JOTCS

Journal of the Turkish Chemical Society Chemistry

Section: A

Volume: 1, Iss:1

June 2015

An Open-Access-Based Scholarly Chemical Journal

www.dergipark.ulakbim.gov.tr/Jotcsa

Published, in English, Biannually
(every June and December)
Turkish Translations of Titles and Abstracts are Available.

TURKISH
CHEMICAL SOCIETY

jotcsa@turchemsoc.org

Correspondance to:
Dr. Barbaros AKKURT, PHD, Managing Editor

Turkish Chemical Society
Halaskargazi Str. Uzay. Apt. No:25 D:8, Harbiye-Sisli-Istanbul/Turkey

Journal of the Turkish Chemical Society, Section A: Chemistry (JOTCSA)

e-ISSN: 2149-0120

A biannual, open-access chemical journal, hosted by Dergipark

(Published, in English, in every February and August)

Address: Halaskargazi Str. Uzay Apt. No: 15/8, 34373 Harbiye, Istanbul/Turkey.

Fax: +90 212 231 70 37

E-mail: jotcsa@turchemsoc.org
Website: http://dergipark.ulakbim.gov.tr/jotcsa

Note: Do not forget to register on the new journal engine at http://turchemsoc.dergipark.gov.tr/jotcsa. From now on, the journal's updated address will be the latter.

(*)JOTCSA is a peer-reviewed publication of the Turkish Chemical Society.
(*)The ideas outlined by the authors cannot be attributed to the journal management nor the editorial board.

ETHICAL GUIDELINES

Guidelines for the Editors

An editor (editors, associate editors, etc.) should provide impartial consideration to all manuscripts offered for publication, judging each on its particular feature without regard to race, religion, nationality, sex, seniority, or institutional affiliation of the author(s). An editor should review and treat a manuscript submitted for publication with all reasonable speed. An editor takes the sole responsibility for accepting or rejecting a manuscript for publication. An editor may seek assistance on a manuscript from specialists chosen for their expertise and fair judgment. An editor should not reveal any information about the manuscript under consideration to anyone other than the author and designated reviewers until after the evaluation process is complete. An editor should respect the intellectual independence of authors.

Authors

Our journal considers a person as an author who is responsible at least for a part of the work. Authors should be able to explain the problem in study in a deep manner. For our journal, all authors are responsible for the content they submitted. The corresponding author is responsible for the agreement of all the authors and to keep them informed about the submission process since first submission of their manuscript. He/she is responsible for providing the license to publish, in case of acceptance, on behalf of all the authors. Our journal assumes that submitting the paper implies in total agreement from all the authors. For manuscripts with more than 8 authors, all the authors should provide a declaration specifying what was their contribution to the manuscript. It is not acceptable for JOTCSA to consider for publication anything that was previously published, neither entirely nor partly in other journals. Anything sent to our journal must not be under analysis by anywhere else. Simultaneous submissions to JOTCSA and any other journal, is considered a major conduct flaw, and all the authors will be definitely banned, and all their previous publications in JOTCSA will be publicly retracted. Plagiarism and self-plagiarism will be treated in the same way. Multiple manuscripts, dealing with closely related subjects and/or variables are discouraged as long as they could figure in a single paper.

Reviewers

JOTCSA invites peers to review its submissions, relying on their expertise, curricula, and their will to review them as volunteers. By accepting to review a manuscript, the reviewer commits himself to do so in due time. Delays are extremely negative to the review process and makes it last much longer than it should. When a reviewer is requested, he/she is gently asked to answer the invitation e-mail, informing if he/she is willing or not willing to review the manuscript. It is a gesture of politeness, and it avoids delays too. By accepting to review a manuscript, the reviewer declares that no conflicts of interests do exist, and he/she is doing his/her revision for the wealth and progress of Science. Those reviewers who answer our requests, agreeing or not, and those who respect the deadlines, are scored positively, and eventual submissions they could send to JOTCSA will be treated with priority.

The online version of this declaration can be viewed on http://dergipark.ulakbim.gov.tr/public/journals/5106/ethical_guidelines.pdf.

Journal of the Turkish Chemical Society, Section A: Chemistry (JOTCSA)

e-ISSN: 2149-0120

A biannual, open-access chemical journal, hosted by Dergipark

(Published, in English, in every February and August)

Editorial, Vol. 4, issue 1 (2017): Submissions between

August, 2016-February, 2017

We are very happy to present the volume 4, issue 1 of "Journal of the Turkish Chemical Society, Section A: Chemistry" which has already been indexed in **TR-Dizin** of TÜBİTAK (The Scientific and Technological Research Council of Turkey) (http://cabim.ulakbim.gov.tr/?s=Journal+of+Turkish+chemical+society+section+a+chemistry) and **Chemical Abstracts** (http://cassi.cas.org/publication.jsp?P=eCQtRPJo9AQyz133K_ll3zLPXfcr-WXfBFkLh3LyfXFg_e-wSJbBGVqP1LcMb11IqcF_LtPabBIcxTi1U3hLSzLPXfcr-WXfOYGMrpflh97uS_W7bNp1NzLPXfcr-WXfYacegenFFY3CFMZeDSK6wQ).

This issue includes 27 papers, 8 by authors of various nationalities and 19 by Turkish authors.

We wish to thank all the authors and reviewers of the manuscripts, and to the editorial team of Journal of the Turkish Chemical Society, Section A: Chemistry for their valuable contributions over the last three years to making a success of our journal.

From beginning of 2017, our journal has been moving from the Open Journal System (OJS) to National Journal System (UDS) supported by The Scientific and Technological Research Council of Turkey (TÜBİTAK) and it will be available to submit yours manuscript soon.

You are invited to take a look at the new system and for more information to authors. Please visit to the website of our journal at http://dergipark.ulakbim.gov.tr/jotcsa and send an e-mail to our managing editor, Mr. Barbaros AKKURT, at jotcsa@turchemsoc.org or myself at hasan.kucukbay@inonu.edu.tr.

Best regards,

Prof. Dr. Hasan KÜÇÜKBAY, PhD

Editor-in-chief, JOTCSA

PART I: Microwave-Assisted Synthesis of Benzimidazoles: An Overview (Until 2013)

Hasan Küçükbay[1]*

[1]*Department of Chemistry, Faculty of Arts and Sciences, İnönü University, 44280 Malatya-Turkey.*

Abstract: Benzimidazole derivatives are interesting heterocycles and are found in many naturally occurring products and various drugs. They exhibit several pharmacological activities such as antitumor, diuretic, fungicidal, bactericidal, antihelmintic, antiallergic, antihistaminic, vasodilator, hypotensive, spasmolytic activities and local analgesic. Owing to the importance of these heterocyclic compounds, the aim of this review is to present the main aspects of the microwave synthetic methods of the benzimidazole derivatives until 2013.

Keywords: Benzimidazoles, benzimidazole synthesis, heterocycles, microwave.

Cite this: Küçükbay H. PART I: Microwave-Assisted Synthesis of Benzimidazoles: An Overview (Until 2013). JOTCSA. 2017; 4(1):1–22.

DOI: 10.18596/jotcsa.91217.

*Corresponding author. E-mail: hkucukbay@inonu.edu.tr. Tel: +90-422-3773881; Fax: +90-422-3410037.

INTRODUCTION

Benzimidazole is a privileged heterocyclic structure for exploring chemical functionality in biological active molecules (1). They have been studied extensively due to their biological activities such as antivirutic against a lot of viruses including HIV (2,3), herpes (HSV-1) (4), RNA (5), influenza (6) and human cytomegalovirus (HCMV) (7), potent antiparasitic agents (8), topoisomerase I inhibitors (9), potential antitumor agents (10), selective neuropeptide Y Y1 receptor antagonists, angiotensin II (AII) inhibitors (11), inhibitors of the hepatitis C virus RNA polymerase (12), antibacterial (13), antifungal (14), antiulcer (15), anti-inflammatory (16), antiprotozoal (17), anticonvulsant (18), antitubercular (19), antidepressant (20), antileishmanial (21), antihypertensive (22), antioxidant (23), and anticoagulant (24, 25).

Moreover, benzimidazole structures behave as good ligands to the transition metal atoms using one of the nitrogen atom and these type of complexes have been found in a variety of biological molecules including ion-heme systems, vitamin B_{12} and its derivatives, and several metalloproteins. According to a reported study, metal complexes of biological important ligands are sometimes more effective than the free ligands (26). Therefore, their preparations have been continuously increasing and they have become the most studying heterocyclic motif by synthetic organic chemists and biologists. A number of methods have been developed for the synthesis of compounds containing a benzimidazole moiety (27). The most popular synthetic method of benzimidazoles is the dehydration of 1,2-diaminobenzenes with carboxylic acids under vigorous dehydrating reaction conditions in the presence of strong acids such as polyphosphoric acid, hydrochloric acid, boric acid, or *p*-toluenesulonic acid (28). However, the use of milder reagents, such as Lewis acids (29), inorganic clays (30), or mineral acids (31), has improved both the yield and purity of this reaction (1a). Another important synthesis method of benzimidazoles is the condensation of 1,2-diaminobenzenes with aldehydes in the presence of an oxidative reagent such as nitrobenzene, benzoquinone, sodium metabisulfite, mercuric oxide, lead tetracetate, iodine, copper (II) acetate, indium perfluorooctane sulfonates, ytterbium perfluorooctane sulfonates, and even air, have been used for this aim (32). The benzimidazoles could also be synthesized by the coupling of 1,2-diaminobenzenes with carboxylic acid derivatives such as anhydrides, lactones, orthoesters, imidates and nitriles (33). Moreover, several other catalysts, namely iodine (34), hydrogen peroxide (35), boron trifluoride diethyl etherate (36), zirconyl (IV) chloride (37), zeolite (38), and L-proline (39) have been effectively used for the synthesis of benzimidazole derivetives.

Despite their high effectiveness for the synthesis of benzimidazoles, some of the methods need to be improved for the high reaction temperature, long reaction times, toxic solvent and high-priced catalyst, *etc*. (40). Therefore, development of mild, efficient and environmentally benign protocol for the synthesis of benzimidazoles is still a hot topic for researchers. After the first reports of applications of microwaves in synthetic chemistry in 1986 (41), microwave-assisted

synthesis have become popular, particularly, last two decades due to the generally short reaction times, the high purity and yields of the resulting products. Up to now, several microwave-assisted methodologies for the synthesis of benzimidazoles have been reported.

This article aims to review the work reported, microwave-assisted synthesis of benzimidazole derivatives during past years untill 2013.

Microwave-assisted benzimidazole synthesis: a) Benzimidazole synthesis from carboxylic acids/carboxylic acid derivatives and 1,2-diaminobenzenes

The first microwave-assisted benzimidazole synthesis reported in 1995 by Bougrin and Soufaoui (42). They have described a benzimidazole synthesis method using 1,2-diaminobenzene or 4-substituted-1,2-diaminobenzene and ethyl acetoacetate or ethyl benzoylacetate on solid mineral supports in dry media under microwave irradiation in domestic ovens (Scheme 1).

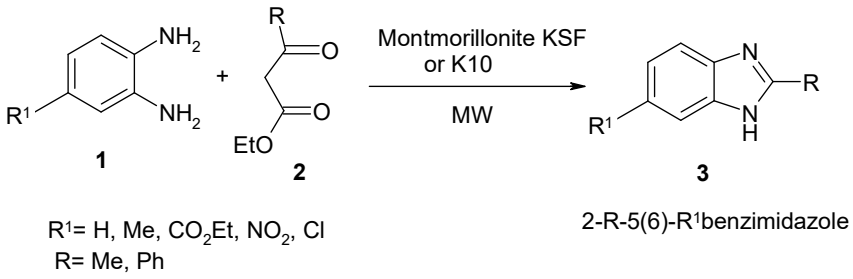

Scheme 1.

Bougrin *et al*. (43) have described in dry media synthesis of 2-trifluoromethylbenzimidazoles through cyclocondensation of N-(carbotrifluoromethyl)-*ortho*-arylenediamines on montmorillonite K10 under domestic microwave oven with good yields (Scheme 2).

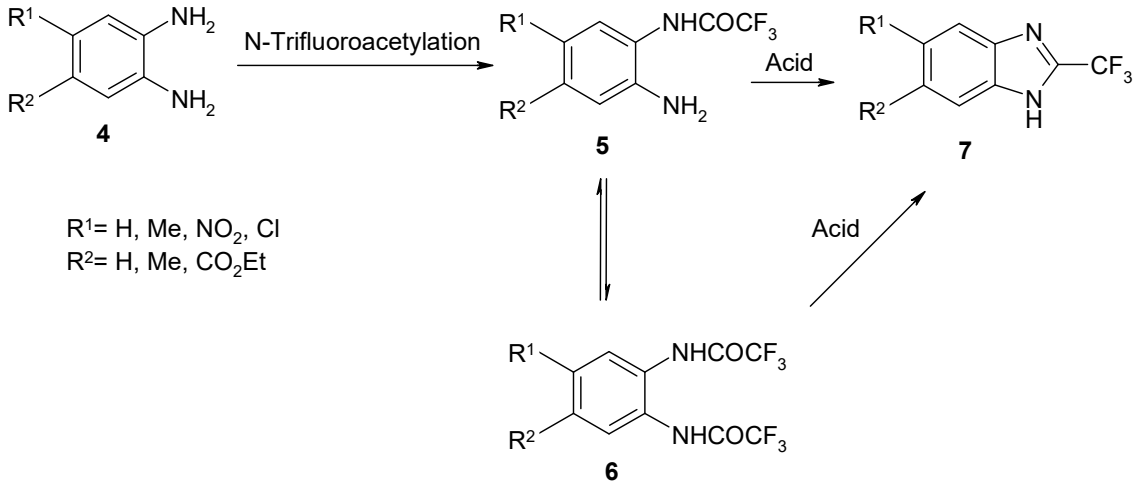

Scheme 2.

Bendale and Sun (44) have described an efficient, facile, and practical liquid-phase combinatorial synthesis of benzimidazoles under microwave irradiation in short time (Scheme 3).

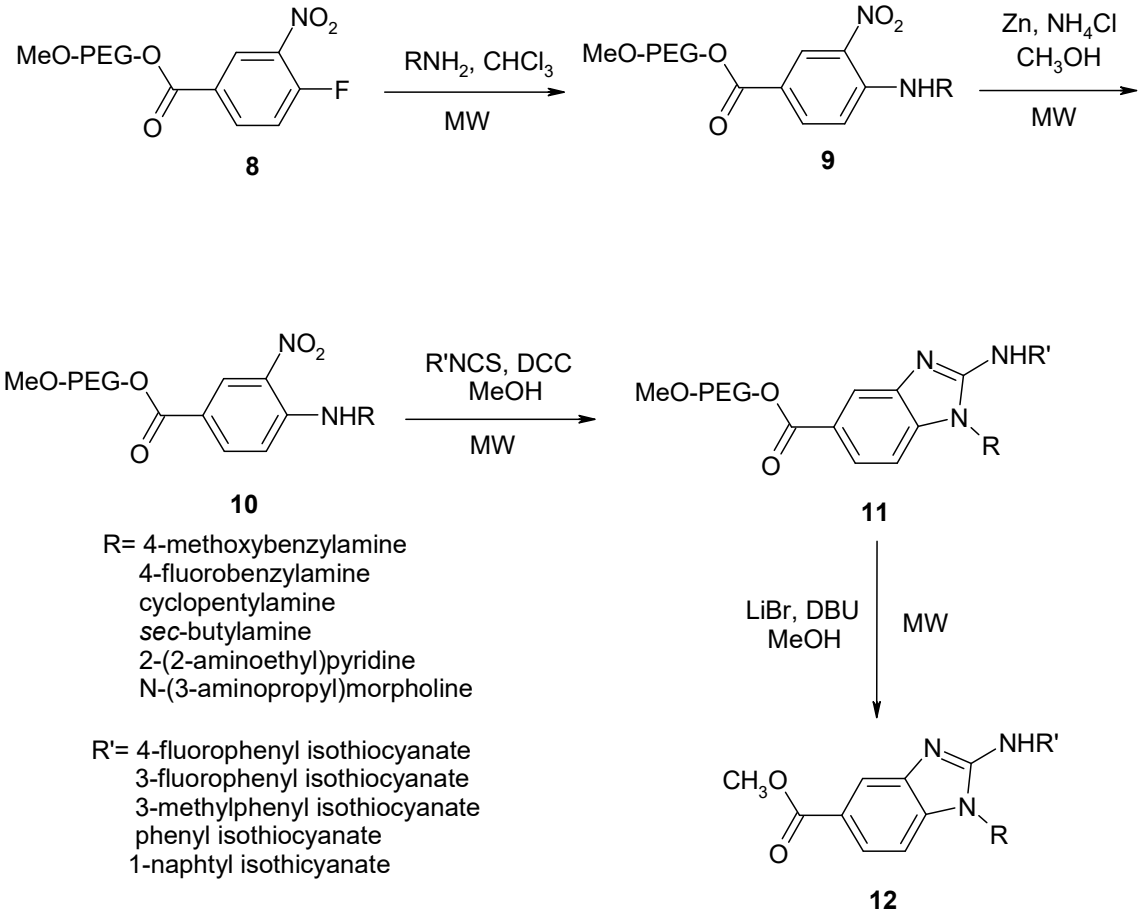

Scheme 3.

Getvoldsen *et al*. (45) developed an *in situ* monitoring method for the reactions in a microwave using UV/Vis spectroscopy. The benzimidazole synthetic reaction from 1,2-diaminobenzene and formic acid has chosen as a model reaction. They have reported that the new method would be an excellent analytical tool for monitoring the progress of a reaction, determination of end points and derivation of quantitative and kinetic data (Scheme 4).

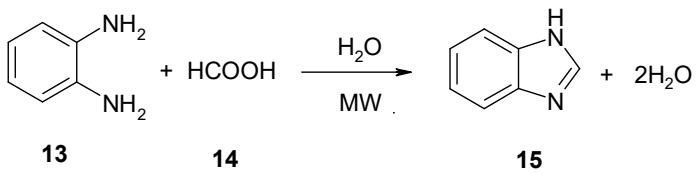

Scheme 4.

Boufatah *et al*. (46) have reported the preperation of some new biologically active benzimidazole-4,7-dione derivatives in 7 steps through the microwave irradiation for the ring closing step to obtain benzimidazole derivative (Scheme 5).

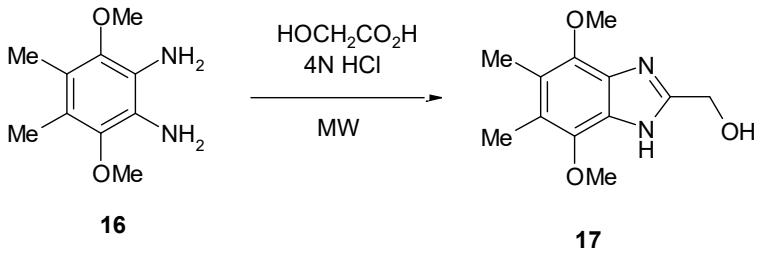

16 **17**

Scheme 5.

Zhang and Tempest (47) have improved the efficiency of the Ugi/de-Boc/cyclization synthesis replaced the normal Boc group with the fluorous-Boc group to protect the diamine. They were used fluorous component as a limiting agent in the Ugi reaction. Hence, they have easily separated designed condensation product containing the F-Boc group from the reaction mixture by fluorous SPE. Compared to the original Ugi/de-Boc/cyclization procedures, which take 1-2 days, the fluorous/microwave approach which modified by Zhang and Tempest has more favorable reaction and purification conditions: less than 20 min for each reaction and no need of the double scavenging step (Scheme 6).

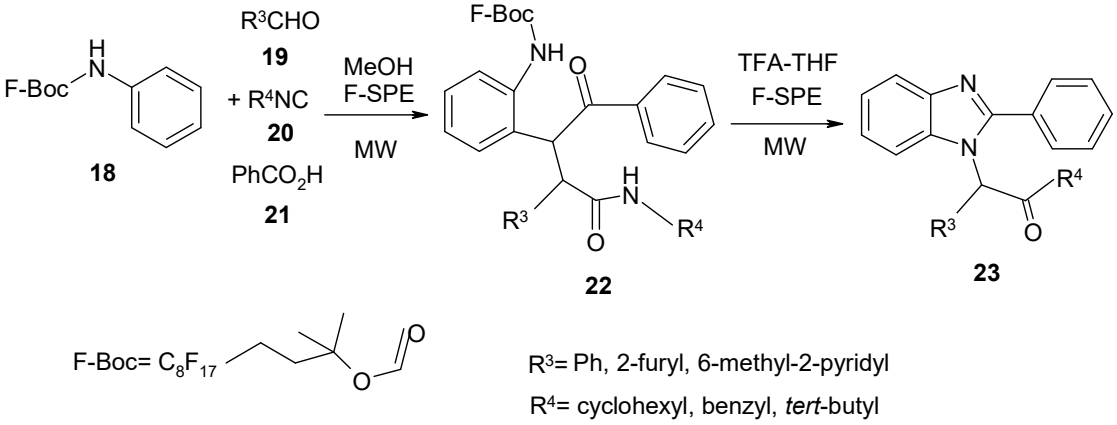

Scheme 6.

Getvoldsen *et al*. (48) have reported 2-([4-^{18}F] fluorophenyl) benzimidazole synthesis from the cyclocondensation reaction of 1,2-diaminobenzene with radiolabelled [4-^{18}F]fluorobenzoic acid in neat methanesulfonic and polyphosphoric acids under microwave (Scheme 7).

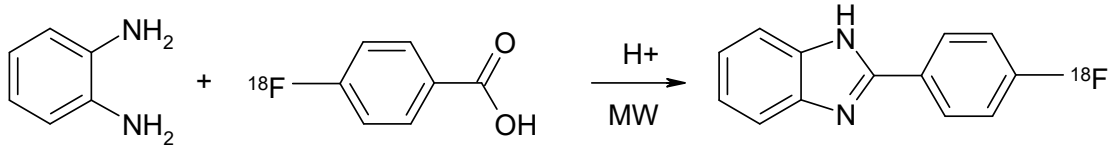

1 **24** **25**

Scheme 7.

Martinez-Palou *et al*. (49) have described 2-long alkyl chain substituted benzimidazole synthesis from the reaction of 1,2-diaminobenzene and stearic acid via mono and multimode microwave irradiation with high yields (Scheme 8).

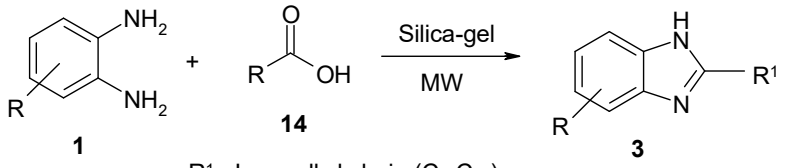

Scheme 8.

Vliet *et al*. (50) have described a simple, rapid, one pot procedure for the generation of 2-substituted benzimidazoles with high-yield directly from 2-nitroanilines using $SnCl_2$ as a reduction agent and carboxylic acid under microwave irradiation at 130 °C in 5 min (Scheme 9).

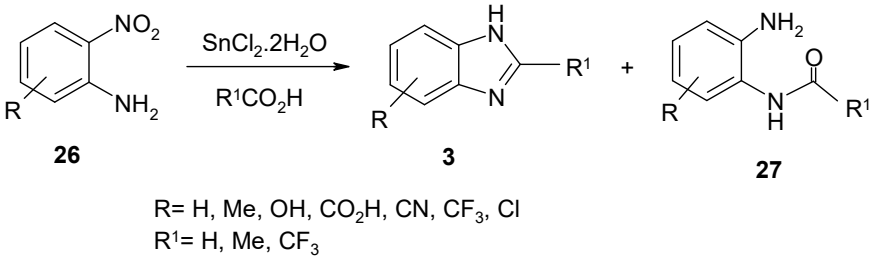

Scheme 9.

Lin *et al*. (51) have reported a microwave-assisted one-pot synthesis of several benzimidazole derivatives from readily available starting compounds such as 1,2-diaminobenzene, 4,5-diaminopyrimidine, *cis*-1,2-diaminocicylohexane and several carboxylic acids including heteroaraomatic carboxylic acids (Scheme 10).

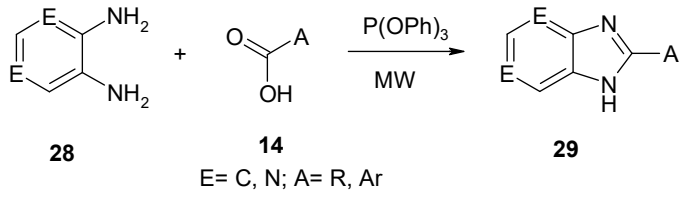

Scheme 10.

Mobinikhaledi and co-workers (38) described a selective synthesis of 2-aryl-1*H*-benzimidazoles through the reaction of 1,2-diaminobenzene with arylcarboxylic acid using zeolite as an efficient catalyst under microwave irradiation (Scheme 11).

Ar= 3-Nitrophenyl,4-nitrophenyl, 4-chlorophenyl
3-chlorophenyl, 4-tolyl, 3-tolyl, 4-methoxyphenyl
4-bromophenyl, 2-pyridyl

Scheme 11.

Jing *et al*. (52) have described a simple and rapid synthesis of benzimidazoles from 1,2-diaminobenzene dihydrochloride and esters under microwave irradiation. This is also the first report for microwave assisted benzimidazole synthesis from esters and 1,2-diaminobenzenes (Scheme 12).

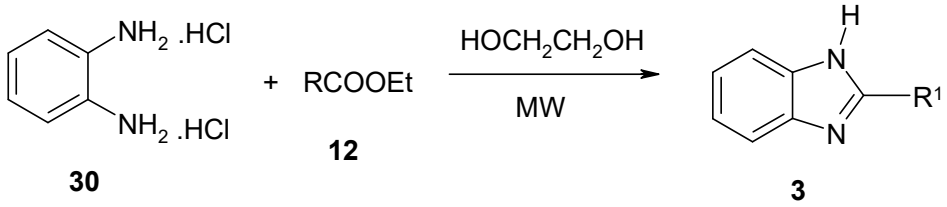

R= $ClCH_2$, CH_3,
$HOCH_2$, Et, H,
n-C_5H_{10}, CH_2CO_2Et

R_1= $ClCH_2$, CH_3,
$HOCH_2$, Et, H,
n-C_5H_{10}, 2-Benzimidazolyl

Scheme 12.

Gellis *et al*. (53) have reported the synthesis a series of variously substituted benzimidazole-4,7-diones in seven steps and antitumor activity results of them. One of them exhibit excellent cytotoxicity comparable to that of mitomycin C (Scheme 13).

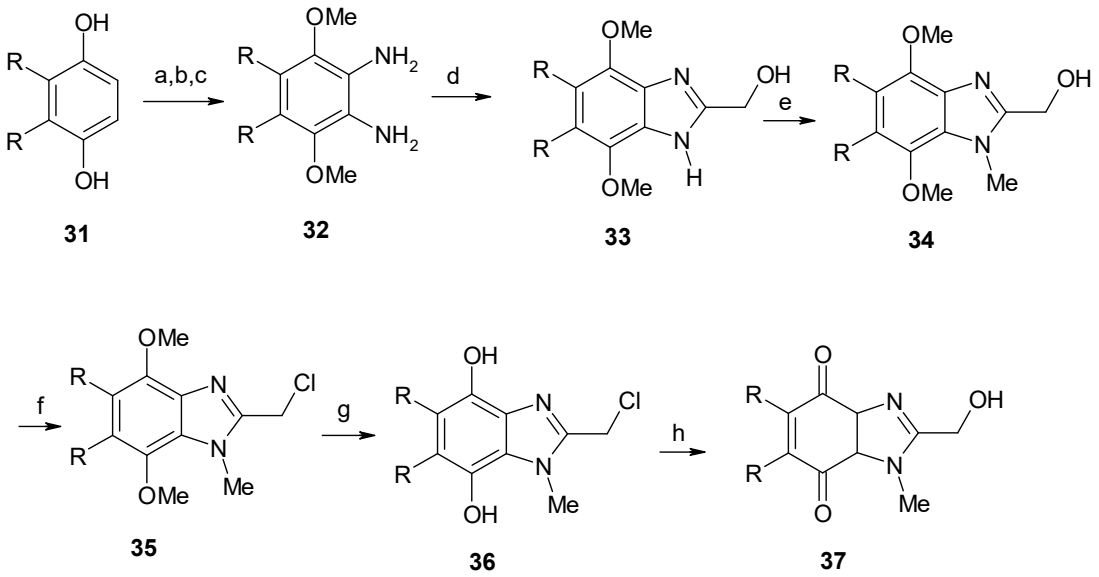

Scheme 13. Reagents and conditions: (a) KOH, $(CH_3)_2SO_4$, CH_3OH, reflux, 1 h; (b) R= H; HNO_3 62%, 1 h at rt, 1 h at 100°C or R= CH_3, $(CH_3CO)_2O$, HNO_3 fuming, 90 °C, 1 h; (c) Sn, HCl; (d) $HOCH_2CO_2H$, 4 N HCl, microwave, 800 W, 1 h 30 min; (e) $LiN(TMS)_2$, THF, 20 min, then CH_3I, 7h; (f) $SOCl_2$, $CHCl_3$, reflux, 4h; (g) BBr_3, CH_2Cl_2, -78 °C, 3 h; (h) $K_2Cr_2O_7$, H_2O, rt, 2 h.

Algül *et al*. (54) have described the synthesis of some 2-substituted benzimidazole, benzothiazole, and indole derivatives using on both microwave irradiation and conventional heating methods. They have also evaluated hyaluronidase inhibitory activity of the compounds (Scheme 14).

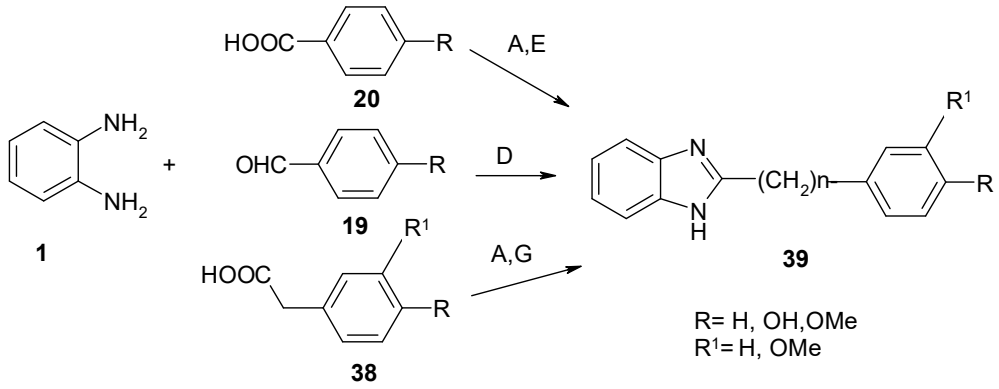

Scheme 14. A= PPA/MW, D= $Na_2S_2O_5$/DMF, E= PPA, G= HCl.

Keri *et al*. (27) have reported an expeditious, novel, and efficient method for the synthesis of benzimidazole derivatives from *o*-phenylendiamines with different phenoxy acid using a Wells-Dawson $H_6P_2W_{18}O_{62}.24\ H_2O$ catalyst (Scheme 15).

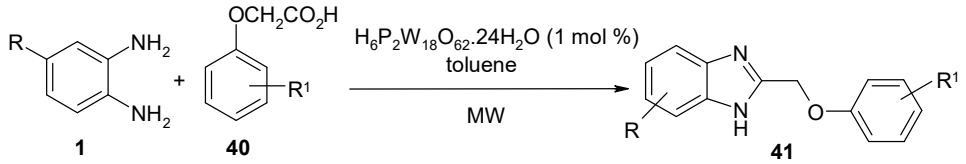

R= H, Br, Me
R^1= H, 2-Me, 3-Me, 4-Me, 2-Cl, 4-Cl, 2-NO_2, 4-NO_2, 2-NH_2, 2,4-Cl

Scheme 15.

Similar to the Keri method, Hosamani and co-workers (55) described a convenient protocol for the preparation of 5-nitro-2-arylsubstituted phenoxymethyl-1*H*-benzimidazole libraries in one pot-synthesis both under microwave irradiation and conventional heating methods using hydrochloride acid as catalyst (Scheme 16).

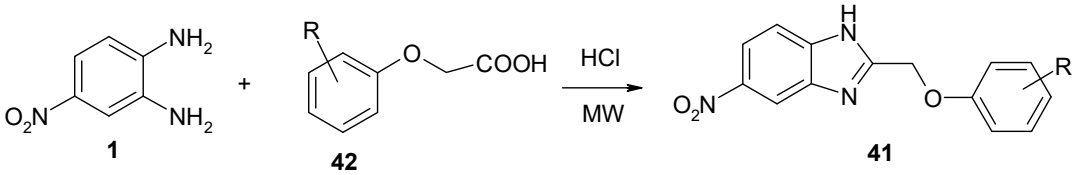

R= H, 2-Me, 3-Me, 4-Me,
2-Cl, 4-Cl, 2-NO_2, 4-NO_2
2-NH_2, 2,4-dichloro

Scheme 16.

Hasaninejad *et al*. (56) have reported the synthesis of some 2-substituted benzimidazole derivatives from benzene-1,2-diamine with mono and dicarboxylic acids under microwave irradiation using silphox [$POCl_{3-n}(SiO_2)_n$] catalyst in highly yield and short reaction times (Scheme 17).

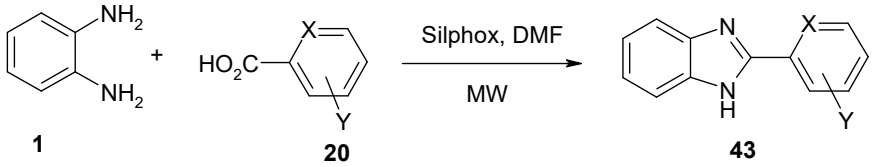

X= C, N
Y= H, Me, OMe, NO_2, Cl,Br

Scheme 17.

Sun and co-workers (57) synthesized angular bis-benzimidazoles on the support with three appendages with good yields and purities through soluble polymer-supported reaction. The integration of microwave irradiation and a soluble polymer support strategy provided an efficient and convenient approach for high throughput and diversity-oriented synthesis of drug-like molecules. Their preliminary screening results have shown that some of these compounds exhibited moderately to good inhabitation against VEGFR 3, which is related to the invasion and migration of cancer cells (Scheme 18).

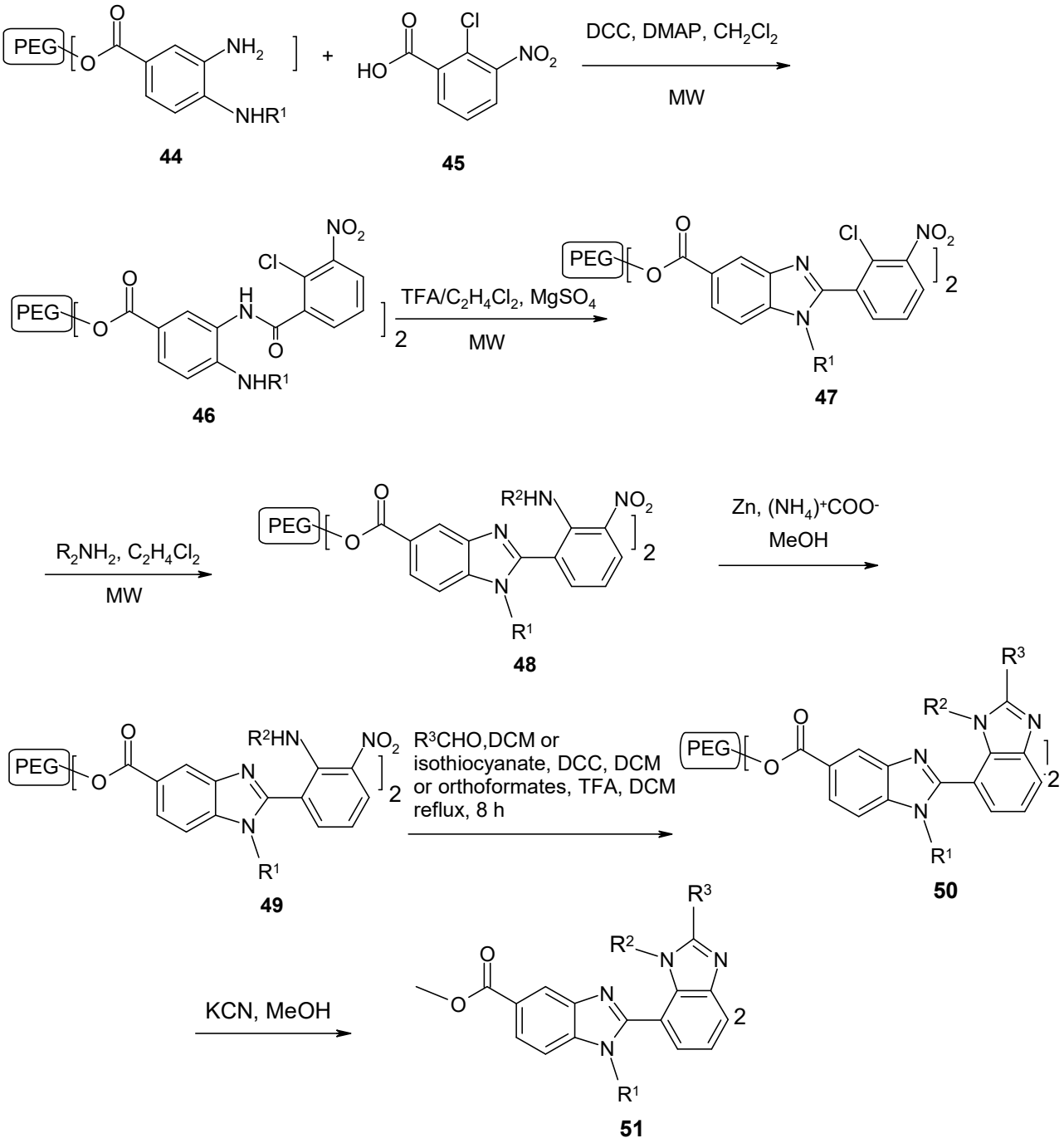

R1= 2-(cyclohexen1-yl)ethyl, isobutyl, 3-methoxypropyl, *n*-butyl, *sec*-butyl
R2= *n*-butyl, isopropyl, 3,3-diphenylpropyl, 2-thenyl, 4-methoxybenzyl, 2-methoxyethyl
R3= *n*-butyl, 4-nitrophenyl, 2-furyl, 2-thienyl, 2-hydroxyphenyl, 3-hydroxyphenyl, 4-hydroxyphenyl, benzylisothiocyanate

Scheme 18.

Sun and co-workers (58-60) reported a novel synthetic method for the substituted benzimidazole derivatives from the starting compounds 1,2-diaminobenzene derivative on soluble polymer support and 3-nitro-4-hydroxy/fluorobenzoic acid in a multistep process under focused microwave irradiation (Scheme 19).

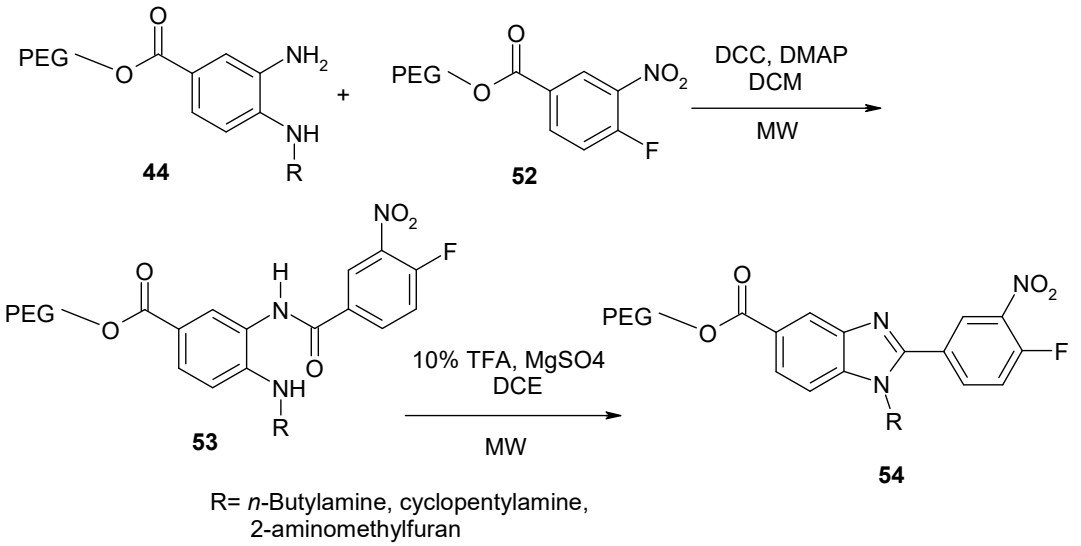

R= *n*-Butylamine, cyclopentylamine, 2-aminomethylfuran

Scheme 19.

The same group has recently described the synthesis of bis-heterocyclic skeletal novel benzimidazole-linked pyrrolo-/pyridobenzimidazolones and benzimidazole-linked isoindolo-benzimidazoleones on ionic liquid support under microwave irradiation by utilizing the cascade cyclization (61) (Scheme 20).

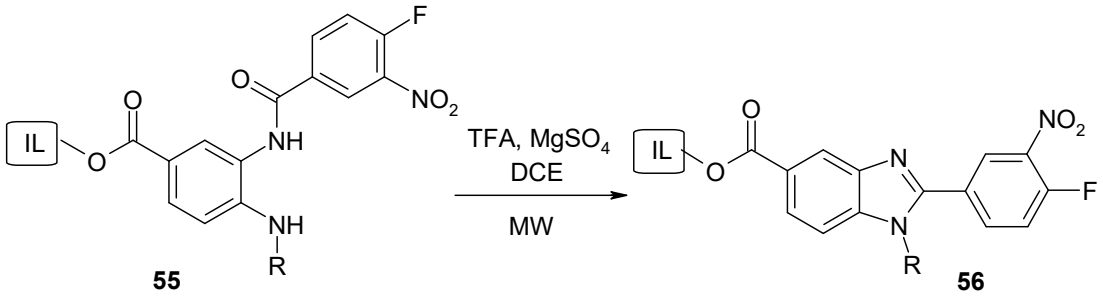

R= Isobutyl, 2-(cyclohexen-1-yl)ethyl, 3-methoxypropyl

Scheme 20.

b) Benzimidazole synthesis from aldehydes and 1,2-diaminobenzenes

Ben-Alloum *et al*. (62) have described oxidative heterocyclization of aldehydes and o-phenylenediamine with nitrobenzene or dimethylsulfoxide impregnated on silica gel irradiated with microwave in good yields and high purity (Scheme 21).

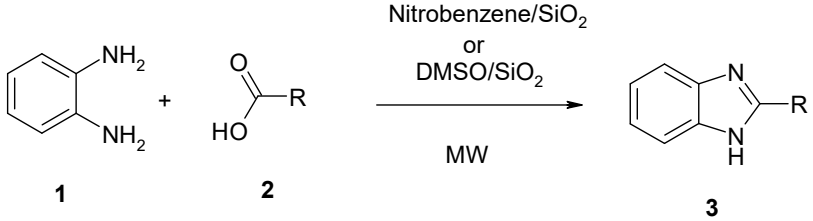

R= Ph, 4-tolyl, 4-anisolyl, 4-ClPh, 4-NO_2Ph, 2-ClPh, 2-HOPh, 2-furyl, *n*-propyl, ethyl

Scheme 21.

Navarrete-Vazquez and co-workers (63) described a simple, rapid, and efficient method for the preparation of several 2-(alkyoxyaryl)-1*H*-benzimidazole compounds under solvent-free conditions using readily available and inexpensive reagents utilizing microwave irradiation (Scheme 22).

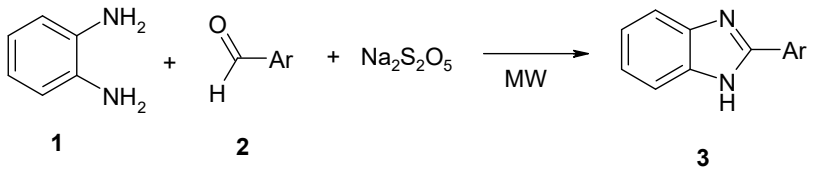

Ar= 2-HOPh, 2-MeOPh, 2-EtOPh, 2-PrOPh, 2-PhCH$_2$OPh
2-NO$_2$Ph, 4-HOPh, 4-pyridyl, 2,4,5-(trimethoxy)phenyl

Scheme 22.

Zahran and co-workers (64) described the synthesis of new heterocyclic compounds containing pyrazol-5-one coupled with benzimidazole under dry media and they also explored antitumor activity of the newly synthesized heterocycles. Some of them were found to be more effective than thalidomide (Scheme 23).

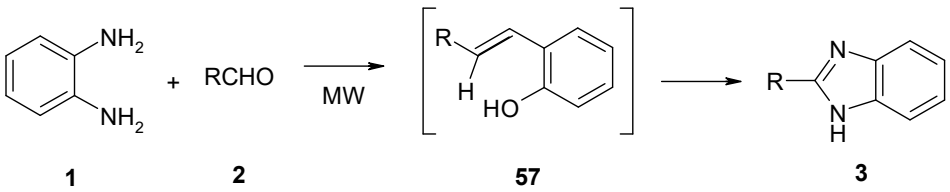

R=

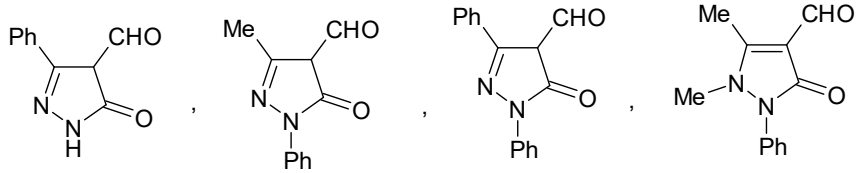

Scheme 23.

Dubey and Moorthy (65) have reported comparative synthesis of 2-alkyl and 2-aryl substituted benzimidazole derivative in the presence of polyphosphoric acid through microwave and conventional methods and also studied the effect of salt form of reactant for completion of the reaction. According to their report, the 2-substituted aryl and alkyl benzimidazole derivative synthesized via microwave and it is beneficial, in respect of yield increases up to 10 to 50%) and time (96 to 98% was reduced) than conventional method of synthesis. They also showed some remarkable inferences while the use of salt form of the reactant (1,2-diaminobenzene dihydrochloride). Navarrete-Vazquez *et al*. (66) have synthesized several benzimidazole derivatives which could be vasorelaxant and spasmolytic properties from the reaction of 1,2-

diaminobenzene with aromatic substituted aldehydes and sodium metabisulfite under microwave irradiation.

Jacob and co-workers (67) described an improved methodology for the selective synthesis of 1,2-disubstituted benzimidazoles by the condensation of 1,2-diaminobenzene and aldehydes using solid-supported catalyst ($SiO_2/ZnCl_2$) in a short time under microwave irradiation.

Mao *et al*. (68) have reported intermittent microwave irradiation for the synthesis 2-benzimidazole derivatives from aromatic aldehydes an 1,2-diaminobenzene only using molecular oxygen as the oxidant and inexpensive KI as the catalyst.

Rathod and co-workers (40) described eco-friendly benzimidazole synthesis from aromatic aldehydes and 1,2-diaminobenzene using $MoO_3/CeO_2.ZrO_2$ as a catalyst under solvent-free conditions both conventional and microwave heating. Azarifar *et al*. (69) have reported 2-aryl-1-(arylmethyl)1H-benzimidazole synthesis from 1,2-diaminobenzene and aldehydes through acetic acid-promoted condensation in air under microwave irradiation (Scheme 24).

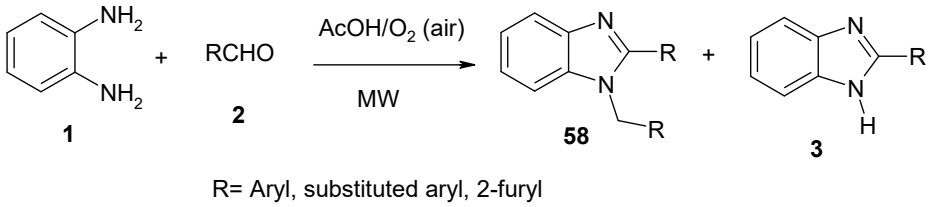

Scheme 24.

Mungra and co-workers (70) described a microwave-assisted synthesis of 4-(benzimidazol-2-yl)tetrazolo[1,5-a]quinoline from 1,2-diaminobenzene and heterocyclic aldehydes catalyzed by an organocatalyst *p*-TsOH (Scheme 25).

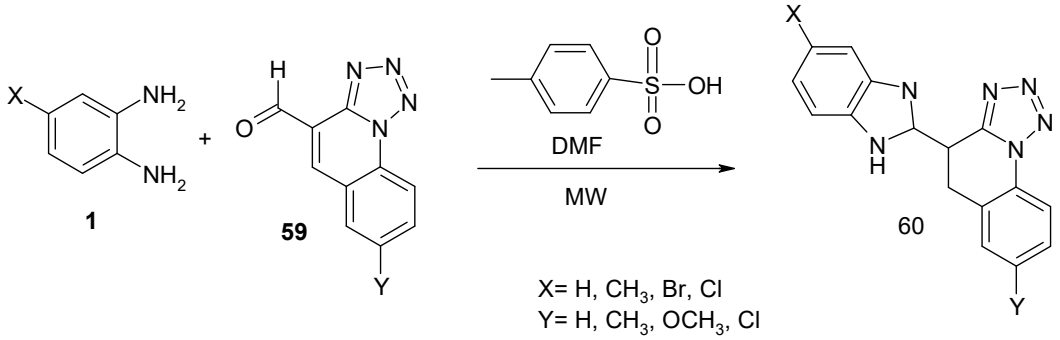

Scheme 25.

Krim *et al*. (71) have reported efficient synthetic routes to prepare fluorescent compounds containing benzimidazoles in the 5-position of pyrimidine nucleosides. Their synthesis is based on the straightforward condensation of 5-formyl-2'-deoxyuridine and arylenediamine

derivatives under a cooperative effect of microwave activation and $NaHSO_3$ catalysis (Scheme 26).

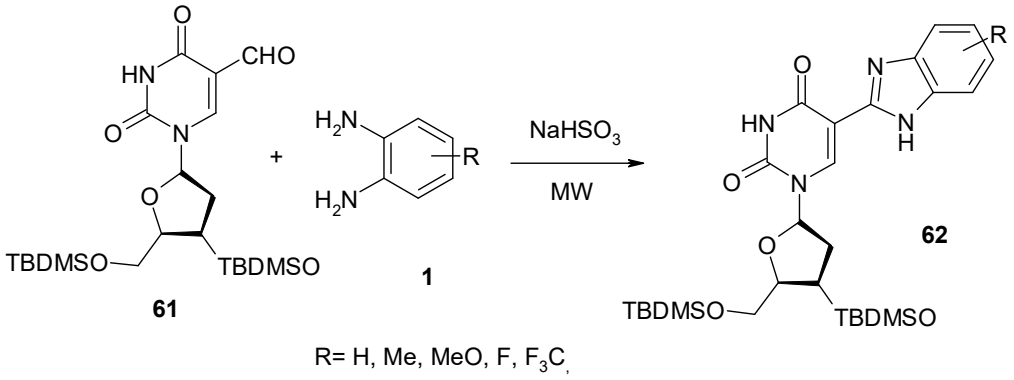

R= H, Me, MeO, F, F_3C,

Scheme 26.

c) Miscellaneous benzimidazole syntheses

Reddy *et al*. (72) have reported microwave assisted synthesis of 5- or 5,6-disubstituted-2-trifluoroacetonylbenzimidazole derivatives (Scheme 27).

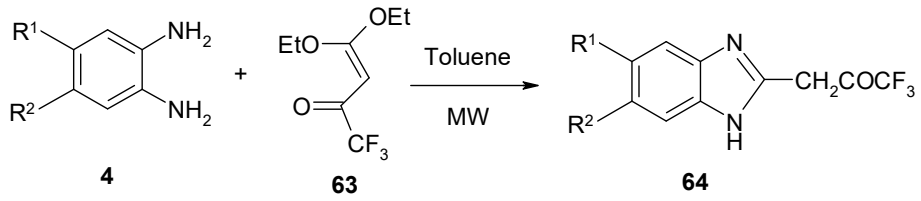

R^1=, R^2= H or Me

Scheme 27.

Hulme and co-workers (73) described a novel two-step solution phase protocol for the synthesis of arrays of triazadibenzoazulenones using the Ugi reaction and two tandem ring closing transfomations. They also used microwave irradiation for 5 or 10 min for the second ring closing steps (Scheme 28).

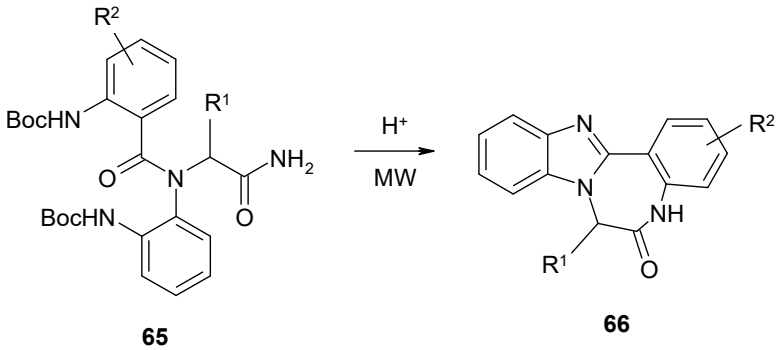

R^1= *n*-Propyl, 2-phenylethyl, *n*-butyl, isopropyl, *sec*-butyl, Me
R^2= H, Cl, MeO

Scheme 28.

Wang *et al*. (74) reported microwave-assisted solvent-dependent chemoselective reaction dealing with 4-arylidene-2-phenyloxazol-5-ones and *ortho*-diamines to obtain benzimidazole scaffold (Scheme 29).

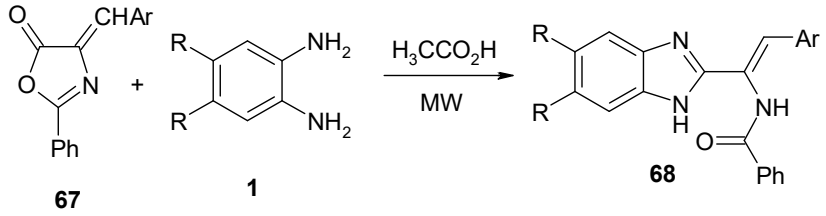

R= H, Me, Cl, CO_2H
Ar= Ph, 4-ClPh, 4-MeOPh, 3,4,5-trimethoxyphenyl, 2-thienyl

Scheme 29.

Shaw and *et al*. (75) described a novel synthetic protocol for the synthesis of unique norstatine analogs bearing benzimidazole moiety through Passerini reaction and following ring closing (Scheme 30).

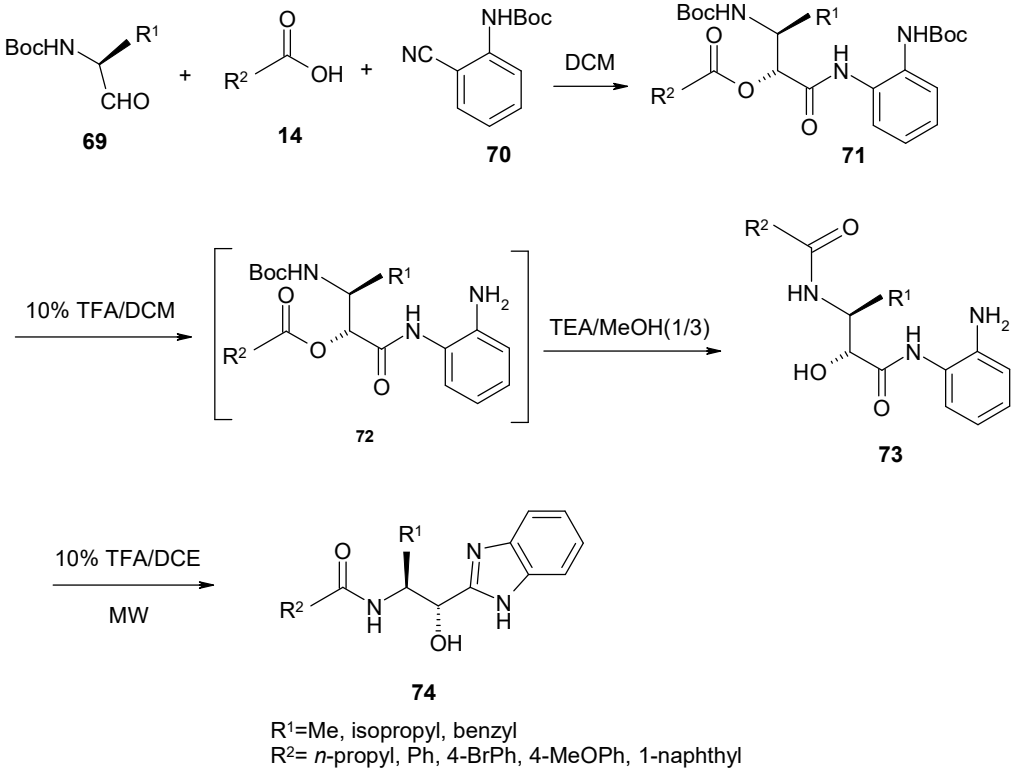

R^1=Me, isopropyl, benzyl
R^2= *n*-propyl, Ph, 4-BrPh, 4-MeOPh, 1-naphthyl

Scheme 30.

Wen *et al*. (76) have reported on eco-friendly, one-pot efficient propylphosphonic anhydride (T3P) mediated synthesis of benzimidazoles from various carboxylic acids and 1,2-diaminobenzene under microwave irradiation (Scheme 31).

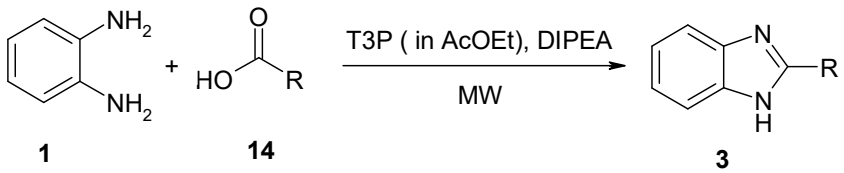

1 **14** **3**

R= Et, Ph, 4-substituted phenyl, 4-pyridyl, 4-chloro-2-phenylethyl

Scheme 31.

CONCLUSION

Properties of benzimidazole and its derivatives have been studied for over a hundred years. Special interest of researchers triggered by the fact that 5,6-dimethylbenzimidazole is a component of naturally occurring vitamin B-12. The benzimidazole ring is an important pharmacophore in modern drug discovery. On the other hand, in the past decade, heating and driving chemical reaction by microwave energy has been an increasingly popular theme in the scientific community. A number of methods have been developed for the synthesis of benzimidazole containing compounds. There are two main synthesis methods for the benzimidazoles: i) from the reaction of 1,2-diaminobenzenes with carboxylic acids or its derivatives, ii) condensation of 1,2-diaminobenzenes with aldehydes presence of an oxidative reagent. Despite their high efficiency for the synthesis of benzimidazoles, some of the methods are plugged by one of the drawbacks such as, high reaction temperature, prolonged reaction times, toxic solvent and expensive catalyst, *etc.* Therefore, development of mild, efficient and environmentally benign protocol for the synthesis of benzimidazoles continues to attract researchers' attentions. This article aims to review the work reported, microwave-assisted synthesis of benzimidazole derivatives published in SCI journals from the first report up to 2013.

ABBREVIATIONS

Ac= Acetyl
Ar= Aryl
Boc= *tert*-Butyloxycarbonyl
DCC= N,N'-Dicyclohexylcarbodiimide
DCE= 1,2-Dichloroethane
DCM= Dichloromethane
DEAD= Diethyl azodicarboxylate
DIPEA= N,N-Diisopropylethylamine
DMAD= Dimethylacetylene dicarboxylate
DMAP= 4-Dimethylaminopyridine
DMF= Dimethylformamide
DMSO= Dimethyl sulfoxide
HCMV= Human cytomegalovirus
HIV= Human Immunodeficiency Virus
HSV= Herpes simplex virus
Me= Methyl
MW= Microwave

PEG= Polyethylene glycol
PPA= Polyphthalamide
RNA= Ribonucleic acid
TBDMS= *tert*-butyldimethylsilyl
TFA= Trifluoroacetic acid
TEA= Triethanolamine
Ts= Tosyl
T3P= propylphosphonic anhydride
VEGFR= Vascular endothelial growth factor receptor

REFERENCES

1. (a) Zhang Z-H, Yin L, Wang Y-M. An expeditious synthesis of benzimidazole derivatives catalyzed by Lewis acids. Catalysis Communications. 2007 Jul;8(7):1126–31. DOI:10.1016/j.catcom.2006.10.022. 1. (b) S Panda S, Malik R, C Jain S. Synthetic approaches to 2-arylbenzimidazoles: A review. Current Organic Chemistry. 012;16(16):1905–19.

2. Porcari AR, Devivar RV, Kucera LS, Drach JC, Townsend LB. Design, synthesis, and antiviral evaluations of 1-(substituted benzyl)-2-substituted-5, 6-dichlorobenzimidazoles as nonnucleoside analogues of 2, 5, 6-trichloro-1-(β-D-ribofuranosyl) benzimidazole. Journal of medicinal chemistry. 1998;41(8):1252–62. DOI: 10.1021/jm970559i.

3. Roth M, Morningstar ML, Boyer PL, Hughes SH, Buckheit Jr RW, Michejda CJ. Synthesis and biological activity of novel nonnucleoside inhibitors of HIV-1 revers transcriptase. 2-aryl-substituted benzimidazoles. Journal of Medicinal Chemistry 1997; Dec; 40(26), 4199-4207. DOI:10.1021/jm970096g.

4. Migawa MT, Girardet J-L, Walker JA, Koszalka GW, Chamberlain SD, Drach JC, et al. Design, synthesis, and antiviral activity of α-nucleosides: D-and L-isomers of lyxofuranosyl-and (5-deoxylyxofuranosyl) benzimidazoles. Journal of Medicinal Chemistry. 1998;41(8):1242–51. DOI: 10.1021/jm970545c.

5. Tamm, I.; Sehgal, P.B. Halobenzimidazole ribosides and RNA synthesis of cells and viruses. Advances in Virus Research. 1978, 22, 187-258. DOI: 10.1016/S0065-3527(08)60775-7.

6. Tamm, I. Ribonucleic acid synthesis and influenza virus multiplication. Science, 195; 126: 1235-1236.

7. Kim JS, Gatto B, Yu C, Liu A, Liu LF, La Voie EJ. Substituted 2,5'-bi-1H-benzimidazoles: Topoisomerase I inhibition and cytotoxicity. Journal of Medicinal Chemistry. 1996; 39: 992-998. DOI: 10.1021/jm950412w.

8. Zarrinmayeh H, Nunes AM, Ornstein PL, Zimmerman DM, Arnold B, Schober DA, Gackenheimer SL, Bruns RF, Hipskind PA, Britton TC, Cantrell BE, Gehlert DR. Synthesis and evaluation of a series of novel 2-[(4-chlorophenoxy)methyl]benzimidazoles as selective neuropeptide Y Y1 receptor antagonists. Journal of Medicinal Chemistry. 1998; 41: 2709-2719. DOI: 10.1021/jm9706630.

9. Kohara Y, Kubo K, Imamiya E, Wada T, Inada Y, Naka T. Synthesis and angiotensin II receptor antagonistic activities of benzimidazole derivatives bearing acidic heterocycles as novel tetrazole bioisosteres. Journal of Medicinal Chemistry.1996; 39: 5228-5235. DOI: 10.1021/jm960547h.

10. a) Denny WA, Rewcastle GW, Baguley BC. Potential antitumor agents .59. structure-activity-relationships for 2-phenylbenzimidazole-4-carboxamides, a new class of minimal DNA-intercalating agents which may not act via topoisomerase-II. Journal of Medicinal Chemistry. 1990; 33: 814-819. DOI: 10.1021/jm00164a054. b) Demirayak S, Mohsen UA, Karaburun AC. Synthesis and anticancer and anti-HIV testing of some pyrazino[1,2-a]benzimidazole derivatives. European Journal of Medicinal Chemistry. 2002; 37: 255-260**.** DOI: 10.1016/S0223-5234(01)01313-7. c) Sharma PS, Sharma R, Tyagi R. Inhibitors of cyclin dependent kinases: Useful targets for cancer treatment. Current Cancer Drug Targets. 2008; 8: 53-75. DOI: 10.2174/156800908783497131.

11. Fonseca T, Gigante B, Gilchrist TL. A short synthesis of phenanthro[2,3-d]imidazoles from dehydroabietic acid. Application of the methodology as a convenient route to benzimidazoles. Tetrahedron. 2001; 57: 1793-1799. DOI: 10.1016/S0040-4020(00)01158-3.

12. LaPlante SR, Jakalian A, Aubry N, Bousquet Y, Ferland J-M, Gillard J, Lefebvre S, Poirer M, Tsantrizos YS, Kukolj G, Beaulieu PL. Binding mode determination of benzimidazole inhibitors of the hepatitis C virus RNA polymerase by a structure and dynamics strategy. Angewandte Chemie International Edition. 2004; 43: 4306-4311. DOI: 10.1002/anie.200460326.

13. a) Fekner T, Gallucci J, Chan MK. Ruffling-induced chirality: Synthesis, metalation, and optical resolution of highly nonplanar, cyclic, benzimidazole-based ligands. Journal of American Chemical Society. 2004; 126: 223-236. DOI: 10.1021/ja030196d. b) Küçükbay H, Çetinkaya E, Durmaz R. Synthesis and antimicrobial activity of substituted benzimidazole, benzothiazole and imidazole derivatives. Arzneimmitel Forschung/Drug Research. 1995; 45: 1331-1334. c) Küçükbay H, Durmaz R, Orhan E, Günal S. Synthesis, antibacterial and antifungal activities of electron-rich olefins derived benzimidazole compounds. Il Farmaco. 2003; 58: 431-437. DOI: 10.1016/S0014-827X(03)00068-5 d) Durmaz R, Köroğlu M, Küçükbay H, Temel İ, Özer MK, Refiq M, Çetinkaya E, Çetinkaya B, Yoloğlu S. Investigationof serum minimal inhibitory concentrations of some benzimidazole, imidazole and benzothiazole derivatives and their effects on liver and renal functions. Arzneimmitel Forschung/Drug Research. 1998; 48: 1179-1184.

14. a) Olander D, Zwawiak J, Lukianchuk V, Lesyk R, Kropacz A, Fojutowski A Zaprutko L. Synthesis of some N-substituted nitroimidazole derivatives as potential antioxidant and antifungal agents. European Journal of Medicinal Chemistry. 2009; 44: 645-652. b) Küçükbay H, Durmaz B. Antifungal activity of organic and organometallic derivatives of benzimidazole and benzothiazole. Arzneimmitel Forschung/Drug Research. 1997; 47: 667-670.

15. a) Carcangue D, Shue YK, Wuonola MA, Nickelsen MU, Joubran C, Abedi JK, Jones J, Kuhler TC. Novel structure's derived from 2-[[(2-Pyridyl)methyl]thio]- 1H-benzimidazole as anti-Helicobacter pylori agents, part 2. Journal of Medicinal Chemistry. 2002; 45: 4300-4309. DOI: 10.1021/jm020868v. b) Lindberg P, Nordberg P, Alminger T, Bradstrom A, Wallmark B. The mechanizm of action of the gastric-acid secretion inhibitor omeprazole. Journal of Medicinal Chemistry. 1986; 29: 1327-1329. DOI: 10.1021/jm00158a001.

16. a) Medzhitov R. Inflammation 2010: New adventures of an old flame. Cell; 2010:140: 771-776. DOI: 10.1016/j.cell.2010.03.006. b) Grivennikov S, Greten FR, Karin M. Immunity, inflammation, and Cancer. Cell. 2010; 140:883889. DOI: 10.1016/j.cell.2010.01.025. c) Nathan C. Points of control in inflammation. Nature. 2002; 420: 846-852. DOI: 10.1038/nature01320. d) Cronstein BN, Weissmann G. Targets for antiinflammatory drugs. Annual Review of Pharmacology and Toxicology. 1995; 35: 449-462. DOI: 10.1146/annurev.pa.35.040195.002313.

17. a) Vazquez GN, Vilehis MMR, Mulia LY, Melendez V, Gerena L, Campos AH, Castillo R, Luis FH. Synthesis and antiprotozoal activity of some 2- (trifluoromethyl)-1H-benzimidazole bioisosteres. Eurpean Journal of Medicinal Chemistry. 2006; 41: 135-141. DOI:10.1016/j.ejmech.2005.09.001. b) Gomez HT, Nunez EH, Rivera IL, Alvarez JG, Rivera RC, Puc RM, Ramos RA, Guttirez MCR, Bacab MJC, Vazquez GN. Design, synthesis and in vitro antiprotozoal activity of benzimidazole-pentamidine hybrids. Bioorganic and Medicinal Chemistry Letters, 2008; 18: 3147-3151. DOI:10.1016/j.bmcl.2008.05.009.

18. Singh J, Grover P, Pathak DP. Synthesis, anticonvulsant activity and comparative QSAR study of some novel 1,2,5-trisubstituted benzimidazole derivatives. Acta Pharmaceutica Sciencia. 2010; 52: 511-522.

19. a) Gupta P, Hameed S, Jain R. Ring-substituted imidazoles as a new class of anti-tuberculosis agents. Eurpean Journal of Medicinal Chemistry. 2004; 39: 805-814. DOI: 10.1016/j.ejmech.2004.05.005. b) Shingalapur RV, Hosamani KM, Keri RS. Synthesis and evaluation of in vitro anti-microbial and anti-tubercular activity of 2-styryl benzimidazoles. Eurpean Journal of Medicinal Chemistry. 2009; 44: 4244-4248. DOI: 10.1016/j.ejmech.2009.05.021. c) Jyoti P, Vinod TK, Shyam VS, Vinita C, Bhatnagar S. Sinha S, Gaikwad AN, Tripathi RP. Synthesis and antitubercular screening of imidazole derivatives. Eurpean Journal of Medicinal Chemistry. 2009; 44: 3350-3355. DOI: 10.1016/j.ejmech.2009.02.013.

20. Hadizadeh F, Hosseinzadeh H, Sadat M-SV, Seifi M, Kazemi S. Synthesis and antidepressant activity of N-substituted imidazole-5-carboxamides in forced swimming test model. Iranian Journal of Pharmaceutical Research. 2008; 7: 29-33.

21. Bhandari K, Srinivas N, Marrapu VK, Verma A, Srivastava S, Gupta S. Synthesis of substituted aryloxy alkyl and aryloxy aryl alkyl imidazoles as antileishmanial agents. Bioorganic and Medicinal Chemistry Letters. 2010; 20: 291-293. DOI:10.1016/j.bmcl.2009.10.117.

22. a) Naik P, Murumkar P, Giridhar R, Yadav MR. Angiotensin II receptor type 1 (AT(1)) selective nonpeptidic antagonists-A perspective. Bioorganic and Medicinal Chemistry. 2010; 18: 8418-8456. DOI: 10.1016/j.bmc.2010.10.043. b) Kubo K, Inada Y, Kohara Y, Sugiura Y, Ojima M, Itoh K, Furukawa Y, Nishikawa K, Nakat T. Nonpeptide angiotensin-II receptor antagonists-synthesis and biological-activity of benzimidazoles. Journal of Medicinal Chemistry. 1993; 36: 1772-1784. DOI: 10.1021/jm00064a011.

23 a) Cole ER, Crank G, Salam-Sheikh A. Antioxidant properties of benzimidazoles. Journal of Agricultural and Food Chemistry. 1974; 22: 918. b) Neochoritis CG, Zarganes-Tzitzikas T, Tsoleridis CA, Stephanidou- Stephanatou J, Kontogiorgis CA, Hadjipavlou-Litina DJ, Choli-Papadopoulou T. One-pot microwave assisted synthesis under green chemistry conditions, antioxidant screening, and cytotoxicity assessments of benzimidazole Schiff bases and pyrimido[1,2-a]benzimidazol-3(4H)-ones. Eurpean Journal of Medicinal Chemistry. 2011; 46: 297-306. DOI: 10.1016/j.ejmech.2010.11.018.

24. Hauel NH, Nar H, Priepke H, Ries U, Stassen JM, Wienen W. Structure-based design of novel potent nonpeptide thrombin inhibitors. Journal of Medicinal Chemistry. 2002; 45: 1757-1766. DOI: 10.1021/jm0109513.

25. Evans BE, Rittle KE, Bock MG, Dipardo RM, Freidinger RM, Whitter WL, Lundell F, Veber DF, Anderson PS, Chang RS, Chang RSL, Lotti VJ, Gerino DJ, Chen TB, Kling PJ, Kunkel KA, Springer JP, Hirshfield J. Methods for drug discovery: development of potent, selective, orally effective cholecystokinin antagonists. Journal of Medicinal Chemistry. 1998; 42: 2235-2246. DOI: 10.1021/jm00120a002.

26. Ahuja IS, Prasad I. Isonicotinamide complexes with some metal(II) halides and pseudohalides, Inorganic and Nuclear Chemistry Letters. 1976; 12: 777-784. DOI:10.1016/0020-1650(76)80065-7.

27. Keri RS, Hosamani KM, Seetharama HR, Reddy RS, Shingalapur RV. Wells-Dawson heteropolyacid: An efficient recyclable catalyst for the synthesis of benzimidazoles under microwave condition. Catalyst Letter. 2009; 131: 552-559. DOI: 10.1007/s10562-009-9966-2.

28. Jing X, Zhu Q, Xu F, Ren X, Li D, Yan C. Rapid one-pot preparation of 2-substituted benzimidazoles from esters using microwave conditions. Synthetic Communication. 2006; 36: 2597-2601.

29. Tandon VK, Kumar M. BF_3 center dot Et_2O promoted one-pot expeditious and convenient synthesis of 2-substituted benzimidazoles and 3,1,5-benzoxadiazepines. Tetrahedron Letters. 2004; 45: 4185-4187.

30. Bougrin K, Loupy A, Petit A, Daou B, Soufiaoui M. Novel synthesis of 2-trifluoromethylarylimidazoles on montmorillonite K10 in a 'dry medium' under microwave irradiation. Tetrahedron. 2001; 57: 163-168.

31. Rastogi R, Sharma S. 2-Aminobenzimidazoles in Organic Synthesis. Synthesis. 1983; 861-882. DOI: 10.1055/s-1983-30546.

32. Hegedus A, Hell Z, Potor A. Zeolite-catalyzed environmentally friendly synthesis of benzimidazole derivatives. Synthetic Communications. 2006; 36: 3625-3630. DOI:10.1080/00397910600943865.

33. Lin SY, Isome Y, Stewart E, Liu JF, Yohannes D, Yu L. Microwave-assisted one step high-throughput synthesis of benzimidazoles. Tetrahedron Letters. 2006; 47: 2883-2886. DOI: 10.1016/j.tetlet.2006.02.127.

34. Sun P, Hu Z. The convenient synthesis of benzimidazole derivatives catalyzed by I_2 in aqueous media. Journal of Heterocyclic Chemistry. 2006;43: 773-775. DOI: 10.1002/jhet.5570430338

35. Bahrami K, Khodaei MM, Kavianinia I. A simple and efficient one-pot synthesis of 2-substituted benzimidazoles. Synthesis. 2007; 547-550.

36. Nagawade RR, Shinde DB. $BF_3.OEt_2$ promoted solvent free synthesis of benzimidazole derivatives. Journal of the Chinese Chemical Society. 2006; 17: 453-456. DOI: 10.1002/jccs.201100591.

37. Nagawade RR, Shinde DB. Zirconyl(IV) chloride-promoted synthesis of benzimidazole derivatives. Russian Journal of Organic Chemistry. 2006; 42: 453-454. DOI: 10.1134/S1070428006030201.

[38] Mobinikhaledi A, Zendehdel M, Jamshidi FH. Zeolite-catalyzed synthesis of substituted benzimidazoles under solvent-free condition and microwave irradiation. Synthesis and Reactivity in Inorganic, Metal-Organic and Nano-Metal Chemistry. 2007; 37: 175-177. DOI: 10.1080/15533170701301496.

39. Varala R, Nasreen A, Enugala R, Adapa SR. L-proline catalyzed selective synthesis of 2-aryl-1-arylmethyl-1H-benzimidazoles. Tetrahedron Letters. 2007; 48: 69-72. DOI: 10.1016/j.tetlet.2006.11.010.

40. Rathod SB, Lande MK, Arbad BR. Synthesis, characterizaion and catalytic application of MoO_3/CeO_2-ZrO_2 solid heterogeneous catalyst fort he synthesis of benzimidazole derivatives, Bulletin Korean Chemical Society. 2010; 31: 2835-2840. DOI: 10.5012/bkcs.2010.31.10.2835.

41. Gedye R, Smith F, Westaway K, Ali H, Baldisera L, Laberge L. The Use of Microwave-Ovens for rapid Organic-Synthesis. Tetrahedron Letters. 1986; 27: 279-282. DOI: 10.1016/S0040-4039(00)83996-9.

42. Bougrin K, Soufiaoui M. Nouvelle voie de synthèse des arylimidazole sous irradiation micro-ondes en milieu sec. *T*etrahedron Letters. 1995; 36: 3683-3686. DOI: 10.1016/0040-4039(95)00611-F.

43. Bougrin K, Loupy A, Petit A, Daou B, Soufiaoui M. Nouvelle voie synthése des 2-trifluorométhylarylimidazoles sur montmorillonite K10 en 2milieu sec2 sous micro-onde. Tetrahedron. 2001; 537: 163-168.

44. Bendale PM, Sun C-M. Rapid microwave-assisted liquid-phase combinatorial synthesis of 2-(arylamino)benzimidazoles. J. Comb. Chem. 2002; 4: 359-361. DOI: 10.1021/cc0200080.

45. Getvoldsen GS, Elander N, Stone-Elander AA. UV monitoring of microwave-heated reactions-A feasibility study. Chemistry Eurepan Journal. 2002; 8: 2255-2260. DOI: 10.1002/1521-3765(20020517)8:10<2255::AID-CHEM2255>3.0.CO;2-R.

46. Boufatah N, Gellis A, Maldonado J, Vanelle P. Efficient microwave-assisted synthesis of new sulfonylbenzimidazole-4,7-diones: heterocyclic quinones with potential antitumor activity. Tetrahedron. 2004; 60: 9131-9137. DOI: 10.1016/j.tet.2004.07.070.

47. Zhang W, Tempest P. Highly efficient microwave-assisted fluorous Ugi and post-condensation reactions for benzimidazoles and quinoxalinones. Tetrahedron Letters. 2004; 45: 6757-6760. DOI: 10.1016/j.tetlet.2004.07.039.

48. Getvoldsen G, Fredriksson A, Elander N, Stone-Elander S. Microwave-assisted cyclocondensation of 1,2-diaminobenzene with [4-^{18}F]fluorobenzoic acid: microwave synthesis of 2-(4-18F]fluorophenyl)benzimidazole. Journal of labelled compounds and radiopharmaceuticals. 2004; 47: 139-145. DOI: 10.1002/jlcr.807.

49. Martinez-Palou R, Zepeda LG, Höpfl H, Montoya A, Guzmán-Lucero DJ, Guzmán J. Parallel and automated library synthesis of 2-long alkyl chain benzoazoles and azole[4,5-*b*]pyridines under microwave irradiation. Molecular Diversity. 2005; 9: 361-369. DOI: 10.1007/s11030-005-6357-5.

50. VanVilet DS, Gillespie P, Scicinski JJ. Rapid one-pot preparation of 2-substituted benzimidazoles from 2-nitroanilines using microwave conditions. Tetrahedron Letters. 2005; 46: 6741-6743. DOI: 10.1016/j.tetlet.2005.07.130.

51. Lin A-Y, Isome Y, Stewart E, Liu J-F, Yohannes D, Yu L. Microwave-assisted one step high-throughput synthesis of benzimidazoles. Tetrahedron Letters. 2006; 47: 2883-2886. DOI: 10.1016/j.tetlet.2006.02.127.

52. Jing X, Zhu Q, Xu F, Ren X, Li D, Yan C. Rapid one-pot preparation of 2-substituted benzimidazoles from esters using microwave conditions. Synthetic Communication. 2006; 36: 2601-2606. DOI: 10.1080/00397910600764204.

53. Gellis A, Kovacic H, Boufatah N, Vanelle. Synthesis and cytotoxicity evaluation of some benzimidazole-4,7-diones as bioreductive anticancer agents. Eurepan Journal of Medicinal Chemistry. 2008; 43: 1858-1864. doi:10.1016/j.ejmech.2007.11.020.

54. Algül O, Kaessler A, Apcin Y, Yılmaz A, Jose J. Comparative studies on conventional and microwave synthesis of some benzimidazole, benzothiazole and indole derivatives and testing on inhibition of hyaluronidase. Molecules. 2008; 13: 736-748.

55. Hosamani KM, Seetharamareddy HR, Keri RS, Hanamanthagouda MS, Moloney MG. Microwave assisted, one-pot synthesis of 5-nitro-2-aryl substituted-1H-benzimidazole libraries: Screening in vitro for antimicrobial activity. Journal of Enzyme Inhibition and Medicinal Chemistry. 2009; 24: 1095-1100. DOI: 10.1080/14756360802632716.

56. Hasaninejad A, Niknam K, Zare A, Farsimadan E, Shekouhy M. Silphox [$POCl_{3-n}$ $(SiO_2)_n$] as a new, efficient, and heterogeneous reagent for the synthesis of benzimidazole derivatives under microwave irradiation. Phosphorus, Sulfur, and Silicon. 2009; 184: 147-155. DOI: 10.1080/10426500802080931.

57. Chen C-H, Chien M-H, Kuo M-L, Chou C-T, Lai J-J, Lin S-F, Thummanagoti S, Sun C-M. Diversity-oriented synthesis of angular bis-benzimidazole derivatives under microwave irradiation. Journal of Combinatorial Chemistry. 2009; 11: 1038-1046. DOI: 10.1021/cc7002045.

58. Chen L-H, Hsiao Y-S, Yellol GS, Sun C-M. Microwave Promoted Simple, Efficient and Regioselective Synthesis of Trisubstituted Imidazo[1,2- *a*]benzimidazoles on Soluble Support. ACS Combinatorial Science. 2011 Mar 14;13(2):112–9. DOI:10.1021/co1000037.

59. Chanda K, Maiti B, Yellol GS, Chien M-H, Kuo M-L, Sun C-M. Polymer supported synthesis of novel benzoxazole linked benzimidazoles under microwave conditions: In vitro evaluation of VEGFR-3 kinase inhibition activity. Organic & Biomolecular Chemistry. 2011; 9: 1917-1926. DOI: 10.1039/c0ob00547a.

60. Chou C-T, Yellol GS, Chang W-J, Sun M-L, Sun C-M. Microwave assisted straightforward synthetic method for benzimidazole linked quinoxalinones on soluble polymer support. Tetrahedron. 2011; 67: 2110–2117. DOI: 10.1016/j.tet.2011.01.040.

61. Thummanagoti S, Yellol GS, Sun C-M. Ionic liquid supported multistep divergent synthesis of benzimidazole linked pyrrolo-/pyrido-/isoindolo-benzimidazolones. Tetrahedron Letters. 2011; 52: 2818-2822. DOI: 10.1016/j.tetlet.2011.03.046.

62. Ben-Alloum A, Bakkas S, Soufiaoui M. Benzimidazoles: Oxydation hétérocyclisante par le nitrobenzéne ou le diméthylsulfoxyde sur silice et sous irradiation micro-ondes ou ultra-violet. Tetrahedron Letters. 1998; 39: 4481-4484.

63. Navarrete-Vazquez G, Moreno-Diaz H, Aguirre-Crespo F, Leon-Rivera I, Villalobos-Molina R, Munoz-Muniz O, Estrada-Soto S. Design, microwave-assisted synthesis, and spasmolytic activity of 2-(alkyloxyaryl)-1*H*-benzimidazole derivatives as constrained stilbene bioisosteres. Bioorganic & Medicinal Chemistry Letters. 2006; 16: 4169-4173. DOI: 10.1016/j.bmcl.2006.05.082.

64. Zahran MA–H, El-Essawy FA-A, Yassin SM, Salem TA-R. Rapid and efficient synthesis of 4-substituted pyrazol-5-one under microwave irradiation in solvent-free conditions. Archive der Pharmzie. 2007; 340: 591-598.DOI: 10.1002/ardp.200700121.

65. Dubey R, Moorthy NSHN. Comparative studies on conventional and microwave assisted synthesis of benzimidazole and their 2-substituted derivative with the effect of salt form of reactant. Chemical Pharmaceutical Bulletin. 2007; 55: 115-117. DOI: 10.1248/cpb.55.115.

66. Navarrete-Vazquez G, Moreno-Diaz H, Estrada-Soto S, Torres-Piedra M, Leon-Rivera I, Tlahuext H, Munoz-Muniz O, Torres-Gomez H. Microwave-assisted one-pot synthesis of 2-(substituted phenyl)-1H-benzimidazole derivatives. Synthetic Communications. 2007; 37: 2815-2825. DOI: 10.1080/00397910701147332 5.

67. Jacob RG, Dutra LG, Radatz CS, Mendes SR, Perin G, Lenardao EJ. Synthesis of 1,2-disubstituted benzimidazoles using $SiO_2/ZnCl_2$. Tetrahedron Letters. 2009; 50: 1495-1497. DOI: 10.1016/j.tetlet.2009.01.076.

68. Mao Z, Wang Z, Li J, Song X, Luo Y. Rapid and cheap synthesis of benzimidazoles via intermittent microwave promotion: A simple and potential industrial application of air as oxidant. Synthetic Communication. 2010; 40: 1963-1977. DOI: 10.1080/00397910903219328.

69. Azarifar D, Pirhayati M, Maleki B, Sanginabadi M, Yami RN. Acetic acid-promoted condensation of o-phenylenediamine with aldehydes into 2-aryl-1- (arylmethyl)-1H-benzimidazoles under microwave irradiation. Journal of the Serbian Chemical Society. 2010; 75: 1181-1189. DOI: 10.2298/JSC090901096A.

70. Mungra DC, Patel MP, Patel RG. Microwave-assisted synthesis of some new tetrazolo[1,5-*a*]quinoline-based benzimidazoles catalyzed by p-TsOH and investigation of their antimicrobial activity. Medicinal Chemistry Research. 2011; 20: 782-789. DOI: 10.1007/s00044-010-9388-0.

71. Krim J, Grünewal C, Taourirte M, Engels JW. Efficient microwave-assisted synthesis, antibacterial activity and high fluoresence of 5 benzimidazole-2'-deoxyuridines. Biorganic and Medicinal Chemistry. 2012; 20: 480-486. DOI: 10.1016/j.bmc.2011.10.041.

72 Reedy ACS, Rao PS, Venkataratnam RV. Fluoro organics: Facile synthesis of novel 2- or 4-trifluoromethyl-1H-arylo-1,5-diazepines, oxazepines, thiazepines, 2- (1,1,1-trifluoraacetonyl)imidazoles, oxazoles and thiazoles. Tetrahedron. 1997; 53: 5847-5854. DOI: 10.1016/S0040-4020(97)00244-5.

73. Hulme C, Chappeta S, Griffith C, Lee Y-S, Dietrich J. An efficient solution Phase synthesis of triazadibenzoazulenones: 'designer isonitrile free' methodology enabled by microwaves. Tetrahedron Letters. 2009; 50: 1939-1942. DOI: 10.1016/j.tetlet.2009.02.099.

74. Wang S-L, Ding J, Jiang B, Gao Y, Tu S-J. Microwave-Assisted Solvent-Dependent Reaction:Chemoselective Synthesis of Quinoxalin-2(1*H*)-ones, Benzo[*d*]imidazoles and Dipeptides. ACS Combinatorial Science. 2011. Sep 12;13(5):572–7. DOI: 10.1021/co2001247.

75. Shaw AY, Medda F, Hulme C. Facile and rapid route for the synthesis of novel norstatine analogs via PADAM-cyclization methodology. Tetrahedron Letters. 2012; 53: 1313–1315. DOI: 10.1016/j.tetlet.2011.12.073.

76. Wen Xiaoan, El Bakali J, Deprez-Poulain R, Deprez B. Efficient propylphosphonic anhydride (®T3P) mediated synthesis of benzothiazoles, benzoxazoles and benzimidazoles. Tetrahedron Letters. 2012; 53: 2440-2443. DOI:10.1016/j.tetlet.2012.03.007.

Construction of an Electrochemical Xanthine Biosensor Based on Graphene/Cobalt Oxide Nanoparticles/Chitosan Composite for Fish Freshness Detection

Berna Dalkıran*, Pınar Esra Erden, Esma Kılıç

Ankara University, Faculty of Science, Department of Chemistry, Tandoğan, 06100, Ankara.

Submitted: June 19, 2016. **Revised:** July 21, 2016. **Accepted:** August 9, 2016.

Abstract: A xanthine biosensor based on glassy carbon electrode (GC) modified with graphene (GR), Co_3O_4 nanoparticles, and chitosan (CH) composite was fabricated. Xanthine oxidase (XAO) solution was dropped on the surface of Nafion/Co_3O_4/CH/GR/GC and the electrode was placed in saturated glutaraldehyde vapor for the crosslinking of the enzymes. The modified electrode was characterized by scanning electron microscopy, cyclic voltammetry and electrochemical impedance spectroscopy. Under the optimized experimental conditions, xanthine was detected in the concentration range from 5.0×10^{-4} to 8.0×10^{-2} mM with a detection limit of 2.0×10^{-4} mM. The low Michaelis–Menten constant (0.17 mM) suggested enhanced enzymic affinity for the immobilized enzyme as compared to previously reported xanthine biosensors. Moreover, the biosensor exhibited some advantages, such as short response time (10 s), high sensitivity (6.58 μA/mM or 74.8 μA/mMcm^2), and good reproducibility (RSD = 1.2%). The suitability of the device was verified by xanthine assay in a fish meat sample. The biosensor provided to be a reliable, easy, fast and economical method for the evaluation of fish freshness.

Keywords: Amperometric biosensor, Co_3O_4 nanoparticle, graphene, xanthine, fish freshness.

Submitted: June 19, 2016. **Revised:** July 21, 2016. **Accepted:** 09 August, 2016.

Cite this: Dalkıran B, Erden P, Kılıç E. Construction of an Electrochemical Xanthine Biosensor Based on Graphene/Cobalt Oxide Nanoparticles/Chitosan Composite for Fish Freshness Detection. Journal of the Turkish Chemical Society, Section A: Chemistry. 2017;4(1):23–44.

DOI: 10.18596/jotcsa.54485.

***Corresponding author:** Dr. Berna Dalkıran; bernadalkiran@gmail.com.

INTRODUCTION

Estimation of fish freshness is important in the food industry for the manufacture of high quality products. After the death of fish, ATP (adenosine triphosphate) decomposition proceeds according to the sequence ATP $\rightarrow$ ADP $\rightarrow$ AMP $\rightarrow$ IMP$\rightarrow$ HxR $\rightarrow$ Hx $\rightarrow$ X$\rightarrow$ U where ADP is adenosine diphosphate, AMP is adenosine 5'-phosphate, IMP is inosine 5'-phosphate, HxR is inosine, Hx is hypoxanthine, X is xanthine, and U is uric acid [1]. Among various indicators of freshness such as total volatile basic nitrogen [2], ammonia [3], volatile acids [4] and pH [5], nucleotides produced by ATP decomposition are considered the most reliable and useful indicators for estimating fish freshness. IMP is one of the major contributing factors to the pleasant flavor of fresh fish whereas, its degradation product hypoxanthine/xanthine contributes to the "off-taste" [6]. In general, enzymatic decomposition of hypoxanthine is the rate-determining step, so hypoxanthine and xanthine accumulate in fish tissue. Thus, the quantification of both hypoxanthine and xanthine may be used to indicate fish freshness [7]. Moreover, determination of xanthine level in blood and tissue is essential for diagnosis and medical management of various diseases like hyperuricemia, gout, xanthinuria, and renal failure [8]. Obviously a rapid and reliable method for the detection of xanthine is of great significance in clinical assay and food quality control.

According to the literature, several analytical methods are available for the analysis of xanthine. Among these are capillary column gas chromatography [9], HPLC [10], chemiluminesence [11] and spectrophotometry [12]. In general, the methods already in use are time-consuming and tedious or expensive and difficult to operate. They are also inadequate for real time monitoring. Biosensors possess the characteristics of being simple for operation, highly sensitive and selective. Various electrochemical biosensors have been reported for xanthine analysis [13-16] notwithstanding the fact that most of these biosensors have drawbacks such as being relatively less stable, less sensitive and their reproducibility being somewhat poor. So, some improvement is still needed. On the other hand, graphene has attracted tremendous research interest in recent times because of its unique physicochemical properties, such as high surface area, strong mechanical strength, excellent thermal and electric conductivity, and ease of functionalization. It comprises a single layer of sp^2 hybridized carbon atoms joined by covalent bonds to form a flat hexagonal lattice. The idealized structure of graphene is completely two dimensional [17]. In the field of electrochemistry, graphene is considered

as an ideal material for sensing application since it can play an important role in improving the performance of sensors due to its high specific surface area and good electrical conductivity [18-19].

Recently, metal or metal oxide nanoparticles have been widely used in the fabrication of nanocomposites. They have many excellent properties such as large surface-to-volume ratio, good electrical properties, high surface reaction activity, high catalytic efficiency, chemical stability, and strong adsorption ability [20]. Among various types of nanoparticles, Co_3O_4 nanoparticles are of special interest in recent years as the material is cheap, biocompatible, easily available, and has highly prospective electrocatalytic properties [21]. Up to now, various metal or metal oxide nanoparticles and graphene composites such as Pd–graphene [22], Fe_3O_4–graphene oxide [23], TiO_2–graphene [24], Pt nanoparticles–graphene [25], and Au–graphene [26] have been investigated for biosensor construction and synergistic effects of these composites in electrocatalytic applications have been reported. With its extraordinary properties such as film forming capability, superior mechanical strength, high permeableness, and nontoxicity, chitosan (CH) appears to be the biocompatible polymer of choice. As such, it serves as a matrix for the assembly of biomolecules, nanoparticles and other substances [27]. Combinations of chitosan with graphene or metal/metal oxide nanoparticles have also been tested as the electrochemical biosensing platforms [25-26]. In this paper, the construction of a new amperometric xanthine biosensor for fish freshness detection based on immobilization of xanthine oxidase on Nafion/Co_3O_4/CH/GR composite film modified GC is presented. The experimental conditions related to the preparation and the characterization of the biosensor were studied in detail. Optimum parametric studies such as enzyme loading, pH, and working potential were conducted. The analytical performance parameters of the biosensor including the linear range, detection limit, sensitivity, response time, repeatability and stability were also reported. The biosensor developed was also employed in the analysis of xanthine in fish samples as a means for the estimation of fish freshness.

MATERIALS AND METHODS

Chemicals

Graphene solution (2 mg/mL) was obtained from Dropsense (Llanera, Spain). Xanthine oxidase (from microbial source with a specific activity of 8 Units/mg solid), Co_3O_4 nanoparticles (<50 nm particle size (TEM), 99.5% trace metals basis) $K_3Fe(CN)_6$, $K_4Fe(CN)_6$, uric acid, ascorbic acid, and glutaraldehyde were obtained from Sigma (St. Louis, MO, USA). Chitosan (90% deacetylation) was from Aldrich. Xanthine and glucose were from Fluka (Buchs, Switzerland). All other chemicals were purchased from Merck (Darmstadt, Germany).

Apparatus and measurements

Electrochemical measurements were carried out with IVIUM electrochemical analyzer (Ivium Technologies, Netherlands). A three-electrode configuration was employed, consisting of a modified glassy carbon electrode (3 mm in diameter) serving as the working electrode, and Ag/AgCl (BAS MF 2052) and platinum wire (BAS MW 1034) serving as the reference and counter electrodes, respectively. Scanning electron microscope (SEM) images were obtained using SEM from Carl Zeiss AG, EVO® 50 Series. ORION Model 720A pH/ion meter and ORION combined pH electrode (Thermo Scientific, USA) was used to check the pH of test solutions. Double distilled water was used for preparing all solutions (ELGA PURELAB). Electrochemical impedance spectroscopy (EIS) and cyclic voltammetry (CV) measurements were performed in the presence of 5.0 mM $K_3[(Fe(CN)_6]$, 5.0 mM $K_4[(Fe(CN)_6]$ and 100 mM KCl solution. EIS measurements were performed at the frequency range of 10^5 Hz–0.05 Hz with 10 mV amplitude. The amperometric measurements were performed at an applied potential of +0.70 V in 50 mM phosphate buffer solution (PBS pH 7.5) under stirring at room temperature. All amperometric measurements were performed in oxygen-saturated solutions.

Biosensor preparation and modification

Prior to coating, firstly the unmodified GC was polished with 0.05 μm alumina slurry, and then rinsed throughly with double distilled water, followed by ultrasonication in ethanol for 5 minutes. 0.025 g of chitosan (CH) was dissolved in 5.0 mL of acetate buffer solution

(pH 5.0) via magnetic strirring at room temperature. Co_3O_4 nanoparticles were dispersed in chitosan solution with 4 h of ultrasonication to obtain a concentration of 1.0 mg mL^{-1}.

5 μL of GR solution (2 mg/mL) was drop-casted on the cleaned surface of GC. After being dried at room temperature, 5 μL of Co_3O_4/CH solution was drop-casted on the surface of graphene modified GC to prepare the Co_3O_4/CH/GR/GC electrode. 10 μL of XAO solution (0.0248 Units μL^{-1}) was dropped on the surface of Co_3O_4/CH/GR/GC to fabricate XAO/Co_3O_4/CH/GR/GC. XAO modified electrode was placed in 2.5% glutaraldehyde vapor for 15 min in order to induce chemical cross-linking and then dried at room temperature. Finally, 7.5 μL of nafion solution (0.5%) was dropped on the enzyme electrode and the solvent was allowed to evaporate. The biosensor was dipped in 50 mM PBS (pH 7.5) to wash off the unbound constituents from the electrode surface. The fabrication process of the biosensor is presented in Scheme 1.

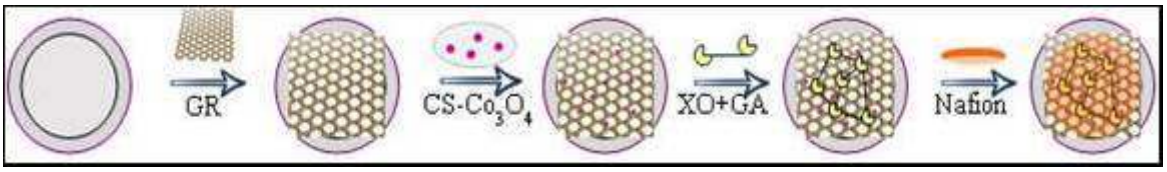

Scheme 1. Stepwise fabrication processes of the modified electrode.

(GR:Graphene, Co_3O_4, CH:Chitosan, XAO:Xanthine oxidase, GA:Glutaraldehyde, Nafion).

Preparation of fish sample for real sample analyses

The trout fish was cut into small pieces by chopping and homogenized. The homogenate was then divided into three parts. One part was stored at room temperature, the second part was stored at +4 °C and the last part was stored at -18°C. Before each experiment, the homogenate preparation was mechanically stirred and then centrifuged. This homogenate suspension was filtered through a Whatman filter paper to obtain fish meat extract. Distilled water was then added into the extract producing a total volume of 25.0 mL of homogenized sample solution.

RESULTS and DISCUSSION

Surface morphologies of composite electrodes

The surface morphologies of GR/GC, Co_3O_4/CH/GR/GC, and XAO/Co_3O_4/CH/GR/GC were investigated by SEM (Fig. 1). Image a shows wavy and crumpled shapes of graphene. Image b indicates that the Co_3O_4 nanoparticles are distributed throughout the porous chitosan network. The resulting porous film is suitable for immobilization. The surface of the composite (XAO/Co_3O_4/CH/GR) shows globular structures (image c), indicating that enzymes were successfully immobilized on the surface of Co_3O_4/CH/GR/GC.

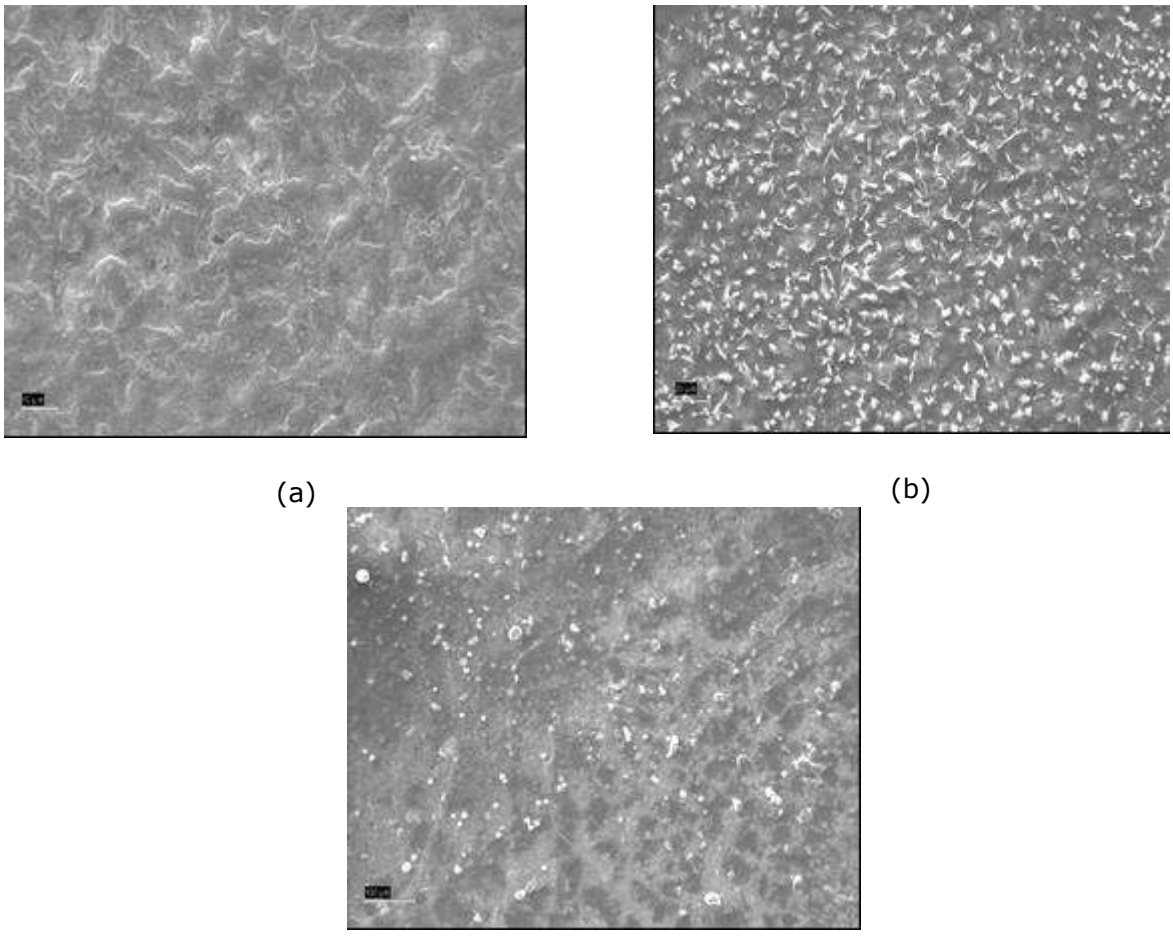

(a) (b)

(c)

Fig. 1 SEM images of (a) GR/GC, (b) Co_3O_4/CH/GR/GC and (c) XAO/Co_3O_4/CH/GR/GC.

Electrochemical characteristics of composite electrodes

$[Fe(CN)_6]^{3-/4-}$ solution containing 100 mM KCl was used as redox probe to evaluate the electrochemical characteristics of modified electrodes. Figure 2A compares the CVs of unmodified GC, CH/GC, GR/GC, Co_3O_4/CH/GC and Co_3O_4/CH/GR/GC in this probe. The CV curve obtained with unmodified GC indicates a well-defined reduction and oxidation peak (curve b) that belongs to $[Fe(CN)_6]^{3-/4-}$ redox couple. After the modification of the GC with CH, a decrease is observed in the peak current (curve a); leading to the conclusion that CH is acting as an inert blocking layer making the electron transfer more difficult. CH is known to have a relatively poor conductivity and some decrease in the peak current has also been reported previously [14]. GC coated with a layer of GR produce a CV (curve c), with a remarkable enhancement in the peak currents compared to those with unmodified GC and CH/GC. These changes could be ascribed to the enhanced surface area of graphene. The CV obtained with Co_3O_4/CH/GC (curve d) shows an increase in the peak current compared to the ones with unmodified GC and CH/GC. We suggest that the Co_3O_4 nanoparticles play some role in the enlargement of the electroactive surface area of the electrode.

In the case of GR/GC and Co_3O_4/CH/GC the peak potential separation ($\Delta E = E_{pa}$-E_{pc}) was found to be smaller than for the GC and CH/GC indicating that faster electron transfer reaction. The treatment of the GR/GC surface with Co_3O_4/CH composite leads to an increase in the redox peak currents of $[Fe(CN)_6]^{3-/4-}$ system (curve e) relative to the other four-electrode systems. This observation assures that the Co_3O_4/CH composite have been successfully combined onto the electrode surface, and the electron transfer of $[Fe(CN)_6]^{3-/4-}$ at the electrode surface was made easier. The peak potential separation ΔE at Co_3O_4/CH/GR/GC was smaller than for the GC, CH/GC and Co_3O_4/CH/GC demostrating faster electron transfer behavior due to the synergistic action of the Co_3O_4 nanoparticles and graphene.

The effective surface area of the GC, GR/GC, Co_3O_4/CH/GC and Co_3O_4/CH/GR/GC was estimated according to the Randles-Sevcik equation [28]. The effective surface area of the GC, GR/GC, Co_3O_4/CH/GC, and Co_3O_4/CH/GR/GC was 0.071 cm^2, 0.100 cm^2, 0.122 cm^2 and 0.210 cm^2, respectively. In comparison with the unmodified GC, the effective surface area of the GR, Co_3O_4/CH and Co_3O_4/CH/GR/GC modified electrodes was increased about 1.5, 1.2 and 2.9 times, respectively. These results were expected, as

Co_3O_4 nanoparticles and GR facilitate enhanced electron transfer for the redox process of $Fe(CN)_6^{3-/4-}$ [18; 29-30], thus increasing the effective surface area. The surface area of the Nafion/XAO/Co_3O_4/CH/GR/GC was also calculated as 0.088 cm^2 and further used for the sensitivity estimation of the enzyme electrode.

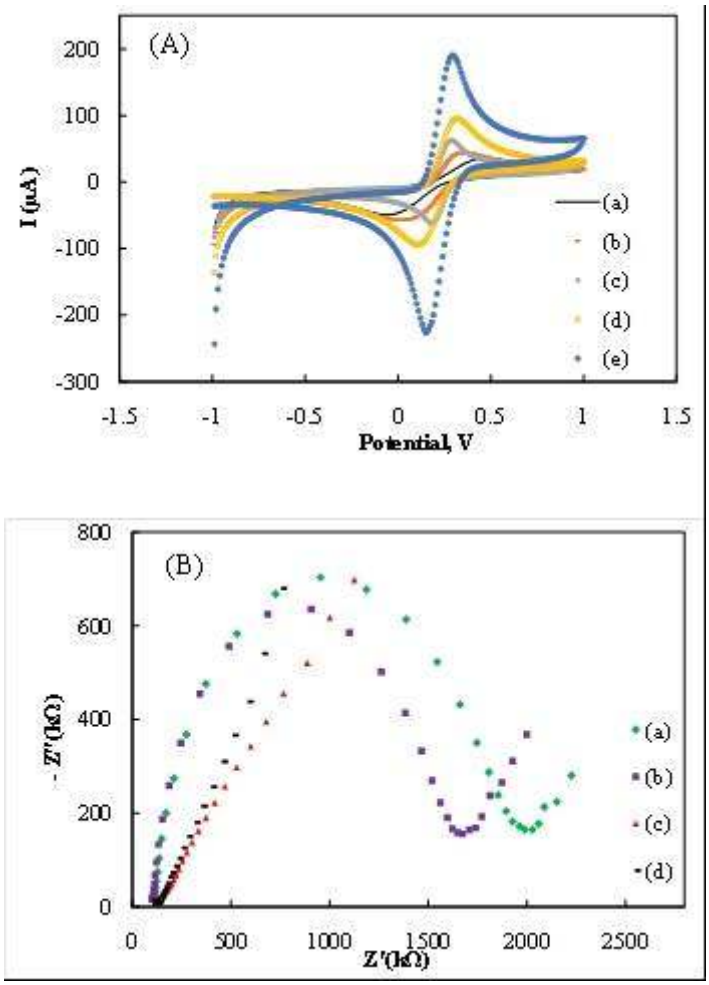

Fig. 2 (A) Cyclic voltammograms of (a) CH/GC, (b) GC, (c) GR/GC, (d) Co_3O_4/CH/GC and (e) Co_3O_4/CH/GR/GC at 50 mVs^{-1}, in 100 mM KCl solution containing 5.0 mmol L^{-1} $Fe(CN)_6^{3-/4-}$ (B) The Nyquist curves of in (a) CH/GC, (b) GC, (c) GR/GC, and (d) Co_3O_4/CH/GR/GC 100 mM KCl solution containing 5.0 mM$Fe(CN)_6^{3-/4-}$

In this study, EIS was employed to probe the electron transfer kinetics at the unmodified GC, CH/GC, GR/GC and Co_3O_4/CH/GR/GC (Fig. 2B). The Nyquist plots of the EIS consist of a semicircular portion and a linear portion, which correspond to the electron transfer limited process and the diffusion limited process, respectively. The electron transfer resistance (R_{ct}) at electrode surface is equal to the semicircle diameter, which can be used to describe the interface properties of the electrode [31]. With unmodified GC, a semicircle curve (Fig. 2B (b)) was obtained. When the electrode was modified with CH

film (Fig. 2B (a)), the diameter of the semicircle is larger indicating that a layer of CH coated the electrode surface supposedly, this layer blocks the diffusion of the electroactive species to the electrode surface. With GC covered with GR, the diameter of the semicircle decreases (Fig. 2B (c)), relative to the ones obtained with unmodified GC and CH/GC. The smallest semicircle was observed with Co_3O_4/CH/GR/GC in accordance with the expectation (Fig. 2B (d)) suggesting that Co_3O_4 and GR have a synergetic effect and this composite can make the electron transfer easier. The results of EIS study is constistent with the results reported in the literature for Co_3O_4 and graphene modified electrodes [30; 32].

Optimization of experimental parameters

A study was carried out to assess the optimum GR amount on the GC. 5; 7.5 and 10 μL of GR solution (2 mg/mL) was casted on the cleaned surface of GC and dried at room temperature. The electrode response was determined by CV in 100 mM KCl solution containing 5.0 mM $Fe(CN)_6^{3-/\mathbf{4-}}$. The highest peak currents were obtained with 10 μL graphene (data not shown). However, the peak currents of three different graphene concentrations were close to each other. Thus, 5 μL GR solution was used for further experiments to prevent the waste of this expensive reagent. The effect of the Co_3O_4 amount for the preparation of Co_3O_4/CH composite was investigated by dispersing in the range of 0.5 to 1.5 mg Co_3O_4 in 1 mL of CH solution. The electrode response was determined by CV in 100 mM KCl solution containing 5 mM $Fe(CN)_6^{3-/\mathbf{4-}}$. The highest peak currents were obtained with 1.0 mg Co_3O_4 (data not shown). Thus, a 1.0 mg Co_3O_4 amount was selected for the preparation of Co_3O_4/CH composite.

The effect of varying the concentration of XAO (0.1–0.5 U) during preparation was studied. The optimal amount of 0.3 Unit of XAO was obtained for the immobilization on the working electrode. This loading was therefore used for all biosensors in further experiments. Higher enzyme loadings caused the current decrease which is most likely due to the blocking of the electrode surface area by the large amount of immobilized protein. On the other hand, lower enzyme quantities caused the decrease of biosensor response.

Since enzymic activity is extremely affected by pH, the influence of pH on the biosensor response was investigated with 0.06 mM xanthine by using 50 mM PBS between pH 5.5 and 8.5. The response increases from pH 5.5 to 7.5. At pH values higher than 7.5, a decrease of the response was found. This results indicated that the maximum response of the biosensor occured at pH 7.5. Thus, pH 7.5 was selected as optimum pH value for further experiments. The optimum pH value found is within the pH between (7.0–8.5) reported for free XAO from microbial sources [33]. These results indicate that this immobilization procedure does not significantly effect the optimum pH of XAO.

The optimum working potential was investigated after the optimal composition of electrode was established. We have determined the optimum working potential by evaluating the xanthine response of the enzyme electrode at different potentials. The best response was obtained at +0.70 V and this potential was selected as the optimum working potential of the enzyme electrode.

The electrochemical reactions involved are known to be as follows at +0.70 V [14]:

$$\text{Xanthine} + O_2 + H_2O \xrightarrow{\text{XAO}} \text{Uric acid} + H_2O_2 \qquad \text{(Eq. 1)}$$

$$H_2O_2 \xrightarrow[+0.70\,\text{V}]{\text{Nafion/Co}_3\text{O}_4\text{-NPs-GR}} 2H^+ + 2e^- + O_2 \qquad \text{(Eq. 2)}$$

The electron transfer mechanism of the biosensor developed also involves the H_2O_2 formed from xanthine by XAO immobilized on the Co_3O_4/CH/GR composite. H_2O_2 molecules are then oxidized on the biosensor surface at +0.70 V. The response current of the biosensor is directly proportional to xanthine concentration (Fig. 3A).

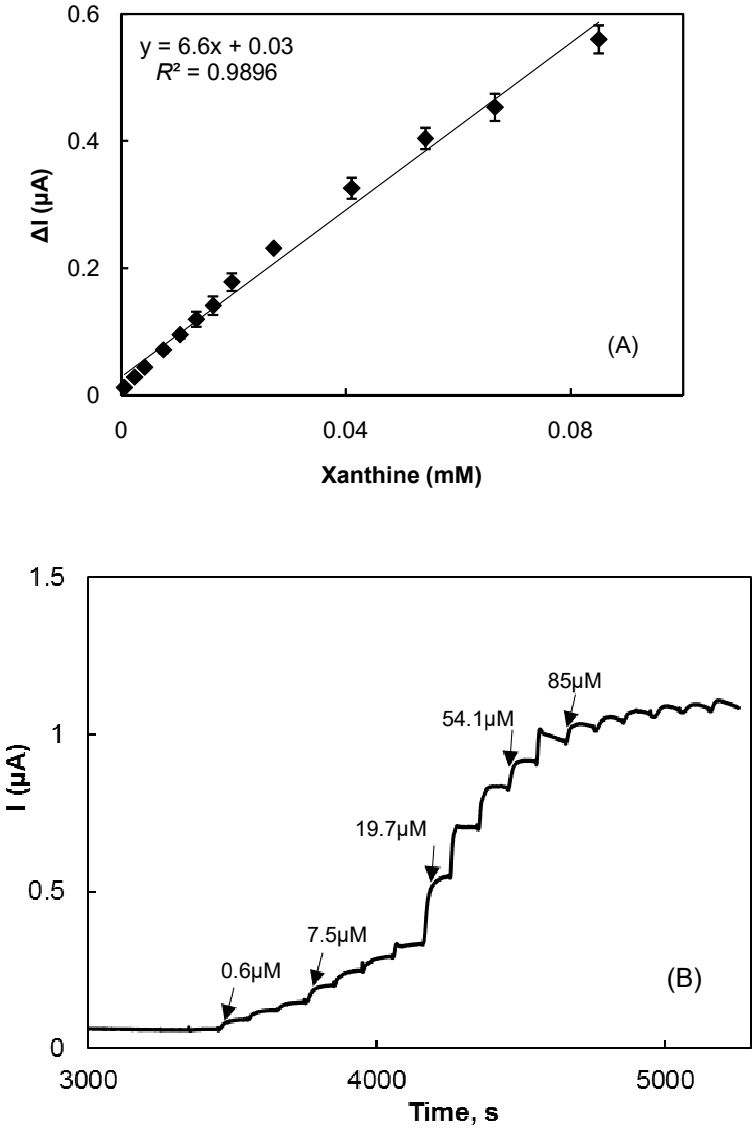

Fig. 3. (A) Calibration curve of the Nafion/XAO/Co_3O_4/CH/GR/GC. (B) Typical current–time response of the on successive injection of xanthine into a stirred solution of 50 mM PBS (pH 7.5).

Performance parameters

Fig. 3 shows the calibration curve and the chronoamperometric response of the biosensor the sequential additions of xanthine in 50 mM PBS (pH 7.5). In Figure 3A, *Δi* is the difference between the response current of the biosensor (*i*) and background current. After the addition of xanthine, the anodic current increased and reached a stationary state within 10 s. The linear response range of the biosensor to xanthine concentration was from 5.0×10^{-4} mM to 8.0×10^{-2} mM with a correlation coefficient of 0.9896 and

sensitivity of 6.6 μA/mM or 74.8 μA/mMcm^2. The limit of detection (LOD) of the biosensor, which is the minimum concentration at which the ratio of signal to noise is not less than 3, is 2.0×10^{-4} mM (S/N = 3). This detection limit is lower than that of ferrocene modified polypyrrole coated Pt electrode (1.0×10^{-6} M) [34] and mesoporous graphite material micro-structured with palladium-platinum deposits (1.5×10^{-6} M) [35] but comparable to silver nanoparticles/cysteine modified Au electrode (1.5×10^{-7} M) [36] and poly(glycidyl methacrylate-co-vinylferrocene)/MWCNT nanocomposite layer modified pencil graphite electrode (1.2×10^{-7} M) [37]. In order to evaluate the effect of direct oxidation of xanthine the response of Nafion/Co_3O_4/CH/GR/GC and Nafion/XAO/Co_3O_4/CH/GR/GC to xanthine were determined. The sensitivity of Nafion/XAO/Co_3O_4/CH/GR/GC (y=6.6x+0.03 R^2=0.9896) was found to be four times higher than Nafion/Co_3O_4/CH/GR/GC (y=1.7x+0.06 R^2=0.9896). Hence we can decide that the direct oxidation of xanthine has a contribution to biosensor response

Lineweaver–Burk plot gave the apparent Michaelis–Menten constant (K_m^{app}) value of 0.17 mM for immobilized enzyme, and this value is lower than those of a $CuPtCl_6$/glassy carbon chemically modified electrode based xanthine biosensor (1.11 mM) [38] polypyrrole and ferrocene modified Pt electrode based xanthine biosensor (1.33 mM) [34], and a platinum electrodeposited polyvinylferrocenium perchlorate matrix modified Pt electrode based xanthine biosensor (3.45 mM) [39]. These results show that the current biosensor possesses higher affinity to xanthine compared with some of earlier biosensors.

As a measure of the repeatability of the Nafion/XAO/Co_3O_4/CH/GR/GC, five successive calibration curves were prepared using the same biosensor. The relative sensitivity standard deviation (RSD) was around 1.0%. The reproducibility was also good (use of three different electrodes resulted in a relative standard deviation of 1.2%).

Long-term stability is one of the most important properties of biosensors due to the tendency of the enzymes to lose their activity when not stored in appropriate conditions. The long–term stability of the biosensor was tested by storing it in a dry atmosphere at +4 °C when not in use. There was no significant change in the amperometric response within the first 15 days. At the end of a 30 day storage period, some 90% of the original sensitivity was retained. Even after 2 months, the biosensor was found to have reserved

(83%) of its initial activity. The high stability of this biosensor may be attributed to the chemical and mechanical stability of Co_3O_4/CH/GR composite and thus it can be used as a useful platform for immobilising enzymes to enhance biosensor performances.

The common issue in the electrochemical determination of xanthine is the interference from species, such as glucose, uric acid, and ascorbic acid. The interference of glucose (0.02 mM), uric acid (0.02 mM), ascorbic acid (0.02 mM), and sodium benzoate (0.02 mM) were investigated. The response of the biosensor to 0.02 mM xanthine was found to have changed by −3%, 15%, 20% and −4% respectively. The high interferences due to uric acid (15%) and ascorbic acid (20%) are no surprise as the working potential is fairly high.

Table 1 lists the response characteristics of the proposed xanthine biosensor compared to the some other xanthine biosensors previously reported. The results presented in Table 1 demonstrate that the different characteristics of the developed xanthine biosensor based on Nafion/Co_3O_4/CS/GR modified GC are better in some situations or comparable with earlier sensors reported.

Analysis of the fish sample

The analytical reliability and application potential of the presented biosensor was evaluated for the determination of the concentration of xanthine accumulated in fish continuously after death, which attracts much interest as an indicator for estimating the freshness of fish [37]. After freshly killed and stored for 6, 12, 24 and 48 h at room temperature, the concentration of xanthine in fish meat was determined by Nafion/XAO/Co_3O_4/CH/GR/GC. Xanthine level of fish samples were determined by the standard addition method. The concentrations of the analyte were arranged so as to fall into the linear working range; using fish meat extract as a matrix. The multiple addition calibration curve was found to be linear and the original xanthine concentration in the fish meat sample was 62.8±0.2 mg L^{-1} (n=3). After 6, 12, 24, and 48 h, the concentration of xanthine increased from 62.8 to 113.7, 119.3, 123.3, and 253.5 mg L^{-1}, respectively. The level was doubled after 6 h, increases slowly up to 24 h of storage and beyond 24 h it increases very rapidly (Fig. 4a). The increase in xanthine accumulation with storage time is an expected result. To investigate the effect of storage conditions on

fish freshness, the change of xanthine concentration with time was also investigated in fish meat samples stored at +4 °C and -18 °C. In the fish sample stored at +4 °C xanthine level was increased from 62.6 to 245.8 and 340.2 mg L^{-1} after 8 and 15 days, respectively. (Fig. 4b). In the fish sample stored at room temperature xanthine level was found to be 253.5 mg L^{-1} after 2 days. Thus, it can be concluded that degradation is very high at room temperature compared to +4°C. In the fish sample stored at -18 °C xanthine level was only increased from 62.4 to 71.7 mg L^{-1} after 15 days. (Fig. 4c). The results obtained demonstrated that the degradation is higher at 4°C than at -18 °C. In the fish sample stored at -18 °C xanthine level was nearly constant after 3 days. On the basis of the measurements of the fish sample stored at -18 °C, one can conclude that no significant degradation occurred over this time period and storage temperature is very important to reduce the spoilage of fish meat.

Table 1: Various amperometric xanthine biosensors reported in recent years.

No	Enzyme /Working potential	Immobilization matrix/ Immobilization technique	Linearity/Detection limit	pH	Response time/Repeat ability	Storage stability	Reference
1	XAO/+0.55 V vs.SCE	Nano $CaCO_3$ particles and XAO modified electrode/cross-linking	2.0×10^{-6}–2.5×10^{-4} M/2.0×10^{-6} M(XAO-Nano$CaCO_3$ electrode)	7.5	<5 s/RSD 4.9% (XAO-Nano$CaCO_3$)	15% loss after 28 days (XAO-Nano $CaCO_3$)	[33]
	XAO-HRP/-0.05V vs.SCE	Nano $CaCO_3$ particles, XAO and HRP modified electrode/cross-linking	4.0×10^{-7}–5.0×10^{-5}M/1.0×10^{-7} M(XAO-HRP Nano$CaCO_3$ electrode)				
2	XAO/-0.05 V vs. Ag/AgCl	Mesoporous graphite material micro-structured with palladium-platinum deposits/adsorption	1.5– 70 µM/1.5 µM	8.4	60 s	-	[35]
3	XAO/+0.70 V vs.Ag/AgCl	Co_3O_4 nanoparticle/chitosan/multiwalled carbon nanotube/ composite film/cross-linking	2.0×10^{-7}–1.6×10^{-5} M/2.0×10^{-7}	7.0	5 s/2.9%	35% loss after 1 month	[14]
	XAO/HRP/–0.30 V		2.0×10^{-5}–3.6×10^{-4} M/2.0×10^{-5}			(XAO/Co_3O_4/MWCNTs/CH/GC)	
4	XAO/+0.38 V vs. Ag/AgCl	Zinc oxide nanoparticles–polypyrrole composite/physiosorption	0.8 µM–40 µM /0.8 µM	7.0	5 s/<5.1%	40% loss after 100 days	[40]
5	XAO/+0.60 V vs. Ag/AgCl	Supramolecular assembly between single walled nanotube surface and an adamantane-modified xanthine oxidase via β-cyclodextrin-modified pyrene derivative	5.0–600 µM/2 µM	7.0	10 s/6.1%	67%loss after 1 month	[15]
6	XAO/+0.35 V vs. Ag/AgCl	Reduced *expanded* graphene oxide sheets decorated with iron oxide nanoparticles into poly(glycidyl methacrylate-covinylferrocene)/covalent immobilization	2–36 µM /0.17 µM	7.0	3 s	30% loss after 25 days	[13]

7	XAO/+0.20 V vs. Ag/AgCl	Cadmium oxide nanoparticles/carboxylated multiwalled carbon nanotube (c-MWCNT) composite film electrodeposited on the surface of Au electrode/covalent immobilization	0–120 μM/0.05 μM	7.5	4 s	50% loss after 120 days	[41]
8	XAO/+0.50 V vs. Ag/AgCl	Silver nanoparticles/cysteine modified Au electrode/covalent immobilization	2 μM–16 μM/0.15 μM	7.0	5 s/<2.6%	20% loss after 60 days	[36]
9	XAO/+0.35 V vs. Ag/AgCl	Poly(glycidyl methacrylate-co-vinylferrocene)/MWCNT nanocomposite layer modified pencil graphite electrode/adsorption	2–48 μM 28–46μM 46–86μM/0.12 μM	7.0	4 s	30% loss after 25 days	[37]
10	Nafion/XAO/ +0.70 V vs.Ag/AgCl	Cobalt oxidenanoparticle/ chitosan/graphene/ composite/cross-linking	5.0×10^{-4}–8.0×10^{-2} mM/2.0×10^{-4} mM	7.5	10 s/1.0%	17% loss after 2 months	This work

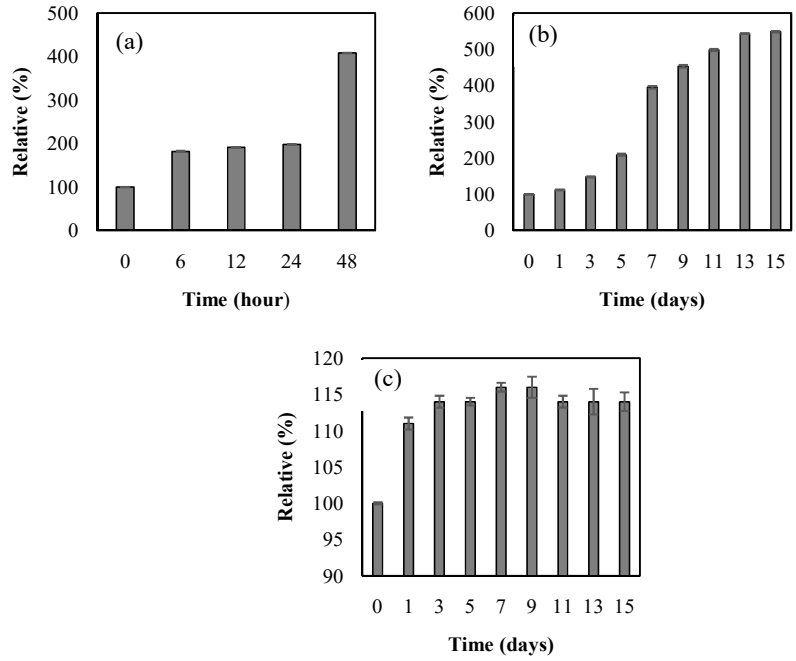

Fig. 4. Change of xanthine concentration in fish meat with time at different storage conditions: (a) room temperature (b) +4ºC and (c) -18ºC.

CONCLUSIONS

With the electrocatalytic synergy of graphene and Co_3O_4 nanoparticles to xanthine, a sensitive xanthine biosensor was achieved. Nafion/XAO/Co_3O_4/CH/GR composite of known composition was coated on GC to act as a biosensor for xanthine. The use of Nafion/Co_3O_4/CH/GR composite resulted in the improved analytical performance of the xanthine biosensor in terms of low response time (10 s), high reproducibility (1.2%), good sensitivity (6.58 μA/mM), wider linear range (5.0×10^{-4}–8.0×10^{-2} mM), and low detection limit (2.0×10^{-4} mM) compared with some of the previously reported biosensors. The presented biosensor was shown to be adequate for the determination of xanthine in fish samples. The results are used to evaluate the freshness. The purposed strategy may be to be applicable to the development of enzyme-based biosensors for other bioactive species.

ACKNOWLEDGMENTS

Financial support of this research Ankara University Research Fund (Project No: 13L4240002) and a scholarship for B.DALKIRAN of The Scientific and Technological Research Council of Turkey are gratefully acknowledged.

REFERENCES

[1] Niu J, Lee, JY. A new approach for the determination of fish freshness by electrochemical impedance spectroscopy. J. Food Sci. 2000;65(5):780-785.

[2] Anderson AK. Biogenic and volatile amine-related qualities of three popular fish species sold at Kuwait fish markets. Food Chem. 2000;107(2):761–767.

[3] Ota F, Nakamura T. Variation of ammonia contents in fish meat by heating under pressure: relation between the increase of ammonia and the freshness of fish. Bull. Japan. Soc. Sci. Fish. 1952;18:15–20.

[4] Suzuki T. Determination of volatile acids for judging the freshness of fish. Bull. Japan. Soc. Sci. Fish. 1953;19:102–106.

[5] Kawabata T, Fujimaki M, Amano K, Tomiya F. Studies of the pH for fish muscle. Bull. Japan. Soc. Sci. Fish. 1952;18:124–132.

[6] Nakatani HS, Vieira dos Santos L, Pelegrine CP, Gomes STM, Matsushita M, Evelázio de Souza NJ, Visentainer V. Biosensor based on xanthine oxidase for monitoring hypoxanthine in fish meat. Am. J. Biochem. Biotechnol. 2005;1:85–89.

[7] Lawal AT, Adeloju SB. Progress and recent advances in fabrication and utilization of hypoxanthine biosensors for meat and fish quality assessment: A review. Talanta 2012;100:217–228.

[8] Pundir CH, Devi R. Biosensing methods for xanthine determination: A review. Enzyme Microb. Tech. 2014;57:55–62.

[9] Pagliarussi RS, Freitas LAP, Bastos JK. A quantitative method for the analysis of xanthine alkaloids in Paullinia cupana (guarana) by capillary column gas chromatography. J. Sep. Sci. 2002;25:371−374.

[10] Cooper N, Khosravan R, Erdmann C, Fiene J, Lee JW. Quantification of uric acid, xanthine and hypoxanthine in human serum by HPLC for pharmacodynamic studies. J. Chrom. B. 2006;837:1–10.

[11] Hlavay J, Haemmerli S, Gailbult G. Fibre-optic biosensor for hypoxanthine and xanthine based on a chemiluminescence reaction. Biosens. Bioelectron. 1994;9:189-195.

[12] Amigo JM, Coello J, Maspoch S. Three-way partial least-squares regression for the simultaneous kinetic-enzymatic determination of xanthine and hypoxanthine in human urine. Anal. Bioanal. Chem. 2005;382:1380–1388.

[13] Dervisevic M, Custiuc E, Çevik E, Durmuş Z, Şenel M, Durmuş A. Electrochemical biosensor based on REGO/Fe_3O_4 bionanocomposite interface for xanthine detection in fish sample. Food Control 2015; 57:402−410.

[14] Dalkiran B, Kacar C, Erden PE, Kilic E. Amperometric xanthine biosensors based on chitosan-Co_3O_4-multiwall carbon nanotube modified glassy carbon electrode. Sensor. Actuat. B:Chem. 2014;200:83–91.

[15] Villalonga R, Diez P, Gamella M, Reviejo J, Pingarrón JM. Immobilization of xanthine oxidase on carbon nanotubes through double supramolecular junctions for biosensor construction. Electroanal. 2011;23(8):1790-1796.

[16] Oztürk FÖ, Erden, PE, Kacar C, Kilic E. Amperometric biosensor for xanthine determination based on Fe_3O_4 nanoparticles. Acta Chim. Slov. 2013;61(1):19–26.

[17] Chen J, Zheng X, Miao F, Zhang J, Cui X, Zheng W. Engineering graphene/carbon nanotube hybrid for direct electron transfer of glucose oxidase and glucose biosensor. J. Appl. Electrochem. 2012;42:875-881.

[18] Kuila T, Bose S, Khanra P, Mishra AK, Kim NH, Lee JH (2011). Recent advances in graphene-based biosensors. Biosens. Bioelectron. 2011;26(12):4637–4648.

[19] Zhou K, Zhu Y, Yang X, Li C. Preparation and application of mediator-free H_2O_2 biosensors of graphene-Fe_3O_4 composites. Electroanal. 2011;23(4):862-869.

[20] Fei J, Wen J, Yi L, Ge F, Zhang Y, Huang M, Chen X. Electrochemical determination diethylstilbestrol by a single-walled carbon nanotube/platinum nanoparticle composite film electrode. J. Appl. Electrochem. 2008;38:1527–1533.

[21] Kacar C, Dalkiran B, Erden PE, Kilic E. An amperometric hydrogen peroxide biosensor based on Co_3O_4 nanoparticles and multiwalled carbon nanotube modified glassy carbon electrode. Appl. Surf. Sci. 2014;311:139–146.

[22]Zeng Q, Cheng JS, Liu XF, Bai HT, Jiang JH. Palladium nanoparticle/chitosan-grafted graphene nanocomposites for construction of a glucose biosensor. Biosens. Bioelectron. 2011;26(8):3456-3463.

[23] Teymourian H, Salimi A, Khezrian S. Fe_3O_4 magnetic nanoparticles/reduced graphene oxide nanosheets as a novel electrochemical and bioelectrochemical sensing platform. Biosens. Bioelectron. 2013;49:1–8.

[24] Fu L, Zheng YH, Fu ZX. Ascorbic acid amperometric sensor using a graphene-wrapped hierarical TiO_2 nanocomposite. Chem. Pap. 2015;69:655-661.

[25] Wu H, Wang J, Kang X, Wang C, Wang D, Liu J, Aksay IA, Lin Y. Glucose biosensor based on immobilization of glucose oxidase in platinum nanoparticles/graphene/chitosan nanocomposite film. Talanta 2009;80:403–406.

[26] Zhou K, Zhu Y, Yang X, Luo J, Li C, Luan S. A novel hydrogen peroxide biosensor based on Au–graphene–HRP–chitosan biocomposites. Electrochim. Acta 2010;55:3055–3060.

[27] Chuah AM, Kuroiwa T, Ichikawa S, Kobayash I, Nakajima M. Formation of biocompatible nanoparticles via the self-assembly of chitosan and modified lecithin. J. Food Sci. 2008;74(1):1-8.

[28] Zargar B, Parhamand H, Hatamie A. Electrochemical investigation and stripping voltammetric determination of captopril at CuO nanoparticles/multi-wall carbon nanotube nanocomposite electrode in tablet and urine samples. Anal. Methods 2015;7:1026–1035.

[29] Pérez-López B, Merkoci A. Carbon nanotubes and graphene in analytical sciences. Microchim. Acta 2012;179(1-2):1–16.

[30] Dong XC, Hang X, Wang XW, Huang YX, Chan-Park MB, Zhang H, Wang LH, Huang W, Chen P. 3D graphene–cobalt oxide electrode for high-performance supercapacitor and enzymeless glucose detection. ACS Nano 2012;6(4): 3206–3213.

[31] Gokoglan TC, Soylemez S, Kesik M, Toksabay S, Toppare L. Selenium containing conducting polymer based pyranose oxidase biosensor for glucose detection. Food Chem. 2015;172: 219–224.

[32] Qi X, Gao H, Zhang Y, Wang X, Chen Y, Sun W. Electrochemical DNA biosensor with chitosan-Co_3O_4 nanorod-graphene composite for the sensitive detection of staphylococcus aureus nuc gene sequence. Bioelectrochem. 2012;88:42–47.

[33] Shan D, Wang Y, Xue H, Cosnier S. Sensitive and selective xanthine amperometric sensors based on calcium carbonate nanoparticles. Sensor. Actuat. B:Chem. 2009;136:510–515.

[34] Arslan F, Yaşar A, Kilic E. An amperometric biosensor for xanthine determination prepared from xanthine oxidase immobilized in polypyrrole film. Artif. Cell Blood Sub. 2006;34(1):111−126.

[35] Dodevska T, Horozova E, Dimcheva N. Design of an amperometric xanthine biosensor based on a graphite transducer patterned with noble metal microparticles. Cent. Eur. J. Chem. 2010;8(1):19–27.

[36] Devi R, Batra B, Lata S, Yadav S, Pundir CS. A method for determination of xanthine in meat by amperometric biosensor based on silver nanoparticles/cysteine modified Au electrode. Process Biochem. 2013;48,:242–249.

[37] Dervisevic M, Custiuc E, Çevik E, Şenel M. Construction of novel xanthine biosensor by using polymeric mediator/MWCNT nanocomposite layer for fish freshness detection. Food Chem. 2015;181:277-283.

[38] Pei J, Li XY. Xanthine and hypoxanthine sensors based on xanthine oxidase immobilized on a $CuPtCl_6$ emically modified electrode and liquid chromatography electrochemical detection. Anal. Chim. Acta 2000;414:205–213.

[39] Bas SZ, Gulce H, Yıldız S. Amperometric xanthine biosensors based on electrodeposition of platinum on polyvinylferrocenium coated Pt electrode. J. Mol. Catal. B: Enzym. 2011;7:282–288.

[40] Devi R, Thakur M, Pundir C.S. Construction and application of an amperometric xanthine biosensor based on zinc oxide nanoparticles–polypyrrole composite film. Biosens. Bioelectron. 2011;26(8):3420-3426.

[41] Jain U, Narang J, Rani K, Chauhan N. Synthesis of cadmium oxide and carbon nanotube based nanocomposites and their use as a sensing interface for xanthine detection. RSC Advances 2015;5(38):29675-29683.

Türkçe Öz ve Anahtar Kelimeler

Balıkta Tazelik Tayininin Grafen/Kobalt Oksit Nanoparçacıkları/Kitosan Kompozitine Dayanan Elektrokimyasal Ksantin Biyosensörü ile Gerçekleştirilmesi

Berna Dalkıran*, Pınar Esra Erden, Esma Kılıç

Ankara University, Faculty of Science, Department of Chemistry, Tandoğan, 06100, Ankara.

Öz: Camsı karbon elektrodu (GC) grafen (GR), Co_3O_4 nanoparçacıkları ve kitosan (CH) kompoziti üretilmiştir. Ksantin oksidaz (XAO) çözeltisi Nafion/Co_3O_4/CH/GR/GC yüzeyine damlatıldı ve elektrot doymuş glutaraldehit buharında enzimlerin çapraz bağlanması için tutuldu. Modifiye elektrot taramalı elektron mikroskopisi, döngülü voltammetri ve elektrokimyasal impedans spektroskopisi ile karakterize edildi. Optimize deneysel koşullar altında, ksantinin 5,0 x 10^{-4} ile 8,0 x 10^{-2} mM arasında, tayin sınırı 2,0 x 10^{-4} mM olmak üzere tayin edildiği bulundu. Düşük Michaelis-Menten sabiti (0,17 mM), daha önce bildirilen ksantin biyosensörleriyle karşılaştırıldığında immobilize enzimin artmış aktivitesini gösterdiği tespit edildi. Bunun dışında, biyosensör bazı avantajlar da sunmaktadır, bunlar arasında kısa tepki zamanı (10 s), yüksek hassasiyet (6,58 μA/mM ya da 74,8 μA/mMcm^2), ve iyi tekrarlanabilirlik (RSD = %1,2) öne çıkmaktadır. Cihazın uygunluğu balık eti örneğinde ksantin tayini yapılarak doğrulandı. Biyosensör güvenilir, kolay, hızlı ve ekonomik bir şekilde balık tazeliğini değerlendirilmesi için bir yol sunmaktadır.

Anahtar kelimeler: Amperometrik biyosensör, Co_3O_4 nanoparçacık, grafen, ksantin, balık tazeliği.

Sunulma: 19 Haziran 2016. **Düzeltme :** 21 Temmuz 2016. **Kabul:** 09 Ağustos 2016.

JOTCS
Journal of the Turkish Chemical Society
Section: A
Chemistry
TURKISH CHEMICAL SOCIETY

DFT Studies and Crystal Structure of Synthesized 1,3-bis(2-thiophenylmethyl)-4,5-dihydroimidazolidinium hexafluorophosphate Salt

Senem Akkoç[1*], Sevim Türktekin Çelikesir[2], Yetkin Gök[3], Sevtap Çağlar Yavuz[1], Mehmet Akkurt[2] and Namık Özdemir[4]

[1]*Erciyes University, Faculty of Science, Department of Chemistry, 38039 Kayseri, Turkey.*
[2]*Erciyes University, Faculty of Science, Department of Physics, 38039 Kayseri, Turkey.*
[3]*Inönü University, Faculty of Science and Arts, Department of Chemistry, 44280 Malatya, Turkey.*
[4]*Ondokuz Mayıs University, Faculty of Science and Arts, Department of Physics, 55139 Samsun, Turkey.*

Abstract: The synthesized compound **5**, $(C_{13}H_{15}N_2S_2)[PF_6]$, was fully characterized with X-ray diffraction method. In this compound, the asymmetric unit contains a 1,3-(2-thiophenylmethyl)-4,5-dihydroimidazolidinium cation and a hexafluorophosphate anion. Due to an 180° rotation about the thiophene-CH_2 bonds, the thiophene rings in the cation are disordered [site-occupancy factors = 0.903(4)/0.097(4) and 0.837(5)/0.163(5), respectively]. The short C—N bond lengths [1.303(4) and 1.287(4) Å] in the imidazolidine ring display partial electron delocalization within the N—C—N fragment. Anion and cations are connected through intermolecular C—H...F hydrogen bonds and three π-π stacking interactions [centroid-centroid distances = 3.890(3), 3.852(5) and 3.816(7) Å] between the thiophene rings of the adjacent cations, forming layers parallel to (011). Furthermore, we studied theoretical studies of this compound, too. Geometry optimization was carried out in gas phase by Density Functional Theory (DFT) method with B3LYP applying 6-311++G** basis set. The obtained results from experimental and theoretical structural properties of compound **5** had been compared to each other.

Keywords: Imidazolidinium salt, synthesis, crystal structure, DFT, C—H...F hydrogen bonds, π-π stacking interactions.

Submitted: July 15, 2016. **Revised:** August 9, 2016. **Accepted:** August 22, 2016.

Cite This: Akkoç S, Türktekin Çelikesir S, Gök Y, Çağlar Yavuz S, Akkurt M, Özdemir N. DFT Studies and Crystal Structure of Synthesized 1,3-bis(2-thiophenylmethyl)-4,5-dihydroimidazolidinium hexafluorophosphate Salt. JOTCSA. 2017;4(1):45–58.
DOI: 10.18596/jotcsa.67666.
***Corresponding author**· E-mail address: senemakkoc@erciyes.edu.tr; T: +90 352 437 52 62; F: +90 352 437 49 33.

INTRODUCTION

Heterocyclic salts are significant in terms of being used as a carbene ancillary ligand in catalytic reactions. Complexes containing heterocyclic groups have high catalytic activities for many useful organic transformations such as C—C and C—N cross-coupling reactions, C—H bond activation and metathesis [1-7]. The catalytic activity can be changed with the substituents on the N atom of the salts such as imidazolium, imidazolidinium or bis-benzimidazolium [5, 8]. Carbon-carbon cross-coupling reactions, which play an important role in the synthesis of natural products, drug design and industrially important starting materials, have been an area of interest for organic chemists for a long time [9-11].

To estimate the structural properties of the compounds, *ab initio* methods such as DFT in the computational chemistry are significant tools. Some chemical and physical properties of the chemical compounds and materials are extensively investigated due to *ab initio* calculations based on the quantum mechanics [12]. DFT is the most widely used for "*ab initio*" calculations of the structure of molecules, atoms, surfaces, crystals and their interactions [13].

Herein, we prepared a heterocyclic salt (**5**) containing thiophene moiety (Scheme 1). The crystalline structure of 1,3-bis(2-thiophenylmethyl)-4,5-dihydroimidazolidinium hexafluorophosphate salt (**5**) was reported in this study. Moreover, we studied the compound's theoretical structural properties with DFT software.

EXPERIMENTAL SECTION

General Method for the Preparation of the Imidazolidinium Salt

The study was made according to method defined in the literature [14, 15]. To a solution of diamine **1** (15 mmol) in toluene (20 mL), heteroaryl-2-carbaldehyde **2** (29 mmol) was added at ice bath temperature. After the obtained mixture was stirred at 0 ºC for 18 h, the solvent in the medium was removed *in vacuo*. The formed Schiff base **3** was crystallized from diethyl ether/hexane (1:2) mixture at 25 °C. To a solution of Schiff base **3** (24 mmol) in methyl alcohol (40 mL), $NaBH_4$ (48 mmol) was added. After the mixture was stirred for 24 h, the solvent was removed. The heteroaryl-substituted diamine **4** as the product was crystallized from a mixture of dichloromethane/diethyl ether (1:1). Ammonium hexafluorophosphate (NH_4PF_6) (1.0 mmol) was added to a solution of heteroaryl-substituted diamine **4** (1.0 mmol) in $CH(OEt)_3$ (5 mL) and the reaction mixture was heated for 12 h at 80 °C. A solid was seen to precipitate. Then the heteroaryl-substituted heterocyclic salt **5** was crystallized from ethyl alcohol/diethyl ether (1:2) mixture. Results of ^1H NMR, ^{13}C NMR (by using Bruker AC300P FT spectrometer operating) and melting point (by using an Electrothermal 9200 melting point apparatus) can be found in a previous study [15].

X-ray Crystal Structure

Single-crystal diffraction data were gathered by a STOE IPDS II diffractometer with graphite monochromated Mo-Kα radiation (λ = 0.71073 Å), in the rotation method, at 25 °C. All data were made accurate for polarization, Lorentz and absorption effects [16]. Crystal structure was solved by direct methods using program SHELXS97 and refined by the full-matrix least-squares method for all F^2 data using the SHELXL97 [17] programs. With the anisotropic displacement parameters, all non-hydrogen atoms were refined. All H atoms were positioned geometrically and were refined using a riding model with $U_{iso}(H) = 1.2U_{eq}(C)$. The fluorine

atoms of the hexafluorophosphate anion are disordered over two sites with occupancies of 0.588(13) and 0.412(13). The crystallographic data and the refinement procedure details for the title compound are summarized in Table 1. The list of selected geometric parameters is given in Table 2.

Table 1. The crystallographic data and the refinement procedure details for **5**

Chemical formula	$C_{13}H_{15}F_6N_2PS_2$
M_r	408.36
Crystal system, space group	Monoclinic, $P2_1/c$
Temperature (K)	293
a, *b*, *c* (Å)	20.3151 (12), 6.0059 (3), 14.9112 (9)
β (°)	109.987 (4)
V (Å^3)	1709.74 (17)
Z	4
μ (MoKα) (mm^{-1})	0.46
Crystal size (mm)	0.50 × 0.45 × 0.39
No. of measured, independent and observed [$I > 2\sigma(I)$] reflections	10743, 3743, 2447
R_{int}	0.026
θ values (°)	θ_{max} = 27.1, θ_{min} = 2.1
$(\sin \theta/\lambda)_{max}$ (Å^{-1})	0.642
Range of *h*, *k*, *l*	*h* = -25→25, *k* = -7→6, *l* = -18→18
Refinement on	F^2
$R[F^2 > 2\sigma(F^2)]$, $wR(F^2)$, *S*	0.060, 0.182, 1.08
No. of reflections	3743
No. of parameters	262
No. of restraints	40
H-atom treatment	H-atom parameters constrained
$(\Delta/\sigma)_{max}$	< 0.001
$\Delta\rho_{max}$, $\Delta\rho_{min}$ (e Å^{-3})	0.62, -0.48

The computations were carried out at 6-311++G** levels using the SPARTAN 10 software package [18], with operating density functional methods. The calculations were done for the

optimized structures in the gas phase. SPARTAN software [19] is a molecular modeling and computational chemistry application from wavefunction.

RESULTS AND DISCUSSION

Characterization of the Heteroaryl-substituted Heterocyclic Salt

In a previous study, the structure of 1,3-bis(2-thiophenylmethyl)imidazolidinium salt was determined by elemental analysis, ^{1}H and ^{13}C NMR [15]. Furthermore, the structure of this compound was completely characterized with X-ray studies. The ^{1}H NMR spectrum of the salt assigned the structures. The resonance for C(2)-H was observed as a sharp singlet 8.71 ppm [15]. The imino carbon atom was observed at 158.0 ppm in ^{13}C NMR.

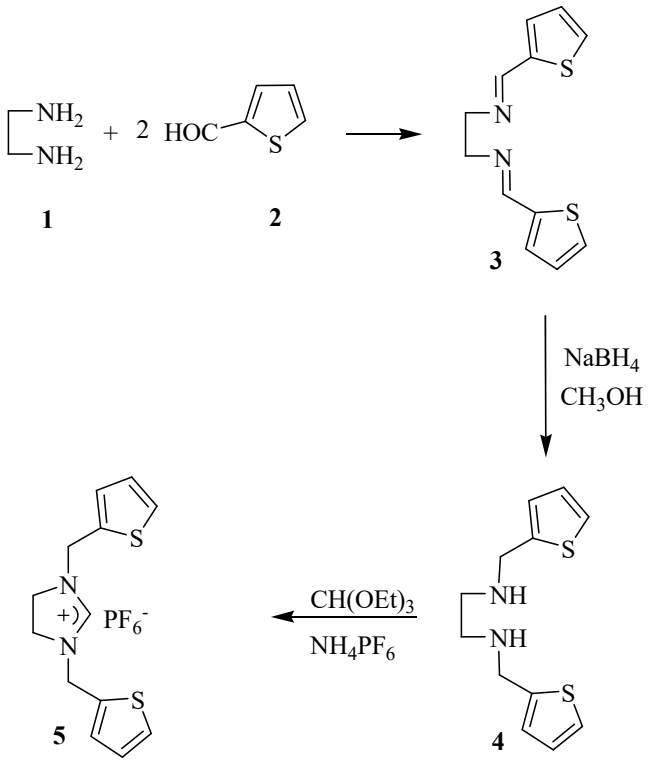

Scheme 1. Synthesis of imidazolidinium salt [15].

Single crystal and molecular structure

A single crystal of the imidazolidinium salt, which is adequate for X-ray diffraction, was acquired by slow diffusion of dichloromethane into diethyl ether solutions at 25 °C. The molecular view of compound is represented in Figs. 1 and 2.

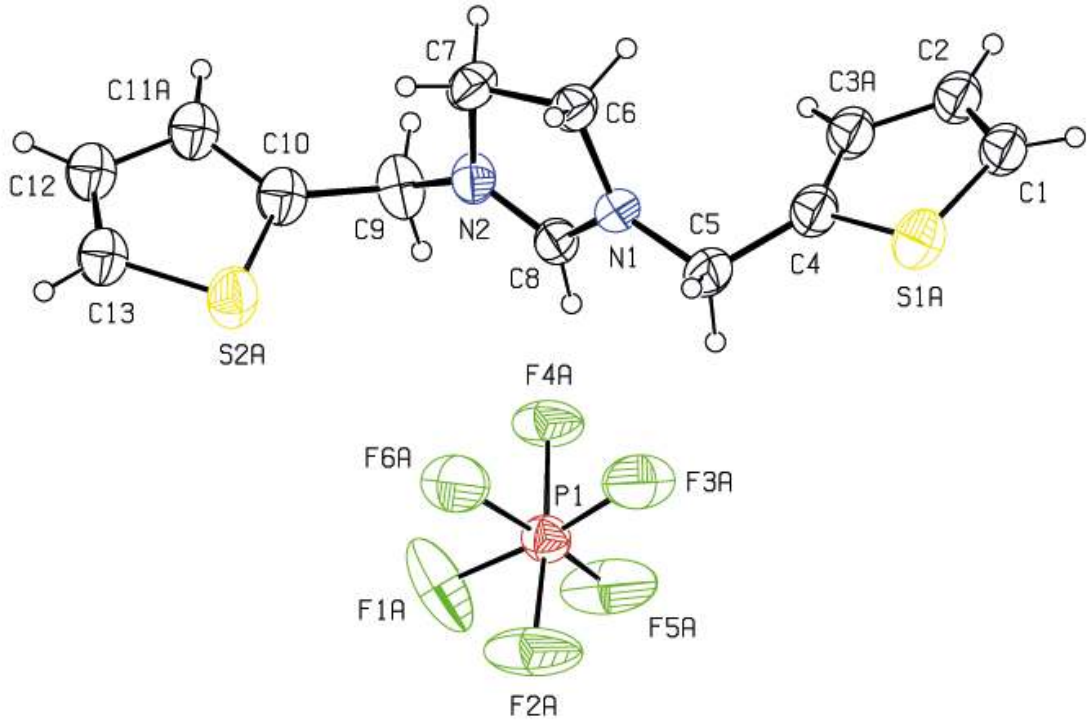

Figure 1. An ORTEP plot [20] of the molecular structure of **5**. At the 30 % probability level, displacement ellipsoids for non-H atoms are drawn. Only major disorder component is shown.

In compound **5** (Figure 1), 1,3-bis(2-thiophenylmethyl)-4,5-dihydroimidazolidinium cation has a thiophenyl-ring flip disorder. Two positions of both thiophene rings in the cation are obtained by an 180° rotation about the thiophene-CH_2 bonds.

A similar thiophene ring disorder has been observed in a thiophene derivative, 1,3-bis(2-thiophenylmethyl)-4,5-dihydroimidazolidinium trichlorido([eta]6-*p*-cymene)ruthenate(II)

[21]. The bond lengths and angles in **5** were found to be similar to those reported for the structures of the related compounds with furfuryl or thenyl moities [22, 23].

The imidazolidine ring (N1/N2/C6–C8) is essentially planar [maximum deviations = -0.008(2) Å for N1 and 0.007(3) Å for C8]. Because of the *π*-electron delocalization on the imidazolium ring, the N1—C8 and N2—C8 bond lengths of 1.303(4) and 1.287(4) Å in the imidazolidine ring are shorter than the average single C—N bond length of 1.48 Å. This case shows double bond character in these C—N bonds and demonstrates a partial electron delocalization within the N1—C8—N2 fragment.

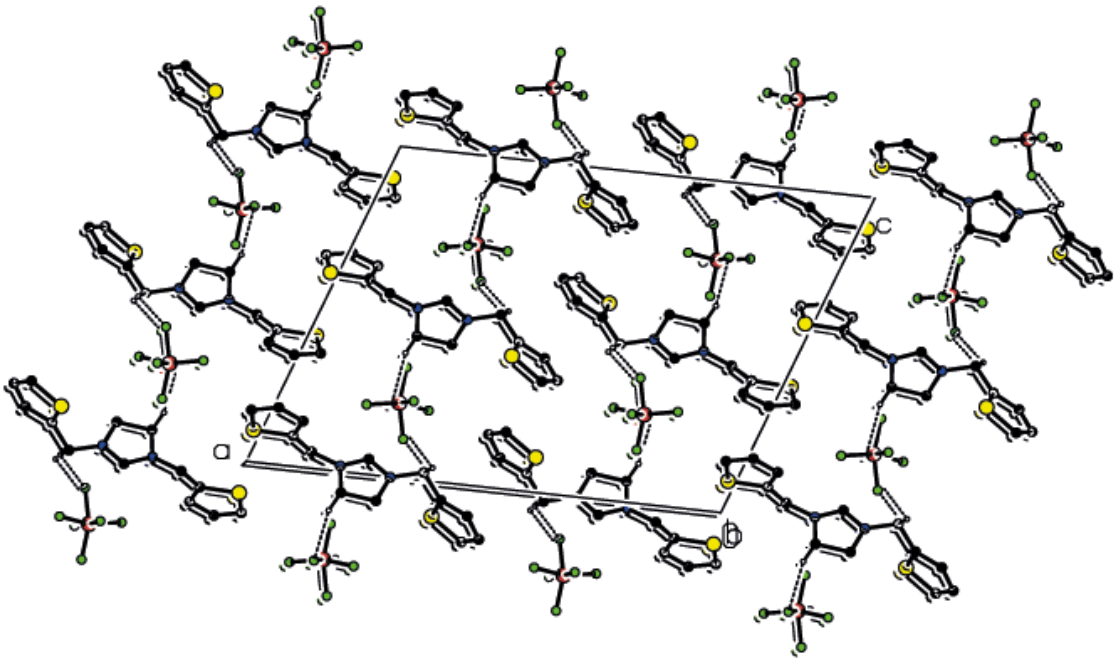

Figure 2. View of the hydrogen bonding and molecular packing of **5** in the unit cell. H atoms not involved in H bonding are omitted for clarity and only major disorder component is shown.

In the crystal structure of compound **5**, adjacent anion and cations are connected by C—H···F hydrogen bonds and slipped π–π inter actions [*Cg2*...*Cg2*^{i}= 3.890(3) Å; where *Cg*2 is

the centroid of the S2A/C10/C11A/C12/C13 thiophene ring; symmetry code (i): 1-x, 1-y, 1-z], with an interplanar distance of 3.660(2) Å and resulting a slipping distance of 1.320Å, forming a three-dimensional network (Table 1 and Figure 2).

Table 2. Selected geometric parameters (Å, º) for **5**

C1—C2	1.330 (5)	C10—S2B	1.616 (11)
C1—C3B	1.492 (19)	C10—S2A	1.704 (4)
C1—S1A	1.679 (4)	C11A—C12	1.420 (9)
C2—C3A	1.389 (7)	S2A—C13	1.667 (4)
C2—S1B	1.544 (13)	C11B—C13	1.518 (18)
C3A—C4	1.402 (7)	S2B—C12	1.566 (10)
S1A—C4	1.709 (4)	C12—C13	1.317 (5)
C3B—C4	1.526 (16)	F1A—P1	1.511 (8)
S1B—C4	1.544 (13)	F2A—P1	1.548 (9)
C4—C5	1.494 (5)	F3A—P1	1.605 (7)
C5—N1	1.455 (4)	F4A—P1	1.593 (6)
C6—N1	1.471 (4)	F5A—P1	1.544 (7)
C6—C7	1.529 (4)	F6A—P1	1.562 (7)
C7—N2	1.465 (4)	F1B—P1	1.507 (12)
C8—N2	1.287 (4)	F2B—P1	1.534 (11)
C8—N1	1.303 (4)	F3B—P1	1.433 (13)
C9—N2	1.454 (4)	F4B—P1	1.484 (13)
C9—C10	1.497 (5)	F5B—P1	1.514 (12)
C10—C11A	1.420 (8)	F6B—P1	1.512 (8)
C10—C11B	1.519 (16)		
C1—S1A—C4	92.45 (17)	C8—N1—C6	109.5 (3)
C4—S1B—C2	98.3 (6)	C5—N1—C6	123.9 (3)
N2—C8—N1	114.5 (3)	C8—N2—C9	125.2 (3)
C13—S2A—C10	92.74 (19)	C8—N2—C7	110.4 (3)
C12—S2B—C10	94.9 (4)	C9—N2—C7	123.8 (3)
C8—N1—C5	126.3 (3)		
C4—C5—N1—C8	-119.8 (4)	C10—C9—N2—C8	-125.8 (4)

Table 3. Hydrogen-bond parameters (Å, °) for **5**

	D—H	H...A	D...A	D—H...A
C6—H6A···F2Ai	0.97	2.48	3.413 (9)	162
C8—H8···F3A	0.93	2.38	3.266 (10)	159
C9—H9A···F6Aii	0.97	2.55	3.231 (11)	128

Symmetry codes: (i) x, 1/2-y, 1/2+z; (ii) x, 1+y, z.

Theoretical studies

Molecular structure and physical properties of the molecule can be predicted accurately by the help of computational methods based on DFT. The theoretical and experimental structural properties of compound **5** were examined. Experimental geometric parameters (bond angles and lengths) were compared with computed values from density functional theory with B3LYP 6-311++G** basis set. The lowest energy conformation of compound **5** was used in theoretical calculations. Theoretical calculation results were obtained in good agreement with experimental data.

Table 4. Experimental and calculated selected geometric parameters for **5**

Bond Lengths (Å)	**Experimental**	**Calculated(Vacuum)**
C1—C2	1.330 (5)	1.364
S1A—C4	1.709 (4)	1.748
C4—C5	1.494 (5)	1.497
C5—N1	1.455 (4)	1.473
C6—N1	1.471 (4)	1.482
C6—C7	1.529 (4)	1.548
C7—N2	1.465 (4)	1.479
C8—N1	1.303 (4)	1.317
C9—N2	1.454 (4)	1.475
C9—C10	1.497 (5)	1.500
C10—S2A	1.704 (4)	1.748
C11A—C12	1.420 (9)	1.425
C12—C13	1.317 (5)	1.366
F3A—P1	1.605 (7)	1.652
Bond Angles (°)		
C1—S1A—C4	92.45 (17)	91.54
C8—N1—C6	109.5 (3)	109.17
C5—N1—C6	123.9 (3)	122.59
N2—C8—N1	114.5 (3)	114.36
C13—S2A—C10	92.74 (19)	91.53
C8—N2—C9	125.2 (3)	125.34
C8—N2—C7	110.4 (3)	109.90
C9—N2—C7	123.8 (3)	124.73

CONCLUSIONS

In this work, the synthesized salt was characterized by using single crystal X-ray diffraction method. The molecular structures were theoretically investigated by the DFT calculations. The obtained geometrical parameters of the optimized geometries were in agreement with X-ray structure results.

ACKNOWLEDGEMENTS

The authors acknowledge the Faculty of Arts and Sciences, Ondokuz Mayıs University, Turkey, for the use of the Stoe *IPDS* 2 diffractometer (purchased under grant F.279 of the

University Research Fund).

SUPPORTING INFORMATION

CCDC 1014061 contains the supplementary crystallographic data for this paper. These data can be obtained, free of charge, from The Cambridge Crystallographic Data Centre via http://www.ccdc.cam.ac.uk/deposit.

REFERENCES

1. Akkoc S, Gok Y. Synthesis and characterization of 1-phenyl-3-alkylbenzimidazol-2-ylidene salts and their catalytic activities in the Heck and Suzuki cross-coupling reactions. Journal of Coordination Chemistry. 2013 Apr;66(8):1396–404. DOI: 10.1080/00958972.2013.786053.

2. Winkelmann OH, Riekstins A, Nolan SP, Navarro O. A Comparative Study on (NHC)Pd(acac)Cl Complexes (NHC = N-heterocyclic carbene): Indications for the Origin of the Different Reactivity of Saturated and Unsaturated NHC in Cross-Coupling Reactions. Organometallics. 2009 Oct 12;28(19):5809–13. DOI: 10.1021/om900677v.

3. Akkoç S, Gök Y, Akkurt M, Tahir MN. Catalytic activities in the direct C5 arylation of novel palladium N-heterocyclic carbene complexes containing benzimidazol-2-ylidene nucleus. Inorganica Chimica Acta. 2014 Mar;413:221–30. DOI: 10.1016/j.ica.2014.01.015.

4. Ritter T, Day MW, Grubbs RH. Rate Acceleration in Olefin Metathesis through a Fluorine−Ruthenium Interaction. Journal of the American Chemical Society. 2006 Sep;128(36):11768–9. DOI: 10.1021/ja064091x.

5. Yılmaz Ü, Şireci N, Deniz S, Küçükbay H. Synthesis and microwave-assisted catalytic activity of novel bis-benzimidazole salts bearing furfuryl and thenyl moieties in Heck and Suzuki cross-coupling reactions. Applied Organometallic Chemistry. 2010;n/a-n/a.

[6] Akkoç S, Gök Y, İlhan İ Ö, Kayser V. N-Methylphthalimide substituted benzimidazolium salts and PEPPSI Pd-NHC complexes: synthesis, characterization and catalytic activity in carbon-carbon bond forming reactions. Beilstein Journal of Organic Chemistry. 2016 Jan; 12: 81-8. DOI:10.3762/bjoc.12.9

[7] Akkoç S, Gök Y, İlhan İ Ö, Kayser V. In situ generation of efficient palladium N-heterocyclic carbene catalysts using benzimidazolium salts for the Suzuki-Miyaura cross-coupling reaction. Current Organic Synthesis. 2016; 13. DOI: 10.2174/1570179413666151218200334

[8] Durap F, Metin Ö, Aydemir M, Özkar S. New route to synthesis of PVP-stabilized palladium(0) nanoclusters and their enhanced catalytic activity in Heck and Suzuki cross-coupling reactions. Applied Organometallic Chemistry. 2009 Oct; 23: 498–503. DOI: 10.1002/aoc.1555

[9] Aktaş A, Akkoç S, Gök Y, Palladium catalyzed Mizoroki-Heck and Suzuki-Miyaura reactions using napthalenomethyl-substituted imidazolidin-2-ilidene ligands in aqueous media. Journal of Coordination Chemistry. 2013 Aug; 66: 2901-9. DOI: 10.1080/00958972.2013.819092.

[10] Resch V, Schrittwieser J H, Siirola E, Kroutil W. Novel carbon-carbon bond formations for biocatalysis. Current Opinion in Biotechnology. 2011 Feb; 22: 793-9. DOI: 10.1016/j.copbio.2011.02.002.

[11] Minto R E, Blacklock B J. Biosynthesis and function of polyacetylenes and allied natural products. Progress in Lipid Research. 2008 Jul; 47(4): 233-306. DOI: 10.1016/j.plipres.2008.02.002.

[12] Kart H H, Özdemir Kart S, Karakuş M, Kurt M. Ab initio/DFT calculations of butyl ammonium salt of O,O′-dibornyl dithiophosphate. Spectrochimica Acta Part A: Molecular and Biomolecular Spectroscopy. 2014 Aug; 129: 421–8. DOI: 10.1016/j.saa.2014.03.076.

[13] Argaman N, Makov G. Density functional theory: An introduction, American Journal of Physics. 68 (2000) 69-79. DOI.org/10.1119/1.19375.

[14] Akkoç S, Gök Y, Akkurt M, Tahir M N, Imidazole, pyrimidine and diazepine containing heteroaryl-substituted heterocyclic salts as efficient ligand precursors for Mizoroki-Heck coupling reaction: synthesis, structural characterization and catalytic activities, Journal of the Iranian Chemical Society. 2014 Mar; 11: 1767-74. DOI: 10.1007/s13738-014-0449-z.

[15] Ozdemir İ, Gurbuz N, Gok Y, Cetinkaya B. *N*-functionalized azolin-2-ylidene-palladium-catalyzed heck reaction. Heteroatom Chemistry. 2008 Jan; *19(1)*: 82-6. DOI: 10.1002/hc.20415.

[16] Stoe & Cie (2002). *X-AREA* and *X-RED32*. Stoe & Cie, Darmstadt, Germany.

[17] Sheldrick G M. A short history of *SHELX*. Acta Crystallographica Section A. 2008; A64: 112–122. DOI:10.1107/S0108767307043930.

[18] Spartan'10; Wavefunction, Inc.: Irvine, CA, 2011.

[19] Young D. Computational Chemistry. Wiley-Interscience, 2001. Appendix A. A.1.6 pg 330, SPARTAN.

[20] Farrugia L J. WinGX and ORTEP for Windows: an update. Journal of Applied Crystallography. 2012 Jun; 45: 849–54. ISSN: 0021-8898.

[21] Arslan H, VanDerveer D, Özdemir I, Gürbüz N, Gök Y, Çetinkaya B. 1,3-bis(2-thienylmethyl)-4,5-dihydroimidazolium trichlorido(6-p-cymene)ruthenate(II). Acta Crystallographica Section E. 2009; E65: 165–6. ISSN: 1600-5368.

[22] Yıldırım S Ö, Akkurt M, Şireci N, Küçükbay H, Kazak C. 2-[(2-Furylmethyl)sulfanyl]-1*H*-3,1-benzimidazol-3-ium chloride dihydrate. Acta Crystallographica Section E. 2007; E63: 2433. ISSN: 1600-5368.

[23] Akkurt M, Şireci N, Deniz S, Küçükbay H, Büyükgüngör O. 1,3-Difurfuryl-benzimidazolium chloride monohydrate. Acta Crystallographica Section E. 2009; E65: 2037–8. ISSN: 1600-5368.

Türkçe Öz ve Anahtar Kelimeler

Sentezlenmiş 1,3-bis(2-tiyofenilmetil)-4,5-dihidroimidazolidinyum heksaflorofosfat Tuzunun DFT Çalışmaları ve Kristal Yapısı

Senem Akkoç, Sevim Türktekin Çelikesir, Yetkin Gök, Sevtap Çağlar Yavuz, Mehmet Akkurt ve Namık Özdemir

Öz: Sentezlenen **5** bileşiği ($C_{13}H_{15}N_2S_2$)[PF_6] X-ışını saçılması yöntemiyle tam olarak karakterize edilmiştir. Bu bileşikte, asimetrik birim 1,3-(2-tiyofenilmetil)-4,5-dihidroimidazolyum katyonu ve bir heksaflorofosfat anyonu içermektedir. Tiyofen –CH_2 bağları etrafında 180 °C dönmeden ötürü, katyondaki tiyofen halkaları düzensizdir [bölge kullanım faktörleri = sırasıyla 0,903(4)/0,097(4) ve 0,837(5)/0,163(5)]. İmidazolidin halkasındaki kısa C-N bağ uzunlukları [1,303(4) ve 1,287(4) Å] N-C-N kısmı içinde kısmi elektron delokalizasyonu göstermektedir. Anyon ve katyonlar intramoleküler C-H...F hidrojen bağları ve üç π-π istiflenmesi ile komşu katyonların tiyofen halkaları arasında bağlanmıştır [merkezler arası uzaklık = 3,890(3), 3,852(5) ve 3,816(7) Å], (011)'e paralel tabakalar meydana gelmiştir. Bunun ötesinde, bu bileşiğin teorik çalışmaları da yapılmıştır. Geometrik en uygunlaştırma gaz fazında Yoğunluk Fonksiyonel Teorisi (DFT) yöntemiyle B3LYP 6-311++G** temel seti kullanılarak yürütülmüştür. **5** bileşiğinin deneysel ve teorik çalışmalardan elde edilen sonuçları birbiriyle karşılaştırılmıştır.

Anahtar kelimeler: İmidazolidinyum tuzu, sentez, kristal yapısı, DFT, C-H…F hidrojen bağları.

Sunulma: 15 Temmuz 2016. **Düzeltme:** 9 Ağustos 2016. **Kabul:** 22 Ağustos 2016.

Preparation and Characterization of TAMP/TIMP-Ti and Zr Compounds and Their Catalytic Activity over Propylene Oxide and ε-Caprolactone

Asgar Kayan*[1]
[1]Department of Chemistry, Kocaeli University, Kocaeli, 41380, Turkey.

Abstract: Titanium and zirconium 2-((p-tolylamino/p-tolylimino)methyl)phenolate (TAMP and TIMP) were prepared by reaction of Ti- and Zr-alcoholates with 2-((p-tolylamino)methyl)phenol (TAMPH) and 2-((p-tolylimino)methyl)phenol (TIMPH) in ethyl alcohol. To characterize these compounds, ^{1}H, ^{13}C NMR, FTIR, mass spectroscopies, and elemental analysis were used. The TAMP and TIMP metal compounds can be formulated as $(TAMP)_3M_2(OR)O_2$ and $(TIMP)_4M_2O_2$, respectively. The catalytic activity of these compounds was checked in polymerization reactions with propylene oxide (PO) and ε-caprolactone (ε-CL) and Ti-TAMP was effective**.** Poly-propylene oxide (PPO) and poly-caprolactone (PCL) were identified by ^{1}H, ^{13}C NMR and gel permeation chromatography (GPC).

Keywords: Metal alkoxide, catalyst, Schiff base, ε-caprolactone, polymer.

Submitted: June 28, 2016. **Revised:** August 06, 2016. **Accepted:** September 06, 2016.

Cite this: Kayan A. Preparation and Characterization of TAMP/TIMP-Ti and Zr Compounds and Their Catalytic Activity over Propylene Oxide and ε-Caprolactone. JOTCSA. 2017;4(1):59–80.

DOI: 10.18596/jotcsa.14346.

*Corresponding author. E-mail: akayan@kocaeli.edu.tr.

INTRODUCTION

Schiff-bases, carboxylate anions, and their derivatives are useful ligands for the construction of new interesting metal catalysts [1-7]. Metal alcoholate compounds modified by carboxylates, β-diketonates, and Schiff-bases have attracted much attention as catalysts for ring opening polymerization of oxirane derivatives, lactides, and ε-caprolactone [8-10]. The chemistry of the compounds of the type Ti- and Zr-(OR) (2-((p-tolylamino/p-tolylimino)methyl)phenolate) in which OR^- is a potentially active ligand for polymerization catalysis remains much less studied. Metal Schiff base compounds have used as catalysts for ring opening of ε-caprolactone and propylene oxide. Among those catalysts, some catalysts were low performance of ring-opening polymerization (ROP) of ε-CL and PO. ROP of ε-CL and PO has been gaining attention due to its wide range of applications such as production of nonionic surfactants, packaging materials, adhesives, plastics, and coating materials [10-13].

Therefore, it is important to synthesize new compounds containing single-site alcoholate group which is active in polymerization reactions. A major interest of this study is to synthesize and characterize zirconium and titanium catalysts containing both an active group of alcoholate and ligands (TAMP and TIMP) with nitrogen and oxygen as donor atoms. The second interest of this study is to compare the reactivity of ligands (TAMP and TIMP) against to metal alcoholates. Finally, seeing their catalytic activity over ring opening of PO and ε-CL in mild reaction conditions was also one of the interests of this study.

EXPERIMENTAL

Materials and instrumentation

Tetraisopropyl orthotitanate (98%, Merck), tetrapropyl zirconate (70% in propyl alcohol, Fluka), tetrabutyl zirconate (80% in *tert*-butanol, Fluka), salicylaldehyde (Sigma-Aldrich), *p*-toluidine (99%, Merck), sodium borohydride (98%, Merck), propylene oxide (99%, Alfa Aesar), ε-caprolactone (97%, Sigma-Aldrich), and tetrahydrofuran (THF) (99.9%, Merck) were used as received. *n*-Butyl alcohol (99%, Merck), n-propyl alcohol (99%, Sigma-Aldrich), chloroform

(99.8%, Sigma-Aldrich) and isopropyl alcohol (99.5%, Merck) were dried over activated 4A° molecular sieves before use. All syntheses were carried out in closed vessels under ambient atmosphere. TAMPH and TIMPH were prepared as in literatures [14,15].

^{1}H and $^{13}C\{^{1}H\}$NMR experiments were performed on a Bruker 300 and 400 MHz NMR spectrometers. FTIR spectra of compounds were measured on a Shimadzu 8201/86601 PC spectrometer. The elemental analyses were performed on a LECO CHNS-932 elemental analyzer. Molecular mass measurements of compounds were performed on SCIEX 4000 QTRAP LC-MS/MS and Waters SYNAPT MS (HRMS, TOF/MS). Electrospray ionization (ESI ±) method was used in both mass spectrometers to produce ions. Gel permeation chromatography measurements (GPC) were carried out on a Shimadzu prominence GPC system including RID-10A refractive index detector, a LC-20AD solvent delivery unit, and two PSS SDV columns (50 and 1000 A˚). The GPC was eluted with THF at 30 °C running at 1.0 mL/min and was calibrated using few polystyrene standards (162 -34300 Da).

Preparation of TIMPH (p-MeC_6H_4)N=CH(C_6H_4-2-OH) (1)

p-Toluidine (6.90 g, 0.064 mol) was added to the stirring solution of salicyl aldehyde (7.98 g, 0.064 mol) in ethanol (50 mL), which was let to react for 3 h at reflux temperature. After that, the solution was cooled to room temperature and an orange solid was formed. It was filtered and washed with ethanol and then dried by vacuum evaporator. Anal. Calcd. For $C_{14}H_{13}NO$ (%), (*Mw* = 211.26 g/mol): C, 79.59; H, 6.20; N, 6.63. Found: C, 79.35; H, 6.28; N, 6.42. MALDI-TOF MS (m/z): [$C_{14}H_{13}NO$] = 212.0 (100%) Da. ^{1}H NMR (300 MHz, $CDCl_3$): δ 2.40 (s, 3H, CH_3), 6.94–7.40 (m, 8 H, PhO, PhN), 8.66 (s, 1 H, CH), 13.40 (s, 1 H, OH) ppm. Elemental analysis, $C_{14}H_{13}NO$ (211.26 g/mol): Calc. C 79.59, H 6.20, N 6.63% ; found: C 79.35, H 6.28, N 6.42. FTIR (KBr pellet, cm^{-1}): 3052, 3022, 2921, 2859, 1616 (C=C, Ar), 1597 (C=C, Ar), 1578 (C=N), 1509, 1498, 1459, 1414, 1367, 1282 (C-O, phenolic), 1181, 1159, 1118, 1033, 910, 851, 835, 816, 788, 750, 634.

Preparation of TAMPH (p-MeC$_6$H$_4$)NHCH$_2$(C$_6$H$_4$-2-OH) (2)

The reaction of salicylaldehyde with p-methylaniline yielded 2-((tolylimino)methyl)phenol. 2-((Tolylimino)methyl)phenol (2×10^{-2} mol) was dissolved in 50 mL of methanol and dioxane at 1: 1 ratio. $NaBH_4$ (2×10^{-2} mol) was added to this solution until the disappearance of yellow color of the Schiff base (1 h). Cold water was added to the solution to form precipitate. The precipitate was recrystallized with methanol to yield 2-((tolylamino)methyl)phenol. ^{1}H NMR ($CDCl_3$, ppm): δ 2.28 (s, 3H, CH_3), 3.87 (s, 1H, NH), 4.34 (s, 2H, CH_2-N), 6.7-6.75 (m, aromatic, 2H), 6.82-6.85 (m, aromatic, 2H), 7.02-7.04 (m, aromatic, 2H), 7.09-7.12 (m, aromatic, 1H), 7.16-7.22 (m, aromatic, 1H), 8.48 (s, 1H, OH). FTIR (KBr pellet, cm^{-1}): 3416 (OH), 3261 (NH), 3011, 2915, 2860, 1612 (C=C, Ar), 1591 (C=C, Ar), 1508, 1454, 1399, 1356, 1290 (C-O, phenolic), 1247, 1184, 1156, 1109, 1055, 975, 909, 862, 817, 751, 716, 704, 609.

Preparation of (TAMP)$_3$Ti$_2$(O^{i}Pr)O$_2$ compound (3)

2-((p-Tolylamino)methyl)phenol (3.10×10^{-3} mol, 0.66 g) was added to the solution of tetraisopropyl orthotitanate (1.55×10^{-3} mol, 0.45 g) in 20 mL of isopropyl alcohol. The reaction mixture was stirred for 3 hours at room temperature. Then, the volatile parts were removed from the yellow-colored product by a vacuum evaporator at 30 ^{o}C. Then the compound was recrystallized from hexane. Elemental analysis ($C_{45}H_{49}N_3O_6Ti_2$, (TAMP)$_3$Ti$_2$(O^{i}Pr)O$_2$, M_w = 823.62 g/mol): Calc. C 65.6, H 6.00, N 5.10%. Found: C, 65.8, H 6.03, N, 5.34%. MS (m/z, for (TAMP)$_3$Ti$_2$(O^{i}Pr)O$_2$): $[C_{45}H_{49}N_3O_6Ti_2{}^{48}Na]^+$ = 848.4 (16%), $[C_{45}H_{49}N_3O_6Ti^{48}]^+$ = 775.4, $[C_{45}H_{49}N_3O_6Ti^{47}]^+$ = 774.4, $[C_{45}H_{49}N_3O_6Ti^{46}]^+$ = 773.4, $[C_{42}H_{42}N_3O_3Ti^{48}]^+$ = 684.3 Da. ^{1}H NMR ($CDCl_3$, ppm): δ 1.23 (d, CH_3, O^{i}Pr), 2.30 (s, CH_3Ph), 4.05 (septet, OCH, O^{i}Pr), 4.43 (s, CH_2N), 6.3-7.4 (m, CH, aromatic). ^{13}C NMR ($CDCl_3$, ppm): δ 20.54 (CH_3Ph), 25.35 (CH_3, O^{i}Pr), 49.37 (CH_2N), 64.50 (OCH, O^{i}Pr), 116.24 (Ar), 116.70 (Ar), 119.90 (Ar), 122.91 (Ar), 128.61 (Ar), 129.17 (Ar), 129.67 (Ar), 130.46 (Ar), 144.8 (=CipsoN, Ar), 157.0 (=C-O, Ar). FTIR (KBr pellet, cm^{-1}): 3261 (NH), 3013, 2916, 2860, 1613 (C=C, Ar), 1593 (C=C, Ar), 1514, 1489, 1456, 1402, 1250, 822, 754.

Preparation of $(TIMP)_4Ti_2O_2$ compound (4)

2-((p-Tolylimino)methyl)phenol (3.12×10^{-3} mol, 0.66 g) was added to the solution of tetraisopropyl orthotitanate (1.56×10^{-3} mol, 0.45 g) in 20 mL of isopropyl alcohol. The reaction mixture was stirred for 3 hours at room temperature. Then, the volatile parts were removed from the yellow product by a vacuum evaporator at 30 °C. Then the compound was washed three times with n-heptane and dried under reduced pressure. Elemental analysis ($C_{56}H_{48}N_4O_6Ti_2$, $(TIMP)_4Ti_2O_2$, M_w = 968.74 g/mol): Calc. C 69.43, H 4.99, N 5.78%. Found: C 68.47, H 5.07, N 5.10%. MS (m/z): [$C_{56}H_{48}N_4O_6Ti_2^{48}$] = 968.33 (100%), [$C_{56}H_{48}N_4O_6Ti$] = 924.25 (16%) Da. ^{1}H NMR ($CDCl_3$, ppm): δ 2.39 (s, CH_3Ph), 6.94 (t, 1H, CH, aromatic), 7.02 (d, 1H, CH), 7.20 (m, 4H, CH), 7.38 (m, 2H, CH), 8.64 (s, CH=N). ^{13}C NMR ($CDCl_3$, ppm): δ 21.26 (CH_3Ph), 117.41 (Ar), 119.18 (Ar), 119.51 (Ar), 121.20 (Ar), 130.20 (Ar), 132.31 (Ar), 133.09 (Ar), 137.10 (Ar), 144.09 (=CipsoN, Ar), 161.32 (=C-O, Ar), 161.91 (CH=N). FTIR (KBr pellet, cm^{-1}): 3055, 3026, 2920, 2860, 1614 (C=C, Ar), 1601 (C=C, Ar), 1549 (C=N), 1502, 1471, 1446, 1379, 1310 (C-O, phenolic), 1184, 1150, 1122, 1016, 922, 864, 818, 754, 608.

Preparation of $(TAMP)_3Zr_2(O^nPr)O_2$ compound (5)

2-((p-Tolylamino)methyl)phenol (3.10×10^{-3} mol, 0.66 g) was added to the solution of tetrapropyl zirconate (1.55×10^{-3} mol, 0.73 g) in 20 mL of n-propyl alcohol. The reaction mixture was stirred for 3 hours at room temperature. Then, the volatile parts were removed from yellow product by vacuum evaporator at 30 °C. Then the compound was recrystallized with hexane. Elemental analysis ($C_{45}H_{49}N_3O_6Zr_2$, $(TAMP)_3Zr_2(O^nPr)O_2$, M_w = 910.34 g/mol): Calc. C 59.37, H 5.43, N 4.62%. Found: C 58.50, H 5.51, N 4.70%. MS (m/z): [$C_{45}H_{49}N_3O_6Zr^{92}Zr^{94}H]^+$ = 915.5, [$C_{45}H_{49}N_3O_4Zr^{90}Zr^{90}H]^+$ =876.6, [$C_{45}H_{49}N_3O_4Zr^{90}Zr^{91}H]^+$ = 877.6, [$C_{45}H_{49}N_3O_4Zr^{90}Zr^{92}H]^+$ = 878.6, [$C_{43}H_{45}N_3O_4Zr_2H]^+$= 850.4, and [$C_{42}H_{43}N_3O_4Zr_2H]^+$= 834.4 Da. ^{1}H NMR ($CDCl_3$, ppm): δ 0.98 (t, CH_3, O^nPr), 1.63 (m, CH_2, O^nPr), 2.34 (s, CH_3Ph), 3.65 (t, OCH_2, O^nPr), 4.42 (s, CH_2N), 6.81 (d, 2H, CH, aromatic), 6.94 (m, 2H, CH), 7.11 (d, 2H, CH), 7.19 (d, 1H, CH), 7.27 (t, 1H, CH). ^{13}C NMR ($CDCl_3$, ppm): δ 10.00 (CH_3, O^nPr), 20.67 (CH_3Ph), 26.00 (CH_2, O^nPr), 49.28 (CH_2NH), 64.85 (OCH_2, O^nPr), 116.26 (Ar), 116.73 (Ar), 120.07 (Ar), 123.22 (Ar), 128.76 (Ar), 129.23 (Ar), 129.99 (Ar), 130.38 (Ar), 144.85 (=C-NH, Ar), 157.03

(=C-O, Ar). FTIR (KBr pellet, cm^{-1}): 3259 (NH), 3013, 2916, 2860, 1614 (C=C, Ar), 1593 (C=C, Ar), 1511, 1484, 1451, 1400, 1357, 1289 (C-O, phenolic), 1249, 1184, 1155, 1109, 1056, 1041, 976, 903, 863, 819, 753, 710, 705.

Preparation of $(TIMP)_4Zr_2O_2$ compound (6)

2-((p-Tolylimino)methyl)phenol (3.12×10^{-3} mol, 0.66 g) was added to the solution of tetrapropyl zirconate (1.56×10^{-3} mol, 0.73 g) in 20 mL of n-propyl alcohol. The reaction mixture was stirred for 3 hours at room temperature. Then, the volatile parts were removed from the yellow product by a vacuum evaporator at 30 °C. Then, the compound was washed three times with heptane and dried under reduced pressure. Elemental analysis ($C_{56}H_{48}N_4O_6Zr_2$, $(TIMP)_4Zr_2O_2$, M_w = 1055.45 g/mol): Calc. C 63.73.12, H 4.58, N 5.31%. Found: C 63.30; H 4.67; N 5.37%. MALDI-TOF MS (m/z): $[C_{56}H_{48}N_4O_6Zr_2]$ = 1029.82 (100%), $[C_{56}H_{48}N_4O_6Zr^{94}]$ = 967.95(85%) Da. ^{1}H NMR ($CDCl_3$, ppm): δ 2.44 (s, C*H*$_3$), 7.0 (t, 1H, CH), 7.10 (d, 1H, CH), 7.26 (m, 4H, CH), 7.43 (d, CH, aromatic), 8.66 (s, CH=N). ^{13}C NMR ($CDCl_3$, ppm): δ 21.21 (CH_3Ph), 117.34 (Ar), 119.13 (Ar), 119.46 (Ar), 121.15 (Ar), 129.90 (Ar), 130.15 (Ar), 132.27 (Ar), 133.04 (Ar), 137.04 (Ar), 146.00 (=CipsoN, Ar), 161.27 (=C-O, Ar), 161.81 (CH=N). FTIR (KBr pellet, cm^{-1}): 3055, 3022, 2920, 2858, 1618 (C=C, Ar), 1599 (C=C, Ar), 1570 (C=N), 1540 (C=N), 1512, 1474, 1458, 1367, 1309 (C-O, phenolic), 1283, 1184, 1150, 1109, 908, 815, 752, 517.

Preparation of $(TAMP)_3Zr_2(O^nBu)O_2$ compound (7)

2-((p-Tolylamino)methyl)phenol (3.10×10^{-3} mol, 0.66 g) was added to the solution of tetrabutyl zirconate (1.55×10^{-3} mol, 0.74 g) in 20 mL of n-butyl alcohol. The reaction mixture was stirred for 3 hours at room temperature. Then, the volatile parts were removed from yellow product by a vacuum evaporator at 35 °C. Then the compound was recrystallized from hexane. Elemental analysis ($C_{46}H_{51}N_3O_6Zr_2$, $(TAMP)_3Zr_2(O^nBu)O_2$, M_w = 924.36 g/mol): Calc. C 59.77, H 5.56, N 4.55%. Found: C 58.89, H 5.83, N 4.74%. ^{1}H NMR ($CDCl_3$, ppm): δ 0.95 (t, CH_3, O^nBu), 1.4 (m, CH_2, O^nBu), 1.55 (m, CH_2, O^nBu), 2.3 (s, CH_3-Ph), 3.65 (t, OCH_2, O^nBu), 3.9 (s, NH), 4.40 (s, CH_2-N), 6.78 (d, CH), 6.78 (d, CH), 6.92-6.38 (m, CH), 7.07 (d, CH)), 7.16 (d, CH), 7.23 (t, CH). ^{13}C NMR ($CDCl_3$, ppm): δ 13.00 (CH_3, O^nBu), 18.00 (CH_2, O^nBu),

20.71 (CH_3Ph), 35.00 (CH_2, O^{n}Bu), 49.44 (CH_2NH), 63.00 (OCH_2, O^{n}Bu), 116.35 (Ar), 116.80 (Ar), 120.10 (Ar), 123.17 (Ar), 128.78 (Ar), 129.30 (Ar), 130.03 (Ar), 130.53 (Ar), 144.84 (=CipsoN, Ar), 157.12 (=C-O, Ar). FTIR (KBr pellet, cm^{-1}): 3261 (NH), 3022, 2920, 2859, 1616 (C=C, Ar), 1595 (C=C, Ar), 1510, 1451, 1365, 1281 (C-O), 1249, 1183, 1151, 1110, 1051, 975, 909, 857, 816, 751, 703.

Preparation of $(TIMP)_4Zr_2O_2$ compound (8)

2-((p-Tolylimino)methyl)phenol (3.12×10^{-3} mol, 0.66 g) was added to the solution of tetrabutyl zirconate (1.56×10^{-3} mol, 0.75 g) in 20 mL of n-butyl alcohol. The reaction mixture was stirred for 3 hours at room temperature. Then, the volatile parts were removed from the yellow product by a vacuum evaporator at 38 ^oC. Then, the compound was recrystallized from heptane. Elemental analysis ($C_{56}H_{48}N_4O_6Zr_2$, $(TIMP)_4Zr_2O_2$, M_w = 1055.45 g/mol): Calc. C 63.73, H 4.58, N 5.31%. Found: C 63.30, H, 4.80, N, 5.37%. MALDI-TOF MS (m/z): [$C_{56}H_{48}N_4O_4Zr_2^{94}$] =1029.74 (100%), [$C_{56}H_{48}N_4O_6Zr^{94}$] = 967.95 (38%), [$C_{56}H_{48}N_4O_5Zr^{90}$] = 945.80 (28%) Da. ^{1}H NMR ($CDCl_3$, ppm): δ 2.39 (s, CH_3-Ph), 6.94 (t, 1H, CH, aromatic), 7.03 (d, 1H, CH), 7.22 (m, 2H, CH), 7.38 (t, 2H, CH), 8.63 (s, CH=N). ^{13}C NMR ($CDCl_3$, ppm): δ 21.25 (CH_3Ph), 117.40 (Ar), 119.18 (Ar), 119.50 (Ar), 121.19 (Ar), 130.20 (Ar), 132.30 (Ar), 133.09 (Ar), 137.10 (Ar), 146.08 (=CipsoN, Ar), 161.31 (=C-O, Ar), 161.90 (CH=N). FTIR, cm^{-1}: 3053, 3022, 2922, 2859, 1617 (C=C, Ar), 1597 (C=C, Ar), 1570 (C=N), 1509, 1451, 1367, 1309 (C-O, phenolic), 1281, 1183, 1148, 1110, 1033, 909, 851, 816, 788, 751.

PPO and PCL prepared with $(TAMP)_3Ti_2(O^iPr)O_2$ (9)

The TAMP-Ti catalyst (40 mg) was taken in a vial and 1.5 mL of PO was added under nitrogen. The mixture was stirred at different temperatures and times as seen in Table 1. ^{1}H NMR ($CDCl_3$, *δ*, ppm): 3.60 (CH_2), 3.40 (CH), 1.10 (d, CH_3). ^{13}C NMR ($CDCl_3$, *δ*, ppm): 75.40 (CH), 73.30 (CH_2), 17.3 (CH_3).

The polymerization reactions of ε-CL (1.5 mL) with Ti-catalyst (20 mg) were carried out at 100 ^oC under solvent free condition. ^{1}H NMR ($CDCl_3$, ppm), δ: 3.46 (t, $^{\varepsilon}CH_2$-O), 2.31 (t, $^{\alpha}CH_2$-C=O), 1.66 (t, $^{\beta,\delta}CH_2$), 1.39 (t, $^{\gamma}CH_2$). ^{13}C NMR ($CDCl_3$, ppm), δ: 173.79 (C=O), 64.38 ($^{\varepsilon}CH_2$O), 34.34

($^{\alpha}CH_2$), 28.57 ($^{\delta}CH_2$), 25.75 ($^{\beta}CH_2$), 24.80 ($^{\gamma}CH_2$). [O=C-$^{\alpha}CH_2{}^{\beta}CH_2{}^{\gamma}CH_2{}^{\delta}CH_2{}^{\varepsilon}CH_2$O-]. Full characterization of PCL and PPO prepared with different catalysts were given in the literatures [16,17].

RESULTS and DISCUSSION

Reactions of $M(OR)_m$ (M-OR: Ti-O^{i}Pr, Zr-O^{n}Bu, Zr-O^{n}Pr, m: 4 for Ti and Zr) with 2-((*p*-tolylamino)methyl)phenol or 2-((*p*-tolylimino)methyl)phenol with 1: 2 mole ratio in alcohols or chloroform at room temperature produced the compounds (3-8). The formulations of compounds were depended on mass measurements, elemental analysis results, ^1H, ^{13}C NMR and FTIR spectra. The masses of TAMP-M /TIMP-M compounds were determined by mass spectrometries (HRMS and MALDI TOF/TOF). The samples were analyzed under positive ionization conditions when HRMS (TOF/MS) was used. The ESI-MS method was chosen because of ions formed upon ESI under soft ionization condition [18]. In the mass spectra of TAMP/TIMP-metal compounds, isotopic patterns clearly identified metal containing ions, because there were a few relevant ions in spectra. For example, zirconium has four isotopes with significant natural abundance from 89.90 to 93.91 Da. The *m/z* spectrum of $(TAMP)_3Zr_2(O^nPr)O_2$ compound showed ions at $[C_{45}H_{49}N_3O_6Zr^{92}Zr^{94}H]^+$ =915.5, $[C_{45}H_{49}N_3O_4Zr^{90}Zr^{90}H]^+$ =876.6, $[C_{45}H_{49}N_3O_4Zr^{90}Zr^{91}H]^+$ = 877.6, $[C_{45}H_{49}N_3O_4Zr^{90}Zr^{92}H]^+$ = 878.6, $[C_{43}H_{45}N_3O_4Zr_2H]^+$= 850.4, and $[C_{42}H_{43}N_3O_4Zr_2H]^+$ = 834.4 Da. (Figure 1). Especially the masses of TIMP compounds were determined by MALDI-TOF mass spectrometry. Although simple linear MALDI-TOF instrument is rather low resolution mass spectrometer, it gives a distribution of fragments of ions. For example, the MALDI-TOF *m/z* spectrum of $(TIMP)_4Ti_2O_2$ compound showed ions at $[C_{56}H_{48}N_4O_6Ti_2{}^{48}]$ =968.33 (100%) and $[C_{56}H_{48}N_4O_4Ti^{48}]$ = 924.25 (16%) Da (Figure 2). The suggested formula of ligands (TAMP and TIMP) and metal compounds (3-8) were consistent with elemental analysis and ^1H NMR results. MS measurements of TAMP and TAMP-metal compounds showed that compounds were dimeric by an oxo bridge in contrast to $ZrCl_2$-amino acid Schiff base compounds [19].

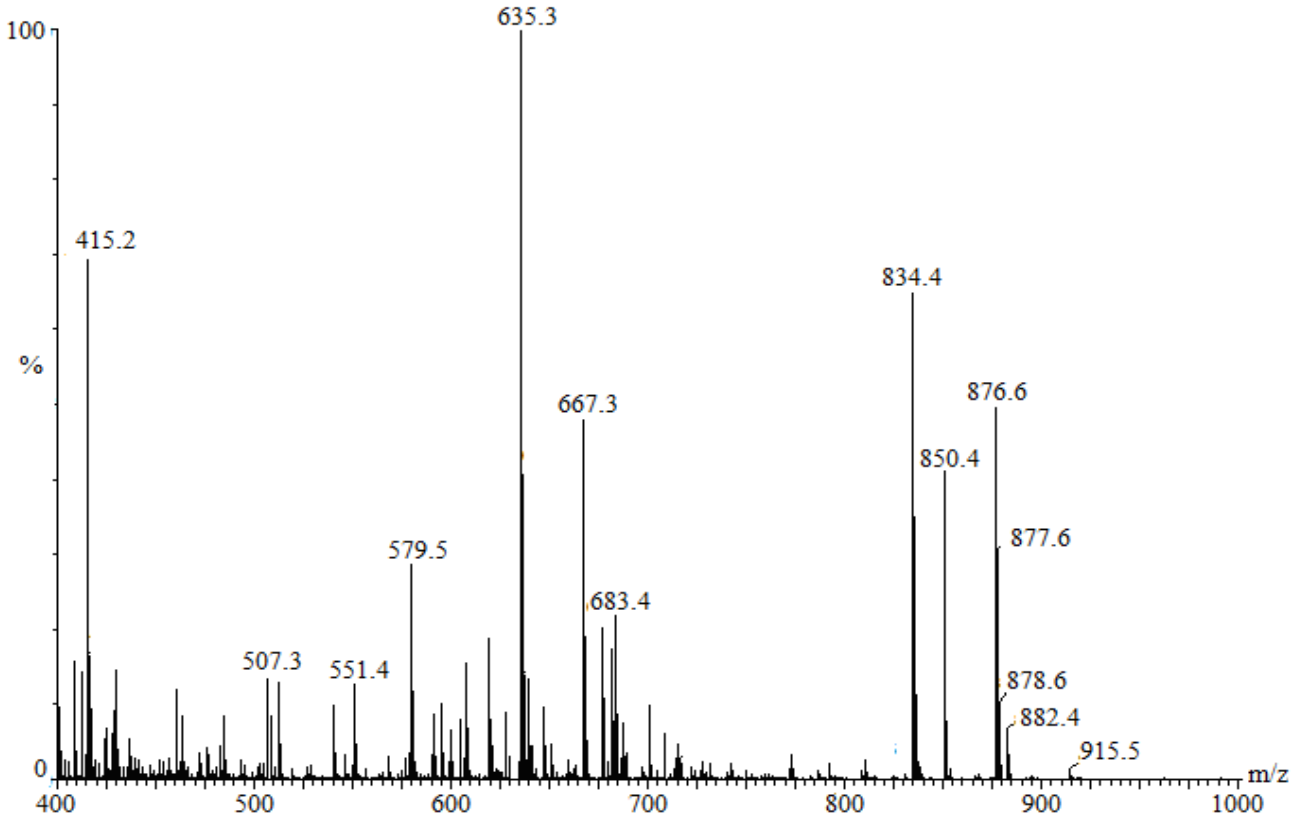

Figure 1. MS spectrum of $(TAMP)_3Zr_2(O^nPr)O_2$ compound under positive ionization conditions.

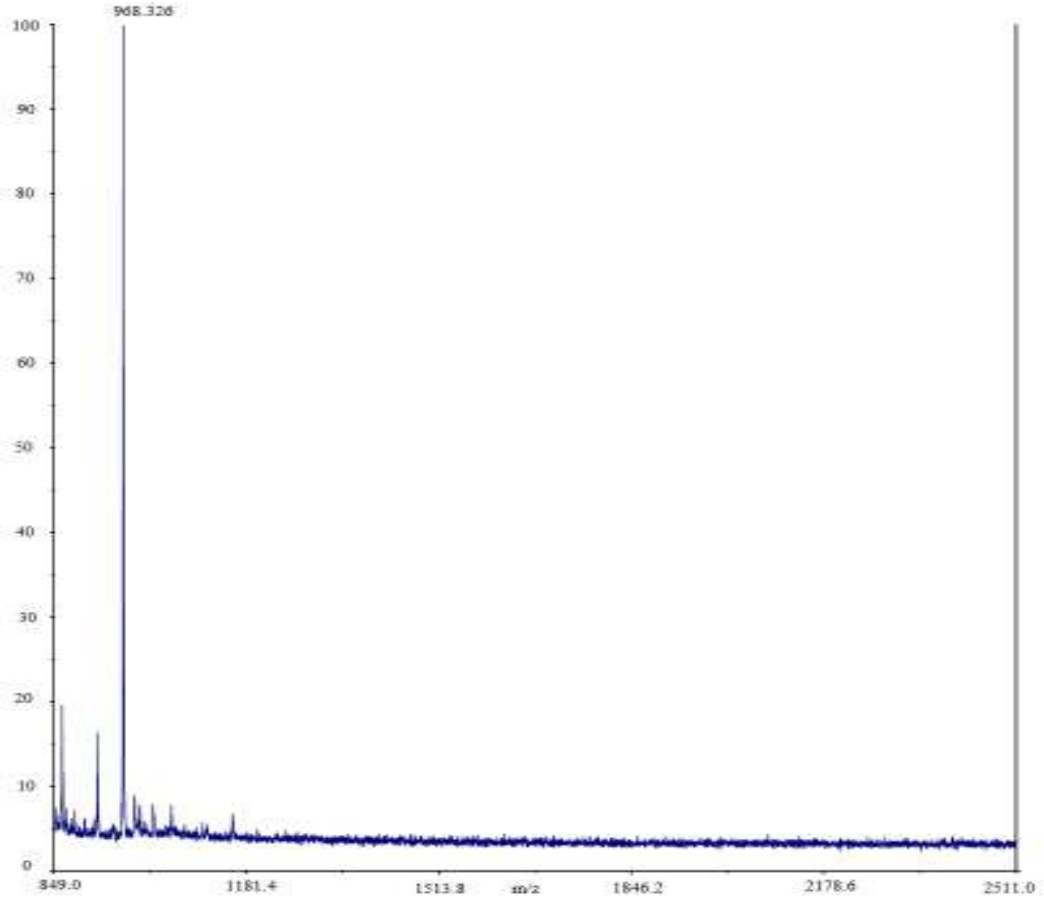

Figure 2. MALDI-TOF/MS spectrum of $(TIMP)_4Ti_2O_2$ compound.

TAMP and TIMP ligands were bound through both O and N atoms at the same time to one metal ion or two metal ions. These bindings are based on FTIR and NMR data of compounds and can be drawn as seen in Scheme 1.

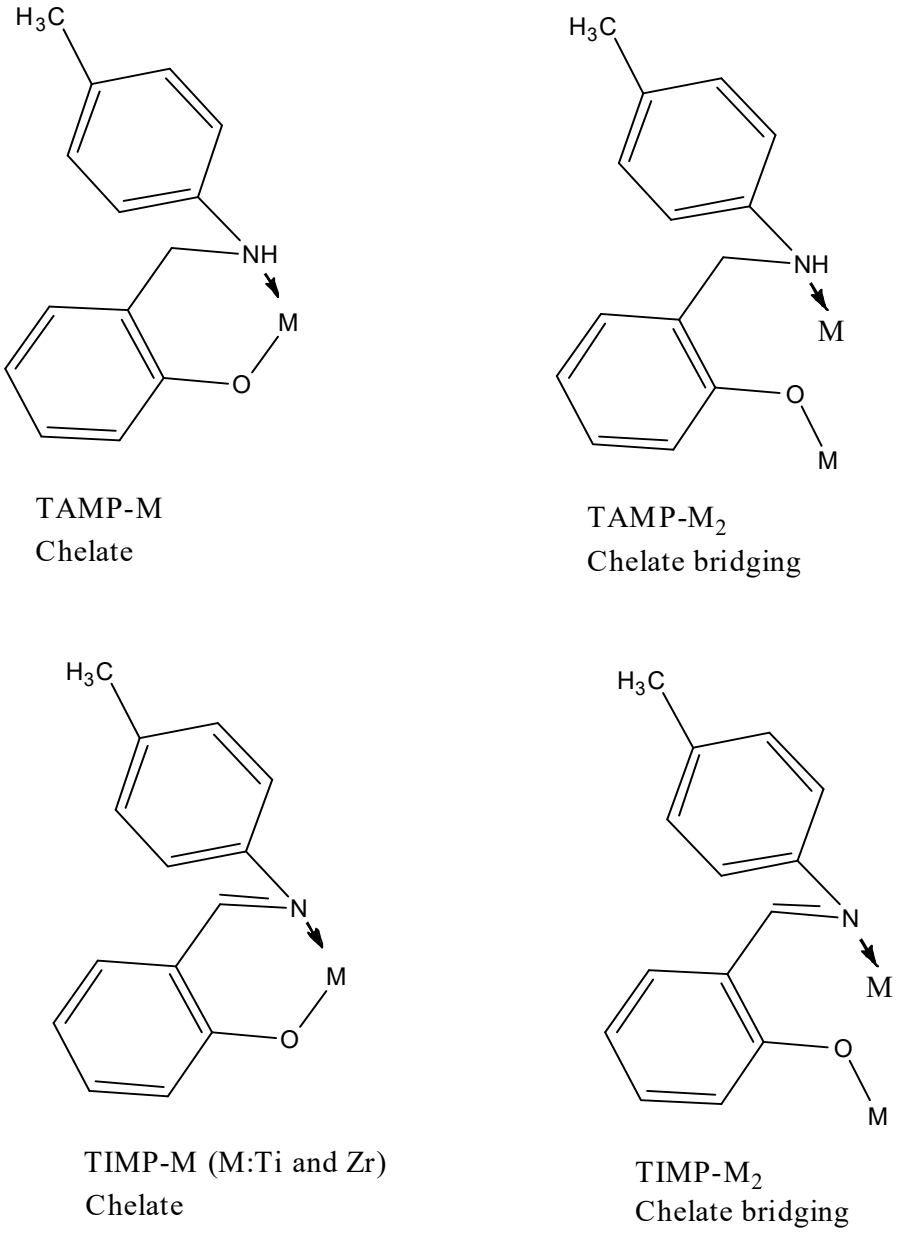

Scheme 1. The structures of TAMP and TIMP-metal compounds.

FTIR spectrum of free 2-((*p*-tolylamino)methyl)phenol exhibited bands at ~3416 and 3261 cm^{-1} corresponding to stretching vibrations of the OH and NH groups, respectively [6,14]. After coordination of TAMP ligand to metal alcoholate, the broad OH band at ~3416 cm^{-1} disappeared and the NH band appeared at slightly different region. These FTIR measurements showed that the formations of metal compounds were stabilized by coordination of the phenoxido ligand and the amine functionality. TIMP ligand was also coordinated to metal centers by forming phenoxido-imino derivatives. A strong band is observed at ~1578 cm^{-1} for

C=N group in the FTIR spectra of TIMPH ligand. Coordination of nitrogen to the metals, the C=N band is shifted to the lower value (1570-1540 cm^{-1}) in the FTIR spectra. The shifting of this group to lower value in the metal compounds suggests the coordination of metal ion through nitrogen atom of C=N group. It is expected that coordination of nitrogen to the metal atom reduces the electron density in the C=N bond and lowers the value of C=N frequency [6,20]. The phenolic C-O stretch appears at ~1282 cm^{-1} in free ligand, whereas it appears at 1312-1308 cm^{-1} in the compounds. This is a sign of bonding through phenolic oxygen. These observations are consistent with literature data [6,20].

The ^1H NMR spectra of TAMP-Zr and TAMP-Ti compounds showed the expected peaks with peak multiplicities. The reaction between $Zr(O^nPr)_4$ and TAMPH can be shown in the Scheme 2.

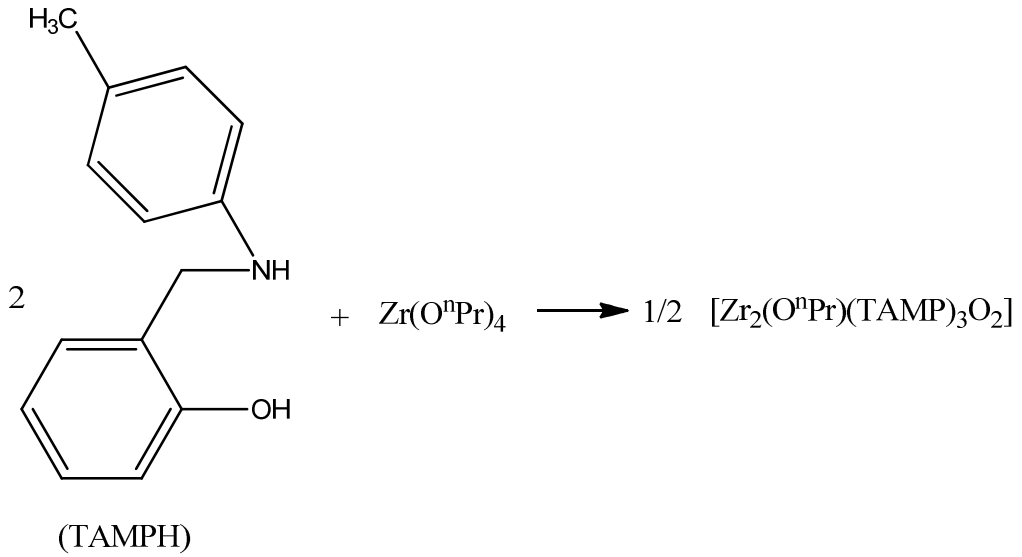

Scheme 2. The reaction between $Zr(O^nPr)_4$ and TAMPH.

^1H NMR spectrum of TAMP-Zr compound showed triplets at 0.98 ppm for CH_3 protons, multiplets at 1.63 ppm for CH_2 protons and triplets at 3.65 ppm for OCH_2 protons of n-propylate groups in TAMP-Zr-O^nPr compound. The signals of TAMP groups appeared at 2.34 (s, CH_3), 4.42 (s, CH_2N), 6.81 (d, 2H, CH, aromatic), 6.94 (m, 2H, CH), 7.11 (d, 2H, CH), 7.19 (d, 1H, CH), 7.27 (t, 1H, CH), respectively (Figure 3). The signal for the C-OH proton is absent in the ^1H NMR spectrum. The lack of a hydroxyl proton signal at around ~8.50 ppm indicates that

TAMP is completely coordinated to zirconium. ^{13}C NMR spectrum of TAMP-Zr compound showed the expected peaks as given in the experimental section (Figure 4). The ^{13}C NMR data of compounds were consistent with literature data given for phenoxyimine/amine-$TiCl_2$, -CpTi, -CpZr compounds [15, 20-23].

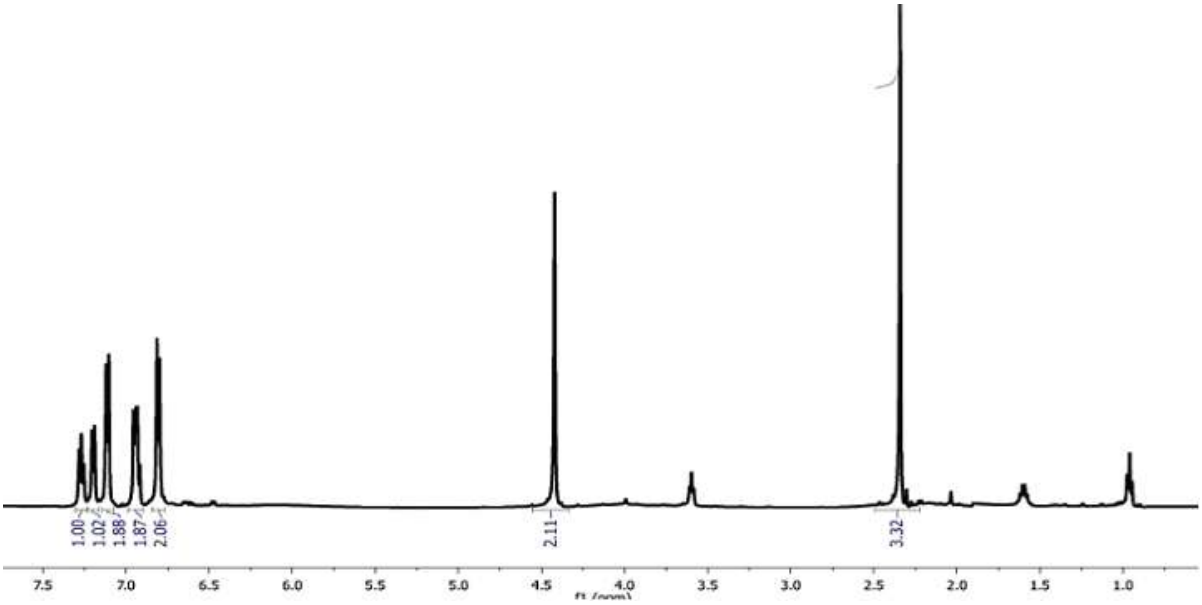

Figure 3. ^{1}H-NMR spectrum of $(TAMP)_3Zr_2(O^nPr)O_2$ compound

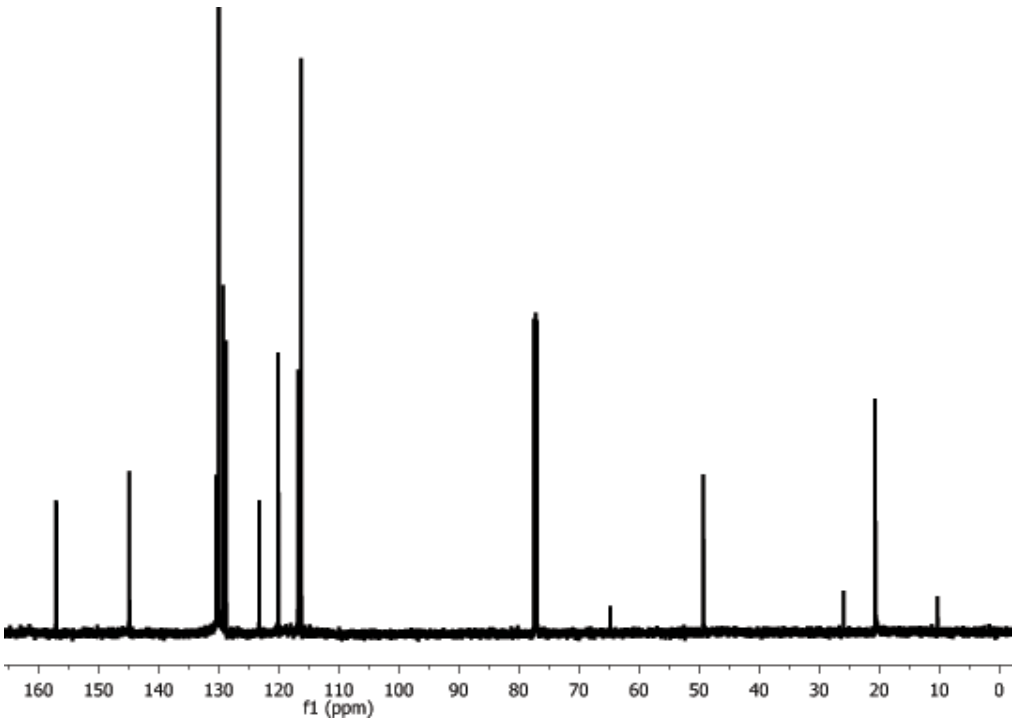

Figure 4. ^{13} C-NMR spectrum of $(TAMP)_3Zr_2(O^nPr)O_2$ compound

The reaction between $Zr(O^nPr)_4$ and TIMPH can be shown in the Scheme 3. In contrast to ^1H and ^{13}C NMR spectra of TAMP-Zr compound, ^1H and ^{13}C NMR spectra of TIMP-Zr compound showed no peaks for n-propylate groups. In other words, in the presence of TIMP ligand the *n*-propylate groups were released from zirconium atom.

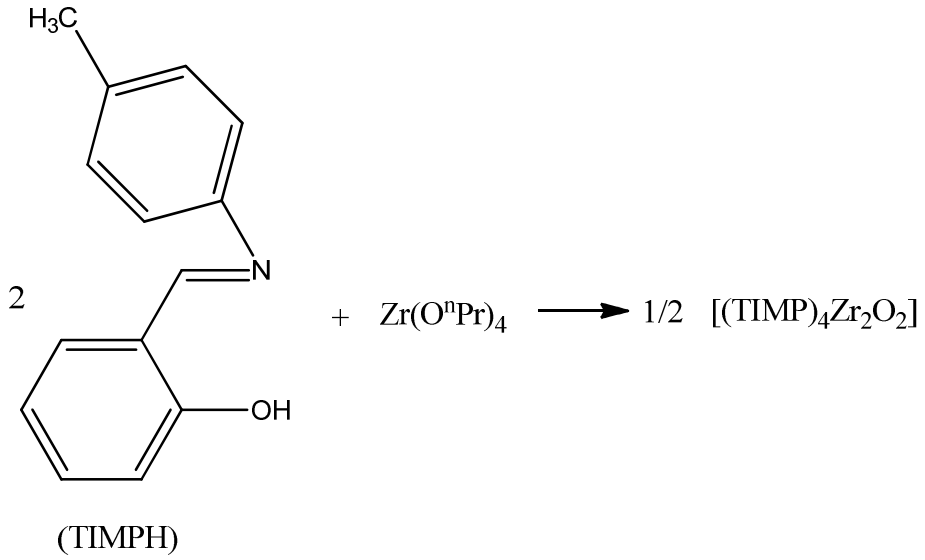

Scheme 3. The reaction between $Zr(O^nPr)_4$ and TIMPH.

^1H NMR and ^{13}C NMR (Figure 5) signals of TIMP groups appeared at 2.44 (s, CH_3), 7.0 (t,1H, CH), 7.10 (d, 1H, CH), 7.26 (m, 4H, CH), 7.43 (d, CH, aromatic), 8.66 (s, CH=), and 21.21 (CH_3Ph), 117.34, 119.13, 119.46, 121.15, 129.90, 130.15, 132.27, 133.04, 137.04, 146.0 (=CipsoN), 161.27 (=C-O, Ar), 161.81 (CH=N), respectively. ^1H NMR spectra of all TIMP-M compounds showed that no alcoholate groups remained as bonded to metals. However, ^1H NMR spectra of TAMP-M compounds showed expected peaks for alcoholate groups. TIMP ligand caused more condensation reactions than TAMP ligand as given in the experimental section. This can be attributed to the strong hygroscopic properties of metal-imine compounds. As written in the experimental section, all reactions (3-8) were conducted in atmospheric conditions instead of inert conditions (Ar, N_2). It was one of the purposes of this study to reduce the number of alcoholate groups of metal alcoholates to form single site catalysts for polymerization reactions. Therefore, some of the alcoholate groups underwent condensation reactions to form oxo groups in the presence of TAMPH and TIMPH ligands under atmospheric

conditions. The presence of moisture was necessary to form oxo groups from metal alcoholates. The resulted oxo groups were bridged between metal atoms. This was the expected results as seen in literature data [24,25]. The number of oxo groups determined by both elemental analysis and ^{1}H NMR measurements. The ^{13}C NMR spectra of the metal compounds gave somewhat similar data for carbon resonances with that of the free TAMPH and TIMPH ligands. Because carbon atoms of TIMP and TAMP ligands (except for =C-O and =C-N carbons) were not affected too much when TAMP and TIMP were bonded to metals. The =CO and =C-N carbon peaks were shifted to somewhat different region when compared those of free ligands peaks in ^{13}C NMR spectra.

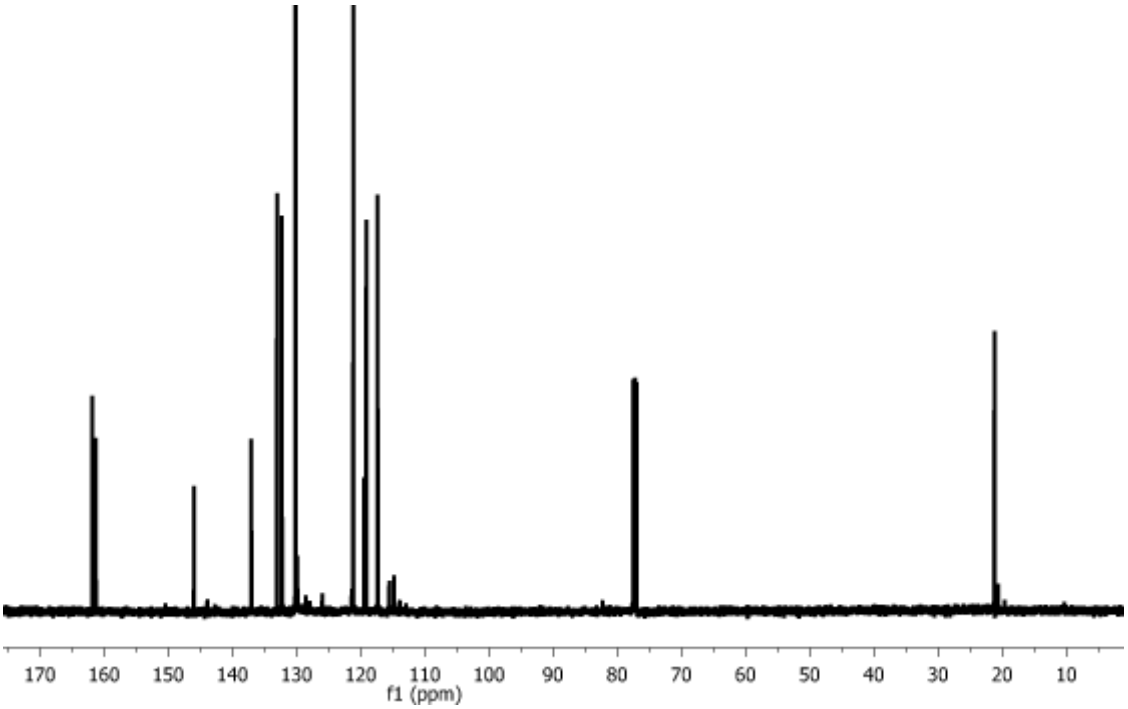

Figure 5. ^{13} C-NMR spectrum of $(TIMP)_4Zr_2O_2$ compound

Since TAMP-metal compounds have an active alcoholate group, TAMP-Ti compound was tested in the polymerization of PO and ε-CL. In order to characterize the PPO and PCL samples, GPC (gel permeation chromatography), ^{1}H NMR, and ^{13}C NMR instruments were used. The obtained data were consistent with the previously published ^{13}C NMR data for PPO [16] and PCL polymers [17]. ^{1}H and ^{13}C NMR spectra illustrated that main changes occurred at the CH and CH_2 protons of oxirane ring when PO was polymerized. For instance, there were shifts from 2.4-2.9 ppm to 3.4-3.7 ppm for the CH_2 and CH protons of PO. The maximum recovery rate of polymer and the maximum polymerization velocities of PO occurred at 75 °C for Ti catalyst.

The conversion of monomer PO and ε-CL to polymers was followed by GPC measurements. GPC was used to determine molecular weight of polymers. Changing the reaction time and temperature caused to obtained different weight average molecular weights (*Mw*) or number average molecular weights (*Mn*) polymers (Table 1). For polymers of PO prepared with TAMP-Ti stirring at 25 °C for 3 days, the main peak appeared at 2070 Da for *Mw* or 1912 Da for *Mn*. The ratio of *Mw/Mn* was 1.08. When the temperature was increased from 25 to 75 °C, the conversions of monomers to polymers increased from 28.6% to 100% and also molecular weight of polymer increased for titanium catalyst (Figure 6). However, as can be seen in Figure 6, the GPC chromatogram of the PO polymer prepared at 75 °C with Ti-TAMP showed bimodal molecular weight distribution. The first peak in Figure 6 has weight average molecular weight 5022 Da or number average molecular weight 3989 Da with the *Mw/Mn* value of 1.26. Ti-TAMP compounds were also tested in the polymerization of ε-caprolactone. The polymerization reactions were conducted without solvent at 100 °C. The conversion of ε-CL monomer as high as 99% was observed after polymerizing for 12 hours. The weight average molecular weight and the number average molecular weight of PCL were ~35000 Da and ~30000 Da, respectively, with the *Mw/Mn* value of ~1.15.

Table 1. Data for PO and ε-CL polymers obtained from GPC measurements.

Catalyst	**T, °C**	**Time, h**	**M_w**	**M_n**	**(M_w/M_n)**	**Conversion (%)**
TAMP-Ti	25	72	2070 PO	1912 PO	1.08	28.6
TAMP-Ti	50	48	2385 PO	2175 PO	1.09	32.7
TAMP-Ti	75	48	5022 PO	3989 PO	1.26	100
TAMP-Ti	75	48	11400 ε-CL	10200 ε-CL	1.12	30
TAMP-Ti	100	12	35656 ε-CL	30835 ε-CL	1.15	99

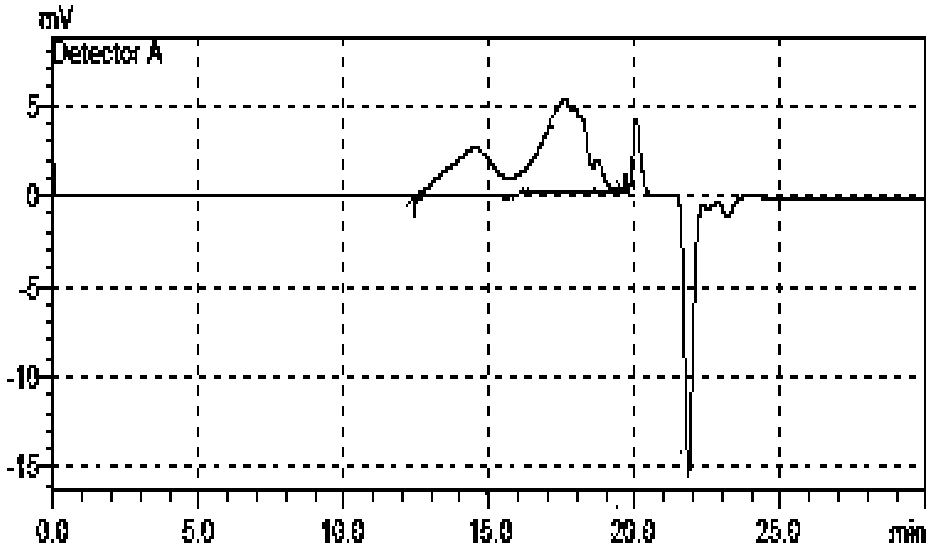

Figure 6. Gel permeation chromatogram of PO polymer prepared at 75 °C with $(TAMP)_3Ti_2(O^iPr)O_2$ compound.

Transition metal compounds carry out ROP of ε-CL and PO via a coordination-insertion mechanism [26-33]. For example, the polymerization mechanism of ε-CL can be shown in Scheme 4. The spectroscopic data suggest that ε-CL attacks the metal-center first and then the nucleophile OR- ion attacks C=O carbon atom in ε-CL.

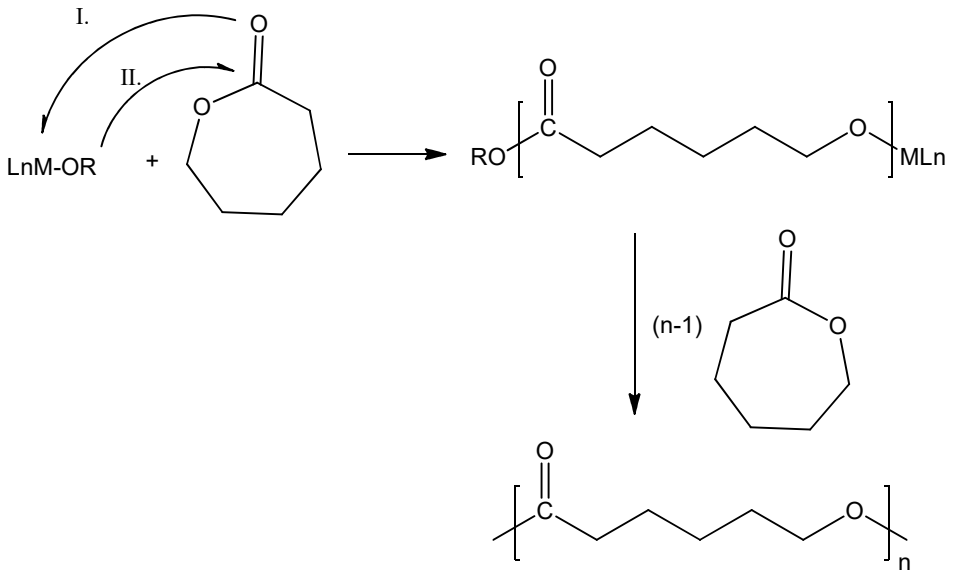

Scheme 4. The attack of ε-caprolactone to metal center of metal-alcoholate compound (I.: first step, II.: second step).

CONCLUSIONS

The result of this study showed that TAMPH and TIMPH were good ligands for modification of Ti and Zr-alcoholates. These compounds were synthesized and characterized by elemental analysis, mass measurements and spectroscopic techniques including ^{1}H NMR, ^{13}C NMR and FTIR spectroscopy. Each product was formulated by combination of techniques mentioned above. The prepared Ti-compound having an active alcoholate group was effective as catalyst for the polymerization of PO and ε-CL at mild reaction conditions. The structures of polymers were characterized by spectroscopic techniques and gel permeation chromatography (GPC).

ACKNOWLEDGMENTS

This study has been supported by the Kocaeli University, (project No: 2014/17).

REFERENCES

1. Yoshinaga I, Yamada N, Katayama S. Effect of metal alkoxide complexes on condensation reactions of hydrolyzed phenyltriethoxysilane. Journal of sol-gel science and technology. 2003;28(1):65-70. DOI: 10.1023/A:1025637103740.

2. Moraru B, Gross S, Kickelbick G, Trimmel G, Schubert U. A new type of methacrylate-substituted oxozirconium clusters:$[Zr_3O(OR)_5(OMc)_5]_2$ and $[Zr_3O(OR)_3(OMc)_7]_2$. Monatshefte für Chemie/Chemical Monthly. 2001;132(9):993-999. DOI: 10.1007/s007060170039.

3. Kayan A. Preparation, characterization and application of inorganic–organic hybrid polymers, poly-GPTS/M (CL) x O (OH). Industrial & Engineering Chemistry Research. 2012;51(41):13339-13345. DOI: 10.1021/ie301470k.

4.Yalcin G, Kayan A. Synthesis and characterization of Zr, Ti, Al-phthalate and pyridine-2-carboxylate compounds and their use in ring opening polymerization. Applied Catalysis A: General. 2012; 433: 223-228. DOI: 10.1016/j.apcata.2012.05.019.

5. Feinle A., Lavoie-Cardinal F, Akbarzadeh J, Peterlik H, Adlung M, Wickleder C, Hüsing N. Novel Sol–Gel Precursors for Thin Mesoporous Eu^{3+}-Doped Silica Coatings as Efficient Luminescent Materials. Chemistry of Materials. 2012;24(19):3674-3683. DOI: 10.1021/cm300996j.

6. Uttamchandani J, Kapoor RN. Titanium (IV) and zirconium (IV) derivatives of tetradentate schiff bases. Transition Metal Chemistry. 1978;3(1):79-81. DOI: 10.1007/BF01393514.

7. Bouyahyi M, Roisnel T, Carpentier JF. Aluminum complexes of fluorinated β-diketonate ligands: syntheses, structures, intramolecular reduction, and use in ring-opening polymerization of lactide. Organometallics. 2009;29(2):491-500. DOI: 10.1021/om9009312.

8. Spassky N, Wisniewski M, Pluta C, Le Borgne A. Highly stereoelective polymerization of rac - (D, L) - lactide with a chiral schiff's base/aluminium alkoxide initiator. Macromolecular Chemistry and Physics. 1996;197(9):2627-2637. DOI: 10.1002/macp.1996.021970902.

9. Ulusoy M, Kilic A, Durgun M, Tasci Z, Cetinkaya B. Silicon containing new salicylaldimine Pd (II) and Co (II) metal complexes as efficient catalysts in transformation of carbon dioxide (CO_2) to cyclic carbonates. Journal of Organometallic Chemistry. 2011;696(7):1372-1379. DOI: http://dx.doi.org/10.1016/j.jorganchem.2011.01.005.

10. Kowalski A, Libiszowski J, Duda A, Penczek S. Polymerization of L, L-dilactide initiated by tin (II) butoxide. Macromolecules. 2000;33(6):1964-1971. DOI: 10.1021/ma991751s.

11. Lee BF, Wolffs M, Delaney KT, Sprafke J K, Leibfarth FA, Hawker CJ, Lynd NA. Reactivity ratios and mechanistic insight for anionic ring-opening copolymerization of epoxides. Macromolecules. 2012;45(9):3722-3731. DOI: 10.1021/ma300634d.

12. Matějka L, Dukh O, Brus J, Simonsick Jr WJ, Meissner B. Cage-like structure formation during sol–gel polymerization of glycidyloxypropyltrimethoxysilane. Journal of non-crystalline solids. 2000;270(1):34-47. http://dx.doi.org/10.1016/S0022-3093(00)00074-0.

13. Hild F, Neehaul N, Bier F, Wirsum M, Gourlaouen C, Dagorne S. Synthesis and Structural Characterization of Various N, O, N-Chelated Aluminum and Gallium Complexes for the Efficient ROP of Cyclic Esters and Carbonates: How Do Aluminum and Gallium Derivatives Compare?. Organometallics. 2013;32(2):587-598. 10.1021/om3011068.

14. Agirbas H, Kemal B, Budak F. Synthesis and structure–antibacterial activity relationship studies of 4-substituted phenyl-4, 5-dihydrobenzo [f][1, 4] oxazepin-3 (2H)-thiones. Medicinal Chemistry Research. 2011;20(8):1170-1180. DOI: 10.1007/s00044-010-9457-4.

15. Alesso G, Sanz M, Mosquera ME, Cuenca T. Monocyclopentadienyl Phenoxido–Amino and Phenoxido–Amido Titanium Complexes: Synthesis, Characterisation, and Reactivity of Asymmetric Metal Centre Derivatives. European Journal of Inorganic Chemistry. 2008;2008(29):4638-4649. DOI: 10.1002/ejic.200800553.

16. Chisholm MH, Navarro-Llobet D, Simonsick WJ. A comparative study in the ring-opening polymerization of lactides and propylene oxide. Macromolecules. 2001;34(26):8851-8857. DOI: 10.1021/ma011328v.

17. Srisaard M, Molloy R, Molloy N, Siripitayananon J, Sriyai M. Synthesis and characterization of a random terpolymer of L - lactide, ϵ - caprolactone and glycolide. Polymer international. 2001;50(8): 891-896. DOI: 10.1002/pi.713.

18. Liu C, Zhao Y, Zhai LL, Lv GC, Sun WY. Syntheses, crystal structures, and properties of silver (I) complexes with oxazoline-containing bidentate ligand. Journal of Coordination Chemistry. 2012;65(1):165-175. DOI: 10.1080/00958972.2011.645813.

19. Singh HL, Singh J. Synthesis of New Zirconium (IV) Complexes with Amino Acid Schiff Bases: Spectral, Molecular Modeling, and Fluorescence Studies. International Journal of Inorganic Chemistry. 2013. DOI:10.1155/2013/847071.

20. Mounika K, Anupama B, Pragathi J, Gyanakumari C. Synthesis Characterization and Biological Activity of a Schiff Base Derived from 3-Ethoxy Salicylaldehyde and 2-Amino Benzoic acid and its Transition Metal Complexes. Journal of Science Research. 2010;2:513-524. DOI: 10.3329/jsr.v2i3.4899.

21. Li CY, Yu CJ, Ko B.T. Facile synthesis of well-defined titanium alkoxides based on benzotriazole phenoxide ligands: efficient catalysts for ring-opening polymerization of cyclic esters. Organometallics. 2012;32(1):172-180. DOI: 10.1021/om300962k.

22. Tanaka R, Viehmann P, Hecht S. Bis (phenoxy-azo) titanium (IV) Complexes: Synthesis, Structure, and Catalytic Activity in Styrene Polymerization. Organometallics. 2012;31(11):4216-4220. DOI: 10.1021/om3001636.

23. Ishii SI, Furuyama R, Matsukawa N, Saito J, Mitani M, Tanaka H, Fujita T. Ethylene and Ethylene/Propylene Polymerization Behavior of Bis (phenoxy - imine) Zr and Hf Complexes with Perfluorophenyl Substituents. Macromolecular rapid communications. 2003;24(7):452-456. DOI: 10.1002/marc.200390072.

24. Gross S. Oxocluster-reinforced organic–inorganic hybrid materials: effect of transition metal oxoclusters on structural and functional properties. Journal of Materials Chemistry. 2011;21(40): 15853-15861. DOI: 10.1039/C1JM10579E.

25. Ivanovici S., Rill C, Koch T, Puchberger M, Kickelbick G. Solvent effects in the formation of hybrid materials based on titanium alkoxide-polysiloxane precursors. New Journal of Chemistry. 2008;32(7):1243-1252. DOI: http://dx.doi.org/10.1039/b800161h.

26. Chmura AJ, Davidson MG, Jones MD, Lunn MD, Mahon MF, Johnson AF, Wong SS. Group 4 complexes with aminebisphenolate ligands and their application for the ring opening polymerization of cyclic esters. Macromolecules. 2006;39(21):7250-7257. DOI: 10.1021/ma061028j.

27. Mert O, Kayan A. Synthesis of silyliminophenolate zirconium compounds and their catalytic activity over lactide/epoxide. Applied Catalysis A: General. 2013;464:322-331. DOI: 10.1016/j.apcata.2013.06.010.

28. Mert O, Kayan A. Synthesis and characterization of substituted salicylate zirconium compounds and their catalytic activity over ε-caprolactone. Journal of Inclusion Phenomena and Macrocyclic Chemistry. 2014; 80(3-4):409-416. DOI: 10.1007/s10847-014-0429-z.

29. Kayan A, Mert O. Preparation of l-Lactide/3-Glycidyloxypropyltrimethoxysilane Copolymeric Materials with Various Catalysts. Journal of Inorganic and Organometallic Polymers and Materials. 2014; 24(6): 1055-1062. DOI: 10.1007/s10904-014-0083-3.

30. Su CK, Chuang HJ, Li CY, Yu CY, Ko BT, Chen JD, Chen MJ. Oxo-bridged bimetallic group 4 complexes bearing amine-bis (benzotriazole phenolate) derivatives as bifunctional catalysts for ring-opening polymerization of lactide and copolymerization of carbon dioxide with cyclohexene oxide. Organometallics. 2014; 33(24):7091-7100. DOI: 10.1021/om500784a.

31. Kayan A. Preparation, Characterization and Application of Hybrid Materials Having Multifunctional Properties. Journal of Inorganic and Organometallic Polymers and Materials. 2015;25(6):1345-1352. DOI: 10.1007/s10904-015-0246-x.

32. Kayan A. Synthesis, Characterization, and Application of Hybrid Inorganic–Organic Composites (K/Na) ZrSi (R) O_x. Journal of Inorganic and Organometallic Polymers and Materials. 2016;26(3):640-647. DOI: 10.1007/s10904-016-0349-z.

33. Horeglad P, Cybularczyk M, Litwińska A, Dąbrowska AM, Dranka M, Żukowska GZ, Michalak M. Controlling the stereoselectivity of rac-LA polymerization by chiral recognition induced the formation

of homochiral dimeric metal alkoxides. Polymer Chemistry. 2016;7(11):2022-2036. DOI: http://dx.doi.org/10.1039/C5PY02005K.

Türkçe Öz ve Anahtar Kelimeler

TAMP/TIMP-Ti ve Zr Bileşiklerinin Hazırlanması ve Karakterizasyonu ve Propilen Oksit ile ε-Kaprolakton Üzerindeki Katalitik Aktivitesi

Asgar Kayan

Öz: Titanyum ve zirkonyum 2((p-tolilamino/p-tolilimino)metil)fenolat (TAMP ve TIMP), etil alkol içinde 2-((p-tolilamino)metil)fenol (TAMPH) ve 2-((p-tolilimino)metil)fenol (TIMPH) bileşiklerinin Ti- ve Zr-alkolatlarının tepkimesinden hazırlanmıştır. Bu bileşiklerin karakterizasyonu için ^{1}H, ^{13}C NMR, FTIR, kütle spektrometrisi ve elementel analiz kullanılmıştır. TAMP ve TIMP metal bileşikleri sırasıyla $(TAMP)_3M_2(OR)O_2$ ve $(TIMP)_4M_2O_2$ olarak gösterilebilir. Bu bileşiklerin katalitik aktivitesi propilen oksit (PO) ve ε-kaprolakton (ε-CL) bileşiklerinin polimerleşmesinde kullanılmıştır ve Ti-TAMP'ın aktif olduğu bulunmuştur. Poli-propilen oksit (PPO) ve poli-kaprolakton (PCL) ^{1}H, ^{13}C NMR ve jel geçirgenlik kromatografisi (GPC) ile tanımlanmıştır.

Anahtar kelimeler: Metal alkoksit, katalizör, Schiff bazı, ε-kaprolakton, polimer.
Gönderilme: 28 Haziran 2016. **Düzeltme:** 06 Ağustos 2016. **Kabul:** 6 Eylül 2016.

JOTCS A
Journal of the Turkish Chemical Society
Section: A
Chemistry
TURKISH CHEMICAL SOCIETY

Novel Antimony(III) Halide Complexes with Some n-Alkyl Thioureas: Synthesis, Characterization and Study of Their Effect upon the Catalytic Oxidation of Linoleic Acid to Hydroperoxylinoleic Acid by Lipoxygenase

Ibrahim Ismet Ozturk*

*Department of Chemistry, Namık Kemal University, 59030 Tekirdag, Turkey

Abstract: Four novel thiourea derivatives of antimony(III) compounds (SbX_3; X = Cl or Br) with N-methylthiourea (NMTU) and N-ethylthiourea (NETU) of formulas $[SbCl_3(NMTU)_3]$ (**1**), $[SbBr_3(NMTU)_3]$ (**2**),$[SbCl_3(NETU)_3]$ (**3**), and $[SbBr_3(NETU)_3]$ (**4**) were synthesized. These new antimony(III) halides were characterized by melting point, elemental analysis, molar conductivity, FT-Infrared spectroscopy, FT-Raman spectroscopy, UV-Vis spectrophotometry, NMR (^1H and ^{13}C) spectroscopy and TG-DTA analysis. The reactions of N-methylthiourea (NMTU) and N-ethylthiourea (NETU) with SbX_3 (X = Cl or Br) in a 2:1 ligand/metal rate but unexpected products were formed in a 3:1 ligand/metal rate. The compounds are non-electrolytes in solution and spectroscopic data of the compounds are appropriate with six coordinate octahedral geometry by three halide ions and three sulfur atoms from thiourea ligands. N-methythiourea and N-ethylthiourea ligands behave as monodentate in compounds **1**-**4** with the binding through sulfur. The influence of these compounds **1**–**4**, N-methythiourea and N-ethylthiourea upon the catalytic peroxidation of linoleic acid to hyperoxolinoleic acid by lipoxygenase was kinetically studied.

Keywords: Antimony(III) halides; N-alkyl thioureas; spectroscopic characterization; lipoxygenase.
Submitted: July 23, 2016. **Accepted:** October 01, 2016.
Cite this: Öztürk İ. Novel Antimony(III) Halide Complexes with Some n-Alkyl Thioureas: Synthesis, Characterization and Study of Their Effect upon the Catalytic Oxidation of Linoleic Acid to Hydroperoxylinoleic Acid by Lipoxygenase. JOTCSA. 2017;4(1):81–98.
DOI: . 10.18596/jotcsa.31798.
***Corresponding author. E-mail:** iiozturk@nku.edu.tr, Tel.:+90 282 250 26 23.

INTRODUCTION

Antimony (Sb) is a pnictogenic element and its ground state electron configuration is $5s^25p^3$ [1]. Antimony(III) halides, interacting with sulfur donor ligands, behave as Lewis acids, while their compounds show a range of structural motifs. One of the reasons of this geometric diversity of antimony(III) compounds is the lone pair electrons located on the antimony atom [2]. Thus, antimony(III) halide compounds with thioamide ligands contain a five coordinated metal center with a stereochemically active lone pair [3–8]. Antimony has been used as a drug for over more than 100 years. The use of antimony in medicine has been reviewed by Hadjikakou *et al*. [9]. Antimonials have been used especially for the treatment of leismaniasis (tropical disease) (*e.g.* melglumineantimoniate (Glucantime) and sodium stibogluconate (Pentostam)) [9]. The potential anticancer activity of antimony compounds is under consideration [9-22]. The last studies indicated that antimony(III) compounds are more active against carcinoma than lymphoma [17]. It is also considerable that antimony(III) compounds demonstrate strong anti-proliferative activity against human cancer cells [17]. Particularly, the antimony(III) compounds demonstrate selectivity against sarcoma and carcinoma cells [17].

Lipoxygenase is a family of iron-containing enzyme which catalyzes the oxidation of arachidonic acid to leukotrienes, in a necessary mechanism for the cell lifetime involving in inflammation mechanism [23-24]. Lipoxygenase inhibition is found to stimulate apoptosis [25], while the lipid peroxides derived from fatty acid metabolism by lipoxygenase can construct cellular proliferation [26]. So, lipoxygenase inhibitions supply a potential new target for the treatment and chemoprevention for a number of diverse cancers.

Thiourea and its derivatives have wide applications in the agricultural area, science of medicine, and analytical chemistry. The chemistry of thioureas has attracted attention owing to their potential use of reagents for the separation of metal ions and as antifungal, antiviral, and antibacterial agents [27-30]. The chemical attention of thiourea derivatives lies in the fact that they are ambidentate ligands with nitrogen and sulfur atoms susceptible for coordination and they have binding sites relevant to those in living organisms [31-32]. The coordination chemistry of thiourea derivatives with p-block elements less well studied than that of the transition metal elements and so this is still a matter of research interest [33-36].

In this work, we report the structural and spectroscopic characterization of four novel antimony (III) halide compounds with the thioureas (Scheme 1), N-methylthiourea (NMTU) and N-ethylthiourea (NETU) of formulae $[SbCl_3(NMTU)_3]$ (**1**), $[SbBr_3(NMTU)_3]$ (**2**), $[SbCl_3(NETU)_3]$ (**3**) and $[SbBr_3(NETU)_3]$ (**4**). These new compounds were used to study their influence upon the catalytic peroxidation of linoleic acid by lipoxygenase.

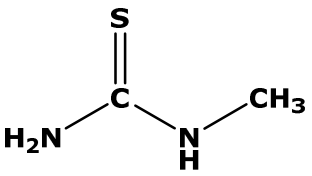

N-methythiourea (NMTU)

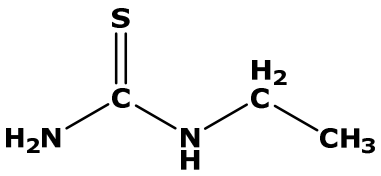

N-ethylthiourea (NETU)

Scheme 1. Formulas of the ligands used.

MATERIALS AND METHODS

Materials and Physical Measurements

All solvents used were of reagent grade; N-methylthiourea, N-ethylthiourea, and antimony(III) chloride were purchased from Sigma-Aldrich, antimony(III) bromide was purchased from Alfa Aesar. Melting points were measured using a Stuart SMP30 scientific apparatus and are uncorrected. Elemental analyses for C, H, N, and S were carried out with a Carlo Erba EA Model 1108 elemental analyzer. The molecular conductivities of compounds in DMSO were measured by means of a VWR Phenomenal conductometer CO 3000 L. FT-Raman spectra of compounds were obtained at room temperature using a low-power (~30mW) green (514.5) mm laser on a Renishaw In Via spectrometer set at 2.0 resolution. FT-Infrared spectra of compounds from 4000-400 cm^{-1}were obtained with Bruker Optics, Vertex 70 FT-Infrared spectrometer using ATR technique. The UV spectra of compounds were collected in a Shimadzu UV-2600 spectrophotometer. NMR spectra of compounds were obtained with a Varian Unity Inova 500 MHz spectrometer in DMSO-d_6 with chemical shifts given in ppm referenced to internal TMS (H). TG–DTA analysis of compounds were carried out on a Seiko SII TG/DTA 7200 apparatus under N_2 flow (50 cm^3 min^{-1}) with a heating rate of 10 °C min^{-1}.

Synthesis of $[SbCl_3(NMTU)_3]$ (1), $[SbBr_3(NMTU)_3]$ (2), $[SbCl_3(NETU)_3]$ (3) and $[SbBr_3(NETU)_3]$ (4)

1.0 mmol of N-methylthiourea (0.090 g) in benzene (10 mL) was added to a benzene (10 mL) solution of $SbCl_3$ (0.5 mmol, 0.114 g) for compound **1** and to $SbBr_3$ (0.5 mmol, 0.181 g) for compound **2**. 1.0 mmol N-ethylthiourea (0.104 g) in benzene (10 mL) was added to a benzene (10 mL) solution of $SbCl_3$ (0.5 mmol, 0.114 g) for compound **3** and to $SbBr_3$ (0,5 mmol, 0,181 g) for compound **4** and then the solutions were stirred for 30 min, then they were filtered off and then the resulting clear solutions were kept in darkness at room temperature to give compounds of the antimony(III) halide. All compounds are soluble in acetone, acetonitrile, dimethyl sulfoxide, ethanol, methanol, and tetrahydrofuran.

Result for **1:** Yellow crystals; yield 89%; mp, 114-118°C; mw, 498.56 g/mol; Found for $C_6H_{18}Cl_3N_6S_3Sb$: C: 14.38; H: 3.51; N: 16.75; S: 19.15, Calc. for C: 14.45; H: 3.64; N: 16.89; S: 19.29. UV-Vis (DMSO): λ_{max} (logε) = 257.50 (4.55). FT-IR (cm^{-1}): 3244m, 3161s, 1626s,

1551s, 1489m, 1452m, 1402m, 1338w, 1292s, 1255w, 1146w, 1122s, 972s, 773s, 715s, 633m, 598w, 544m, 482s. Λ_M = 8.8 $\Omega^{-1}.cm^2.mol^{-1}$.

Result for **2:** Yellow crystals; yield 85%; mp, 86-89°C; mw, 631.91 g/mol; found for $C_6H_{18}Br_3N_6S_3Sb$: C: 11.38; H: 2.91; N: 13.24; S:15.12, Calc. for C: 11.40; H: 2.87; N: 13.30; S: 15.22. UV-Vis (DMSO): λ_{max} (logε) = 258.00 (4.63). FT-IR (cm^{-1}): 3246m, 3161s, 1624s, 1553s, 1487m, 1452m, 1402m, 1338w, 1290s, 1257w, 1147w, 1122s, 972s, 771s, 715s, 632s, 600w, 542m, 476s. Λ_M = 23.1 $\Omega^{-1}.cm^2.mol^{-1}$.

Result for **3:** Light yellow crystals; yield 87%; mp, 63-65°C; mw, 540.64 g/mol; found for $C_9H_{24}Cl_3N_6S_3Sb$: C: 19.84; H: 4.42; N: 15.34; S:17.45,Calc. for C: 19.99; H: 4.47; N: 15.54; S: 17.79. UV-Vis (DMSO): λ_{max} (logε) = 257.50 (4.49). FT-IR (cm^{-1}): 3323w, 3277w, 3230w, 3147s, 2974m, 1618s, 1556w, 1541s, 1500w, 1466m, 1379m, 1344m, 1304w, 1261s, 1080w, 1032w, 1009w, 903w, 891w, 821w, 802s, 739s, 644s, 542w, 486s, 444w, 424w. Λ_M = 13.9 $\Omega^{-1}.cm^2.mol^{-1}$.

Result for **4:** Light yellow crystals; yield 89%; mp, 68-71°C; mw, 673.99 g/mol; found for $C_9H_{24}Br_3N_6S_3Sb$: C: 15.98; H: 3.52; N: 12.35; S: 14.19,Calc. for C: 16.04; H: 3.59; N: 12.47; S: 14.27. UV-Vis (DMSO): λ_{max} (logε) = 258.50 (4.73). IR (cm^{-1}): 3323w, 3277w, 3232w, 3147s, 2974m, 1618s, 1541s, 1498w, 1446w, 1379m, 1344m, 1304w, 1263s, 1171w, 1126s, 1113w, 1080w, 1032w, 1009w, 902w, 891w, 822w, 802s, 739s, 644s, 544w, 488s, 445w, 426w. Λ_M = 23.5 $\Omega^{-1}.cm^2.mol^{-1}$.

Study of lipoxygenase inhibition mechanism

Preparation of the solutions: 0.2 M borate buffer solution was used in all kinetic studies. Borate buffer solution was prepared as defined here: 6.18 g boric acid (H_3BO_3, 0.1 mol) was added to 300 mL distilled water. The pH was calibrated to 9 with 50% w/v sodium hydroxide. Lastly, the solution was diluted to 500 mL with distilled water [37]. Linoleic acid solution was prepared as defined here: 0.05 mL of linoleic acid was dissolved in 0.05 mL of ethanol (95%). 50 mL of H_2O was added in the flask. 5 mL of the prepared solution was added to 30 mL of the buffer solution. Enzyme solution: 10000 U of enzyme solution for each mL of buffer solution was prepared in ice-cold bath [38]. An amount of 500 U for every 3 mL of reaction mixture is used in every experiment. A unit of lipoxygenase causes and increases in absorption at 234 nm equal to 0.001 per minute.

Method

The activity of enzyme was observed by UV spectroscopy. The enzyme solution (0.05 mL) was added to a cell containing 2 mL of linoleic acid solution and a necessary amount of the buffer solution. The temperature of a solution of the inhibitor was preserved constant at 25 °C. No pre-incubation of the enzyme with an inhibitor solution was applied. The enzyme activity was established from an increase in the absorption intensity at 234 nm at 25°C (ε = 25 000 L mol^{-}

$^{1}cm^{-1}$) [39-41] caused by the oxidation of linoleic acid. Solutions of antimony(III) halide compounds **1**-**4** were prepared in dimethyl sulfoxide, concentrations of compounds being 10^{-1} and 10^{-2}mol.L^{-1}. The substrate concentration was preserved constant at a level of 0.3 mmol.L^{-1}, and the amounts of buffer and inhibitor solutions were altered according to the necessary final concentration of the inhibitor. The whole volume of the reaction mixture was 2 mL. Every experiment was repeated three times. All solutions were kept at thermostatic water bath at 25ºC, except from the enzyme solution that was kept at ice cold bath (0ºC).

RESULTS AND DISCUSSION

General Aspects

Antimony(III) halide compounds **1**-**4** were synthesized in benzene solution by reacting the thioureas with antimony(III) halide, as shown in Eq. 1. All the reactions were built in 2:1 ligand to metal rate. N-methythiourea and N-ethythiourea are coordinated to antimony through their neutral forms while no deprotonation occurred. Compounds **1**-**4** were characterized by melting point, elemental analysis, molar conductivity, FT-Infrared spectroscopy, FT-Raman spectroscopy, TG-DTA analysis, UV-Vis spectrophotometry and NMR spectroscopy. All compounds are air-stable. The melting points and elemental analyses of the compounds are given in Table 1. All compounds are neutral with octahedral (O_h) geometry with 3:1 HL/SbX_3 ratio (Figure 1).

$$SbX_3 + 2\,HL \xrightarrow{\text{Benzene}} [SbX_3(HL)_3] \qquad (1)$$

X: Cl or Br

HL : N-methythiourea (NMTU), N-ethylthiourea (NETU)

Table 1. Yields, melting points and elemental analysis of antimony(III) halide compounds.

Compounds	Yield (%)	mp (ºC)	Found (Calculated) (%)			
			C	H	N	S
$[SbCl_3(NMTU)_3]$ (1)	89	114-118 °C	14.38 (14.45)	3.51 (3.64)	16.75 (16.89)	19.15 (19.29)
$[SbBr_3(NMTU)_3]$ (2)	85	86-89 °C	11.38 (11.40)	2.91 (2.87)	13.24 (13.30)	15.12 (15.22)
$[SbCl_3(NETU)_3]$ (3)	87	63-65 °C	19.84 (19.99)	4.42 (4.47)	15.34 (15.54)	17.45 (17.79)
$[SbBr_3(NETU)_3]$ (4)	89	68-71 °C	15.98 (16.04)	3.52 (3.59)	12.35 (12.47)	14.19 (14.27)

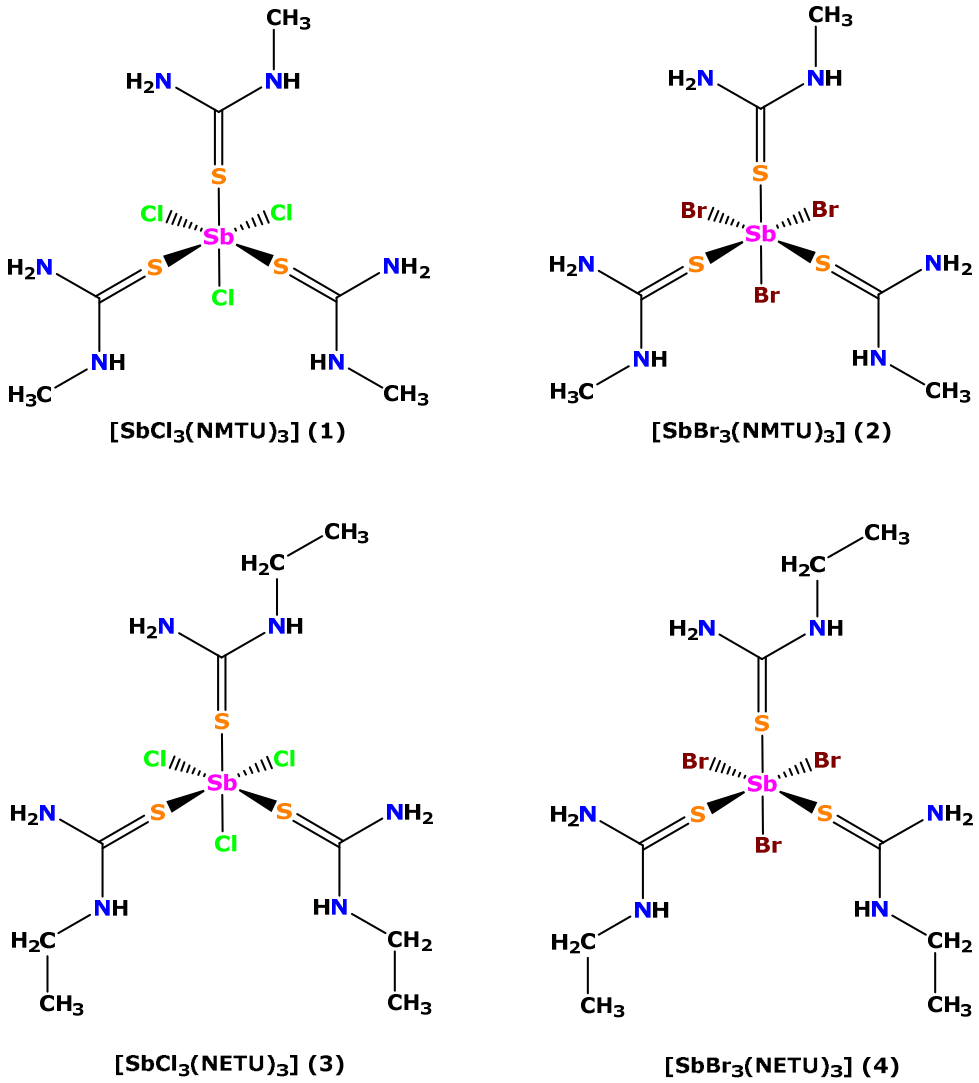

Figure 1. Proposed structures for antimony(III) halide compounds of N-methythiourea and N-ethylthiourea.

Molar Conductivity Studies

The molar conductance values of 10^{-3} M antimony(III) compounds **1-4** were obtained in dimethyl sulfoxide at room temperature. The measured molar conductance values of antimony(III) compounds are 8.8 $\Omega^{-1}.cm^2.mol^{-1}$ (**1**), 23.1 $\Omega^{-1}.cm^2.mol^{-1}$ (**2**),13.9 $\Omega^{-1}.cm^2.mol^{-1}$(**3**) and 23.5 $\Omega^{-1}.cm^2.mol^{-1}$ (**4**) respectively. Generally higher molar conductance values are determinative of the electrolytic nature of the metal compounds and lower values display their non-electrolytic nature [42]. The molar conductance values of antimony(III) compounds indicating that compounds **1**-**4** are non-electrolytes.

FT-Infrared and FT-Raman Spectral Studies

Characteristic infrared bands of the antimony(III) halide compounds and the free thioureas are shown in Table 2 and Figure 2. The characteristic infrared bands, responsive to molecular structure, are the strain modes for the ν(N-H), ν(C=S) and ν(C-N) bands [8,15-16]. The infrared spectra of compounds represent distinct vibration bands at 1551 cm^{-1} (**1**), 1553 cm^{-1} (**2**), 1541

cm^{-1} (**3**) and 1541cm^{-1} (**4**), respectively, which are attributed to the v(C-N) vibrations. Bands at 773 cm^{-1} (**1**), 771cm^{-1} (**2**), 802 cm^{-1} (**3**), and 802 cm^{-1} (**4**) are attributed to the v(C=S) vibrations. Amide v(N-H) vibrations were monitored in the region of 3323-3147cm^{-1} in compounds**1**-**4**. The corresponding vibrations at the free thioureas are found at 3327-3165 cm^{-1}, 1543 cm^{-1} and 775 cm^{-1} (NMTU), 3327-3147 cm^{-1}, 1541 cm^{-1} and 804 cm^{-1} (NETU). A low frequency shifts in the v(C=S) band and high frequency shifts in v(C-N) band indicate that coordination happens through sulfur atoms of the thioureas in the solid state. Since no v(S-H) vibrations are observed in the infrared spectrum of **1-4** indicating that the free ligands are coordinated through their thione forms. Sb-S and Sb-X (X: Cl or Br) vibrations are Raman-active [8,15-16]. Thus, bands at 412/406 cm^{-1} (**1**), 443 cm^{-1}(**2**), 408 cm^{-1} (**3**) and 444 cm^{-1} (**4**) in the Raman spectra of compounds **1**-**4** are owing to the Sb-S vibrations. Bands at 191/136 cm^{-1} in **1** and 199/191/133 cm^{-1} in **3** are attributed to the Sb-Cl vibrations, while band at 108/100 cm^{-1} in **2** and 105 cm^{-1} in **4** has been assigned to the Sb-Br vibrations (Figures S1-S4).

Table 2. Selected IR and Raman spectroscopic data for compounds **1**-**4** and free ligands.

	Mid-IR (cm^{-1})			**Raman (cm^{-1})**	
Compound	**v(N-H)**	**v(C-N)**	**v(C=S)**	**v(Sb-S)**	**v(Sb-X)**
NMTU	3327, 3246, 3165	1543	775	-	-
$[SbCl_3(NMTU)_3]$ (1)	3244, 3161	1551	773	412,406	191,136
$[SbBr_3(NMTU)_3]$ (2)	3246, 3161	1553	771	443	108,100
NETU	3327, 3232, 3147	1541	804	-	
$[SbCl_3(NETU)_3]$ (3)	3323, 3230, 3147	1541	802	408	199,191,133
$[SbBr_3(NETU)_3]$ (4)	3323, 3232, 3147	1541	802	444	105

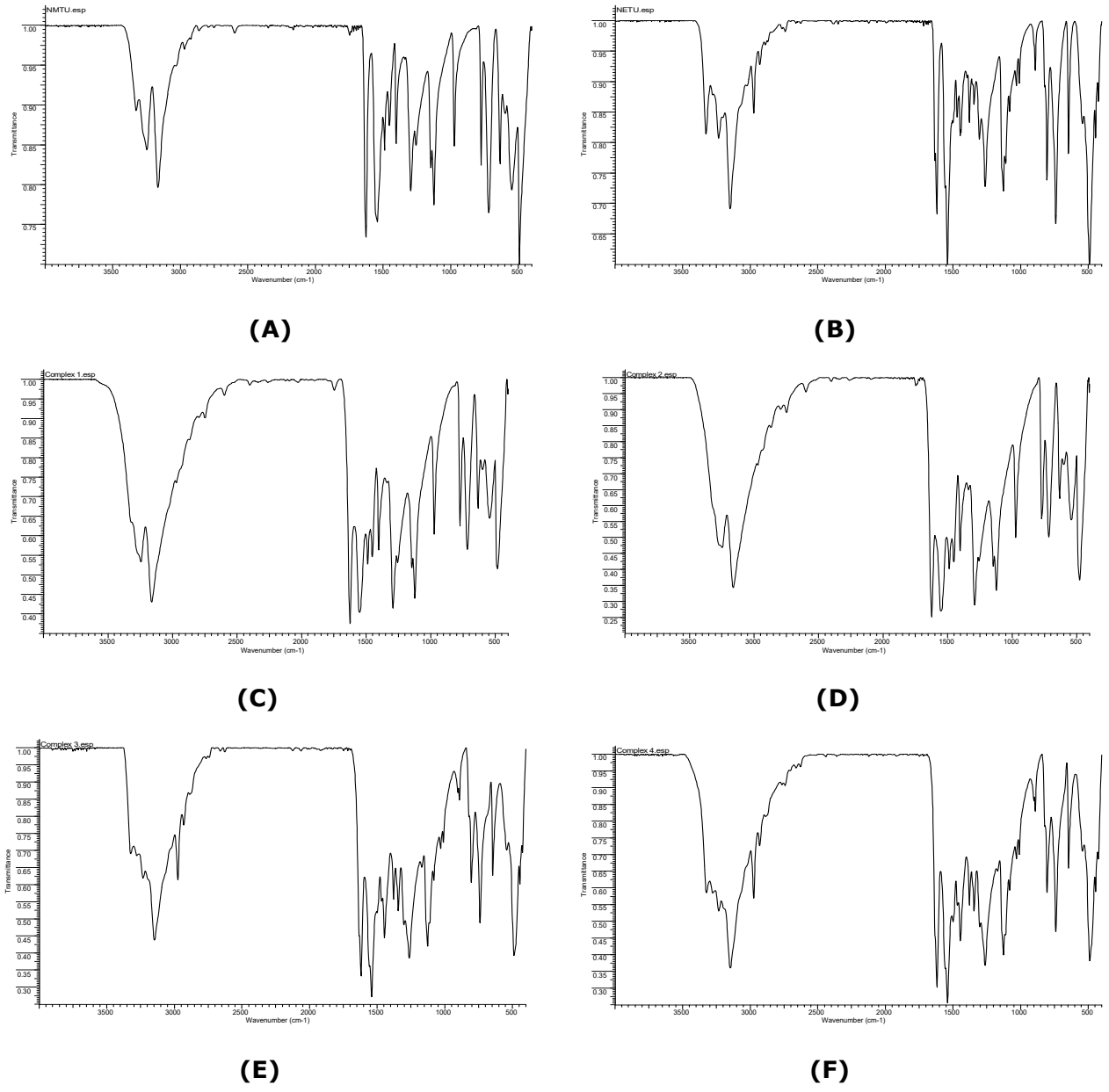

Figure 2. Infrared spectra of: (**A**) N-methylthourea, (**B**) N-ethylthiourea, (**C**) $[SbCl_3(NMTU)_3]$ (**1**), (**D**) $[SbBr_3(NMTU)_3]$ (**2**), (**E**) $[SbCl_3(NETU)_3]$ (**3**) and (**F**)$[SbBr_3(NETU)_3]$ (**4**)

Thermal Analysis

The thermal stability of antimony(III) halide compounds **1**-**4** is tested by TG-DTA analysis in an atmosphere of nitrogen in the range 25-800 ºC. The data show that compounds **1**-**4** remain stable up to 149 ºC (**1**), 138 ºC (**2**), 146 ºC (**3**), and 160 ºC (**4**), respectively (Figure 2). Beyond these temperatures, compounds **1**, **2** and **4** have one decomposition step, while **3** has two decomposition steps.

UV-Vis Spectral Studies

The UV-Vis spectra of the free N-methylthiourea, N-ethylthiourea, and their antimony(III) compounds in dimethyl sulfoxide is described in Figures 3 and 4. Free thioureas and their antimony(III) halide compounds exhibit one major absorption band in the UV region. Compounds **1-4** exhibit at 257.50 nm (**1**), 258.00 nm (**2**), 257.50 nm (**3**) and 258.50 (**4**), respectively,

which are assigned to the n-π* transitions. The corresponding absorption band at the free ligands is found at 256.50 nm (NMTU and NETU). The absorption bands shift to lower energy from chloro to bromo Sb(III) compounds.

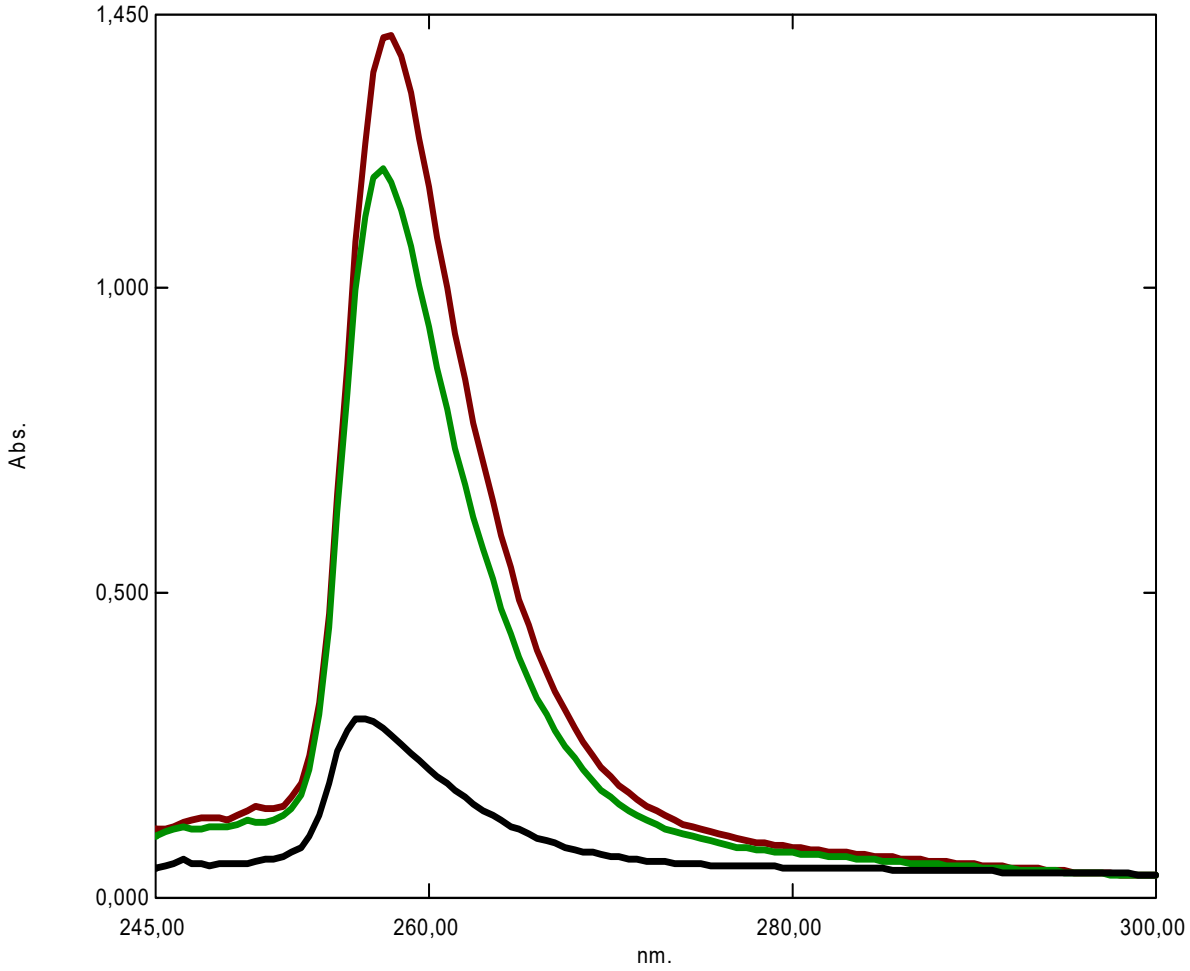

Figure 4. Uv-Vis absorption spectra of N-methylthiourea (—), $[SbCl_3(NMTU)_3]$ (**1**) (—) and $[SbBr_3(NMTU)_3]$ (**2**) (—)

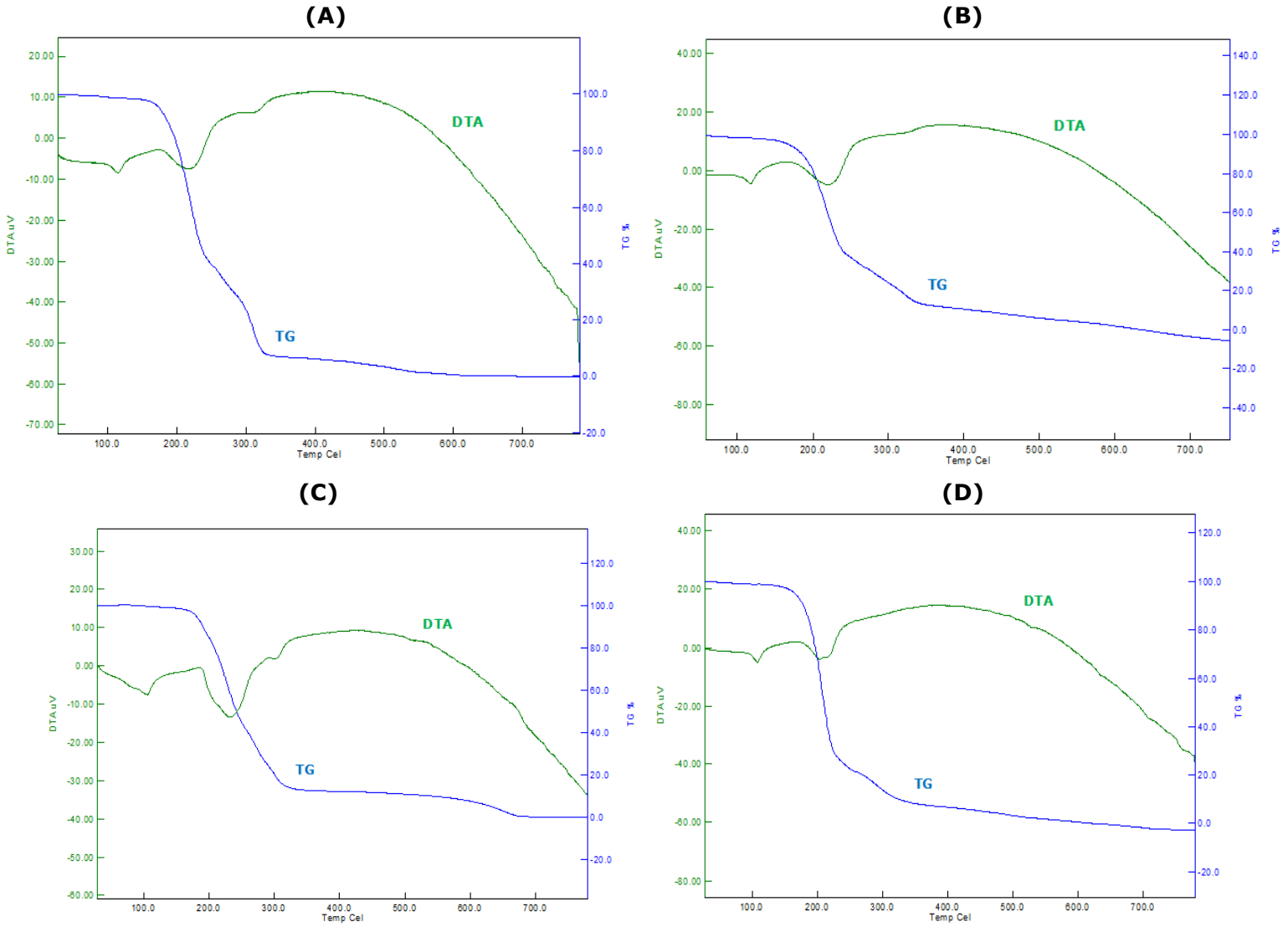

Figure 3. TG and DTA curves for compounds (A) $[SbCl_3(NMTU)_3]$ (**1**),(B) $[SbBr_3(NMTU)_3]$ (**2**), (C) $[SbCl_3(NETU)_3]$ (**3**) and (D) $[SbBr_3(NETU)_3]$ (**4**)

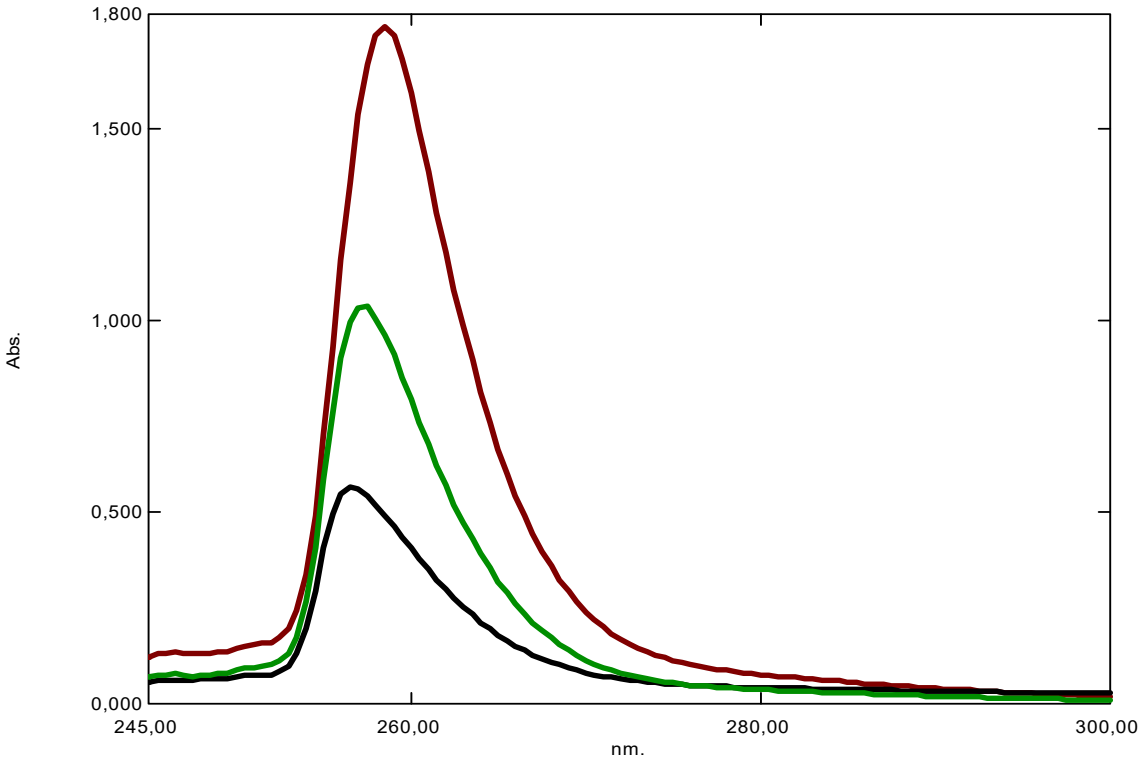

Figure 5. UV-Vis absorption spectra of N-ethylthiourea (—), $[SbCl_3(NETU)_3]$ (**3**) (—) and $[SbBr_3(NETU)_3]$ (**4**) (—).

NMR Spectral Studies

The ^1H and ^{13}C NMR chemical shifts of N-methylthiourea, N-ethylthiourea and those of the antimony(III) halide compounds **1**–**4** in DMSO-d_6 are summarized in Table 3 (Figures S5–S14). In the ^1H NMR spectra of the compounds, the N–H signal of thiourea ligands became less intense upon coordination and shifted downfield from their positions in the free ligands. The deshielding is related to an increase in π-electron density in the C–N bond upon coordination [27, 29, 30, 34]. The appearance of the N–H signal shows that the N-methylthiourea and N-ethylthiourea are coordinated to antimony(III) via the thione group. Table 3 shows that the N–H protons of NMTU and NETU are nonequivalent (NH_2 appears as a doublet) and also after coordination N-H protons of compounds **1**-**4** are nonequivalent. It should be noted that NMTU and NETU in ^{13}C NMR gives two signals for >C=S, -CH_2- and -CH_3 carbons for showing that the compounds exist in two isomeric forms [43]. The new signal observed at 3.49 (**1**), 3.60 (**2**), 3.49 (**3**) and 3.62 (**4**) ppm, respectively in the ^1H NMR spectra. These new signals are attributed to the halogen-hydrogen interaction. All other resonance signals of the thioureas remain un-shifted in the spectra of the compounds. However, such narrow shifts were also monitored for antimony(III) halide compounds with thione ligands [17-20].

Table 3. Chemical shifts (ppm) of the resonance signals observed in ^{1}H and ^{13}C NMR spectra of free thioureas and their antimony(III) compounds **1**–**4** in *DMSO-d*^{6}.

Compounds	^{1}H NMR chemical shifts (ppm)	^{13}C NMR chemical shifts (ppm)
N-methylthiourea (NMTU)	7.64, 7.47, 6.93 (N-H) 2.84, 2.64 (-CH_3)	184.94, 181.87 (>C=S) 31.97, 30.80 (-CH_3)
[$SbCl_3(NMTU)_3$] (**1**)	7.68, 7.50, 6.98 (N-H) 2.84, 2.64 (-CH_3) 3.49 (Cl···H)	184.95, 181.83 (>C=S) 31.92, 30.76 (-CH_3)
[$SbBr_3(NMTU)_3$] (**2**)	7.73, 7.51, 7.16 (N-H) 2.84, 2.65 (-CH_3) 3.60 (Br···H)	184.91, 181.26 (>C=S) 31.96, 30.84 (-CH_3)
N-ethylthiourea (NETU)	7.53, 7.23, 6.88 (N-H) 3.41, 3.07 (-CH_2-) 1.05-1.08, t (-CH_3)	183.83, 180.95 (>C=S) 39.66, 38.60 (-CH_2-) 15.45, 14.88 (-CH_3)
[$SbCl_3(NETU)_3$] (**3**)	7.68, 7.55, 6.90 (N-H) 3.38, 3.06 (-CH_2-) 1.05-1.08, t (-CH_3) 3.49 (Cl···H)	183,83 180.79 (>C=S) 39.66, 38.59 (-CH_2-) 15.48, 14.85 (-CH_3)
[$SbBr_3(NETU)_3$] (**4**)	7.73, 7.56, 6.90 (N-H) 3.38, 3.07 (-CH_2-) 1.05-1.08, t (-CH_3) 3.62 (Br···H)	183.80, 180.37 (>C=S) 38.63, 38.63 (-CH_2-) 15.45, 14.83 (-CH_3)

Kinetic study of the peroxidation of linoleic acid by lipoxygenase in the presence of antimony(III) compounds 1–4 and free thioureas

Because lipoxygenase inhibition is found to induce apoptosis [25] the effect of compounds **1**–**4** and free ligands on the oxidation of linoleic acid by lipoxygenase were studied in a vast concentration area. The degree of lipoxygenase activity (A, %) in the presence of these compounds was calculated according to the process described previously [38]. Figures 6 and 7 compares the inhibitory effect of **1**–**4** in different concentrations. The IC_{50} values which were found for antimony(III) compounds are 44.22 μM (**1**), 39.63 μM (**2**),45.05 μM (**3**) and 53.55 μM (**4**), N-methylthiourea (NMTU) 221.66 μM and for N-ethylthiourea (NETU) 217.65 μM, respectively. Thus, all four compounds show higher inhibitory activity of lipoxygenase than free thioureas (N-methylthiourea (NMTU) and N-ethylthiourea (NETU)) and moreover, antimony(III) halide compounds of N-methylthiourea (**1** and **2**) show higher inhibitory activity of lipoxygenase than antimony(III) halide compounds of N-ethylthiourea (**3** and **4**).

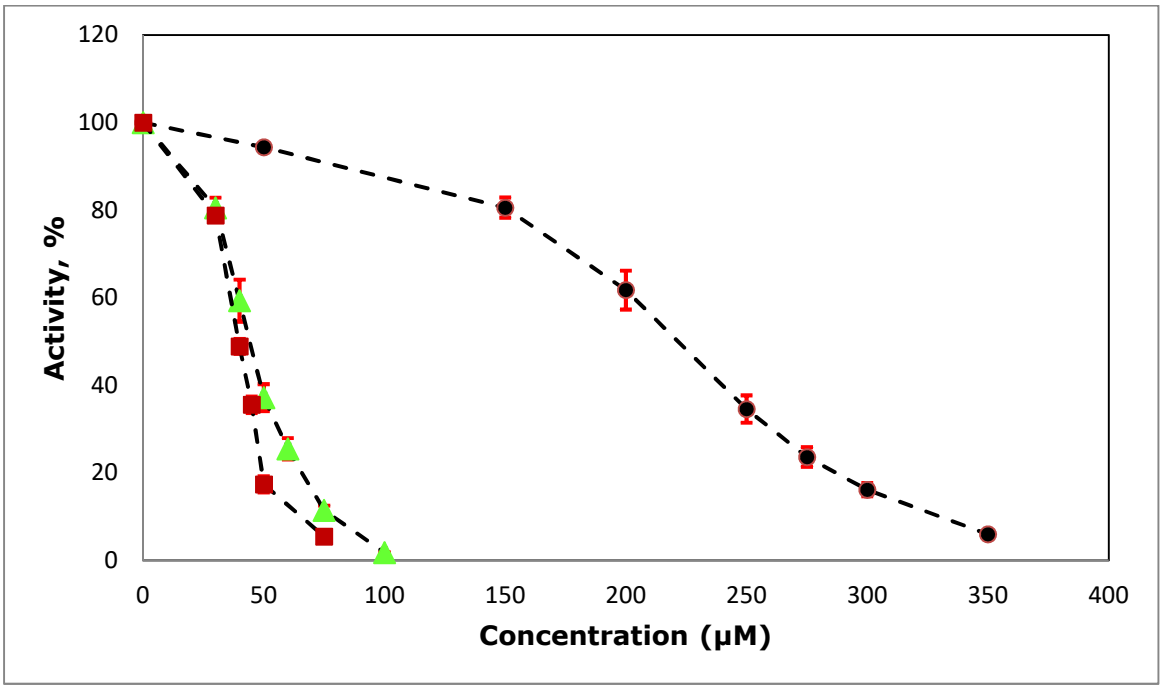

Figure 6. The inhibitory effect against lipoxygenase caused by (▲)[$SbCl_3(NMTU)_3$] (1), (■)[$SbBr_3(NMTU)_3$] (**2**),and (●) N-methythiourea in various concentrations.

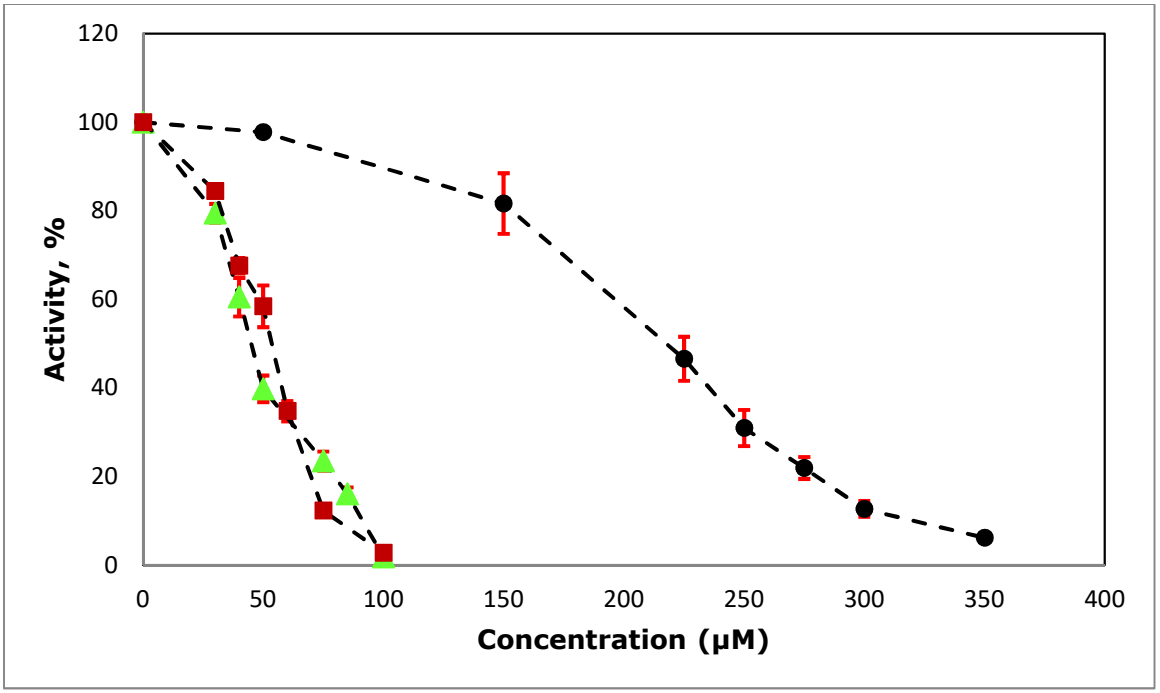

Figure 7. The inhibitory effect against lipoxygenase caused by (▲)[$SbCl_3(NETU)_3$] (3), (■)[$SbBr_3(NETU)_3$] (**4**), and (●) N-ethythiourea in various concentrations.

CONCLUSIONS

N-alkyl thioureas, namely N-methylthiourea (NMTU) and N-ethylthiourea (NETU) react with antimony(III) halides (halide: Cl or Br) to form compounds of formulas $[SbCl_3(NMTU)_3]$ (**1**), $[SbBr_3(NMTU)_3]$ (**2**),$[SbCl_3(NETU)_3]$ (**3**) and $[SbBr_3(NETU)_3]$ (**4**). The reactions of N-methylthiourea (NMTU) and N-ethylthiourea (NETU) with SbX_3 (X = Cl or Br) in a 2:1 HL/SbX_3 rate, but unexpected compounds were formed in a 3:1HL/SbX_3rate. All antimony(III) halide compounds are neutral with octahedral (O_h) geometry. All four compounds show higher inhibitory activity of lipoxygenase than free thioureas (N-methylthiourea (NMTU) and N-ethylthiourea (NETU)) and moreover, antimony(III) compounds of N-methylthiourea (**1**-**2**) show higher inhibitory activity of lipoxygenase than antimony(III) compounds of N-ethylthiourea (**3**-**4**). On the other hand, while antimony(III) halide compounds **1**-**4** display similar lipoxygenase inhibition with other antimony (III) compounds, they display lower lipoxygenase inhibition than the tin compounds in the literature [14, 38].

ACKNOWLEDGEMENTS

This work has been supported by Namik Kemal University (Project No. NKUBAP.01.GA.16.014).

REFERENCES

1. Norman NC, Editor. Chemistry of Arsenic, Antimony and Bismuth. Blackie Academic and Professional; 1998. ISBN: 978-0-7514-0389-3.

2. Sun H, Editor. Biological Chemistry of Arsenic, Antimony and Bismuth. Wiley. 2010. ISBN: 978-0-470-71390-7.

3. Parrilha GL, Dias RP, Rocha WR, Mendes IC, Benítez D, Varela J, Cerecetto H, M. González M, Melo CML, Neves JKAL, Pereira VRA, Beraldo H. 2-Acetylpyridine and 2-benzoylpyridine-derived thiosemicarbazones and their antimony(III) complexes exhibit high anti-trypanosomal activity. Polyhedron, 2012; 31; 614-21.DOI:10.1016/j.poly.2011.10.018.

4. Ajaz H, Hussain S, Altaf M, Stoeckli-Evans H, Isab AA, Mahmood R, Altaf S, Ahmad S. Synthesis and Characterization of Antimony(III) Complexes of Thioamides, and Crystal Structure of $\{[Sb(Imt)_2Cl_2]_2((_2\text{-Imt})\}Cl_2$(Imt=Imidazolidine-2-thione). Chinese Journal of Chemistry, 2011; 29; 254-58. DOI: 10.1002/cjoc.201190074.

5. Barnes NA, Godfrey SM, Pritchard RG, Ratcliffe S. The reactions of SbX_3 (X = Cl, Br, I) with N-methylbenzothiazole-2-thione (mbtt) and N-methylbenzothiazole-2-selone (mbts). Formation of the mixed mer/fac-complex $[mer\text{-}SbBr_3(mbts)_2(\mu\text{-}mbts)fac\text{-}SbBr_3(mbts)_2]\cdot CH_2Cl_2$. Polyhedron, 2010; 29; 1822-32. DOI:10.1016/j.poly.2010.02.029.

6. Bukvetskii BV, Sedakova TV, Mirochnik AG. Crystal structure and luminescence of antimony(III) bromide with aniline. Journal of Structural Chemistry. 2009; 50; 322-27. DOI:10.1007/s10947-009-0044-9.

7. Barnes NA, Godfrey SM, Pritchard RG, Ratcliffe S. The reaction of N,N `-Di-tert-butylthiourea (dtbtu) with antimony(III) halides—formation of the triply bridged [(dtbtu)SbX2(mu-X)(2)(mu-

dtbtu)SbX2(dtbtu)] (X = Cl, Br) dimers. European Journal of Inorganic Chemistry.2008; 3661–67. DOI: 10.1002/ejic.200800252.

8. Yin HD, Zhai J, Sun YY, Wang DQ. Synthesis, characterizations and crystal structures of new antimony (III) complexes with dithiocarbamate ligands. Polyhedron. 2008; 27; 663-70. DOI:10.1016/j.poly.2007.10.019.

9. Hadjikakou SK, Ozturk II, Banti CN, Kourkoumelis N, Hadjiliadis N. Recent advances on antimony(III/V) compounds with potential activity against tumor cells. Journal of Inorganic Biochemistry. 2015; 153; 293-305. DOI:10.1016/j.jinorgbio.2015.06.006.

10. Hadjikakou SK, Antoniadis CD, Hadjiliadis N, Kubicki M, Binolis J, Karkabounas S, Charalabopoulos K. (2005) Synthesis and characterization of new water stable antimony(III) complex with pyrimidine-2-thione and in vitro biological study. Inorganica Chimica Acta. 2005; 358; 2861–66. DOI:10.1016/j.ica.2004.06.028.

11. Ozturk II, Hadjikakou SK, Hadjiliadis N, Kourkoumelis N, Kubicki M, Baril M, Butler IS, Balzarini J. Synthesis, structural characterization, and biological studies of new antimony(III) complexes with thiones. The influence of the solvent on the geometry of the complexes. Inorganic Chemistry. 2007; 46; 8652–61. DOI: 10.1021/ic700756e.

12. Ozturk II, Hadjikakou SK, Hadjiliadis N, Kourkoumelis N, Kubicki M, Tasiopoulos AJ, Scleiman H, Barsan MM, Butler IS, Balzarini J. New antimony(III) bromide complexes with thioamides: synthesis, characterization, and cytostatic properties. Inorganic Chemistry. 2009; 48; 2233–45. DOI: 10.1021/ic8019205.

13. Hadjikakou SK, Ozturk II, Xanthopoulou MN, Zachariadis PC, Zartilas S, Karkabounas S and Hadjiliadis N. Synthesis, structural characterization and biological study of new organotin(IV), silver(I) and antimony(III) complexes with thioamides. Journal of Inorganic Biochemistry. 2008; 102; 1007-15. DOI: 10.1016/j.jinorgbio.2007.12.027.

14. Ozturk I, Filimonova S, Hadjikakou SK, Kourkoumelis N, Dokorou V, Manos MJ, Tasiopoulos AJ, Barsan MM, Butler IS, Milaeva ER, Balzarini J, Hadjiliadis N. Structural motifs and biological studies of new antimony(III) iodide complexes with thiones. Inorganic Chemistry. 2010; 49; 488–501. DOI: 10.1021/ic901442e.

15. Ozturk II, Metsios AK, Filimonova-Orlova S, Kourkoumelis N, Hadjikakou SK, Manos E, Tasiopoulos AJ, Karkabounas S, Milaeva ER and Hadjiliadis N. Study on single crystal structure of the antimony(III) bromide complex with 3-methyl-2-mercaptobenzothiazole and biological activity of some antimony(III) bromide complexes with thioamides. Medicinal Chemistry Research. 2012; 21; 3523-31. DOI 10.1007/s00044-011-9905-9.

16. Ozturk II, Kourkoumelis N, Hadjikakou SK, Manos MJ, Tasiopoulos AJ, Butler IS, Balzarini J and Hadjiliadis N. Interaction of antimony(III) chloride with thiourea, 2-mercapto-5-methyl-benzimidazole, 3-methyl-2-mercaptobenzothiazole, 2-mercaptopyrimidine, and 2-mercaptopyridine. Journal of Coordination Chemistry. 2011; 64; 3859-71. DOI: 10.1080/00958972.2011.633603.

17. Ozturk II, Banti CN, Manos MJ, Tasiopoulos AJ, Kourkoumelis N, Charalabopoulos K and Hadjikakou SK. Synthesis, characterization and biological studies of new antimony(III) halide complexes with ω-thiocaprolactam. Journal of Inorganic Biochemistry. 2012; 109; 57-65. DOI: 10.1016/j.jinorgbio.2012.01.014.

18. Ozturk II, Urgut OS, Banti CN, Kourkoumelis N, Owczarzak AM, Kubicki M, Charalabopoulos K and Hadjikakou SK. Synthesis, structural characterization and cytotoxicity of the antimony(III) chloride complex with N,N-dicyclohexyldithiooxamide Polyhedron. 2013; 52; 1403-10. DOI: 10.1016/j.poly.2012.04.038.

19. Ozturk II, Urgut OS, Banti CN, Kourkoumelis N, Owczarzak AM, Kubicki M and Hadjikakou SK. Synthesis, structural characterization and cytostatic properties of N,N-dicyclohexyldithiooxamide complexes of antimony(III) halides (SbX3, X: Br or I). Polyhedron. 2014; 70; 172-79. DOI: 10.1016/j.poly.2013.12.025.

20. Han A, Ozturk II, Banti CN, Kourkoumelis N, Manoli M, Tasiopoulos AJ, Owczarzak AM, Kubicki M and Hadjikakou SK. Antimony(III) halide compounds of thioureas: Structures and biological activity. Polyhedron. 2014; 79; 151-60. DOI: 10.1016/j.poly.2014.05.014.

21. Urgut OS, Ozturk II, Banti CN, Kourkoumelis N, Manoli M, Tasiopoulos AJ and Hadjikakou SK. New antimony(III) halide complexes with dithiocarbamate ligands derived from thiuram degradation: The effect of the molecule's close contacts on in vitro cytotoxic activity. Materials Science and Engineering C. 2016; 58; 396–408. DOI: 10.1016/j.msec.2015.08.030.

22. Urgut OS, Ozturk II, Banti CN, Kourkoumelis N, Manoli M, Tasiopoulos AJ and Hadjikakou SK. Addition of tetraethylthiuram disulfide to antimony(III) iodide; synthesis, characterization and biological activity.InorganicaChimicaActa. 2016; 443; 141-150. DOI: 10.1016/j.ica.2015.12.028.

23. Samuelsson B, Dahlen SE, Lindgren J, Rouzer CA, Serhan CN. Leukotrienes and lipoxins: structures, biosynthesis, and biological effects. Science. 1987; 237; 1171-76. DOI: 10.1126/science.2820055

24. Knapp MJ, Klinman JP. Kinetic Studies of Oxygen Reactivity in Soybean Lipoxygenase-1. Biochemistry. 2003; 42; 11466-75. DOI: 10.1021/bi0300884.

25. Ding XZ, Kuszynski CA, El-Metwally TH, Adrian TE. Lipoxygenase Inhibition Induced Apoptosis, Morphological Changes, and Carbonic Anhydrase Expression in Human Pancreatic Cancer Cells. Biochemical and Biophysical Research Communications. 1999; 266; 392-99. DOI: 10.1006/bbrc.1999.1824.

26. Pidgeon GP, Lysaght J, Krishnamoorthy S, Reynolds JV, O'Byrne K, Nie D, Honn KV. Lipoxygenase metabolism: roles in tumor progression and survival. Cancer Metastasis Reviews. 2007; 26; 26 (2007) 503-24. DOI: 10.1007/s10555-007-9098-3.

27. Bourne S, Koch KR. Intramolecular hydrogen-bond controlled unidentate co-ordination of potentially chelating N-acyl-N'-alkylthioureas: crystal structure of cis-bis(N-benzoyl-N'-propylthiourea) dichloroplatinum(II). Journal of the Chemical Society, Dalton Transactions. 1993; 13; 2071–72. DOI: 10.1039/DT9930002071.

28. Kucukguzel I, Kucukguzel SG, Rollas S, Kiras M. Some 3-Thioxo/alkylthio-1,2,4-triazoles with a substituted thiourea moiety as possible antimycobacterials. Bioorganic Medicinal Chemistry Letters. 2001; 11; 1703–07. DOI: 10.1016/S0960-894X(01)00283-9.

29. Venkatachalam TK, Sudbeck EA, Uckun FM. Regiospecific synthesis, X-ray crystal structure and biological activities of 5-bromothiophenethyl thioureas. Tetrahedron Letters. 2001; 42; 6629–32. DOI: 10.1016/S0040-4039(01)01290-4.

30. Campo RD, Criado JJ, Gheorghe R, Gonzalez FJ, Hermosa MR, Sanz F, Manzano JL, Monte E, Rodrıguez-Fernandez E. N-benzoyl-N′-alkylthioureas and their complexes with Ni(II), Co(III) and Pt(II) – crystal structure of 3-benzoyl-1-butyl-1-methyl-thiourea: activity against fungi and yeast. Journal of Inorganic Biochemistry. 2004; 98; 1307–14. DOI: 10.1016/j.jinorgbio.2004.03.019.

31. Ahmad S, Isab AA, Ahmad S. ^{1}H, ^{13}C, ^{15}N NMR and IR Spectroscopic Studies of a Rh(II) Complex of Thiourea. Journal of Coordination Chemistry. 2003; 56; 1587-95.DOI: 10.1080/0095897031000164168 8.

32. Rodríguez-Fernández E, Manzano JL, Benito JJ, Hermosa R, Monte E, Criado JJ. Thiourea, triazole and thiadiazine compounds and their metal complexes as antifungal agents. Journal of Inorganic Biochemistry. 2005; 99; 1558-72. DOI: 10.1016/j.jinorgbio.2005.05.004.

33. Plutín AM, Alvarez A, Mocelo R, Ramos R, Castellano EE, da Silva MM, Colina-Vegas L, Pavan FR, Batista AA. Anti-Mycobacterium tuberculosis activity of platinum(II)/N,N-disubstituted-N'-acyl thiourea complexes. Inorganic Chemistry Communications. 2016; 63; 74–80. DOI: 10.1016/j.inoche.2015.11.020.

34. Schwade VD, Kirsten L, Hagenbach A, Lang ES, Abram U. Indium(III), lead(II), gold(I) and copper(II) complexes with isophthaloylbis(thiourea) ligands. Polyhedron. 2013; 55; 155–61. DOI: 10.1016/j.poly.2013.03.008.

35. Bowmaker GA, Pakawatchai C, Saithong S, Skelton BW, White AH, Structural and spectroscopic studies of some adducts of silver(I) halides withthiourea and N-ethyl substituted thioureas. Dalton Transactions. 2010; 39; 4391–4404. DOI: 10.1039/C001398F.

36. Hough E, Nicholson DG. Stereochemical role of lone pairs in main-group elements. Part 2. Structure and bonding in trichloro(tetramethylthiourea)antimony(III) studied by means of X-ray crystallography and antimony-121 Mössbauer spectroscopy. Journal of the Chemical Society, Dalton Transactions. 1981; 10; 2083-87. DOI: 10.1039/DT9810002083.

37. Xanthopoulou MN, Hadjikakou SK, Hadjiliadis N, Milaeva ER, Gracheva YA, Tyurin VY, Kourkoumelis N, Christoforidis KC, Metsios AK, Karkabounas S, and Charalabopoulos K. Biological studies of new organotin(IV) complexes of thioamide ligands.European Journal of Medicinal Chemistry. 2008; 43; 327-35. DOI: 10.1016/j.ejmech.2007.03.028.

38. Xanthopoulou MN, Hadjikakou SK, Hadjiliadis N, Kubicki M, Karkabounas S, Charalabopoulos K, Kourkoumelis N, and Bakas T. Synthesis and characterization of a new chloro-di-phenyltin(IV) complex with 2-mercapto-nicotinic acid: Study of its influence upon the catalytic oxidation of linoleic acid to hydroperoxylinoleic acid by the enzyme lipoxygenase. Journal of Organometallic Chemistry. 2006; 691; 1780-89. DOI: 10.1016/j.jorganchem.2005.11.073.

39. Glick D, Editor. Methods of Biochemical Analysis, Volume 2. Interscience Publishers. 1955. ISBN: 9780471304593.

40. Lopez-Nicolas JM, Bru R, Sanchez-Ferrer A, Carcia-Carmona A. An Octaethylene Glycol Monododecyl Ether-Based Mixed Micellar Assay for Lipoxygenase Acting at Neutral pH. Analytical Biochemistry. 1994; 221; 410-15. DOI: 10.1006/abio.1994.1435.

41. Axelrod B, Cheesbrough TM, Laakso S. [53] Lipoxygenase from soybeans: EC 1.13.11.12 Linoleate: oxygen oxidoreductase. Methods Enzymology. 1981; 71; 441-451. DOI:10.1016/0076-6879(81)71055-3.

42. Refat MS, Killa HMA, Fetooh H. Spectroscopic and thermal characterization of Cu(II), Co(II), Ni(II) and Mn(II) complexes of fluorescent dye 4-N,N-dimethyl-ethanolamine-N-allyl-1,8-naphthalimide (4DMEAN). Journal of Molecular Structure. 2010; 983; 122–132. DOI:10.1016/j.molstruc.2010.08.041.

43. Nadeem S, Rauf MK, Ahmad S, Ebihara M, Tirmizi SA, Bashir SA, Badshah A. Synthesis and characterization of palladium(II) complexes of thioureas. X-ray structures of [Pd(N,N'-dimethylthiourea)$_4$]Cl_2.2H_2O and [Pd(tetramethylthiourea)$_4$]Cl_2. Transition Metal Chemistry. 2009; 34; 197–202. DOI: 10.1007/s11243-008-9177-5.

Türkçe Öz ve Anahtar Kelimeler

Bazı n-Alkil Tiyoüreler İçeren Yeni Antimon(III) Halojenür Kompleksleri: Sentez, Karakterizasyon ve Linoleik Asidin Hidroperoksilinoleik Aside Lipoksijenaz ile Katalitik Yükseltgenmesindeki Etkilerinin İncelenmesi

Ibrahim Ismet Ozturk

Öz: Dört yeni tiyoüre-antimon(III) bileşiği (SbX_3; X=Cl veya Br) sentezlenmiştir. Kullanılan üre türevleri N-metiltiyoüre (NMTU) ve N-etiltiyoüre (NETU) olup oluşan komplekslerin kapalı formülleri $[SbCl_3(NMTU)_3]$ (**1**), $[SbBr_3(NMTU)_3]$ (**2**),$[SbCl_3(NETU)_3]$ (**3**) ve $[SbBr_3(NETU)_3]$ (**4**) olarak belirlenmiştir. Bu yeni antimon(III) halojenürler erime noktası, elementel analiz, molar iletkenlik, FT-Kızılötesi spektroskopisi, FT-Raman spektroskopisi, UV-Vis spektrofotometrisi NMR (^1H ve ^{13}C) spektroskopisi ve TG-DTA analizi ile karakterize edilmiştir. N-Metiltiyoüre (NMTU) ve N-etiltiyoüre (NETU) ile SbX_3 (X = Cl veya Br) arasındaki 2:1 ligand/metal oranındaki tepkimeden 3:1 ligand metal oranına sahip beklenmeyen ürünler elde edilmiştir. Bileşikler çözeltide non-elektrolit olarak bulunur ve bileşiklerin spektroskopik verileri altı koordinasyonlu oktahedral geometri ile uyumludur, bu komplekslerde üç halojenür iyonu ve üç tiyoüre kükürt atomu bulunmaktadır. N-Metiltiyoüre ve N-etiltiyoüre ligandları **1-4** bileşiklerinde kükürt üzerinden bağlanan monodentat bir karaktere sahiptir. **1-4** bileşiklerinin, N-metiltiyoüre ve N-etiltiyoürenin, linoleik asidin hidroperoksilinoleik aside lipoksijenaz ile katalitik peroksidasyonu ile dönüşmesi kinetik olarak çalışılmıştır.

Anahtar kelimeler: Antimon(III) halojenürler; N-alkil tiyoüreler; spektroskopik karakterizasyon; lipoksijenaz.
Sunulma: 23 Temmuz 2016. **Kabul:** 01 Ekim 2016.

JOTCS A
Journal of the Turkish Chemical Society
Section: A
Chemistry
TURKISH CHEMICAL SOCIETY

Anti-Diabetic Efficacy and Phytochemical Screening of Methanolic Leaf Extract of Pawpaw (*Carica papaya*) Grown in North Central Nigeria.

Ayorinde Victor Ogundele*[1], Kabir Opeyemi Otun[1], Abdulfatai Ajiboye[1], Bolatito Eunice Olanipekun[1], and Rasheed Bolaji Ibrahim[2]

1. Chemistry unit, Department of Chemical, Geological and Physical Science, Kwara State University, P.M.B 1530, Malete, Nigeria.

2. Biochemistry unit, Department of Biosciences and Biotechnology, Kwara State University, P.M.B 1530, Malete, Nigeria.

Abstract: *Carica papaya* leaf samples (Green) were freshly harvested and dried for six consecutive days. The leaves were extracted with methanol; the resulting extracts were screened for the phytochemical constituents using a standard procedure. Phytochemical screening revealed the presence of bioactive compounds such as tannins, saponins, terpenoids, glycosides, and alkaloids. The *in vitro* anti-diabetic potential of the plant was also determined so as to justify the traditional usage of the plant in treating diabetes. The result of the present study confirmed that the methanolic extract of *C. papaya* leaves possess significant anti-diabetic activity *in vitro*, this shows that the leaves has the potential for the development of drugs in combating diabetes.

Keywords: *Carica papaya* leaves; phytochemical screening; bioactive substances; anti-diabetic property; *in-vitro* analysis.

Submitted: August 09, 2016. **Revised:** September 23, 2016. **Accepted:** October 14, 2016.

Cite this: Ogundele A, Otun K, Ajiboye A, Olanipekun B, Ibrahim R. Anti-Diabetic Efficacy and Phytochemical Screening of Methanolic Leaf Extract of Pawpaw (Carica papaya) Grown in North Central Nigeria. JOTCSA. 2017;4(1):99–114.

DOI: 10.18596/jotcsa.52813.

*Corresponding author. E-mail: vicshow2001@gmail.com.

INTRODUCTION

Human beings have been plagued with diverse types of diseases such as HIV/AIDS, cancer, cholera, hepatitis, leprosy, measles, and diabetes among others. Diabetes mellitus is among the leading causes of death worldwide and it is prevalent in developing nations which may be partly due to the nature of the diets in this part of the world and other factors such as heredity and environmental factors. (1). This disease is caused by an unusual high concentration of sugar in the blood which might be a direct consequence of deficiency of insulin (2). The control or the cure of diabetes without side effects is a serious challenge militating against the development of anti-diabetic therapeutics over the centuries. Of core importance to the development of an anti-diabetic therapeutic is controlling hyperglycaemia, which is the milestone of diabetes and its complications. Thus, controlling excess sugar in the blood is the most crucial aim in reducing the risks associated with diabetes and its complications (3). One of the major means of treating the disease includes, but not limited to, insulin and various oral anti-diabetic agents such as sulfonylureas, biguanides and glinides. However, these agents are not devoid of adverse effects as such, there has been renewed search for hypoglycaemic agents with far lesser or no effect whatsoever.

Diabetes mellitus is an age-long disease and medicinal plant extracts have remained rich repository of therapeutically useful phytoconstituents and viable alternative in combating various diseases plaguing the mankind. There are some plants which possess bioactive compounds which have been reported to be used in combating diabetes worldwide and have been used in treating diabetes. Anti-hyperglycaemic properties of the plants are in direct relationship with their ability to restore the function of pancreatic tissues by causing an increase in insulin output or inhibit the intestinal absorption of glucose or to the facilitation of metabolites in insulin dependent processes (4).

Structures of some anti-diabetic compounds that have been successfully isolated from different plants are given below:

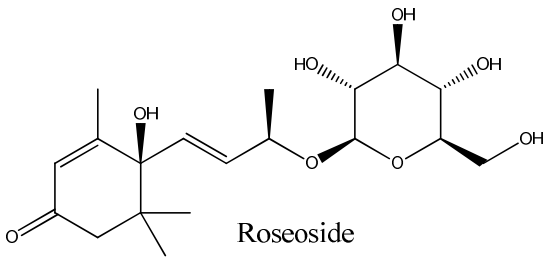

Roseoside

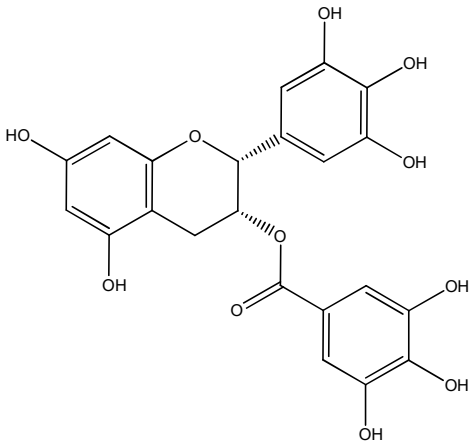

epigallocatechin gallate

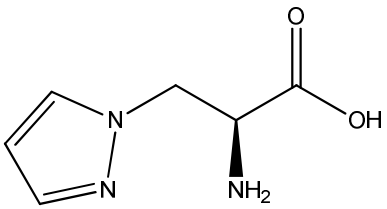

beta-pyrazol-1-ylalanine

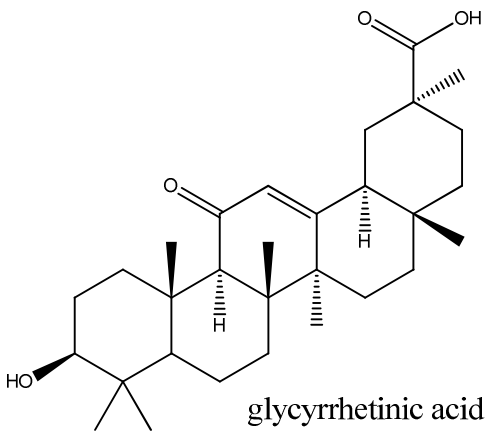

glycyrrhetinic acid

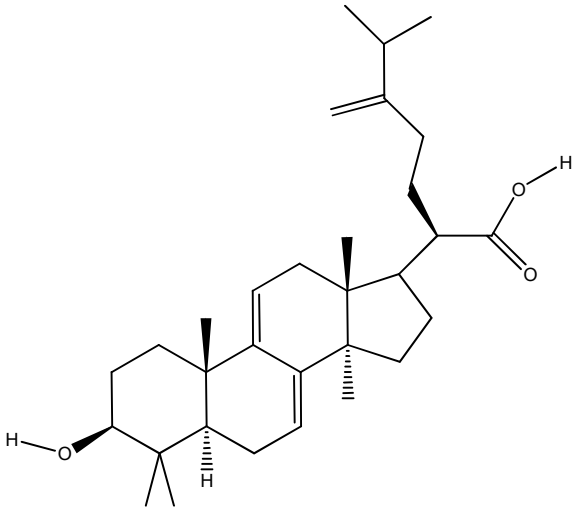

dehydrotrametenolic acid

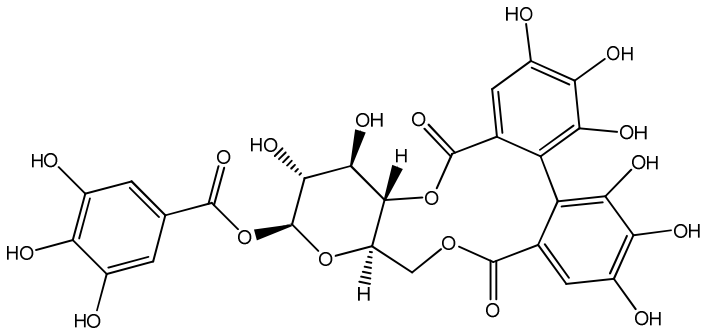

strictinin

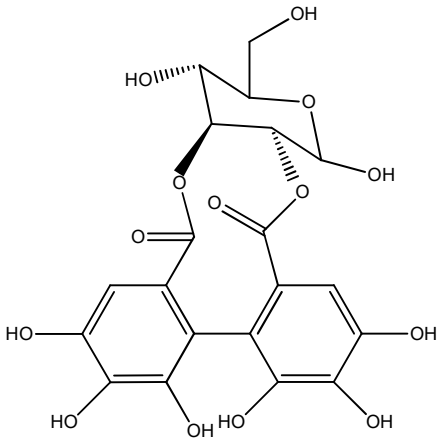

isostrictinin

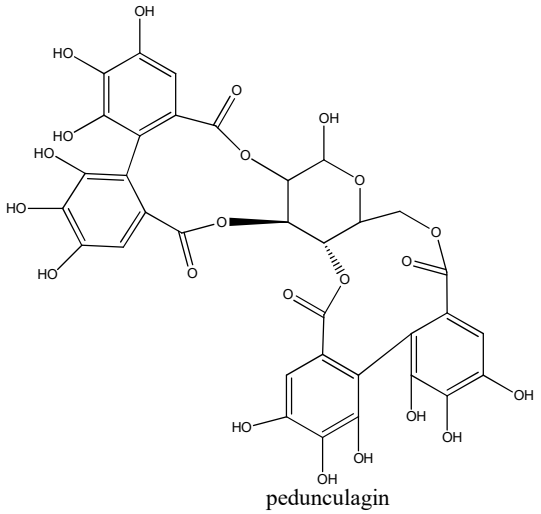

pedunculagin

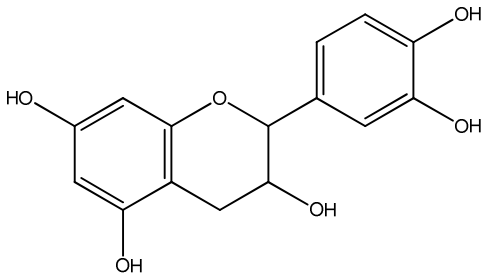

epicatechin

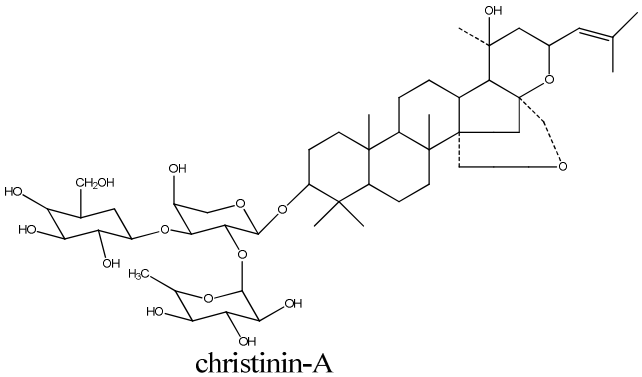

christinin-A

Plants are normally made use of in folk medicine to combat different ailments among which diabetes belong to, such plants include; *Allium cepa* (Onions), *Cynodon dactylon, Clerodendron phlomoides, Cinnamomum tamala, Coccinia indica, Enicostemma littorale, Ficus bengalensig, Gymnema sylvestre* leaves (Gurnar), *Momordica charantia* (Bitter melon), *Pterocarpus marsupium, Syzygium cumini (6,7), Vernonia amygdalina, Pandanus amaryfollius* (Pandan), *Ocimum basilicum L. (Lamiaceae), Phyllanthus niruri L.* (Euphoribiaceae), *Viscum album L.* (Viscaceae or Loranthaceae) (8), *Allium sativum* (Garlic), *Aloe vera, Cinnamomum cassie, Catharanthus roseus* (Madagascar periwinkle), *Muurrayi komingii, Ocimum santum, panax ginseng, Trigonella foemum-graecum* (Fenugreek), *Pterocarpus marsupium* (Indian kino) and *Syzigium cumini* (9-11). The isolated compounds from these plants are currently undergoing clinical trials so as to ascertain their efficacy and conformability to the standard.

Medicinal plants that have been confirmed to possess anti-diabetic properties in Nigeria are- *Vinca major L, Azadirachta indica, Carica papaya, Gongronema latifolium, Securridaca langepedunculat, Sclerocarya birrea* [CA. Rich], *Momordica balsamina L, Hypoxis*

*hemerocallidea (*Africa potato), *Harpagophylum procumbens DC, Clauseria anisata* (wild), *Cissampelos capensis, Brachylaena discolour,* (12-17).

Quite a number of researches have been conducted on various parts of *Carica papaya* family Caricaceae*.* The plant is home to various types of bioactive compounds (18). The leaves of *Carica papaya* are used traditionally to treat numerous ailments such as malaria, dengue, jaundice, immunomodulatory, and antiviral activity (19). Other diseases that have been reported to be controlled by *Carica papaya* traditionally in Nigeria includes; abdominal discomfort, pain, malaria, diabetes, obesity, infections, and oral drug poisonings. Adeneye and Olagunju, 2009 and Ahmad *et al*., 2011 reported the therapeutic potential of *Carica papaya* on dengue and malaria while Owoyele *et al*., 2008 confirmed the anti-inflammatory potency of the plant, similarly, Aruoma reported the effect of *Carica papaya* fruits and leaves on the sugar reducing tendency of the plant (20-23).

Despite the enormous work which have been done to probe the anti-diabetic potency of various parts of *C. papaya* over the world, report is scanty on the efficacy of the leaves of this plant in lowering the abnormally high blood sugar usually associated with diabetes hence, the present study aimed at investigating the phytochemical profile and also evaluate *the in vitro anti-diabetic potency of C. papaya leaves.*

MATERIALS AND METHODS

Sample collection

Green leaves of *Carica papaya* were collected from Islamic village in Ilorin, Ilorin West Local Government, Kwara State, Nigeria. The plant was authenticated at the herbarium of Plant and Environmental Biology Department, Kwara State University Malete, Nigeria.

Preparation of Sample

The leaves were dried under ambient conditions for six consecutive days and subsequently pulverized. A 70-gram-sample of the pulverized leaves was extracted with methanol for 72 hours and the resultant crude extract obtained was filtered. The crude extract was concentrated under reduced pressure using rotary evaporator to obtain a solvent-free methanol extract and stored in an air-tight bottle for further analyses.

Phytochemical analysis

The qualitative phytochemical tests were carried out to determine the presence and absence of various phytochemical constituents such as of alkaloids, saponins, glycosides, terpenoids, and tannins using the standard method (24).

***In vitro* anti-diabetic activity test**

The *Carica papaya* leaf extract was subjected to non-enzymatic glycosylation of haemoglobin assay, and α-amylase inhibition assay. Anti-diabetic efficacy of *C. papaya* was carried out by estimating the degree of non-enzymatic haemoglobin glycosylation, measured colorimetrically at 520 nm. Glucose (2%), haemoglobin (0.06%) and gentamycin (0.02%) solutions were prepared in phosphate buffer 0.01 M and pH 7.4. 1 mL each of above solution was mixed. 1 mL of the concentrated extract was added to the mixture. It was incubated in dark at ambient condition for 72 hrs. The degree of glycosylation of haemoglobin was measured colorimetrically at 520 nm. % inhibition was calculated using standard literature procedure (34). α-Tocopherol (Trolox) was used as a standard drug for assay (25).

Alpha amylase inhibition assay

A starch solution (0.1% w/v) was obtained by stirring 0.1 g of potato starch in 100 mL of 16 mM of sodium acetate buffer. The enzyme solution was prepared by mixing 27.5 mg of alpha amylase in 100 mL of distilled water. The colorimetric reagent is prepared by mixing sodium potassium tartrate solution and 3, 5-dinitrosalicylic acid solution at 96 mM. In alpha amylase inhibition method, 1 mL of substrate - potato starch (1% w/v), 1 mL of plant extract of four different concentrations (40, 60, 80, and 100 µg/mL), 1 mL of alpha amylase enzyme (1% w/v) and 2 mL of acetate buffer (0.1 M, pH 7.2) were added. Both control and plant extracts were added with starch solution and left to react with α- amylase solution under alkaline conditions at 25^0C. The reaction was monitored for 3 minutes. The generation of maltose was quantified by the reduction of 3, 5-dinitrosalicylic acid to 3-amino-5-nitrosalicylic acid. This reaction is detectable at 540 nm (26).

Glucose uptake in yeast cells

Commercial baker's yeast was washed by repeated centrifugation (3000 g; 5 mins) with distilled water until the supernatant fluids were clean and 10 % (v/v) suspension was prepared in distilled water. Various concentrations of extracts (1-5 mg) were added to 1 mL of glucose solution (5, 10 and 25 mM) and incubated together for 10 mins at 37 ºC. Reaction started by adding 100 mL of yeast suspension, vortexed and further incubated at 37 ºC for 60 mins. After that time, the tubes were centrifuged (2500 g, 5 min) and glucose was estimated in the supernatant. Metronidazole was taken as standard drug (27). The increase in the percentage of glucose uptake by yeast cells was calculated based on standard literature procedure.

RESULTS AND DISCUSSION

Phytochemical analysis

The result of the qualitative phytochemical screening (secondary metabolites) present in the methanolic extract of *C. papaya* leaves is presented in Table 1. The screening revealed the presence of various bioactive constituents like polyphenol, tannins, saponins, terpenoids, flavonoids, glycosides and alkaloids. Anthocyanin was absent in the leaves studied. This result is in concordance with the reports (28-31). Various medicinal values of plants are functions of the phytochemicals that are present in such plant and may therefore be responsible for their anti-hyperglycemic properties.

Ayoola & Adeyeye reported (30) that saponins, cardiac glycosides, and alkaloids are the major bioactive components present in the leaves of *Carica papaya*. The presence of saponins supports the fact that pawpaw leaf has cytotoxic effects (32). The presence of alkaloids in the leaves shows that this plant can be effective anti-malarial, since alkaloids consist of quinine, which is an anti-malarial drug (33).

Table 1. Phytochemical screening of methanolic extracts of *Carica papaya* extract.

Phytochemical compounds	MTH/CP
Polyphenol & Tannins	+
Flavonoids	+
Saponins	+
Terpenoids	+
Anthocyanins	-
Glycosides	++
Alkaloids	+

Key terms: +=trace amount, ++= strongly present, -= absent, MTH/CP= Methanolic extract of *Carica papaya*

α-amylase inhibitory effect of methanolic *C.papaya* extract

Alpha-amylase is a digestive enzyme found in the secretions of the intestinal mucosa, pancreas, and the saliva. It is responsible for the breakdown of α-1, 4-glycosidic bonds in starch. Thus, the catalytic activities of the enzyme (especially in the small intestine), increase the availability of glucose in the blood, since the pH of the intestine is around 6.9, α–amylase has access to starch at this pH and catalyses the breakdown of this polysaccharide into monosaccharide and disaccharide. At a concentration of 100 µg/mL, *C. papaya* leaf shows the highest percentage of inhibition of 25.2%. There was a dose dependent increase in percentage inhibitory activity against α–amylase enzyme as shown in Table 2. From the data, the results suggest that the extract possesses significant inhibitory activity since the percentage inhibition varied from 19.63 to 25.2 in the concentration range of 80 µg/mL - 100 µg/mL which was higher when compared to that of the standard drug within the same range. The α–amylase inhibitors act as an anti-nutrient that obstructs the digestion and absorption of carbohydrates (36).

Table 2. Effect of methanol extract of *Carica papaya* leaf on α-amylase inhibition.

Concentration (µg/mL)	Standard % Inhibition	Methanolic extract of *Carica papaya* leaf % Inhibition
20	5.65%	9.6%
40	9.58%	13.2%
60	13.20%	16.54%
80	13.20%	19.63%
100	22.50%	25.2%

Values are expressed as mean ± SMD. Absorbance of blank= 0.217±0.00

Glucose uptake action of methanolic *C.papaya* extract

Glucose transport across yeast cellular membrane occurs via facilitated diffusion down concentration gradient. The rate of glucose transport across the membrane in yeast cell system at different glucose concentrations, *i.e.* 20, 40, 60, 80, and 100 µg/mL respectively, is

presented in Table 3. The mechanism of glucose transport across the yeast cell membrane has been receiving attention as *in vitro* screening method for hypoglycaemic effect of various compounds present in medicinal plants. Recent studies on the transport of non metabolizable sugars and certain metabolizable glycosides suggest that sugar transport across the yeast cell membrane is mediated by stereospecific membrane carriers. This implies that the dose-dependent increase in the glucose uptake of yeast (Table 3) is a reflection of the extract's ability to enhance the utilization of glucose by yeast. This is because transport of glucose is only attained (and continued) if there is removal of intracellular glucose. The result obtained suggest that methanol extract of *C. papaya* leaves were capable of enhancing glucose uptake (utilization) thereby controlling the blood glucose level (25).

Table 3. Effect of methanolic extract of *Carica papaya* leaf on the uptake of glucose by yeast cells.

Concentration (µg/mL)	**Methanolic extract of *Carica papaya* leaf**
% Glucose uptake	
20	9.17%
40	16.2%
60	16.2%
80	19.3%
100	24.82%

Values are expressed as mean ± SMD. Absorbance of blank=0.225 ±0.00

In vitro non-enzymatic glycosylation of haemoglobin

The inhibitory effect of methanolic *C. papaya samples* on non-enzymatic glycosylation of haemoglobin is shown in Table 4. *C. papaya* exhibits a concentration-dependent increase in % inhibition of glycosylation, which suggests that the plant extract decreases the formation of the glucose haemoglobin complication and thus the amount of free haemoglobin increases. Interestingly, at a concentration of 100 µg/mL, *C. papaya* showed the highest percentage inhibition of 20.6% which compared favorably with that of the standard. Increased concentration of glucose in the blood leads to its binding to haemoglobin which may result in the formation of the reactive oxygen species (37).

Table 4. Effect of methanolic extract of *C. papaya* leaf extract on haemoglobin glycosylation.

Concentration (µg/mL)	**Standard**	**Methanolic extract of *Carica papaya* leaf**
	% Inhibition	**% Inhibition**
20	5.38%	5.38%
40	8.8%	12.1%
60	17.8%	15.2%
80	23.1%	18%
100	29.7%	20.6%

Values are expressed as mean ± SMD. Absorbance of blank= 0.246 ± 0.00

CONCLUSION

The result of the present study demonstrated that the qualitative phytochemical analysis of methanolic extract of *C. papaya* leaves confirmed the presence of the following phytoconstituents; polyphenol, tannins, saponins, terpenoids, flavonoids, glycosides, and alkaloids. The *in vitro* anti-diabetic potential of the plant extract was confirmed through α-amylase inhibition, glucose uptake by yeast cells and non-enzymatic glycosylation methods. The result of this research confirms the claim of Yoruba herbalists in using the leaves of the plant to control diabetes, however; further exploration of the various bioactive compounds should be isolated and developed into drugs to combat the disease. The result of the present study confirmed that the methanolic extract of *C. papaya* leaves possess significant anti-diabetic activity *in vitro,* this shows that the leaves has the potential for the development of drugs in combating diabetes.

REFERENCES

1. World Health Forum; Controller of Publication, United States of America, *Ministry of Health Sciences forum*, WHO, 1993;**14**(6): 390-396

2. Narkhede, M.B., Ajimire, P.V., Wagh, A.E., Manoj, M. and Shivashanmugam, A.T. In vitro antidiabetic activity of *Caesalpina digyna (*R.) methanol root extract. Asian J. Plant Sci. Res., 2011;**1**(2):101-106.URL: https://www.researchgate.net/publication/266871671_In_vitro_antidiabetic_activity_of_Caesalpina_digyna_R_methanol_root_extract

3. Polonsky, K.S.,. The past 200 years in diabetes. *N. Engl. J. Med.* 2012; **367**, 1332-1340. DOI: 10.1056/NEJMra1110560

4. DK Patel, SK Prasad, R Kumar, S Hemalatha.. An overview on antidiabetic medicinal plants having insulin mimetics property *Asian Pac J Trop Biomed,* 2012; **2** (4), pp. 320–330. DOI: 10.1016/S2221-1691(12)60032-X

5. Jung M, Park M, Lee HC, Kang YH, Kang ES, Kim SK. Anti-diabetic agents from medicinal plants. Curr med chem. 2006; 13(10): 1203-1218. URL: https://www.ncbi.nlm.nih.gov/pubmed/16719780

6. Modak M, Dixit P, Londhe J, Ghaskadbi S, Paul A, Devasagayam T. Indian herbs and herbal drugs used for the treatment of diabetes. *J. Clin Biochem Nutri*. 2007; **40** (3): 163-173. DOI: 10.3164/jcbn.40.163

7. Jarald E, Joshi SB, Jain DC. Diabetes and herbal medicines. *Iran J Pharmacol Ther.* 2008;**7**(1): 97-106. URL: http://ijpt.iums.ac.ir/index.php/ijpt/article/viewFile/369/331

8. Simon JE (1995). Basil New crop Factsheet Centre for New Crops and Plant Products, Purdue University. URL: http:// www.hort.purdue.edu/newcrop/CropFactSheets/basil.html.

9. Grover JK, Yadav S, Vats V. Medicinal plants of india with anti-diabetic potential*. J Ethnopharmacol.* 2002; **81**: 81-100. DOI: 10.1016/S0378-8741(02)00059-4

10. Brai BIC, Odetola AA, Agomo PU. Anti-hyperglycemic activity of *Cassia kleinii* leaf extract in normal rats and alloxan-induced diabetic rats. Indian J. Pharmcol. 2007; 34: 409-415. URL: http://medind.nic.in/ibi/t02/i6/ibit02i6p409.pdf

11. Gondwe M, Okoro. PK, Juta R. Effect of diabetes on kidney. *Diabetes*.2008; **52**: 283-291

12. Ojiako AO, Chikezie PC, Ogbuji CA (2015) Blood glucose level and lipid profile of alloxan-induced hyperglycaemic rats treated with single and combinatorial herbal formulations *J.Tradit Compl*. DOI:10.1016/j.jtcme.2014.12.005

13. Ojiako AO and Chikezie PC. Comparative proximate composition and hypoglycaemic properties of three medicinal plants (*Verononiа amygdalina, Azadirachata indica* and *Moringa oleifera)*. *Pharmacogn commun* .2014;**4**: 40-48. DOI:10.5530/pc.2014.3.4

14. Ugochukwu NH, Fafunso PJ, Boba AT, Babady NE. The various medicinal effects of Gongronema *latifolium. Phytother Res*.2005;**12**:46-52.

15. Ojewole JAO. Analgesic, anti-inflammatory and hypoglycaemic effects of *Securidaca longepedunculata (Fresen.)* [*Polygalaceae*] root-bark aqueous extracts inflammo-pharmacol. 2008;16: 174-181. DOI: 10.1007/s10787-007-0016-7

16. Ibegbulem CO, Chikezie PC. Hypoglycaemic properties of ethanolic extracts of *Gongronema latifolium, Aloe perryi, Viscum album* and *Allium sativum* administered to alloxan-induced diabetic albino rats (*Rattus norvegicus*). *Pharmacogn commun.*2013;**3**:12-16. DOI: 10.5530/pc.2013.2.4

17. Chikezie PC, Uwakwe AA. Activities of three erythrocyte enzymes of hyperglycaemic rats (*Rattus norvegicus)* treated with *Allium sativa* extract. J Diabetes *Meta Discord*.2014;**13**:50. DOI: 10.1186/2251-6581-**13-50**

18. Sathasivam K, Ramanathan S, Mansor S, Haris M, Wernsdorfer W."*Thrombocytecount in mice after administration of papaya leaf suspension"*, *The Middle European Journal of Medicine*, 2009; **121**(3), 19-22. DOI: 10.1007/s00508-009-1229-0

19. Yogiraj Vijay, Pradeep Kumar Goyal, Chetan Singh Chauhan, Anju Goyal, Bhupendra Vyas. *Carica papaya* Linn: An Overview*. International Journal of Herbal Medicine*, 2014;**2** (5): 01-08 URL: http://www.florajournal.com/vol2issue5/jan2015/2-4-12.1.pdf

20. Adeneye, A.A., & Olagunju, I.A. Preliminary hypoglycemic and hypolipidemic activities of the aqueous seed extract of Carica papaya Linn. in Wistar rats. *Biology and Medicine*.2009;**1**:1–10. DOI: http://www.biolmedonline.com/Articles/vol1_1_1-10.pdf

21. Ahmad, N., Fazal, H., Ayaz, M., Abbasi, B.H., Mohammad, I., Fazal, L.. Dengue fever treatment with Carica papaya leaves extracts. *Asian Pac. J. Trop. Biomed*.2011; **1**:330-333. DOI: 10.1016/S2221-1691(11)60055-5

22. Owoyele, B.V., Adebukola, O.M., Funmilayo, A.A., Soladoye, A.O. Anti-inflammatory activities of ethanolic extract of Carica papaya leaves. *Inflammopharmacol*. 2008; **16**: 168-173. DOI: 10.1007/s10787-008-7008-0

23. Aruoma, O.I., Hayashi, Y., Marotta, F., Mantello, P., Rachmilewitz, E., Montagnier, L. Applications and bioefficacy of the functional food supplement fermented papaya preparation. *Toxicology*. 2010; **278**: 6-16. DOI: 10.1016/j.tox.2010.09.006

24. William PJ, Douglas K. Extraction of plant secondary metabolites in natural products isolation. 2nd ed. Humana Press, *New Jersey*.2006;**20**: 323-35. DOI: 10.1385/1-59259-955-9:323

25. Gupta D, Kondongala S.C, Girish P. In vitro antidiabetic activity of pentacyclic tritrprnoida and fatty acid ester from bauhinia purpurea. *Inter. J. Pharmacol*. *Pharmaceut. Tech*.2013; Vol-2. ISSN-2277- 3436

26. Shekib L.A, Iraq E.I, Abo Baker S.M. "Studies on amylase inhibitors in some Egyptian legume seeds" *Plant Foods Human Nutr*; 1988;**38**, 325–332. DOI: 10.1007/BF01091730

27. Rajesh P. Dinesh Kumar Damiki Laloo, Siva Hemalatha. Evaluation of phytochemical and antioxidant activities of the different fractions of Hybanthus enneaspermus Linn F Muell Violaceae. *Asian Pacific J of Tropical Medicine*: 2009; **39:**1-6. URL:www.journal homepage:www.elsevier.com/locate/apjtm

28. Akhila S., and N. G. Vijayalakshmi., "Phytochemical Studies *On Carica Papaya Leaf Juice", IJPSR*, 2015; **6** (2), 880883. DOI: 10.13040/IJPSR.0975-8232.6(2).880-83

29. Sheikh Fauziya and R Krishnamurthy. *"Papaya (carica papaya): source material for anticancer", CIBTech Journal of Pharmaceutical Sciences*, 2013;**2**(1), 25-34. URL: http://www.cibtech.org/cjps.htm.

30. Ayoola P.B. and A. Adeyeye. "Phytochemical and nutrient evaluation of *Carica papaya* (pawpaw) leaves*",IJRRAS*,2010;**5**(3),325-328.URL: www.arpapress.com/Volumes/Vol5Issue3/IJRRAS_5_3_15.pdf.

31. Baskaran C., V. Ratha bai, S.Velu, Kubendiran Kumaran. "The efficacy of *Carica Papaya* leaf extract on some bacterial and a fungal strain by well diffusion method*", Asian Pacific Journal of Tropical Disease*, 2012;**2** (2), S658-S662 DOI: 10.1016/S2222-1808(12)60239-4

32. Okwu, D.E. and M.E. Okwu. Chemical Composition of Spondia Momb in plants *J. Sustain. Agri. Environ*., 2004;**6**: 140-147

33. Roman-Ramos, R., Flores-Saenz, J.L., and Alarcon-Aguilar, F.J. Anti-hyperglycemic effect of some edible plants. *Journal of Ethnopharmacology*.1995;**48**,25-32. URL: https://www.ncbi.nlm.nih.gov/pubmed/8569244

34. Megha G, Chaudhari Bhoomi B, Joshi Kinnari N, Mistry Brijesh Dabhi, Sanjay lal*. In Vitro* Antimicrobial Activity of Stem Bark of *Bauhinia Purpurea*. J Int Sci Press (India) 2013*;* 4:29-35. URL: *https://www.researchgate.net/profile/**Brijesh_Dabhi**/publications*

35. Rajbhar,K., Dawda, H. and Mukundan, U. Quantitative spectrophotometric estimation of specific monosaccharides by DNSA method. International journal of Research and Development Organization, 2016; 29(1):112-126. ISSBN: **2455-7676**

36. Adesegun, S. A., Fayemiwo, O., Odufuye, B. Coker, H.A.B. α-amylase inhibition and antioxidant activity of *Pterocarpus osun* Craib. Journal of Natural Products, 2013; 6: 90-95. URL: http://journalofnaturalproducts.com/Volume6/13_Res_paper-12.pdf

37. Clifford J.B, Caroline D. Review article: Traditional Plant Medicines as Treatments for Diabetes, Diabetes care.1989; 12(8). DOI: 10.2337/diacare.12.8.553.

Türkçe Öz ve Anahtar Kelimeler

Anti-Diabetic Efficacy and Phytochemical Screening of Methanolic Leaf Extract of Pawpaw (*Carica papaya*) Grown in North Central Nigeria.

Ayorinde Victor Ogundele, Kabir Opeyemi Otun, Abdulfatai Ajiboye, Bolatito Eunice Olanipekun, Rasheed Bolaji Ibrahim

Öz: *Carica papaya* yaprak örnekleri (Yeşil) taze iken toplanmış ve altı tam gün kurutulmuştur. Yapraklar metanolle ekstrakte edilmiştir; elde edilen ekstraktlar standart bir prosedür kullanarak fitokimyasal içerik bakımından gözden geçirilmiştir. Fitokimyasal görüntülemeye göre tanenler, saponinler, terpenoidler, glikozidler ve alkaloidler gibi biyoaktif maddelerin varlığı ortaya konmuştur. Bitkinin *in vitro* antidiyabetik potansiyeli, geleneksel kullanımı doğrulamak amacıyla belirlenmiştir. Bu çalışmanın sonucuna göre *C. papaya* yapraklarının *in vitro*'da belirgin antidiyabetik aktivite gösterdiği ortaya konmuştur, buna göre, bitkinin yaprakları diyabetle savaşta kullanılabilecek ilaçların geliştirilmesi için potansiyele sahiptir.

Anahtar kelimeler: *Carica papaya* yaprakları; fitokimyasal görüntüleme; biyoaktif maddeler; anti-diyabetik maddeler; *in-vitro* inceleme.

Gönderme: 09 Agustos 2016. **Düzenleme:** 23 Eylül 2016. **Kabul:** 14 Ekim 2016.

JOTCS A Journal of the Turkish Chemical Society Section A Chemistry
TURKISH CHEMICAL SOCIETY

Effect of Cooking Method on the Proximate, Amino Acid, and Fatty Acid Compositions of *Clarias gariepinus* and *Oreochromis niloticus*

Omolara Olusola Oluwaniyi[1]*, Omotayo Olutola Dosumu[1] and Gbonjubola Victoria Awolola[1]
[1] Department of Industrial Chemistry, University of Ilorin, Ilorin, Nigeria

Abstract: The proximate, amino acid and fatty acid compositions of the fillet and oil of two commonly consumed fresh water fishes - *Clarias gariepinus* (Catfish) and *Oreochromis niloticus* (Tilapia) - were evaluated in this study. The samples were separately boiled, roasted (over hot charcoal) and fried using different types of oils (palm oil, groundnut oil, soybean oil and refined palm oil) and the effect of the processing methods on the nutritional composition was determined. The moisture content ranged from 76.27% for catfish to 79.97% for tilapia while the oil content ranged from 7.80% for tilapia and 11.00% for catfish. Ash content was in the range 8.03 – 9.16% and the protein content was 15.83 - 18.48%. The cooking methods resulted in a variation in the nutrient composition but no significant variation was observed in the amino acid composition except for the samples fried with palm oil which recorded significantly reduced essential amino acid contents. All the fish samples – both fresh and processed – have amino acid scores less than 100, with lysine, threonine and the sulfur-containing amino acids being among the limiting amino acids. Both fish samples contain more unsaturated than saturated fatty acids.

Keywords: Fish; proximate composition; fatty acid; amino acid.

Submitted: September 02, 2016. **Revised:** September 28, 2016. **Accepted:** October 20, 2016.

Cite this: Oluwaniyi O, Dosumu O, Awolola G. Effect of Cooking Method on the Proximate, Amino Acid, and Fatty Acid Compositions of Clarias gariepinus and Oreochromis niloticus. JOTCSA. 2017;4(1):115–32.

DOI: 10.18596/jotcsa.53143.

*Corresponding author. E-mail: laraoluwaniyi@yahoo.com, Tel: +234-8033947875.

INTRODUCTION

Fishes are highly nutritious, tasty, and easily digested protein source for a large population in many developing countries. While marine fishes are generally cheaper when compared with fresh water fishes in Nigeria (1), fresh water fishes are increasingly becoming more abundant, constituting close to 70% of the total fish supply in Nigeria (2). Freshwater fishes are found in freshwater bodies, including streams, rivers, ponds and so on (3). They are available and abundant in riverine areas. About 41% of all known fish species are found in fresh water. In Nigeria and other developing nations of the world, fish is a very common and abundant animal protein source because it is cheaper than meat and the supply is relatively stable (4). About 60% of people in many developing countries are believed to depend on fish for more than 30% of their animal protein supplies (5).

Fishes generally contain very high moisture content, very little carbohydrate, and vitamins and minerals in trace quantities (1). Most fish species contain between 60 – 80% moisture, 15 – 26% protein and 2 – 13 % fat (6). The fat contents vary with species, age, size, and season. Fishes that are high in oil are known as fatty or oily fish and the dry matter may contain as much as 30% oil, while those that are low in oil are known as white fish. Fishes are generally rich in all essential amino acids, especially those that are in low quantity in cereals such as lysine. Fish protein can therefore serve as an amino acid supplement, improving the amino acid supply and the quality of protein in the diet (7).

The part of fish that is mostly consumed is the muscle (8) and it contributes both fatty acids and amino acids to diets. Ordinarily, consumption of animal protein usually results in a high consumption of saturated fats which is quite unhealthy for the heart; however, fish consumption does not have that problem because of its low content of fats generally and saturated fatty acids in particular. It affords the patient the opportunity to obtain good quality dietary protein without excessive fat consumption. Fish is therefore recommended for a good cardiac health.

Several varieties of fish species abound in the various water bodies in Nigeria and they serve both as food and as economic resource to the country. Prominent among these species are croakers, catfishes, tilapias, threadfins, soles and the clupeids and these account for close to 90% of Nigeria's fishes (9). This represents a major source of animal protein supply to Nigeria, which ordinarily has low protein consumption (10). In recent times, there has been an increase in fish farming in Nigeria, especially of African catfish (*Clarias gariepinus*) and the tilapia family because they grow very fast and also because of their ability to tolerate different environmental conditions and temperatures (11).

The two fish species chosen for this work were because of their abundance and good consumer acceptance. *Clarias gariepinus* is one of the most farmed fish in tropical and sub-tropical Africa and many Nigerians now farm the species either as a hobby or as a means of livelihood. *Oreochromis niloticus*, though not as farmed as *C. gariepinus,* is highly prolific and low in fat. In spite of the economic values and availability of these fishes, there is limited data on the nutritional composition of the samples and especially how processing may affect the nutritional quality. Previous report on marine water fishes (1), (4) have shown that processing does affect the nutritional and amino acid composition of marine water fishes, generally leading to a reduction in the nutritional values.

This work therefore aims to determine the proximate, fatty acid and amino acid composition of two freshwater fish species and to determine how the different methods of boiling, roasting and frying with different types of oil may affect these parameters.

MATERIALS AND METHODS

Collection and preparation of samples

Two freshwater fish species were used in this study - African sharp-tooth Catfish *(Clarias gariepinus)* and Tilapia (*Oreochromis niloticus)*. The samples were obtained fresh in October 2013 from different sources. African catfish (average weight: 0.9 kg, length: 340 mm) was obtained from a private fish farm (pond) in Tanke area, Ilorin, Kwara State, Nigeria while Tilapia (average weight: 0.5 kg, length: 190 mm) was obtained from Kainji Dam, Niger State, Nigeria. The fishes were obtained live.

Sample Treatment

Upon arrival at the laboratory, the fish samples were washed and cut into pieces. The head and viscera were removed and the pieces were thoroughly washed again with domestic water and then with distilled water. The pieces (about 90 g each) were separated into seven parts. One of the seven divisions was set apart as the control (raw), one was boiled and another roasted. The remaining four parts were separately deep-fried in four different cooking oils (palm oil, soybean oil, refined, decolorized palm oil and groundnut oil). Common procedures for preparation of fish for table consumption were followed. The boiling was done with domestic water for 10 minutes until the pieces were tender; the roasting was carried out with heat from hot charcoal for about 15 minutes and the deep – frying was done in a frying pan for 15 minutes. No ingredient or additive was added for the cooking. The bones were removed from the samples but the skin was not removed. The fish fillets were then mashed and the moisture content was determined immediately. The dried samples (after moisture content determination) were ground using mortar and pestle, wrapped in aluminum foil and then polyethylene bags before they were labelled and refrigerated (4).

Analytical Procedures

Standard methods of the Association of Official Analytical Chemists (AOAC) were adopted for the analyses of the samples (12). 2.0 g of each sample was heated to a constant weight in a crucible placed in an oven maintained at 105 °C to determine the moisture content. Crude fat was determined using a Soxhlet extractor and n-hexane as the extractant. Nitrogen content was determined by the Kjeldahl method, using 2.0 g of dried, defatted samples the crude protein was calculated as % total nitrogen x 6.25. Ash was determined by the incineration of 1.0 g of dried, defatted samples placed in a muffle furnace at 550°C for 5 hours.

The fatty acid profile of the oils extracted from the samples was determined by Gas Chromatography. The oil samples were re- extracted with redistilled n-hexane, filtered through anhydrous Na_2SO_4 and the solvent was removed using a rotary evaporator (12). The oil sample was then saponified for about 5 min at 95 °C with 0.5 M KOH in dry ethanol. The mixture was neutralized using 0.7 M HCl followed by the addition of 14 % BF_3 in methanol. The methylation process was completed by heating for 5 min at 90 °C. Identification and quantification of the fatty acids were done by injecting the esterified fat into the injection port of the gas chromatography equipment (HP 6890 powered with HP ChemStation Rev. A 09.01 [1206] Software) with nitrogen as the carrier gas.

Amino acid content determination was carried out by ion exchange chromatography (13), using the Technicon Sequential Multisample (TSM) Amino Acid Analyzer (Technicon Instruments Corporation, Dublin, Ireland). 2.0 g of sample was defatted using chloroform/methanol, hydrolyzed using 6 M HCl and the hydrolysate was injected into the TSM analyzer for separation and characterization. Tryptophan content was not determined.

The amino acid score for the essential amino acids was calculated using the formula (Eq. 1) (14):

$$Amino\ acid\ score = \frac{Amount\ of\ amino\ acid\ per\ sample\ protein\ [mg/g]}{Amount\ of\ amino\ acid\ per\ protein\ in\ reference\ protein\ [mg/g]} \quad \text{(Eq. 1)}$$

The total and percentage essential amino acids [TEAA and TEAA%], total acid amino acids [TAAA], sulfur-containing amino acids [TSAA] and aromatic amino acids [TArAA] were evaluated from the amino acid profile and the predicted protein efficiency ratio (P-PER) was determined using one of the equations of Alsmeyer and co-workers (15) adapted by Adeyeye (16) [*i.e.* P-PER = -0.468 + 0.454(Leu) – 0.105(Tyr)].

Statistical analysis

Results are expressed as mean ± standard deviation of triplicate trials. SPSS version 16.0 was used for the statistical analysis. One way analysis of variance (ANOVA) and Duncan's multiple

range tests were carried out and statistical significance of differences were accepted at the 5% limit ($P \leq 0.05$).

RESULTS AND DISCUSSION

The results of the proximate composition of the two species are presented in Table 1. The moisture contents of catfish samples range from 76.27% in the fresh sample to 54.29% in the sample fried in soybean oil. For tilapia fish samples, moisture contents range from 79.97% in the fresh sample to 32.62% in the groundnut oil-fried sample. The moisture content of the two species are in the same range (76.27 – 79.97%) for the fresh samples but tilapia fish appeared to be more affected by processing, especially frying, resulting in a greater loss of the moisture content observed in tilapia than catfish. Catfish has a higher fat content (11%) than tilapia (7.8%). However, tilapia absorbs more fat during frying than catfish, resulting to a higher fat content observed in the fried samples of tilapia than catfish. The ash contents of both species reduce with processing while the protein content of both increase with processing except the protein content of *C. gariepinus* which decreased slightly but not significantly on boiling.

Table 1. Proximate composition of fresh and processed *Clarias gariepinus* and *Oreochromis niloticus*

Proximate Quality	***C. gariepinus* (Fresh)**	***C. gariepinus* (Boiled)**	***C. gariepinus* (Roasted)**	***C. gariepinus* (SOF)**	***C. gariepinus* (GOF)**	***C. gariepinus* (ReOF)**	***C. gariepinus* (POF)**
Moisture	76.27 ± 1.07^{a}	74.87 ± 0.15^{a}	63.11 ± 2.16^{b}	54.29 ± 1.89^{c}	60.94 ± 1.06^{b}	60.70 ± 0.91^{b}	62.05 ± 1.00^{b}
Fat (on Dry basis)	11.00 ± 1.21^{a}	14.21 ± 0.12^{a,b}	12.82 ± 0.34^{a,b}	26.52 ± 1.22^{c}	20.07 ± 2.81^{d}	16.53 ± 2.45^{b,d}	26.19 ± 4.23^{c}
Ash (on dry basis)	8.03 ± 0.88^{a}	6.50 ± 2.09^{a,c}	6.73 ± 0.59^{a,c}	4.67 ± 0.26^{b,c}	7.64 ± 2.57^{a,c}	2.39 ± 1.78^{b}	6.25 ± 1.78^{a,c}
Protein (on dry basis)	18.48 ± 0.91^{a}	18.18 ± 0.13^{a}	26.74 ± 1.64^{b,c}	28.23 ± 1.01^{c}	25.60 ± 1.16^{b,d}	28.39 ± 0.49^{c}	23.82 ± 1.96^{d}
	***O. niloticus* (Fresh)**	***O. niloticus* (Boiled)**	***O. niloticus* (Roasted)**	***O. niloticus* (SOF)**	***O. niloticus* (GOF)**	***O. niloticus* (ReOF)**	***O. niloticus* (POF)**
Moisture	79.97 ± 0.16^{a}	74.89 ± 0.81^{b}	66.03 ± 0.34^{c}	46.09 ± 0.41^{d}	32.62 ± 0.61^{f}	48.55 ± 0.21^{e}	33.77 ± 0.83^{g}
Fat (on Dry basis)	7.80 ± 0.39^{a}	13.08 ± 0.63^{b}	13.59 ± 0.48^{b}	36.08 ± 1.29^{c,d}	32.54 ± 4.43^{c}	32.46 ± 0.54^{c}	37.80 ± 1.23^{d}
Ash (on dry basis)	9.16 ± 0.62^{a}	6.69 ± 1.49^{b,d}	8.67 ± 0.85^{a,c}	5.86 ± 0.81^{b,d}	7.42 ± 0.57^{c,d}	5.13 ± 0.36^{b}	5.78 ± 0.29^{b}
Protein (on dry basis)	15.83 ± 0.08^{a}	18.49 ± 0.50^{b}	24.62 ± 0.37^{c}	26.32 ± 0.36^{c,d}	38.24 ± 2.63^{e}	28.41 ± 0.34^{d}	36.05 ± 1.03^{e}

a, b,..Values are means ± standard deviations of triplicate determinations; Values in the same row sharing the same letters are not significantly different ($p<0.05$ level); POF= Fish sample fried in palm oil; SOF= Fish sample fried in soybean oil; ReOF= Fish sample fried in refined palm oil; GOF = Fish sample fried in groundnut oil.

The moisture contents obtained for the two fish species were in the ranges previously reported by other workers (5), (17), (18), *etc*. The moisture contents generally reduced with processing with the reduction being more pronounced and significant in the fried samples than in the other processed samples. On the other hand, the fat content increased as a result of processing with the increase being more pronounced in the fried samples. The fat content results showed that *C. gariepinus* is a medium fat fish while *O. niloticus* is a low fat fish species. Several factors affect the fat content of fish samples including species, geographical region, age, and diet (19). *C. gariepinus* used in this study were farmed and thus fed with artificial and controlled diets, whereas the *O. niloticus* was free and thus were feeding on

naturally available diets; this could significantly impact on the proximate compositions, hence the observed variations. Though *O. niloticus* had less fat than *C. gariepinus* originally, the fried samples of *O. niloticus* have higher fat contents than the fried *C. gariepinus*. Candela *et al.* (20) had earlier reported that the frying process affect different fish species in different ways and that this should be taken into account in determining the total fat consumed in a fish meal. This could therefore account for the different behaviors of the fishes to frying. The ash contents of both species reduced with processing, though the reduction did not follow any particular order and the reduction was attributed to the possible loss of some water soluble and heat-labile minerals during processing. The protein contents of the samples increased after processing and this is quite noteworthy because fishes are generally consumed as a protein source in food and it is therefore very important that processing or preparation methods should not have a negative impact on either the protein content or quality. The processing techniques involved here did not result in a reduction in the protein contents. While only a slight difference was observed in the protein content of the fresh and boiled samples, other treatments resulted in large differences in the protein contents.

Tables 2 - 4 present the amino acid composition and amino acid scores of the two species with tilapia having a slightly better amino acid profile than catfish. Although a greater loss of total amino acids was observed following the processing of catfish than tilapia, there is an increase in the total and percentage of essential amino acids following the processing of catfish. The amino acids lost in catfish as a result of processing were mainly the acid amino acids. Of all the processing techniques investigated, frying with palm oil appeared to have the worst effect on the amino acid contents of the fish samples, resulting in the loss of essential amino acids for the two species.

Table 2. Amino Acid Composition of Fresh and Processed *Clarias gariepinus* (g/100 g protein)

Amino Acid	***C. gariepinus* (Fresh)**	***C. gariepinus* (Boiled)**	***C. gariepinus* (Roasted)**	***C. gariepinus* (SOF)**	***C. gariepinus* (GOF)**	***C. gariepinus* (ReOF)**	***C. gariepinus* (POF)**
Lysine (Lys)[a]	5.00	5.40	5.00	5.27	4.92	5.62	4.92
Histidine (His)[b]	2.21	2.33	2.24	2.24	2.21	2.46	1.89
Arginine (Arg)	5.26	5.61	5.26	5.52	4.92	5.78	4.66
Aspartic acid (Asp)	23.26	10.92	10.02	10.61	9.87	11.26	21.21
Threonine (Thr)[a]	3.26	3.20	3.01	3.09	2.95	3.28	2.65
Serine (Ser)	4.26	3.53	3.47	3.5	3.07	3.66	3.96
Glutamic acid (Glu)	15.98	13.18	12.80	12.88	12.12	13.33	15.3
Proline (Pro)	4.69	3.46	3.05	3.15	3.15	3.56	4.27
Glycine (Gly)	4.18	5.52	4.95	5.19	4.32	5.60	3.51
Alanine (Ala)	5.05	4.82	4.22	4.48	4.03	5.05	4.72
Cystine (Cys)[a]	1.19	0.99	0.86	0.86	0.80	0.99	1.72
Valine (Val)[a]	3.82	3.65	3.27	3.42	3.01	3.50	3.86
Methionine (Met)[a]	0.68	2.29	2.19	2.24	2.08	2.40	0.86
Isoleucine (Ile)[a]	3.17	3.39	3.04	3.2	2.92	3.39	3.01
Leucine (Leu)[a]	5.95	6.85	6.50	6.66	6.23	6.94	5.21
Tyrosine (Tyr)[a]	3.02	3.33	3.02	3.18	3.02	3.65	2.70
Phenylalanine (Phe)[a]	4.05	4.44	4.39	4.40	4.47	4.47	3.37
Total Amino acids	**95.03**	**82.91**	**77.29**	**79.89**	**74.09**	**84.94**	**87.82**
% Difference		-12.12	-17.74	-15.14	-20.94	-10.09	-7.21

Total Essential amino acids [EAA]	28.14 (29.61%)	31.55 (38.05%)	29.64 (38.35%)	30.52 (38.20%)	28.79 (38.86%)	32.06 (37.74%)	25.77 (29.34%)
Total Acid amino acids [AAA]	39.24 (41.29%)	24.10 (29.07%)	22.82 (29.53%)	23.49 (29.40%)	21.99 (29.68%)	24.59 (28.95%)	36.51 (41.57%)
Sulfur amino acids [SAA]	1.87 (1.97%)	3.28 (3.96%)	3.05 (3.95%)	3.10 (3.88%)	2.88 (3.89%)	3.39 (3.99%)	2.58 (2.94%)
Aromatic amino acids [ArAA]	9.28 (9.77%)	10.10 (12.18%)	9.65 (12.49%)	9.82 (12.29%)	9.70 (13.09%)	10.58 (12.46%)	7.96 (9.06%)

[a] Essential amino acids according to FAO/WHO (1975); [b] Indispensable amino acid in human adult according to FAO/WHO/UNU (1985); ND = Not determined; POF= Fish sample fried in palm oil; SOF= Fish sample fried in soybean oil; ReOF= Fish sample fried in refined oil; GOF = Fish sample fried in groundnut oil. Values in parenthesis are % of TAA

Table 3. Amino Acid Composition of Fresh and Processed *Oreochromis niloticus* (g/100 g protein)

	***O. niloticus* (Fresh)**	***O. niloticus* (Boiled)**	***O. niloticus* (Roasted)**	***O. niloticus* (SOF)**	***O. niloticus* (GOF**	***O. niloticus* (ReOF)**	***O. niloticus* (POF)**
Lysine (Lys)[a]	5.21	4.38	3.92	3.40	4.02	3.62	5.02
Histidine (His)[b]	2.21	2.30	2.37	2.02	2.24	2.02	2.24
Arginine (Arg)	5.35	5.26	5.61	5.26	5.01	4.92	5.35
Aspartic acid (Asp)	10.08	10.11	10.55	9.02	11.26	10.05	23.6
Threonine (Thr)[a]	3.01	3.45	3.29	3.01	3.15	3.01	3.15
Serine (Ser)	3.42	3.61	2.96	2.52	3.01	2.55	4.15
Glutamic acid (Glu)	12.72	13.63	12.20	11.59	12.72	11.29	16.35
Proline (Pro)	3.26	3.87	3.66	3.26	3.97	3.15	4.78
Glycine (Gly)	4.90	4.01	3.65	3.55	3.94	3.41	4.20
Alanine (Ala)	5.51	4.21	3.99	3.68	4.41	3.87	5.24
Cystine (Cys)[a]	0.93	1.39	1.26	1.19	1.32	1.13	1.26
Valine (Val)[a]	3.18	4.20	3.71	3.42	4.00	3.42	3.91
Methionine (Met)[a]	2.19	1.51	1.41	1.35	1.64	1.30	0.70
Isoleucine (Ile)[a]	3.20	3.68	3.11	3.01	3.55	3.01	3.42
Leucine (Leu)[a]	6.53	7.21	6.94	6.55	7.02	6.09	6.03
Tyrosine (Tyr)[a]	3.17	3.33	3.02	2.70	3.18	3.33	3.02
Phenylalanine (Phe)[a]	4.22	4.81	4.55	4.22	4.81	4.02	3.96
Total Amino acids	**79.09**	**80.96**	**76.2**	**69.75**	**79.25**	**70.19**	**96.38**
% Difference		1.87	-2.89	-9.34	0.16	-8.90	17.29
Total Essential amino acids [EAA]	29.75 (37.62%)	31.54 (38.96%)	29.30 (38.45%)	26.98 (38.68 %)	30.43 (38.40 %)	26.49 (37.74%)	28.43 (29.50%)
Total Acid amino acids [AAA]	22.8 (28.83%)	23.74 (29.32%)	22.75 (29.86%)	20.61 (29.55 %)	23.98 (30.26 %)	21.34 (30.40%)	39.95 (41.45%)
Total Sulfur amino acids [SAA]	3.12 (3.94%)	2.90 (3.58%)	2.67 (3.50%)	2.54 (3.64%)	2.96 (3.74%)	2.43 (3.46%)	1.96 (2.03%)
Total Aromatic amino acids [ArAA]	9.60 (12.14%)	10.44 (12.90%)	9.94 (13.04%)	8.94 (12.82 %)	10.23 (12.91 %)	9.37 (13.35%)	9.22 (9.57%)

[a] Essential amino acids according to FAO/WHO (1975); [b] Indispensable amino acid in human adult according to FAO/WHO/UNU (1985); ND = Not determined; POF= Fish sample fried in palm oil; SOF= Fish sample fried in soybean oil; ReOF= Fish sample fried in refined oil; GOF = Fish sample fried in groundnut oil. Values in parenthesis are % of TAA

Table 4. Amino Acid Score of Fresh and Processed *Clarias gariepinus* and *Oreochromis niloticus*

	Ile	Leu	Lys	Met + Cys	Phe + Try	Thr	Try	Val	His
Standard	2.8	6.6	5.8	2.5	6.3	3.4	1.1	3.5	1.9
***C. gariepinus* (Fresh)**	113	90	86	**75**	112	96	ND	109	116
***C. gariepinus* (Boiled)**	121	104	**93**	131	123	94	ND	104	123
***C. gariepinus* (Roasted)**	109	98	**86**	122	118	89	ND	93	118
***C. gariepinus* (SOF)**	114	101	91	124	120	**91**	ND	98	118
***C. gariepinus* (GOF**	104	94	**85**	115	119	87	ND	86	116
***C. gariepinus* (ReOF)**	121	105	97	136	129	**96**	ND	100	129
***C. gariepinus* (POF)**	108	79	85	103	96	**78**	ND	110	99
***O. niloticus* (Fresh)**	114	99	90	125	117	**89**	ND	91	116
***O. niloticus* (Boiled)**	131	109	**76**	116	129	101	ND	120	121
***O. niloticus* (Roasted)**	111	105	**68**	107	120	97	ND	106	125
***O. niloticus* (SOF)**	108	99	**59**	102	110	89	ND	98	106
***O. niloticus* (GOF)**	127	106	**69**	118	127	93	ND	114	118
***O. niloticus* (ReOF)**	108	92	**62**	97	117	89	ND	98	106
***O. niloticus* (POF)**	122	91	87	**78**	111	93	ND	112	118

ND = Not determined

Although the amino acid analysis did not reveal an increase in the amino acid contents as one may have expected from the protein contents, there was an observed increase in both the quantity and percentage of the total essential amino acids except for the sample fried with crude palm oil which recorded a reduction in the total essential amino acids for both *C. gariepinus* and *O. niloticus*. For *C. gariepinus*, there was also observed an increase in the sulfur-containing amino acids and aromatic amino acids and a reduction in the acid amino

acids while for *O. niloticus,* the acid amino acids increased slightly while both the sulfur-containing amino acids and the aromatic amino acids recorded only slight variations. Frying with crude palm oil appeared to have the worst effect on the quality of amino acids for both fish species. Although it resulted in an increase in total amino acids for *O. niloticus* and only a slight decrease for *C. gariepinus*, the number of limiting amino acids increased as a result of the loss of the essential amino acids.

Previous workers have reported varying effects of processing on the protein and amino acid contents of fish samples. While some reported no significant effect on protein and amino acid contents following boiling and frying (21), others reported that heat processing resulted in reduction in protein value by destroying the constituent amino acids or making them unavailable (22). This may imply that the length of time of heat treatment also contributed to the change in amino acid contents of the fish samples. Our previous work on marine water fishes (4) had reported that boiling and roasting had no significant effect on the amino acid composition of the four fish samples investigated while frying resulted in a significant reduction in essential, sulfur-containing and aromatic amino acids. Samples fried with palm oil also reported the lowest values of essential amino acids and they were also the only samples with limiting amino acids. These results therefore suggest that processing has different types of effects on different fish types but frying has the worst kind of effect as far as protein quality is concerned. One can also deduce that increase in protein content does not necessarily imply an increase in the quality of the protein. The results also show that both *C. gariepinus* and *O. niloticus* are not sources of complete proteins. They have several essential amino acids with scores less than 100 including lysine, threonine, methionine, cysteine, leucine, and valine whereas the marine water fishes have no limiting amino acids except when fried (4). Amino acid scoring provides a way to predict how efficiently a protein will meet a person's amino acid needs. This concept assumes that tissue protein synthesis is limited unless all required amino acids are available at the same time and in appropriate amounts at the site of tissue protein synthesis.

The results of the fatty acid analysis of both fish species, presented in Tables 5 and 6, show that both species contain more unsaturated fatty acids than saturated, and that palmitic acid is the main saturated fatty acid in both species. Oleic acid is the major unsaturated fatty acid in both species with linoleic acid, linolenic acid and palmitoleic acid also being present in varying amounts.

Table 5: Fatty Acid Composition of Fresh and Processed *Clarias gariepinus*

Fatty acid	***C. gariepinus* (Fresh)**	***C. gariepinus* (Boiled)**	***C. gariepinus* (Roasted)**	***C. gariepinus* (SOF)**	***C. gariepinus* (GOF**	***C. gariepinus* (ReOF)**	***C. gariepinus* (POF)**
Caprylic acid (C8:0)	0.00	0.00	0.00	0.00	0.00	0.00	0.00
Capric acid (C10:0)	0.00	0.00	0.00	0.00	0.00	0.00	0.00
Lauric acid (C12:0)	2.81	2.51	0.00	2.51	0.00	0.00	3.49
Myristic acid (C14:0)	4.77	5.10	0.31	5.07	0.36	0.32	4.71
Palmitic acid (C16:0)	22.40	18.97	26.99	23.76	23.40	26.03	23.16
Palmitoleic acid (C16:1)	3.96	5.23	10.42	5.20	11.99	10.87	2.82
Margaric acid (C17:0)	1.22	1.61	1.89	1.60	2.18	1.97	0.51
Stearic acid (C18:0)	5.56	7.34	5.74	7.30	6.61	5.99	10.21
Oleic acid (C18:1)	29.94	28.26	30.95	27.37	28.34	29.73	30.08
Linoleic acid (C18:2)	14.94	16.89	6.42	13.16	7.23	7.05	16.72
α-Linolenic acid (C18:3)	5.34	7.05	11.05	7.02	12.72	11.53	4.49
Arachidic acid (C20:0)	1.32	1.74	0.00	1.73	0.00	0.00	0.56
Arachidonic acid (C20:4)	1.45	1.91	2.25	1.90	2.59	2.34	0.61
Behenic acid (C22:0)	0.54	0.71	0.83	0.71	0.96	0.87	0.23
Erucic acid (C22:1)	5.76	2.67	3.15	2.66	3.62	3.28	2.42
Lignoceric acid (C24:0)	0.00	0.00	0.00	0.00	0.00	0.00	0.00
TOTAL FATTY ACIDS	**100.00**	**100.00**	**100.00**	**100.00**	**100.00**	**100.00**	**100.00**
TOTAL SATURATED FATTY ACIDS	38.61	37.98	35.77	42.69	33.51	35.19	42.86
TOTAL UNSATURATED FAs	61.39	62.02	64.23	57.31	66.49	64.81	57.14

Values are % of eluted methyl esters; ND = Not detected

Table 6. Fatty Acid Composition of Fresh and Processed *Oreochromis niloticus*

Fatty acid	***O. niloticus* (Fresh)**	***O. niloticus* (Boiled)**	***O. niloticus* (Roasted)**	***O. niloticus* (SOF)**	***O. niloticus* (GOF**	***O. niloticus* (ReOF)**	***O. niloticus* (POF)**
Caprylic acid (C8:0)	0.00	0.00	0.00	0.00	0.00	0.00	0.00
Capric acid (C10:0)	0.00	0.00	0.00	0.00	0.00	0.00	0.00
Lauric acid (C12:0)	0.00	2.62	0.00	3.82	2.66	0.00	2.41
Myristic acid (C14:0)	0.30	4.44	0.31	6.21	4.50	0.31	4.86
Palmitic acid (C16:0)	27.97	25.39	30.71	24.16	23.81	26.71	24.32
Palmitoleic acid (C16:1)	10.18	3.68	10.46	5.54	3.74	10.31	4.98
Margaric acid (C17:0)	1.85	1.13	1.90	1.01	1.15	1.87	1.53
Stearic acid (C18:0)	5.61	5.17	5.77	4.59	5.24	5.69	6.99
Oleic acid (C18:1)	30.84	33.85	26.63	27.24	31.37	31.02	27.56
Linoleic acid (C18:2)	6.35	10.33	6.87	15.54	13.94	6.99	13.91
α-Linolenic acid (C18:3)	10.80	4.96	11.10	4.41	5.04	10.94	6.72
Arachidic acid (C20:0)	0.00	1.23	0.00	1.09	1.25	0.00	1.66
Arachidonic acid (C20:4)	2.20	1.34	2.26	1.19	1.36	2.22	1.82
Behenic acid (C22:0)	0.82	0.50	0.84	0.44	0.51	0.83	0.68
Erucic acid (C22:1)	3.08	5.35	3.16	4.76	5.43	3.11	2.55
Lignoceric acid (C24:0)	0.00	0.00	0.00	0.00	0.00	0.00	0.00
TOTAL FATTY ACIDS	**100.00**	**100.00**	**100.00**	**100.00**	**100.00**	**100.00**	**100.00**
TOTAL SATURATED FATTY ACIDS	36.56	40.47	39.53	41.32	39.12	35.40	42.46
TOTAL UNSATURATED Fas	63.44	59.53	60.47	58.68	60.88	64.60	57.54

Values are % of eluted methyl esters; ND = Not detected

Fish lipids are very desirable because of their rich content of long-chain omega-3 polyunsaturated fatty acids (LC ω-3 PUFA), especially eicosapentaenoic acid (EPA) and docosahexaenoic acid (DHA). EPA and DHA can be synthesized from α-linoleic acid (ALA) thus; ALA and linoleic acid (LA) are the two truly essential fatty acids. Though the percentage quantities of DHA and EPA were not determined, the results of the fatty acid composition revealed that both fish samples contain the two essential fatty acids in sizeable quantities. These two acids account for 20.28% of the fatty acids in fresh *C. gariepinus* (with ALA accounting for 5.34%) and 17.15% in fresh *O. niloticus* (with 10.80% ALA). Though these values vary in the processed samples, the range remains fairly constant. Apart from the two essential fatty acids, the two fish samples contain rich supply of other fatty acids. Both samples are very rich in oleic acid and palmitic acid. Generally, the fish samples contain more unsaturated fatty acids (61.39 – 63.44%) than the saturated fatty acids (36.56 – 38.61%). PUFAs regulate prostaglandin synthesis and accelerate wound healing (23), (24) and the ω-3

and ω-6 PUFAs have been reported to contribute positively to the treatment of cardiovascular diseases and cancers (25). Increasing the consumption of fish and fish products, which are rich in polyunsaturated fatty acids, is therefore desirable for human health (26), (27). The contents of PUFAs in different fish species and even among freshwater and marine fish may vary (28) and the results obtained here have indicated that there was indeed a variation in the composition of PUFA in the two fish species.

CONCLUSION

This study has shown that *C. gariepinus* had medium oil content while *O. niloticus* was low in oil contents. The two species have also been shown to be low in some essential amino acids and the methods of table preparation may further reduce the amino acid composition. Frying did exert a significant effect on the amino acid composition of the samples but when palm oil was used in the frying process, there was observed a significant reduction in protein quality in terms of loss of the amino acids, especially the essential amino acids; thus frying with palm oil is not a nutritionally beneficial method of table preparation of fresh water fish.

REFERENCES

1. Oluwaniyi OO, Dosumu OO. Preliminary Studies on the effect of processing methods on the quality of three commonly consumed marine fishes in Nigeria. Biokemistri 2009; 21(1):1-7. URL: http://www.bioline.org.br/request?bk09001.

2. Federal Office of Statistics. Nigerian Fish Production by Sectors. Lagos 1990. Nigerian Government Printers. Nigeria. 40.

3. www.ucmp.berkeley.edu/exhibits/biomes/freshwater.php.

4. Oluwaniyi OO, Dosumu OO, Awolola GV. Effect of local processing methods (boiling, frying and roasting) on the amino acid composition of four marine fishes commonly consumed in Nigeria. *Food Chemistry 2010;* 123: 1000–1006. DOI: 10.1016/j.foodchem.2010.05.051.

5. Osibona AO, Kusemiju K, Akande GR. Fatty acid composition and amino acid profile of two freshwater species, African catfish (*Clarias gariepinus*) and Tilapia (*Tilapia zillii*). *Afri. Jour. Food Agr. Nutr. Dev. (AJFAND)* 1990; 9(1): 608 – 621. URL: http://www.ajfand.net/Volume9/No1/Adesola2965.pdf.

6. Pearson D, Cox HE. The Chemical Analysis of Foods (7th edition) Churchill Livingstone. 1976. 575 p. ISBN: 0443014116, 9780443014116.

7. United Nations Food & Agriculture Organization, Nutritional elements of fish. FAO, Rome. 2005.

8. Ackman RG. Seafood lipids and fatty acids. *Food Reviews International*. 1990; 6 (4): 617-646. DOI: 10.1080/87559129009540896.

9. Federal Department of Fisheries, Abuja Nigeria. 3rd Edition. Publisher Fisheries Statistics of Nigeria. 2004; 45.

10. Afolabi AO, Arawomo OA, Oke OL. Quality changes of Nigerian traditionally processed fresh water fish species I. Nutritive and organoleptic changes. *J. Food Techno*. 1984; 19: 333-340. DOI: 10.1111/j.1365-2621.1984.tb00356.x.

11. Hecht J, Oellermann L, Verheust L. Perpectives on clariid catfish culture in Africa. *Aquat. Living Resour*. 1996; 9: 197-206 (Hors Serie). URL: www.alr-journal.org/articles/alr/pdf/1996/05/alr96hs16.pdf.

12. Official Methods of Analysis of the Association of Official Analytical Chemists (AOAC), Vols. I and II, Association of Analytical Chemists, Arlington. 1994.

13. FAO/WHO Protein quality evaluation. Report of joint FAO/WHO expert consultation. FAO food and nutrition paper 51. 1991. Italy: Rome.

14. FAO/WHO Energy and protein requirements. Technical report series no. 522. 1973. Geneva, Switzerland: WHO.

15. Alsmeyer RH, Cunningham AE, Hapich ML. (1974). Equations predict PER from amino acid analysis. Food Technology 1974; 28: 34–38. URL: http://agris.fao.org/agris-search/search.do?recordID=US201303166075.

16. Adeyeye EI. Amino acid composition of three species of Nigerian fish: Clarias anguillaris, Oreochromis niloticus and Cynoglossus senegalensis. Food Chemistry 2009; 113(1), 43–46. DOI: 10.1016/j.foodchem.2008.07.007.

17. Elagba Mohamed HA, Rabie A, Mohammed MH. Proximate composition, amino acid and mineral contents of five commercial Nile fishes in Sudan. *Afri. Jour. Food Sci.* 2010; 4(10): 650 – 654. URL: http://www.academicjournals.org/article/article1380732813_Elagba%20et%20al.pdf.

18. Ogbonnaya C, Ibrahim MS. Effects of drying methods on proximate compositions of catfish (*Clarias gariepinus*) *World Jour. of Agr. Sci.* 2009; 5(1): 114 – 116. URL: http://citeseerx.ist.psu.edu/viewdoc/download?doi=10.1.1.415.5187&rep=rep1&type=pdf.

19. Piggott GM, Tucker BW. Seafood: Effects of technology on nutrition.CRC Press New York, USA. 1990. 384 p. ISBN: 0824779223, 9780824779221.

20. Candela M, Astiasaran I, Bello J. Deep-fat frying modifies high fat fish lipid fraction. J. Agric. Food Chem. 1998; 46: 2793 – 2796. URL: http://pubs.acs.org/doi/abs/10.1021/jf9709616.

21. Ismail A, Hainida E, Ikram K. Effects of cooking practices (boiling and frying) on the protein and amino acids contents of four selected fishes. *Nutrition and Food Science* 2004; 34(2): 54–59. DOI: 10.1108/00346650410529005.

22. Burger IH, Walters CL. The effect of processing on the nutritive value of flesh foods. Symposium on the effect of processing on the nutritive value of food held on 10th November 1972. *Proceedings of Nutrition Society* 1973; 32: 1–8. DOI: 10.1079/PNS19730002.

23. Bowman WC, Rand MJ. Textbook of pharmacology (2nd. Ed.) Wiley - Blackwell Oxford. 1991. 1928 p. ISBN: 0632099909, 978-0632099900.

24. Gibson RA. Australian fish – an excellent source of both arachidonic acid and 3 polyunsaturated fatty acids. *Lipids* 1983; 18:743-752. URL: http://link.springer.com/article/10.1007/BF02534631.

25. Connor WE. The beneficial effects of omega-3 fatty acids: cardiovascular diseases and neurodevelopment. *Current Opinion in Lipidology* 1997; 8: 1-3. URL: http://www.ncbi.nlm.nih.gov/pubmed/9127702.

26. Burr ML. Fish and cardiovascular system. *Progress in Food and Nutrition Science* 1989; 13: 291-316. URL: http://www.ncbi.nlm.nih.gov/pubmed/2699044.

27. Sargent JR. Fish oils and human diet. *British Journal of Nutrition* 1997; 78 (Suppl. 1): S5-S13 DOI: 10.1079/BJN19970131.

28. Abd Rahnan S, Teh SH, Osman H, Daud NM. Fatty acid composition of some Malaysian fresh water fish. *Food Chemistry* 1995; 54: 45-49. DOI: 10.1016/0308-8146(95)92660-C.

Türkçe Öz ve Anahtar Kelimeler

Clarias gariepinus ve Oreochromis niloticus Türlerindeki Yakın Sonuçlar, Amino Asit ve Yağ Asidi Bileşenleri Üzerinde Pişirme Yönteminin Etkisi

Omolara Olusola Oluwaniyi, Omotayo Olutola Dosumu and Gbonjubola Victoria Awolola

Öz: Bu çalışmada, yakın analiz, amino asit ve yağ asidi bileşenleri fileto ve yağ kısmında incelendi ve yaygın tüketilen iki balık türü olan *Clarias gariepinus* (yayın balığı) ve *Oreochromis niloticus* (tatlısu çipurası) üzerinde çalışıldı. Örnekler ayrı ayrı pişirildi, sıcak kömür ateşinde kızartıldı ve farklı yağlar kullanılarak (hurma yağı, yerfıstığı yağı, soya fasülyesi yağı ve rafine edilmiş hurma yağı) kızartıldı. Besin bileşimi üzerine işleme tekniklerinin etkisi belirlendi. Nem içeriği yayın balığında %76,27 ve tatlısu çipurasında %79,97 olarak bulundu, yağ içeriği ise yayın balığı için %11,00 ve tatlısu çipurası için ise %7,80 olarak tespit edildi. Kül içeriği %8,03 – 9,16 aralığında bulunurken protein içeriği ise %15,83 – 18,48 olarak tespit edildi. Pişirme yöntemleri besin içeriğinde bir değişmeye neden olmakla birlikte, örnekler hurma yağı ile kızartılmadığı müddetçe amino asitlerde belirgin bir değişme olmamaktadır, hurma yağı esansiyel amino asit içeriklerinde ciddi bir azalmaya neden olmaktadır. Bütün balık örnekleri hem taze, hem de işlenmiş olarak amino asit skoru bakımından 100'Den düşüktür, sınırlayıcı amino asitler lizin, treonin ve kükürtlü amino asitlerdir. Her iki balık türü, doymuş yağ asitlerine nazaran daha fazla doymamış yağ asidi içermektedir.

Anahtar kelimeler: Balık; yakın bileşim; yağ asidi; amino asit.

Sunulma: 02 Eylül 2016. **Düzeltme:** 28 Eylül 2016. **Kabul:** 20 Ekim 2016.

The Adsorption of Calmoduline via Nicotinamide-Immobilized Poly(HEMA-GMA) Cryogels

Kadir Erol*[1]

[1]Hitit University, Osmancık Ömer Derindere Vocational Higher School, Department of Property Protection and Safety, Çorum, Turkey

Abstract: The separation and purification of an important biomolecule calmoduline is extremely important. The adsorption technique is quite popular, and the cryogels as adsorbents with the macroporous structure and interconnected flow channels are preferred in this field. In this study, the adsorption of calmoduline via Ca(II) immobilized poly(2-hydroxyethyl methacrylate-glycidyl methacrylate), poly(HEMA-GMA), cryogels was studied through changing interaction time, calmoduline initial concentration, and temperature conditions. For the characterization of cryogels, the swelling test, Fourier Transform Infrared (FT-IR) Spectroscopy, Scanning Electron Microscopy (SEM), surface area (BET), elemental analysis and ICP-OES methods were performed. Nicotinamide molecule was used as Ca(II) being the chelating agent and the adsorption capacity of the cryogels was estimated as 1.812 mg calmoduline/g cryogel. The adsorption models of the process were examined via the Langmuir and Freundlich isotherm models.

Keywords: Adsorption; calmoduline; cryogel; nicotinamide.

Submitted: September 28, 2016. **Revised**: October 31, 2016. **Accepted**: November 03, 2016.

Cite this: Erol K. The Adsorption of Calmoduline via Nicotinamide-Immobilized Poly(HEMA-GMA) Cryogels. JOTCSA. 2017;3(3):747–62.

DOI: To be assigned.

*Corresponding author. E-mail: kadirerol86@gmail.com

INTRODUCTION

Calmoduline (CaM) is an acidic protein with the molecular weight of 17 kDa. This protein consists of two globular regions or lobe (N-lobe or expressed as C-lobe), each joined by long flexible helix centre. These regions consist of a pair of EF-hand motif (1). It binds to the four calcium ions via the four EF-hand motifs with binding in micromolar range. As a result of binding, there are conformational changes, the hydrophobic fields come into the outer surface (2-4). The calmoduline regulates a variety of cellular functions such as the concentration of abdominal muscle (5), cell cycle (6), and metabolism (7). This protein constitutes at least 0.1% of the total cellular protein concentration in most cells and exists in higher levels in the brain, testicles, and stimulated and rapidly growing cells (8). It also helps the regulation of functions (by contributing the signaling pathway in organisms) such as cell proliferation, learning and memory, growth, exocytosis, endocytosis, and movement (9). The regulation of these functions can be accomplished through the direct interaction of calmoduline protein with a large number of proteins such as kinase, phosphatase, cytoskeleton to increase in calcium concentration within the cell. Moreover, the calmoduline carries the calcium signal in the cell (10-12).

Immobilized metal affinity chromatography (IMAC) has been developed first in 1975 by Porath *et al* (13). This technique is fast, reliable and used generally for the purification of proteins recombined with histidine (14-18). IMAC resins consist of a solid support (*e.g.* agarose), a linker, a chelating compound (iminodiacetic acid, nitrilotriacetic acid or carboxymethyl ethylenediamine) and a divalent transition metal ion (Zn^{2+}, Cu^{2+}, Ni^{2+}, Co^{2+}, *etc.*). The chelating compounds are being immobilized to the solid support via a linker and are coordinated with metal ions (19).

Metal ions interact with nitrogen atoms locating within the structure of amino acids (especially nitrogen atoms in the imidazole ring of histidine amino acids) on the surface of proteins (20).

In this study, the nicotinamide molecules were bonded on the poly(HEMA-GMA) cryogels as a chelating agent. The Ca(II) ion was used as the metal ion. A significant conclusion was achieved as a result of comparison of results with the literature (21). In addition, there was no recent study encountered about the calmoduline adsorption using cryogels. The adsorption of calmoduline from an aqueous solution of this protein was studied and the optimum adsorption conditions (interaction time, initial concentration and temperature) were determined.

MATERIALS AND METHODS

Materials

2-Hydroxyethyl methacrylate (HEMA), glycidyl methacrylate (GMA), ethylene glycol dimethacrylate (EGDMA), calcium chloride dihydrate, ammonium persulfate (APS), sodium dodecyl sulfate (SDS), N,N,N',N'-tetramethylethylenediamine (TEMED), nicotinamide, and calmoduline were supplied from the company Sigma (St. Louis, USA). All other chemicals are of analytical purity and ultra-pure water (18 MΩ.cm) was used in all studies.

Methods

The Synthesis of poly(HEMA-GMA) Cryogels: GMA (500 µL), HEMA (5000 µL) and distilled water (6500 µL) were mixed to obtain the monomeric phase. The disperse phase was prepared using SDS (1 g), distilled water (25.60 mL) and EGDMA (2.4 mL) and then the two phases were mixed with each other. It was cooled in an ice bath for 10-15 minutes. TEMED (100 µL) and APS (20 mg) were added. The mixture remained at -20°C for 24 hours.

The resulting cryogels were cut in the shape of membrane (disc). The cryogels were washed using a rotator (Multi Bio RS-24 Biosen, Latvia) at 10 rpm with distilled water for the removal of sodium dodecyl sulfate and other unwanted chemicals and then the washing water was changed in every 15 minutes until it becomes clear.

The Immobilization of Nicotinamide and the Binding of Ca(II) to the Poly(HEMA-GMA) Cryogels: The number of 20 cryogel membrane was stirred in NaOH (1 M, 10 mL) for 2 hours. Membranes washed several times were interacted with nicotinamide solution (50 mg/mL, 10 mL) for 24 h. At the end of this process, the color of membranes turned from white to yellow. Then the cryogels was washed again with distilled water and stirred in $CaCl_2.2H_2O$ solution (10 mL, 5 mg/mL). The yellow color of Ca(II) attached membranes was brightened a little bit and washed with distilled water-ethanol mixture several times (Figure 1).

Characterization Studies

Swelling Test: The water retention capacity of poly(HEMA-GMA)@Nic-Ca(II), cryogels was determined using distilled water. The dry cryogel membranes were carefully weighed and then placed into the distilled water in the isothermal water bath and remained at 25°C for 30 minutes. The membranes were placed on a filter paper and the water retained on the surface was removed by clinging. At the end, the water retention capacity was calculated according to the formula given below:

$$\text{Water Retention Capacity \%} = [(W_s - W_o)/ W_o] \times 100 \qquad \text{(Equation1)}$$

Wherein, W_o and W_s are the weights (g) of dry and water retained membranes, respectively.

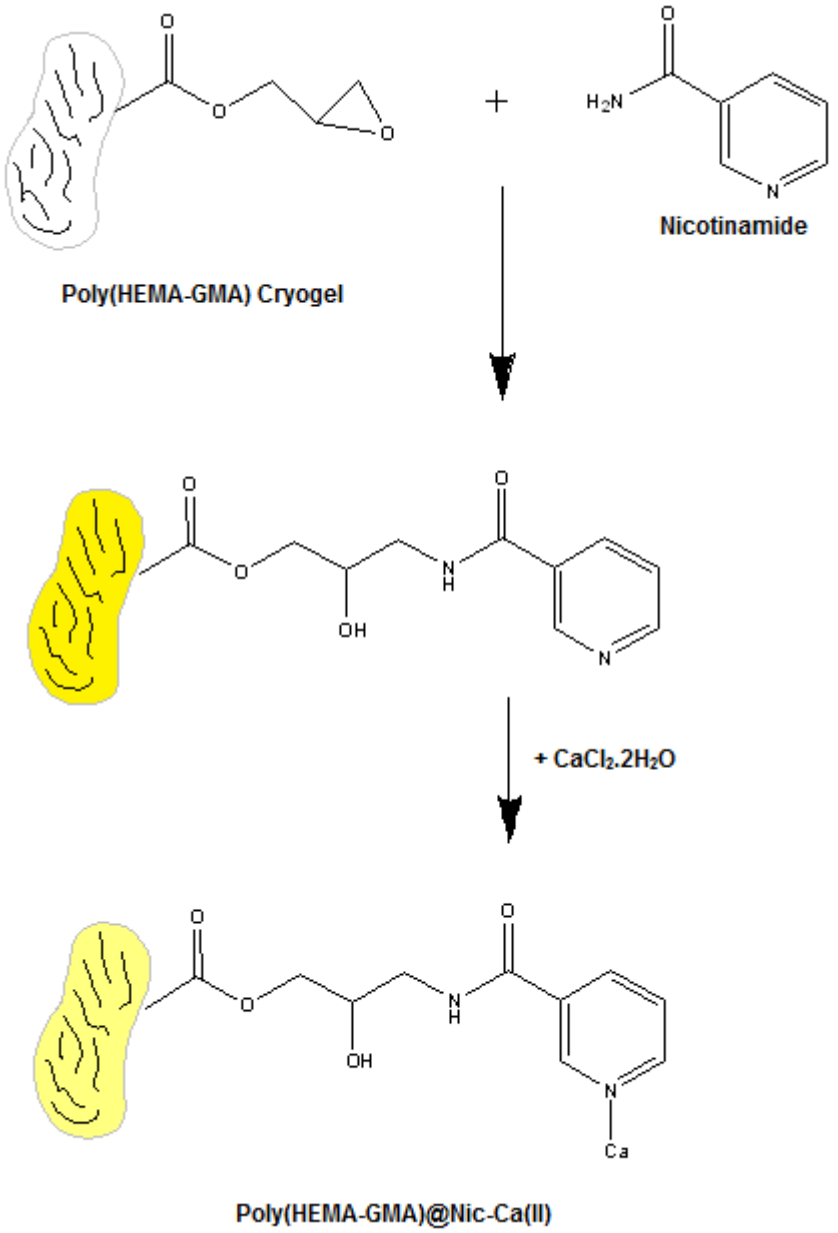

Figure 1. The schematic representation of Poly(HEMA-GMA)@Nic-Ca(II) cryogel synthesis.

SEM Analysis: The surface morphology of cryogel membranes was examined using Scanning Electron Microscopy (SEM, FEI / Quanta 450 FEG, USA). The membrane dried via lyophilization was tailored for SEM analysis and attached on double-sided carbon tape on the SEM holder. The sample was then coated under vacuum with a thin gold layer. The sample obtained was then placed in the SEM device and imaged.

FT-IR Analysis: The characteristic functional groups of poly(HEMA-GMA) cryogels were determined using Fourier Transform Infrared (FT-IR, Thermo Scientific Nicolet 6700 FT-IR spectrometer, USA). The cryogels were dried and pulverized primarily (about 2 mg) and made into pellets by mixing homogeneously by anhydrous potassium bromide powder (KBr) (98 mg, IR grade, Merck, Germany) and the FT-IR spectrum was obtained in the wavenumber range of 400-4000 cm^{-1}.

Elemental Analysis: The dry sample was weighed and placed into the elemental analysis (Elementar Vario PYRO cube, Germany) container. The analysis was performed under the condition of the combustion tube at 1120°C and the reduction tube at 850°C and then the N% value obtained.

The Determination of Ca(II) Amount Bound to the Cryogels : To determine the amount of Ca(II) attached to the poly(HEMA-GMA)@Nic cryogels, the ICP-OES (Spectro Arcos, Germany) were used. In this technique, the sample was excited by electromagnetic induction to the temperature of 10,000 K by argon plasma and the quantity of elements excited was determined by the specific wavelength emitted by these elements. Plasma is obtained by the stimulation of argon gas electromagnetically using a radio frequency (RF) generator on the induction coils. This process was performed by the ionization of incoming gas via hot plasma successively.

Surface Area Analysis: The specific surface area of the membranes was determined via Brunauer-Emmett-Teller (BET; Quantachrome Autosorb® iQ-Chemi, USA) device. The cryogels samples dried with lyophilization remained at 35°C under 100 mbar vacuum for 6 hours to eliminate oxygen and moisture in the pores. Then, the cryogel samples were treated with nitrogen gas at room temperature.

The Adsorption-Desorption Studies: The calmoduline adsorption onto the poly(HEMA-GMA)@Nic-Ca(II) was studied in a batch system. For the adsorption experiment, the buffer solution (4 mL, pH 7.5, 0.1 M Tris-HCl) and the calmoduline solution (1 mL) were mixed and stirred in a rotator for 15 minutes. To determine the calmoduline concentration prior to adsorption, the sample (200 µL) was taken. A cryogel was placed into the adsorption medium and stirred in a rotator at 20 rpm. The membrane was then removed from the adsorption medium and sample (2 mL) was taken to be analyzed in UV-Vis to determine the protein concentration after adsorption. The adsorbed amount of calmoduline was determined using a UV-Vis spectrophotometer (Double Beam PC 8 Auto Cell Scanning UVD-3200 Labomed, INC., USA) at 280 nm wavelength. The calmoduline adsorption capacity of cryogel was determined according to the formula given below.

$$q = [(C_i - C_f) \times V] / m \quad \text{(Eq. 2)}$$

Where q is the amount of adsorption (mg / g), C_i is the concentration of calmoduline solution before adsorption (mg / L), C_f is the concentration of calmoduline solution after adsorption (mg / L), V is the volume of the adsorption medium (L) and m is the amount of dry adsorbent (g).

For desorption studies, NaCl solution (1 M, 10 mL) was used. To determine the reusability of cryogels, the adsorption-desorption cycle was performed using NaOH solution (50 mM, 10 mL) for the regeneration of cryogels exposed to the desorption process.

RESULTS and DISCUSSIONS

Characterization Studies

The swelling ratio of cryogels was calculated as 764% which is quite a good result as compared to the literature (22, 23). Accordingly, the dry cryogel (1 g) has retained about 7.64 g of water. The SEM image of cryogels shows the macro-pores and the interconnecting flow channels (Figure 2). When the FT-IR spectra are examined, the peaks at 3423 cm^{-1} (alcohol, -OH), 2947 (alkane C-H), 1731 (carboxylic acid, C = O), 1619 and 1558 cm^{-1} (amine, NH) are obvious for the poly(HEMA-GMA)@Nic-Ca(II) cryogels (Figure 3). In the case of elemental analysis results, the poly(HEMA-GMA)@Nic-Ca(II) cryogels have the N% value corresponding the ligand amount of 32.9 mg/g cryogel (nicotinamide 1.175 mmol/g cryogel). The surface area of cryogels was estimated as 8.736 m^2/g which quite comparable with the literature (24, 25). The Ca(II) amount immobilized on the cryogels was found as 455 mmoles/g.

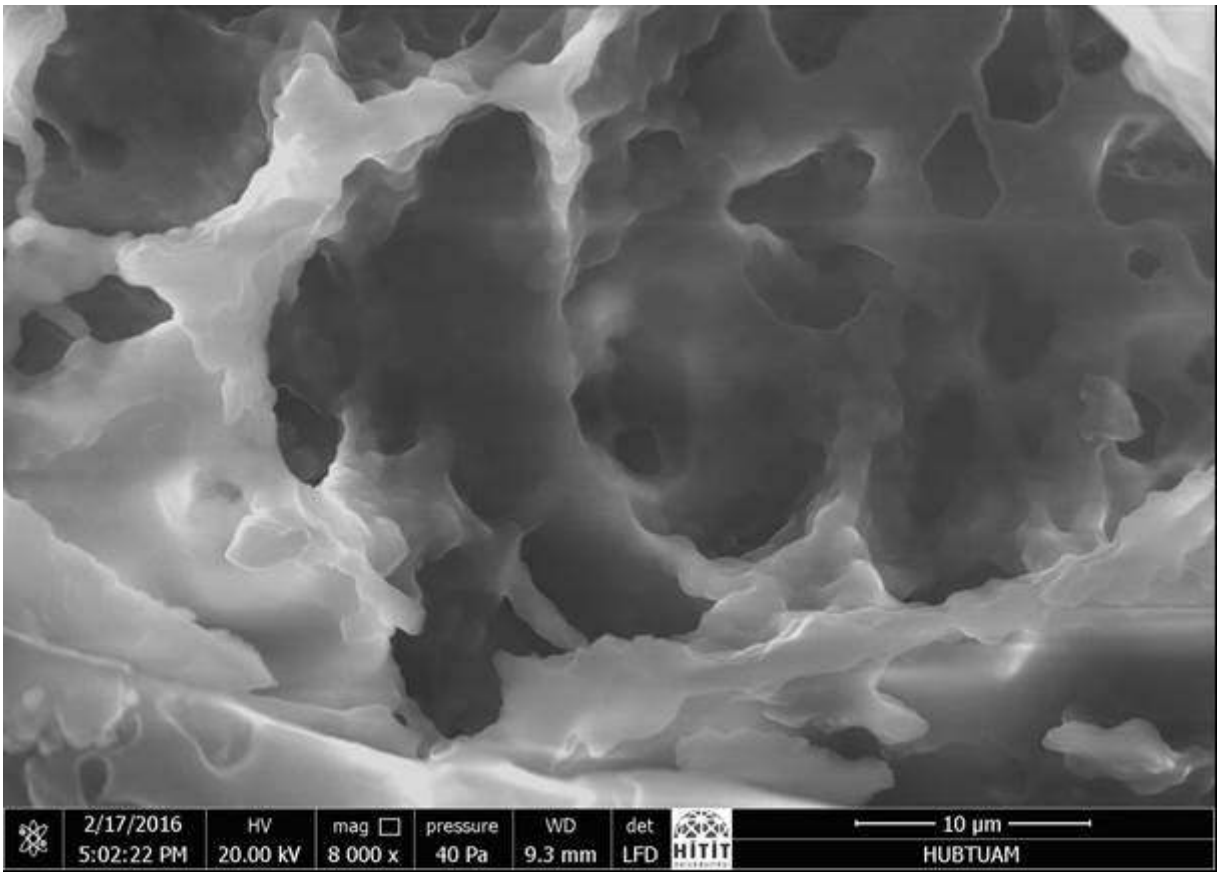

Figure 2. The SEM images of poly(HEMA-GMA)@Nic-Ca(II) cryogels.

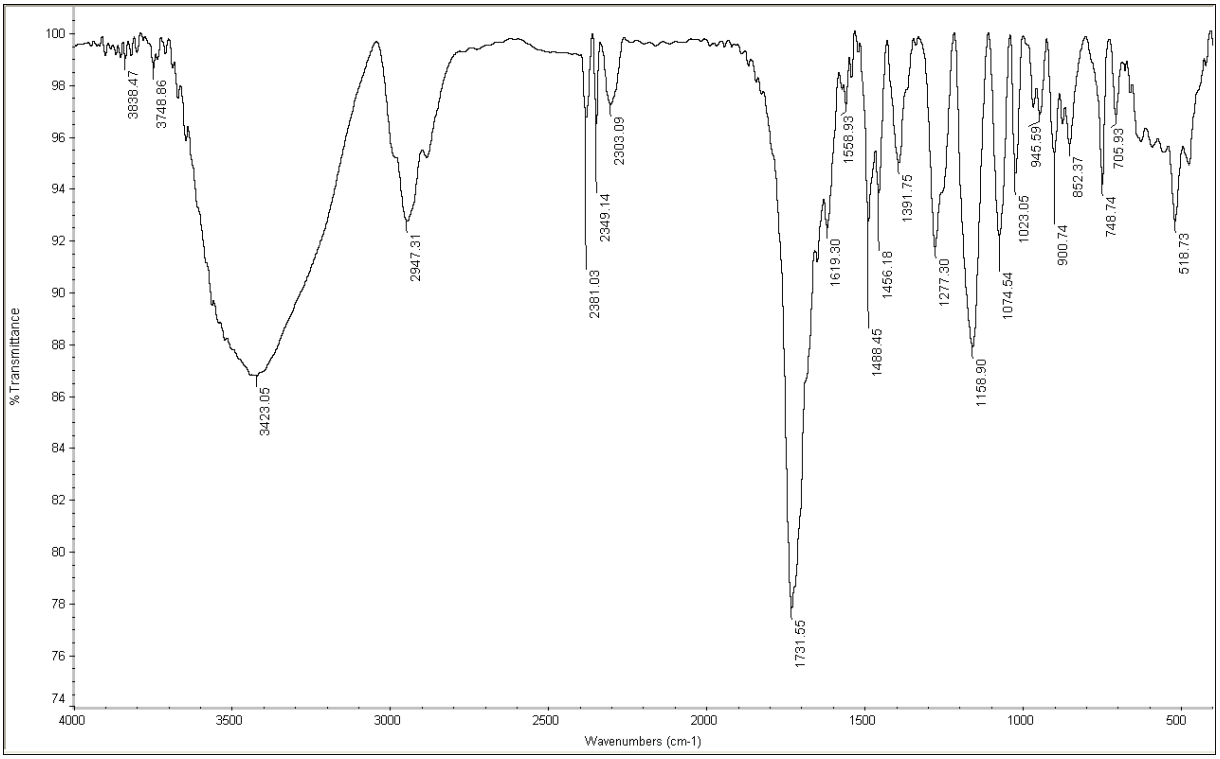

Figure 3. The FT-IR spectrum of poly(HEMA-GMA)@Nic-Ca(II) cryogels.

Adsorption-Desorption Experiments

To determine the environmental condition within the scope of adsorption studies, the adsorption time, calmoduline initial concentration, and temperature parameters were investigated. At the end of the studies performed, the 20 minute-interaction time was sufficient to achieve the maximum adsorption capacity (Figure 4-a). During this time, the calmoduline adsorption capacity of poly(HEMA-GMA)@Nic-Ca(II) cryogels was reached the maximum value and not changed significantly at subsequent time intervals because of the saturation of binding zone on the surface of cryogels. The adsorption capacity of cryogels was increased with the concentration of calmoduline solution used in adsorption, but there was no significant change observed in the adsorption capacity after the concentration value of 5 mg/L (Figure 4-b). This situation can also be explained by the saturation of cryogels in terms of target molecules. The decrease observed on the adsorption capacity with increasing temperature has shown that the interaction between poly(HEMA-GMA)@Nic-Ca(II) cryogels and calmoduline molecules were electrostatic interaction (Figure 4-c). The electrostatic interaction was weakened with increasing temperature and decreased the adsorption capacity by causing the partial breaking of the bonds.

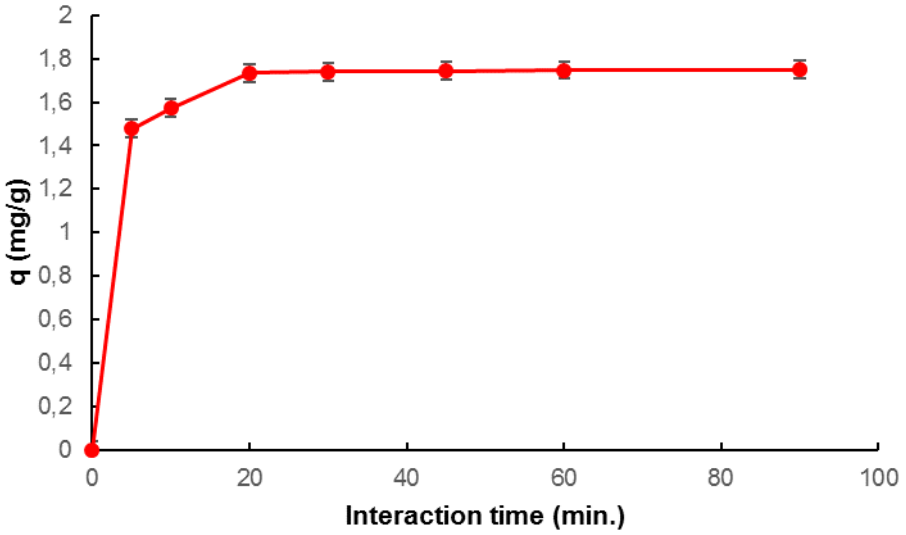

a

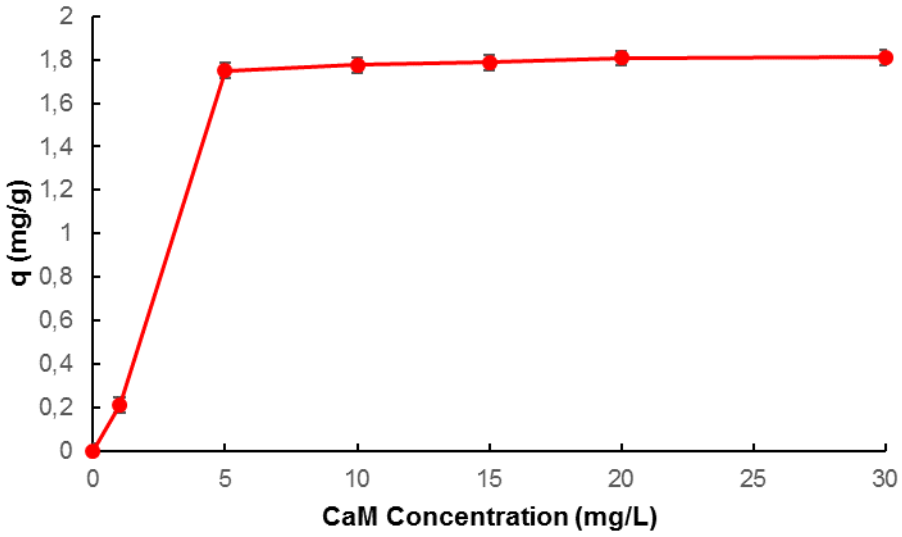

b

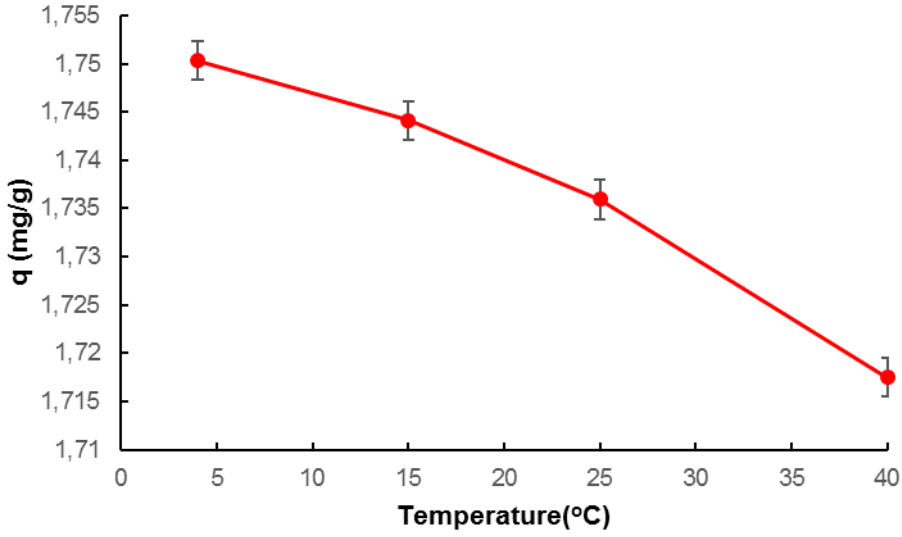

c

Figure 4. The effect of a) Interaction time. $C_{Calmodulin}$: 5 mg/L; temperature: 25°C. b) Calmoduline initial concentration. Interaction time: 20 min.; temperature: 25°C. c) Temperature. $C_{Calmodulin}$: 5 mg/L; interaction time: 20 min. on the adsorption process. All experiments were repeated three times applying 95% confidence interval for calculating mean values reported.

To test the reusability properties of the poly(HEMA-GMA)@Nic-Ca(II) cryogels, the same cryogel was used 5 times for the adsorption-desorption process. There was no significant decrease was observed in the adsorption capacity of cryogel at the end of the 5 cycles (from 1.753 to 1.7391) (Figure 5). This result has shown that the reusability performance of poly(HEMA-GMA)@Nic-Ca(II) cryogels are significantly high.

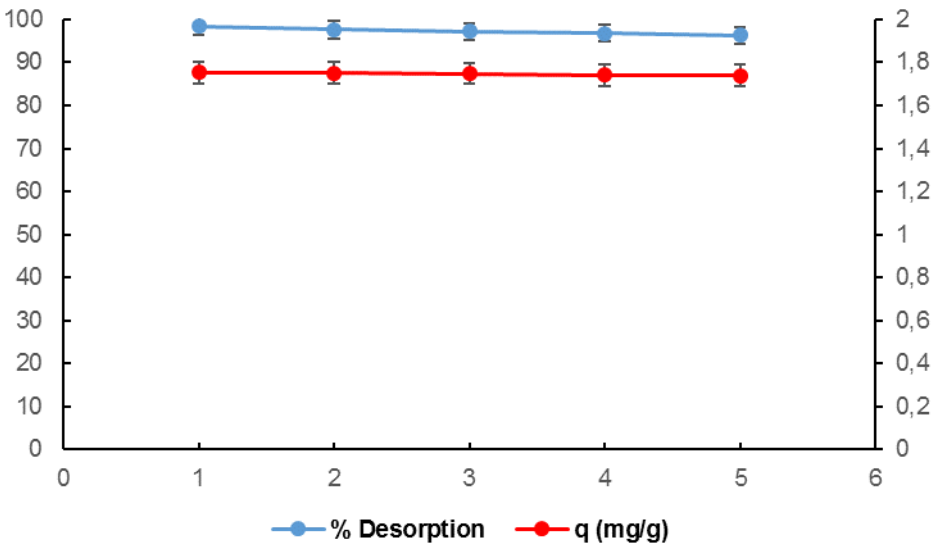

Figure 5. The reusability of poly(HEMA-GMA)@Nic-Ca(II) cryogels.

The calmoduline adsorption performance of poly(HEMA-GMA), poly(HEMA-GMA)@Nic and poly(HEMA-GMA)@Nic-Ca(II) cryogels were compared with each other under predetermined optimum adsorption conditions (interaction time: 20 min., calmoduline initial concentration: 5.0 mg/L). As can be seen from Figure 6, the calmoduline adsorption capacity of poly(HEMA-GMA) (0.125 mg/g) is very much lower than that of poly(HEMA-GMA)@Nic-Ca(II) cryogel (1.75 mg/g). According to this result, the incorporation of nicotinamide and Ca(II) into the structure has provided a substantial increase of calmoduline affinity of the cryogel. In the method performed before (26), the calmoduline adsorption amount of 0.2 µg was achieved per procedure, and thus the high performance of cryogels used in this study is remarkable as a conclusion of the comparison with this result.

Adsorption Isotherms

The characterization of the adsorption of calmoduline molecule onto poly(HEMA-GMA)@Nic-Ca(II) cryogels, the adsorption isotherms were examined. According to the Langmuir adsorption isotherm, the adsorption phenomena is on the surface, uniform and assumed to have occurred in one layer (27), whereas according to the Freundlich adsorption isotherm, the adsorption is not limited to a single layer and are considered to be heterogeneous (28). The following equations were used for the Langmuir and Freundlich isotherms.

$$\text{Langmuir equation: } C_{eq}/Q = 1/(Q_{max.}\, b) + (C_{eq}/Q_{max.}) \qquad \text{(Eq.2)}$$

If it is linearized, Eq. 3 is obtained:

$$1 / Q_{eq} = [1 / (Q_{max.}\ b)][\ 1 / C_{eq}] + [1 / (Q_{max})] \quad \text{(Eq. 3)}$$

Where, the y-intercept of the plot $1/C_{eq}$ vs $1/Q_{eq}$ is $1/Q_{max}$ and the slope is $1/Q_{max.}b$. Q_{eq} is the adsorbed calmoduline amount (mg/g), C_{eq} is the calmoduline concentration at equilibrium, b is the Langmuir adsorption constant (L/mg), and $Q_{max.}$ is the maximum adsorption capacity (mg/g).

$$\text{Freundlich equation: } \ln Q_{eq} = \ln K_f + (n \times \ln C_{eq}) \quad \text{(Eq. 4)}$$

Where K_f and n are the Freundlich isotherm constants. The y-intercept of the $\ln Q_{eq}$ vs $\ln C_{eq}$ plot is the $\ln K_f$ and the slope is the n value.

The necessary adsorption and correlation coefficients for both adsorption isotherms were calculated and given in Table 1.

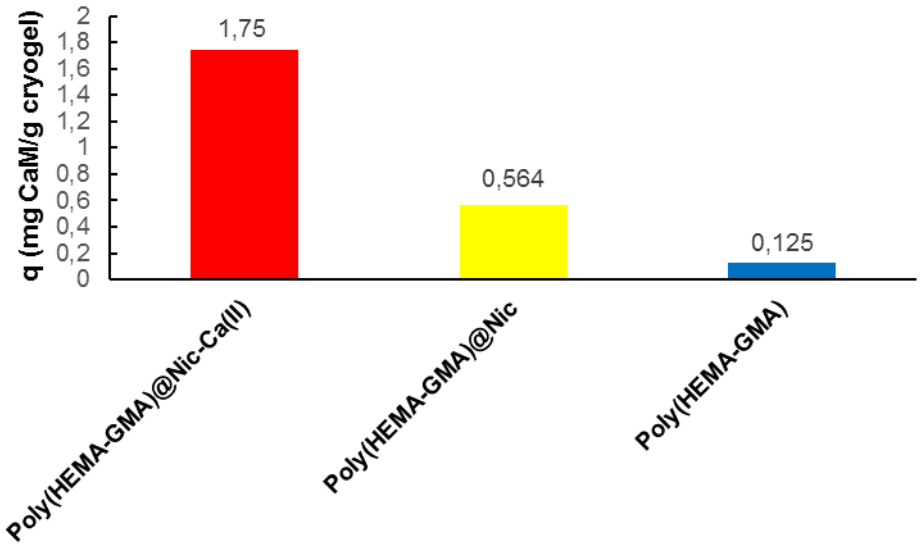

Figure 6. The comparison of the calmoduline adsorption capacities of poly(HEMA-GMA), poly(HEMA-GMA)@Nic and poly(HEMA-GMA)@Nic-Ca(II) cryogels.

Table 1. The parameters obtained from adsorption isotherms.

	Langmuir Constants			Freundlich Constants			
$Q_{exp.}$ (mg/g)	$Q_{max.}$(mg/g)	b (L/mg)	R^2	K_f	n	1/n	R^2
1.812	1.821	7.358	0.9349	1.74	0.0133	75.19	0.925

According to the experimental data obtained, the correlation coefficient of the Langmuir isotherm is higher and the Q_{max} value corresponds to the value obtained in the experiment.

CONCLUSIONS

It was determined that poly(HEMA-GMA)@Nic-Ca(II) cryogel is a suitable adsorbent for the adsorption of calmoduline molecule. It is thought that the interaction occurs between Ca(II) ion within the structure of cryogel and the charged groups on the calmoduline molecule. The decrease in the amount of adsorption with increasing temperature and ionic strength is an indicator of the electrostatic interaction. The interaction between the cryogel and calmoduline fits well the Langmuir adsorption model. Therefore, according to this model, the calmoduline molecules are adsorbed onto the poly(HEMA-GMA)@Nic-Ca(II) cryogels on a monolayer homogeneously.

ACKNOWLEDGEMENT

Because of the contribution to the work, I would like to express my heartfelt thanks of Assoc. Prof. Dr. Dursun Ali Köse (Hitit University, Faculty of Arts and Sciences, Department of Chemistry).

REFERENCES

1. Sudhakar Babu, Y., C. Bugg, and W. Cook, Structure of calmodulin refined at 2.2 Å resolution. Journal of molecular biology, 1988. 2041: p. 191-204. URL: https://www.ncbi.nlm.nih.gov/pubmed/3145979.

2. Zhang, M., T. Tanaka, and M. Ikura, Calcium-induced conformational transition revealed by the solution structure of apo calmodulin. Nature Structural & Molecular Biology, 1995. 29: p. 758-767. DOI:10.1038/nsb0995-758.

3. Hitoshi Kuboniwa, N.T., et al., Solution structure of calcium-free calmodulin. Nature structural biology, 1995. 29. URL: https://www.ncbi.nlm.nih.gov/pubmed/7552748.

4. Yamniuk, A.P. and H.J. Vogel, Calmodulin's flexibility allows for promiscuity in its interactions with target proteins and peptides. Molecular biotechnology, 2004. 271: p. 33-57. DOI: 10.1385/MB:27:1:33.

5. Webb, R.C., Smooth muscle contraction and relaxation. Advances in physiology education, 2003. 274: p. 201-206. DOI:10.1152/advan.00025.2003.

6.

7. Means, A.R., Calcium, calmodulin and cell cycle regulation. FEBS letters, 1994. 3471: p. 1-4. DOI:10.1016/0014-57939400492-7.

8.

7. Racioppi, L. and A.R. Means, Calcium/calmodulin-dependent protein kinase kinase 2: roles in signaling and pathophysiology. Journal of Biological Chemistry, 2012. 28738: p. 31658-31665. DOI:10.1074/jbc.R112.356485.

8. Kulej, K., et al., Optimization of calmodulin-affinity chromatography for brain and organelles. EuPA Open Proteomics, 2015. 8: p. 55-67. http://dx.doi.org/10.1016/j.euprot.2015.05.004.

9. O'Day, D.H., CaMBOT: profiling and characterizing calmodulin-binding proteins. Cellular signalling, 2003. 154: p. 347-354. URL: https://www.ncbi.nlm.nih.gov/pubmed/12618209.

10. Clapham, D.E., Calcium signaling. Cell, 2007. 1316: p. 1047-1058. DOI: 10.1016/j.cell.2007.11.028.

11. Ikura, M., M. Osawa, and J.B. Ames, The role of calcium-binding proteins in the control of transcription: structure to function. Bioessays, 2002. 247: p. 625-636. DOI: 10.1002/bies.10105.

12. West, A.E., et al., Calcium regulation of neuronal gene expression. Proceedings of the National Academy of Sciences, 2001. 9820: p. 11024-11031. DOI: 10.1073/pnas.191352298.

13. Porath, J., et al., Metal chelate affinity chromatography, a new approach to protein fractionation. Nature, 1975. 258: p. 598-599. URL: https://www.ncbi.nlm.nih.gov/pubmed/1678.

14. Block, H., et al., Immobilized-metal affinity chromatography IMAC: a review. Methods in enzymology, 2009. 463: p. 439-473. DOI: 10.1016/S0076-68790963027-5.

15. Cheung, R.C.F., J.H. Wong, and T.B. Ng, Immobilized metal ion affinity chromatography: a review on its applications. Applied microbiology and biotechnology, 2012. 966: p. 1411-1420. DOI: 10.1007/s00253-012-4507-0.

16. Westra, D.F., et al., Immobilised metal-ion affinity chromatography purification of histidine-tagged recombinant proteins: a wash step with a low concentration of EDTA. Journal of Chromatography B: Biomedical Sciences and Applications, 2001. 7601: p. 129-136. URL: http://europepmc.org/abstract/med/11522055.

17. Yip, T.-T. and T.W. Hutchens, Immobilized metal-ion affinity chromatography. Protein Purification Protocols, 2004: p. 179-190. DOI:10.1385/1-59259-655-X:179.

18. Charlton, A. and M. Zachariou, Immobilized metal ion affinity chromatography of histidine-tagged fusion proteins. Affinity Chromatography: Methods and Protocols, 2008: p. 137-149. URL: https://www.ncbi.nlm.nih.gov/pubmed/18826053.

19. Kågedal, L., Immobilized metal ion affinity chromatography. Protein Purification, Principles, High Resolution Methods, and Applications, 2011: p. 183-201. URL: https://www.ncbi.nlm.nih.gov/pubmed/21954778?dopt=Abstract.

20. Karakus, C., et al., Evaluation of immobilized metal affinity chromatography kits for the purification of histidine-tagged recombinant CagA protein. Journal of Chromatography B, 2016. 1021: p. 182-187. DOI: 10.1016/j.jchromb.2015.11.045.

21. Hincke, M.T., Conditions for improved adsorption of calmodulin to nitrocellulose: detection by 45Ca binding. Electrophoresis, 1988. 97: p. 303-306. DOI: 10.1002/elps.1150090704.

22. Kose, K., et al., Affinity purification lipase from wheat germ: comparison of hydrophobic and metal chelation effect. Artif Cells Nanomed Biotechnol, 20162169-141X Electronic: p. 1-10. DOI: 10.3109/21691401.2016.1161642.

23. Erol, K., et al., Polyethyleneimine assisted-two-step polymerization to develop surface imprinted cryogels for lysozyme purification. Colloids Surf B Biointerfaces, 2016. 146: p. 567-76. DOI: 10.1016/j.colsurfb.2016.06.060.

24. Kose, K., et al., PolyAdenine cryogels for fast and effective RNA purification. Colloids Surf B Biointerfaces, 2016. 146: p. 678-86. DOI: 10.1016/j.colsurfb.2016.07.003.

25. Kose, K. and L. Uzun, PolyGuanine methacrylate cryogels for ribonucleic acid purification. J Sep Sci, 2016. 3910: p. 1998-2005. DOI: 10.1002/jssc.201600199.

26. Maruyama, K., T. Mikawa, and S. Ebash, Detection of calcium binding proteins by 45Ca autoradiography on nitrocellulose membrane after sodium dodecyl sulfate gel electrophoresis. Journal of Biochemistry, 1984. 952: p. 511-519. URL: http://jb.oxfordjournals.org/content/95/2/511.short.

27. Langmuir, I., The adsorption of gases on plane surfaces of glass, mica and platinum. Journal of the American Chemical society, 1918. 409: p. 1361-1403. DOI: 10.1021/ja02242a004.

28. Freundlich, H.M.F., Uber die adsorption in losungen. Zeitschrift fur Physikalische Chemie, 1906. 57: p. 385-471. URL: https://openlibrary.org/books/OL15094118M/Über_die_Adsorption_in_Lösungen.

Türkçe Öz ve Anahtar Kelimeler

Nikotinamid Tutuklanmış poli(HEMA-GMA) Kriyojelleri ile Kalmodulinin Adsorpsiyonu

Kadir Erol

Öz: Önemli bir biyomolekül olan kalmodulinin ayrılması ve saflaştırılması son derece önemlidir. Adsorpsiyon tekniği oldukça popülerdir, makro-gözenekli yapıları ve içinde barındırdığı akış kanalları ile kriyojellerin adsorban olarak kullanıldığı görülmektedir. Bu çalışmada, kalmodulinin Ca(II) tutuklanmış poli(2-hidroksietil metakrilat-glisidil metakrilat, poli(HEMA-GMA)) ile kalmodulinin adsorpsiyonu çalışılmış ve etkileşim süresi, kalmodulinin ilk derişimi ve sıcaklık değiştirilerek deneyler yapılmıştır. Kriyojellerin karakterizasyonu için, şişme testi, Fourier Dönüşüm Kızılötesi Spektroskopisi (FT-IR), Taramalı Elektron Mikroskopisi (SEM), yüzey alanı (BET), elementel analiz ve ICP-OES yöntemleri kullanılmıştır. Nikotinamid molekülü, Ca(II) için kelatlama aracı olarak kullanılmış ve 1,812 mg kalmodulin/g kriyojel olarak, adsorpsiyon kapasitesi bulunmuştur. Sürecin adsorpsiyon modelleri Langmuir ve Freundlich izoterm modellerine göre incelenmiştir.

Anahtar kelimeler: Adsorpsiyon; kalmodulin; kriyojel; nikotinamid.

Sunulma: 28 Eylül 2016. **Düzeltme**: 31 Ekim 2016. **Kabul**: 03 Kasım 2016.

JOTCS A Journal of the Turkish Chemical Society Chemistry Section A
TURKISH CHEMICAL SOCIETY

Effect of Collection Time on Chemical Composition and Antibacterial Activity of Flower Essential Oil of *Ocimum canum* (Sims) Grown in Nigeria

Usman Lamidi Ajao[1*], Yusuf Abdulrauf Olaniyi[1], Saliu Bola Kudirat[2], Olanipekun Bolatito Eunice[3], Elelu Nusirat[4].

[1]Department of Chemistry, Faculty of Physical Sciences University of Ilorin, PMB 1515 Ilorin, Nigeria.
[2]Department of Microbiology, Faculty of Life Sciences, University of Ilorin, PMB 1515 Ilorin, Nigeria.
[3]Department of Chemical, Geological and Physical Sciences, Kwara State University, Malete, Nigeria.
[4]Department of Veterinary Public Health and Preventive Medicine, Faculty of Veterinary Medicine University of Ilorin, PMB 1515, Nigeria.

Abstract: Flowers (1000 g) of *Ocimum canum* harvested at different times (7 am, 10 am, 1 pm, 4 pm, and 7 pm) in a day were separately hydrodistilled and yielded 0.19 - 0.27% (w/w) of essential oils. GC and GC-MS analyses revealed that the oils were predominated by oxygenated monoterpenoids (51.2-74.4%). Hydrocarbon monoterpenoids constituted 6.2-10.2% of the oils. Percentage composition of hydrocarbon and oxygenated sesquiterpenoids in the oils were in the range of 1.3-22.0%. The most abundant constituent of the oils was linalool (40.5-58.7%). Other principal constituents were as follows: Limonene (0.6 –7.5%), terpinen-4-ol (1.4–5.6%), eugenol (4.4–8.9%), geranyl acetate (0.2–4.9%), α-trans-bergamotene (3.2–9.4%) and (*E)*-isoeugenol (4.1–5.5%). The predominance of linalool in the oils showed that the oils were of linalool chemotype. Antibacterial activity of the oils was evaluated against *Staphylococcus aureus and Escherichia coli* using agar diffusion method. Irrespective of the time of collection of the flower, the oils were found to be active against the tested organisms. However, they are more active on *Escherichia coli* than *Staphylococcus aureus*. The activity of the oils on the organisms was concentration-dependent.

Keywords: *Ocimum canum*; Chemotype; linalool; terpene synthase; antibacterial activity.

Submitted: September 29, 2016. **Revised:** October 25, 2016. **Accepted:** 07 November, 2016.

Cite this: Usman L, Yusuf A, Saliu B, Olanipekun B, Elelu N. Effect of Collection Time on Chemical Composition and Antibacterial Activity of Flower Essential Oil of *Ocimum canum* (Sims) Grown in Nigeria. JOTCSA. 2017;4(1):149–64.

DOI: to be assigned.

*Corresponding author. E-mail: usmanlamidi@unilorin.edu.ng, tel: +2348035032378.

INTRODUCTION

Ocimum canum is an annual, odorous herb with several folkloric uses (1). They are used in treating conjunctivitis and headaches (2). The aerial parts of the plant are used as febrifuge and as an ingredient of many remedies of cold and sinusitis. An infusion of its leaves is used as a diaphoretic (3, 4). Biochemical and biological activities of the plant extracts account for their use in herbal medicine (5-7). The presence of phenolics, flavonoids, tannins and terpenoids that were established in the plant extracts is responsible for the activities exhibited by the plant (8).

The existence of linalool, eugenol, *trans*-methylcinnamate, methyl chavicol, eucalyptol, and camphor chemotypes of leaf oil of *O. canum* have been reported in Rwanda, Nigeria, Sao Tome, Brazil, India, and Cameroon (5, 9-14). Similarly, linalool, *cis*- and *trans*- piperitol chemotypes of flower oil of the plant grown in Rwanda and Burkina-Faso have been discovered (9, 15).

Variation in the chemotypes of the oils is attributable to environmental and physiological factors at various locations of the plant that bears the essential oils (5). These factors determine the activity of the enzyme that facilitates the biosynthesis of terpenoid constituents of essential oils from their respective precursors in plants (16). Hence, the factors could cause a variation in phytochemical profiles and biological activities of the oils. At a particular plant location, the factors could vary from time to time in a day. It is on the basis of this that this work aimed at monitoring the effect of collection time on the chemical composition and antibacterial activity of essential oil from flower of the plant on *Escherichia coli* and *Staphylococcus aureus*.

MATERIALS AND METHODS

Sample Collection and Preparation

Flowers of *O. canum* were harvested from its mature plant at park and garden of University of Ilorin, Ilorin, Kwara State Nigeria. The harvests were carried out at various times in a day (7 am, 10 am, 1 pm, 4 pm, and 7 pm). Identification of the plant was done in the herbarium of Plant Biology Department, University of Ilorin, Ilorin where a voucher sample was deposited (UILH/001/608). The harvested samples were separately pulverized. The test organisms were obtained from the culture collection of the Department of Microbiology, University of Ilorin. The organisms were isolated and characterized by colonial, microscopic, and biochemical techniques in a previous study (17).

Isolation of the Oil

1000 g of each of the pulverized flowers of *Ocimum canum* was hydro-distilled for 3 hours in a Clevenger-type apparatus, according to the British Pharmacopoeia specification (18). The resulting oil from each sample was collected, preserved in a sealed sample tube, and stored under refrigeration until analysis.

Gas chromatography (GC) analysis

Essential oil from each of the harvests was diluted in n-hexane by 1000-fold and subjected to GC analysis. The GC analyses were performed on an Orion micromat 412 double focusing gas chromatography system fitted with two capillary columns coated with Cp- Sil 5 and Cp-Sil 19 (fused silica, 25 m x 0.25 mm, 0.15µm film thickness) and flame ionization detector (FID). The volume injected was 0.2 µL, and the split ratio was 1:30. Oven temperature was programmed from 50 – 230 °C at 3 °C/min using hydrogen as a carrier gas. Injection and detector temperatures were maintained at 200 °C and 250 °C, respectively. Qualitative data were obtained by electronic integration of FID area percent without the use of correction factors.

Gas Chromatography – Mass Spectrometry (GC/MS) Analysis

A Hewlett – Packard HP 5890A GC, interfaced with a VG analytical 70-250s double focusing mass spectrometers was used. The MS operating conditions were: ionization voltage 70 eV, ion source and transfer line temperature was maintained at 230 ^{o}C. The GC operating conditions were identical with those of GC analyses. The MS data were acquired and processed by on-line desktop with a computer equipped with disk memory. The percentage composition of the oils' constituents were computed in each case from GC peak areas. The identification of the components was based on comparison of retention indices (determined relative to the retention times of series of n-alkanes) and mass spectra with those of authentic samples and with data from the literature (19-21).

Antibacterial Assay (Agar Diffusion Method)

Antibacterial activity of the oils was determined using agar diffusion method described by Sartoratto *et al.* (22) Inoculums were prepared with the fresh cultures of bacteria, grown in nutrient broth for 24 hours at 37 ^{o}C and standardized to McFarland scale 0.5. Five wells (4 mm) were made on the Mueller-Hinton agar plates already seeded with bacteria by spread plate technique using flame sterilized Cork Borer. The essential oils were diluted with Tween 80 to obtain 25%, 50%, and 100% (v/v) concentrations and 0.1 mL each was transferred to separate,

appropriately labelled wells**.** An aliquot (0.1 mL) of Tween 80 was used as negative control while streptomycin served as positive control. Plates were incubated at 37 °C for 24 hrs. Antibacterial activity was determined by clearance around loaded wells. MIC was determined as lowest concentration of oil that inhibited growth of bacteria.

RESULTS AND DISCUSSION

Fresh flowers of *Ocimum canum* afforded 0.19-0.27% (w/w) of essential oil. The yield increased from 0.19% (w/w) in 7 am harvest to 0.21% (w/w) in 10 am harvest. It subsequently decreased to 0.20% (w/w) in 1 pm harvest. The yield later increased from 0.24% (w/w) in 4 pm harvest to 0.27% (w/w) in 7 pm harvest. Variations in oil yields from various harvests signified that the time of harvest affects the yield.

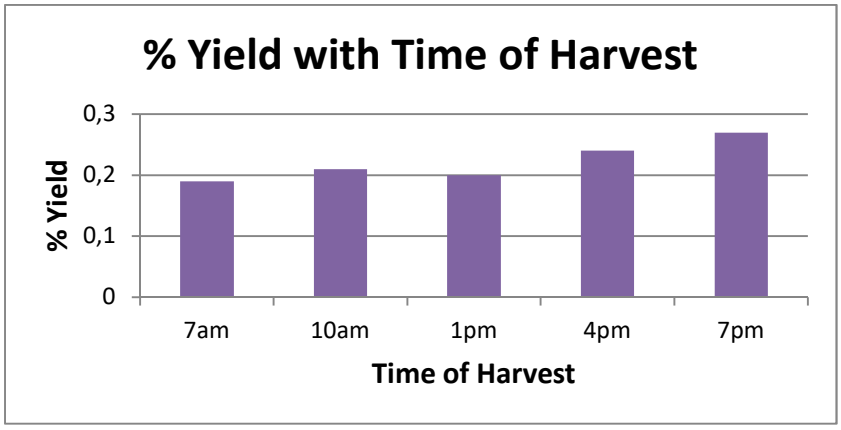

Figure 1: Yield of Oils from *Ocimum canum.*

Table 1: Chemical Composition (%) of Flower Essential Oil of *Ocimum canum.*

Compound[a]	**RI**[b]	**RI**[c]	**% Composition**	**Mass Spectral Data**			
			7 am	**10 am**	**1 pm**	**4 pm**	**7 pm**	
α-pinene	937	939	0.2	0.3	0.4	-	-	136,121,**93**,91,77
Car-2-ene	1001	1002	2.2	0.4	0.3	0.2	-	136,121,105,**93**,41
Car-3-ene	1009	1011	2.4	1.2	2.2	-	-	136,121,105,**93**,91
α-terpinene	1018	1015	-	-	0.3	0.4	-	136,**121**,105,93,77
p-cymene	1024	1024	1.3	-	-	0.3	0.4	134,**119**,103,91,77
o-cymene	1026	1026	-	0.4	-	-	-	134,**119**,105,91,77
Sylvestrene	1027	1030	-	0.3	0.5	-	-	136,121,107,**93**,68
Limonene	1031	1029	1.4	0.6	0.6	-	7.5	136,121,93,79,**68**
β-phellandrene	1031	1029	-	0.6	-	0.6	-	136,121,**93**,79,77
Eucalyptol	1033	1031	2.9	1.2	2.2	0.5	1.5	154,139,108,81,**43**
cis-β-ocimene	1040	1050	-	1.0	1.7	1.1	1.0	136,121,**93**,79,41
γ-terpinene	1062	1059	-	0.9	0.7	0.8	0.7	136,121,105,**93**,77
m-cymenene	1082	1082	-	0.5	-	0.6	0.6	134,119,103,91,77
α-terpinolene	1088	1088	0.5	0.3	0.6	-	-	136,121,105,**93**,79
Linalool	1098	1096	48.1	55.4	40.5	68.1	58.7	154,121,93,**71**,41
Octylacetate	1121	1112	2.4	-	-	-	-	187, 169,157,109,43
Lavandulol	1166	1163	-	-	0.1	0.5	0.5	136,123,93,**69**,41
Terpinen-4-ol	1177	1174	1.4	5.5	5.6	3.5	5.2	154,136,111,93,**71**
α-terpineol	1185	1188	-	0.4	-	0.5	0.4	136,121,93,81,**59**
Nerol	1228	1229	-	-	0.2	0.2	-	154,121,93,**69**,41
Geranial	1270	1268	1.6	1.8	0.6	0.9	1.1	152,109,**69**,53,41
Geranyl-formate	1300	1298	-	-	-	0.2	-	182,136,93,**69**,41
α-cubebene	1351	1351	0.1	0.2	0.1	-	-	204,161,119,**105**,41
Eugenol	1356	1359	8.7	8.9	6.6	4.4	4.8	**164,**149,131,103,91
Nerylacetate	1365	1361	-	-	1.5	-	-	154,121,93,**69**,41
β-elemene	1375	1374	1.8	1.1	1.0	0.7	0.5	204,161,121,**93**,81
α-copaene	1376	1376	1.9	-	0.8	-	-	204,**161**,119,105,91
Geranyl acetate	1383	1382	-	0.2	-	4.9	-	154,121,93,**69**,41
β-cubebene	1390	1388	0.2	0.2	0.2	-	-	204,**161**,105,91,41
β-caryophyllene	1418	1417	2.8	1.4	-	-	-	204,161,133,93,**41**
α-*trans*-bergamotene	1436	1435	-	-	9.4	3.2	5.3	204,161,119,**93**,41
α-guaine	1439	1439	1.7	0.8	0.8	0.5	0.6	204,161,**105**,93,41
(Z)-β-farnesene	1443	1442	2.3	0.3	-	0.2	-	204,133,93,69,**41**
(E)-isoeugenol	1447	1451	-	-	5.5	4.1	-	**164**,149,131,93,77
α-caryophyllene	1454	1454	0.2	0.2	-	-	-	204,161,133,**93**,79
(E)-β-farnesene	1458	1456	-	-	-	0.1	-	204,161,93,**69**,41
γ-gurjunene	1473	1471	-	0.2	0.2	-	-	204,**161**,119,91,41

β-chamigrene	1475	1473	-	-	1.0	-	-	204,**189**,105,93,41
γ-muurolene	1477	1475	1.2	0.3	1.7	-	0.8	204,**161**,119,91,41
Germacrene D	1480	1479	1.5	1.4	1.7	-	1.5	204,**161**,119,105,41
α-selinene	1494	1494	-	-	-	0.5	-	204,**189**,161,133,41
Bicyclogermacrene	1494	1500	-	0.9	0.8	0.2	0.4	204,161,**121**,93,41
β-himachalene	1499	1500	-	-	0.2	-	-	204,134,**119**,105,41
α-bulnesene	1505	1509	2.4	1.3	1.2	0.4	0.6	204,189,**107**,93,41
Amorphene	1506	1511	-	0.5	1.7	0.8	0.8	204,161,**133**,105,41
γ-cadinene	1513	1513	0.4	1.7	0.7	1.0	1.4	204,**161**,119,91,41
β-sesquiphellandrene	1521	1522	-	0.5	0.4	0.8	0.7	204,161,93,**69**,41
cis-nerolidol	1534	1563	-	-	1.2	0.2	-	204,161,136,69,**41**
Germacrene B	1560	1561	1.6	-	-	0.5	0.4	204,161,**121**,93,41
trans-nerolidol	1564	1532	0.3	-	-	0.2	-	204,161,105,**69**,41
Spathulenol	1576	1578	0.2	-	-	-	-	220,205,119,91,**43**
Caryophyllene oxide	1581	1583	-	0.2	-	-	-	219,161,121,79,**41**
β-eudesmol	1649	1650	0.2	0.2	0.1	-	-	222,204,189,149,**59**
Bisabolol	1683	1685	0.2	-	-	-	-	204,119,109,69,**43**
Patchoulene	1793	1756		0.8				204,161,**107**,93,79
TOTAL			**92.1**	**92.4**	**93.7**	**98.8**	**97.7**	
No of Compounds			**30**	**37**	**36**	**33**	**25**	

[a]:- compounds are listed in order of elution from silica capillary column coated on cp-sil 5;

[b]:- Retention indices on fused silica capillary column coated with cp-sil; [c]:- Retention Indices from literature.

Identities, retention indices, and percentage composition of the constituents of flower essential oils of *Ocimum canum* harvested at 3 hours interval in a day (7 am, 10 am, 1 pm, 4 pm, and 7 pm) is presented in Table 1. In the table, compounds 25-37 representing 92.1-98.8% of the oils were identified from their mass spectra. Hydrocarbon monoterpenoids constituted 6.2-10.2% of the oils while percentage composition of oxygenated monoterpenoids was 51.2-74.4%. Meanwhile, 1.3-22.0% of the oils was hydrocarbons and oxygenated sesquiterpenoids.

The most abundant constituent of the oil was linalool (40.5-68.1%). Other major constituents were limonene (0.6 – 7.5%), terpinen-4-ol (1.4 – 5.6%), eugenol (4.4 – 8.9%), geranyl acetate (0.2 – 4.9%), α-*trans*-bergamotene (3.2 – 9.4%) and (*E)*-isoeugenol (4.1 – 5.5%). Car-2-ene (0.2 – 2.2%), car-3-ene (1.2 – 2.4%), eucalyptol (0.5 – 2.9%), *cis*-β-ocimene (1.0 – 1.7%), octylacetate (2.4%), neryl acetate (1.5%), β-elemene (0.5 – 1.8%), α-copaene (0.8 – 1.9%), β-caryophyllene (1.4 – 2.8%), δ-guaine (0.5 – 1.7%), (*Z*)-β-farnesene (0.2 – 2.3%), γ-muurolene (0.3 – 1.7%), germacrene D (1.4 – 1.7%), α-bulnesene (0.4 – 2.4%), γ-cadinene (0.7 – 1.7%), *cis*-nerolidol (0.2– 1.2%) and germacrene B (0.4 – 1.6%) were also detected in appreciable quantities.

Comparison of the oils revealed that there were variations in their composition patterns. Qualitatively, octyl acetate and bisabolol in the oil from 7 am harvest were not detected in the oils from other harvests. Similarly, oil from 10 am harvest bears *p*-cymene, caryophyllene oxide, and patchoulene that were not found in other oils. Furthermore, the presence of neryl acetate, β-himachalene and β-chamigrene were established in the oil of 1 pm harvest but did not exist in other oils. Oil from 4 pm harvest also had geranyl formate, *(E)*-β-farnesene, and α-selinene that were not detected in other oils.

Eucalyptol, *cis*-β-ocimene, γ-terpinene, β-sesquiphellandrene, bicyclogermacrene and amorphene occurred in the oils except for the oil from 7 am harvest. Similarly, limonene, γ-muurolene and germacrene D were detected in the oils except oil of 4 pm harvest. 2-carene was found in the oils with the exception of the oil of 7 pm harvest. Absence of some compounds in the oils may be due to unfavorable physiological conditions of the plant at the time of harvest that did not favor their biosynthesis.

Quantitatively, linalool was more abundant in the oil of 4 pm harvest than other oils. Similarly, terpinen-4-ol was of greater abundance in the oil of 1 pm harvest than other oils. Geranial and eugenol were more abundant in the oil of 10 am harvest than other oils. β-Elemene was detected

in higher quantity in the oil of 7 am and 10 am harvests than other oils. However, β-cubebene and δ-cadinene were found in higher quantities in the oils of 4 and 7 pm harvests than other oils.

Terpinen-4-ol and eugenol occurred in appreciable quantities in the oils but more abundant in the oils from 7 am and 1 pm harvests, respectively. δ-Guaine was more abundant in the oil of 7 am harvest than other oils. Quantitative variations in the oil constituents are attributable to difference in activity of synthases that mediate the formation of the compounds from their respective precursors (23).

The biosynthesis of terpenoids is usually catalyzed by the synthase of the most abundant mono- and sesquiterpenoids in the presence of a divalent metal ion via cationic intermediates. These intermediates subsequently undergo series of reactions such as; hydride shift, cyclization, and other rearrangements until the reaction is terminated by proton loss or hydration to form various terpenoids (21, 23). The reactions do proceed by cationic mechanism.

Reaction mechanisms

The predominance of linalool in the oils implied that its synthase mediates the transformation of geranyl and neryl pyrophosphates to all monoterpenoids in the oils via cationic intermediates (Figure 1). In the figure, linalool synthase aided the transformation of geranyl **(1)** and neryl pyrophosphates **(2)** to geranyl **(4)** and neryl **(5)** cations. Isomerization of each of the ions (**4** and **5**) formed linalyl cation **(3).** Hydration of linalyl and geranyl cations produced linalool **(6)** in the oils. Hydration of geranyl cation that was oxidized and acetylated gave geranial **(8)** and geranyl acetate **(9)** in the oils from 10 am and 4 pm harvests, respectively**.** Neryl cation **(5)** was hydrated to nerol **(10)** in oil from 1 pm and 4 pm harvests and subsequent acetylation of nerol formed neryl acetate **(11)** in oil from 1 pm harvest. Electrophilic attack of the ion **(5)** on C_6-C_7 double bond produced α-terpinyl cation **(12)**. Deprotonation of the ion **(12)** at C_5 and C_1 followed by its electrophilic attack on the deprotonated carbons formed 3-carene **(13)** in oil from 7 am to 1 pm harvests and 2-carene (14) in oils from 7 am to 4 pm harvests. Deprotonation of α-terpinyl cation at C_8 **(12)** gave limonene **(15)** in the oils except oil from 4pm harvest. Folding of the ion **(12)** towards C_2-C_3 double bond followed by its electrophilic attack via C_2 produced pinyl cation **(16).** Deprotonation of the ion (**16**) at C_4 formed α-pinene **(17)** in the oils with the exception of oils from 4 pm and 7 pm harvests. 1, 6-hydride shifts of the ion **(12)** followed by delocalization of C2 – C3 π electrons to C1 – C2 formed phellandryl cation **(18).** Deprotonation of the ion **(18)** at C_{10} formed β- phellandrene **(19)** in oils from 10 am and 4 pm harvests. 6, 7-hydride shift of the ion **(12)** gives terpinyl-4-yl cation **(20).** Subsequent deprotonation of the latter **(20)** at C_1 and C_7

produced α-terpinene **(21)** in oils from 1 and 4pm harvests and α-terpinolene **(22)** in oils from 7 am, 10 am and 1 pm harvests respectively. Dehydrogenation of α-terpinene **(21)** at C_4 and C_5 formed p-cymene **(23)** in oil from 10am harvest. Hydration of α-terpinyl cation (**12**) formed α-terpineol **(24)** in oils from 10am, 4pm and 7pm harvests. Nucleophilic attack of hydroxyl oxygen of α-terpineol on C2-C3 double bond and subsequent protonation of the product formed eucalyptol (**25**) in the oils.

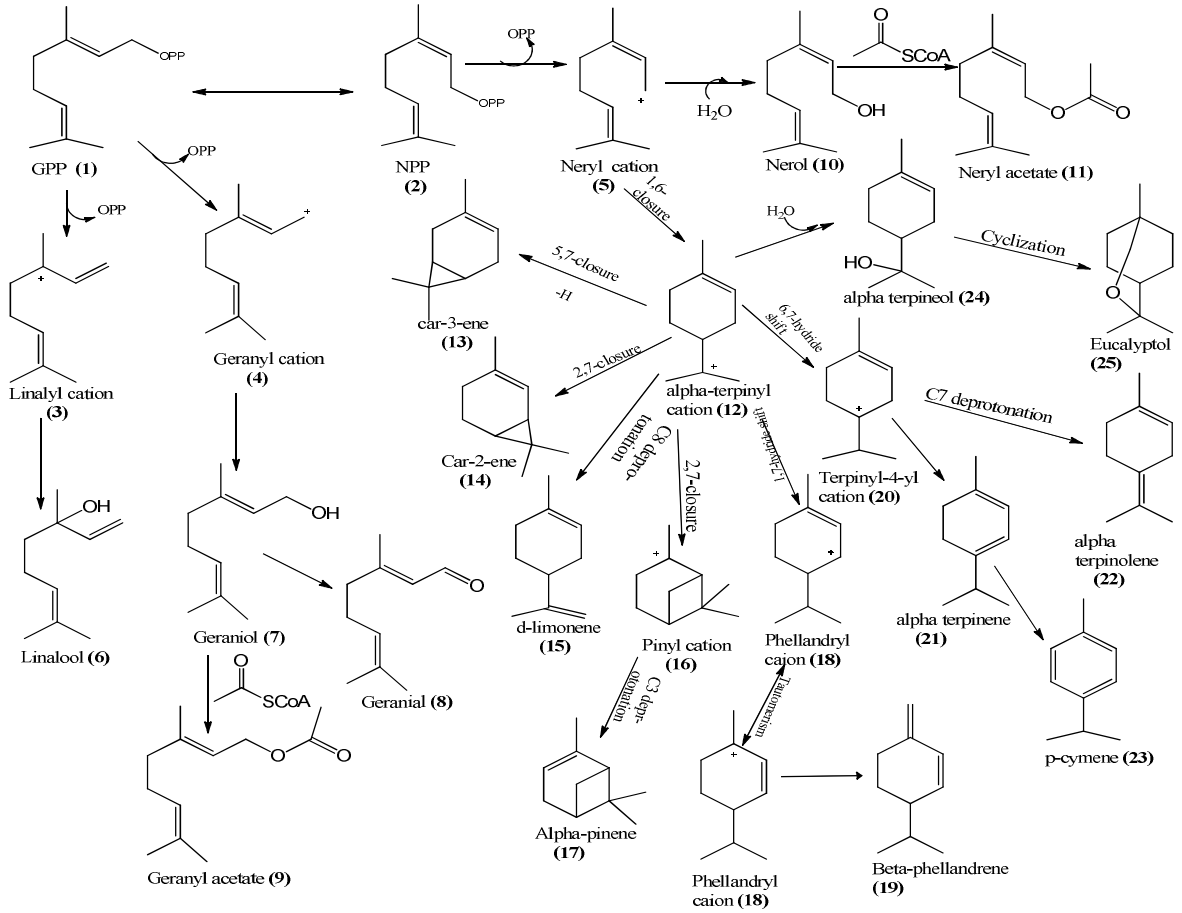

Reaction Scheme 1: Biosynthesis of monoterpenoids mediated by linalool synthase.

The abundance of β-caryophyllene, γ-cadinene and α-*trans*-bergamotene in the oils of 7 am, 10 am and 1-7 pm harvests implied that their synthases mediated the biosynthesis of all the sesquiterpenoids in the oils, where each of the compounds predominated (reaction scheme 2). In Scheme 2, the synthases catalyzed the ionization of *cis*- and *trans*-farnesyl pyrophosphates **(27** and **26)** to their respective cationic intermediates **(48** and **49).** Isomerization of the ions **(48, 49)** formed *cis*- and *trans*- nerolidyl cations **(50, 28)**. Hydration of the ions **(50, 28)** formed *cis*-nerolidol **(51)** in oils of 1 pm and 4 pm harvests and *trans* nerolidol in oils from 7 am and 4 pm

harvests (**29**). Electrophilic attack of the ion **(48)** on C_{10}-C_{11} double bond via C_{10} formed (Z)-germacrenyl cation **(30)**. Delocalization of the pi electrons from C_6-C_7 to C_6-C_5 followed by electrophilic addition of the *(E)*-germacrenyl cation (**52**) on C_2-C_3 double bond via C_2 formed eudesmanyl cation **(31)**. Bond cleavage at C_4-C_5 followed by deprotonation at C_{15} gave β-elemene **(32)** in the oils**.** Hydride shift followed by electrophilic attack of the ion **(30)** on the C_6-C_7 double bond via C_6 formed cadinyl cation **(33)**. Deprotonation of the ion at C_3 produced ϒ-cadinene **(34)** in the oils. Electrophilic attack of the ion **(33)** on the C_2-C_3 double bond via C_2 followed by deprotonation at C_4 formed α-copaene **(35)** in oils from 7 am and 1 pm harvests. Electrophilic attack of *(E)*-farnesyl cation **(48)** on C_{10}-C_{11} double bond via C_{11} formed humulyl cation **(36).** Subsequent electrophyllic attack of the ion (**36**) on C_2-C_3 double bond via C_2 formed caryophyllyl cation **(37)**. Deprotonation of the ion **(37)** at C_4 and C_{15} form α-caryophyllene **(38)** and β-caryophyllene **(39)** respectively in the oils from 7 am and 10 am harvests. Epoxidation of the compound **(39)** at C_6-C_7 double bond produced caryophyllene oxide **(40)** in oil from 10 am harvest. C_{11}-C_{10} and C_{10}-C_1 hydride shifts followed by delocalization of C_2-C_3 pi electron to C_1-C_2 and subsequent deprotonation at C_{15} of the ion **(30)** formed germacrene D **(41)** in the oils with the exception of oil from 4 pm harvest. C_{11}-C_{10} and C_{10} -C_1 hydride shifts followed by electrophilic attack of the ion **(30)** on the C_6 and C_7 double bond via C_6 formed armophenyl cation **(42)**. Deprotonation of the ion **(42)** at C_8 formed α-amorphene **(43)** in the oils except oil from 7 am harvest. Electrophyllic attack of the *(E)*-farnesyl cation (**49**) on C_6-C_7 double bond formed bisabolyl cation **(46).** Electrophyllic attack of the ion **(46)** on the C_2-C_3 double bond via C_2 followed by deprotonation at C_4 produced α-bergamotene **(47)** in the oils from 1-7 pm harvests.

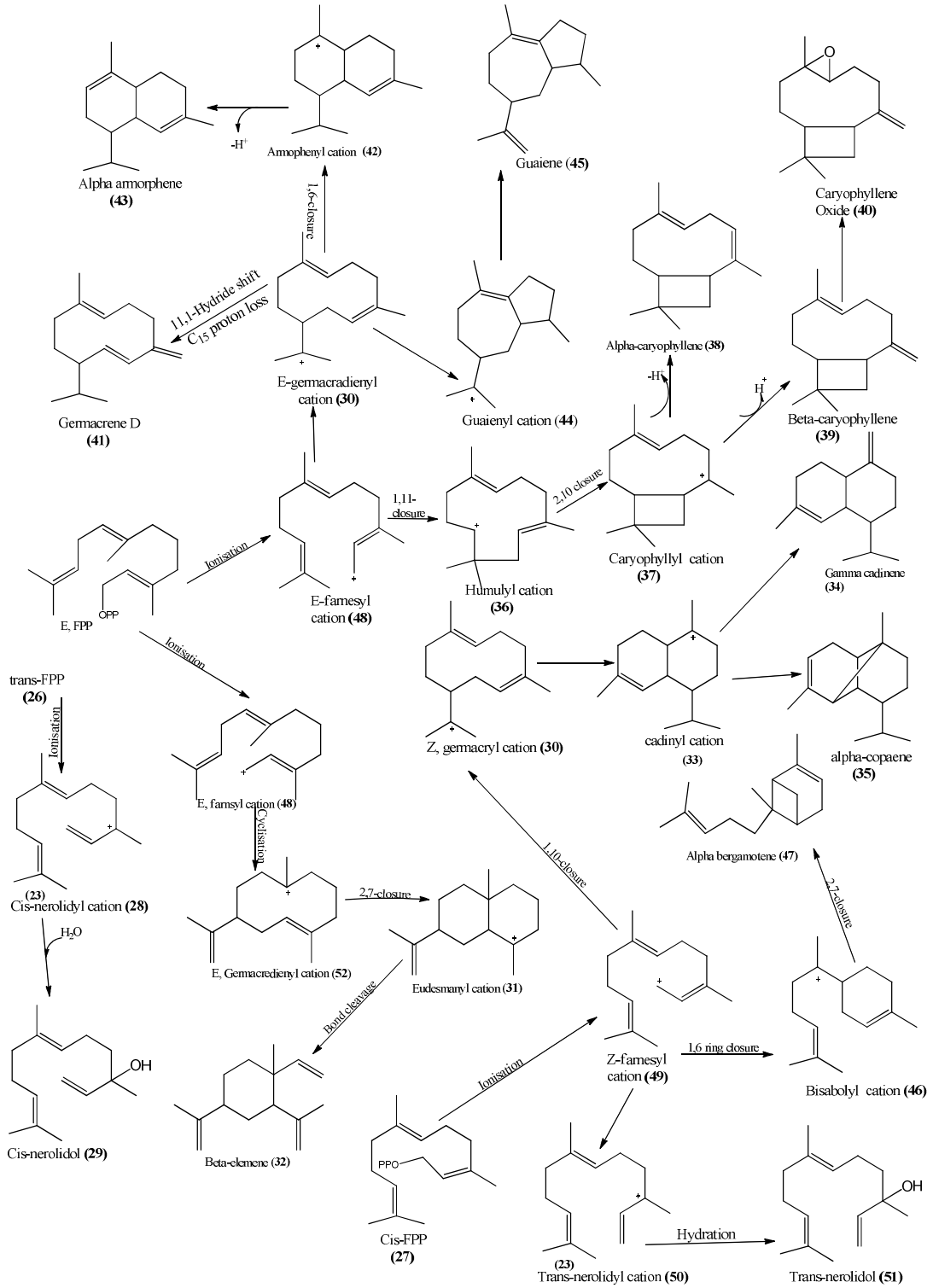

Reaction Scheme 2: Biosynthesis of Sesquiterpenoids mediated by β-caryophyllene, γ-cadinene, and α-*trans*-bergamotene synthases.

Table 2: Antibacterial Activity of Fruit Essential Oil of *Ocimum Canum* Harvested at Different Hour in a Day.

Oil samples	Organisms	Activity as Diameter Zone of Clearance Around Bacterial Colony (mm)				
		25%	50%	100%	Streptomycin	Tween 80
A	*S. aureus*	-	-	12.2	15.6	0
	E. coli	-	-	15.2	12.4	0
B	*S. aureus*	-	14.8	18.9	16.8	0
	E-coli	-	24.1	28.2	28.1	0
C	*S. aureus*	-	14.7	18.1	16.7	0
	E-coli	-	24.0	24.9	24.1	0
D	*S. aureus*	-	14.6	15.6	14.7	0
	E-coli	-	26.1	31.6	30.5	0
E	*S. aureus*	-	14.0	16.0	17.0	0
	E-coli	-	13.0	19.1	9.9	0

KEY: A= Essential oil from 7 am harvest. B= Essential oil from 10 am harvest. C= Essential oil from 1 pm harvest. D= Essential oil from 4 pm harvest. E= Essential oil from 7 pm harvest. *S. aureus- Staphylococcus aureus. E-coli- Escherichia coli.*

The oils inhibited the test organisms at 50 and 100% concentrations irrespective of the time of collection (Table 2). No activity was however obtained at 25% oil concentration. Activity of the oils compared favorably with that of streptomycin in most of the tests except for sample collected at 7 am where no inhibition occurred at 50% concentration. Also, Tween 80, which was the solvent used for dilution, had no inhibitory activity on the test organisms. Judging by the diameter zone of inhibition, *Escherichia coli,* which is a Gram negative bacteria, was more susceptible to the antibacterial effect of the oils compared to the Gram positive *Staphylococcus aureus*. This is an indication that the essential oils of *O. canum* may be more active on Gram negative rather than Gram positive organisms. Since activity discriminate based on cell wall type, the mechanism of inhibition by the oil can be likened to that of the β lactam antibiotics which inhibits cell wall synthesis. Bassole *et al.* (15) and Jeferson *et al.* (12) also reported higher antibacterial activity of oils of *O. canum* on *E. coli* compared to *S. aureus*.

CONCLUSION

Essential oil yields from flowers of various harvests differ significantly. This implied that environmental factors and physiological conditions of plants that determine essential oil yield varied at various times of harvest of the flowers, hence, causes differences in their yields. The most abundant monoterpenoid in the oils was linalool of which its synthase aided the formation of all monterpenoids in the oils. However, the composition patterns of monoterpenoids in the oils varied appreciably due to changes in the activity of linalool synthase as determined by environmental and physiological conditions of the plant at various times of harvests. Similarly, β-caryophyllene, γ-cadinene, and α-*trans*-bergamotene were the most abundant sesquiterpenoids in oils from various harvests. Hence, their synthases mediated the biosynthesis of all sesquiterpenoids in the oils where each of the compounds predominates. Variations in sesquiterpenoids profile in the oils are attributable to differences in activity of the synthases.

The oils were active against *Escherichia coli* and *Staphylococcus aureus*. Furthermore, it was noticed that the essential oils of *O. canum* showed higher inhibitory activity against the test organism than the positive control (streptomycin). Although, they were more active against *Escherichia coli* (gram negative) than *Staphylococcus aureus* (gram positive) bacteria, concentration and modelling of such oil with inhibitory activity into antibiotics can serve as an intervention to the ever growing problem of antibiotic resistivity.

REFERENCES

1. Iwu MM, 1993. Handbook of African medicinal plants. CRC Press, New York, pp: 164-166.
2. Ngassoum MB, Ousmaila H, Ngamo LT, Maponmetsem PM, Jirovetz L, Buchbauer G. Aroma compounds of essential oils of two varieties of the spice plant Ocimum canum Sims. From northern Cameroon. J. Food Comp. Anal., 2004; **17**: 197–204. DOI: 10.1016/j.jfca.2003.08.002.
3. Bauer K, Garbe D, Surburg H. Common Fragrance and Flavour Materials, 2 edn., VCH Verlagsgesellschaft mbH, Weinheim. 1990.
4. Fun CE, Baerheim-Svendsen A. Composition of the essential oils of Ocimum basilicum var. canum Sims and O. gratissimum L. Grown on Aruba. Flavour Frag. J. 1990; **5:** 173—177. DOI: 10.1002/ffj.2730050308.
5. Tamil Selvi M, Thirugnanasampandan R, Sundarammal S. Antioxidant and cytotoxic activities of essential oil of *Ocimum canum* Sims. from India. *Journal of Saudi Chemical Society*. 2015; **19**: 97–100. DOI: 10.1016/j.jscs.2011.12.026.

6. Bhattacharya A, Ashok A, Navnota S, Jagbeer C. Evaluation of some anti-oxidative constituents of three species of *Ocimum*. International Journal of Life Science. 2014; **8**(5): 14-17. DOI: 10.3126/ijls.v8i5.11858.

7. Pradyut B. Evaluation of antibacterial activities of leaf extracts of two medicinal plants *Ocimum canum* Sims and *Ocimum tenuiflorum* Linn., *J. Microbiol. Biotech. Res.*, 2013; **3** (3):20-23. URL: http://scholarsresearchlibrary.com/JMB-vol3-iss3/JMB-2013-3-3-20-23.pdf.

8. Behera S, Babu SM, Ramani YR, Choudhury PK, Panigrahi R. Phytochemical Investigation And Study On Antioxidant Properties Of *Ocimum Canum* Hydro-Alcoholic Leaf Extracts. *Journal of Drug Delivery & Therapeutics.* 2012: **2**(4), 122-128. URL: http://jddtonline.info/index.php/jddt/article/view/198/133.

9. Ntezurubanza L, Scheffer JJC, Looman A. Composition of the essential oil of *Ocimum canum* grown in Rwanda. *Pharmaceutisch Weekblad Scientific Edition.* 1985; *273,* Vol. 7.. DOI: 10.1007/BF01959201.

10. Ekundayo O, Laakso I, Hiltunen R. Constituents of the Volatile Oil from Leaves of *Ocimum canum* Sims. *Flavour and fragrance journal.* 1989; **4**.17-18. DOI: 10.1002/ffj.2730040104.

11. Martins AP, LIgia R, Salgueirol R, Felix T, Salvador C, Joseph C, Antonio PC, Tomás A. Composition of the Essential Oils of *Ocimum canum*, *0. gratissimum* and *0. Minimum*, *Planta Med.*, 1999; 65. DOI: 10.1055/s-2006-960465.

12. Jeferson C, Nascimento L, Barbosa CA, Vanderlucia FP, Jorge MD, Renato F, Luiz AMS, Robson SA. Chemical composition and antimicrobial activity of essential oils of *Ocimum canum* Sims. and *Ocimum selloi* Benth. *Annals of the Brazilian Academy of Sciences.* 2010; **83**(3): 787-799. DOI: 10.1590/S0001-37652011005000019.

13. Philippe B, Ntonga PA, Eric- Moïse BF, Gisèle AFD, Joseph LT. Chemical composition and residue activities of *Ocimum canum* Sims and *Ocimum basilicum L* essential oils on adult female Anopheles funestus ss, *Journal of Animal &Plant Sciences.* 2013; **19(**1): 2854-2863. URL: http://www.m.elewa.org/JAPS/2013/19.1/4.pdf.

14. Ntonga PA, Nicolas B, Elisabeth M, Lengo M, Philippe B, Philippe G. Activity of *Ocimum basilicum, Ocimum canum*, and *Cymbopogon citratus* essential oils against *Plasmodium falciparum* and mature-stage larvae of Anopheles funestus s.s. *EDP Sciences Parasite.* 2014; **21:** 33. DOI:10.1051/parasite/2014033.

15. Bassole IHN, Nebie R, Savadogo A, Ouattara CT, Barro N, Traore SA. Composition and antimicrobial activities of the leaf and flower essential oils of *Lippia chevalieri* and *Ocimum canum* from Burkina Faso. *African Journal of Biotechnology.* 2005; **4 (**10): 1156-1160. URL: http://www.ajol.info/index.php/ajb/article/view/71260/60215.

16. Usman LA, Watti OI, Ismaeel RO, Ojumoola AO. Effect of drying on yield, chemical composition and Insecticidal activity of leaf essential oil of sweet orange (Citrus sinensis). *Journal of the Turkish Chemical Society (JOTCS)*. 2016; **3**(1):1-18. DOI: 10.18596/jotcsa.09331.

17. Saliu BK, Agbabiaka TO, Sule IO, Gambari-Ambali RO. Assessment of Local Methods of Processing for the Preservation of the Physico-Chemical Properties and Microbiological Quality of two Local Cheeses in Ilorin, Nigeria. *Journal of Microbiology Biotechnology and Food Science.* 2014; *3 (4) 337-342. URL:* http://search.proquest.com/docview/1648082027?pq-origsite=gscholar.

18. British Pharmacopoeia, London, H.M. Stationary. 1980; **11**: 109. ISBN: 9780113206889.

19. Jennings W, Shibamoto T. Qualitative Analysis of Flavour volatiles by Glass Capillary Gas Chromatography. Academic Press, 1980; New York. ISBN: 0-12-384250-6.

20. Adams RP. Identification of Essential Oil components by Gas Chromatography and Mass Spectrometry. 4th ed. Allured Publ. Corp.Carol Stream. IL. USA. 2012; ISBN: 978-1-932633-21-4.

21. Joulain D, Koenig WA. The Atlas of Spectra data of sesquiterpene hydrocarbons. 1998; E.B. Verlog Hamburg, Germany. ISBN: 9783930826483.

22. Sartoratto A, Machado ALM, Delarmelina C, Figueira GM, Duarte MCT, Rehder VLG. Oils from Aromatic Plants used in Brazil. Brazilian J. Microbiology. 2004; **35**: 275-280. DOI: 10.1590/S1517-83822004000300001.

23. Degenhardt J, Kollner TG, Gershenzon J. Monoterpene and sesquiterpene synthases and the origin of terpene skeletal diversity in plants. Phytochem. 2009; 70: 1621–1637. DOI: 10.1016/j.phytochem.2009.07.030.

Türkçe Öz ve Anahtar Kelimeler

Nijerya'da Yetiştirilen *Ocimum canum* (Sims) Çiçek Esansiyel Yağının Kimyasal Bileşimi ve Antibakteriyel Aktivitesi Üzerine Toplama Zamanının Etkisi

Usman Lamidi Ajao, Yusuf Abdulrauf Olaniyi, Saliu Bola Kudirat, Olanipekun Bolatito Eunice, Elelu Nusirat.

Öz: Bir günün farklı zamanlarında (7 öö, 10 öö, 1 ös, 4 ös, 7 ös) hasat edilen *Ocimum canum* çiçekleri (1000 g) ayrı ayrı hidrodistilasyona tabi tutulmuş ve %0,19-0,27 (w/w) esansiyel yağ vermiştir. GC ve GC-MS analizleri, yağların oksijenli monoterpenoidler (%51,2-74,4) içerdiğini göstermiştir. Hidrokarbon monoterpenoidleri yağların %6,2-10,2'sini oluşturmuştur. Hidrokarbon ve oksijenli seskiterpenoidlerin yağlardaki yüzde bileşimi %1,3-22,0 arasında değişmektedir. Yağlarda en baskın bileşen linalooldür (%40,5-58,7). Diğer birincil bileşenler şöyle sıralanabilir: Limonen (%0,6-7,5), terpinen-4-ol (%1,4-5,6), eugenol (%4,4-8,9), geranil asetat (%0,2-4,9), α-trans-bergamoten (%3,2-9,4) ve *(E)*-izoeugenol (%4,1-5,5). Linaloolün yağlarda baskın olması, yağların linalool kemotipinde olduğunu göstermiştir. Yağların antibakteriyel aktivitesi *Staphylococcus aureus ve Escherichia coli* bakterilerine karşı agar diffüzyon yöntemi ile değerlendirilmiştir. Çiçeğin toplandığı zamandan bağımsız olarak, yağların test edilen organizmalara karşı aktif olduğu bulunmuştur. Ancak, bunlar *Staphylococcus aureus*'a nazaran *Escherichia coli*'ye karşı daha aktiftir. Yağların organizmalar üzerindeki aktivitesi derişime bağlıdır.

Anahtar kelimeler: *Ocimum canum*; kemotip; linalool; terpen sentaz; antibakteriyel aktivite.

Sunulma: 29 Eylül 2016. **Düzeltme:** 25 Ekim 2016. **Kabul:** 07 Kasım, 2016.

JOTCS A Journal of the Turkish Chemical Society Chemistry Section A
TURKISH CHEMICAL SOCIETY

Optimization of Extraction Parameters for Fat-Soluble Vitamins and Major Element Analysis in *Polygonum cognatum Meissn* Plant (Madımak)

Halil İbrahim Ulusoy[1,*], Hilal Acıdereli[2], Uğur Tutar[3]

[1]*Cumhuriyet University, Faculty of Pharmacy, Department of Analytical Chemistry, 58140, SIVAS, TURKEY*
[2]*Cumhuriyet University, Faculty of Pharmacy, Department of Biochemistry, 58140, SIVAS, TURKEY*
[3]*Cumhuriyet University, Faculty of Health Sciences, Department of Nutrition and Diet, 58140, SIVAS, TURKEY*

Abstract: The concentrations of fat-soluble vitamins (A and E) and various metal ions (Ca, Cd, Cr, Co, Cu, Fe, Mg, Mn, Pb, Zn) have been determined in *Polygonum cognatum Meissn* plant samples collected in Sivas, Turkey. Analysis of vitamins were carried out by HPLC after Soxhlet extraction and metal ions were determined by FAAS after microwave digestion, respectively. The study is focused on two main purposes: optimization of sample preparing parameters prior to determination and chemical analysis of a common edible plant in Anatolia. There was not enough information about this plant in point of vitamins and various metal species. Consequently, useful and detailed data were introduced to literature for a well-known and so consumed edible plant.

Keywords: *Polygonum cognatum meissn* (Madımak); vitamin A; vitamin E; metal analysis; HPLC; FAAS.

Cite this: Ulusoy H, Acıdereli H, Tutar U. Optimization of Extraction Parameters for Fat-Soluble Vitamins and Major Element Analysis in Polygonum cognatum Meissn Plant (Madımak). JOTCSA. 2017;4(1):165–78.

DOI: To be assigned.

*Corresponding Author. E-mail: hiulusoy@yahoo.com. Tel. : +90 346 219 1010 -3905 . Fax : +90 346 219 11 86.

INTRODUCTION

The analysis of micronutrients in food samples is of great interest both regarding nutrition and commercial aspects. This kind of analysis is so important in order to know the contents of foods and environmental samples in view of their toxicity and essential properties (1, 2). Trace elements play an important role in the formation of the active chemical constituents present in medicinal plants. However, most of the research work on medicinal plants pertain to constituents such as essential oils, vitamins, glycosides, and other organic compounds, while little attention has been paid to the elemental composition of the plants (3, 4).

Vitamins A and E are essential food ingredients that are usually supplied with the diet (5). Normally, the human organism cannot synthesize vitamins, and for this reason, they must be included in the human diet. The determination of fat-soluble vitamins A and E plays an important role in nutritional and biochemical studies, and analytical methods available and capable of determining these vitamins in different samples are imperative (6). The possible protective effect of vitamin E against environmental and drug toxicity has also attracted the attention of many investigators (7). The dietary reference intake of vitamin E for an adult person is 15 $mg.day^{-1}$ (8). Measurements of these vitamins in real samples like drugs, biological liquids, and foods are an important research area in order to check their intakes.

Due to their similar chemical properties, vitamins A and E are generally determined using an identical sample workup procedure. Typically, this includes a saponification step, extraction of the vitamins into an organic solvent, and separation by normal or reversed-phase HPLC coupled to UV or fluorescence detection (9, 10). Many analytical methods including colorimetry, thin-layer chromatography, gas chromatography, and high-performance liquid chromatography (HPLC) have been used for the analysis of fat soluble vitamins. HPLC is preferred for vitamin E quantification due to simplicity, giving more precision, and more specific than other methods (11). The most critical and time consuming step in the vitamin analysis is the extraction of the vitamin from real samples. So, newly developed methods are proposed together a useful sample preparation step.

The essential metal species play an important role in many biological systems due to their functions in metabolic activities. So, there are a lot of studies based on trace metals in food samples (12-14). The following of trace metals in food samples helps to understanding of their possible toxic effects. In addition, some of these metals are necessary for vital functions and they are taken by diet via food additives. Heavy metals may enter the food chain as a result of their intake by edible plants. So, determination of heavy metals in plant samples is a very important analytical problem. Some of these metals have significantly toxic and have hazardous effects on human health (15).

In food samples, a pre-treatment and separation procedure is often necessary to isolate the components of interest from sample matrices, to purify and concentrate the analyte (16). In order to release vitamins, various extraction methods such as soxhlet extraction (17), cloud point extraction (18), ultrasound assisted extraction (19), and accelerated solvent extraction (20) have been applied depending on the nature of the sample. The success of applied pre-treatment procedure affects directly the reliability of analysis results.

Polygonum Cognatum Meissn (Figure 1) is a wild edible plant called "madımak" in Turkish. This edible plant is perennial of slender woody stock. It grows on roadsides, slopes, and cliffs at altitudes of 720–3000 m (21-23). The young shoots with leaves are collected in the spring. In Turkish folk medicine, it has been used for various purposes, such as its diuretic effect and for the treatment of diabetes mellitus (24). According to Ozbucak *et al.* (25), the amount of protein in Madımak is higher that similar plants which are consumed as foods. Some wild plant species used as vegetables in the black sea region of Turkey were investigated by Civelek and Balkaya. The results of this study was shown that mineral and nutrient contents of *Polygonum cognatum Meissn* was comparable levels respect to other vegetables (26).

Figure 1. An image taken in a local bazaar in Sivas.

This study aims to examine the chemical contents of *Polygonum cognatum Meissn* (Madımak) in terms of fat-soluble vitamins and various metals. As far as we know, this is the first study reporting the detail chemical analysis of this plant although it is overly consumed in the Anatolia. The soxhlet extraction method was optimized and used for sample preparation in vitamin analysis and the contents of vitamins A and E were determined by HPLC-DAD system. Microwave digestion system was also optimized to digest samples before metal analysis and the concentrations of metals were determined by flame atomic absorption spectrometer (FAAS).

EXPERIMENTAL

Instrumentation

The chromatographic system used is equipped with a pump model LC20-AD (Shimadzu), a thermostatic oven, CTO-10 AS (Shimadzu), auto sampler, SIL-20Ac (Shimadzu) and detectors: a DAD detector model SPD-M20A (Shimadzu). An LC solution software (Shimadzu) was used to transfer the data to the computer. An Inertsil C18 (250 mm×4,6×5 µm) column was used for chromatographic separation.

An atomic absorption spectrometer (Shimadzu AAS-6300), equipped with D_2-background correction, a hollow cathode lamp and an air-acetylene flame atomizer, was used for all determinations. All metal determinations were carried out according to manufacturer proposals.

SE (Soxhlet extraction apparatus, VWR Scientific Products, catalog no. 27611-049) was performed as described in EPA Method 3540. A microwave digestion system (CEM Mars X6, USA) was used to dissolve and prepare the samples to analysis. The pH measurements were carried out with a pH meter (Selecta 2001 pH-meter).

Chemicals

All chemicals were of chromatographic and analytical reagent grade. α-tocopherol (Vitamin E) and Retinol (Vitamin A) were purchased from Sigma (St. Louis, Steinheim, Germany), and n-hexane and isopropyl alcohol were from Merck (Darmstadt, Germany). Stock metal solutions were prepared by using their nitrate salts bought from Merck. Ultra-pure water with a resistivity of 18.2 MΩ cm was used in all experiments provided by ELGA (Flex III, UK) water purification system. The stock standard solutions of vitamins were prepared in ethanol, and the standards used were prepared by dilution of the appropriate volume of the stock in colored bottles and stored at –20 ^{0}C. Stock standard solutions of metal salts were prepared in 0.01 M HNO_3.

Sample Preparation

Madımak samples were collected from the flora of Sivas district on May, 2014. The experiments were carried out with two samples obtained from two different sub-districts and symbolized as M1 and M2. Edible parts of plant were cut and dried in laboratory conditions. Dried samples were ground by using a blender and kept in a refrigerator until analysis.

Sample preparation is one of the most critical steps of chemical analysis, which determines the quality and the credibility of the analytical results obtained, and it is estimated that it accounts for about 60 % of all errors during the whole analytical process (27). Manipulation is time consuming, expensive, and is the main source of errors and, therefore, it should be kept at a minimum if possible. Nevertheless, the relative amount of target species in the sample be analyzed can be very low, and it sometimes requires pre-concentration or separation procedures. Samples were prepared by using two different way for vitamin and metal analysis. Soxhlet

extraction was preferred in order to extract vitamins A and E from Madımak plant. Microwave digestion method was applied to samples before metal analysis.

Soxhlet Extraction

Conventional Soxhlet extraction method was applied to samples prior to the HPLC analysis. A 20 g sample portion of the dried plant was refluxed with 400 mL of organic solvent for 8 h at the boiling temperature of ethanol by using Soxhlet apparatus. Five parallel extraction were carried for repetition analysis. The extracts were filtered and concentrated by using a rotary evaporator until dryness. Approximately, 1 g of concentrated sample was obtained from each extraction system.

In the second step, the obtained extracts were re-dissolved by using various solvents such as acetonitrile, ethanol, methanol, n-hexane, and acetone. 100 mg of extract was weighed and 2.5 mL of solvent was added onto the extracts. Then, the samples were mixed vigorously by a vortex for 10 minutes. Finally, the samples were filtered by using 0.45 µm membrane and transferred to HPLC vials.

Microwave Digestion

The samples were digested by using a microwave digestion system prior to metal analysis. The microwave parameters were given in Table 1. After digestion, the samples were filtered through 0.45 µm filter paper and neutralized by a few drops of ammonia until its acidity was eliminated. Then, they were diluted to a 10 mL final volume with 0.1 M HNO_3 and the metal contents of samples were determined by using FAAS.

Table 1. Microwave parameters for digestion procedure

Amount of sample	0.50 g of plant sample	
Digestion reagent	+ 10 mL of HNO_3	
Steps	0-5 min.	100 ºC
	5-10 min.	150 ºC
	10-20 min.	180 ºC

Analysis of samples

Analysis of vitamin A and E by HPLC-DAD: For determination of vitamins A and E, a reverse-phase column (Inertsil C18 (250 mm×4.6×5 µm)) was used throughout the experiments. The mobile phase consisted of methanol/acetonitrile (95:5) with a flow rate of 1.2 mL/min at isocratic mode. Injection volume was 20 µL for each analysis. A DAD detector was used for quantification of vitamins A and E at 324 nm and 292 nm, respectively. Retention times were 4.49 min for vitamin A and 11.20 min for vitamin E. The results were calculated with the help of the peak areas of standard solutions. Lab solution software provided by Shimadzu was used for evaluation of chromatograms.

Analysis of metals by FAAS: An atomic absorption spectrometer was used to determine metals in digested samples by microwave digestion system. All samples were filtered before analysis by a 0.45 μm filter. All determinations were performed in air/acetylene flame at conditions proposed by the manufacturer.

RESULTS AND DISCUSSIONS

Optimization of Soxhlet Extraction Parameters

Soxhlet extraction technique was employed for the extraction and separation of chemical constituents in Madımak. 20.00 g of plant sample was refluxed in 400 mL of solvent for 8 hours. Three different solvents (ethanol, methanol, and n-hexane) were used in order to choose the best extraction conditions. Five parallel extraction systems were used for repetitive analyses. The extracts were filtered and concentrated by using a rotary evaporator until dryness. After extraction, solvents were evaporated and raw extracts were obtained about 1 g for each samples. The concentrated extracts were re-solved (diluted) prior to HPLC analysis. The solvent selection in this step is also very critical for sensitive and reliable determinations. We tried five different solvents in this step namely ethanol, methanol, acetonitrile, n-hexane, and acetone. Analysis results were illustrated in Figure 2. Standard addition method was applied to samples in order to evaluate the recovery of extraction procedures. 20.00 μg mL^{-1} of vitamin was spiked into the samples and recovery values were calculated by considering the measured and added concentrations.

As seen in Figure 2, the best signals were obtained by ethanol. According to experimental results, ethanol is a good solvent both for main extraction and re-dissolution of the extract. So, subsequent extractions were carried out by using ethanol.

A series of experiments were also made to choose ideal extraction time. The extraction of 20.00 g of the sample was carried out by using ethanol throughout 3, 6, 8, and 12 hours. According to the experimental results, there is not an important change in the amount of extractable vitamins after 8 hours. So, the samples were refluxed for 8 h in the next studies.

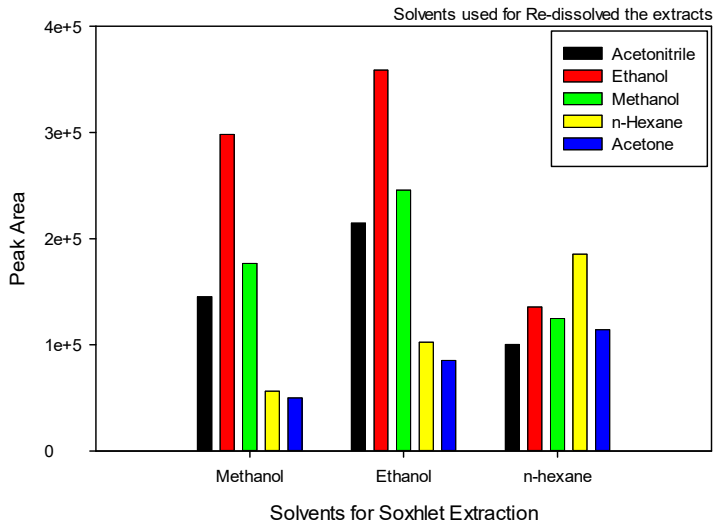

Figure 2. The effects of various solvents on extraction

Amounts of Vitamin A and E in the Plant Samples

After the conditions were optimized, samples were prepared and their vitamins A and E contents were determined by HPLC-DAD system. Chromatograms obtained from the standard and the sample were shown in Figure 3. As can be seen from the figure, the peak of vitamin A was not observed in the samples. Analysis results were presented in Table 2.

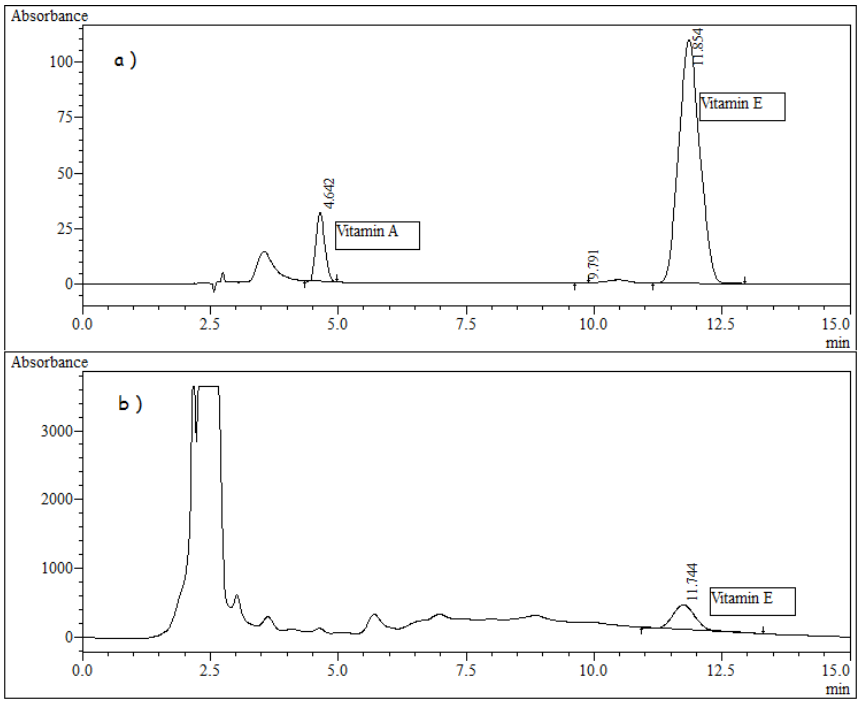

Figure 3. Chromatograms for standard solution (a) and sample (b)

Table 2. The contents of vitamins A and E in Madımak (N:5)

Vitamins		**M1**			**M2**		
	Added	**Found mg kg^{-1}**	**% RSD**	**% R**	**Found mg kg^{-1}**	**% RSD**	**% R**
	0	Not detected	-	-	Not detected	-	-
A	20.00	21.26±1.42	6.67	106.30	20.65±1.39	6.73	103.25
	40.00	40.92±2.02	4.94	102.30	39.88±2.22	5.57	99.70
	0	63.01±4.55	7.22	-	59.18±5.14	8.69	-
E	20.00	84.20±5.88	6.98	101.43	78.66±5.55	7.06	99.30
	40.00	101.99±6.24	6.12	99.00	97.87±6.12	6.25	98.67

Optimization of Metal Analysis Procedure

The preparation of samples were carried out by microwave digestion system explained in the previous section. For this purpose, the explained procedure in Table 1 was applied to the samples. The concentrations of metal ions were determined by using a flame atomic absorption spectrometer.

Firstly, the concentration of nitric acid used in digestion procedure was optimized to avoid the high acidic medium. According to manufacturer's proposals, digestion procedure was applied by using 0.50 g of sample and 8.0 mL HNO_3 as solvent at different concentrations. The extraction of spiked model solutions were repeated with various concentration of HNO_3 in the range of 5-16 mol L^{-1}. As seen in Figure 4, there is not an important change on amounts of extractable metals after 10 mol L^{-1} concentration. In addition, it needs as little as possible acidic conditions in the digestion in order to avoid high ionic strength. If the solution is more acidic, it will be more difficult to neutralize the solution prior to determination. So, 10 mol L^{-1} of HNO_3 was selected in the digestion procedure. As seen in Figure 4, 10 mol L^{-1} HNO_3 is enough for a quantitative digestion. So, determination of metal species were carried out by using these optimal parameters.

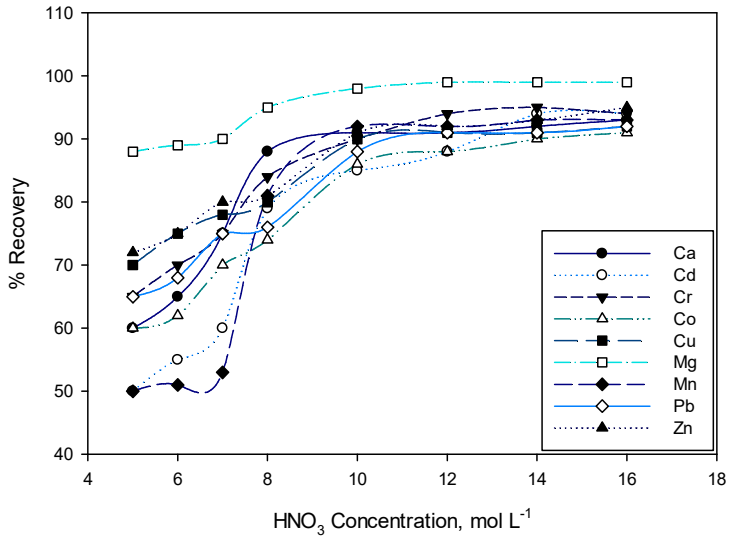

Figure 4. Optimization of HNO_3 concentration

Amounts of Various Metals in the Plants Samples

The plant samples were prepared by using the optimized digestion method as explained in previous section and their analysis were performed by flame atomic absorption spectrometer (FAAS). The obtained results were presented in Table 3.

CONCLUSIONS

In this study, the detailed chemical analysis of *Polygonum cognatum Meissn* (Madımak) has been performed for the first time. There are a few studies in literature dealing with some properties of Madımak such as anti-microbial activity, antioxidant activity (20) but they are inadequate to display its nutrient properties. According to vitamin analysis results, the plant includes vitamin E at important amounts while does not include vitamin A. Both direct analysis and spiked analyses were shown that the amount of vitamin A was under the limit of detection for our detection method. When analysis results and recommended values were considered together, it can be said that Madımak contributes to intake essential elements and vitamin E by daily diet.

Table 3. Results of metal analysis in Madımak Plant (N:5)

Elements		**M1**			**M2**		
	Added	**Found mg kg^{-1}**	**% RSD**	**% R**	**Found mg kg^{-1}**	**% RSD**	**% R**
Ca	0	65.190±2.553	3.9	-	44.500±4.473	8.4	-
	20.000	81.255±3.895	4.8	95.39	63.545±4.985	7.8	98.5
	40.000	96.847±5.587	5.8	92.07	88.384±5.354	6.1	104.6
Cd	0	0.045±0.003	6.7	-	0.105±0.006	6.1	-
	0.020	0.063±0.004	6.4	96.92	0.128±0.010	7.8	102.4
	0.040	0.090±0.005	5.6	105.88	0.144±0.014	9.7	99.3
Cr	0	0.080±0.002	1.9	-	0.079±0.007	8.8	-
	0.020	0.096±0.004	4.1	96.0	0.103±0.008	7.8	104.0
	0.040	0.115±0.009	7.8	95.8	0.125±0.010	8.0	105.0
Co	0	0.091±0.008	8.8	-	0.124±0.011	8.4	-
	0.020	0.115±0.010	8.7	103.6	0.140±0.012	8.6	97.2
	0.040	0.136±0.012	8.8	103.8	0.161±0.013	8.1	98.2
Cu	0	0.399±0.031	7.8	-	0.351±0.012	3.4	-
	0.100	0.487±0.041	8.4	97.5	0.463±0.021	4.5	102.7
	0.200	0.586±0.043	7.3	97.8	0.569±0.025	4.4	103.3
Fe	0	6.774±0.445	6.6	-	7.646±0.237	3.1	-
	2.000	8.650±0.551	6.4	98.6	9.815±0.443	4.5	101.8
	4.000	10.698±0.612	5.7	99.3	11.843±0.563	4.8	101.7
Mg	0	66.522±2.550	3.8	-	66.983±1.483	2.2	-
	20.000	88.147±3.654	4.1	101.8	87.548±3.654	4.2	100.6
	40.000	109.224±5.552	5.1	102.6	110.278±4.654	4.2	103.1
Mn	0	4.535±0.123	2.7	-	4.289±0.095	2.2	-
	2.000	6.866±0.254	3.7	105.1	6.120±0.107	1.7	97.3
	4.000	8.442±0.360	4.3	98.9	6.250±0.101	1.6	99.4
Pb	0	0.046±0.004	7.8	-	0.047±0.004	8.5	-
	0.020	0.065±0.006	9.2	98.4	0.070±0.006	8.6	104.5
	0.040	0.083±0.007	8.4	96.7	0.085±0.007	8.2	97.7
Zn	0	10.364±0.433	4.2	-	9.139±0.230	2.5	-
	2.000	12.875±0.687	5.3	104.1	11.312±0.645	5.7	101.6
	4.000	14.215±0.702	4.9	98.9	13.444±0.727	5.4	102.3

Results of metal analysis can be evaluated according to their toxicity and essential functions. The amounts of Cd, Cr, Co, and Pb in the analyzed samples were lower than legal limits according to FDA. As seen in Table 3, the amounts of these metals are under 0.15 mg kg^{-1}. So, it can be said that the studied plant samples does not include common toxic metal components according

to our determination conditions. Cu concentration in the samples were determined as 0.351 and 0.399 mg kg^{-1} in samples. We think that herbicides or insecticides may cause this results. Because, this kind of chemicals are used on April-May period in the sampling region to destroy unwanted plants. As known, most of these chemicals may include copper. So, the amount of copper is higher than expected. One of important results of study is the content of Mn, Fe and Zn in Madımak. As known, Zn, Fe and Mn are essential elements for a healthy diet.

COMPLIANCE WITH ETHICAL STANDARDS

The authors declare that there is not unethical situation.

CONFLICT OF INTEREST

The authors declare that they have no conflict of interest.

REFERENCES

1. Delgado-Zamarreño MM, Bustamante-Rangel M, Sanchez-Perez A, Hernandez-Mendez J. Analysis of vitamin E isomers in seeds and nuts with and without coupled hydrolysis by liquid chromatography and colorimetric detection. Journal of Chromatography A. 2001;935:77–86. DOI: 10.1016/S0021-9673(01)00991-8.

2. Ulusoy HI. Simple and useful method for determination of inorganic selenium species in real samples based on UV-VIS spectroscopy in a micellar medium. Analytical Methods. 2015;7:953-960. DOI: 10.1039/C4AY02691H.

3. Ebrahim AM, Etayeb MA, Khalid H, Manale N, Roumie M, Michalke B. PIXE as a complement to ICP-OES trace metal analysis in Sudanese medicinal plants. Applied Radiation and Isotopes. 2014; 90:218–224. DOI: 10.1016/j.apradiso.2014.04.013.

4. Kumar A, Nair AG, Reddy AV, Garg AN. Analysis of essential elements in Pragya-peya a herbal drink and its constituents by neutron activation. J Pharm Biomed Anal 2005;37(4):631–638. DOI: 10.1016/j.jpba.2004.11.051.

5. Höller U, Wolter D, Hofmann P, Spitzer H. Microwave-Assisted Rapid Determination of Vitamins A and E in Beverages. J Agric Food Chem. 2003; 51(6):1539–1542. DOI: 10.1021/jf0260038.

6. Ortega AC, Silva DC, Visentainer JV, Souza NE, Almeida VC, Oliveira CC. Determination of vitamins A and E exploting cloud point extraction and micellar liquid chromatograpy. Analytical Letters. 2011; 44:778–786. DOI: 10.1080/00032711003783184.

7. Monsen ER. Dietary Reference Intakes for The Antioxidant Nutrients: Vitamin C, Vitamin E, Selenium, and Carotenoids. Journal of the American Dietetic Association. 2000; 100(6):637–640. DOI: 10.1016/S0002-8223(00)00189-9.

8. Aslanturk A, Uzunhisarcikli M, Kalender S, Demir F. Sodium selenite and vitamin E in preventing mercuric chloride induced renal toxicity in rats. Food and Chemical Toxicology. 2014;70:185–190. DOI: 10.1016/j.fct.2014.05.010.

9. Bilic N, Sieber R. Use of a column for extraction, drying, and purification of retinol and R-tocopherol prior to their determination in milk and dairy products by HPLC. Fresenius' Anal Chem. 1988; 330:143-145. DOI: 10.1016/j.fct.2014.05.010.

10. Ruperez FJ, Martin D, Herrera E, Barbas C. Chromatographic analysis of a-tocopherol and related compounds in various matrices. Journal of Chromatography A. 2001; 935: 45–69. DOI: 10.1016/S0021-9673(01)01101-3.

11. Lee J, Ye L, Landen WO, Eitenmiller RR. Optimization of an Extraction Procedure for the Quantification of Vitamin E in Tomato and Broccoli using Response Surface Methodology. Journal of food composition and analysis. 2000; 13:45-57. DOI:10.1006/jfca.1999.0845

12. Ulusoy HI, Aksoy U, Akçay M. Simultaneous pre-concentration of Pb and Sn in food samples and determination by atomic absorption spectrometry. Eur Food Res Technol. 2013; 236:725–733. DOI 10.1007/s00217-013-1929-6.

13. Nollet LML. Handbook of Water Analysis (Food Science and Technology). 2000, New York: Marcel Dekker ISBN: 9780849370335.

14. Ulusoy HI, Yilmaz O, Gurkan R. A micellar improved method for trace levels selenium quantification in food samples, alcoholic and nonalcoholic beverages through CPE/FAAS. Food Chemistry. 2013; 139:1008–1014. DOI: 10.1016/j.foodchem.2013.01.087.

15. Bakirdere S, Yaman M. Determination of lead, cadmium and copper in roadside soil and plants in Elazig, Turkey. Environ Monit Assess. 2008; 136:401–410. DOI 10.1007/s10661-007-9695-1.

16. Reto M, Figueira ME, Filipe HM, Almeida CMM. Analysis of vitamin K in green tea leafs and infusions by SPME–GC-FID. Food Chemistry. 2007; 100:405–411. DOI: 10.1016/j.foodchem.2005.09.016.

17. Durante M, Lenucci MS, Rescio L, Mita G, Caretto S. Durum wheat by-products as natural sources of valuable nutrients. Phytochem Rev. 2012; 11:255–262. DOI: 10.1007/s11101-012-9232-x.

18. Heydari R, Elyasi NS. Ion-pair cloud-point extraction: A new method for the determination of water-soluble vitamins in plasma and urine. Journal of Separation Science. 2014;37:2724–2731. DOI:10.1002/jssc.201400642.

19. Le HV, Le VM. Comparison of enzyme-assisted and ultrasound-assisted extraction of vitamin C and phenolic compounds from acerola (Malpighia emarginata DC.) fruit. International Journal of Food Science and Technology. 2012; 47:1206–1214. DOI: 10.1111/j.1365-2621.2012.02960.x.

20. Saha S, Walia S, Kundu A, Sharma K, Paul RK. Optimal extraction and fingerprinting of carotenoids by accelerated solvent extraction and liquid chromatography with tandem mass. Food Chemistry. 2015;177:369–375. DOI: 10.1016/j.foodchem.2015.01.039

21. Yıldırım A, Mavi A, Kara AA. Antioxidant and antimicrobial activities of *Polygonum cognatum Meissn* extracts. J Sci Food Agric. 2003; 83:64–69. DOI: 10.1002/jsfa.1288.

22. Davis PH. Flora of Turkey and the East Aegean Islands, Vol. 7; University Press: Edinburgh, 1982. pp 349-382 ISBN-13: 978-0852241592.

23. Tatli A. Important Range Plants of Erzurum Province. Food and Agriculture Organisation of the United Nations, Rome, 1988. pp 43-52.

24. Baytop T. Türkiye'de Bitkilerle Tedavi. Nobel Tip Kitab Evleri, İstanbul, 1999. p480. ISBN 9754200211.

25. Ozbucak TB, Akcin ÖE, Yalçin S. Nutrition Contents of the Some Wild Edible Plants in Central Black Sea Region of Turkey. International Journal of Natural and Engineering Sciences. 2007; 1:11-13.

26. Civelek C, Balkaya A. The Nutrient Content of Some Wild Plant Species Used as Vegetables in Bafra Plain Located in the Black Sea Region of Turkey. The European Journal of Plant Science and Biotechnology. 2013; 7(1):62-65.

27. Madej K. Microwave-assisted and cloud-point extraction in determination of drugs and other bioactive compounds. Trends in Analytical Chemistry. 2009; 28(4):437-446. DOI: 10.1016/j.trac.2009.02.002.

Türkçe Öz ve Anahtar Kelimeler

Polygonum Cognatum Meissn Bitkisinin (Madımak) Temel Element Analizi ve Yağda Çözünen Vitaminleri için Ekstraksiyon Parametrelerinin Uygunlaştırılması

Halil İbrahim Ulusoy, Hilal Acıdereli, Uğur Tutar

Öz: Yağda çözünen vitaminlerin (A ve E) ve çeşitli metal iyonlarının (Ca, Cd, Cr, Co, Cu, Fe, Mg, Mn, Pb, Zn) derişimi Sivas, Türkiye'de toplanan *Polygonum cognatum Meissn* bitki örneklerinde tespit edilmiştir. Vitamin analizleri Soxhlet ekstraksiyonunun ardından HPLC ile, metal iyonlarının varlığı ise mikrodalga çözünürleştirmesinin ardından FAAS ile tayin edilmiştir. Çalışma iki ana hedefe odaklanmıştır: Anadolu'da yetişen yaygın bir yenebilir bitki türünün kimyasal analizi ve tayinden önce örnek hazırlama parametrelerinin en uygun hale getirilmesi. Vitamin ve çeşitli metal türleri açısından bu bitki hakkında yeterli bilgi bulunmamaktadır. Sonuç olarak, iyi bilinen ve bolca tüketilen bir bitki için literature faydalı ve ayrıntılı bilgiler sunulmuştur.

Anahtar kelimeler: *Polygonum cognatum meissn* (Madımak); vitamin A; vitamin E; metal analizi; HPLC; FAAS.

On the Systematics of Mass Spectrometry: A New Graph-Theoretical Method

Berkay Sütay*[1]

[1]Istanbul Technical University, Department of Chemistry, Istanbul, 34469, Turkey.

Abstract: The systematic background of mass spectrometry (MS) was established by using the Valency Interaction Formula theory in an efficient manner. A new graph theoretical method was developed as a pure quantum mechanical survey and applied on a variety of molecules and assemblies to elucidate the quantum mechanical systematics behind mass spectrometry. The topological indexes and graph theoretical methods in chemistry and physics as the striking features of this new method were applied onto the mass spectra of several molecules and assemblies due to the insufficiencies of the obsolete fragmentation procedures. These fundamental topological indexes were determined to make quick deductions pictorially on the mass spectra of molecules. The major fragmentation pathways for several molecules, as the striking features of Mass Spectometry, were examined in a pure theoretical way and *a priori* decomposition products were predicted. The systematic theory was provided in the light of our examination and a great deal of qualitative information was obtained just by knowing which interactions are soft among the others. The results are of general validity in comparison with the experimental data.

Keywords: Mass spectrometry; valency interaction formula; electron impact ionization; topology; graph theory.

Gönderme: 19 Ağustos 2016**. İkinci tur:** 20 Ekim 2016**. Kabul: .**09 Kasım 2016

Cite this: Sütay B. On the Systematics of Mass Spectrometry: A New Graph-Theoretical Method. JOTCSA. 2017;4(1):179–96.

DOI: To be assigned.

*Corresponding author. E-mail: sutay@itu.edu.tr.

INTRODUCTION

Chemistry is a science that explains everything in the sense of molecular structures. This is the reason for a need in working with structural formulas by a pictorial language. Such a pictorial method allows the determination of the stabilities, reactivities, molecular properties and the strength of the bonding interactions, *etc.*; in an efficient manner. For this purpose, the Valency Interaction Formula (VIF) Theory is well enough to make such chemical deductions (1, 2) by supplying us with the very fundamental LPI (Level Pattern Indices) topological indexes as the direct number of bonding, nonbonding, and antibonding molecular orbitals (MO). The advantage of the VIF theory is that it enables a practical usage theoretically without requiring large scale computer calculations. It is possible to compare the bonding interactions as to their strengths and to find the soft interaction in the molecular structure which is required to explain the mass spectra in terms of the fragments.

Quantum Mechanics machinery was built on an abstract linear algebraic space –and also the linear operators– in terms of the superposition principle as a fundamental aspect (3). The eigenvectors of any Hermitian operator form a complete basis set which is also orthonormal. Then, a unitary transformation from such a complete basis set (4) to another becomes possible in the Hilbert space. Although these orthonormal basis sets have been used more often in quantum chemical computations, there is not a strict requirement for basis sets to be orthonormal. Even in many cases, the vectors of a basis set are not the eigenvectors of a physical observable. On the other hand, the orthonormal basis sets facilitate both algebraic and algorithmic convenience which may easily manifest itself by the well-known unity operator (I). In such a complete orthonormal basis of $\{|e_i>\}$ ket vectors, this operator may be written as

$$I = \sum_{i \geq 1}^{\infty} |e_i\rangle\langle e_i| \qquad \text{(Eq. 1)}$$

where $\delta_{ij} = \langle e_i | e_j \rangle$. Then, the representation of an arbitrary operator (A) in this basis becomes A=IAI. For our particular interest into the molecular structure, one lets this operator be Hamiltonian (H) and find Eq. 2.

$$H = IHI = \sum_{i,j} |e_i\rangle\langle e_i|H|e_j\rangle\langle e_j| = \sum_{i,j} H_{ij}|e_i\rangle\langle e_j| \qquad \text{(Eq. 2)}$$

However, the non-orthonormal basis sets are also used. These basis sets are the ones allowed by the superposition principle in a countably infinite dimensional linear vector space. Such a linear vector space is the Hilbert space (L2) which the quantum mechanics was built on rigorously by P.A.M. Dirac (3). The most general linear transformations on Hilbert space should include non-orthonormal bases. Mostly in Valence Bond (VB) theory, the atomic orbitals (AO) centered on the nuclei are not strictly orthogonal to each other which supports the overlaps ($S_{ij}=<e_i|e_j>$) and naturally the chemical bonding. In this particular case, VB and MO theories reflect very different formalisms, *e.g.* VB theory is based on the non-orthonormal bases and holds the chemist's intuitive structural picture of bonds and lone pairs while these localized orbitals remain lost in the MO picture. Both the expense of the nonorthogonality problem in VB theory and the plague of the delocalized orbitals of MO theory make it difficult to recover a pictorial language for chemists. *The principle of linear covariance* which was developed by Sinanoğlu (1, 2) unifies different formalisms of quantum chemistry (*e.g.* MO and VB formalisms), involves the largest group of transformations whether they are orthonormal or non-orthonormal and also leads to a comprehensive analysis of the higher symmetries of Hilbert space in the Euclidean space (ε_3) in a very easy and elegant manner.

> *Principle of Linear Covariance: "The vectors, operators and their quantum mechanical equations are to be viewed as invariant under any linear transformations between different basis sets, in other words they should be linearly covariant in their tensor algebraic form." (1, 2).*

On the basis of this principle, for a general non-orthonormal basis {|fi>}, Eq. 2 may be written in the tensorial form (5), Eq. 3.

$$H = IHI = \left|f_i\right\rangle\left\langle f^i\right|H\left|f^j\right\rangle\left\langle f_j\right| = H^{ij}\left|f_i\right\rangle\left\langle f_j\right|\underline{\underline{or}}H_{ij}\left|f^i\right\rangle\left\langle f^j\right| \qquad \text{(Eq. 3)}$$

where H^{ij} and H_{ij} are the contravariant and covariant components of Hamiltonian operator. In the sense of our chemical intuition, the one-electron Hilbert space requires to be projected onto the valency vector space (Vn) including the valence shell AOs. That means the Hilbert space for a molecule with M number of atoms would be a tensor product of the one-electron Hilbert space L2(Ri) located at Ri ϵ ε3, Eq. 4.

$$\mathcal{L}_2(\vec{R}) = \mathcal{L}_2(\vec{R}_1) \otimes \mathcal{L}_2(\vec{R}_2) \otimes \ldots\ldots \otimes \mathcal{L}_2(\vec{R}_M) \qquad \text{(Eq. 4)}$$

and the corresponding V_n space of the molecular assembly as a direct sum,

$$V_n(\vec{R})=V_{n_1}(\vec{R}_1)\oplus V_{n_2}(\vec{R}_2)\oplus.....\oplus V_{n_M}(\vec{R}_2) \qquad \text{(Eq. 5)}$$

In this projected valency vector space, the valency becomes 1 for H and He, 4 for Li, Be, ..., F, Ne and 9 for transition metals, *etc.*, corresponding to {1s}, {2s,2p_x,2p_y,2p_z}, {3d_{x2-y2},3d_{z2},3d_{xy},3d_{xz},3d_{yz},4s,4p_x,4p_y,4p_z } respectively, and so on. Thus, each atom is represented by a graph which is called a *VIF picture* (1) as in Fig. 1.

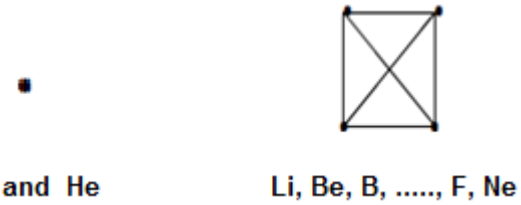

Figure 1. The graph representations of 1st and 2nd row elements as their VIF pictures.

In these graphs which reflect the topology of the molecular assembly in Hilbert space as a projection into Euclidean space, H_{ij} tensor components (matrix elements) correspond to the strengths of the bonding interaction between the nearest-neighbour atomic orbitals. For the sake of simplicity, these H_{ij} values are assumed to be the same and taken as unity.

Hitherto, one may conclude that the unity operator (I) projects the full Hilbert space onto the valency shell space V_n C L_2 and depicts the molecular structure in Euclidean space which leaves a very practical tool for chemists and keeps their chemical intuition alive. This VIF theory overcomes the insufficiencies of previous approaches in the area of chemical graph theory (6-9) and other topological treatments by giving the direct LPI of any molecule in a very easy way.

Every molecule is represented by a VIF structure which depicts the one-electron interactions given in one-electron hamiltonian (h). For any molecule made up of main group elements with the valency shell size n=4, the four atomic orbitals (s and p valencies only) are joined to each other and therefore each atom appears as a tetrahedron, and combining the neighboring tetrahedra leads to the VIF pictures. The two following pictorial rules are applied to these VIF structures:

Rule 1: A valency point may be multiplied by a nonzero constant (κ) which can be positive or negative (Multiplication rule).

Rule 2: A valency point may be superimposed on another valency point bringing its valency interactions with it (Addition rule).

These rules may be applied any number of times, in any desired combination until the VIF is fully reduced by eliminating the non-nearest neighbour interaction lines, at last one reads off the LPI from the final picture; $\{n_+ , n_0 , n_-\}$. The number of free dots giving the number of nonbonding MOs and each single interaction line indicates the presence of a pair of bonding and antibonding MOs. Finally the electrons are assigned to the MOs to get the Electron Count Index (ECI); $\{N_+ , N_0 , N_-\}$. A simple example illustrates the rules and their use in Fig. 2.

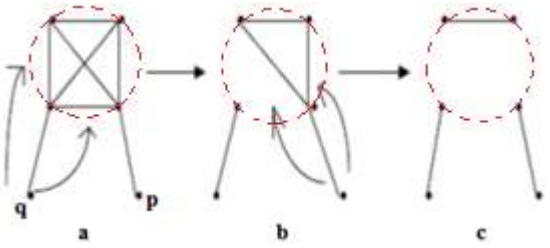

Figure 2. The reduction of the VIF picture for water molecule. **a**. Point q is multiplied by -1, then the line ended with point q gains -1 strength and superimposed onto three neighbouring lines with initial strength 1. **b**. The same is applied to point p. **c**. Finally only three lines of the initial eight remain free. This final reduced-VIF corresponds to LPI={3,0,3} as indicated in (9).

Recently, VIF theory was applied to copper clusters and iron(II)-oxygen bonding in hemoglobin molecule via one-electron density operator version of the theory (10, 11).

In view of this theory, we will deal with a number of examples by predicting the decomposition products (fragments) before getting a mass spectrum data, each providing a systematical approach. The obselete fragmentation procedures are only capable of dealing with small molecules and hard to perform in making quick *a priori* deductions. The previously developed topological indices and graph theoretical methods on the molecular structure are also insufficient and none of these methods could explain the mass spectra of molecules.

There are several different ways to ionize a sample in mass spectrometry from electron impact to electron spray or chemical ionization displaying different fragmentation products. Each of these methods has its own disadvantages, *e.g.* in the case of the most

commonly used electron impact ionization, the molecule must be volatile, thermally stable and its extensive fragmentation -due to the hard ionization process- beclouds the selection of important peaks among the others most of which correspond to many unnecessary second generation product ions. There is not even a method or theory in dealing with the mass spectra purely. Now, it can be possible that knowing an *a priori* mass spectrum of any molecule by using our new method in the present paper. The most important advantage of this new method is its highly user-friendly character, without requiring to know the mathematics behind the method essentially and lets us get *a priori* predictions on the fragments, even for very large or complex molecules. It is applicable to any molecule without considering its thermal stability under the conditions of "electron impact (EI) ionization" procedure. The second important advantage of this method is about the direct determination of the first generation fragments (*e.g.* positively charged molecular ions) which supplies an easy picking of the useful peaks and leaving several unimportant peaks directly eliminated.

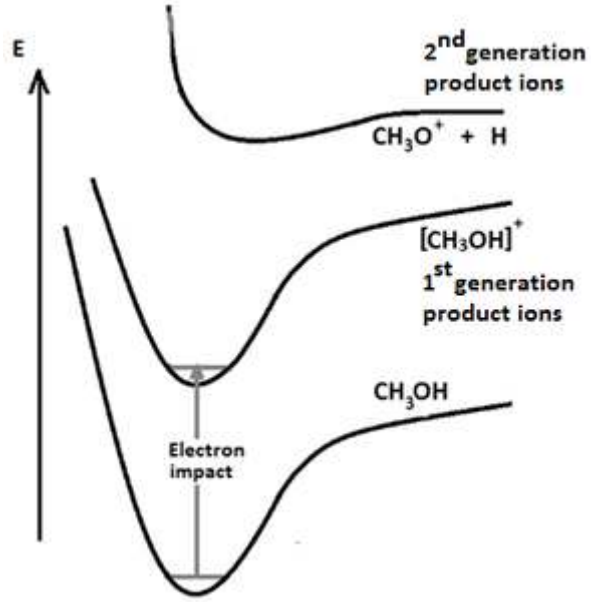

Figure 3. The potential energy change in methanol molecule after electron impact treatment (12).

The fragmentation in electron ionization can be described using potential curves as in the diagram. The electron impact energy is enough to remove an electron from the analyte and form a molecular ion (see Figure 3). The standard electron ionization source to induce analyte ionization is about 70 electron volt (eV) electrons, but this level of energy is so much higher than the energy required for ionization of most common compounds (typically between 6 and 12 eV). Most of the excess energy is dissipated via vibroelectronic excitation modes. Due to the higher energy supplied by 70 eV accelerated electrons, several other bond dissociation reactions become possible which produce

second generation product ions by breaking the stronger bonds in the molecule. In the case of methanol, the molecular ion is formed after the electron impact treatment, but second generation fragments (CH_3O^+) starts forming at higher levels of energy through 70 eV. The VIF picture of methanol molecule was shown in Table 1.

Table 1. VIF picture of methanol molecule.

VIF picture	reduced VIF picture
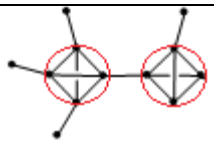	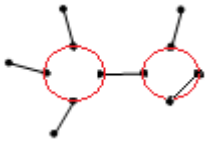

It is clear to see that all C-H, C-O and O-H bonds survive after the reduction of VIF picture. This verifies the first generation product as CH_3OH^+ molecular ion in its mass spectrum, Figure 4.

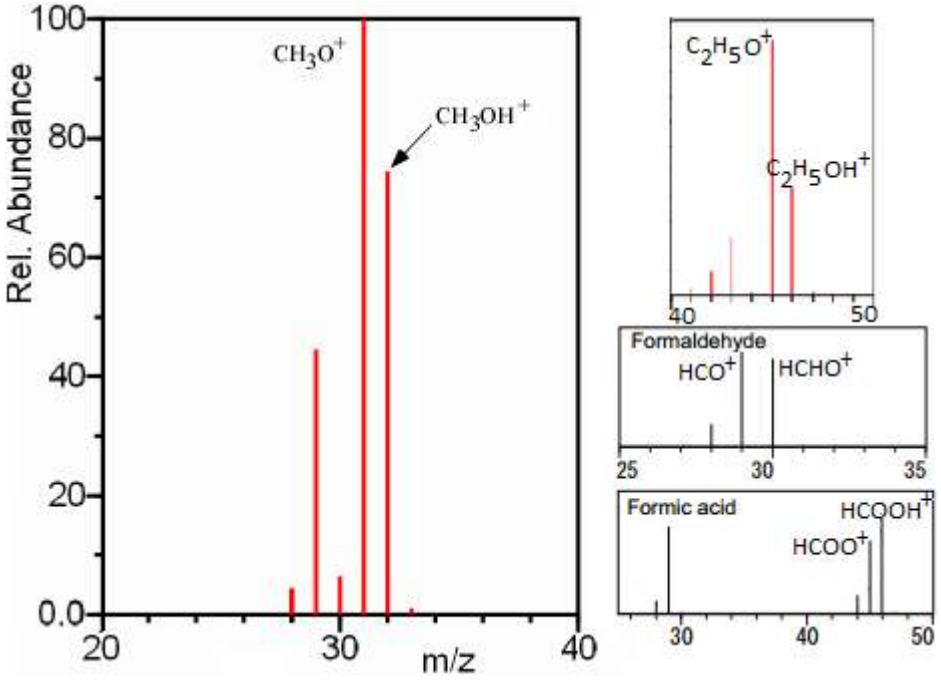

Figure 4. Mass spectra of methanol, ethanol, formaldehyde, and formic acid (15).

A similar situation may also be seen in the mass spectra of ethanol, formaldehyde, and formic acid molecules which produce their molecular ions as well. Then, CH_3O^+, $C_2H_5O^+$, HCO^+ and $HCOO^+$ ions (one hydrogen losing) in the given spectra remain as the secondary products. The higher dissociation energy of CH_3O – H bond (440 $kJ.mol^{-1}$) in methanol molecule (16) along with the VIF reduction argument leaves those ions as the second generation ones. The solid localized orbital scheme of methanol (9) and its water

molecule analogy with methyl linkage (1) also verify this argument, in other words, any weak bond interaction in these systems does not exist. To clarify this argument and relate it to mass spectrometry, it is necessary to go one step further in terms of looking for the weaker or softer interactions inside a molecule.

In Fig. 5, several well-known explosive molecules were shown.

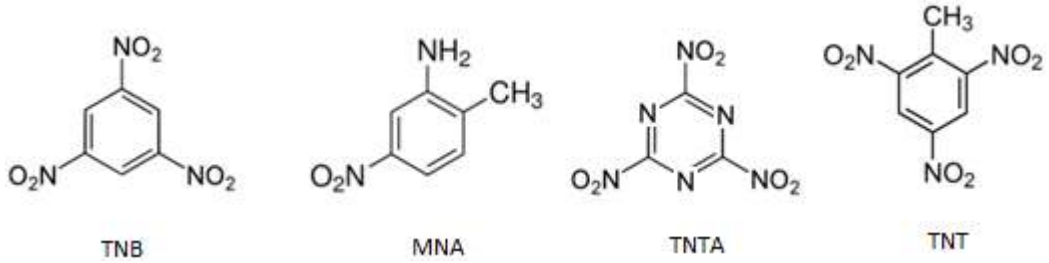

Figure 5. Structures of several well-known explosives (TNB: trinitrobenzene, MNA: methylnitroaniline, TNTA: trinitrotriazine, TNT: trinitrotoluene).

Various DFT computations (17-20) along with AIM analysis on several well-known expulsive molecules predicted that the significantly low C-NO_2 bond electron density (~1.76-1.83 e/Å^3) as well as its Laplacian (~ -17 e/Å^5) indicate highly charge depletion (very low charge accumulation) in this bond in comparison to other bonds in the molecules (see Table 2). All those confirm that C-NO_2 bonds are the weakest linkages in the molecule.

Table 2. Topological properties of C–NO_2 bond in various explosives.

	ρ [e/Å^3]	**$\nabla^2\rho$ [e/Å^5]**
TNB[a]	1.77	-16.7
MNA[b]	1.76	-16.4
TNTA[c]	1.83	-18.3
TNT[d]	1.78	-17.1

(**a.** ref.17, **b.** ref.18, **c.** ref.19, **d.** ref.20.)

Table 2 also supports the transferability of these two topological properties between highly similar molecules, *e.g.* the same values may be assigned to C-N bonds in nitrobenzene (NB) and dinitrobenzene (DNB) which only differs in the number of nitro groups from TNB. On the other hand, the trend in the change of Laplacian of bond electron densities for all bonds in TNB molecule was drastically decreased in three C-NO_2 bond regions (17). That situation indicates another realistic bond sensitivity in the molecule, whereas the other bonds does not exhibit this kind of relationship (In the present work, this sensitive bonds will be called as *soft interactions*). The VIF picture of nitrobenzene (NB) molecule was shown in Table 3.

Table 3. VIF picture of NB molecule.

VIF picture *	reduced VIF picture**
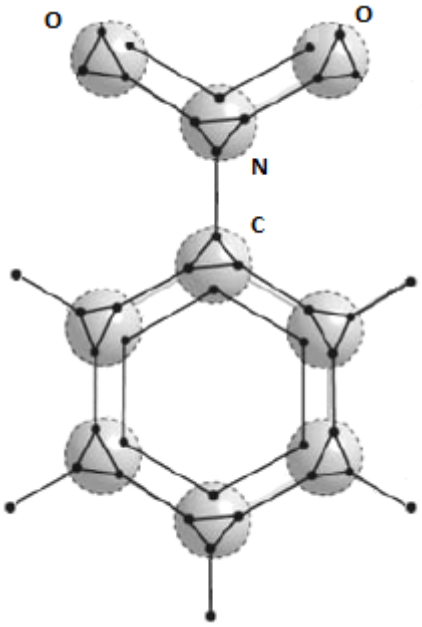	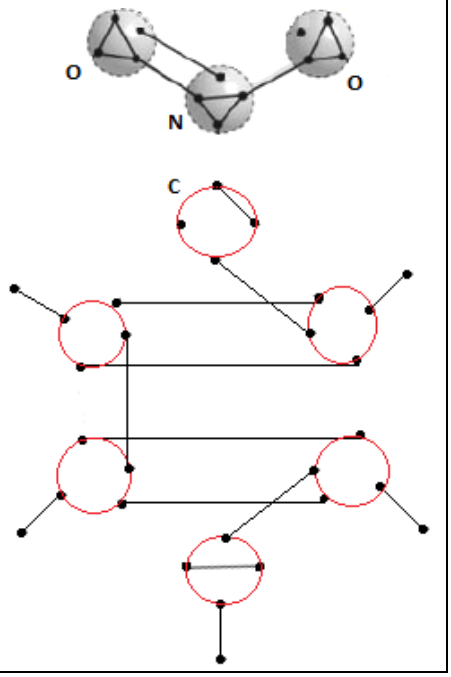

(* pi resonance of nitro group with benzene cloud was not shown ** for reduction, please see *appendix*)

It may be already seen that C-N bond line has vanished which makes it a soft interaction in NB molecule (M=123 g.mol^{-1}). This result verifies the topological argument above for the weakness of C-N bond above. Then it is expected to observe m/z=77 peak in its mass spectrum due to the loss of nitro group, (see Figure 6).

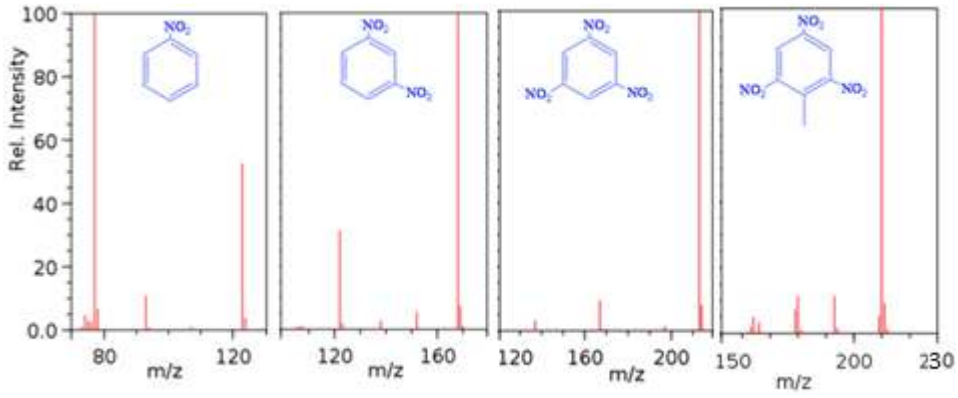

Figure 6. Mass spectra of NB, DNB, TNB and TNT (15).

The validity of the same argument was also clear in the mass spectra of DNB (168 g.mol^{-1}), TNB (213 g.mol^{-1}) and TNT (227 g.mol^{-1}) molecules, each of those has m/z=122, 167 and 181 peaks in their spectra respectively.

Applications

First, we will handle the mass spectrum of a general hydrocarbon, consisting of C-H and C-C bonds only. Since there are no heteroatoms in a hydrocarbon molecule, there are no nonbonding MOs and nonbonding valence shell electrons as well. Consequently, the cationic character of a hydrocarbon molecular ion is delocalized over all the bonds. We may also deduce that, from the full-reduced VIF picture in Table 4, there is no soft interaction between any two atoms; therefore there is no specific cleavage region in the molecule (the wiggly line indicates the long carbon chain).

Table 4. VIF pictures for a general hydrocarbon.

General VIF picture	General Full-reduced VIF picture
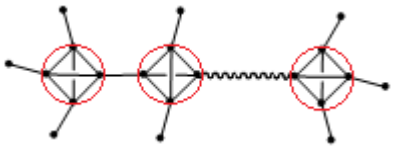	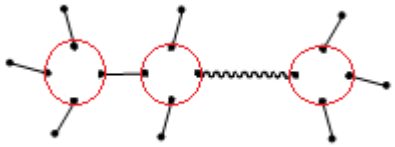

The C-C bonds are weaker than C-H bonds and thus, we except the fragmentation of C-C bonds that causes producing of a mixture of alkyl carbocations, easily seen in the mass spectrum of any hydrocarbon. All these significant fragment ions, the corresponding carbocations, are CH_3^+ (m/z= 15), $C_2H_5^+$ (m/z= 29), $C_3H_7^+$ (m/z= 43), $C_4H_9^+$ (m/z= 57); *etc*. One can see the corresponding peaks in Figure 7, as a model spectrum.

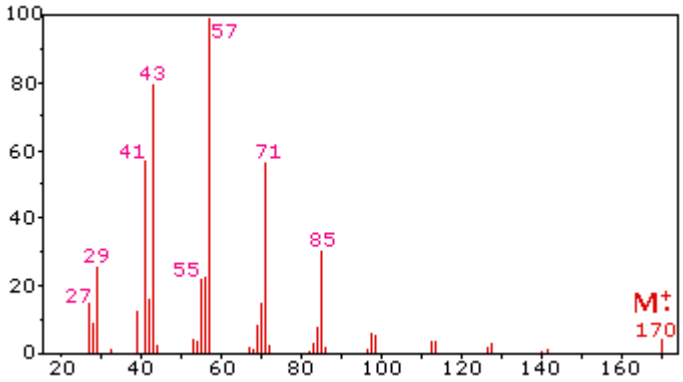

Figure 7. The mass spectrum of dodecane molecule (21).

Another group of compounds is oximes. An oxime molecule has a variety of bonds with different polarity and different strengths; such as C-H, C-N, C-C, C-O, *etc.* It seems a bit difficult and complicated to determine the possible cleavage regions for oximes, but now, it is possible to deduce the decomposition products by using the VIF theory. The VIF picture for a general oxime molecule is given in Table 5.

Table 5. The VIF pictures for a general oxime molecule.

Structure	VIF	Semi-reduced VIF	Full-reduced VIF
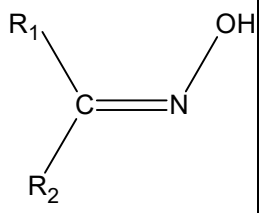	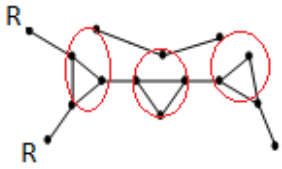	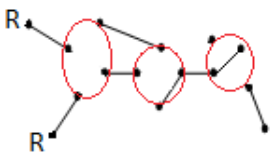	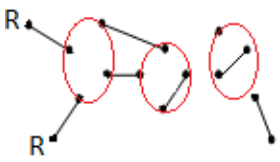

One may get the result that the intraatomic interaction lines of nitrogen and oxygen tend to decompose the N-O bond; in other words, the N-O interaction is the soft one among the other heteronuclear bonds. By this way, N-O interaction line does not appear in the full-reduced VIF which means, an oxime molecule always decomposes by the cleavage of a N-O bond (Figure 8).

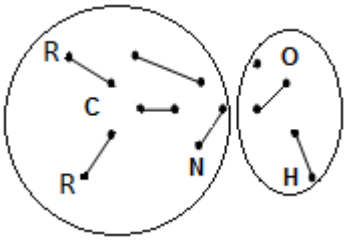

Figure 8. Fragments of a typical oxime molecule. The cleavage of N-O bond was clearly shown.

Thus, we get two main fragments; one of which is always hydroxyl (OH^-) ion, corresponding peak having the m/z value 17, and the other is the remaining part. These two fragments, as two major peaks, exist in the mass spectra of all oximes, Fig. 9.

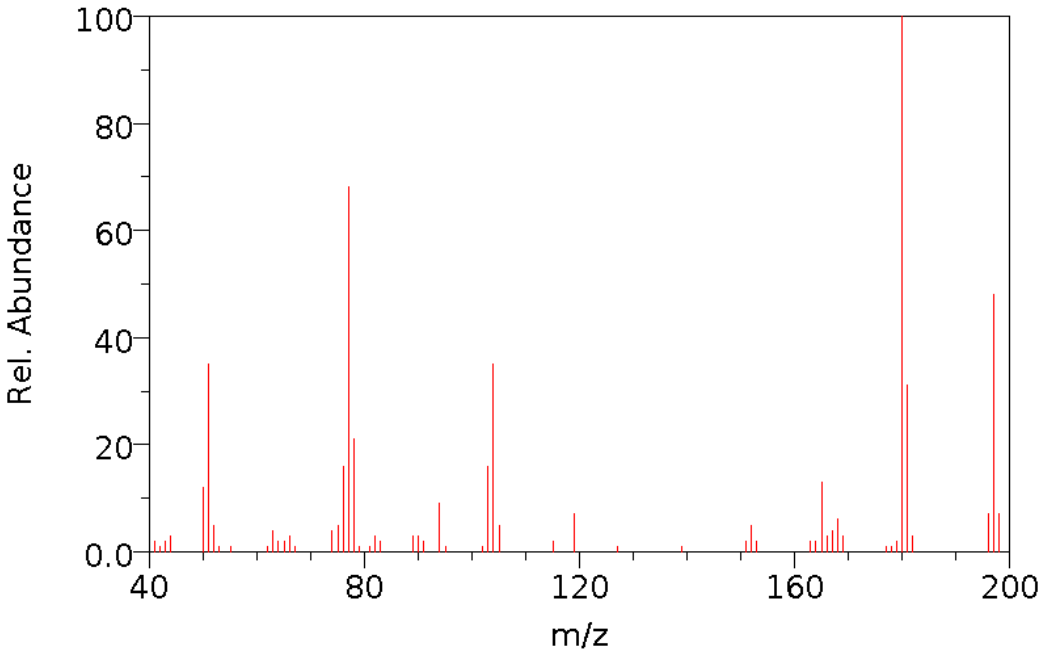

Figure 9. The mass spectrum of methanone, diphenyl-, oxime (M=197) molecule. The M-17 peak was not showed in the spectrum (21).

The spectrum of the oxime shows an appreciable M-180 peak indicating that it is mainly due to loss of the hydroxyl group with a remaining part as a second fragment. Of course, if there is a oxygen-substituted oxime molecule, *e.g.* for $-OCH_3$, there will be a m/z=31 peak instead of m/z=17, the cleavage of the N-O bond still holds.

Our final interest is Schiff bases which have different kind of bonds than the oxime molecules. Likewise, it is a bit complicated to estimate the fragments of the Schiff bases in their mass spectra. We will use the VIF theory again to determine the decomposition products in a completely theoretical approach. The VIF picture for a general Schiff base is given in Table 6.

Table 6. The VIF pictures for a general Schiff base molecule.

Structure	VIF	Semi-reduced VIF	Full-reduced VIF
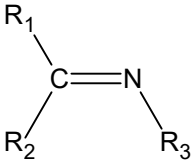	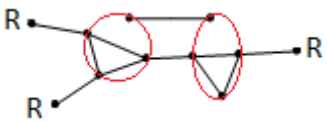	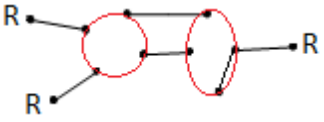	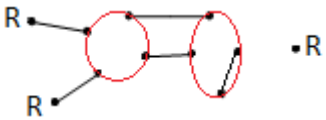

The semi-reduced VIF indicates the cleavage of the C-N bond, from the amine side of the molecule, by the intraatomic interaction line of nitrogen atom, in other words, this C-N

interaction is soft, which is also implicit in the full-reduced VIF picture. Consequently, a Schiff base molecule tends to be divided into two main parts by the cleavage of this bond. These two main fragments exist in the mass spectra of all Schiff base molecules as two major peaks. For example, these two fragments for the molecule given below can be deduced readily in the light of a recent study (22);

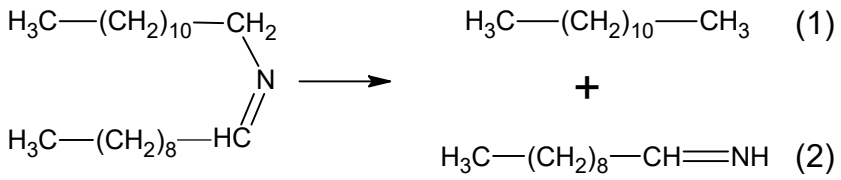

the m/z values are 170 and 156 for (1) and (2) fragments respectively. These two major peaks can easily be seen in the mass spectra of this Schiff base in Fig. 10.

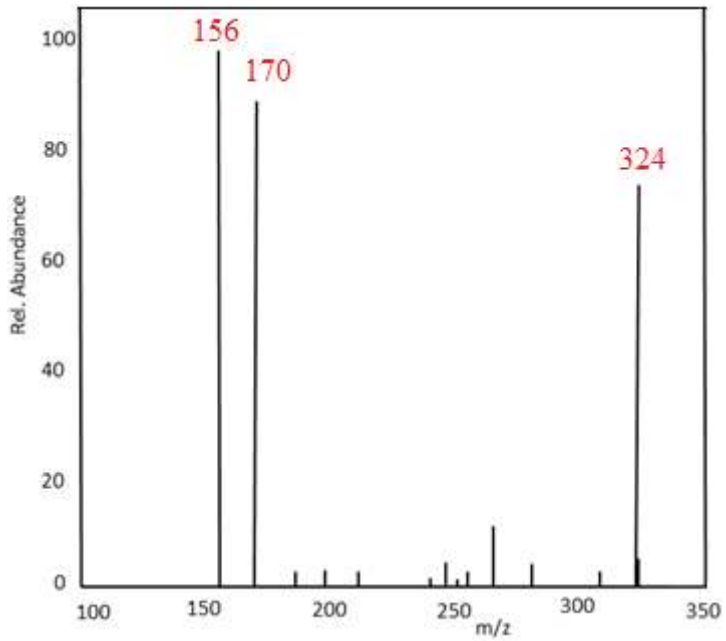

Figure 10. The mass spectrum of the Schiff base molecule (22).

One may increase the number of the examples even further(23-25); but we want to end this argument with a comprehensive example; the mass spectrum of a 2-substituted cyclohexanone oxime which is worthwhile to examine. Table 7 shows the molecule and its VIF picture (the wiggly lines indicate the remaining parts of the molecule, we only used the necessary parts).

Table 7. A somewhat simplified VIF pictures of the 2-substituted oxime molecule.

Structure	Clarified VIF	Semi-reduced VIF
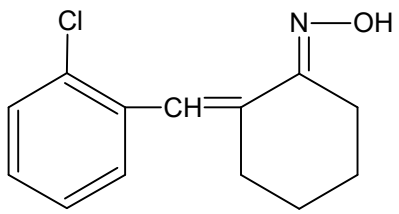	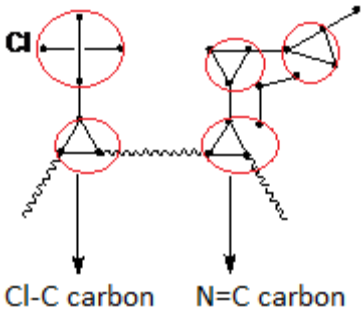	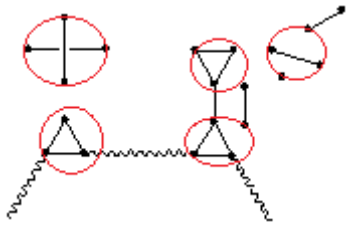

We see that, from the semi-reduced-VIF, there are three main segments; chlorine (m/z=35), hydroxyl group (m/z=17), and the final segment which is due to the loss of the hydroxyl group, namely the remaining part (m/z=218).

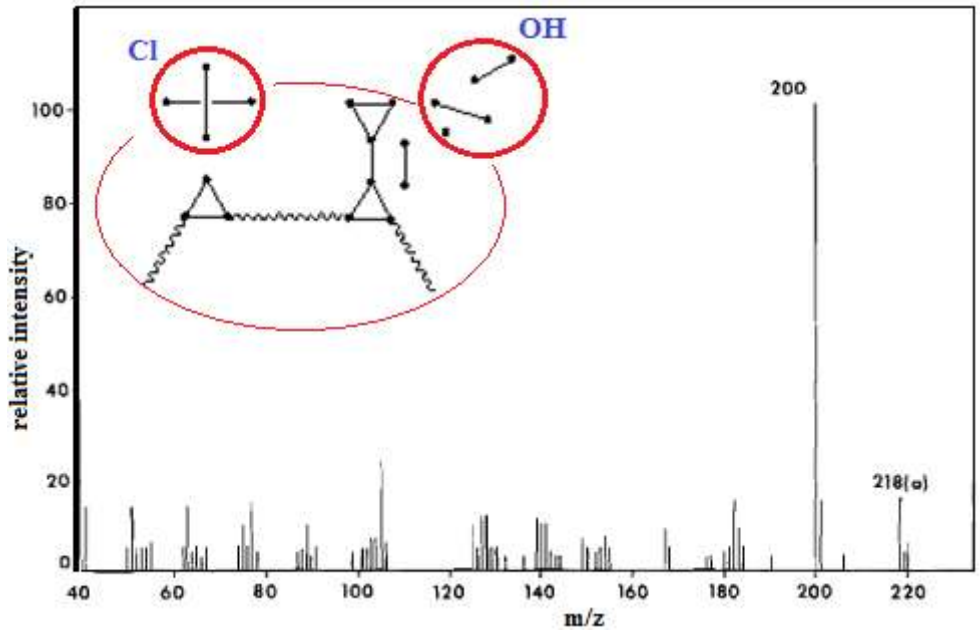

Figure 11. The mass spectrum of the oxime molecule from Table 7 (23). (m/z=17 and 35 peaks are not available in the experimental spectrum in which m/z axis starts from value 40).

These peaks have major importance and may easily be seen in the mass spectrum (see Figure 11) (23).

Conclusion. A new approach was presented in this paper for the development of the systematics of mass spectrometry in the sense of modern quantum mechanical methods. This aforementioned method was quite simplified and one may easily quickly manipulate

this method for the quick predictions of *a priori* mass spectra. It is also possible that we may get the main fragmentation results in the generalized form for a given compound family as to type of their bonding characteristics; like we have shown in this paper. Such an *a priori* work will also be helpful for enlightening the characterization of newly synthesized molecules.

REFERENCES

1. Sinanoğlu O. New method for qualitative quantum chemical deductions on organic or inorganic molecules or clusters directly from structural formulas or ORTEP diagrams. Theoretica Chimica Acta. 1985 Oct;68(4):251–70.

2. Sinanoğlu O. A theorem for qualitative deductions in organic or inorganic chemistry regarding the relative stabilities, distortions and reactions of molecules. Chemical Physics Letters. 1984; 103, 315.

3. Dirac PAM. The principles of quantum mechanics. 4. ed. (rev.), repr. Oxford: Clarendon Press; 2009. 314 p. (The international series of monographs on physics).

4. Courant R, Hilbert D. Methods of mathematical physics. New York: Interscience Publishers; 1989. 2 p. (Wiley classics library).

5. Schultz-Piszachich, W., Tensor Algebra Analysis, 4th ed., Teubner, Leipzig (1988).

6. King, R.B., eds., Chemical Applications of Topology and Graph Theory, Elsevier (1983).
King RB, United States, editors. Chemical applications of topology and graph theory: a collection of papers from a symposium held at the University of Georgia, Athens, Georgia, U.S.A., 18-22 April 1983. Amsterdam ; New York: Elsevier; 1983. 494 p. (Studies in physical and theoretical chemistry).

7. Bonchev D, Rouvray DH, editors. Chemical graph theory: introduction and fundamentals. New York: Abacus Press; 1991. 288 p. (Mathematical chemistry).

8. Balaban AT, editor. Chemical applications of graph theory. London ; New York: Academic Press; 1976. 389 p.

9. Sinanoglu O, Alia J, Hastings M. Valency Interactions in AHm0,.-+. (Hydrides of Main Group Elements, Radicals, Cations, Anions) and MO Energy Level Patterns Directly from the Pictorial "VIF" Method Compared with Computer Calculations. The Journal of Physical Chemistry. 1994 Jun;98(23):5867–77.

10. Alia J. Chemical Reasoning Based on an Invariance Property: Bond and Lone Pair Pictures in Quantum Structural Formulas. Symmetry. 2010 Jul 23;2(3):1559–90.

11. Alia JD. Molecular Structural Formulas as One-Electron Density and Hamiltonian Operators: The VIF Method Extended. The Journal of Physical Chemistry A. 2007 Mar;111(12):2307–18.

12. This figure was depicted from the arguments of reference 13 and 14.

13. Borkar S, Sztaray B, Bodi A. Dissociative photoionization mechanism of methanol isotopologues (CH_3OH, CD_3OH, CH_3OD and CD_3OD) by iPEPICO: energetics, statistical and non-statistical kinetics and isotope effects. Phys. Chem. Chem. Phys. 2011; 13:13009.

14. Thapa B, Schlegel HB. Molecular Dynamics of Methanol Monocation (CH_3OH^+) in Strong Laser Fields. Journal of Physical Chemistry A. 2014; 118:10, 1769.

15. Mass spectra of "methanol, ethanol, formaldehyde, formic acid, NB, DNB, TNB and TNT" molecules, in NISTchemistry web book, NIST Standard Reference Database Number 69. National Institute of Standards and Technology, Gaithersburg, MD, 20899, (http://webbook.nist.gov)

16. Blanksby SJ, Ellison GB. Bond Dissociation Energies of Organic Molecules. Accounts of Chemical Research. 2003 Apr;36(4):255–63.

17. Stephen AD, Kumaradhas P, Pawar RB. Charge Density Distribution, Electrostatic Properties, and Impact Sensitivity of the High Energetic Molecule TNB: A Theoretical Charge Density Study. Propellants, Explosives, Pyrotechnics. 2011 Apr;36(2):168–74.

18. Ellena J, Goeta AE, Howard JAK, Punte G. Role of the Hydrogen Bonds in Nitroanilines Aggregation: Charge Density Study of 2-Methyl-5-nitroaniline. The Journal of Physical Chemistry A. 2001 Sep;105(38):8696–708.

19. SRINIVASAN P, MAHESHWARI K, JOTHI M, Kumaradhas P. Charge Density Distribution, Electrostatic Properties and Sensitivity of the Highly Energetic Molecule 2,4,6-Trinitro-1,3,5-triazine: A Theoretical Study. Central European Journal of Energetic Materials. 2012;9(1):59–76. URL: http://yadda.icm.edu.pl/yadda/element/bwmeta1.element.baztech-article-BAT1-0041-0077/c/httpwww_wydawnictwa_ipo_waw_plcejemvol-9-1-2012srinivasan.pdf.

20. Stephen AD, Pawar RB, Kumaradhas P. Exploring the bond topological properties and the charge depletion-impact sensitivity relationship of high energetic TNT molecule via theoretical charge density analysis. Journal of Molecular Structure: THEOCHEM. 2010 Nov;959(1–3):55–61.

21. Mass spectra of "dodecane" and "methanone, diphenyl-, oxime" molecules, in NISTchemistry web book, NIST Standard Reference Database Number 69. National Institute of Standards and Technology, Gaithersburg, MD, 20899, (http://webbook.nist.gov)

22. Tuncel EF, Berkay S, Berna O, Nebahat D. Synthesis, characterization and biological activity of a new long-chain imine ligand and some transition metal complexes in solvent-free conditions. Main Group Chemistry. 2012;(3):217–222.

23. Smith P, Dimmock J, Turner W. Mass Spectrometry of Some Substituted 2-Benzylidenecyclohexanone Oximes. Can J Chem. 1973;51(9):1471–5. DOI: 10.1139/v73-221.

24. Smith PJ, Dimmock JR, Turner WA. Mass Spectrometry of Some Substituted 2-Benzylidenecyclohexanones and 2,6-bis-Benzylidenecyclohexanones. Canadian Journal of Chemistry. 1973 May;51(9):1458–70. DOI: 10.1139/v73-220.

25. Smith PJ, Dimmock JR, Taylor WG. Mass Spectrometry of some Nuclear Substituted Styryl Ketones. Canadian Journal of Chemistry. 1972 Mar 15;50(6):871–9. DOI: 10.1139/v72-136.

Türkçe Öz ve Anahtar Kelimeler

Kütle Spektrometrisinin Sistematikleri Üzerine: Yeni bir Graf-Teorik Yöntem

Berkay Sütay

Öz: Kütle spektrometrisinin (MS) sistematik artalanı Değerlik Etkileşim Formülü teorisinin etkin bir şekilde kullanılmasıyla ortaya konmuştur. Yeni graf teorik yöntem, saf bir kuantum mekanik araştırma olarak geliştirilmiştir ve kütle spektrometrisinin arkasındaki kuantum mekanik sistematikleri aydınlatmak için bir seri molekül ve birleşiklere uygulanmıştır. Kimya ve fizikteki topolojik indisler ve graf teorik yöntemler bu yeni yöntemin çarpıcı özellikleri olup pek çok molekül ve birleşiğin kütle spektrumlarına uygulanmıştır (artık kullanılmaz hale gelmiş parçalanma prosedürlerinden dolayı). Bu esaslı topolojik indisler, moleküllerin kütle spektrumları üzerinde hızlı tahminler yapma ve kararlar alma olanağı vermesi için kullanılmıştır. Kütle Spektrometrisinin çarpıcı yönlerinden biri olarak, pek çok molekülün temel parçalanma yolları tamamen teorik bir yolla incelenmiş ve *a priori* bozunma ürünleri tahmin edilmiştir. Sistematik teori incelememizin ışığında ortaya konmuştur ve hangi etkileşimlerin diğerleri arasında yumuşak tabiatlı olduğu öğrenildikten sonra çok miktarda kalitatif bilgi elde edilmiştir.

The results are of general validity in comparison with the experimental data.

Sonuçlar, deneysel verilerle kıyaslandığında genel olarak geçerli bulunmuştur.

Anahtar kelimeler: Kütle spektroskopisi; değerlik etkileşim formülü; elektron çarpma iyonlaştırması; topoloji; graf teorisi.

Gönderme: 19 Ağustos 2016**. İkinci tur:** 20 Ekim 2016**. Kabul: .**09 Kasım 2016

Nutrition Profile of the Sea of Marmara Between Years 2010 and 2013

Bahattin Yalçın[1*], Umut E. Yılmaz[2] and M. Levent Artüz[2]

[1] Department of Chemistry, Faculty of Science and Arts, Marmara University, Göztepe, 34722 Istanbul, Turkey
[2]Sevinç-Erdal İnönü Foundation, MAREM (Marmara Environmental Monitoring) project, Department of Marine Sciences, Anadoluhisarı Toplaroönü No: 8, 34810, Istanbul, Turkey

Abstract: In order to determine the nutrition load in the Sea of Marmara, sampling was realised on appointed 25 stations, at standard vertical sections from surface to deepest point of the station, bi-annually between 2010 and 2013. NO_2–N, NO_3–N, NH_4–N, and PO_4–P were analysed from unfiltered water samples; in addition, some physicochemical parameters that play important roles, such as salinity, temperature, dissolved oxygen, and pH, were measured for each station. This study reports on nutrients load in the Sea of Marmara for a preliminary assessment of the status of these nutrients and a brief discussion about the unique oceanographic status of the Sea of Marmara.

Keywords: Sea of Marmara; nutrient; pycnocline; thermocline; halocline; pollution.

Submitted: May 05, 2016. **Revised:** May 31, 2016. **Accepted:** October 13, 2016.

Cite this: Yalçın B, Yılmaz U, Artüz M. Nutrition Profile of the Sea of Marmara Between Years 2010 and 2013. JOTCSA. 2017;4(1):197–226.
DOI: To be assigned.
*Corresponding author. E-mail: byalcin@marmara.edu.tr.

INTRODUCTION

The Sea of Marmara and Turkish Straits extend from the Aegean Sea to the Black Sea trough the Dardanelles (60 km), Sea of Marmara (210 km), and Bosphorus (31 km). The total length of the system is approximately 300 km, with a maximum depth of 1273 m **(1)**.

Because of huge density differences between the waters of the Mediterranean and the Black Sea, occurs a two-layer current system along the Sea of Marmara and Turkish Straits (TS) flowing in opposite direction.

The watermasses of the Black Sea are entirely different from those of the Mediterranean Sea originated watermasses. In the Black Sea precipitation and runoff exceeds evaporation, for which reason a surface layer of relatively low salinity and correspondingly low density is present.

Owing to the distribution of density, the surface waters of Black Sea flow through the Bosphorus and the Dardanelles into the Aegean Sea basin and Mediterranean Sea originated water flows in along the bottom. The outflow from the Black Sea basin is a function of its water budget and carries runoff from the large rivers and surface waters during into the Black Sea **(2)**.

Intensive mixing takes place mainly along the Bosphorus as well as in the other parts of the straits and Sea of Marmara. The salinity of the inflowing Mediterranean Sea originated watermass which is over 38.50 ‰ at the entrance of the Dardanelles strait decreases slowly with the distance travelled in the Sea of Marmara down to 29 ‰, where the bottom current enters the Black Sea at the Northern end of the Bosphorus. At the same time, the salinity of the outflowing water is increased from 16 ‰ in origin in the Black Sea to 30 ‰ leaving the Dardanelles **(3)**.

The in- and outflowing water masses are separated by a well-defined transition layer, which oscillates in accordance to the contours of the bottom. This layer of transition also represents the discontinuity layer for temperature and salinity and called thermo-halocline **(4, 5)**.

The exponentially growing pollution since 1980 is the main problem in the Sea of Marmara. All the settled areas around and also in the hinterland of the Sea of Marmara are discharging the wastes using "deep sea discharges" without any treatment directly under the pycnocline–thermocline layer in the Sea of Marmara **(3)**.

In 1980's the Istanbul municipality started a project in contemplation of using the Mediterranean Sea originated upper current as a conveyor for transport and discard the waste

water to the Black Sea without any treatment, and applied it despite the countering measurements **(2)**.

Now it is known that the Mediterranean originated undercurrent only reaches 30% to the Black Sea with the most optimistic estimate due to the changes of the salinity stratification of the surface water and the seasonal volumetric fluctuations of the surface currents, the undercurrent does not reach continuously to the Black Sea basin **(3)**.

The role of nutrients in limiting and/or boosting primary production in the sea is widely acknowledged.

Dissolved Nitrite Nitrogen (NO_2-N), Nitrate Nitrogen (NO_3-N), Ammonium Nitrogen (NH_4-N), and Phosphate Phosphorus (PO_4-P) are large and important fractions of marine nutrient pools, especially in euphotic zones. Compounds of nitrogen, and especially those of phosphorus, are major cellular components of organisms **(6)**.

There are no adequate studies of nutrients across the Sea of Marmara. Some of the studies are, with the topics of; "Organic carbon distribution in the surface sediments of the Sea of Marmara and its control by the inflows from adjacent water masses" **(7)**. "Elemental composition of seston and nutrient dynamics in the Sea of Marmara" **(8)**; "Nutrient exchange fluxes between the Aegean and Black Seas through the Marmara Sea" **(9)**, respectively.

During the last four decades, drastic changes have occurred in the Sea of Marmara ecosystem because of anthropogenic pressures. Therefore, this study was designed to monitoring of the seasonal variations in nutrients of this area between years 2010 and 2013 (and ongoing).

MATERIALS AND METHODS

The present study is based on data gathered during survey cruises in the Sea of Marmara waters between 2010 and 2013 and realized biannually as winter and summer seasons measurements on 23 stations (Figure 1).

Figure 1. Map with the location of the sampling stations.

Data gathering conducted on winter and summer seasons due to direct effect of temperature and precipitation on the solubility and concentration of nutrients in sea water and also availability of MAREM project stuff.

The network of stations is shown in Figure 1 and locations in Table 1. All 24 stations were observed with the standard depths from 0.5 to 1000 m or less for the bottom.

Table 1. The location table of the stations with maximum depths of the station.

Station Nº	Coordinate	Depth	Station Nº	Coordinate	Depth
2	40° 50.333' N : 028° 59.733' E	515 m	**32**	40° 23.283' N : 027° 26.950' E	39 m
3	40° 42.383' N : 029° 04.367' E	1000 m	**33**	40° 39.883' N : 027° 26.650' E	138 m
6	40° 53.883' N : 028° 58.350' E	52 m	**34**	40° 54.350' N : 027° 33.783' E	187 m
12	40° 26.750' N : 029° 01.067' E	83 m	**35**	40° 28.750' N : 027° 00.100' E	58 m
15	40° 26.117' N : 028° 33.950' E	53 m	**38**	40° 30.733' N : 027° 14.433' E	65 m
17	40° 40.583' N : 028° 33.900' E	442 m	**3c**	40° 18.517' N : 026° 34.683' E	46 m
19	40° 56.600' N : 028° 33.083' E	59 m	**40**	40° 48.283' N : 027° 26.950' E	997 m
1b	41° 12.817' N : 029° 07.350' E	87 m	**5i**	40° 44.633' N : 029° 39.133' E	121 m
1i	40° 44.717' N : 029° 15.050' E	380 m	**6b**	41° 01.283' N : 028° 58.950' E	39 m
23	40° 43.933' N : 027° 59.950' E	850 m	**6c**	40° 07.083' N : 026° 21.483' E	86 m
25	40° 23.167' N : 027° 56.100' E	33 m	**7i**	40° 44.050' N : 029° 50.283' E	32 m
29	40° 21.500' N : 027° 48.783' E	33 m			

The chemical parameters were measured by collecting seawater samples with Niskin bottles, and analysed using a Shimadzu spectrophotometer UV-240 in the laboratory on board. NO_2–N, NO_3–N, NH_4–N, and PO_4–P were analysed from unfiltered water samples, according to Standard Methods for the Examination of Water and Wastewater **(10)**.

All oceanographic parameters were measured *in situ* with a CTD YSI 6600 V2 multi-parameter data probe and MIDAS ECM with additional probes (pH and Dissolved Oxygen) along the water

column with 1 sec duration (approximately 10 cm intervals) from the surface (0.5 m) to the deepest section of the station.

All the data are stored in MAREM database and processed with the HIDRO-QL software. (10)

Remarks: The measurements in highly polluted areas, such as Golden Horn and the tip of the İzmit Bay, are present in hydrographical tables but that values and corresponding stations are left out of accounts by mean maximum and minimum values to characterize the water masses.

RESULTS

Temperature

Table 2. Average long-term temperature distribution/fluctuation of the whole Sea of Marmara area incl. Turkish Straits, during summer seasons, in depth basis between years 2010 and 2013 in the summer seasons.

Beginning Date: **28/02/2010**				Emin: **029° 55.050' E**				Nmin: **37° 13.000' N**			
Ending Date: **27/08/2013**				Emax: **026° 07.000' E**				Nmax: **41° 20.000' N**			
PARAMETER: **T°C**				PROJECT: **MAREM**							
DEPTH. (m)	**MIN.**	**MAX.**	**DIFF.**	**QUAN.**	**MEAN**	**ST.DEV.**	**VAR.**	**SEM.**	**MEAN COR.**	**VOL. AV.**	**VOL. ST.DEV.**
0.5	19.59	29.89	10.30	222	26.20	1.785	3.173	0.120	26.20	26.20	1.785
5.0	17.82	29.86	12.04	222	25.07	2.375	5.617	0.159	24.91	25.63	2.173
10.0	14.96	29.81	14.85	215	23.31	3.223	10.342	0.220	21.59	24.87	2.783
25.0	10.97	18.92	7.95	208	14.66	1.621	2.616	0.112	17.09	22.42	5.057
50.0	13.20	18.09	4.89	126	15.72	0.780	0.604	0.069	15.32	21.57	5.234
100.0	14.60	15.73	1.13	43	15.19	0.294	0.084	0.045	15.32	21.31	5.280
250.0	14.41	16.08	1.67	27	15.16	0.442	0.188	0.085	15.16	21.15	5.302
500.0	14.03	16.29	2.26	20	15.12	0.684	0.444	0.153	15.10	21.04	5.316
750.0	14.02	16.05	2.03	13	15.02	0.612	0.346	0.170	14.99	20.97	5.325
1,000.0	14.01	16.11	2.10	6	14.79	0.828	0.571	0.338	14.85	20.93	5.330

(MIN=minimum value; MAX=maximum value; DIFF=difference; QUAN=quantity of measurements; MEAN= mean value; S.DEV=standard deviation; VAR= variance; SEM=standard error of mean; MEAN COR= mean correction; VOL. AV. = volumetric average; VOL. S. DEV. = volumetric standard deviation).

The temperature conditions seem to have the same main characteristics in all the cross-sections (Tables 2-3). This also flows from the longitudinal section. The water temperatures of the upper water mass which is Black Sea-originated water change between 7.9 °C and 29.9 °C, depending on the meteorological conditions. The deeper layers are consequently more homogeneous with respect to the temperature than the upper layers between 10.8°C and 18.2°C with a constant average of 14.2°C, in summer seasons.

Also the temperatures in the winter season of the upper water mass changes between 5.8°C and 16.2°C, depending on the meteorological conditions. The deeper layers are consequently more homogeneous with respect to the temperature than the upper layers between 10.1°C and 16.2°C.

Salinity

The salinity conditions in the Sea of Marmara provide a striking example of the difference between the Black Sea water and the Mediterranean originated water. The transition layer is very prominent, the mean salinity rising about 22.5 ‰ from surface to 35.6 ‰ on 50 m depth (Tables 4-5). The upper layer has an average salinity of about 25 ‰. This water mixture, which is composed of the Black Sea and Mediterranean Sea-originated water, takes place mainly in the turbulent channel of the Bosphorus. The deeper layer is uniform with respect to salinity, varying between 38.5 and 38.8 ‰.

Table 3. Average long-term temperature distribution/fluctuation of the whole Sea of Marmara area incl. Turkish Straits, during winter seasons, in depth basis between years 2010 and 2013 in the winter seasons.

Beginning Date: **28/02/2010**			Emin: **029° 55.050' E**					Nmin: **37° 13.000' N**			
Ending Date: **27/08/2013**			Emax: **026° 07.000' E**					Nmax: **41° 20.000' N**			
PARAMETER: **T°C**			PROJECT: **MAREM**								
DEPTH. (m)	**MIN.**	**MAX.**	**DIFF.**	**QUAN.**	**MEAN**	**ST.DEV.**	**VAR.**	**SEM.**	**MEAN COR.**	**VOL. AV.**	**VOL. ST.DEV.**
0.5	5.81	10.90	5.09	146	6.81	1.080	1.159	0.089	6.81	6.81	1.080
5.0	5.90	11.10	5.20	146	6.96	1.030	1.054	0.085	7.08	6.89	1.056
10.0	5.90	14.85	8.95	144	7.59	1.871	3.478	0.156	8.20	7.12	1.417
25.0	6.40	15.94	9.54	138	10.68	3.582	12.740	0.305	10.87	7.98	2.628
50.0	10.10	16.15	6.05	98	14.53	1.215	1.462	0.123	13.64	8.93	3.387
100.0	13.00	15.75	2.75	32	14.82	0.853	0.705	0.151	14.61	9.20	3.533
250.0	13.10	14.97	1.87	22	14.27	0.465	0.206	0.099	14.42	9.35	3.587
500.0	13.30	14.85	1.55	16	14.34	0.417	0.163	0.104	14.30	9.46	3.622
750.0	13.30	14.67	1.37	12	14.27	0.387	0.137	0.112	14.27	9.54	3.644
1,000.0	13.20	14.64	1.44	8	14.20	0.470	0.193	0.166	14.22	9.59	3.656

Table 4. Average long-term salinity distribution/fluctuation of whole Sea of Marmara area incl. Turkish Straits, during summer seasons, in depth basis between years 2010 and 2013.

Beginning Date: **28/02/2010**			Emin: **029° 55.050' E**				Nmin: **37° 13.000' N**				
Ending Date: **27/08/2013**			Emax: **026° 07.000' E**				Nmax: **41° 20.000' N**				
PARAMETER: **SAL ‰**			PROJECT: **MAREM**								
DEPTH. (m)	**MIN.**	**MAX.**	**DIFF.**	**QUAN.**	**MEAN**	**ST.DEV.**	**VAR.**	**SEM.**	**MEAN COR.**	**VOL. AV.**	**VOL. ST.DEV.**
0.5	12.70	25.36	12.66	222	20.50	2.439	5.922	0.164	20.50	20.50	2.439
5.0	13.20	26.30	13.10	222	20.84	2.373	5.605	0.159	20.93	20.67	2.410
10.0	13.90	35.89	21.99	215	21.55	2.688	7.189	0.183	24.12	20.96	2.535
25.0	16.79	38.29	21.50	208	32.55	4.592	20.989	0.318	30.78	23.74	5.871
50.0	27.85	40.22	12.37	126	36.47	2.638	6.905	0.235	35.52	25.36	6.995
100.0	31.10	40.05	8.95	43	36.59	2.558	6.393	0.390	36.93	25.82	7.224
250.0	34.80	40.02	5.22	27	38.06	1.327	1.696	0.255	37.84	26.13	7.390
500.0	36.71	40.19	3.48	20	38.65	1.139	1.233	0.255	38.63	26.36	7.515
750.0	37.71	40.49	2.78	13	39.16	1.017	0.955	0.282	39.07	26.52	7.598
1,000.0	38.05	40.73	2.68	6	39.32	1.097	1.003	0.448	39.28	26.59	7.636

Table 5. Average long-term salinity distribution/fluctuation of whole Sea of Marmara area incl. Turkish Straits, during winter seasons, in depth basis between years 2010 and 2013.

Beginning Date: **28/02/2010**				Emin: **029° 55.050' E**					Nmin: **37° 13.000' N**		
Ending Date: **27/08/2013**				Emax: **026° 07.000' E**					Nmax: **41° 20.000' N**		
PARAMETER: **SAL ‰**				PROJECT: **MAREM**							
DEPTH. (m)	**MIN.**	**MAX.**	**DIFF.**	**QUAN.**	**MEAN**	**ST.DEV.**	**VAR.**	**SEM.**	**MEAN COR.**	**VOL. AV.**	**VOL. ST.DEV.**
0.5	13.00	29.70	16.70	146	22.26	3.006	8.974	0.249	22.26	22.26	3.006
5.0	14.07	29.80	15.73	146	23.09	2.867	8.161	0.237	23.20	22.67	2.962
10.0	14.58	34.78	20.20	144	24.36	3.301	10.824	0.275	25.42	23.23	3.175
25.0	20.14	38.46	18.32	138	29.86	5.764	32.983	0.491	29.72	24.82	4.861
50.0	26.57	39.39	12.82	98	34.78	3.782	14.154	0.382	33.34	26.28	5.882
100.0	26.69	38.90	12.21	32	33.96	4.691	21.314	0.829	34.72	26.62	6.047
250.0	32.00	39.30	7.30	22	36.16	2.582	6.366	0.550	35.66	26.91	6.190
500.0	33.73	39.54	5.81	16	36.38	2.033	3.875	0.508	36.52	27.12	6.283
750.0	34.87	39.80	4.93	12	37.16	1.824	3.050	0.527	37.21	27.28	6.362
1,000.0	35.83	39.98	4.15	8	38.13	1.659	2.409	0.587	37.89	27.39	6.427

The striking feature is that the transition layer is not found at the same depth in the different sections of the Sea of Marmara. If we have to divide the water mass of the Sea of Marmara into four parts from east to west, the transition layer is between 10 and 25 m in the first eastern part; and in the next, it is at 25-50 m; in the third quadrant, it is again found at 10-25 m, and finally, in the outermost section the transition layer reaches the surface in the southern part. The middle transition layer lies about 25-50 m and in the northern part between 10 and 25 m.

Dissolved Oxygen

As usual, the upper layer is well oxygenated relative to the deeper layers. The content of dissolved oxygen (DO) decreases from 5.7 mgL^{-1} at 0.5 m to 2.6 mgL^{-1} at about 50 m in summer (Table 6) and from 7.3 mgL^{-1} at 0.5 m to 3.9 mgL^{-1} at about 50 m in winter (Table 7). The decrease is not always regular. One characteristic feature is an intermediate minimum occurring in the western part of the Sea of Marmara. At the entrance of the Dardanelles, there is an intermediate maximum layer at about 125 to 150 m. The DO content of in moving water is slightly higher than elsewhere in the depths of the Sea of Marmara. The effect can be traced along the southern shore.

Table 6. Average long term dissolved oxygen (mg/l) distribution/fluctuation of whole Sea of Marmara area incl. Turkish Straits, during summer seasons, in depth basis between years 2010 and 2013.

Beginning Date: **28/02/2010** Emin: **029° 55.050' E** Nmin: **37° 13.000' N**
Ending Date: **27/08/2013** Emax: **026° 07.000' E** Nmax: **41° 20.000' N**
PARAMETER: **DO (mg/l)** PROJECT: **MAREM**

DEPTH. (m)	MIN.	MAX.	DIFF.	QUAN.	MEAN	ST.DEV.	VAR.	SEM.	MEAN COR.	VOL. AV.	VOL. ST.DEV.
0.5	2.46	8.89	6.43	222	5.68	1.203	1.441	0.081	5.68	5.68	1.203
5.0	2.25	7.77	5.52	222	5.10	1.128	1.267	0.076	5.15	5.39	1.201
10.0	1.35	7.00	5.65	215	4.71	1.057	1.111	0.072	4.52	5.16	1.198
25.0	0.80	7.22	6.42	208	3.56	1.198	1.429	0.083	3.61	4.78	1.380
50.0	0.14	6.49	6.35	126	2.62	1.371	1.866	0.122	2.61	4.51	1.555
100.0	0.04	4.36	4.32	43	1.64	0.974	0.927	0.149	1.76	4.39	1.638
250.0	0.15	3.47	3.32	27	1.15	0.794	0.607	0.153	1.20	4.30	1.700
500.0	0.02	3.13	3.11	20	0.88	0.891	0.755	0.199	0.97	4.24	1.750
750.0	0.09	3.01	2.92	13	0.97	1.002	0.927	0.278	0.80	4.20	1.778
1,000.0	0.03	1.55	1.52	6	0.36	0.592	0.292	0.242	0.51	4.18	1.796

Table 7. Average long term dissolved oxygen (mg/L) distribution/fluctuation of whole Sea of Marmara area incl. Turkish Straits, during winter seasons, in depth basis between years 2010 and 2013.

Beginning Date: **28/02/2010** Emin: **029° 55.050' E** Nmin: **37° 13.000' N**
Ending Date: **27/08/2013** Emax: **026° 07.000' E** Nmax: **41° 20.000' N**
PARAMETER: **DO (mg/l)** PROJECT: **MAREM**

DEPTH. (m)	MIN.	MAX.	DIFF.	QUAN.	MEAN	ST.DEV.	VAR.	SEM.	MEAN COR.	VOL. AV.	VOL. ST.DEV.
0.5	4.41	9.77	5.36	146	7.52	0.837	0.695	0.069	7.52	7.52	0.837
5.0	3.50	8.90	5.40	146	7.11	0.977	0.949	0.081	7.09	7.31	0.930
10.0	3.10	8.60	5.50	144	6.61	1.096	1.194	0.091	6.41	7.08	1.041
25.0	1.70	7.64	5.94	138	5.32	1.384	1.900	0.118	5.34	6.66	1.361
50.0	1.10	6.66	5.56	98	4.11	1.194	1.411	0.121	4.29	6.29	1.611
100.0	2.02	5.22	3.20	32	3.61	0.910	0.803	0.161	3.40	6.16	1.681
250.0	0.80	4.04	3.24	22	2.27	0.800	0.611	0.171	2.52	6.05	1.790
500.0	1.01	3.81	2.80	16	1.94	0.975	0.891	0.244	1.93	5.96	1.873
750.0	0.80	3.12	2.32	12	1.57	0.882	0.712	0.255	1.54	5.89	1.941
1,000.0	0.38	2.65	2.27	8	1.06	0.808	0.571	0.286	1.19	5.84	1.994

pH Values

pH range, compared to the long-term data of the horizontal and vertical directions, seems to be constant. The average pH mean value ranges from 7.70 to the 7.75 in the upper layer with an average of 7.67, and in the layer under the halocline (approx. 30 m) ranges between 7.69 and 8.05 with an average pH of 7.8 (Table 8-9).

Usually, the alkaline ratios increase direct proportionally depending depth level in the Sea of Marmara. The relative acidity levels are found in the bays mainly with anthropogenic activity in the Sea of Marmara.

Nutrients

The seasonal variability of all the nitrogen compounds was somewhat chargeable, by the presence of many concentration peaks the highest concentrations of nitrate (910.00 μgL^{-1}) in the Sea of Marmara were observed in the winter period at the year of 2010 at 10 metres depth (Table 10), which is explained by the increase in coastal water influx due to rains and decrease in phytoplankton activity.

The observed concentrations of nitrate generally decreased in winter periods and increased in summer with a regular fluctuation in Sea of Marmara. While in winter, concentrations were significantly higher, and their variability was of a stepwise nature. A relatively small increase (up to 63.00 μgL^{-1}) in concentration was observed in 2010. A maximum nitrate nitrogen value was reached at the end of 2010 winter study during stepwise increases in concentrations in the spring and at the end of the summer-to-fall period concentrations of this variable temporarily increased to 395.00 μgL^{-1} (Table. 10).

These concentrations are abnormal even for nearshore surface waters and can be related only to shore outflow.

The type of nitrite variation values (NO_2) was more or less similar to a period in Sea of Marmara. The maximum concentrations of nitrites in Sea of Marmara prove the active mineralization of organic matter.

Table 8. Average long-term pH distribution/fluctuation of whole Sea of Marmara area incl. Turkish Straits, during summer, in depth basis between years 2010 and 2013.

Beginning Date: **28/02/2010** Emin: **029° 55.050' E** Nmin: **37° 13.000' N**
Ending Date: **27/08/2013** Emax: **026° 07.000' E** Nmax: **41° 20.000' N**
PARAMETER: **pH** PROJECT: **MAREM**

DEPTH. (m)	MIN.	MAX.	DIFF.	QUAN.	MEAN	ST.DEV.	VAR.	SEM.	MEAN COR.	VOL. AV.	VOL. ST.DEV.
0.5	6.61	8.99	2.38	222	8.00	0.374	0.139	0.025	8.00	8.00	0.374
5.0	6.51	8.91	2.40	222	8.04	0.363	0.131	0.024	8.03	8.02	0.369
10.0	6.53	8.91	2.38	215	8.03	0.356	0.126	0.024	8.02	8.02	0.364
25.0	6.75	8.94	2.19	208	8.00	0.307	0.094	0.021	8.01	8.02	0.351
50.0	6.80	8.75	1.95	126	8.01	0.319	0.101	0.028	7.98	8.02	0.347
100.0	6.83	8.46	1.63	43	7.88	0.292	0.084	0.045	7.90	8.01	0.346
250.0	7.24	8.42	1.18	27	7.83	0.303	0.088	0.058	7.83	8.01	0.346
500.0	6.44	8.49	2.05	20	7.77	0.529	0.266	0.118	7.82	8.00	0.352
750.0	7.22	8.25	1.03	13	7.89	0.312	0.090	0.087	7.84	8.00	0.351
1,000.0	6.83	8.11	1.28	6	7.80	0.488	0.199	0.199	7.82	8.00	0.352

Table 9. Average long-term pH distribution/fluctuation of whole Sea of Marmara area incl. Turkish Straits, during winter, in depth basis between years 2010 and 2013.

Beginning Date: **28/02/2010** Emin: **029° 55.050' E** Nmin: **37° 13.000' N**
Ending Date: **27/08/2013** Emax: **026° 07.000' E** Nmax: **41° 20.000' N**
PARAMETER: **pH** PROJECT: **MAREM**

DEPTH. (m)	MIN.	MAX.	DIFF.	QUAN.	MEAN	ST.DEV.	VAR.	SEM.	MEAN COR.	VOL. AV.	VOL. ST.DEV.
0.5	6.01	8.80	2.79	146	7.30	0.645	0.413	0.053	7.30	7.30	0.645
5.0	6.20	8.80	2.60	146	7.35	0.599	0.356	0.050	7.35	7.33	0.622
10.0	6.14	8.81	2.67	144	7.39	0.529	0.278	0.044	7.38	7.35	0.593
25.0	6.31	8.10	1.79	138	7.39	0.440	0.192	0.037	7.40	7.36	0.560
50.0	6.45	8.18	1.73	98	7.45	0.433	0.186	0.044	7.43	7.37	0.544
100.0	6.60	8.00	1.40	32	7.44	0.390	0.148	0.069	7.54	7.37	0.538
250.0	7.04	8.38	1.34	22	7.82	0.334	0.106	0.071	7.77	7.39	0.538
500.0	7.09	8.92	1.83	16	8.01	0.504	0.238	0.126	8.00	7.40	0.545
750.0	7.14	9.02	1.88	12	8.17	0.601	0.331	0.173	8.16	7.41	0.553
1,000.0	7.71	9.15	1.44	8	8.27	0.641	0.359	0.227	8.25	7.42	0.561

Table 10. Nutrients' fluctuations based on years and periods 2010 and 2013.

	NO_2^- ($\mu g.L^{-1}$)		NO_3^- ($\mu g.L^{-1}$)		$PO_4 - P$ ($\mu g.L^{-1}$)		$NH_3 - N$ ($\mu g.L^{-1}$)	
	Min.	**Max.**	**Min.**	**Max.**	**Min.**	**Max.**	**Min.**	**Max.**
2010 Winter	1.00 station no:24 0.5 m	8.00 station no:23 0.5 m	63.00 station no:22 10 m	910.00 station no:33 10 m	118.00 station no:19 0.5 m	980.00 station no:1b 0.5 m	30.00 station no:24 0.5 m	830.00 station no:19 0.5 m
2010 Summer	0.04 station no:33 0.5 m	12.10 station no:23 0.5 m	136.00 station no:2 100 m	395.00 station no:6b 30 m	483.00 station no:1b 20 m	525.00 station no:1b 0.5 m	23.20 station no:17 10 m	628.00 station no:33 100 m
2011 Winter	0.41 station no:1b 0.5 m	28.80 station no:40 0.5 m	161.00 station no:6i 10 m	326.00 station no:15 0.5 m	300.00 station no:17 0.5 m	600.00 station no:8 0.5 m	100.00 station no:1i 10 m	391.00 station no:15 10 m
2011 Summer	0.28 station no:3i 0.5 m	21.38 station no:1i 300 m	193.90 station no:23 0.5 m	817.70 station no:1b 50 m	11.160 station no:40 0.5 m	234.70 station no:2 0.5 m	274.20 station no:1b 0.5 m	908.80 station no:5i 50 m
2012 Winter	0.04 station no:19 0.5 m	21.30 station no:12 10 m	41.83 station no:6c 10 m	384.68 station no:23 50 m	39.13 station no:29 0.5 m	285.38 station no:33 10 m	14.568 station no:3 500 m	477.82 station no:23 400 m
2012 Summer	0.04 station no:23 0.5 m	6.86 station no:1i 0.5 m	131.42 station no:40 1000 m	881.42 station no:3 100 m	37.43 station no:40 1000 m	268.42 station no:6 10 m	10.00 station no:40 1000 m	751.80 station no:6c 50 m
2013 Winter	0.04 station no:2 0.5 m	13.377 station no:23 400 m	186.46 station no:23 10 m	665.83 station no:1b 50 m	119.40 station no:17 0.5 m	1560.20 station no:23 10 m	26.816 station no:2 50 m	2413.40 station no:38 10 m
2013 Summer	0.04 station no:19 0.5 m	4.072 station no:1b 50 m	131.42 station no:40 900 m	603.44 station no:6b 0.5 m	99.735 station no:40 900 m	418.37 station no:38 0.5 m	108.60 station no:23 0.5 m	2309.60 station no:38 10 m

Ammoniacal nitrogen was characterized by a similar variability (the winter maximum gradually gives way to the summer decrease in concentrations). The annual trend of ammoniacal nitrogen had no significant changes (Table. 10).

Especially during the winter period, when consumption of phosphate was insignificant, the concentration fluctuated to 37.43 μgL^{-1} (Table. 10). Exhaustion of phosphate in the summer period in 2010-2013 coincides with such seasonal features as a lack of precipitation and absence of intensive mixing. Only by the end of the summer period did the concentration of phosphates see an increase. While the seasonal trend in Sea of Marmara consisted of many concentration peaks, they are more pronounced in the Sea of Marmara. Phosphate background was significantly higher here as well, most likely a result of a large quantity of organics in the intake of the Sea of Marmara and hindered water exchange.

Analysis of the inter-annual distribution of phosphorus shows a gradual increase in concentrations. Abnormal peaks (525.00 μgL^{-1}) of phosphorus were observed in 2010 summer study. In the same periods, the contents of nitrate (395.00 μgL^{-1}) and ammonia (628.00 μgL^{-1}) were very high. Such abnormal peaks are most likely the result of waste water that pollutes the Sea of Marmara inflow, since at this time meteorological cataclysms take place, *e.g.* local floods and waterspouts damaging the coast. A comparison of phosphate concentrations in the summer period in 2010-2013 suggests a general tendency towards an increase in phosphate concentration from year to year (Table. 11).

Table 11. Mean Nutrient values basis on years and seasons between 2010 and 2013.

	NO_2^- ($\mu g.L^{-1}$)	**NO_3^- ($\mu g.L^{-1}$)**	**$PO_4 - P$ ($\mu g.L^{-1}$)**	**$NH_3 - N$ ($\mu g.L^{-1}$)**
2010 Winter	2,07	518,42	516,67	350,56
2010 Summer	1,96	187,81	498,00	371,74
2011 Winter	3,59	245,78	382,64	260,59
2011 Summer	3,84	265,91	125,22	502,33
2012 Winter	4,37	210,00	99,62	282,40
2012 Summer	1,26	416,95	152,18	254,73
2013 Winter	2,26	314,01	429,71	737,46
2013 Summer	0,55	425,10	172,39	655,31

NO_2-N concentration: The earliest observed NO_2-N concentrations where the mean concentration between 2010 and 2011 was 2.86 μgL^{-1} (Table. 11) and the concentration had increased by the mid-2011's to 3.839 μgL^{-1}; this was followed by a slight, but statistically significant, decrease to 0.548 μgL^{-1} by 2012–2013 in the Sea of Marmara (Figure 2).

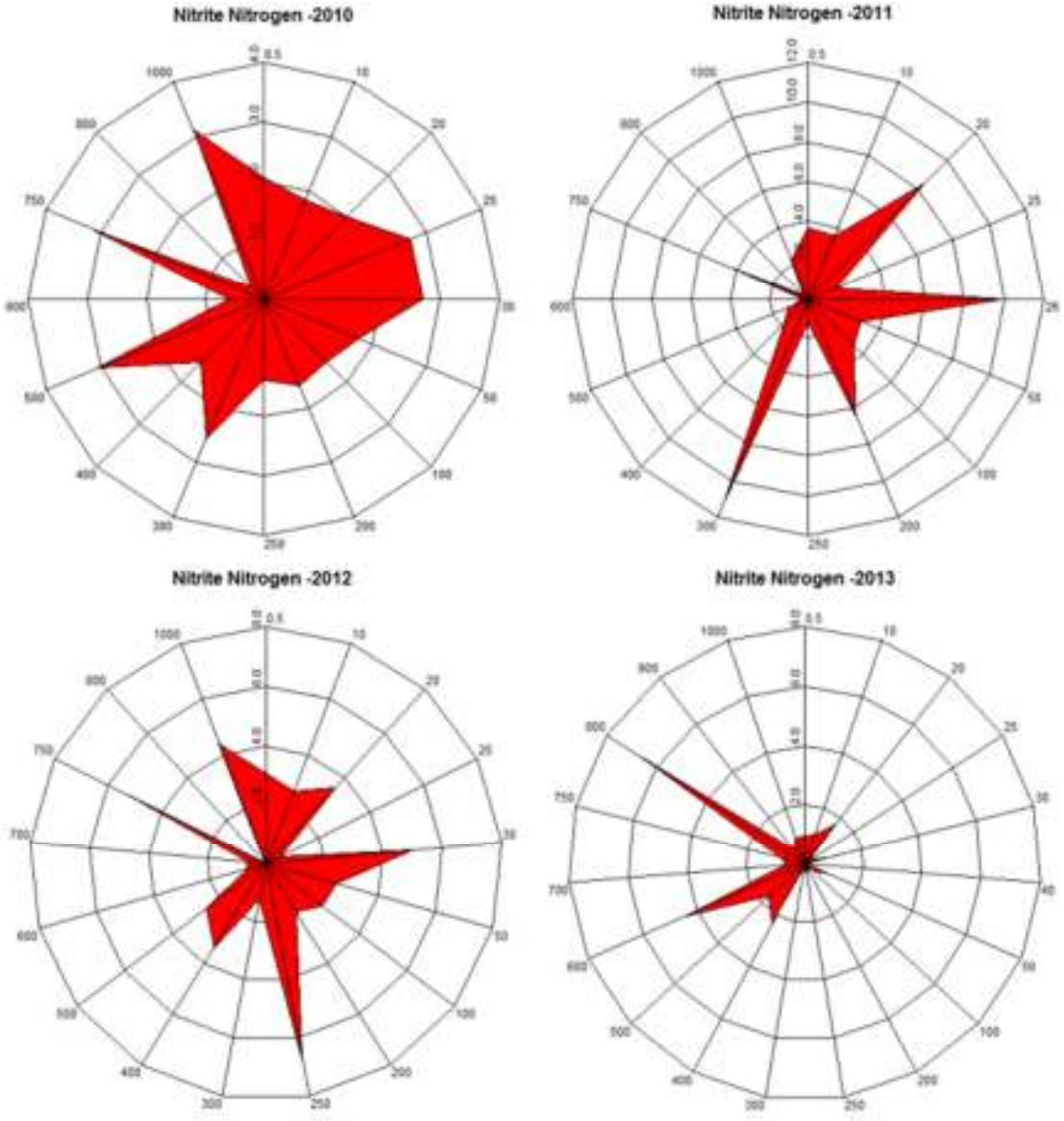

Figure 2. Average long-term nitrite nitrogen distribution/fluctuation of whole Sea of Marmara area incl. Turkish Straits, in depth basis between years 2010 and 2013.

The mean ratio fluctuates between a maximum value of 4.51 μgL^{-1} in the Mediterranean Sea originated lower layer, with the other words under the pycnocline, with a mean salinity of 38‰, in 900 m depth and with a minimum value of 0.57 μgL^{-1} in upper, Black Sea originated water mass, in depth of 26 m, in a converse manner, between years 2010 and 2013 (Table. 12).

Mean NO_2-N (μgL^{-1}) value fluctuations against salinity (‰Sal) between 2010 and 2013 are given in Figure. 3.

NO_3-N concentration: The development of the NO_3-N concentration in the Sea of Marmara between 2010 and 2013 is quite uniform with a minimum mean concentration of 213.12 μgL^{-1}, and with a maximum mean concentration of 502.5 μgL^{-1} in the Black Sea originated water.

(Figure 4). The deeper sections below 50 m, in other words; the layer under the halocline, have a semi-constant mean value in a range of 179.37 μgL^{-1} and 534.33 μgL^{-1}(Table. 12).

Table 12. Mean nutrient values based on layers (upper and lower) between years of 2010 and 2013.

		2010		2011		2012		2013	
		Winter	**Summer**	**Winter**	**Summer**	**Winter**	**Summer**	**Winter**	**Summer**
NO_2-N ($\mu g.L^{-1}$)	Upper Layer	2.14	2.09	3.85	4.26	3.95	0.90	1.48	0.46
	Lower Layer	1.99	1.91	3.32	3.69	4.51	1.37	2.73	0.57
NO_3-N ($\mu g.L^{-1}$)	Upper Layer	502.5	213.12	241.78	237.81	221.03	333.16	335.82	353.36
	Lower Layer	534.33	179.37	249.78	275.27	206.31	442.73	307.29	445.59
PO_4-P ($\mu g.L^{-1}$)	Upper Layer	516.83	504	381.94	119.40	98.11	163.42	473.60	210.09
	Lower Layer	516.5	486	383.33	127.15	100.12	150.10	416.2	161.61
NH_4-N ($\mu g.L^{-1}$)	Upper Layer	378.89	298.62	261.5	348.04	243.23	220.52	396.18	804.32
	Lower Layer	322.22	396.12	259.67	553.75	295.45	265.26	438.67	494.79

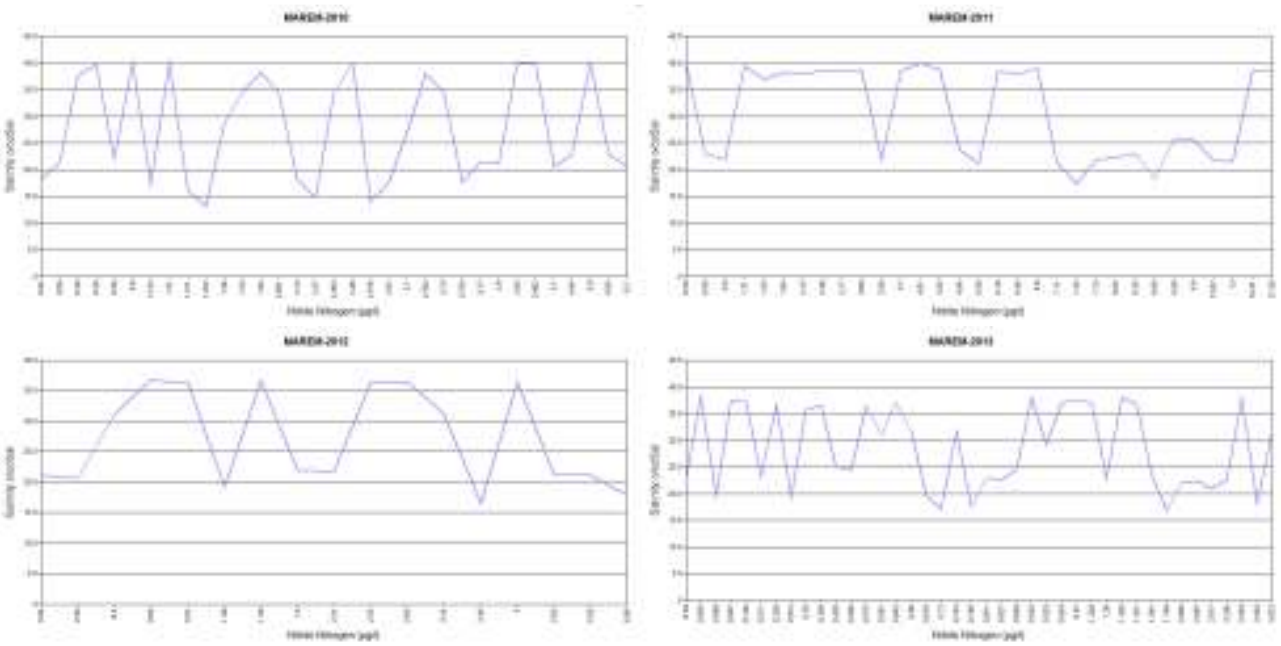

Figure 3. Average long-term nitrite nitrogen - salinity distribution/fluctuation of whole Sea of Marmara area incl. Turkish Straits, in depth basis between years 2010 and 2013.

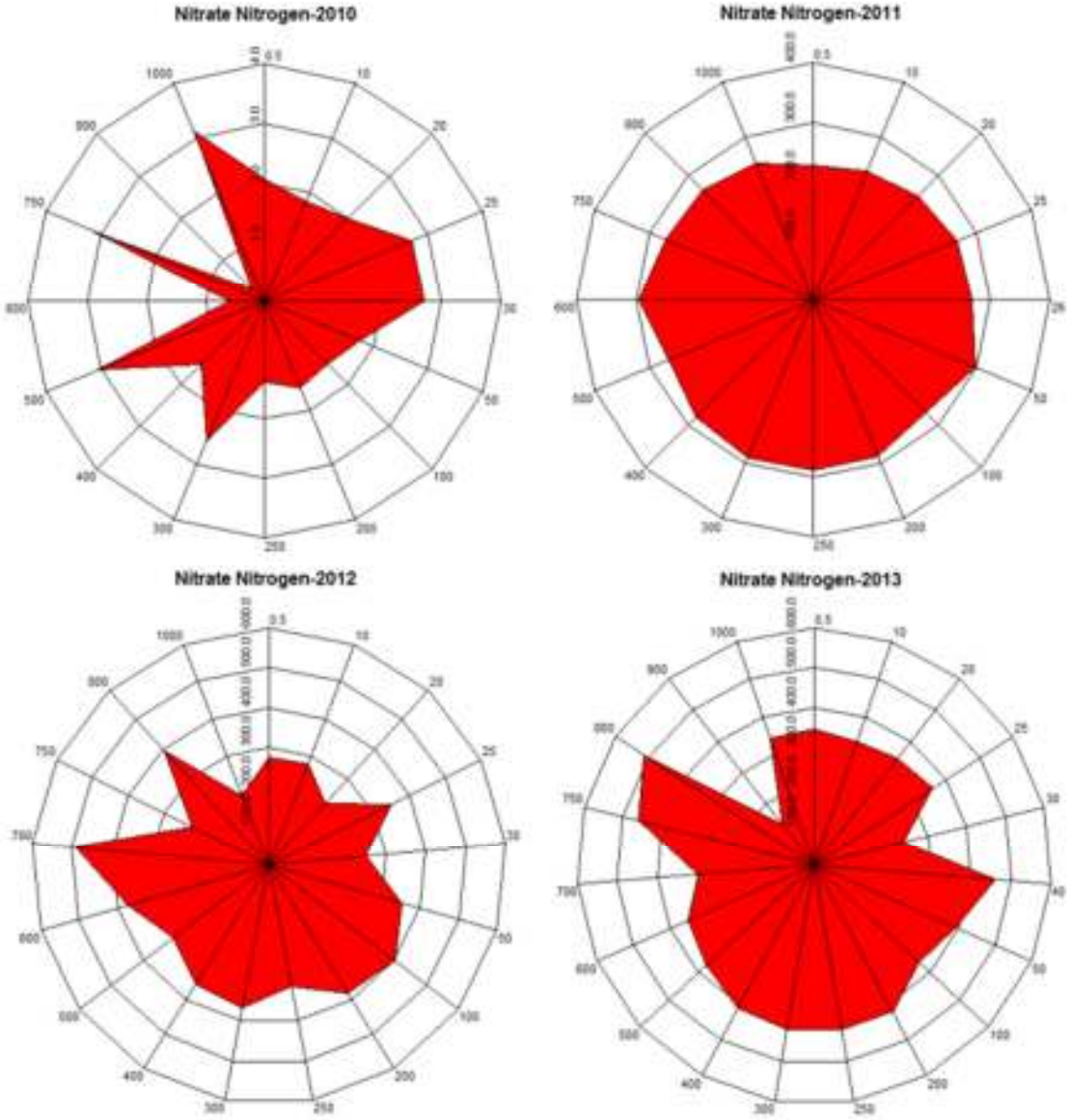
Nitrate Nitrogen-2010
Nitrate Nitrogen-2011
Nitrate Nitrogen-2012
Nitrate Nitrogen-2013

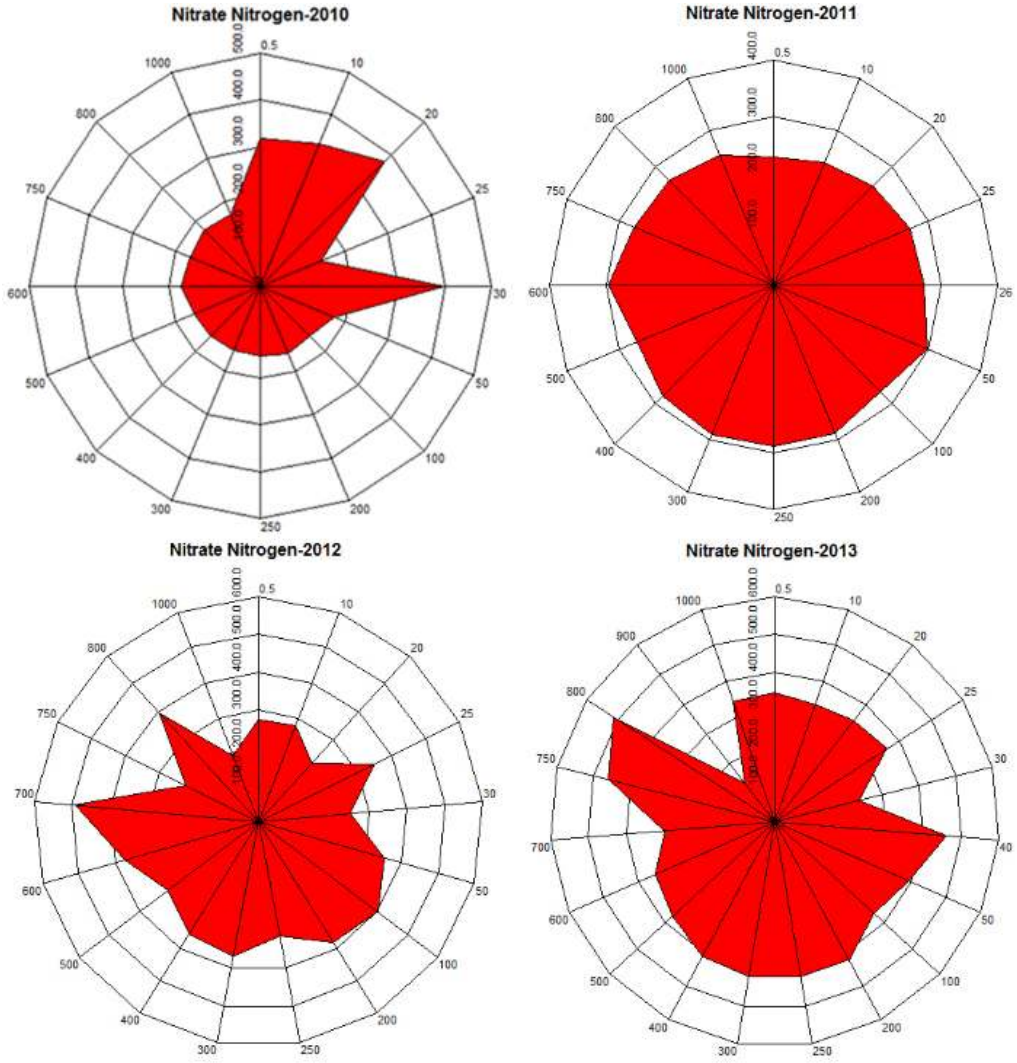

Figure 4. Average long-term nitrate nitrogen distribution/fluctuation of the whole Sea of Marmara area incl. Turkish Straits, in depth basis between years 2010 and 2013.

Regarding the measurements in the period of 2010 and 2013, a regular time-dependent change of the development of the NO_3-N concentration in either layer can be mentioned. Mean NO_3-N (μgL^{-1}) value fluctuations against Salinity (‰Sal) between 2010 and 2013 are given in Figure 5.

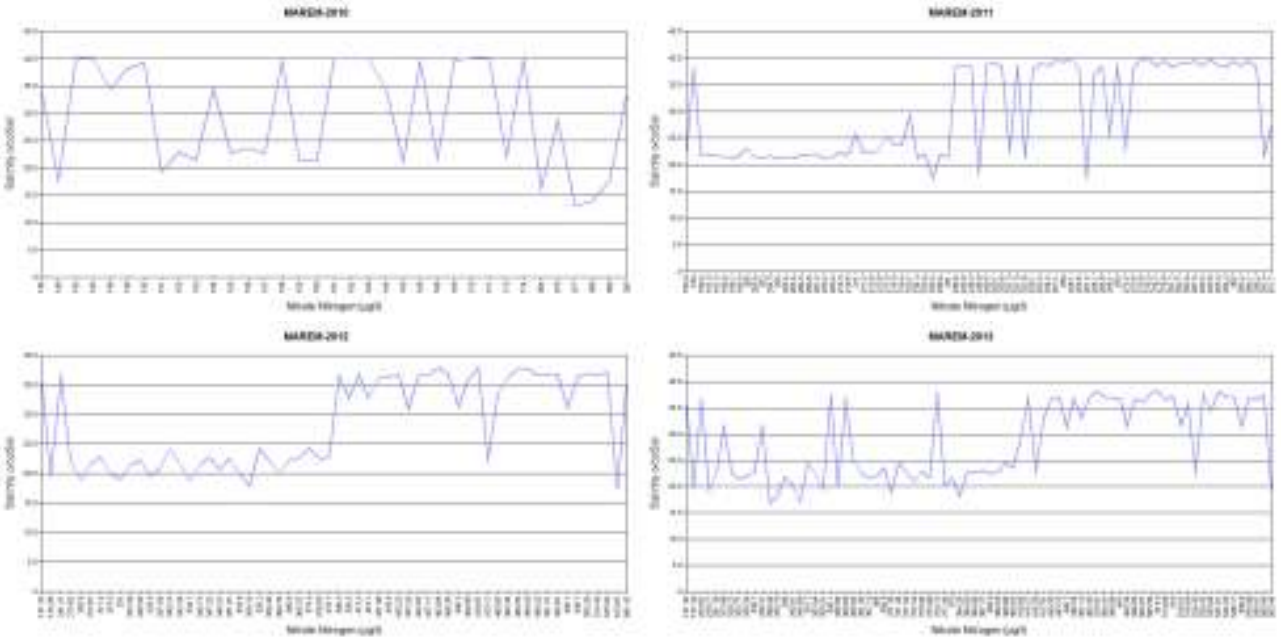

Figure 5. Average long-term nitrate nitrogen - salinity distribution/fluctuation of whole Sea of Marmara area incl. Turkish Straits, in depth basis between years 2010 and 2013.

NH_4-N concentration: Throughout the study period, the mean concentration of NH_4-N between 2010 and 2011 was 371.30 μgL^{-1}, increasing to 482.47 μgL^{-1} in the 2012–2013 period as an average value for the whole Sea of Marmara (Table. 11) (Figure 6).

The mean ratio fluctuates between a maximum value of 553.75 μgL^{-1} in the Mediterranean Sea originated lower layer, with the other words under the pycnocline, with a mean salinity of 38‰, in 900 m depth and with a minimum value of 259.67 μgL^{-1} in upper, Black Sea originated water mass, in depth of 26 m, in a converse manner (Figure 6) (Table. 12).

Mean NH_4-N (μgL^{-1}) value fluctuations against Salinity (‰Sal) between 2010 and 2013 are given in Figure 7.

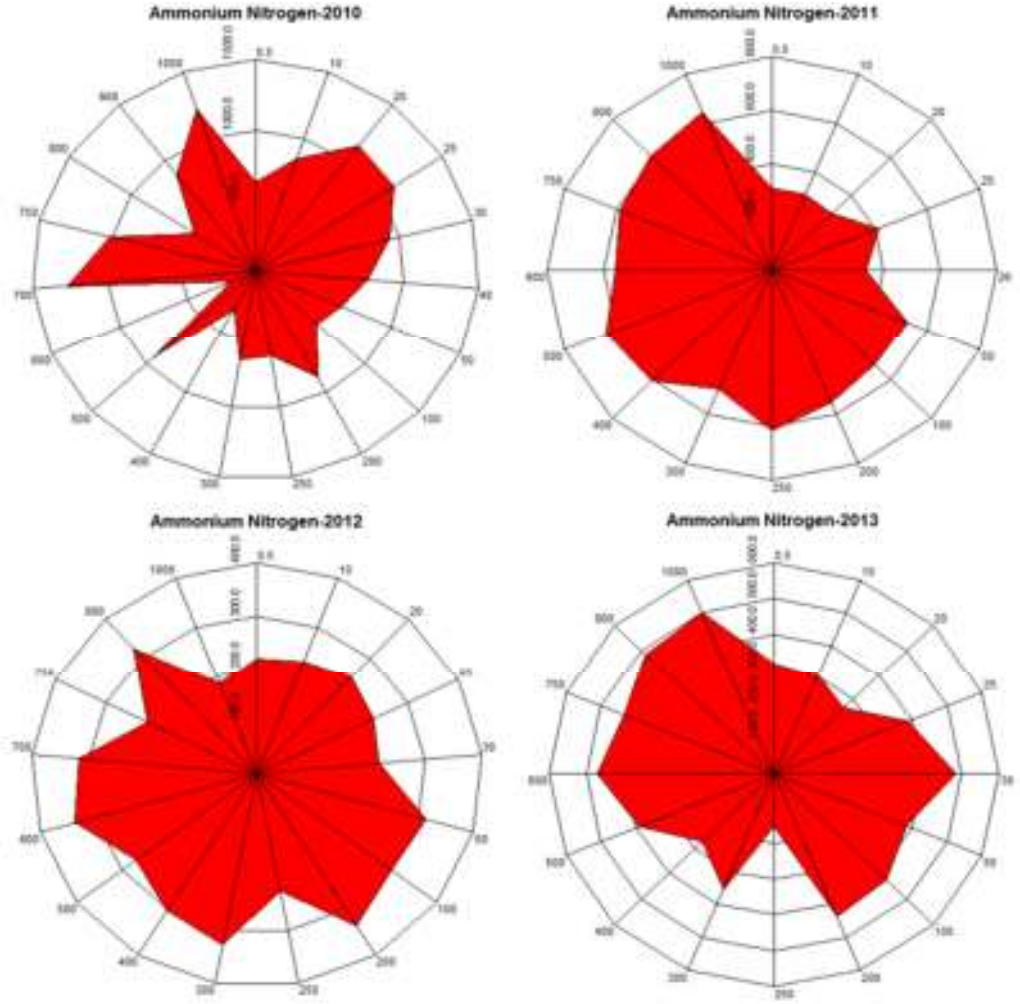

Figure 6. Average long-term ammonia nitrogen distribution/fluctuation of the whole Sea of Marmara area incl. Turkish Straits, in depth basis between years 2010 and 2013.

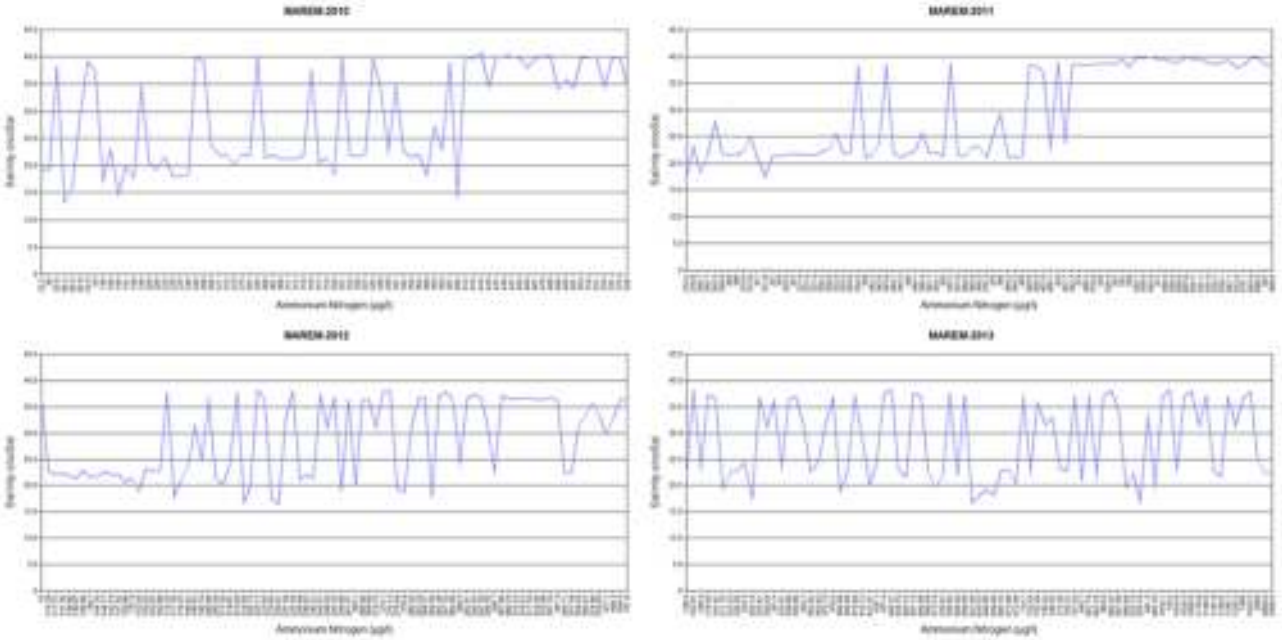

Figure 7. Average long-term ammonia nitrogen - salinity distribution/fluctuation of whole Sea of Marmara area incl. Turkish Straits, in depth basis between years 2010 and 2013.

Also, the upper layer comprises a mean maximum of 804.327 μgL^{-1} and a mean minimum of 220.52 μgL^{-1}, whereas the lower layer with a mean maximum of 553.755μgL^{-1} and a mean minimum of 259.67 μgL^{-1} (Table. 12)

PO_4-P concentration: The PO_4-P ratio shows an extraordinary dispersion in the Sea of Marmara with all sub-regions including bays and straits and water masses. The PO_4-P mean ratio is remained with minimum 98.11 μgL^{-1}, winter 2012, and with a maximum 516.83 μgL^{-1}, in winter 2010, in the Black Sea originated upper layer with average salinity of 28‰; whereas with minimum 100.12 μgL^{-1} in winter 2012, and with a maximum 516.50 μgL^{-1}, in winter 2010, below the pycnocline in the Mediterranean originated water mass with a mean salinity of 38‰ throughout the study period (Figure 8) (Table. 12).

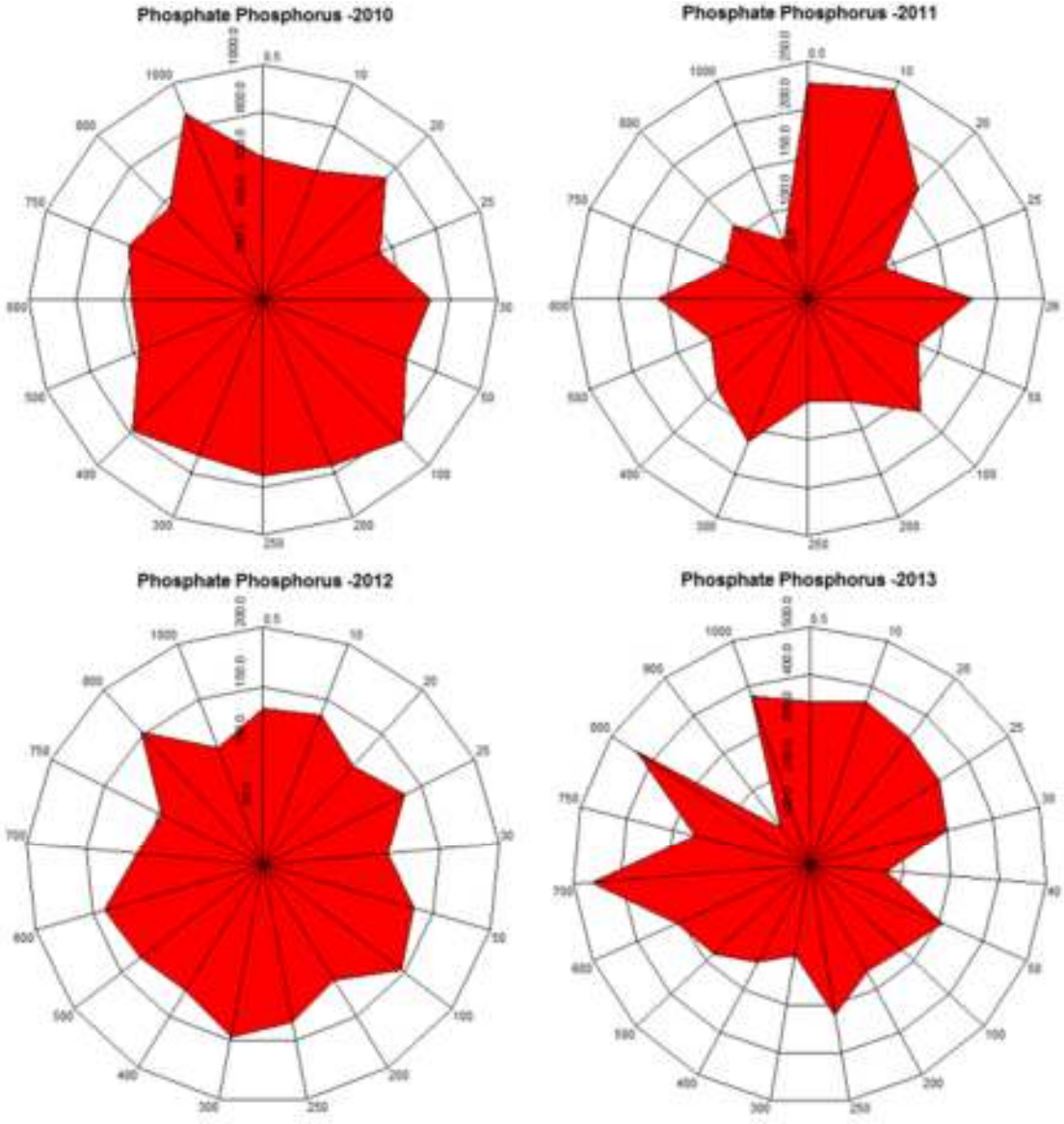

Figure 8. Average long-term phosphate phosphorus distribution/fluctuation of the whole Sea of Marmara area incl. Turkish Straits, in depth basis between years 2010 and 2013.

Mean PO_4-P (μgL^{-1}) value fluctuations against Salinity (‰Sal) between 2010 and 2013 are given in Figure 9.

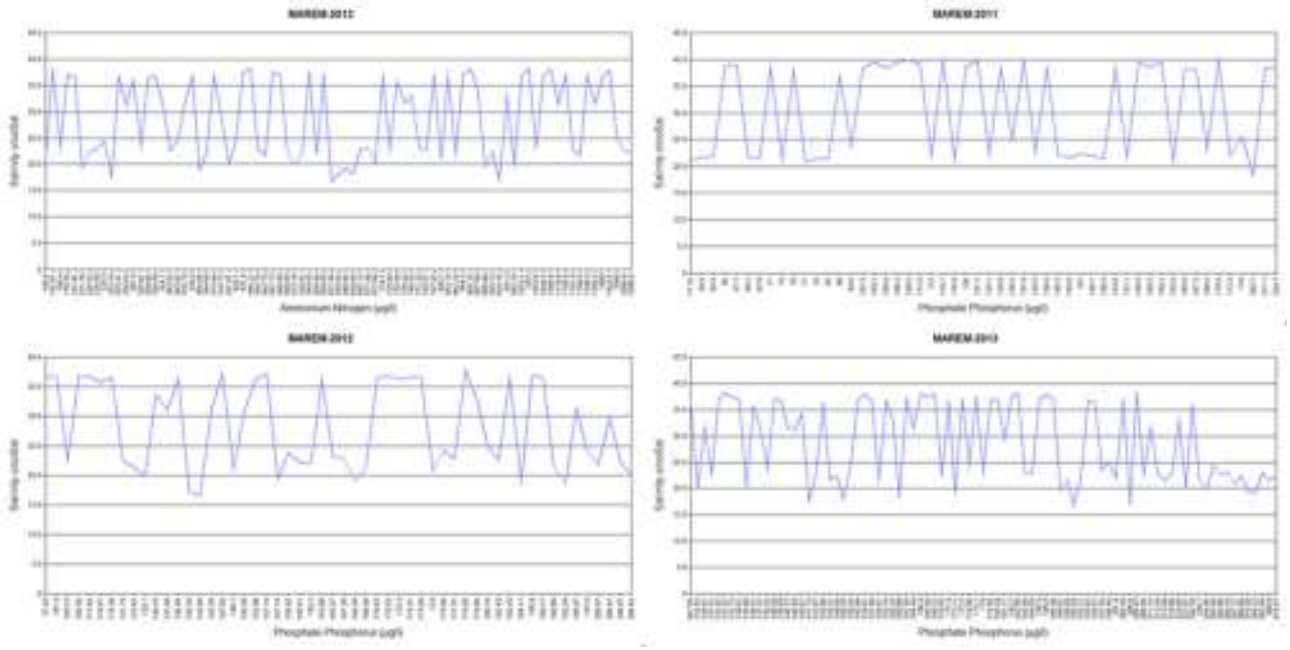

Figure 9. Average long-term phosphate phosphorus- salinity distribution/fluctuation of whole Sea of Marmara area incl. Turkish Straits, in depth basis between years 2010 and 2013.

DISCUSSION

The Sea of Marmara has unique hydrodynamic features, which connect it to the Mediterranean Sea via Dardanelles and to the Black Sea via Bosphorus.

The Sea of Marmara receives heavy inputs of municipal and industrial wastewater from Istanbul and adjacent populated areas around the region. Significant industrial wastewater and more amount of municipal wastewater still enter unthreatened. Especially critical areas, which receive wastes from Turkey's major industrial centres, are in need of stronger pollution control measures including İzmit and Gemlik Bays.

The major pollution source here and in the Straits are the release of wastewaters without any treatment via "deep sea discharges" with the principal to use the below water mass, that flows from the Aegean Sea to the Black Sea, as a conveyor. However, the whole Sea of Marmara behaves as a semi-enclosed system, retaining most of the substances arriving there. It is caused by three factors: the morphology of the straits, bi-directional current event, and the dominating wind regime **(3)**.

Water quality and biodiversity along Sea of Marmara coastline is under heavy pressure from extensive domestic and industrial wastewater inflow, and from intensifying the development of uniquely and fragile areas for maritime transport based landing facilities and power plants.

On the other hand, especially in narrow and shallow thresholds such as Turkish straits with several points with strong divergence and convergence mixture points, that raids the density differences and enables mixture **(3)**.

It should be noted that almost all sea currents flow in circular direction because of the Coriolis force effect. However, the outflow from the Black Sea basin is a function of its water budget and carry runoff from the large rivers and surface waters run into the Black Sea and forces the flux to the north-west direction, and on the contrary, the below flux is a function of density of Mediterranean-originated heavy saline water that flows to the opposite direction. They are both directional fluxes.

The DO content of the deeper waters (under the pycnocline layer) of the Sea of Marmara is dramatically low. This is most probably due to the increased pollution caused by the discharge of the sewages under the pycnocline layer without any treatment and by the great difference in density between the surface layer and the deeper waters, which impedes convection.

The concentrations of the nutrients (phosphate, nitrate, nitrite, ammonium, *etc*.) are the main limiting factors for the primary productivity. Concentration and depth (*i.e.,* origin of the water mass) during mid and late winter, when the phytoplankton standing stocks are their lowest levels nutrients reach high values trough out the winter water column. The highest phosphate and nitrate in the waters of the area is also attributed to the runoff from Black Sea Rivers which occupies the surface layers.

Very large changes take place as the surface waters are warmed and by the growth of plant life and phytoplankton blooms in spring. The nutrient concentrations decrease rapidly during the summer months, where concentrations of nutrients at the surface layers fall to very low values, but the levels below the thermocline are maintained or may be somewhat increased.

A calculation of primary productivity from the concentrations of nutrients in the seawater cannot be applied to the whole working area, due to horizontal irregularities in the distribution of these values. (As shown in Figures 2-8 of the present paper) Another obstacle for such a calculation will be the anthropogenic impact on the marine environment regarding the concentrations of the nutrients. This impact can be clearly traced southwards of the Sea of Marmara, including the impact area of mega city Istanbul. The effect is prominent in the south of Bosphorus and in the Izmit Bay where the nutrients are in excess of that required by marine life, causing heavy eutrophication in this water. Because of heavy sewage load to the strait a rapid increase in nutrient content has been observed in the waters of Sea of Marmara.

Changes in the concentration of PO_4 in the different layers of the Sea of Marmara are striking. As will be clearly seen the average concentration of PO_4 has about four times increased in

between 2012 winter and 2013 winter period (Table. 10). Changes which is about 12 times at phosphate concentration is not only at different layers but also at the same water masses and same period with a value of 142.070 $\mu g.L^{-1}$ at the 2013 summer study and 11.160 $\mu g.L^{-1}$ at 2011 summer study(station 40 surface water) Table 8.

Therefore, nutrient surveys in the waters of the Sea of Marmara should take the anthropogenic nutrient load into consideration to explain the anomalies in nutrient distribution. As it has been suggested by several authors for similar conditions, the dissolved oxygen content of the water column may be used for calculation of the primary production. For the primary productivity, vertical mixing of the water layers of the Sea of Marmara is more important than the strength of the of the Black Sea current to the straits limiting the distribution of nutrients and as well as the distribution of the dissolved oxygen content.

Same trends may be observed in the nitrogen concentrations in the area. The periodical increases of the NO_3 may be an explanation for the progressively and dense red-tide in the Sea of Marmara.

Except red-tide concentrations of *Noctiluca scintillans* (Macartney) Kofoid & Swezy, 1921 at the surface, the highest accumulations of planktonic organisms are found at the pycnocline (on whole isopycnal zone), which may be observed on echograms **(5)**.

The unaffected mass of water, which occupies all depths below 200 m in the Sea of Marmara, has a constant average temperature of 14.2°C, without any seasonal variations **(3-5, 12)**.

CONCLUSIONS

Excess nutrient inputs lead to eutrophication and degradation of the aquatic system. Depending on the distribution of the nutrient salt concentrations, clear signs of eutrophication can be seen in the Sea of Marmara proper.

In general -although with some exceptions due to biochemical processes- nutrients have a conservative relationship with salinity, so their concentrations are lower when salinity levels are higher.

Regarding to the complex, two-layer system of the Sea of Marmara, the concentration of nutrients in the both layers fluctuates simultaneously with a decrease in oxygen concentrations and increases in the salinity, depending on the distance to the origin of the water masses such as low salinity/density of Black Sea water and high salinity/density Mediterranean water.

In the previous studies, the low salinity water that flows from the Black Sea were presented as the reason for a possible load of the additional nutrient amount to the Sea of Marmara via Bosphorus. This led to different and wrong interpretations.

However, the real reason of fluctuating distribution ranges of nutrients in different parts of the Sea of Marmara waters is the underlying cause of the unique hydrographical conditions of the Sea of Marmara.

As lower-salinity waters remain confined in the upper part of the water column, the higher nutrient concentrations are generally located in the surface layers. Pollutants follow a similar pattern. As in the case of the Sea of Marmara, discharges without any treatment to the below and dense water mass are affecting the whole water column of different degrees, regarding the density equivalency.

Also the 3 basins with more than 1000 m depth with the position each one of the other, located in a course under main and both direction water masses, acts as a sink for waterborne particles (Sediments, nutrients and pollutants), most of which remain trapped there.

This picture indicates that a considerable accumulation of trapped dangerous particles, must be taking place in the Sea of Marmara sediments.

As previously mentioned as biological view **(3)** it clearly appears as a result of the steady erosion of biodiversity of the Sea of Marmara, in last two decades.

ACKNOWLEDGMENTS

The authors would like to state that the MAREM project would not have been possible without the kind support of the Sevinç-Erdal İnönü Foundation and the project crew: we thank them sincerely for their help. Thanks are also due to Bülent Artüz, especially for modelling, programming, and database facilities of Hidro-QL software.

REFERENCES

1. Rangin C, Demirbağ E, İmren C, Crusson A, Le Picon X, Şengör A. Marine Atlas of the Sea of Marmara (Turkey): data collected on Board R.V. Le Suroit. Brest, France: Ifremer; 2000.

2. Artüz İ, Baykut F, Aydın A. Scientific Aspects of the Black Sea. İstanbul: Istanbul University; 1982.

3. a) Artüz ML, Okay I, Mater B, Artüz OB, Gürseler G, Okay N. Bilimsel Açıdan Marmara Denizi. Türkiye Barolar Birliği Yayınları. 2007;119. b) Artüz ML, Artüz OB, Aydemir A, Sönmez B, Özel D, Öztaş G, et al. Marmara Denizi'nin Değişen Oşinografik Şartlarının İzlenmesi Projesi 2007 Yaz Ayağı, 2007 Temmuz-Ağustos dönemi Hidrografik, Biyolojik, Klimatolojik istasyon çalışmaları. İstanbul: T.C. Kültür Üni. Yayını; 2008. 107 p. (Kitap No: 82). c) Artüz ML, Gülen D, Aydın A, Yalçın B, Artüz OB, Gürseler G, Bargu S, Koç

Torcu H, et al. Marmara Denizi'nin Değişen Oşinografik Şartlarının İzlenmesi Projesi (MAREM) 2011 senesi çalışma verileri (Ön Raporlar). İstanbul: Marmara Üniversitesi; 2011 256 p. (Kitap No: 803)

4. Artüz M, Artüz O, Gülen D, Torcu K, Üzen E, Aydemir A, et al. MAREM 2008 araştırma raporları: Marmara Denizi'nde Değişen Oşinografik Koşullar. İstanbul: T.C. Piri Reis Üniversitesi; 2009.

5. a) (Artüz 2010a) Artüz ML, Artüz OB, Aydın A, Gülen D, Koç H, Akdemir D, et al. Marmara Denizi'nin Değişen Oşinografik Şartlarının İzlenmesi Projesi (MAREM) 2009 senesi çalışma verileri (Ön Raporlar). İstanbul: Marmara Üniversitesi; 2010. 271 p. (Kitap No: 799). b) Artüz ML, Gülen D, Aydın A, Yalçın B, Artüz OB, Gürseler G, Sakınç M, Demir G, et al. Marmara Denizi'nin Değişen Oşinografik Şartlarının İzlenmesi Projesi (MAREM) 2012 senesi çalışma verileri (Ön Raporlar). İstanbul: Sevinç – Erdal İnönü Vakfı; 2012 158 p. (Kitap No: 803) c) Artüz ML, Artüz OB, Gürseler G, Gülen D, Sakınç M, Yalçın B, et al. Marmara Denizi'nin Değişen Oşinografik Şartlarının İzlenmesi Projesi (MAREM) 2013 senesi çalışma verileri (Ön Raporlar) 2013 Kış ve Yaz Dönemi Oşinografik-Hidrografik-Biyolojik-Kimyasal-Sedimantolojik Klimatolojik-Mikrobiyolojik İstasyon Çalışmaları. Ankara: Türkiye Barolar Birliği; 2014. 171 p. (Kitap No: 252)

6. Wetzel R, Likens G. Inorganic nutrients: nitrogen, phosphorus, and other nutrients. In: Limnological Analysis. New York, USA: Springer; p. 85–111.

7. Ergin M, Bodur MN, Ediger D, Ediger V, Yilmaz A. Organic carbon distribution in the surface sediments of the Sea of Marmara and its control by the inflows from adjacent water masses. Marine Chemistry. 1993 Feb;41(4):311–26.

8. Polat S, Tuğrul S, Çoban Y, Baştürk O, Salihoğlu İ. Elemental composition of seston and nutrient dynamics in the Sea of Marmara. Hydrobiologia. 363(1):157–67. URL: http://link.springer.com/article/10.1023/A:1003117504005.

9. Tugrul S, Besiktepe T, Salihoglu I. Nutrient exchange fluxes between the Aegean and Black Seas through the Marmara Sea. Mediterranean Marine Science [Internet]. 2002 Jun 1 [cited 2016 Oct 15];3(1). Available from: http://www.medit-mar-sc.net/index.php/marine/article/view/256.

10. Artüz B. Hidro-QL, Hydrobiological-Oceanographical Management Software and Database. İstanbul: MAREM; 1990.

11 Apha A. WEF (2005) Standard methods for the examination of water and wastewater. American Public Health Association, American Water Works Association, and Water Environment Federation. 2005.

12. (Artüz 2010b) Artüz M, Artüz O, Aydın A, Gülen D, Koç H, Yalçın B, et al. Marmara Denizi'nin Değişen Oşinografik Şartlarının İzlenmesi Projesi (MAREM) 2010 senesi çalışma verileri (Ön Raporlar). İstanbul: Marmara Üniversitesi; 2010. 306 p.

Türkçe Öz ve Anahtar Kelimeler

Nutrition Profile of the Sea of Marmara Between Years 2010 and 2013

Bahattin Yalçın, Umut E. Yılmaz and M. Levent Artüz

Öz: Marmara Denizi'nde beslenme yükünü tayin etmek için, 25 istasyonda örneklemeler yapılmış ve yüzeyin standart dikey bölgelerinden istasyonun en derin noktasına kadar örnek alınmıştır. Örneklemeler 2010 ve 2013 yılları arasında yılda iki kere yapılmıştır. Nitrat azotu, nitrit azotu, amonyum azotu ve fosfat fosforu süzülmemiş su örneklerinde analiz edilmiştir; buna ilave olarak, tuzluluk, sıcaklık, çözünmüş oksijen ve pH gibi önemli roller oynayan bazı fizikokimyasal parametreler de her istasyonda ölçülmüştür.Bu çalışma Marmara Denizi'ndeki besleme yükünü, bu besleyicilerin durumu üzerine öncül değerlendirme olarak bildirmekte ve Marmara Denizi'nin benzersiz oşinografik durumu hakkında kısa bir tartışma sunmaktadır.

Anahtar kelimeler: Marmara Denizi; besleyici; piknoklin; termoklin; haloklin; kirlilik.

Sunulma: 5 Mayıs 2016. **Düzeltme:** 31 Mayıs 2016. **Kabul:** 13 Ekim 2016.

JOTCS Journal of the Turkish Chemical Society Section: A Chemistry
TURKISH CHEMICAL SOCIETY

Comparison of Catalytic Activities both for Selective Oxidation and Decomposition of Ammonia over Fe/HZβ Catalyst

Yeliz Durak-Çetin[1,2*], Alper Sarıoğlan[1], Hasancan Okutan[2]

[1] TÜBİTAK Marmara Research Center, Energy Institute, P.O.21, 41470, Gebze/KOCAELI, TURKEY
[2]Faculty of Chemical and Metallurgical Engineering, Istanbul Technical University, 34469, Maslak/ISTANBUL, TURKEY

Abstract: Ammonia is one of the syngas contaminants that must be removed before using the syngas downstream applications. The most promising hot-gas clean-up techniques of ammonia are selective catalytic oxidation (SCO) and catalytic decomposition. In this study, the catalytic activities over Zeolite Hβ-supported iron catalyst (Fe/HZβ) were compared both for the two catalytic routes. For SCO experiments, temperature (300-550 °C), O_2 (2000-6000 ppmv) and (0-10%) H_2 concentrations were investigated with the presence of 800 ppm of NH_3 in each final gas mixture. In the second route, catalytic ammonia decomposition experiments were carried out with H_2 in balance N_2 (0-30%) containing 800 ppm of NH_3 at 700 °C and 800 °C. In the SCO, NH_3 conversions were increased with increasing reaction temperatures with the absence of H_2 in the reaction mixture. With 10% H_2, it was shown that NH_3 conversions increased with decreasing the reaction temperature. This was interpreted as the competing H_2 and NH_3 oxidations over the catalyst. On the other hand, in the catalytic decomposition, thermodynamic equilibrium conversion of almost 100% was attained at both 700 and 800 °C. Upon H_2 addition, all conversions decreased. The decrease in conversion seemed to be linear with inlet hydrogen concentration. Hydrogen was seen to inhibit the decomposition of ammonia. It was shown that Fe/HZβ catalyst is better to use for catalytic decomposition of NH_3 in syngas rather than SCO of NH_3 in spite of higher reaction temperatures needed in the decomposition reaction.

Keywords: Ammonia; decomposition; selective catalytic oxidation (SCO); hot-gas clean-up.

Submitted: July 01, 2016. **Revised:** November 11, 2016. **Accepted:** November 18, 2016.

Cite this: Durak-Çetin Y, Sarıoğlan A, Okutan H. Comparison of Catalytic Activities both for Selective Oxidation and Decomposition of Ammonia over Fe/HZβ Catalyst. JOTCSA. 2017;4(1):227–42.

DOI: To be assigned.

*Corresponding author. E-mail: yeliz.durak@tubitak.gov.tr

INTRODUCTION

Gasification is a thermochemical conversion technology applied for the production of synthetic fuels and chemicals from coal and biomass. A syngas containing H_2 and CO is released as a result of gasification reactions [1]. The integrated gasification combined cycle (IGCC) uses the syngas to meet heat and power demand. Synthetic fuels and chemicals are catalytically produced from this syngas through the Fischer-Tropsch (FT) process as well. Before FT reaction, the syngas should be cleaned to remove all nitrogenous (NH_3, HCN) and sulfurous (H_2S, COS) pollutants in ppm level, otherwise they lead to the poisoning of the FT catalysts shortly [2-3]. While NH_3 concentrations can be reached up to 10000 ppmv in syngas as a function of the nitrogen content of the solid fuel [4], its threshold level is below 1 ppmv [5]. NH_3 removal can be achieved via three different ways; scrubbing, thermal incineration, and catalytic routes. In the scrubbing as a wet process, the waste gas is washed with a chemical solution and it is necessary to treat the waste water later. In the thermal incineration, ammonia is thermally burnt and NO_x is formed. In the catalytic processes; NH_3 is passed through a column packed with a catalyst. In the one way of catalytic routes, NH_3 in the syngas can oxidatively be converted into harmless nitrogen and water in an exothermic manner. This process is called as selective catalytic oxidation (SCO). In the second way of the catalytic route, NH_3 can be decomposed into hydrogen and nitrogen via the non-oxidative endothermic reaction (Reaction 1) [6].

$$2NH_3 \leftrightarrow N_2 + 3H_2 \qquad \text{(Eq. 1)}$$

Catalytic decomposition of ammonia occurs on a variety of transition metals and natural minerals. Many metals, mainly Fe, Co, Ni, Ru, Rh, Pd, Os, Ir, Pt, W, and Cu, have been tested for ammonia decomposition and it was found that ruthenium is the most active among them [7,8]. The cost of ruthenium is a major concern for commercial utilizations. Therefore, iron based catalysts have been investigated for NH_3 decomposition [9-12]. In the review study of Hongrapipat *et al.,* it was stated that ferrous minerals are promising catalysts for NH_3 decomposition [4]. For example iron sinter, iron pellets, and ferrous dolomite all catalyze the decomposition of 2500 ppm NH_3 in product gas from a peat fueled gasifier at 900°C and about 85% conversions were achieved [9]. In a study by Xu *et al.*, pyrolysis chars from low rank coals were tested and found that the inherently present Fe and Ca minerals in the coal chars were responsible for their activities towards ammonia decomposition [11]. Ohtsuka and co-workers demonstrated that low-valued iron ore, namely limonite, rich in goethite (α-FeOOH) can achieve the almost complete decomposition of 2000 ppm NH_3 in inert atmosphere at 500°C. They also discovered that the presence of phosphorous in the carbon-supported Fe catalysts could greatly promote

catalytic decomposition of ammonia [13-14]. But in these studies, typically temperatures above 850°C were needed when the reaction was run in the presence of fuel gases. The catalytic performance of the catalysts was severely affected by the fuel gases. The requisite of high temperatures is the drawback of decomposition of NH_3. On the other hand, selective catalytic oxidation (SCO) of ammonia is one of the most efficient technologies for ammonia removal from oxygen-containing waste gases. SCO of ammonia involves the controlled addition of an oxidizer (O_2, NO, NO/O_2) to the gasification gas to quantitatively and selectively transform NH_3 into N_2 and H_2O. The catalytic oxidation of ammonia usually occurs between 400-600 °C and depending on operating conditions and the type of catalysts used, can proceed in the three principal reactions (Reactions 2-4).

$$4NH_3 + 3O_2 \rightarrow 2N_2 + 6\ H_2O + 302\ kcal \quad \text{(Eq. 2)}$$

$$4NH_3 + 6NO \rightarrow 5N_2 + 6\ H_2O \quad \text{(Eq. 3)}$$

$$4NH_3 + 4NO + O_2 \rightarrow 4N_2 + 6H_2O \quad \text{(Eq. 4)}$$

But in the presence of O_2, undesirable competing reactions with Reaction 2 can occur and NOx emissions can be released (Reactions 5-7) [15-16].

$$4NH_3 + 4O_2 \rightarrow 2N_2O + 6H_2O + 264\ kcal \quad \text{(Eq. 5)}$$

$$4NH_3 + 5O_2 \rightarrow 4NO + 6H_2O + 216\ kcal \quad \text{(Eq. 6)}$$

$$4NH_3 + 7O_2 \rightarrow 4NO_2 + 6H_2O \quad \text{(Eq. 7)}$$

Or alternatively N_2O emission may be formed through Reaction 8:

$$4NO + 4NH_3 + 3O_2 \rightarrow 4N_2O + 6H_2O \quad \text{(Eq. 8)}$$

When the ammonia removal from gasification gas is needed, it is more convenient to use oxygen as oxidant rather than nitrogen oxides. The oxygen that used as oxidant on SCO of ammonia should not affect the syngas composition which contains combustible gases like CO, H_2, CH_4, *etc*. Also it is undesirable to convert ammonia to nitrogen oxides. In the patented study of Y. Shioya *et al.*, it is said that the optimal O_2 amount should be two moles or more O_2 for one mole of ammonia [17]. Catalysts used for SCO of ammonia are classified in three groups: One is metallic catalysts, the other is transition metal catalysts and their oxides (Co_3O_4, MnO_2 or V_2O_5, Al_2O_3 supported Ni, Fe and Mn, CuO/Al_2O_3 or Fe_2O_3-Al_2O_3, Fe_2O_3-TiO_2, Fe_2O_3-ZrO_2 *etc.*), and zeolites. Precious metal catalysts (Pt, Pd, Ir, Ru, Ag, *etc*.) show high activity at temperatures lower than 200 °C. On the other hand, transition metal oxide catalysts are active at higher temperatures (<400 °C) than precious catalysts but show higher selectivity to N_2. Another potential group is transition metal oxide impregnated zeolite (ZSM5, Y, mordenite, beta, ferrierite, chabazite, *etc.*)

catalysts. Zeolite supported catalysts are active at relatively high temperatures [15]. High acidity ZSM5, Zeolite Beta and Zeolite Y supported iron catalysts were tried at 350, 400 and 450 °C and it was seen that with the increase in temperature NH_3 conversion and N_2 selectivity increased as well. The highest ammonia conversions (95-100%) were achieved at 450 °C. 450 °C is a relatively low temperature when compared with catalytic ammonia decomposition temperatures which are typically 750-850 °C. High iron content of catalysts, low Si/Al ratio of zeolites and low ammonia concentration is advantageous cases in selective catalytic oxidation of ammonia [18]. A detailed PhD study on SCO of ammonia showed that activity of different active metals at 300°C decrease in this order: Pt>Pd>Cu>Ag>Au>Fe>W>Ti. High ammonia conversions and N_2 selectivities can be achieved with copper based catalysts at atmospheric pressure. But at high pressures, the ammonia conversion can decrease under 30% [19]. In this study, the catalytic activities of Zeolite Hβ supported iron catalyst (Fe/HZβ) were compared both for the selective catalytic oxidation and catalytic decomposition of 800 ppmv ammonia.

MATERIALS AND METHODS

Zeolite support, namely Zeolite Hβ, was supplied by Zeolyst International Incorporation. The silica-to-alumina ratio of the zeolite was 38. Wet impregnation method was used to prepare the catalyst. Zeolite Hβ was in ammonium form prior to impregnation. For preparation of the catalyst, iron nitrate ($Fe(NO_3)_3.9H_2O$, Alfa Aesar) was dissolved in a minimum volume of water and the zeolite was added to the solution so as to achieve a nominal iron content of 10% by weight. The slurry was subsequently dried at 90 °C overnight. Zeolite-supported iron catalyst was labeled as Fe/HZβ through the article. Chemical analysis of the catalyst was performed using inductively coupled plasma spectroscopy (Perkin Elmer Optima 2100 ICP-OES). Iron content of the synthesized catalyst was analyzed to be 12.96%. Fe/HZβ catalyst was milled and sieved under 500 μm before the catalytic experiments. A 5 cc (~3 g) sample of the dry catalyst powder was placed in a vertical stainless steel reactor with 310 grade (17 mm i.d.), calcined in dry air at 420°C for 5 hours and reduced under pure hydrogen flow at the same temperature for 10-12 hours as previously explained in detail [20]. After the reduction of the catalyst, different gas mixtures composed of 800 ppmv ammonia were prepared. For selective catalytic oxidation experiments, 2000-6000 ppmv O_2 and 0-10% H_2 concentrations were prepared in balance with N_2 at the temperatures of 300-550 °C. For decomposition experiments; 0-10-20-30% H_2 and balance N_2 were flown over the catalyst bed for 5h at the temperatures of 700 °C and 800 °C and a GHSV of 60 000 h^{-1}. Reaction products were analyzed in line using a UV-Vis NH_3 Analyzer and a Mass

Spectrometer. NH_3 conversion to hydrogen was calculated from the measured NH_3 in the product stream, reaction stoichiometry, and the differential reactor assumption, as $P_{NH3\ to\ H2}/P_{NH3,\ inlet.}$ NO_x concentrations were measured with off-line Analytic Jena multi EA® 5000 Total Nitrogen (TN) measuring device equipped with Nitrogen Chemiluminescence Dedector (NCD).

RESULTS AND DISCUSSION

Comparison of Catalytic Activities Under N_2 Atmosphere

Approximately 3 g (~5 cc) of Fe/HZβ catalyst was charged to the reactor and calcined with air at 420°C for 5 h. Then the reduction procedure was started by shifting to pure H_2 flow at the same temperature and the catalyst was reduced for 10 h. In the first set of experiments (selective catalytic reduction labelled as SCO), a gas mixture consisting of 800 ppm NH_3, 2000 and 4000 ppm O_2 and balance N_2 was flown over the catalyst with a gas flow rate of 5 L/min (GHSV=60,000 h^{-1}). SCO reaction tests were conducted at 300, 350, 400, 450 and 500 °C. In the second set of experiments (catalytic decomposition), a gas mixture of 800 ppm NH_3 and balance N_2 was flown over the reduced catalyst with the same gas flow rate and catalytic decomposition of NH_3 was carried out at 700 °C and 800 °C in the absence of O_2. In the last set, blank reactor tests were conducted with the same gas mixture used for catalytic decomposition of NH_3. Reaction products were analyzed in line using a UV-Vis NH_3 analyzer and a mass spectrometer. Calculated NH_3 conversions versus reaction temperature were plotted in Figure 1.

For the first set of SCO experiment, 4% of ammonia conversion (based on UV-Vis measurements) was achieved at 300 °C in the presence of 2000 ppm O_2. When the reaction temperature was increased stepwise to 500°C, NH_3 conversions were steadily increased. 100% ammonia conversion was reached at 500 °C under SCO conditions. SCO tests were conducted at 350 and 400 °C by increasing the oxygen concentration from 2000 ppm to 4000 ppm to see the effect of O_2 on NH_3 conversion. At 350 °C, ammonia conversions of 12.5% and 8.8% at the reactor exit were obtained with the presence of 2000 and 4000 ppm O_2, respectively. When the reaction temperature was increased to 400 °C, while NH_3 conversion was reached to 31.2% in the presence of 2000 ppm O_2, it was 41.2% for 4000 ppm O_2. It was shown that higher NH_3 conversions could be achieved with increasing O_2 concentrations.

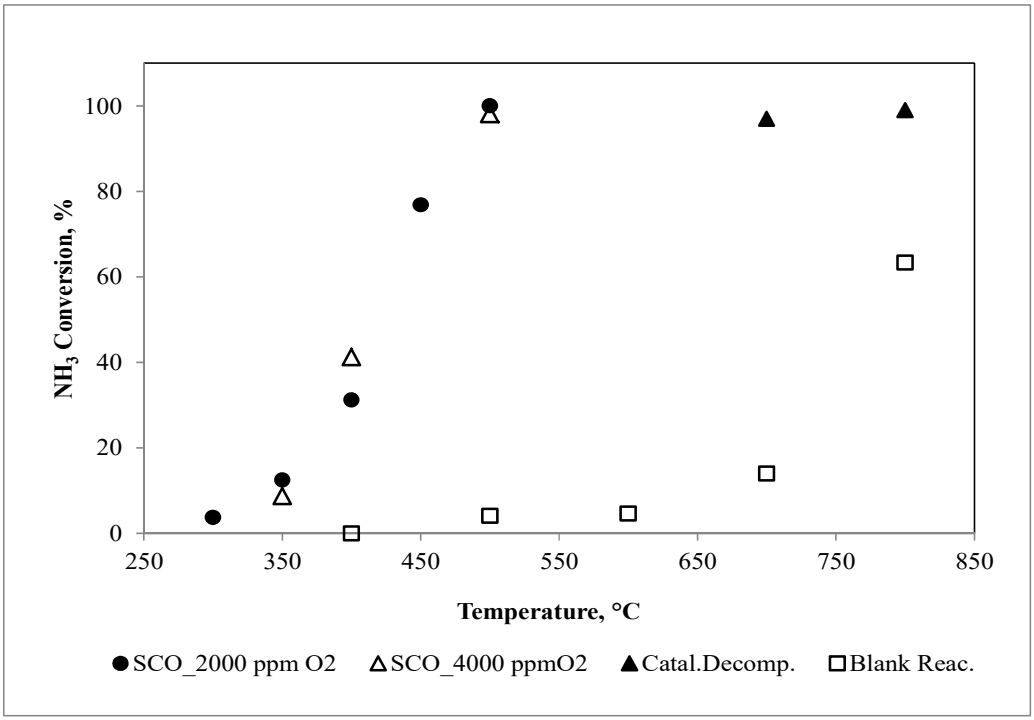

Figure 1: The change of NH_3 conversion with temperature in N_2 atmosphere at atmospheric pressure and 800 ppm inlet NH_3 concentration ●Selective Catalytic Oxidation (SCO) over Fe/HZβ at 2000 ppm O_2 ΔSCO over Fe/HZβ at 4000 ppm O_2 ▲catalytic decomposition over Fe/HZβ □ blank reactor test without O_2.

During the tests, NO_x and H_2O concentrations in the reactor exit were followed by mass spectrometer as well. Figure 2 shows the m/z peak intensities of these components (m/z=30 for NO/NO_2, m/z=18 for H_2O, m/z=46 for the fragment of NO_2, m/z=44 for N_2O and m/z=18 for H_2O). It must be pointed out here that measuring the NO_x components with mass spectrometer have some difficulties because of the overlapping m/z values at m/z=30 for NO and NO_2. On the other, these measurements give an idea on the formation of NO_x components. As seen from the Figure 2, NO_x formation was apparent for all reaction temperature. As expected, water vapor was also formed upon Reactions 2-7. The rate of water vapor formation was started decreasing at 500°C where 100% NH_3 conversion was achieved. This was attributed to a possible secondary reaction between NO_2 and H_2O in the stoichiometric excess of O_2 according to Reaction 9. On the other hand, further verifications are needed to make sure on the occurrence of this reaction.

$$4\ NO_2\ (g) + O_2\ (g) + 2\ H_2O\ (vapor) \rightarrow 4\ HNO_3\ (vapor) \qquad \text{(Eq. 9)}$$

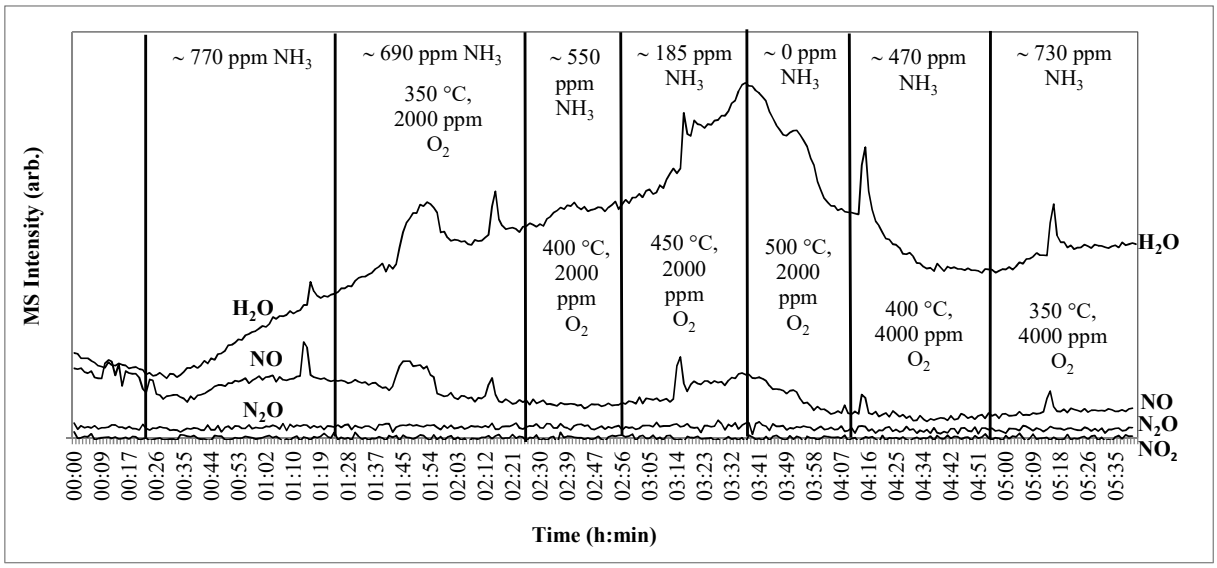

Figure 2: Effects of temperature and O_2 amount on SCO of ammonia on Fe/HZβ catalyst: MS data of H_2O and NO_x in the reactor exit.

Unfortunately, mass spectrometric measurements did not let the selectivity and yield calculations due to the qualitative monitoring of NO_x components and excess N_2 in the reaction atmosphere.

In the second set of catalytic decomposition of NH_3 experiments, the reaction was intentionally carried out at high temperatures, namely at 700 and 800 °C, due to the endothermic nature of the ammonia decomposition. Quite close conversions were achieved for 700 and 800 °C under nitrogen atmosphere by giving H_2 and N_2 as the decomposition products according to Reaction 1. Thermodynamic equilibrium conversion of almost 100% was attained over both at 700 and 800 °C under nitrogen atmosphere.

In the last set of experiments, blank reactor tests were carried out under NH_3 decomposition reaction conditions in the absence of O_2. NH_3 decomposition reaction started at 500 °C with a conversion of 4.1%. The rate of NH_3 decomposition reaction was seen to be increased after 700 °C. While NH_3 conversion was 14% at 700°C, it was peaked to 63% at 800 °C where it was still below the value obtained over the catalyst.

It was shown that under N_2 atmosphere, 100% of NH_3 conversion was achieved over Fe/HZβ catalyst through selective catalytic oxidation reaction at 500 °C while 94% of conversion was obtained over the same catalyst through the catalytic decomposition at 800°C. These results indicated that while selective catalytic oxidation was promoted below 500 °C, catalytic decomposition of NH_3 to H_2 and N_2 was favored above 600 °C.

To investigate the effect of O_2 on SCO activity of Fe/HZβ catalyst in detail, additional tests were conducted at both 400 and 500 °C. SCO tests were carried out at changing O_2 concentrations with an inlet gas composition of 800 ppmv NH_3 in balance N_2. O_2

concentrations were changed between 2000 ppm and 6000 ppm. Obtained results are given in Figure 3. As it was seen in the Figure, conversions at 500 °C were slightly increased from ~94% to ~98% at increasing O_2 concentrations. On the other hand, the highest ammonia conversion (41%) at 400 °C was achieved with 4000 ppm O_2. Relatively lower conversion values were observed with 2000 and 6000 ppm O_2.This indicates that there seemed to be an optimal O_2 concentration at 400°C for an acceptable surface adsorption and NH_3 oxidation. K. Duan *et al.* reported the similar case over Cu-Mn/TiO_2 catalyst for 0.5%, 3% and 5% O_2 concentrations. In their study, the highest NH_3 conversion (~%85) was achieved in the presence of 3% O_2 at 250 °C [21]. This study supported the finding that there is an optimum O_2 concentration related with temperature.

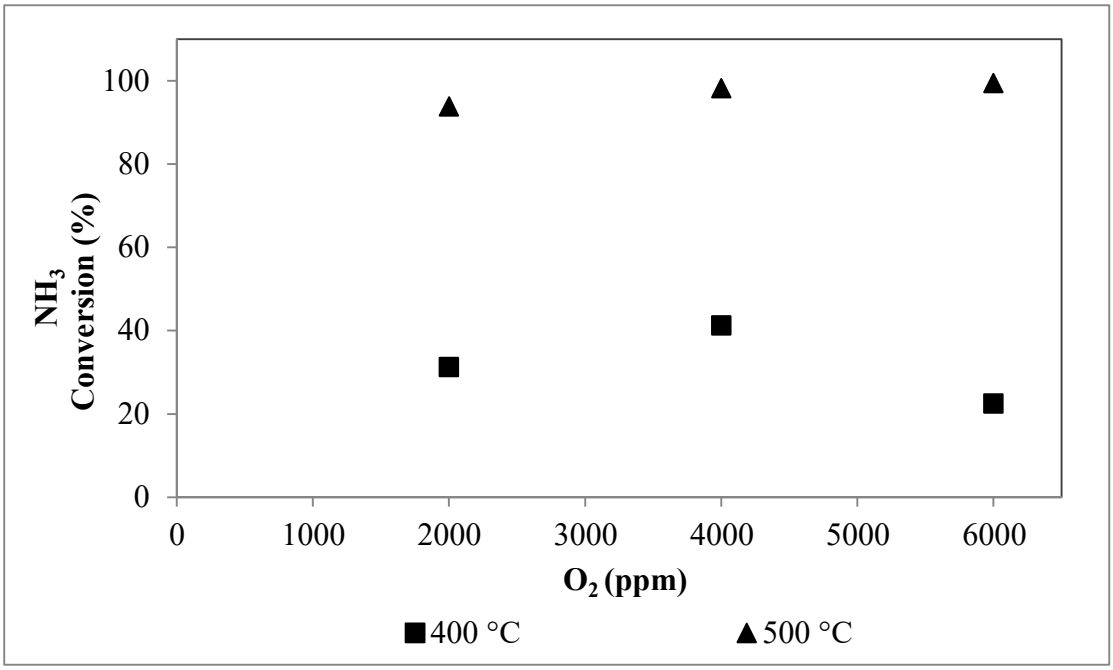

Figure 3: Effect of O_2 concentration on ammonia conversion at 400 and 500 °C.

To get the main picture of the catalytic decomposition and selective catalytic oxidation of ammonia results over Fe/HZβ and in blank reactor, ammonia conversion values were also given in Table 1.

Table 1: The change of NH_3 conversion with temperature and O_2 amount without H_2 at atmospheric pressure and 800 ppm inlet NH_3 concentration: Selective Catalytic Oxidation (SCO) and catalytic decomposition over Fe/HZβ

		Ammonia Conversion, %				
		Ammonia Decomposition	**Blank Reactor Test**	**Selective Catalytic Oxidation of Ammonia**		
O_2 amount (ppm)		0	0	2000	4000	6000
	300	-	-	4	-	-
	350	-	-	13	9	-
	400	-	0	31	41	23
Temperature	450	-	-	77	-	-
(°C)	500	-	4	100	98	99
	600	-	5	-	-	-
	700	97	14	-	-	-
	800	99	63	-	-	-

In order to evaluate the selectivity of the reaction, gas samples were collected into the Tedlar bags after each test conducted at 500 °C and 2000, 4000 and 6000 ppm O_2. Collected gas samples were analyzed with Analytic Jena multi EA® 5000 Total Nitrogen (TN) measuring device equipped with Nitrogen Chemiluminescence Detector (NCD). NO_x concentrations of the samples were measured and results were drawn in Figure 4. As seen from the Figure, NO_x concentration is linearly decreasing with increasing oxygen concentration. This might be due to the further oxidation of NO species according to Reaction 4 or N_2O formation through Reaction 8 under excess oxygen atmosphere. Therefore, excess O_2 might lead to the undesired N_2O emissions.

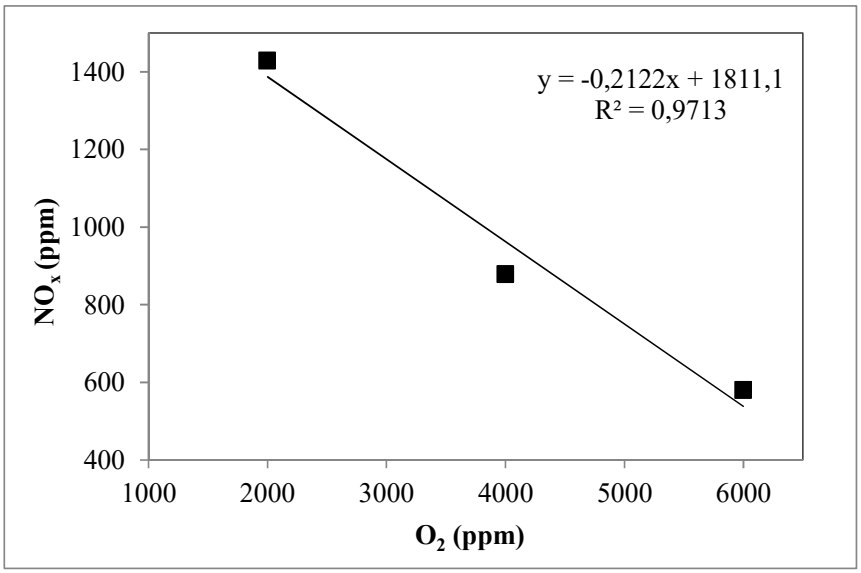

Figure 4: Effect of O_2 concentration on NO_x exit from the SCO reactor at 500 °C.

Comparison of Catalytic Activities Under H_2 Atmosphere

Fe/HZβ catalyst was pretreated in the way of the experimental work conducted under N_2 atmosphere. Similarly, three sets of experiments were carried out, namely selective catalytic oxidation, catalytic decomposition and blank reactor test for decomposition. Selective catalytic oxidation (SCO) experiment was conducted with a gas mixture consisting of 4000 ppm O_2, 800 ppm NH_3, 10% H_2 and balance N_2. The effect of reaction temperature on NH_3 conversion was screened between 400 and 550°C. The same gas mixture in the absence of O_2 was flown over the reactor to carry out the catalytic decomposition of NH_3 to H_2 and N_2 with or without catalyst. Decomposition reaction was tested at 700 and 800 °C. Conversion results were plotted in Figure 5 and also given in Table 2. Contrary to the observation for SCO reaction under N_2 atmosphere, NH_3 conversions decreased with increasing reaction temperatures.

Figure 6 shows the trends for H_2O formation and O_2 consumption through the mass spectrometer. It is apparent that the main reaction product, H_2O, was formed at all reaction temperatures. On the other hand, its concentration decreased with concomitant increase in O_2 concentration when the reaction temperature was decreased from 450 °C to 400 °C. Although a decrease in reaction temperature and water vapor and an increase in O_2 concentration, NH_3 conversion was increased from 35% to 41%. This is the clear indication of unselective oxidation of H_2 at increasing temperatures. To clear the situation, H_2 flow was cut from the mixture at 400 °C and it was shown that H_2O concentration continued decreasing but the NH_3 conversion remained the same. Therefore it was believed that H_2 oxidation reaction competes with selective catalytic oxidation reaction of ammonia to N_2 and H_2O.

$$4NH_3+3O_2 \rightarrow 2N_2+6H_2O+302 \text{ kcal} \quad \text{(Eq. 10)}$$

$$4H_2+2O_2 \rightarrow 4H_2O+231 \text{ kcal} \quad \text{(Eq. 11)}$$

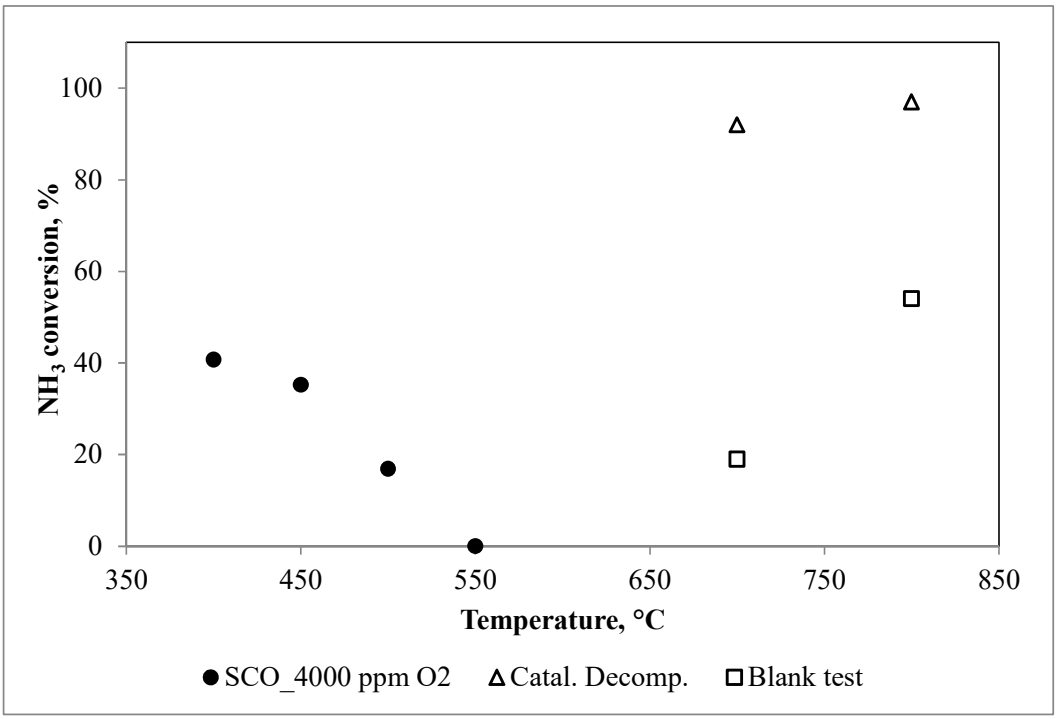

Figure 5. The change of NH_3 conversion with temperature in 10% H_2 balance N_2 atmosphere at atmospheric pressure and 800 ppm inlet NH_3 concentration. ●Selective Catalytic Oxidation over Fe/HZβ ΔCatalytic Decomposition over Fe/HZβ □Blank reactor test without O_2.

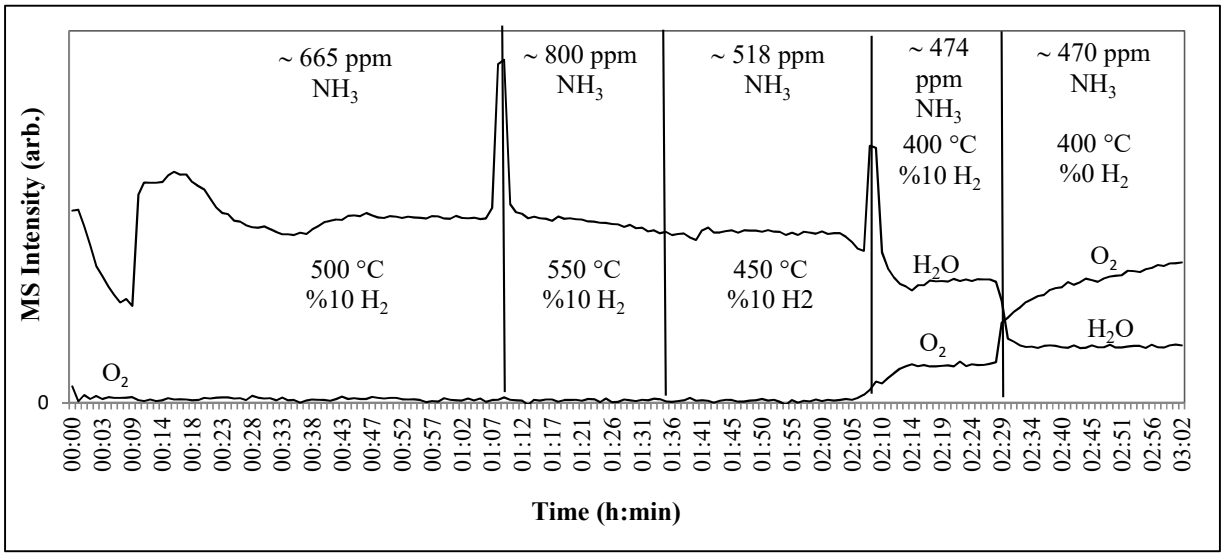

Figure 6: H_2 effect on SCO of ammonia at different temperatures with 4000 ppm O_2.

In the second case, catalytic decomposition of NH_3 to H_2 and N_2 was tested under 10% H_2 concentration. Although high NH_3 conversions over 90% were achieved upon H_2 addition, these conversions under N_2 atmosphere were close to 100%. For the third case, where catalytic decomposition of NH_3 was tested without catalyst, it was seen that while NH_3 conversion was 63% at 800°C, it was decreased to 54% with H_2 addition. On both

cases, loss of activity upon H_2 addition was apparent. Therefore, a new set of experiments were conducted to investigate the effect of H_2 concentration on the activity of Fe/HZβ catalyst for NH_3 decomposition. To do this, H_2 concentration was changed between 10% and 30% for the same inlet NH_3 concentration (800 ppm). Reactions were conducted at 700 °C and 800 °C. The change of conversions with H_2 concentration was plotted in Figure 7 and the corresponding conversion values were given in Table 2. It was shown that all conversions decreased. The decrease in conversion seemed to be linear with inlet hydrogen concentration. Hydrogen was seen to inhibit ammonia decomposition reaction. Conversion loss in the presence of hydrogen is reasonable for the dehydrogenation reactions regarding unfavorable thermodynamic conditions. On the other hand, competing kinetically relevant steps, namely N-H bond breaking and atomic nitrogen association might also be responsible for this inhibition. Rate determining step might be NH_3 dissociation due to hydrogen surrounding the active site [22]. Therefore, restricted N−H bond breaking might limit the number of active sites to be occupied by N-N pairs.

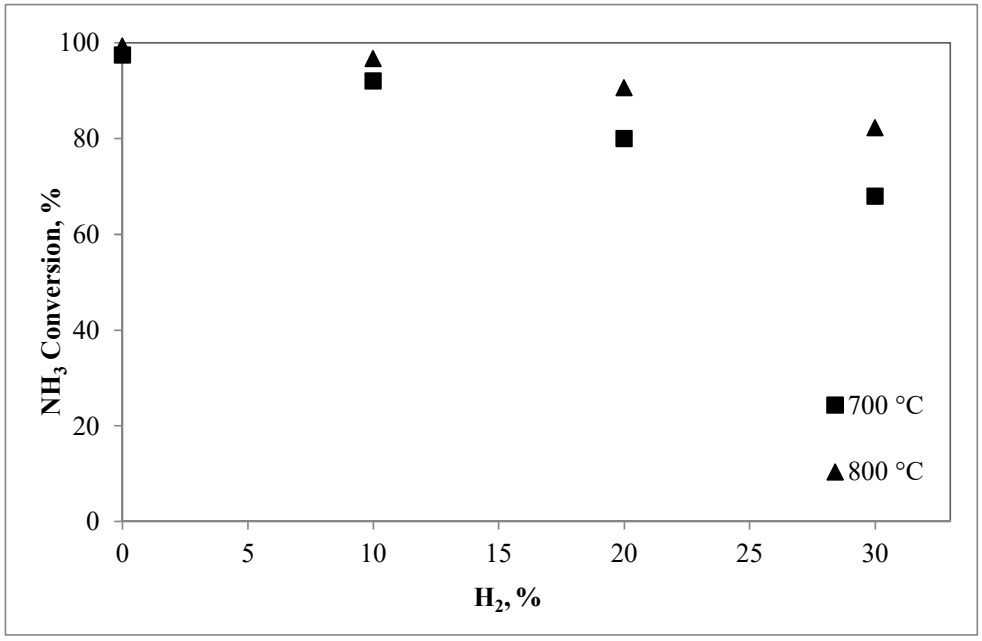

Figure 7: NH_3 decomposition conversions changing with inlet H_2 concentration at 700 and 800 °C.

Table 2: The change of NH_3 conversion with temperature, O_2 and H_2 amounts at atmospheric pressure and 800 ppm inlet NH_3 concentration: Selective Catalytic Oxidation (SCO) and catalytic decomposition over Fe/HZβ.

		Ammonia Conversion, %					
		Ammonia Decomposition				**Blank Reactor Test**	**Selective Catalytic Oxidation of Ammonia**
O_2 amount (ppm)		0				0	4000
H_2 amount (%)		0	10	20	30	10	10
Temperature (°C)	400	-	-	-	-	-	41
	450	-	-	-	-	-	35
	500	-	-	-	-	-	17
	550	-	-	-	-	-	0
	700	97	92	80	68	19	-
	800	99	97	91	82	54	-

CONCLUSIONS

In this study, the catalytic activities over Zeolite Hβ supported iron catalyst (Fe/HZβ) were compared both for the two catalytic routes, namely SCO and Catalytic Decomposition. It was shown that SCO of ammonia reaction is directly related with temperature and O_2 amount. Although comparably higher conversions can be achieved under N_2 atmosphere through SCO reaction, the presence of a fuel gas like H_2 inhibits the selective oxidation of NH_3 and leads to the poor conversions. The loss of SCO activity under H_2 atmosphere was interpreted as the competing H_2 and NH_3 oxidations over the catalyst. On the other hand, although decomposition reaction of NH_3 to H_2 and N_2 requires higher reaction temperatures, it was seen to be less sensitive to the presence of hydrogen. Activity loss with H_2 addition in the case of decomposition reaction was considered to be due to both unfavorable thermodynamic conditions for dehydrogenation and restricted N−H bond breaking due to the hydrogen surrounding the active sites.

ACKNOWLEDGMENTS

The authors greatly acknowledge to "The Scientific and Technological Research Council of Turkey (TÜBİTAK)" for supporting of "Liquid Fuel Production from Biomass and Coal Blends" project (Contract Code: 108G043) in which this study was carried out. The authors would also like to thank the State Planning Organization of Turkey for their

laboratory infrastructure funding (Project: Excellency Center for Gas Technologies, 2011K120040).

REFERENCES

1. Basu, P. (2006). Combustion and Gasification in Fluidized Beds, Taylor & Francis Group, LLC.

2. Rönkkönen, H., Simell, P., Reinikainen, M., Krause, O. ve Niemela, M.V., (2010). Catalytic clean-up of gasification gas with precious metal catalysts – A novel catalytic reformer development, Fuel, 89, 3272-3277. DOI: 10.1016/j.fuel.2010.04.007.

3. Xu C., Donald J., Byambajav E., Ohtsuka Y., (2010). Recent Advances in Catalysts for Hot Gas Removal of Tar and NH3 from Biomass Gasification, Fuel, 89, 1784-1795. DOI: 10.1016/j.fuel.2010.02.014.

4. Hongrapipat J, Saw W.L, Pang S. Removal of Ammonia from Producer Gas in Biomass Gasification: Integration of Gasification Optimisation and Hot Catalytic Gas Cleaning. Biomass Conversion and Biorefinery. 2012, 2 (4), 327-348. DOI: 10.1007/s13399-012-0047-1.

5. Hu J, Yu F, Lu Y. Application of Fischer–Tropsch Synthesis in Biomass to Liquid Conversion. Catalysts. 2012; 2(2), 303-326; DOI: 10.3390/catal2020303.

6. Durak-Çetin Y, Sarıoğlan A, Sarıoğlan Ş, Okutan H. The Effect of Support Type on the Activity of Zeolite Supported Iron Catalysts for the Decomposition of Ammonia. Reaction Kinetics, Mechanisms and Catalysis. 2016; in press, DOI: 10.1007/s11144-016-0981-1.

7. Pansare SS, Torres W, Goodwin J G. Ammonia decomposition on tungsten carbide. Catalysis Communications. 2007;8:4, 649-654. DOI: 10.1016/j.catcom.2006.08.016.

8. Zheng W, Zhang J, Xu H. NH3 Decomposition Kinetics on Supported Ru Clusters: Morphology and Particle Size Effect. Catalysis Letters. 2007;119:3, 311-318. DOI: 10.1007/s10562-007-9237-z.

9. Leppalahti J, Simell P, Kurkela E. Catalytic conversion of nitrogen compounds in gasification gas. Fuel Processing Technology. 1991; 29:1-2, 43-56.

10. Ohtsuka Y, Xu C, Kong D, Tsubouchi N. Decomposition of ammonia with iron and calcium catalysts supported on coal chars. Fuel. 2004 83:6, 685-692. DOI:10.1016/j.fuel.2003.05.002.

11. Donald J, Xu CC, Hashimoto H, Byambajav E, Ohtsuka Y. Novel carbon-based Ni/Fe catalysts derived from peat for hot gas ammonia decomposition in an inert helium atmosphere, Applied Catalysis A: General. 2010; 375:1, 124-133. DOI:10.1016/j.apcata.2009.12.030.

12. Simell P, Kurkela E, Stahlberg P, Hepola J. Catalytic hot gas cleaning of gasification gas. Catalysis Today. 1996; 27(1-2):55-62. DOI:10.1016/0920-5861(95)00172-7.

13. Tsubouchi N, Hashimoto H, Ohtsuka Y. High Catalytic Performance of Fine Particles of Metallic Iron Formed from Limonite in the Decomposition of a Low Concentration of Ammonia. Catalysis Letters. 2005; 105(3-4):203-208. DOI: 10.1007/s10562-005-8691-8.

14. Xu C, Tsubouchi N, Hashimoto H, Ohtsuka Y. Catalytic decomposition of ammonia gas with metal cations present naturally in low rank coals. Fuel. 2005; 84:14-15, 1957-1967. DOI: 10.1016/j.fuel.2005.03.019.

15. Jabłońska M, Chmielarz L, Węgrzyn A. Selective catalytic oxidation (SCO) of ammonia into nitrogen and water vapor over hydrotalcite originated mixed metal oxides: a short review.

CHEMIK. 2013; 67, 8, 701-710. YADDA identifier: bwmeta1.element.baztech-6167861c-0171-499d-b857-8e5d837c4b2f.

16. Torres W, Pansare S S, Goodwin J G. Hot Gas Removal of Tars, Ammonia, and Hydrogen Sulfide from Biomass Gasification Gas. Catalysis Reviews: Science and Engineering. 2007; 49, 4, 407-456. DOI: 10.1080/01614940701375134.

17. Shioya Y, Miyaki Y, Ammonia decomposition catalyst and process for decomposition of ammonia using the catalyst. European patent application. 2009; EP1872852A1.

18. Long R Q, Yang R T. Selective Catalytic Oxidation (SCO) of Ammonia to Nitrogen over Fe-Exchanged Zeolites. Journal of Catalysis. 2001; 201, 145–152. DOI: 10.1006/jcat.2001.3234.

19. Kurkela E, Kurkela M. Advanced Biomass Gasification for High Efficiency Power, Final Activity Report of BIGPower Projec. VTT Research Notes 2511, ISBN 978-951-38-7537-4 (URL: http://www.vtt.fi/publications/index.jsp); 2009.

20. Baranak M, Gürünlü B, Sarıoğlan A, Ataç Ö, Atakül H. Low acidity ZSM-5 supported iron catalysts for Fischer-Tropsch synthesis. Catalysis Today 2013;207:57-64. DOI: 10.1016/j.cattod.2012.04.013.

21. Duan K, Tang X, Yi H, Ning P, Wang L. Rare earth oxide modified Cu-Mn compounds supported on TiO_2 catalysts for low temperature selective catalytic oxidation of ammonia and in lean oxygen. Journal of Rare Earths, Dec.2010; 28, 338-342. DOI: 10.1016/S1002-0721(10)60277-3.

22. Guo W, Vlachos DG. Patched bimetallic surfaces are active catalysts for ammonia decomposition. Nature Communications 2015; 6:8619. DOI: 10.1038/ncomms9619.

Türkçe Öz ve Anahtar Kelimeler

Fe/HZβ Katalizörü Üzerinde Amonyağın Seçici Katalitik Yükseltgenme ve Bozunma Aktivitelerinin Karşılaştırılması

Yeliz Durak-Çetin, Alper Sarıoğlan, Hasancan Okutan

Öz: Amonyak, sentez gazı kullanılmadan önce giderilmesi gereken sentez gazı kirleticilerinden biridir. Amonyağın en umut vaat eden sıcak gaz temizleme yöntemi seçici katalitik yükseltgeme (SCO) ve katalitik bozunmadır. Bu çalışmada; Zeolit Hβ-destekli demir katalizör (Fe/HZβ) üzerindeki amonyak giderim aktiviteleri iki katalitik yol için de karşılaştırılmıştır. SCO deneyleri için, sıcaklık (300-550 °C), O_2 (2000-6000 ppmv) ve H_2 (%0-10) konsantrasyonlarının etkisi her gaz karışımında 800 ppm NH_3 olacak şekilde incelenmiştir. İkinci yolda ise, katalitik amonyak bozunma denemeleri N_2 içinde H_2 (%0-30) varlığında 800 ppm NH_3 içeren gaz karışımı ile 700 ve 800 °C'de gerçekleştirilmiştir. SCO'da, NH_3 dönüşümlerinin reaksiyon ortamında H_2 olmadığı durumda artan reaksiyon sıcaklığı ile arttığı görülmüştür. %10 H_2 varlığında ise, azalan reaksiyon sıcaklığı ile NH_3 dönüşümlerinin arttığı tespit edilmiştir. Bu durum katalizör üzerinde H_2 ve NH_3 yükseltgenmesinin yarışmalı olarak gerçekleştiği şeklinde yorumlanmıştır. Diğer taraftan, katalitik bozunma reaksiyonunda, hem 700 ve hem de 800 °C'de termodinamik denge dönüşümüne yakın, yaklaşık %100, amonyak dönüşümleri elde edilmiştir. Ortama H_2 ilavesi ile bütün dönüşümlerde azalma görülmüştür. Dönüşümlerdeki azalma giriş hidrojen konsantrasyonu ile doğrusal bir ilişki göstermiştir. Hidrojenin, amonyağın bozunma reaksiyonunu engellediği görülmüştür. Fe/HZβ katalizörünün, sentez gazındaki NH_3'ün giderilmesinde NH_3'ün seçici katalitik yükseltgenmesinden ziyade, daha yüksek sıcaklıklara ihtiyaç duyulmasına rağmen (700-800 °C), amonyak bozunma reaksiyonunda kullanılmasının daha etkili olacağı gösterilmiştir.

Anahtar kelimeler: Amonyak; bozunma; seçici katalitik yükseltgeme (SCO); sıcak gaz temizleme.

Sunulma: 01 Temmuz 2016. **Düzeltme:** 11 Kasım 2016. **Kabul:** 18 Kasım 2016.

Docking and Molecular Dynamics Calculations of Some Previously Studied and Newly Designed Ligands to Catalytic Core Domain of HIV-1 Integrase and an Investigation to Effects of Conformational Changes of Protein on Docking Results

Selami Ercan[1]*

[1]Batman University, School of Health Sciences, 72060, Batman, Turkey

Abstract: Nowadays, AIDS still remains as a worldwide pandemic and continues to cause many deaths which arise from HIV-1 virus. For nearly 35 years, drugs that target various steps of virus life cycle have been developed. HIV-1 integrase constitutes one of these steps which is essential for virus life cycle. Computer-aided drug design is being used in many drug development and drug improvement studies as also used in development of the first HIV-1 integrase inhibitor Raltegravir. In this study, 3 ligands which are already used as HIV-1 integrase inhibitors and 4 newly designed ligands were docked to catalytic core domain of HIV-1 integrase. Each ligand docked to three different conformations of protein. Prepared complexes (21 items) were carried out by 50 ns MD simulations and results were analyzed. Finally, the binding free energies of ligands were calculated. It was determined that designed ligands L01 and L03 gave favorable results. The questions about the ligands which have low docking scores in a conformation of protein could give better scores in another conformation of protein and if the MD simulations carry the different oriented and different localized ligands in same position at the end of simulation were answered.

Keywords: HIV-1 integrase; drug design; docking; molecular dynamics; binding free energy.

Submitted: September 09, 2016. **Revised:** October 13, 2016. **Accepted:** October 24, 2016.

Cite this: Ercan S. Docking and Molecular Dynamics Calculations of Some Previously Studied and Newly Designed Ligands to Catalytic Core Domain of HIV-1 Integrase and an Investigation to Effects of Conformational Changes of Protein on Docking Results. JOTCSA. 2017;4(1):243–70.

DOI: To be assigned.

*Corresponding author. E-mail: slmrcn@gmail.com. Tel: +90 488 217 3767, fax: +90 488 217 3601.

INTRODUCTION

Human immunodeficiency virus (HIV) is a member of lentiviruses genus from retroviruses family, which causes a worldwide pandemic of acquired immunodeficiency syndrome (AIDS). It was recently reported that there are about 35 million (33.2 million-34.0 million) people living with human immunodeficiency virus type 1 (HIV-1) at 2015, 1.5 million (1.4 million-1.7 million) deaths that related to AIDS, and 2.1 million (1.9 million – 2.4 million) newly infected people [1].

HIV-1 pol gen encodes three essential enzymes, namely reverse transcriptase (RT), integrase (IN), and protease (PR) which are essential for virus life cycle [2]. Because of the roles of these enzymes they attract most attention in HIV-1 drug discovery studies. Although the first FDA-approved HIV-1 drug Zidovudine [3, 4] (AZT), was a nucleoside reverse-transcriptase inhibitor (NRTI) in the following years another drugs of different targets were discovered. Besides NRTIs, nucleotide reverse-transcriptase inhibitors (NtRTIs), non-nucleoside reverse-transcriptase inhibitors (NNRTIs) are discovered which also target RT enzyme. Other anti-HIV drug groups are as follows: Protease inhibitors (PIs), fusion inhibitors (FIs), co-receptor inhibitors (CRIs) and integrase inhibitors (INIs) [5, 6]. However, instead of using single drugs, a combination of RT and PR drugs, named Highly Active Antiretroviral Therapy (HAART) is used to suppress viral replication of HIV-1 [7-9]. HAART has an achievement on reducing disease progression, but it is also related to collateral problems like resistance of antivirals, toxicity and dosing which are preventing successful treatment of HIV [8, 10-19]. These shortfalls of HAART drugs' combinations point out the need for new drugs. Therefore, in this study, we tried to get some new inhibitors whose analogues showed good docking scores and interactions with IN in our previous work [20]. In contrast to many approved drugs which target RT and PR, only three IN inhibitors are currently approved as antiviral drugs. After approving Raltegravir (RAL: N-[2-[4-[(4-fluorophenyl)methylcarbamoyl]-5-hydroxy-1-methyl-6-oxopyrimidin-2-yl]propan-2-yl]-5-methyl-1,3,4-oxadiazole-2-carboxamide) [21, 22] as the first IN inhibitor in 2007, US Food and Drug Administration (FDA) also approved Elvitegravir (EVG: 6-[(3-chloro-2-fluorophenyl)methyl]-1-[(2S)-1-hydroxy-3-methylbutan-2-yl]-7-methoxy-4-oxoquinoline-3-carboxylic acid) [23], and Dolutegravir (DLG: (4R,12aS)-N-[(2,4-difluorophenyl)methyl]-7-hydroxy-4-methyl-6,8-dioxo-3,4,12,12a-tetrahydro-2H-pyrido [5,6]pyrazino[2,6-b][1,3]oxazine-9-carboxamide) [24] for market distribution.

HIV-1 integrase is a 32 kDa protein consisting of 288 amino acids and is a polynucleotidyl transferase enzyme. IN have structurally and functionally three different domains; N-terminal domain (NTD, 1-49 residues) containing Zn atom and a "His_2Cys_2" (HHCC) motif

which is highly conserved among all integrases, catalytic core domain (CCD, 50-212 residues) containing one or two divalent metal ion such as Mg^{2+} or Mn^{2+} and Asp64, Asp116 and Glu152 which is called "D,D-35-E" motif that is essential for catalysis, C-Terminal domain (CTD) is nonspecific DNA binding domain and consist of 213-288 residues.

Integrase mediates the insertion of viral DNA to host chromosomal DNA. It cuts a copy of double-stranded DNA of reverse transcribed viral RNA from the 3' ends and inserts into the host DNA. Integration occurs in two distinct steps. In the first step called 3' processing integrase cuts two or three nucleotides from the long terminal repeats (LTR) of vDNA at highly conserved CA bases which expose 3'-hydroxyl groups. Second step, involving insertion of processed vDNA to host DNA, is strand transfer reaction. IN catalyzes 3'-hydroxyl groups exposed from first step to attack host DNA from phosphate groups [25]. Thus, these reactions also make IN a specific target because human body does not need such a process.

Due to solubility and inter-domain flexibility problems, full-length structure of integrase could not be solved yet. This issue also is one reason of later development of IN inhibitors. However, individual structure of domains and combination of core domain with N-terminal domain [26] and C-terminal domain [27] have been solved by crystallography and nuclear magnetic resonance (NMR) techniques. Among these structures, only 1BL3 [28] and 2ITG [29] contain the flexible loop that consists of residues between 140-149. After identifying a crystal structure of catalytic core domain with a ligand (5CITEP: 1-(5-chloro-1H-indol-3-yl)-3-hydroxy-3-(2H-tetrazol-5-yl)) [30], IN catches attention as a new target of antiviral drug studies. An advantage of targeting IN is that there is not any homologue enzyme of IN in human body. However, beside use of different sets of chemical molecule types for inhibition of integrase, only β-diketo acids and their bioisosteres are the approved inhibitors and some of them are in clinical trial [31]. Furthermore, in recent years the crystal structures of prototype foamy virus integrase (PFV IN) with viral DNA and also contain the integrase inhibitors RAL, EVG, and DLG have been reported [32, 33]. Notwithstanding the only 15% sequence similarity between HIV integrase and PFV integrase the structure of integrase with vDNA provide new perspectives for researchers to understand inhibitor interactions with receptor and also DNA and researchers used these structures as templates for modelling full-length HIV-1 integrase by computational tools [32-34].

Drug development and improvement are expensive and time-consuming processes. Computational methods such as docking, molecular dynamics, and free energy computations are widely used to help development of new drugs, understanding interactions of drugs with receptors and also reaction mechanisms taking place in

inhibition. It is known that receptors are flexible *in vivo* and even though some docking programs allow flexible protein and ligand docking, but it is a time-consuming process and such a process also could be performed by molecular dynamics after docking process. Therefore, this study also aspires to detail interactions of ligands with receptor in different conformations of protein and to define whether a docking program could mislead a researcher for obtaining best ligand. Namely, in general, a researcher uses docking program for one conformation of protein to dock a series of ligands, but this is only a snapshot of dynamic protein. A ligand could be an inappropriate candidate in a conformation of protein according to docking score and could be a good candidate in another conformation of protein. Also we want to define if the molecular dynamics studies carry these complexes; which different conformations of receptor have differently oriented ligands in it, to same point at (in terms of conformation of ligand and also ligand-receptor interactions) the end of simulation. Two such like studies have been performed by Brigo and co-workers [35, 36]. They have studied differences between wild and mutant type proteins containing 5CITEP as ligand without docking. The coordinates of studied structures are taken from cluster analyses' trajectories in one of these works [35]. In the second work [36], they studied MD behaviors of protein which some diketo acid derivatives and also 5CITEP docked in.

In this study, approved HIV-1 IN inhibitors (INSTs) RAL, EVG and DLG and four newly designed ligands (Figure 1) which are derivatives of previously studied [20] ones used for docking, molecular dynamics and Molecular Mechanic Poison-Boltzmann Surface Area (MM/PBSA) [37]. Approved inhibitors were selected to make an accurate comparison about interactions of ligands with receptor. Furthermore, the fact that these molecules studied by many researchers and the existence of crystal structures of these molecules with protein (PFV IN) may allow us to look from a more accurate perspective to analyze results. The docking modes of ligands with different conformations of receptor, dynamic behaviors of protein and complexes, and binding energies of ligands analyzed widely in this work. Moreover, the restrained electrostatic potential (RESP) charges of used ligands derived from quantum mechanics studies for more compatible results with *in vivo*.

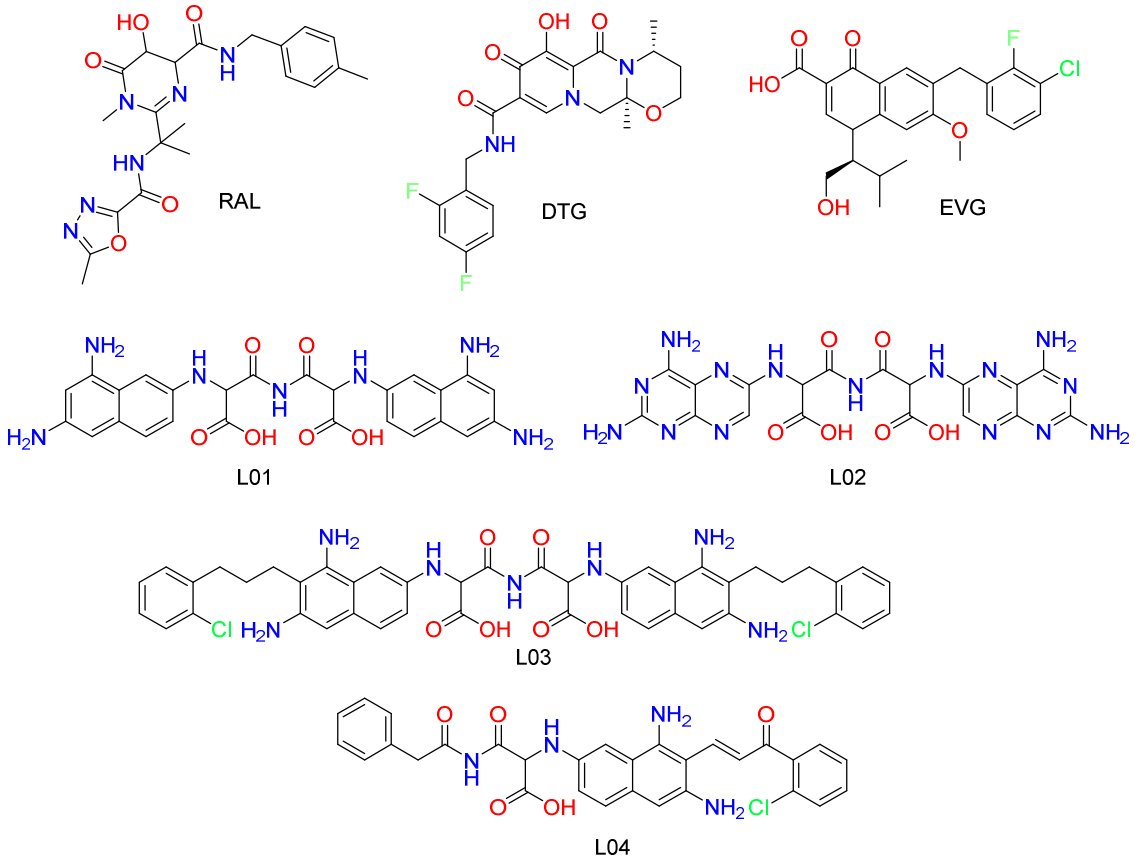

Figure 1. HIV-1 Integrase inhibitors and newly designed ligands those used in the study.

MATERIALS AND METHODS

Preparation of Used Protein Model

The crystallographic structure of CCD was obtained from the Protein Data Bank (www.rcsb.org) [38] with the code 1BL3.pdb. This structure contains A, B, and C chains. We used chain C because it has 50-209 residues (others have missing residues) and one Mg atom in the catalytic site. It is known that integrase catalyzes strand transfer reaction when we have two metal atoms [39]. Therefore, second Mg atom was inserted to model by superimposing C chain of 1BL3.pdb with chain A of the recently solved crystal structure of PFV integrase with pdb code 4BE2 [40]. Superimposition showed that the E152 residue of 1BL3.pdb is in an inappropriate conformation which results in being far from second Mg atom. So it also replaced with E152 residue of 4BE2.pdb. All crystal water molecules were kept in simulation.

The model loaded to *Xleap* module of AMBER 12 [41] and hydrogen atoms were added automatically by module. Model was neutralized by adding Cl^- ions and solvated with TIP3P [42] water model in a truncated octahedral box having at least 10 Å distance around the

receptor and a distance of 0.4 Å between protein and solute. The Amber ff99SB force field was used for the protein.

Preparation of the ligands

The ligands were designed on the basis of structures those are previously studied such as folic acid, methotrexate, and designed compounds LGA and LGB[20]. Ligand optimizations were performed by Gaussian 09 [43] program in three steps. In the first step, all ligands were optimized with semi-empirical AM1 method, followed by B3LYP/6-31+(d,p) optimization and finally latest optimizations were carried out by HF/6-31G* level to produce partial charges of ligands with RESP. *Antechamber* and *parmchk* modules of ABMER package program was used to prepare ligands for *Xleap* program and to create additional force field files which contain missing parameters of any ligands. After docking studies, the RESP charges (Supp. Inf.) of each ligand were added in *Xleap* program by editing molecules.

Molecular Dynamics Studies of Receptor

The minimization of receptor carried out in three steps. In the first step, all the system without water was kept fixed to minimize water molecules. In the second step, water and H atoms of protein are taken free while protein and Mg atoms were kept fixed. In the first and second step, a force constant of 5.0 kcal $mole^{-1}$ $Å^{-2}$ was used to restrain fixed atoms. In final minimization, all the system was released free. Minimizations carried out as 1000 steps steepest descent method followed by 1000 steps conjugate gradient method.

Minimization and MD simulations were carried out with *pmemd* module of AMBER 12. Minimized structure was used as starting point of MD simulation. Before production simulations, the system was heated to 300 K for 500 ps where protein except hydrogens and Mg atoms restrained with 1.0 kcal $mole^{-1}$ $Å^{-2}$ force constant. Heating followed by a 500 ps equilibration simulation.

MD simulations were performed at 300 K temperature. Langevin thermostat with a collision frequency of 2 was used to maintain the temperature of system. The long-range electrostatic interactions were treated by the Particle Mesh Ewald (PME) protocol [44] with a 10 Å cut-off distance. To constrain bond lengths involving hydrogens, SHAKE [45] algorithm was applied. A time step of 2 fs and periodic boundary conditions were employed throughout simulation.

After 20 ns MD simulation of receptor cluster analyses were carried out by *kclust* tool of MMTSB Toolset [46] based on RMSD mode. Three different cluster sets of receptor were defined and best models of each clusters were used for docking, MD simulations of complexes and MM/PB(GB)SA calculations.

Docking Studies

All docking studies were carried out with AutoDock 4 [47] docking program and with the aid of MGL Tools [47] in preparing structures for docking and analyses of results. Lamarckian Genetic Algorithm was used for docking with the settings of 150 individuals in a population, maximum energy evaluations of 2,500,000, maximum generations of 27,000 and 50 docking runs for each ligand. Autodock 4 scores docking of ligands by calculating their binding energies and the best scored conformations of ligands were selected for further studies.

Molecular Dynamics Studies of Complexes

Ligands having best scores for each conformation of receptor combined in Xleap program and also RESP charges of ligands were added. The way and conditions detailed in molecular dynamics studies of receptor followed for molecular dynamics studies of complexes for 50 ns.

MM/PB(GB)SA Studies

The binding free energies of ligands were calculated by MM/PBSA and MM/GBSA methods which implemented in AMBER 12 suite program as MMPBSA.py [37]. A schematic representation of thermodynamic cycle of method shown in Figure 2. With an interval of 10 ps, 1000 snapshots were extracted from MD production trajectories. The binding free energy was computed from the free energy difference of the free ligand, free receptor and ligand-receptor complex as formulated below:

$$\Delta G_{binding,solvated} = \Delta G_{complex,solvated} - (\Delta G_{receptor,solvated} + \Delta G_{ligand,solvated}) \quad (Eq.1)$$

where $G_{complex}$, $G_{receptor}$, and G_{ligand} are the free energy of complex, receptor and ligand molecules, respectively. These energy values are calculated using an average over the extracted snapshots taken from single MD trajectories. Each state can be estimated from molecular mechanics energy E_{MM}, solvation free energy G_{sol}, and solute entropy S.

$$\Delta G_{binding} = \Delta H - T\Delta S \approx \Delta E_{MM} + \Delta G_{sol} - T\Delta S \quad (Eq.2)$$

$$\Delta E_{MM} = \Delta E_{internal} + \Delta E_{electrostatic} + \Delta E_{vdw} \quad (Eq.3)$$

$$\Delta G_{sol} = \Delta G_{PB/GB} + \Delta G_{SA} \qquad (Eq. 4)$$

In Eq. (2), the terms ΔE_{MM}, ΔG_{sol}, and $-T\Delta S$ are dedicated to the changes of gas phase energy, solvation free energy, and the conformational entropy upon binding, respectively. ΔE_{MM} is the sum of internal energy, ΔE_{int}, (bond, angle, and dihedral energies), electrostatic, $\Delta E_{electrostatic}$, and van der Waals energies, ΔE_{vdw} which are computed from MD simulations. Solvation free energy, ΔG_{sol}, depends on polar and nonpolar contributions. $\Delta G_{PB/GB}$, is the electrostatic solvation free energy (polar contribution), and ΔG_{SA} is the nonelectrostatic solvation energy (nonpolar contribution). The polar contribution is calculated from either PB or GB model. Dielectric constants for solute and solvent were set to 1 and 80, respectively. The nonpolar solvation energy, ΔG_{SA}, was computed from the solvent accessible surface area (SASA) with a probe radius of 1.4 Å (Eq. (5)).

$$\Delta G_{SA} = \gamma SASA + \beta \qquad (Eq. 5)$$

where γ is the surface tension constant and β is the offset constant. These values are set to 0.0072 kcal mol^{-1} $Å^{-2}$ and 0 kcal mol^{-1} for MMGBSA and 0.0378 kcal mol^{-1} $Å^{-2}$ and -0.5692 kcal mol^{-1} for MMPBSA. Besides free energy calculations, normal mode analyses (*nmode*) also were performed for defining entropy contribution to binding energies by using an interval of 100 ps 100 frames were extracted from MD trajectories. Less snapshots selected from snapshots used for free energy calculations due to time consuming of *nmode* analyses.

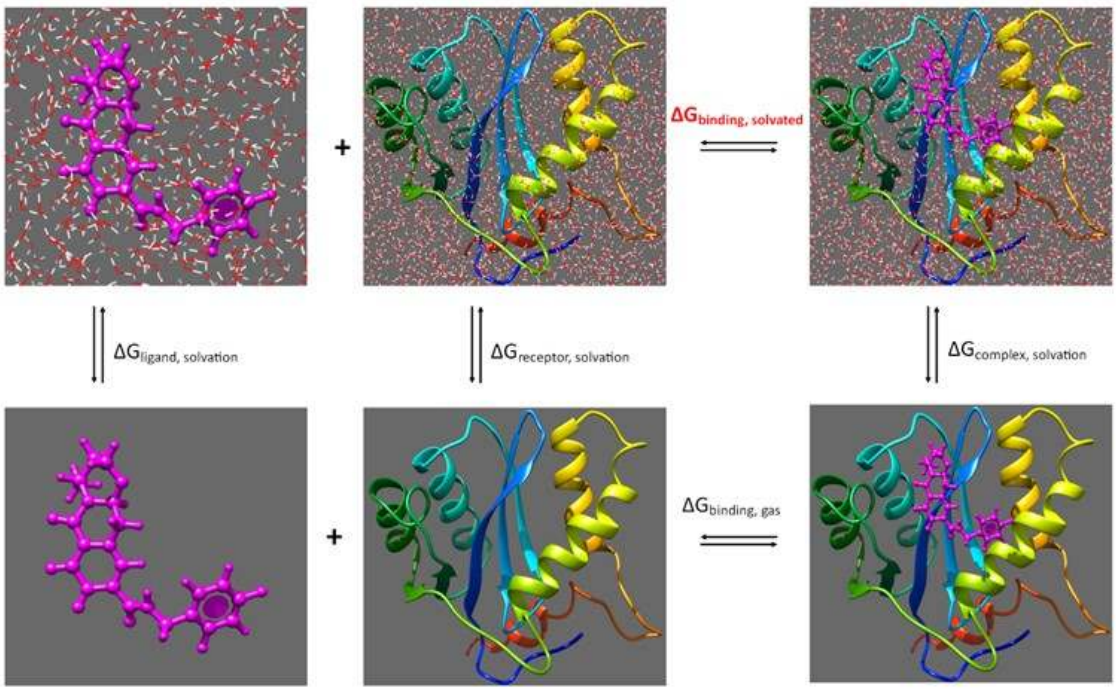

Figure 2. Thermodynamic cycle of MM-PB(GB)SA method.

RESULTS AND DISCUSSION

Molecular Dynamics Studies of Receptor

An important point in MD simulation is to evaluate the stability of system which can be defined by root mean square deviations (RMSD) of time-varying backbone atoms coordinates respect to MD starting frame (Figure 3.). Small changes in RMSD values suggest that there are not significant movements in the CCD and system reaches a plateau after 2.5 ns with a value of ~2.3 Å. This situation could be attributed to structure of CCD having less flexible subdomains, only 140-149, 166-171 and 186-194 residues are flexible in CCD. The RMSD plot of 138-150 which also contains the flexible loop shows that it undergoes a conformational change approximately at 4.5 ns which is ratified by MD simulation movie (Figure 3).

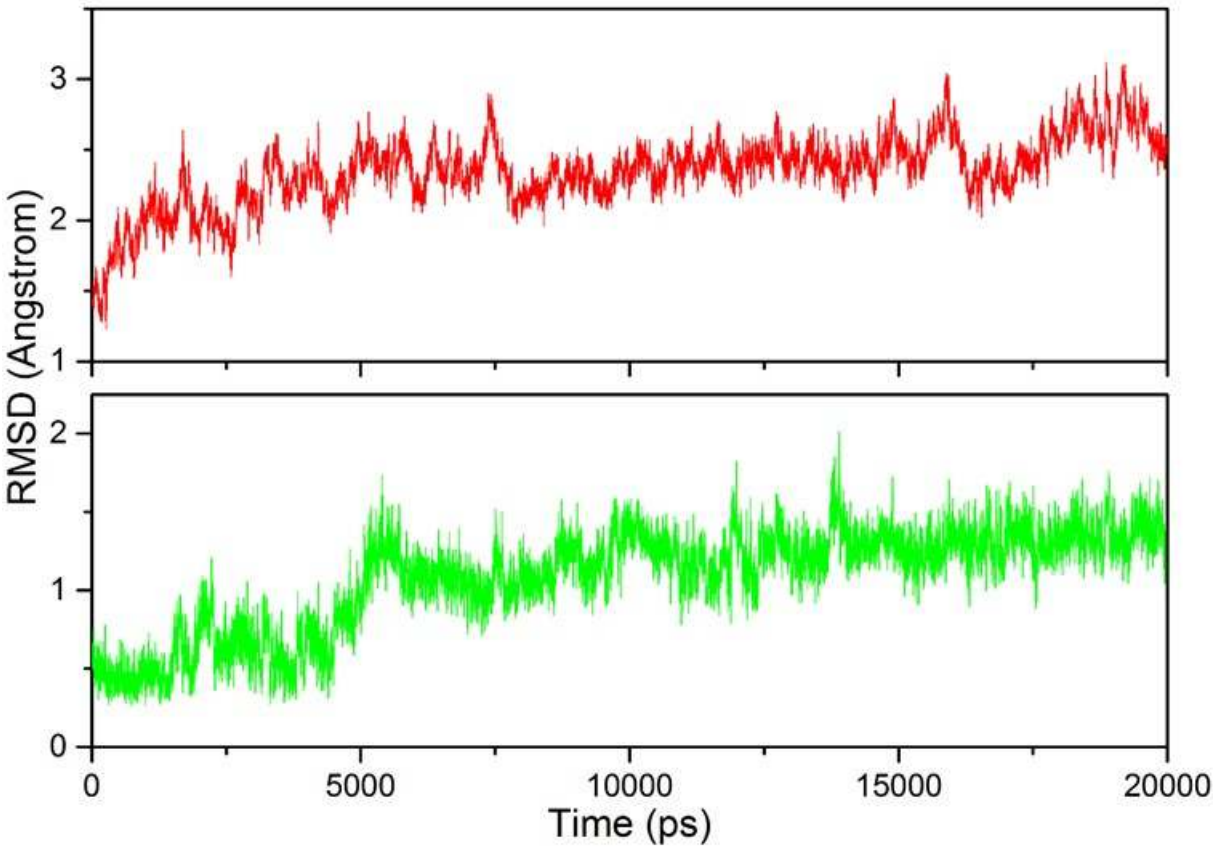

Figure 3. The time evolution of the RMSD values of backbone atoms for all residues (red) and for 140-149 residues (green) in the HIV-1 IN catalytic core.

The distances of Mg^{2+} ions with concerned residue atoms extracted from MD simulation revealed that the catalytic center is reached a stabilization point (Supp. Inf. Figures 1, 2.).

One of the Mg^{2+} ion coordinates with OD1 and OD2 oxygen atoms of D64 and D116 respectively, and oxygen of four water molecules, while second Mg^{2+} ion coordinates with OD2 atom of D64 and OE1 and OE2 atoms of E152 alongside three waters' oxygen atoms. After MD simulation of receptor three conformationally different structures of CCD were defined by cluster analyses. Superimposition of clusters' members named C1, C2 and C3 is represented as ribbon and basic style in Figure 4. C1 constitutes 23.77% of 10,000 frames, where C2 and C3 constitute 61.51 % and 14.72 % of 10,000 frames, respectively. As denoted from evaluation of RMSD plots there is not a major conversion in CCD structure.

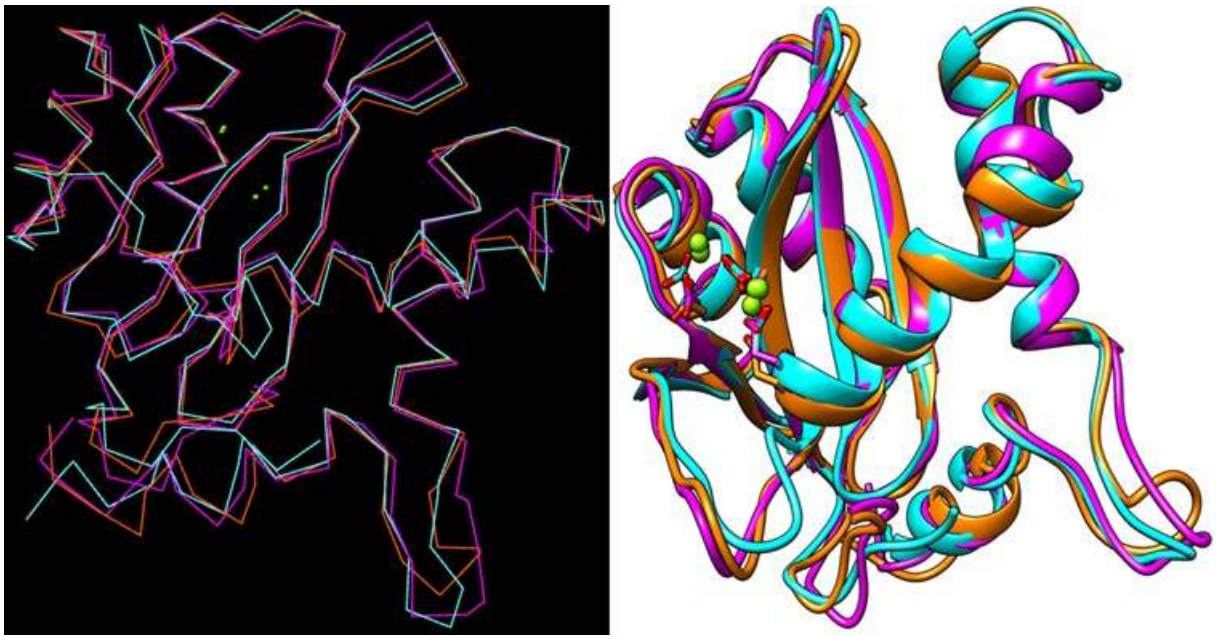

Figure 4. Superimposition of three different conformations of protein obtained from clustering analyses which are represented as C1, C2, and C3 as basic (left) and as ribbon (right) view.

Docking Studies of Ligands

The approved HIV-1 integrase inhibitors RAL, EVG, and DTG and newly designed ligands L01 (3,3'-azanediylbis(2-((6,8-diaminonaphthalen-2-yl)amino)-3-oxopropanoic acid)), L02 (3,3'-azanediylbis(2-((2,4-diaminopteridin-6-yl)amino)-3-oxopropanoic acid)), L03 (3,3'-azanediylbis(2-((6,8-diamino-7-(3-(2-chlorophenyl)propyl)naphthalen-2-yl)amino)-3-oxopropanoic acid)) and L04 ((E)-2-((6,8-diamino-7-(3-(2-chlorophenyl)-3-oxoprop-1-en-1-yl)naphthalen-2-yl)amino)-3-oxo-3-(2-phenylacetamido)propanoic acid) were docked to CCD active site. The docking scores of ligands in C1, C2 and C3 structures are listed in Table 1 while hydrogen bonds seen between ligands and receptors and ligand atoms interacted with metals are shown in Table 2. As an example of docking, the sites of three conformations of protein which L04 posed are depicted in Figure 5 and others were shown in Supporting Information (see Figure 3). Differentiation of docking ligand to three conformations of protein structure obviously seen from figure. L04 is the best scored ligand

in C1 while L01 has best score in both C1 and C3. All ligands seem to be best docked to C1 conformation of protein except EVG. Its docking score higher in C3 than in C1.

Table 1. Docking scores (kcal/mole) of ligands in different conformations of catalytic core domain.

	C1	**C2**	**C3**
L01	-11.55	-11.08	-11.50
L02	-9.06	-8.04	-7.44
L03	-11.31	-10.09	-9.87
L04	-12.14	-9.28	-8.34
DTG	-11.70	-10.69	-11.21
EVG	-10.90	-10.32	-11.04
RAL	-11.49	-9.98	-9.31

Unsurprisingly, the docking scores of ligands, their docked place in catalytic center and the interactions of ligands with receptor are different from each other. These results were expected to some degree, on the other hand the confirmation given by the calculation presented in this study is also is an important element in the field of drug discovery. The docking score of L04 is -12.14 kcal/mole in C1 conformation of receptor while -8.34 kcal/mole in C3 conformation of receptor. We can think like this: Anyone who searches for a ligand library may eliminate L04 in C3 conformation of receptor due to its low docking score. And also this result directs us to MD simulations. Because we use MD simulations to detail dynamics and behaviors of protein or complexes. So the MD simulation analyses of complexes will inform us to know if a ligand having different orientation, docking score and interactions in different conformation of a receptor will change to same orientation and give same interactions with protein after MD simulation or not.

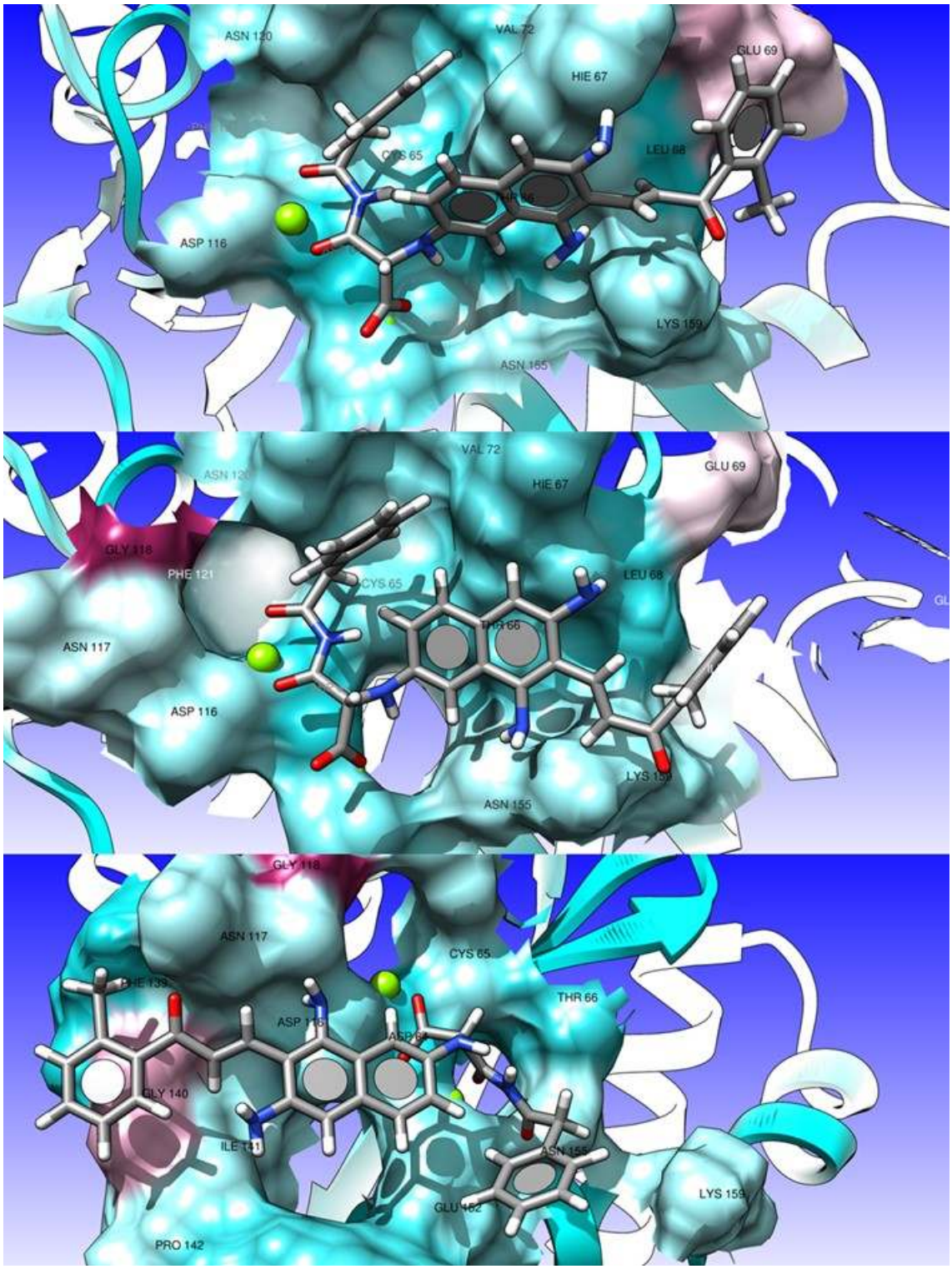

Figure 5. Docking sites and orientations of L04 in C1, C2, and C3 protein conformations.

RAL, EVG, and DTG have been used in many theoretical and experimental studies [40, 48-50]. Recently, crystal structures of PFV integrase with viral DNA including RAL, EVG, and DTG have been obtained. From these structures, 3L2V.pdb and 3OYA.pdb contain RAL, 3L2U.pdb contains EVG and 3S3M.pdb contains DTG. While Raltegravir interacts with

Tyr212 and Gly215 equivalent residues of HIV-1 IN Tyr143 and Gln146, it is also in interaction with Pro214 (Pro145 in HIV-1 IN) in 3OYA crystal structure. In their contained structures, EVG and DTG interact with same residues and also DTG interact with Glu221 (GLu152 in HIV1) in addition to Tyr212 and Pro214 residues. Notwithstanding our docking studies show that in all three conformation of protein, RAL interacts with Tyr143, the docked position of RAL is very different from position it is placed in crystal structure. This is referred to flexible loop, being in very different conformations in PFV structures and 1BL3 structure (used in this study), and also is referred to PFV having vDNA in catalytic site. The docking test of EVG to 3L2U crystal structure supports our consideration (Supporting information, see Figure 4). Performed test run docked the ligand pretty much to the same position of crystal structure while only some substituents of ligand are in different conformations. It is also must be noted that existence of DNA or RNA in structure changes docking results positively (EVG docking test score is 17.6 kcal/mole). Sharma *et al.* have also reported this issue in their study [19]. Besides, one must bear in mind that docking programs consider crystal structures containing ligand for developing program algorithms.

From Table 2 it has been seen that while all ligands interact with Mg atoms, some of ligands have four oxygen atoms in interaction with two Mg atoms. HIE67, GLU92, and ASN117 residues are found to create H bond with ligand atoms. The interactions of all ligands with protein residues at their docked sites are generally given in Table 3. C1 conformation of protein has vdW interactions with all ligands. It is consistent with docking scores of ligands.

Table 2. Hydrogen bonds and metal contacts obtained from docking results between ligand atoms and protein residues.

	C1		**C2**		**C3**	
	H bonds (Residue and Ligand atoms)	Mg-Ligand atoms	H bonds (Residue and Ligand atoms)	Mg-Ligand atoms	H bonds (Residue and Ligand atoms)	Mg-Ligand atoms
L01	GLU152OE1-H49 GLN148OE1-H47 ASN117OD1-H61	MG210-O18,O27 MG211-O17,O26	HIE67O-H48 HIE67ND1-H45 ASP116OD1-H53 ASN117O-H62	MG210-O23,O21 MG211-O18, O27	ASN117O-L01H62 ASN155HD22-L01O17 HIE67O-H48 ASP116OD1-L01H53	MG210-O23,O21 MG211-O18,O27
L02	HIE67H-O LYS159HZ1-N4 LYS159HZ3-N5 CYS65O-H GLU92OE1-H7 GLU92OE2-H11 THR66HA-O	MG210-O3,O5 MG211-O2	HI67HN-N10 ASN155HD22-O5 GLU92OE1-H3 GLU92OE2-H4 SER119OG-H5,H6 HIE67ND1-H9	MG210-O2 MG211-O4	LYS159HZ1-L02N11 ASP116OD2- L02H2 ASN117O- L02H3 GLU152OE1- L02H7 LYS156HE2- L02N11	MG210-O2 MG211-O4,O3
L03	HIE67ND1-H7 ASN155HD21-O5 ASN155HD22-O5 LYS156HZ2-O4 LYS156HZ3-O4 LYS156HZ3-O5	MG210-O,O2 MG211-O,O1,O4	ASP116OD1-H1 CYS65O-H6 HIE67ND1-H10	MG210-O, O1 MG11-O2,O5	HIE67O-L03H3 ASP116OD2-L03H3 ASP116OD2-L03H10 ASN117O-L03H9	MG210-O4 MG211-O2
L04	LYS159HZ2-O4 LYS159HZ3-N2 THR66OG1-H HIE67O-H2 HIE67ND1-H5	MG210-O,O1 MG211-O3	LYS159HZ1-O4 ASP64OD2-H CYS65O-H1 HIE67O-H5,	MG210-O,O1; MG211-O3	ASN117HD22-L04O4 ASN155HD22-L04O ASP116OD2-L04H3 ASN117O-H	MG210-O2 MG211-O1,O3,O

Table 3. Hydrogen bonds and metal contacts obtained from docking results between ligand atoms and protein residues (Continued).

	C1		**C2**		**C3**	
	H bonds (Residue and Ligand atoms)	Mg-Ligand atoms	H bonds (Residue and Ligand atoms)	Mg-Ligand atoms	H bonds (Residue and Ligand atoms)	Mg-Ligand atoms
DTG	GLU152OE1-H13 LYS156HZ1-F LYS156HZ3-F1	MG210-O2,O3 MG211-O2,O4	GLU92OE1-H3 CYS65O-H8 GLU152OE1-H4	MG210-O3,O2,O1 MG211-O2,O4	HIE67H-DTGO ASN155HD22-DTGO1 SER119H-DTGF1 SER119H-F30 HIE67O-DTGH6,H7 GLU92OE1-DTGH13,H14 GLU92OE2-DTGH9	MG210-O4,O2 MG211-O3,O2,O1
EVG	THR66OG1-H21 HIE67-H8 GLU152OE1-H20	MG210-O,O4 MG211-O2,O3	ASN117O-H21 ASP64OD1-H20 ASN117O-H10,	MG210-O2 MG211-O,O4	CYS65O-EVGH21 GLU92OE2-EVGH21 THR66HA-EVGO3 CYS65O-EVGH ASN117O-EVGH10	MG210-O2 MG211-O4,O
RAL	CYS65H-O2 GLU152OE2-H13 GLY118HA3-N4 TYR143HA-F CYS65O-H2	MG210-O2,O4 MG211-O1	LYS159HZ2-RALN4 GLU152OE1-RALH15	MG210-O,O1 MG211-O4,O1	HIE67H-RALO2 THR66HA-RALO2 HIE67HD2-RALN4 GLU92OE2-RALH1 GLU92OE1-RALH15	MG210-O,O1 MG211-O4,O1

Table 4. Various interactions between ligand atoms and protein residues composed by docking.

	C1	C2	C3
L01	π-cation: LYS156NZ vdW: ASP64, CYS65, THR66, GLY140, ILE141, ASN155, LYS159	π-sigma: HIE67 vdW: ASP64, THR66, LEU68, GLY118, ASN155, LYS159	vdW: CYS65, THR66, GLY118
L02	ASP64, THR66, ASP116, GLU152	vdW: THR66, ASN117, GLY118, GLU152	π-alkyl: LYS156 vdW: CYS65, THR66, GLY118, ASN155, LYS156
L03	Charge interactions: LYS156, THR66, VAL72, TYR143, GLU92 vdW: ASP64, CYS65, ASP116, ILE141, PRO142, GLN148, LYS159	π-sigma:THR66 Charge interactions: HIE67 vdW: LEU68, GLU92, ASN117, GLY118, SER119, ASN120, LYS159	π-π: TYR143 π-cation: LYS159 Charge interactions: LEU68, LYS159 vdW: ASP64, THR66, GLY118, TYR143, GLU152, ASN155, ILE162,
L04	Charge interactions: LEU68, HIE67 vdW: ASP64, CYS65, GLU69, GLY70, VAL72, GLU92, ASP116, GLU152, ASN155	π-sigma:THR66 Charge interactions: LEU68, LYS159 VAL72, ASP116	Charge interactions: PHE139 vdW: ASP64, CYS65, GLY140, PRO142, TYR143, GLU152
DTG	Charge interactions: HIE67, VAL72, LYS156 vdW: ASP64, CYS65, THR66, GLU92, ASP116, GLN148, ASN155	Charge interactions: HIE67, VAL72 vdW: ASP64, THR66, ASP116, TYR143, ASN155, LYS159	Charge interactions: CYS65 π-lone pair vdW: ASP64, THR66, ASP116, ASN117, GLY118, GLU152
EVG	π-sigma: THR66 vdW: CYS65, HIE67, VAL72, GLU92, ASP116, GLN148, GLU152, ASN155, LYS156, LYS159	vdW: CYS65, GLU92, GLY118, PRO142, TYR143, GLU152	vdW: THR66, HIE67, GLY118, GLY140, ILE141, PRO142, TYR143, GLU152, ASN155
RAL	Charge interactions: ILE141 vdW: THR66, HIE67, ASN117, SER119, TYR143, ASN144, ASN155	π-π T-shaped:TYR143 Charge interactions: LEU68 vdW: ASP64, CYS65, THR66, GLU92, ASP116, ASN155	π-π t-shaped: HIE67 Charge interactions: HIE67, VAL72 vdW: CYS65, ALA91, ASN117 GLY118, THR143, ASN155

Molecular Dynamics Studies of the Complexes

From the RMSD plots of complexes versus time, it is seen that the proteins reached stable states (Figure 6). In the plot of C1 complex of Dolutegravir, an ascension is seen at about 1.5-5 ns. MD movies of this complex showed the flexible loop between residues 185-198 are causing this rise. It is also seen from the RMSD plots of mentioned residues (not shown here).

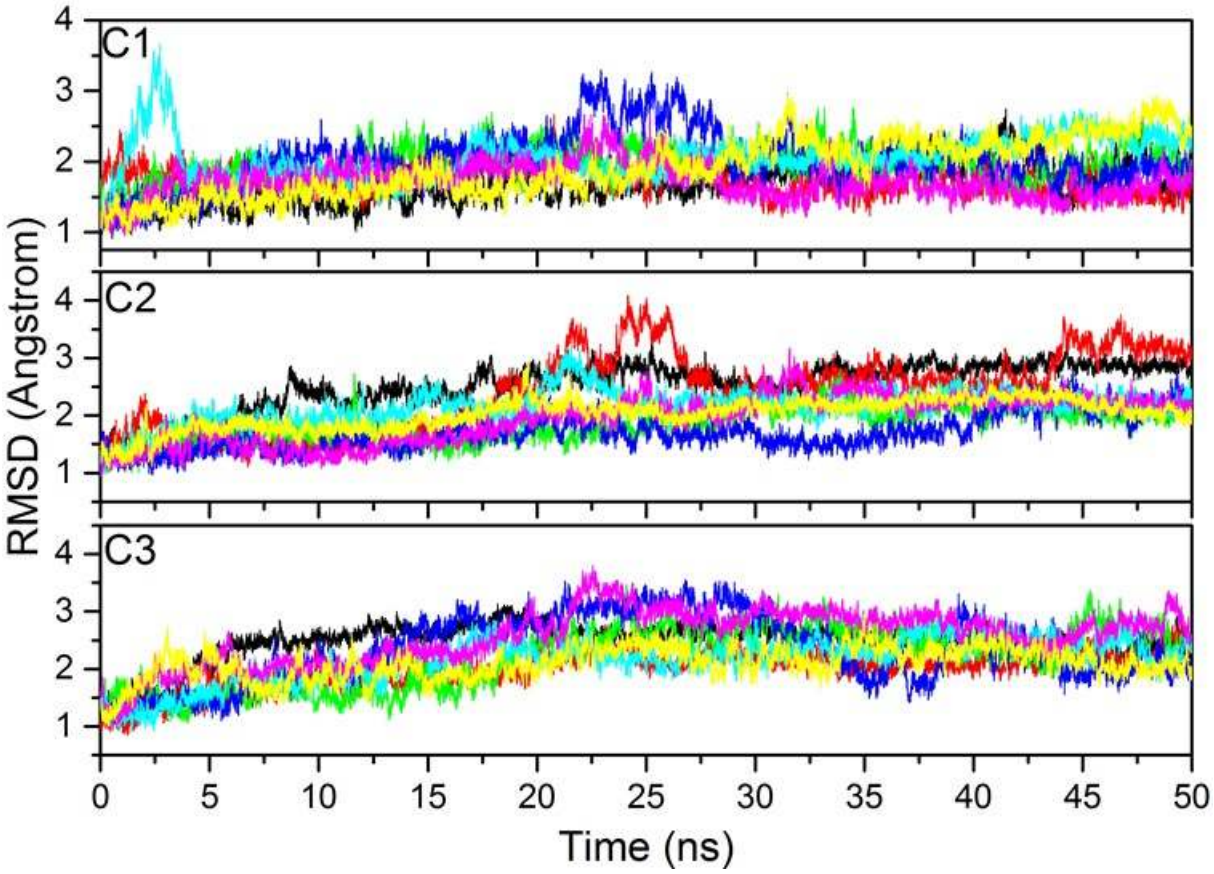

Figure 6. The time evolution of RMSD values for backbone atoms of complexes, C1, C2, and C3 (L01 black, L02 red, L03 green, L04 blue, DTG cyan, EVG magenta, and RAL yellow).

All ligands seem to be in a stable state despite the high RMSD values of L02 and L03 in C1 (Figure 7). We also determined the ligands docked to different conformations of protein with diverse orientations and interactions did not resemble each other by MD simulations (Figure 8). As an example, L01 docked to three different conformations of protein. Each docking orientation is different. And it could be seen that MD simulation did not put those three orientations of L01 to the same position (Figure 8). We would like to point out that this is not an absolute result because an MD simulation of 50 ns (a sufficient time for an MD simulation) was performed in this study and it is not definite to know there will be a change or not by extending time. However, the clustering analyses performed for the 50 ns simulation show that the conformations of complexes are close to each other and so it

is not necessary to depict the achieved clusters here. By the way, the images of structures having lowest energies illustrated here for each complex.

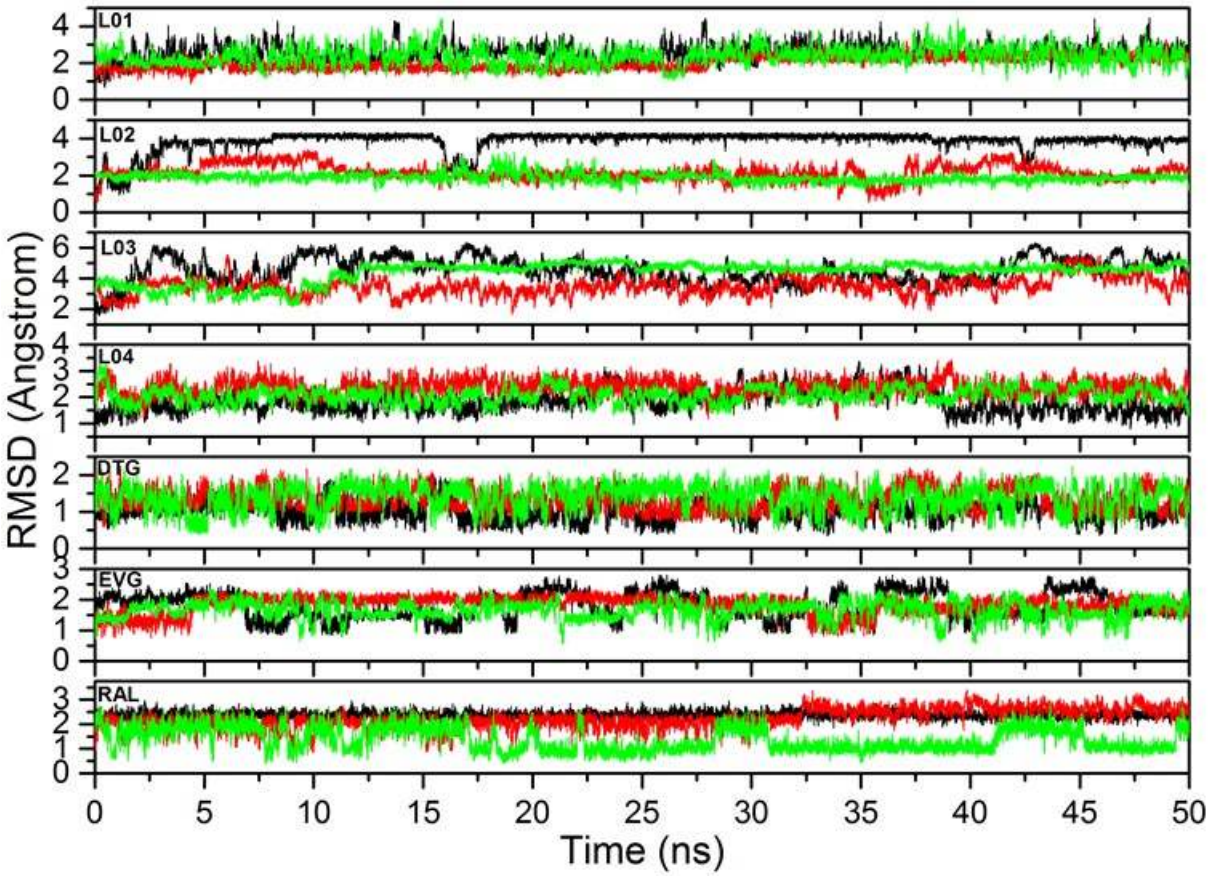

Figure 7. 50 ns time evolution of RMSD values of ligand atoms (C1 black, C2 red, and C3 green).

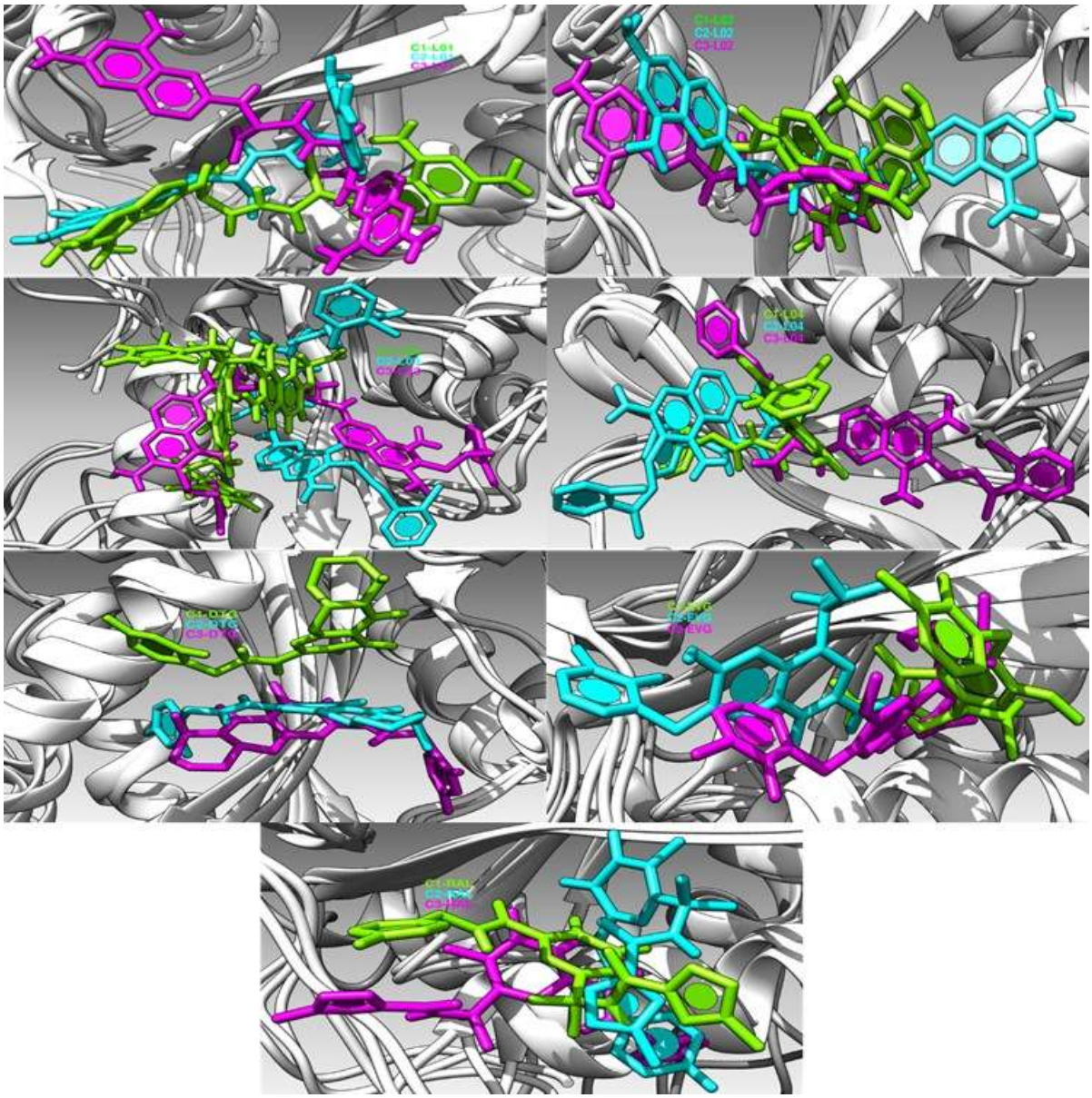

Figure 8. The positions of ligands in each protein structure. Superimposed structures are taken from a lower-energy structure of each complex's MD simulation.

Ligand-residue interactions, which are observed from docking results, seem to change significantly by MD simulations. Especially, most of hydrogen bonds and electrostatic interactions of ligands with residues obtained from docking disappeared by MD simulations (Table 4).

Table 5. Ligand-residue interactions observed from the structures with lowest energies located from MD simulations.

	C1	C2	C3
L01	vdW: ASP64, HIE67, ASP116, 3 water molecules H bonds: 1 water molecule	π-π T shaped: HIE67 vdW: CYS65, HIE67, ASN117, PHE139, LYS159 and 3 water molecules H bonds: THR66, ASP116, ASN155 and 1 water molecule	vdW: ASP64, CYS65, GLU92, ASP116, GLY118, ASN120, GLU152 and 1 water molecule H bonds: THR66, SER119, ASN155 and 4 water molecules
L02	THR66, CYS65, ASP116, ASN155, 2 water molecules H bonds: GLU152 and 4 water molecules	π-alkyl: LYS156, LYS159 vdW: TCYS65, HIE67, ASN117, GLU152, ASN155 and 1 water molecule H bonds: THR66, LYS159 and 1 water molecule	Electrostatic: LYS159 vdW: ASP64, CYS65, ASP116, GLY118, GLU152 and 2 water molecules H bonds: SER119, ASN120, ASN155 and 3 water molecules
L03	vdW: THR66, HIE67, LEU68, ASP116, ASN117, ASN155 and 2 water molecules H bonds: 1 water molecule	π-π stacked:HIE67 π-alkyl: HIE67 vdW: CYS65, THR66, GLY70, GLU92, ASN117 and 2 water molecules H bonds: ASP64, ASP116, GLU152, ASN155 and 2 water molecules	Electrostatic: ASP64 Amid π-stacked: ALA91 π-alkyl: VAL72, LYS159 alkyl-alkyl: LEU68 vdW: THR66, HIE67, ILE89, PRO90, GLU92, SER119, ASN120, ASN155, LEU158, ILE162 and 3 water molecules H bonds: CYS65, ASP116 and 1 water molecule
L04	vdW: ASP64, THR66, GLU69, HIE67, VAL72, ILE73, ASP116, GLU152 and 4 water molecules π-alkyl: CYS65	π-π T shaped: HIE67 vdW: ASP64, CYS65, THR66, GLU92, ASP116 and 4 water molecules	π-cation: LYS159 π-alkyl: TYR143, PRO145 vdW: ASP64, THR66, HIE67, ASP116, GLU152, ASN155 and 2 water molecules H bonds: 1 water molecule
DTG	vdW: ASP64, ASP116, ILE141, TYR143 H bonds: GLN148 and 2 water molecules	π-alkyl: LYS159 vdW: CYS65, THR66, ASP116, GLU152, ASN155, LYS156 and 1 water molecule H bonds: 1 water molecule	vdW: CYS65, GLU92, ASP92, ASP116, GLY118, GLU152, LYS159 and 3 water molecules H bonds: ASN155 and 1 water molecule
EVG	vdW: ASP64, THR66, HIE67, ASP116, ASN155, LYS159 and 5 water molecules H bonds: GLN148 and 2 water molecules	π-anion: ASP116 vdW: ASP64, GLY118, PHE139, GLY140, GLU152 and 4 water molecules H bonds: ASN117 and 2 water molecules	π-anion: ASP64 vdW: HIE67, GLU92, ASP116, GLU152 and 2 water molecules H bonds: CYS65, THR66, ASN155 and 1 water molecule
RAL	π-π stacked: TYR143 vdW: ASP64, ASP116 and 2 water molecules H bonds: 1 water molecule	vdW: ASP64, CYS65, THR66, HIE67, ASP116, TYR143, LYS159 and 5 water molecules H bonds: 1 water molecule	alkyl-alkyl: ILE141 π-anion: GLU152 vdW: ASP64, ASP116, TYR143, LYS156, LYS159 and 4 water molecules

Binding Free Energies of Ligands

The binding modes of the ligands to the different conformations of HIV-1 integrase catalytic core domain were competed by end point energy method, (MM-PB(GB)/SA). Calculated values are shown in Table 5.

Table 6. Binding free energies of ligands calculated by MM-PB(GB)SA method and contribution of entropy to binding free energies.

	ΔE_{elec}	ΔE_{vdW}	ΔG_{PB}	ΔG_{GB}	$-T\Delta S$	ΔG_{bind}^{PB}	ΔG_{bind}^{GB}
C1_L01	-482.0850	-4.2186	-13.0748	-16.5701	28.6627	15.5879	12.0926
C1_L02	-413.9868	-3.1813	-2.3425	-5.6870	22.4444	20.1019	16.7574
C1_L03	-512.5300	-13.5305	-35.9332	-49.3102	27.2606	-8.6726	-22.0496
C1_L04	-294.7430	-9.4281	-14.7613	-2.3909	24.3747	9.6134	21.9838
C1_DTG	-336.6129	-8.0492	-7.5524	-11.5279	23.6320	16.0796	12.1041
C1_EVG	-422.7991	-1.9412	-39.7112	-41.0937	24.8457	-14.8655	-16.2480
C1_RAL	-278.8543	-6.2337	0.0161	-2.4443	21.3160	21.3321	18.8717
C2_L01	-539.7636	-5.0295	-49.4787	-52.4085	27.7591	-21.7196	-24.6494
C2_L02	-532.3656	-6.4072	-25.1195	-15.7172	26.7391	1.6196	11.0219
C2_L03	-512.5300	-13.5305	-35.9332	-49.3102	30.7403	-5.1929	-18.5699
C2_L04	-296.6142	-6.6585	-13.3614	0.3272	22.4650	9.1036	22.7922
C2_DTG	-338.2980	-0.1855	-17.6762	-7.9015	25.0018	7.3256	17.1003
C2_EVG	-311.6691	-7.5985	-8.0243	-16.2065	24.9792	16.9549	8.7727
C2_RAL	-277.6655	-9.7355	-3.8454	-4.3016	20.6870	16.8416	16.3854
C3_L01	-518.1380	-6.6245	-4.8480	-34.2500	29.0603	24.2123	-5.1897
C3_L02	-443.3987	-13.3996	6.4690	-11.4051	28.1492	34.6182	16.7441
C3_L03	-498.7371	-27.6130	-31.0748	-37.0633	31.3367	0.2619	-5.7266
C3_L04	-279.6095	-14.7686	3.2340	-9.2501	26.8973	30.1313	17.6472
C3_DTG	-338.2980	-0.1855	-17.6762	-7.9015	25.8882	8.2120	17.9867
C3_EVG	-383.1383	-3.2655	-37.1270	-35.7265	25.2536	-11.8734	-10.4729
C3_RAL	-285.5304	-10.2197	-9.3601	-3.8106	-22.5998	13.2397	18.7892

ΔE_{elec}: Contribution of electrostatic energy to binding energy, **ΔE_{vdW}:** Contribution of van der Waals interactions to binding energy, **ΔG_{PB}** and **ΔG_{GB}:** Binding energies according to Poisson-Boltzmann and Generalized-Born methods. Mean energies are in kcal mol^{-1}.

Binding free energies of ligands were calculated by Poisson-Boltzmann (PB) [37, 51] and Generalized-Born (GB) [37, 51] approaches. As the varying docking scores, interactions and orientations of ligands in different conformations of protein, binding free energies of ligands also differ from each other. In general, the scores of PB approach are at the lowest than scores of GB approach but in this study some of ligands gave greater PB scores than GB scores such as c1_L04, c2_L02, c2_L04, c2_dtg and c3_dtg/evg/ral. In the complexes which ligands having low binding energy, the electrostatic contributions seem to be lower and mainly the lower binding energy values are complying with this parameter.

From all ligands, the best binding free energy belongs to L01 in C2 protein while Elvitegravir shows favorable values except in C2 protein ($C1_{PB}$: -39.71, $C1_{GB}$= -41.09, $C3_{PB}$: -37.13, $C3_{GB}$= -35.73). Elvitegravir is also well bounded to protein than RAL and DTG inhibitors. The most surprising result is that Raltegravir seems to be the worst ligand overall ligands according to binding free energies. Besides, it has the lowest average binding score in three conformations of protein. This situation is also in contrast with conception of RAL binds rather electrostatically to protein because obtained electrostatic energies of RAL are low in generally.

From the designed ligands, while the results of L01 and L03 are favorable, L04, which has the best docking score (-12.09 kcal/mole) in C3 complex showed low binding free energies (ΔG_{PB}= 3.23 and ΔG_{GB}= -9.25) in contrast to its docking score. Nevertheless, from plotting (Figure 9) docking scores with binding free energies of ligands, it has seen in general the docking scores of ligands are compatible with their binding free energies. We can make an inference that used docking program has a strong estimating property of binding free energies.

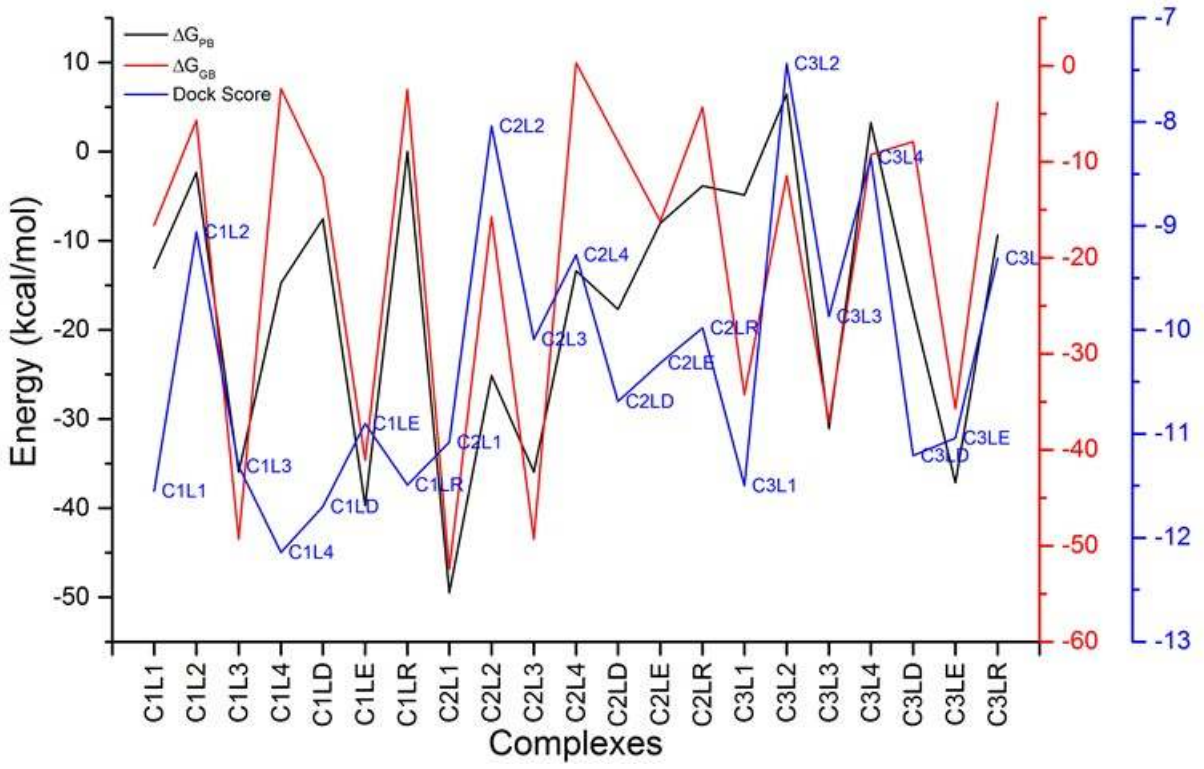

Figure 9. The relation between docking scores and binding free energies calculated by MM-PB(GB)SA.

The contribution of entropy to binding free energies were also computed. While electrostatic energies, vdW energies, and non-polar solvation terms have positive

contribution on binding ligands to protein, polar solvation and entropy terms have negative effect on binding ligands.

CONCLUSION

As a conclusion, three ligands which are currently in use as HIV-1 In inhibitors and four newly designed ligands were used in this study. A molecular dynamics simulation of 10 ns was performed to protein before docking studies. And docking studies were run for three conformations of protein obtained from cluster analyses. Ligands are bound to three conformations of protein in different orientations and so have diverse binding free energies. L04 is the ligand having best docking score (-12.14 kcal/mole) in C1 protein conformation while docking of L02 into C3 protein conformation has the lowest docking score (-7.44 kcal/mole).

After docking studies, a 50 ns MD simulation was performed for each complex and results were analyzed. Ligands' binding free energy calculations were carried out by MM-PB(GB)SA and the results were contributed by entropy calculations. The calculations showed that the binding of L01 to C2 protein is the best bound ligand over other ligands. Besides, ligand having the best docking score, L04, did not demonstrate a good binding to protein. This issue was the one of purposes to search in study and we can say that docking scores could believe a researcher for selecting proper ligands, according to results. It is also should be noted the MM-PB(GB)SA calculations could not produce absolute experimental results but produce outcomes those are compatible with experimental results [52-54].

Another aim of the study was to evaluate new molecules as new HIV-IN inhibitors. From designed ligands L01 (3,3'-azanediylbis(2-((6,8-diaminonaphthalen-2-yl)amino)-3-oxopropanoic acid)) and L03 (3,3'-azanediylbis(2-((6,8-diamino-7-(3-(2-chlorophenyl)propyl)naphthalen-2-yl)amino)-3-oxopropanoic acid)) showed promising results. As the last aim of this study, we could see that MD calculations do not convert conformations of different oriented ligands (in different conformations of protein) to same positions in terms of location and interactions of ligand protein. We also should remark that even though the simulations were carried out for a meaningful time of MD calculations, it is only a simulation of 50 ns and so those issues may vary *in vivo*.

ACKNOWLEDGMENTS

The author is grateful to the Research Foundation of Batman University (Project 2012-FED-7) for the financial support.

REFERENCES

1. Global Aids Response Progress Reporting 2015. 2015.www.unaids.org/sites/default/files/media.../JC2702_GARPR2015guidelines_en.pdf.

2. Miri L, Bouvier G, Kettani A, Mikou A, Wakrim L, Nilges M, Malliavin TE. Stabilization of the integrase-DNA complex by Mg2+ ions and prediction of key residues for binding HIV-1 integrase inhibitors. Proteins. 2014;82(3):466-78.10.1002/prot.24412.

3. Pendri A, Meanwell NA, Peese KM, Walker MA. New first and second generation inhibitors of human immunodeficiency virus-1 integrase. Expert Opin Ther Patents. 2011;21(8):1173-89.10.1517/13543776.2011.586631.

4. Zhang D, Debnath B, Yu S, Sanchez TW, Christ F, Liu Y, Debyser Z, Neamati N, Zhao G. Design and discovery of 5-hydroxy-6-oxo-1,6-dihydropyrimidine-4-carboxamide inhibitors of HIV-1 integrase. Bioorganic & medicinal chemistry. 2014;22(19):5446-53.10.1016/j.bmc.2014.07.036.

5. Mehellou Y, De Clercq E. Twenty-six years of anti-HIV drug discovery: where do we stand and where do we go? J Med Chem. 2010;53(2):521-38.10.1021/jm900492g.

6. De Luca L, De Grazia S, Ferro S, Gitto R, Christ F, Debyser Z, Chimirri A. HIV-1 integrase strand-transfer inhibitors: design, synthesis and molecular modeling investigation. Eur J Med Chem. 2011;46(2):756-64.10.1016/j.ejmech.2010.12.012.

7. DeGruttola V, Dix L, D'Aquila R, Holder D, Phillips A, Ait-Khaled M, Baxter J, Clevenbergh P, Hammer S, Harrigan R, Katzenstein D, Lanier R, Miller M, Para M, Yerly S, Zolopa A, Murray J, Patick A, Miller V, Castillo S, Pedneault L, Mellors J. The relation between baseline HIV drug resistance and response to antiretroviral therapy: re-analysis of retrospective and prospective studies using a standardized data analysis plan. Antiviral therapy. 2000;5(1):41-8,1359-6535 (Print)

8. Goethals O, Van Ginderen M, Vos A, Cummings MD, Van Der Borght K, Van Wesenbeeck L, Feyaerts M, Verheyen A, Smits V, Van Loock M, Hertogs K, Schols D, Clayton RF. Resistance to raltegravir highlights integrase mutations at codon 148 in conferring cross-resistance to a second-generation HIV-1 integrase inhibitor. Antiviral Res. 2011;91(2):167-76.10.1016/j.antiviral.2011.05.011.

9. Richman DD. Antiviral drug resistance. Antiviral Res. 2006;71(2-3):117-21.10.1016/j.antiviral.2006.03.004.

10. Calmy A, Hirschel B, Cooper DA, Carr A. A new era of antiretroviral drug toxicity. Antiviral therapy. 2009;14(2):165-79,1359-6535 (Print).

11. Clavel F, Hance AJ. HIV drug resistance. N Engl J Med. 2004;350(10):1023-35.10.1056/NEJMra025195.

12. Emini EA, Graham DJ, Gotlib L, Condra JH, Byrnes VW, Schleif WA. HIV and multidrug resistance. Nature. 1993;364(6439):679.10.1038/364679b0.

13. Geeraert L, Kraus G, Pomerantz RJ. Hide-and-seek: the challenge of viral persistence in HIV-1 infection. Annu Rev Med. 2008;59:487-501.10.1146/annurev.med.59.062806.123001.

14. Johnson VA, Brun-Vezinet F, Clotet B, Gunthard HF, Kuritzkes DR, Pillay D, Schapiro JM, Richman DD. Update of the drug resistance mutations in HIV-1: December 2010. Top HIV Med. 2010;18(5):156-63,2161-5845 (Electronic), 1542-8826 (Linking).

15. Malta M, Magnanini MM, Strathdee SA, Bastos FI. Adherence to antiretroviral therapy among HIV-infected drug users: a meta-analysis. AIDS Behav. 2010;14(4):731-47.10.1007/s10461-008-9489-7.

16. Marcello A. Latency: the hidden HIV-1 challenge. Retrovirology. 2006;3:7.10.1186/1742-4690-3-7.

17. Moyle G, Gatell J, Perno CF, Ratanasuwan W, Schechter M, Tsoukas C. Potential for new antiretrovirals to address unmet needs in the management of HIV-1 infection. AIDS Patient Care STDS. 2008;22(6):459-71.10.1089/apc.2007.0136.

18. Paredes R, Clotet B. Clinical management of HIV-1 resistance. Antiviral Res. 2010;85(1):245-65.10.1016/j.antiviral.2009.09.015.

19. Sharma H, Sanchez TW, Neamati N, Detorio M, Schinazi RF, Cheng X, Buolamwini JK. Synthesis, docking, and biological studies of phenanthrene beta-diketo acids as novel HIV-1 integrase inhibitors. Bioorg Med Chem Lett. 2013;23(22):6146-51.10.1016/j.bmcl.2013.09.009.

20. Ercan S, Pirinccioglu N. Computational design of a full-length model of HIV-1 integrase: modeling of new inhibitors and comparison of their calculated binding energies with those previously studied. J Mol Model. 2013;19(10):4349-68.10.1007/s00894-013-1943-4.

21. Desimmie BA, Demeulemeester J, Suchaud V, Taltynov O, Billamboz M, Lion C, Bailly F, Strelkov SV, Debyser Z, Cotelle P, Christ F. 2-Hydroxyisoquinoline-1,3(2H,4H)-diones (HIDs), novel inhibitors of HIV integrase with a high barrier to resistance. ACS Chem Biol. 2013;8(6):1187-94.10.1021/cb4000426.

22. Summa V, Petrocchi A, Bonelli F, Crescenzi B, Donghi M, Ferrara M, Fiore F, Gardelli C, Gonzalez Paz O, Hazuda DJ, Jones P, Kinzel O, Laufer R, Monteagudo E, Muraglia E, Nizi E, Orvieto F, Pace P, Pescatore G, Scarpelli R, Stillmock K, Witmer MV, Rowley M. Discovery of raltegravir, a potent, selective orally bioavailable HIV-integrase inhibitor for the treatment of HIV-AIDS infection. J Med Chem. 2008;51(18):5843-55.10.1021/jm800245z.

23. Sax PE, DeJesus E, Mills A, Zolopa A, Cohen C, Wohl D, Gallant JE, Liu HC, Zhong L, Yale K, White K, Kearney BP, Szwarcberg J, Quirk E, Cheng AK, team G-U-s. Co-formulated elvitegravir, cobicistat, emtricitabine, and tenofovir versus co-formulated efavirenz, emtricitabine, and tenofovir for initial treatment of HIV-1 infection: a randomised, double-blind, phase 3 trial, analysis of results after 48 weeks. Lancet. 2012;379(9835):2439-48.10.1016/S0140-6736(12)60917-9.

24. Dow DE, Bartlett JA. Dolutegravir, the Second-Generation of Integrase Strand Transfer Inhibitors (INSTIs) for the Treatment of HIV. Infect Dis Ther. 2014;3(2):83-102.10.1007/s40121-014-0029-7.

25. Delelis O, Carayon K, Saib A, Deprez E, Mouscadet JF. Integrase and integration: biochemical activities of HIV-1 integrase. Retrovirology. 2008;5:114.10.1186/1742-4690-5-114.

26. Wang JY, Ling H, Yang W, Craigie R. Structure of a two-domain fragment of HIV-1 integrase: implications for domain organization in the intact protein. EMBO J. 2001;20(24):7333-43.10.1093/emboj/20.24.7333.

27. Chen JC, Krucinski J, Miercke LJ, Finer-Moore JS, Tang AH, Leavitt AD, Stroud RM. Crystal structure of the HIV-1 integrase catalytic core and C-terminal domains: a model for viral DNA binding. Proc Natl Acad Sci U S A. 2000;97(15):8233-8.10.1073/pnas.150220297.

28. Maignan S, Guilloteau JP, Zhou-Liu Q, Clement-Mella C, Mikol V. Crystal structures of the catalytic domain of HIV-1 integrase free and complexed with its metal cofactor: high level of similarity of the active site with other viral integrases. Journal of molecular biology. 1998;282(2):359-68.10.1006/jmbi.1998.2002.

29. Bujacz G, Alexandratos J, Qing ZL, Clement-Mella C, Wlodawer A. The catalytic domain of human immunodeficiency virus integrase: ordered active site in the F185H mutant. FEBS letters. 1996;398(2-3):175-8,0014-5793 (Print).

30. Goldgur Y, Craigie R, Cohen GH, Fujiwara T, Yoshinaga T, Fujishita T, Sugimoto H, Endo T, Murai H, Davies DR. Structure of the HIV-1 integrase catalytic domain complexed with an inhibitor: a platform for antiviral drug design. Proc Natl Acad Sci U S A. 1999;96(23):13040-3,0027-8424 (Print).

31. Wang Y, Rong J, Zhang B, Hu L, Wang X, Zeng C. Design and synthesis of N-methylpyrimidone derivatives as HIV-1 integrase inhibitors. Bioorganic & medicinal chemistry. 2015;23(4):735-41.10.1016/j.bmc.2014.12.059.

32. Costi R, Metifiot M, Chung S, Cuzzucoli Crucitti G, Maddali K, Pescatori L, Messore A, Madia VN, Pupo G, Scipione L, Tortorella S, Di Leva FS, Cosconati S, Marinelli L, Novellino E, Le Grice SF, Corona A, Pommier Y, Marchand C, Di Santo R. Basic quinolinonyl diketo acid derivatives as inhibitors of HIV integrase and their activity against RNase H function of reverse transcriptase. J Med Chem. 2014;57(8):3223-34.10.1021/jm5001503.

33. Hare S, Gupta SS, Valkov E, Engelman A, Cherepanov P. Retroviral intasome assembly and inhibition of DNA strand transfer. Nature. 2010;464(7286):232-6.10.1038/nature08784.

34. Chen Q, Cheng X, Wei D, Xu Q. Molecular dynamics simulation studies of the wild type and E92Q/N155H mutant of Elvitegravir-resistance HIV-1 integrase. Interdiscip Sci. 2015;7(1):36-42.10.1007/s12539-014-0235-8.

35. Brigo A, Lee KW, Iurcu Mustata G, Briggs JM. Comparison of multiple molecular dynamics trajectories calculated for the drug-resistant HIV-1 integrase T66I/M154I catalytic domain. Biophys J. 2005;88(5):3072-82.10.1529/biophysj.104.050286.

36. Brigo A, Lee KW, Fogolari F, Mustata GI, Briggs JM. Comparative molecular dynamics simulations of HIV-1 integrase and the T66I/M154I mutant: binding modes and drug resistance to a diketo acid inhibitor. Proteins. 2005;59(4):723-41.10.1002/prot.20447.

37. Miller BR, 3rd, McGee TD, Jr., Swails JM, Homeyer N, Gohlke H, Roitberg AE. MMPBSA.py: An Efficient Program for End-State Free Energy Calculations. J Chem Theory Comput. 2012;8(9):3314-21.10.1021/ct300418h.

38. Berman HM, Westbrook J, Feng Z, Gilliland G, Bhat TN, Weissig H, Shindyalov IN, Bourne PE. The Protein Data Bank. Nucleic acids research. 2000;28(1):235-42,0305-1048 (Print).

39. Sechi M, Carcelli M, Rogolino D, Neamati N. Role of Metals in HIV-1 Integrase Inhibitor Design. HIV-1 Integrase: John Wiley & Sons, Inc.; 2011. p. 287-307.9781118015377.

40. Metifiot M, Maddali K, Johnson BC, Hare S, Smith SJ, Zhao XZ, Marchand C, Burke TR, Jr., Hughes SH, Cherepanov P, Pommier Y. Activities, crystal structures, and molecular dynamics of dihydro-1H-isoindole derivatives, inhibitors of HIV-1 integrase. ACS Chem Biol. 2013;8(1):209-17.10.1021/cb300471n.

41. DA Case TD, TE Cheatham III, CL Simmerling, J Wang, RE Duke, R Luo, RC Walker, W Zhang, KM Merz, B Roberts, S Hayik, A Roitberg, G Seabra, J Swails, AW Goetz, I Kolossváry, KF Wong, F Paesani, J Vanicek, RM Wolf, J Liu, X Wu, SR Brozell, T Steinbrecher, H Gohlke, Q Cai, X Ye, J Wang, MJ Hsieh, G Cui, DR Roe, DH Mathews, MG Seetin, R Salomon-Ferrer, C Sagui, V Babin, T Luchko, S Gusarov, A Kovalenko, PA Kollman. University of California; 2012.

42. Jorgensen WL, Chandrasekhar J, Madura JD, Impey RW, Klein ML. Comparison of simple potential functions for simulating liquid water. The Journal of chemical physics. 1983;79(2):926-35,0021-9606.

43. Frisch MJT, G. W.; Schlegel, H. B.; Scuseria, G. E.; Robb, M. A.; Cheeseman, J. R.; Scalmani, G.; Barone, V.; Mennucci, B.; Petersson, G. A.; Nakatsuji, H.; Caricato, M.; Li, X.; Hratchian, H. P.; Izmaylov, A. F.; Bloino, J.; Zheng, G.; Sonnenberg, J. L.; Hada, M.; Ehara, M.; Toyota, K.; Fukuda, R.; Hasegawa, J.; Ishida, M.; Nakajima, T.; Honda, Y.; Kitao, O.; Nakai, H.; Vreven, T.; Montgomery, J. A., Jr.; Peralta, J. E.; Ogliaro, F.; Bearpark, M.; Heyd, J. J.; Brothers, E.; Kudin, K. N.; Staroverov, V. N.; Kobayashi, R.; Normand, J.; Raghavachari, K.; Rendell, A.; Burant, J. C.; Iyengar, S. S.; Tomasi, J.; Cossi, M.; Rega, N.; Millam, J. M.; Klene, M.; Knox, J. E.; Cross, J. B.; Bakken, V.; Adamo, C.; Jaramillo, J.; Gomperts, R.; Stratmann, R. E.; Yazyev, O.; Austin, A. J.; Cammi, R.; Pomelli, C.; Ochterski, J. W.; Martin, R. L.; Morokuma, K.; Zakrzewski, V. G.; Voth, G. A.; Salvador, P.; Dannenberg, J. J.; Dapprich, S.; Daniels, A. D.; Farkas, Ö.; Foresman, J. B.; Ortiz, J. V.; Cioslowski, J.; Fox, D. J. Gaussian 09, Revision E.01 ed: Gaussian, Inc., Wallingford CT,; 2009.

44. Darden T, York D, Pedersen L. Particle mesh Ewald: An N· log (N) method for Ewald sums in large systems. The Journal of chemical physics. 1993;98(12):10089-92,0021-9606.

45. Ryckaert J-P, Ciccotti G, Berendsen HJ. Numerical integration of the cartesian equations of motion of a system with constraints: molecular dynamics of n-alkanes. Journal of Computational Physics. 1977;23(3):327-41,0021-9991.

46. Feig M, Karanicolas J, Brooks CL, 3rd. MMTSB Tool Set: enhanced sampling and multiscale modeling methods for applications in structural biology. J Mol Graph Model. 2004;22(5):377-95.10.1016/j.jmgm.2003.12.005.

47. Morris GM, Huey R, Lindstrom W, Sanner MF, Belew RK, Goodsell DS, Olson AJ. AutoDock4 and AutoDockTools4: Automated docking with selective receptor flexibility. J Comput Chem. 2009;30(16):2785-91.10.1002/jcc.21256.

48. Bera S, Pandey KK, Vora AC, Grandgenett DP. HIV-1 integrase strand transfer inhibitors stabilize an integrase-single blunt-ended DNA complex. Journal of molecular biology. 2011;410(5):831-46.10.1016/j.jmb.2011.01.043.

49. Sharma H, Cheng X, Buolamwini JK. Homology model-guided 3D-QSAR studies of HIV-1 integrase inhibitors. J Chem Inf Model. 2012;52(2):515-44.10.1021/ci200485a.

50. Hare S, Smith SJ, Metifiot M, Jaxa-Chamiec A, Pommier Y, Hughes SH, Cherepanov P. Structural and functional analyses of the second-generation integrase strand transfer inhibitor dolutegravir (S/GSK1349572). Mol Pharmacol. 2011;80(4):565-72.10.1124/mol.111.073189.

51. Homeyer N, Gohlke H. Free Energy Calculations by the Molecular Mechanics Poisson-Boltzmann Surface Area Method. Molecular informatics. 2012;31(2):114-22.10.1002/minf.201100135.

52. Xue W, Liu H, Yao X. Molecular mechanism of HIV-1 integrase-vDNA interactions and strand transfer inhibitor action: a molecular modeling perspective. J Comput Chem. 2012;33(5):527-36.10.1002/jcc.22887.

53. Kuhn B, Kollman PA. Binding of a diverse set of ligands to avidin and streptavidin: an accurate quantitative prediction of their relative affinities by a combination of molecular mechanics and continuum solvent models. J Med Chem. 2000;43(20):3786-91,0022-2623 (Print).

54. Wang J, Morin P, Wang W, Kollman PA. Use of MM-PBSA in Reproducing the Binding Free Energies to HIV-1 RT of TIBO Derivatives and Predicting the Binding Mode to HIV-1 RT of Efavirenz by Docking and MM-PBSA. Journal of the American Chemical Society. 2001;123(22):5221-30.10.1021/ja003834q.

Türkçe Öz ve Anahtar Kelimeler

Bazı Önceden Çalışılmış ve Yeni Tasarlanmış Ligandların HIV-1 İntegraz'ın Katalitik Çekirdek Bölgesine Bağlanması ve Moleküler Dinamik Hesapları ve Bağlanma Sonuçları Üzerinde Proteinin Yönelimsel Değişimlerinin Etkisinin İncelenmesi

Selami Ercan*

Öz: Günümüzde AIDS kontrolden çıkmış bir salgın hastalık görünümündedir ve HIV-1 virüsünden kaynaklanan çok sayıda ölüme neden olmaktadır. Yaklaşık 35 yıldır virus hayat çevriminin çeşitli adımlarını hedef alan ilaçlar geliştirilmiştir. HIV-1 integraz, virus hayat çevrimi için esas olan bu adımlardan birini oluşturur. Bilgisayarlı ilaç tasarımı pek çok ilacın geliştirilmesinde ve iyileştirme çalışmalarında kullanılmakta olup ilk HIV-1 integraz inhibitörü olan Raltegaravir'in geliştirilmesinde de kullanılmıştır. Bu çalışmada, dört yeni tasarım ligand ile daha önce HIV-1 integraz inhibitörü olarak kullanılan üç ligandın HIV-1 integrazın katalitik merkez bölgesine bağlanması incelenmiştir. Her ligand proteinin üç farklı biçimine bağlanmıştır. Hazırlanan kompleksler (21 adet) 50 ns MD simülasyona tabi tutulmuş ve sonuçlar incelenmiştir. Son olarak, ligandların bağlanma serbest enerjileri incelenmiştir. Tasarlanan ligandlardan L01 ve L03 uygun sonuçlar vermiştir. Bir protein yapısında düşük bağlanma skoruna sahip ligandların başka bir konformasyonda daha iyi skor verip veremeyeceği ve MD simülasyonlarının, simülasyonun sonunda aynı konumda ancak farklı konumlanmış ve farklı yönlenmiş ligandları barındırıp barındırmayacağı hakkında sorulan sorulara cevap bulunmuştur.

Anahtar kelimeler: HIV-1 integraz; ilaç tasarımı; bağlanma; moleküler dinamik; bağlanma serbest enerjisi.

Sunulma: 09 Eylül 2016. **Düzenleme:** 13 Ekim 2016. **Kabul:** 24 Ekim 2016.

Optimization of Doping Process Parameters of Cerium Vanadate Doped with Be, Mg, Ca, Sr, and Ba Ions

Gülşah Çelik Gül[1]*

[1]University of Balıkesir, 10145, Balıkesir, Turkey

Abstract: In this research, Taguchi method was applied to determine optimum parameters of doping process of cerium vanadate with Be, Mg, Ca, Sr, and Ba ions. Percentage and type of doping ions are used as parameters in optimization process applied as orthogonal array to decrease the number of experiments. The calculated unit cell volume by Rietveld Refinement analysis via X-ray diffraction data (XRD) were used to confirm the formation of doped cerium vanadates. ANOVA method was applied to determine the effectiveness of the parameters.

Keywords: Cerium vanadate; metal doping; X-ray diffraction; Rietveld refinement method; Taguchi optimization method.

Submitted: July 27, 2016. **Revised:** November 19, 2016. **Accepted:** November 21, 2016.

Cite this: Çelik Gül G. Optimization of Doping Process Parameters of Cerium Vanadate Doped with Be, Mg, Ca, Sr, and Ba Ions. JOTCSA. 2017;4(1):271–82.

DOI: To be assigned.

*Corresponding author. E-mail: gulsahcelik9@gmail.com. Tel: +90 266 612 1067/2012.

INTRODUCTION

The fundamental key of the industry's success is product quality concerning of the customers and manufacturers with consistency and production rate (1). There are many factors contributing to production which is directly related to quality. In 1920s, Fisher (2) determined the optimum treatments in order to produce the best conditions called Design of Experiments (DOE) as a statistical approach to investigation of a system or process. DOE as a statistical approach give only the relationship between input and output data. On the other hand, a fractional factorial design can be described by selecting a limited number of experiments including the most informative possibilities in order to reduce costly and time-consuming experimental procedure (3, 4). The complexity and non-clear guideline of this optimization method caused to form innovative approaches. Dr. Genichi Taguchi (1) developed an optimization method entitled Taguchi Method to consider these difficulties of the previous methods (5, 6). In the last two decades, Taguchi Method has drawn much more attention in many applications such as process optimization (7, 8), component design (9), and manufacturing system (10) due to its practical application for determining optimum parameters for high quality systems.

The third period of transition metals in the periodic table is called lanthanides or rare earths which contain fifteen different elements such as La, Ce, Pr, Nd, *etc*. Among them, cerium exists in several organisms instead of calcium to accumulate in the bones in very little amounts. Also, human blood, bones, and tissue contain 0.001 ppm, 3 ppm and 0.3 ppm of cerium, respectively. Cerium's biological role has not yet been known, but it is estimated that cerium salts can stimulate metabolism, and be toxic in excessive quantities (11). On the other hand, vanadium is a transition metal in the second period that is found in high concentrations in the earth's crust, fossil fuels, soils, and oceans. Vanadium plays an active role in biological systems due to the diversity of oxidation states changing from 1+ to 5+ (12). The rare earth orthovanadates ($REVO_4$), containing both a rare earth metal and vanadium, have been intensively studied to investigate their biological, physical and chemical properties since their crystal structures were determined (13, 14). The desired cerium- and vanadium-containing compound can be obtained considering this unique structure. Rao and Palanna synthesized cerium orthovanadate for the first time via conventional solid-state ceramic method, in 1995 (15), and investigated electrochemical properties of the material after four years (16). Our research group synthesized cerium vanadate by innovative microwave method using cerium sulfate and vanadium(V) oxide (17), and applied this compound and derivatives against xanthine oxidase as inhibitor (18). Since the 2000s, doping processes of cerium orthovanadate with rare earths, heavy metal, alkaline and alkaline earth metals have been studied (19-29).

In this work, we have investigated a previously unreported microwave-assisted synthesis route for doping cerium vanadate with alkaline earth elements. The host material cerium vanadate

has been purely obtained in a short time (10 min) by using microwave irradiation as previously described (15). The commonly presence in nature alkaline earth elements in doping process are chosen to reduce the possible toxic effects of cerium. Taguchi method and ANOVA have been applied to identify the significance of selected parameters related to doping process of cerium vanadate with Be, Mg, Ca, Sr, and Ba ions. The conformation of formation of the doped cerium vanadate derivatives have been controlled via calculation of unit cell volume by Rietveld Refinement analysis using X-ray diffraction data (XRD).

MATERIALS AND METHODS

Mathematical approach of Taguchi

Taguchi approach utilizes orthogonal arrays from design of experiments theory to study a large number of parameters with a small number of experiments. A significant advantage of the Taguchi method is that it performs an experiment with a decreased number of tests, protection the fastness in the analysis (30). The number of experiment can be reduced by using orthogonal arrays. An example typical orthogonal array is shown in Table 1 describing all combination of parameters. That is, nine experiments are to be carried out to study four variables at three levels. Thus, this design reduces 81 configurations to 9 experimental evaluations. Table 2 displays doping process variables and chosen levels for each experiment. Two independent variables at five levels each were selected because of increasing diversity and not applied before: doping element type (Be, Mg, Ca, Sr, and Ba) and doping percentage (2%, 4%, 6%, 8%, and 10%). The following parameters were maintained constant in all tests during experimentation: Temperature of synthesis (800 °C), time of synthesis (2 hours), host material ($CeVO_4$), and starting material types as oxides (BeO, MgO, CaO, SrO, and BaO). Table 3 shows Taguchi orthogonal array for doping parameters of cerium vanadate to decrease number of experiment.

Table 1: Orthogonal array suggested by Taguchi method.

	Variables			
Sample	**A**	**B**	**C**	**D**
1	1	1	1	1
2	1	2	2	2
3	1	3	3	3
4	2	1	2	3
5	2	2	3	1
6	2	3	1	2
7	3	1	3	2
8	3	2	1	3
9	3	3	2	1

Table 2: Doping process variables with definite levels.

Processing variables	Level 1	Level 2	Level 3	Level 4	Level 5
Variable 1: Doping element	Be	Mg	Ca	Sr	Ba
Variable 2: Doping percentage (% w)	2	4	6	8	10

Table 3: Taguchi orthogonal array for doped cerium vanadate.

	Variables	
Sample	**Doping percentage**	**Doping element type**
Be1	2	Be
Be2	4	Be
Be3	6	Be
Be4	8	Be
Be5	10	Be
Mg1	2	Mg
Mg2	4	Mg
Mg3	6	Mg
Mg4	8	Mg
Mg5	10	Mg
Ca1	2	Ca
Ca2	4	Ca
Ca3	6	Ca
Ca4	8	Ca
Ca5	10	Ca
Sr1	2	Sr
Sr2	4	Sr
Sr3	6	Sr
Sr4	8	Sr
Sr5	10	Sr
Ba1	2	Ba
Ba2	4	Ba
Ba3	6	Ba
Ba4	8	Ba
Ba5	10	Ba

Optimal working conditions which determined at the end of the experiment must be given very close performance at different conditions and times. The optimization criteria used to realize this can be summarized that variability around performance value must be under control at minimum level. The signal to noise ratio (S/N) is a performance criterion according to Taguchi and classified in three subsections: *lower is better, higher is better or nominal is better*. In this optimization study, the aim is obtaining minimum expansion means the lowest unit cell volume after doping process, the statistical evaluation is chosen as *'lower is better'*. The S/N ratios for the 'lower is better' option was described by the following equation (31):

$$SN_S = -10 * \log\left(\frac{1}{n}.\sum_{t=1}^{n} Y_t^2\right) \quad \text{(Eq. 1)}$$

where t, n, Y stand for experiment number, trial number and performance criteria, respectively. The quantitative effect and the percent contribution of the above mentioned processing parameters to the unit cell volume of doped cerium vanadate was determined using analysis of variance (ANOVA).

SYNTHESIS AND CHARACTERIZATION

All reagents were supplied as analytically pure by Sigma and Merck companies. Ceric sulfate and sodium orthovanadate were employed for preparation of host material cerium vanadate. The preparation of cerium orthovanadate was carried out by grinding $CeSO_4$ and Na_3VO_4 in a molar ratio 1:1 in an agate mortar followed by microwave treatment in a domestic oven (2.45 GHz, 850 W power) for 10 min as described before (15). Doping elements Be, Mg, Ca, Sr, and Ba as metal oxides were weighted according to selected percentage 2, 4, 6, 8, and 10, and added to host material cerium vanadate. Then, regrounded materials were treated at 800 °C for 2 hours to complete the doping process.

Powder X-ray diffraction (XRD) measurements were carried out by Panalytical X'Pert Pro Diffractometer and Cu K_α radiation (λ=1.54056 Å, 40 mA, 50 kV) with a scan rate of 1 º/min with step size 0.02º. The Rietveld analyses of the samples were done by using the High Score Plus (HS+) Program (License number: 92000029). A Siemens V12 domestic microwave oven was used as the microwave source. Protherm conventional furnace was used to complete the doping process.

RESULTS AND DISCUSSION

Figure 1 displays the XRD pattern of doped materials (a) Be, (b) Mg, (c) Ca, (d) Sr, and (e) Ba in 2%, 4%, 6%, 8%, and 10%. The XRD patterns of all samples are completely matched to basic reflections of undoped cerium vanadate. There is no impurity related to doping elements in the XRD pattern. Pure $CeVO_4$ (Inorganic Crystal Structure Database, ICSD: 98-006-6033) crystallized in tetragonal system with unit cell parameters a=b=7.383 Å. c=6.485 Å and V=353.4889 $Å^3$ with space group I 41/amd. Since the crystal structure of cerium vanadate belongs to a tetragonal system, the lattice parameters *a* and *c* can be calculated using following formula.

$$\frac{1}{d^2} = \frac{4}{3}\frac{h^2 + hk + k^2}{a^2} + \frac{l^2}{c^2} \quad \text{(Eq. 2)}$$

The unit cell volumes calculated by XRD pattern by Rietveld refinement method from the 25 combinations of processing variables and S/N ratios are given in Table 4. The volume of unit cell is a very important criterion both as a success of doping process and as an indicator of doping an element without expansion.

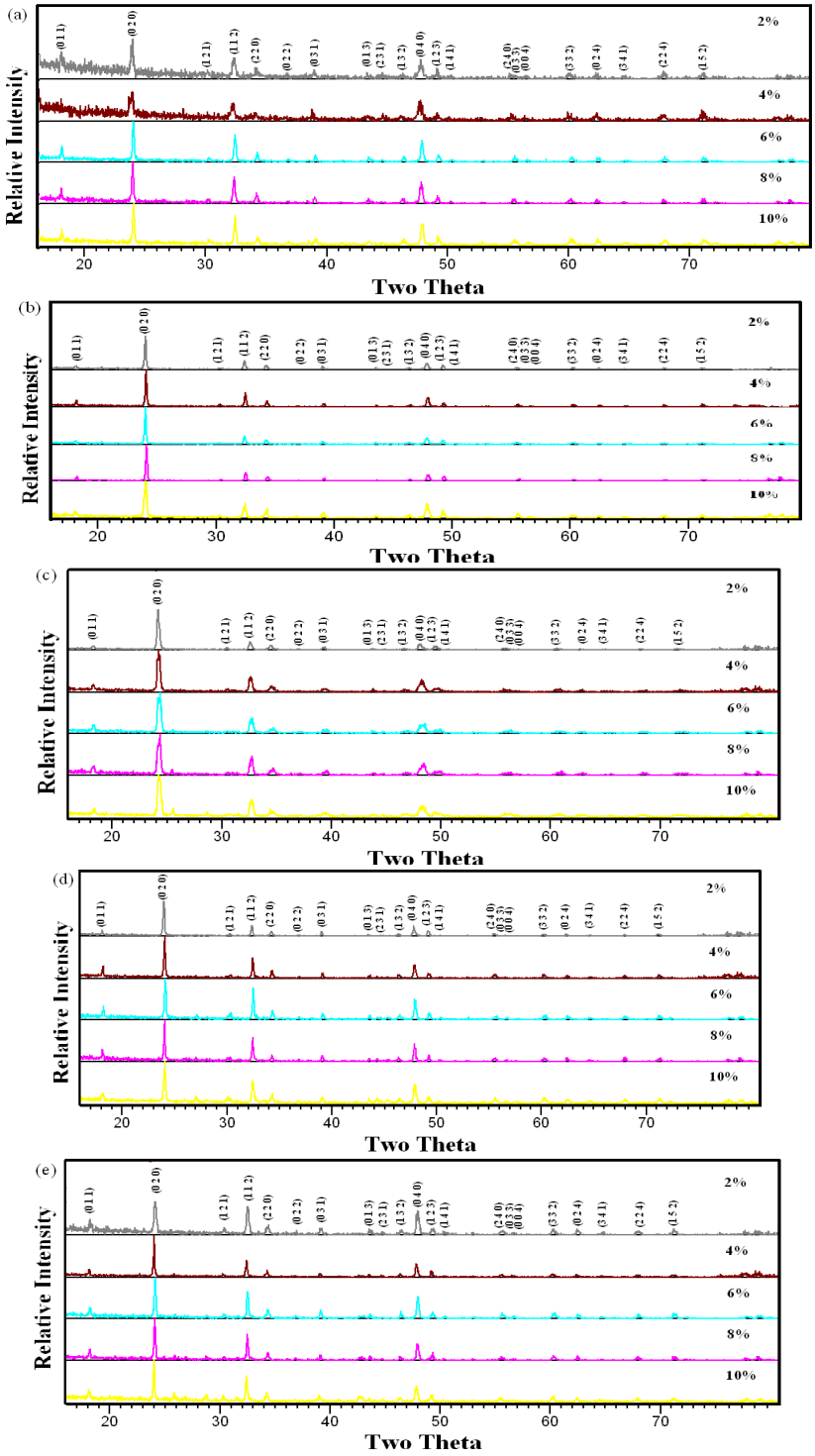

Figure 1: XRD pattern of materials (a) Be, (b) Mg, (c) Ca, (d) Sr, and (e) Ba in 2%, 4%, 6%, 8%, and 10%.

Table 4: Experimental values and corresponding S/N ratios for unit cell volume.

Sample	Doping parameters		Unit cell parameters		Unit cell volume	S/N ratio
	Doping percentage (%w)	Doping element	a=b(Å)	c(Å)		
Be1	2	Be	7.4076	6.4816	355.6623	50.019
Be2	4	Be	7.3983	6.4799	354.6722	50.995
Be3	6	Be	7.4011	6.4705	354.4258	50.991
Be4	8	Be	7.3950	6.4912	354.9781	51.002
Be5	10	Be	7.4005	6.4738	354.5586	50.992
Mg1	2	Mg	7.4023	6.4613	354.0491	50.980
Mg2	4	Mg	7.4009	6.4709	354.4412	50.994
Mg3	6	Mg	7.4017	6.4687	354.3916	50.988
Mg4	8	Mg	7.3404	6.5775	354.4148	50.989
Mg5	10	Mg	7.4004	6.4634	353.9782	50.978
Ca1	2	Ca	7.3806	6.4601	351.9055	50.928
Ca2	4	Ca	7.3476	6.4498	348.2096	50.836
Ca3	6	Ca	7.3640	6.4519	349.8856	50.876
Ca4	8	Ca	7.2982	6.4607	344.1227	50.733
Ca5	10	Ca	7.3541	6.4561	349.1675	50.859
Sr1	2	Sr	7.3915	6.4811	354.0902	50.982
Sr2	4	Sr	7.3911	6.4829	354.1505	50.983
Sr3	6	Sr	7.3905	6.4793	353.8976	50.975
Sr4	8	Sr	7.3924	6.4756	353.8807	50.974
Sr5	10	Sr	7.3838	6.4807	353.3362	50.963
Ba1	2	Ba	7.3936	6.4870	354.6207	50.995
Ba2	4	Ba	7.3920	6.4904	354.6488	50.994
Ba3	6	Ba	7.3895	6.4851	354.1236	50.982
Ba4	8	Ba	7.3915	6.4815	354.1138	50.989
Ba5	10	Ba	7.3910	6.4899	354.5272	50.992

Fig. 2 shows the variations in S/N ratio plots of doping process parameters for the unit cell volume. The ANOVA results of unit cell volume are presented in Table 5 which displays doping element type is the most significant parameter on the success of doping process of cerium vanadate with 95 % confidence interval.

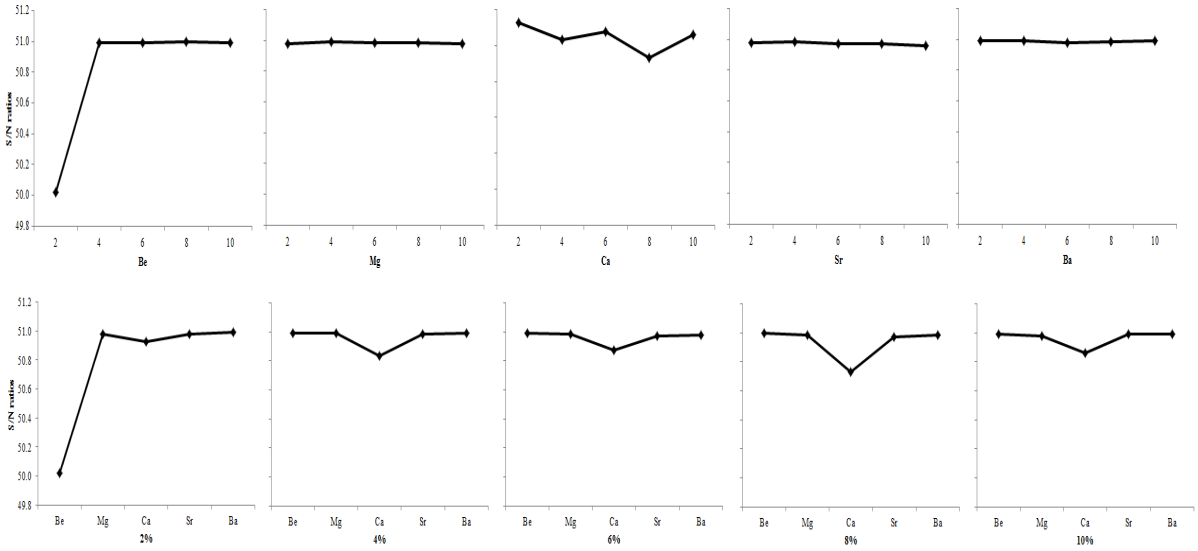

Figure 2: S/N ratios of processing variables for the unit cell volume related to doping percentage and dopant ion type.

Table 5. ANOVA results explaining the significances of doping process parameters on unit cell volume.

Doping process parameters	**Degrees of freedom (*f*)**	**Sum of squares (*S*)**	**Significance *P* (%)**
Doping percentage	5	14.427	5.13
Dopant element type	5	267.072	94.87
Total	8	281.499	100.000

In conclusion, as an optimization technique, Taguchi Method was used to determine the most effective doping process parameters on cerium vanadate doping process with Be, Mg, Ca, Sr and Ba ions. Unit cell parameters and volumes used for comparison were calculated by powder XRD pattern. The type of doping element is the most significant parameter with nearly 95 %. The number of experiments, thereby time and energy consuming were minimized and the significance of the parameters were defined owing to Taguchi method.

ACKNOWLEDGMENTS

We want to thank to The Scientific and Technological Research Council of Turkey and Scientific Research Project Fund of Balikesir University for financial supports and Eng. Metin GÜL for scientific support.

REFERENCES

1. Fei NC. Mehat NM. Kamaruddin S. Practical applications of Taguchi method for optimization of processing parameters for plastic injection moulding: a retrospective review. ISRN Industrial Engineering. 2013 June; 2013:462174. DOI: 10.1155/2013/462174.

2. Dowlatshahi S. An application of design of experiments for optimization of plastic injection molding processes. Journal of Manufacturing Technology Management. 2004 Oct; 15:445–54. DOI: 10.1108/17410380410547852.

3. Farkas K. Hossmann. T. Plattner B. Ruf L. NWC: node weight computation in MANETs. 16th International Conference on Computer Communications and Networks 2007. 2007 Aug; 1059–64. DOI: 10.1109/ICCCN.2007.4317958.

4. Rao RS. Kumar CG. Prakasham RS. Hobbs PJ. The Taguchi methodology as a statistical tool for biotechnological applications: a critical appraisal. Biotechnology Journal. 2008 Apr; 3:510–23. DOI: 10.1002/biot.200700201.

5. Singh H. Kumar P. Optimizing cutting force for turned parts by Taguchi's parameter design approach. The Indian Journal of Engineering and Materials Sciences. 2005 Jan; 12:97–103. http://nopr.niscair.res.in/bitstream/123456789/8419/1/IJEMS%2012(2)%2097-103.pdf.

6. Kamaruddin S. Khan ZA. Foong SH. Application of Taguchi method in the optimization of injection moulding parameters for manufacturing products from plastic blend. IACSIT International Journal of Engineering and Technology. 2010 Dec; 2:574–80. DOI: 10.7763/IJET.2010.V2.184.

7. Mohan NS. Ramachandra A. Kulkarni SM. Influence of process parameters on cutting force and torque during drilling of glass-fiber polyester reinforced composites. Composite Structures. 2005 Dec; 71:407–13. DOI: 10.1016/j.compstruct.2005.09.039.

8. Ariffin M. Ali Sapuan SM. Ismail N. An optimise drilling process for an aircraft composite structure using design of experiments. Scientific Research and Essays. 2009 Oct;4:1109–16. http://www.academicjournals.org/journal/SRE/article-abstract/E509DE018608.

9. Shim HJ. Kim JK. Cause of failure and optimization of V-belt pulley considering fatigue life uncertainty in automotive applications. Engineering Failure Analysis. 2009 Sep; 16:1955–63. DOI: 10.1016/j.engfailanal.2008.10.008.

10. Mahfouz AS. Hassan A. Arisha A. Practical simulation application: evaluation of process control parameters in Twisted-Pair Cables manufacturing system. Simulation Modelling Practice and Theory. 2010 May; 18:471–82. http://202.114.89.42/resource/pdf/4983.pdf.

11. Emsley J. Nature's building blocks: an A-Z guide to the elements (New ed.). New York, NY: Oxford University Press; 2011:375–83, 412–15, 475–81, 511–20, 529–33, 582. ISBN 978-0- 19-960563-7.

12. Mukherjee B. Patre B. Mahapatra S. Vanadium: an element of atypical biological significance. Toxicol Letters. 2004; 150:135–43.

13. Petit CTG. Lan R. Cowin PI. Tao S. Structure and conductivity of strontium-doped cerium orthovanadates $Ce_{1-x}Sr_xVO_4$. Journal of Solid State Chemistry. 2010 Jun; 183:1231–38. DOI: 10.1016/j.jssc.2010.03.032.

14. Rao R. Garg AB. Sakuntala T. Archary SN. Tyagi AK. High pressure Raman scattering study on the phase stability of $LuVO_4$. Journal of Solid State Chemistry. 2009 July; 182:1879–83. DOI: 10.1016/j.jssc.2009.05.003.

15. Rao IS, Palanna OG. Electrical, thermal and infrared studies of cerium(Ill) orthovanadate. Bulletin of Materials Science. 1995 Sep; 18:593–97. DOI: 10.1007/BF02744845.

16. Varma S, Wani BN, Gupta NM. Synthesis, characterization, and redox behavior of mixed orthovanadates $La_{1-x}Ce_xVO_4$. Materials Research Bulletin 2002 Oct; 37:2117–27. DOI: 10.1016/S0025-5408(02)00888-7.

17. Çelik G. Kurtuluş F. Microwave-assisted synthesis of $CeVO_4$ in the mild conditions. characterization and investigation of luminescent properties. Acta Physica Polonica A. 2014 Jan; 125:2-4. DOI:10.12693/APhysPolA.125.357.

18. Kaya MO. Kaya Y. Çelik G. Kurtuluş F. Arslan O. Güler ÖÖ. Differential in vitro inhibition studies of some cerium vanadate derivatives on xanthine oxidase. Journal of Enzyme Inhibition and Medicinal Chemistry 2015 Apr; 30:286-89. DOI: 10.3109/14756366.2014.920837.

19. Watanabe A. Highly conductive oxides. $CeVO_4$. $Ce_{1-x}M_xVO_{4-0.5x}$(M=Ca. Sr. Pb) and $Ce_{1-y}Bi_yVO_4$. with zircon-type structure prepared by solid-state reaction in air. Journal of Solid State Chemistry. 2000 Aug; 153:174–79. DOI: 10.1006/jssc.2000.8773.

20. Hirata T. Watanabe A. Comparison between the Raman Spectra of $Ce_{1-x}Ca_xVO_{4-0.5x}$ ($0 \le x \le 0.41$) and $Ce_{1-x}Bi_xVO_4$ ($0 \le x \le 0.68$). Journal of Solid State Chemistry. 2001 May; 158:264–67. DOI: 10.1006/jssc.2001.9104.

21. Tsipis EV. Kharton VV. Frade JR. Mixed conducting components of solid oxide fuel cell anodes. Journal of European Ceramic Society. 2005 Apr; 25:2623–26. DOI: 10.1016/j.jeurceramsoc.2005.03.114.

22. Tsipis EV. Kharton VV. Vyshatko NP. Shaula AL. Frade JR. Stability and oxygen ionic conductivity of zircon-type $Ce_{1-x}A_xVO_{4+\delta}$ (A=Ca. Sr). Journal of Solid State Chemistry. 2003 Nov; 176:47–56. DOI: 10.1016/S0022-4596(03)00342-6.

23. Tsipis EV. Patrakeev MV. Kharton VV. Vyshatko NP. Frade JR. Ionic and p-type electronic transport in zircon-type $Ce_{1-x}A_xVO_{4\pm\delta}$ (A = Ca. Sr). Journal Materials Chemistry. 2002 Oct; 12:3738–45. DOI: 10.1039/B206004C.

24. Mahapatra S. Vinu R. Saha D. Row. TNG. Madras G. Synthesis. characterization and photocatalytic activity of $M_xCe_{1-x}VO_4$ (M = Li. Ca and Fe). Applied Catalysis A. 2009 Jun; 361:32–41. DOI: 10.1016/j.apcata.2009.03.028.

25. Varma S. Wani BN. Gupta NM. Redox behavior and catalytic activity of La–Fe–V–O mixed oxides. Applied Catalysis A. 2003 Feb; 241:341–48. DOI: 10.1016/S0926-860X(02)00492-1.

26. Varma S. Wani BN. Sathyamoorthy A. Gupta NM. On the role of lattice distortion in the catalytic properties of substituted orthovanadates $La_{1-x}Fe_xVO_4$. Journal of Physics and Chemistry of Solids. 2004 July; 65:1291–96. DOI: 10.1016/j.jpcs.2004.02.009.

27. Pidol L. Noël OG. Harari AK. Viana B. Plenc D. Gourier D. EPR study of Ce^{3+} ions in lutetium silicate scintillators $Lu_2Si_2O_7$ and Lu_2SiO_5. Journal of Physics and Chemistry of Solids. 2006 Apr; 67:643–50. DOI: 10.1016/j.jpcs.2005.10.175.

28. Petkova P. Anisotropic magneto-optical properties of vanadium in $Bi_4Ge_3O_{12}$. Journal of

Magnetism and Magnetic Materials. 2016 July; 410:5-9. DOI: 10.1016/j.jmmm.2016.03.004.

29. Petkova P. Vasilev P. Mustafa M. Parushev I. Vanadium States in Doped $Bi_{12}SiO_{20}$. Materials Science. 2015 Feb; 21:167-72. DOI: http://dx.doi.org/10.5755/j01.ms.21.2.6140.

30. Roy R. A primer on the Taguchi Method. Van Nostrand Reinhold. New York. 1990; 7-10; 40-55.

31. Asl MS. Golmohammadi F. Kakroudi MG. Shokouhimehr M. Synergetic effects of SiC and C_{sf} in ZrB_2-based ceramic composites. Part I:Densification behavior. Ceramics International. 2016 Feb; 42:4498–4506. DOI: 10.1016/j.ceramint.2015.11.139.

Türkçe Öz ve Anahtar Kelimeler

Be, Mg, Ca, Sr ve Ba İyonları ile Doplanmış Seryum Vanadatın Doplama Süreci Parametrelerinin Optimizasyonu

Gülşah Çelik Gül

Öz: Bu çalışmada, Taguchi yöntemi uygulanarak seryum vanadatın Be, Mg, Ca, Sr ve Ba iyonları ile doplama sürecinin en uygun parametreleri bulunmuştur. Doplama iyonunun yüzdesi ve türü, deneylerin sayısını azaltmak için ortogonal dizi şeklinde uygulanmış optimizasyon sürecinde paramatreler olarak kullanılmıştır. Rietveld Düzeltme analizi X-ışını saçılma verilerinden (XRD) hesaplanan birim hücre hacmi, doplanmış seryum vanadatların oluşumunu doğrulamak için kullanılmıştır. Parametrelerin etkinliğini belirlemek için ANOVA yöntemi uygulanmıştır.

Anahtar kelimeler: Seryum vanadat; metal doplama; X-ışını saçılması; Rietveld düzeltme yöntemi; Taguchi optimizasyon yöntemi.

Sunulma: 27 Temmuz 2016. **Düzeltme:** 19 Kasım 2016. **Kabul:** 21 Kasım 2016.

Chemical Characterization of *Lavandula angustifolia* Mill. as a Phytocosmetic Species and Investigation of its Antimicrobial Effect in Cosmetic Products

Aslıhan Cesur Turgut[1]*, Fatih Mehmet Emen[2], Hale Seçilmiş Canbay[3], Ruken Esra Demirdöğen[4], Neslihan Çam[5], Derya Kılıç[6], Tuncay Yeşilkaynak[7]

[1]Mehmet Akif Ersoy University, Scientific and Technological Application and Research Center/ Tefenni Vocational School, 15100, Burdur, Turkey, [2]Mehmet Akif Ersoy University Faculty of Science, Department of Chemistry, 15100, Burdur, Turkey, [3]Mehmet Akif Ersoy University, Scientific and Technological Application and Research Center, 15100, Burdur, Turkey, [4]Cankiri Karatekin University, Faculty of Science, Department of Chemistry, 18100, Cankiri, Turkey, [5]Laber Kimya Ar-Ge San. Tic., Izmir, Turkey, [6]Mehmet Akif Ersoy University Faculty of Science, Department of Chemistry, 15100, Burdur, Turkey. [7] Kahramanmaras Sutcu Imam University, Afsin Vocational School, Kahramanmaras, Turkey.

Abstract: The content of the extracts obtained from *Lavandula angustifolia,* which were grown in Burdur Örtülü locality, was determined via HPLC and GC-MS analysis and the anti-microbial effect of the essential oil *L. angustifolia* was also investigated. The dried flowers of *L. angustifolia* were extracted and the essential oil was distilled from the remaining part. Various phenolic compounds in the extract were quantitatively determined by HPLC. Quantitatively caffeic acid, rosmarinic acid, and 4-hydroxybenzoic acids were the most abundant phenolic acids in the content in decreasing order. 31 different compounds were determined by GC-MS analysis: Linalool and linalyl acetate have the highest concentration. Anti-microbial effects of the essential oil of *L. angustifolia* were determined against the most frequently encountered microorganisms in the cosmetics: *Candida albicans, Staphylococcus aureus, Pseudomonas aeruginosa, and Aspergillus brasiliensis.* It was observed that the essential oil *L. angustifolia* could completely remove the contamination caused by the microorganisms as of the 14th day. According to the results it is concluded that the essential oil of *L. angustifolia*, can be used either directly or incorporated into the cosmetics without the necessity for any other extra preservative against the above mentioned microrganisms.

Keywords: *Lavandula angustifolia* Mill.*;* cosmetic; phenolic compounds; essential oil; antimicrobial activity**.**

Submitted: July 04, 2016**. Revised:** November 24, 2016**. Accepted:** November 25, 2016**.**

Cite this: Cesur Turgut A, Emen F, Seçilmiş Canbay H, Demirdöğen R, Çam N, Kılıç D, et al. Chemical Characterization of Lavandula angustifolia Mill. as a Phytocosmetic Species and Investigation of its Antimicrobial Effect in Cosmetic Products. JOTCSA. 2017;4(1):283–98.
DOI: To be assigned.
*Corresponding author. E-mail: ascesur@gmail.com.

INTRODUCTION

In the last years, usage of aromatic plants in the perfumery, food, and cosmetics industries as the principal raw material as well as its usage in many other fields have increased the demand for medicinal and aromatic plants. Especially the methods, which are named as return to nature, have increased the interest in these plants both in Turkey and in other countries in the world [1].

Lavender (*Lavandula* sp.) is a very valuable essential oil plant from the *Lamiaceae* family. There are 39 lavender species (*Lavandula* sp.) most of which have Mediterranean origin and among them, three have high commercial value. While the essential oil quality of the lavender species (British lavender) is high the lavandin species (hybrid lavender) have high essential oil yield [2, 3]. It plays an important role in the pharmacology and perfumery industries since it contains essential and aromatic oils [4]. 1.8-2 billion dollar-worth of essential oil is exported each year in the world and lavender oil constitutes 50 million dollars of this export [5, 6, 7]. The three commercial lavender species are Lavender (*Lavandula angustifolia* Mill. = *L. officinalis* L. = *L. vera* DC), Lavandin (*Lavandula intermedia* Emeric ex Loisel. = *L. hybrida* L.) and Spike Lavender (*Lavandula spica* = *L. latifolia* Medik.). While the essential oil quality of the Lavender types, which are named as British lavender, is high the essential oil quantity of lavandin, which is named as hybrid lavender [8].

The most important essential oil components of lavender oil are linalyl acetate, linalool, and cineol. Among them, linalyl acetate is the most important component which determines the quality of the lavender oil [9]. There are many studies which indicate that *L. angustifolia* mostly contains linalool and linalyl acetate as essential oil component in essential oil obtained via water vapor distillation of the flowers of *L. angustifolia* [10, 11, 12]. Due to linalool and linalyl acetate, both of which are present in the plant, lavender is used in production of perfume, skin cleaning lotion, bath soap with odor and bath foams in the cosmetics industry [13, 14, 15]. Lavender and its ethanolic extract have high antioxidant activity and its content is rich in phenolic compounds. It is thought that this effect arises from the protective effect that phenolic compounds show against oxidative damage which is caused by the free radicals. Moreover, it is indicated that lavender inhibits bacterial growth [9, 16].

Cosmetic products are not sterile and are open to the growth of microorganism contamination any time. When these products are studied from the microbiological perspective, since they are not produced under aseptic conditions, microorganisms which are not pathogens are observed. Cosmetic products containing pathogenic

microorganisms would put the health of people who use them in danger rather than beautifying them and would either degrade the products or cause diseases. The dangers, which cosmetic products cause, have attracted the attention of those working in this field and intensive studies on this subject [17]. According to the American Pharmacopoeia, *Escherichia coli, Pseudomonas aeruginosa, Staphylococcus aureus* and *Salmonella typhimurium, Candida albicans* and *Aspergillus niger are* microorganisms *which should not be found in c*osmetic products [18]. *Staphylococcus aureus is one of the most common bacterial skin pathogen found in* creams. Presence of these bacteria in creams intensively may cause skin and mucosal infections such as inflammatory skin disease (impetigo), follicular inflammation, and abscess. Infection starts when *Staphylococcus* degrades in the dermal mucosal barrier and enters into the tissues or into the bloodstream [19, 20]. It is reported that the active of the 70% of the skin infections seen in children is *S. aureus* [21]. It is reported that ocular infections are commonly seen in patients who use eye drops. Nosocomial infections and epidemics arising from usage of products contaminated with *P. aeruginosa* are reported [22]. Glycerin used in creams and lotions can be metabolized by microorganisms (especially by *Bacillus, Staphyloccocus* and *Micrococcus)* [23]. Cosmetic products contaminated by *C. albicans* can cause dermatitis [24]. The creams produced by the Ukranian Company Effect which are determined to contain *C. albicans* were collected by the end of 2006 upon notification of Estonia [25].

In the present study, our aim was to examine the content of the extracts obtained from *Lavandula angustifolia,* which were grown in Burdur Örtülü locality and also investigate the anti-microbial effect of the essential oil of *L. angustifolia.* For this purpose, various phenolic compounds were detected in the extracts of Lavender (*Lavandula angustifolia* Mill.) and essential compounds were also detected in its essential oil.

MATERIALS AND METHODS

Chemical Materials

Caffeic acid, p-coumaric acid, and rosmarinic acid were purchased from Sigma, 3,4-dihydroxybenzoic acid, chlorogenic acid, and ferulic acid were purchased from Aldrich, 4-hydroxybenzoic acid, cinnamic acid, and ethanol (absolute for analysis) were purchased from Merck, hexane (for HPLC ≥97.00) and methanol (HPLC grade ≥ 99.9%) were purchased from Sigma-Aldrich, vanilic acid and apigenin were purchased from Fluka, formic acid (analytical reagent grade) was purchased from Fisher Chemical and gallic acid was purchased from Pancreac.

Plant Material (Sampling)

Lavenders (*Lavandula angustifolia* Mill.) collected from Burdur Örtülü locality (37.7167°N-30.2833°E and 959 m above sea level) were used. 2000 g of lavender sample has been dried in the shade after the harvest and the dry flowers were separated from their stems.

Solvent Extraction

Dry flowers separated from their stems were extracted for analysis of their phenolic content. 2-g-sample was dried, powdered and extracted with 10 mL of 96% ethanol for 24 h in water bath at 45 °C. This mixture is centrifuged at 4000 rpm for 5 minutes. Supernatant was concentrated with the rotary evaporator at 45 ^{o}C until complete dryness and dissolved in mobile phase [26].

Clevenger extraction

2000 g stemless dry lavender flowers were weighed. Then the flowers were submitted to hydrodistillation with a Clevenger-type apparatus. As a result of distillation, essential oil yield was found 4.2% .

Instrumentation

Chromatographic analyses were performed using a Shimadzu reversed-phase high-performance liquid chromatography (RP-HPLC) equipped with diode-array detector (DAD). RP-HPLC analysis were done using a 20ACBM system controller, SPD-M20A diode array detector, CTO-10ASVp column oven, SIL 20ACHT autosampler, and a LC20 AT pump. The data were performed using the LC Solution software. The chromatographic separations were achieved on Agilent Eclipse C18 column (250*4,6 mm i.d., 5 µm) the eluates were detected at 280 nm and 320 nm. Analysis of phenolics in Lavandula was achieved by RP-HPLC with gradient elution. The mobile phase used was 3% formic acid in (A) water *vs* (B) methanol. The elution gradient applied at a flow rate of 0.8 mL min^{-1} was: 93%A/7% B for 3 min, 72%A/28%B in 28 min, 67%A/33%B in 60 min, 58%A/42%B in 62 min, 50%A/50%B in 70 min, 30%A/70%B in 75 min, 93%A/7% B in 80 min. Samples were dissolved in mobile phase, and 20 µL of this solution was injected into the column. The column temperature was set at 30 °C. In the HPLC analysis the method of Gomes *et al*. (1999) was modified and used [27]. The volatile compounds were analyzed by using a gas chromatograph 7890 A coupled to a mass spectrometer series MSD 5975 C, (Agilent Technologies) and volatiles were resolved on a CP WAX 52 CB capillary column (50 m * 0.32 mm ID, df :1.2 µm) purchased from Agilent. The carrier gas was helium, at a flow rate of 1.2 mL/min. The temperature program for the GC was as follows; 60 °C initial temperature, after waiting for 2 minutes at 60 °C to

increase 220 °C with 2 °C /min, after reaching this temperature the temperature was kept constant for 20 minutes. The injection was performed in the split mode (20:1). The injection volume was 1 µL. Injector temperature was 240 °C The GC–MS interface was heated at 240°C. MS ion source temperature was 230°C and MS-quadrupole was 150 °C. The electron impact energy was set at 70 eV, and data were collected in the range of 30–500 atomic mass units (amu). Compounds' identification was based on mass spectra by comparison with MS spectral database from Wiley. The integrations were performed with MSDCHEM software [28].

Microorganisms and growth culture

Antimicrobial effects of Lavender essential oil on bacteria-yeast and mold strains were investigated. When choosing the microorganisms, the frequently encountered species in the contaminated creams such as *Candida albicans*, *Staphylococcus aureus*, *Pseudomonas aeruginosa,* and *Aspergillus brasiliensis* were preferred. The methods used in preparation of reference cultures are given in Table 1 and the working cultures, can be seen in Table 2, prior to inoculation, are given below. The protective activity of Lavender oil is determined via challenge test and according to TS EN ISO 11930:2012 standard which is an international method [53]. According to this method the sample was weighed (g/mL) and the bacteria *Staphylococcus aureus* and *Pseudomonas aeruginosa* and the fungi *Candida albicans* and *Aspergillus brasiliensis* were inoculated in the sample at a known level. Following this the samples were incubated in the acclimatization cabin at 25 °C for 28 days. On the 7th and 14th days of incubation and at the end of incubation, samples were analyzed and the number of microorganisms was determined.

Table 1. Preparation of the Reference Stock Cultures.

Reference Strains	Method	Broth Medium Used
Staphylococcus aureus ATCC 6538/ Lot 3221505	Plate	Tryptic Soy Agar
Pseudomonas aeruginosa ATCC 9027/ Lot 3270513	Plate	Tryptic Soy Agar
Candida albicans ATCC 10231/ Lot 8067507	Plate	Sabouraud 4% Dextrose Agar + Supplement
Aspergillus brasiliensis ATCC 16404/ Lot 3175110	Plate	Potato Dextrose Agar

Table 2. Preparation of Working Cultures.

Analysis	Method	Broth Medium Used
Staphylococcus aureus ATCC 6538	Enrichment and Line inoculation in solid broth	Baird-Parker Agar Staphylococcus Selective Agar
Pseudomonas aeruginosa ATCC 9027	Enrichment and Line inoculation in solid broth	Cetrimide Agar Pseudomonas Selective Agar
Candida albicans ATCC 10231	Enrichment and Line inoculation in solid broth	Sabouraud 4% Dextrose Agar + Supplement
Mould- Yeast	Diffusion Plate	Sabouraud 4% Dextrose Agar
Total aerobic mesophilic microorganisms	Diffusion Plate	Tryptic Soy Agar With Polysorbate 80 And Lecithin

RESULTS AND DISCUSSION

HPLC Results

Eleven different phenolic compounds were determined *via* HPLC analysis as it can be seen in Table 3. The antimicrobial phytochemicals are collected in five groups as phenolics, terpenoids-essential oils, alkaloids, lectins-polypeptides and polyacetylenes [29]. Phenolics constitute the largest group among the vegetative antimicrobial agents [30]. The phenolic compounds determined in the lavender extract are gallic acid, 3,4-dihydroxybenzoic acid, 4-hydroxybenzoic acid, chlorogenic acid, vanillic acid, caffeic acid, p-coumaric acid, ferulic acid, apigenin, rosmarinic acid, and cinnamic acid can be seen in Table 4. Its standard chromatogram is given in Figure 1 and the chromatogram of its extract is presented in Figure 2. It is well known that the polyphenols show goof antibacterial effect [31]. High concentrations of phenolic compounds are toxic both for the plants and the microorganisms [32, 33].

Table 3. Concentration of 11 phenolic acids in Lavender sample.

Sample	Gallic Acid	3,4-dihydroxy benzoic Acid	4-hydroxybenzoic Acid	Chlorogenic Acid	Vanillic Acid	Caffeic Acid	p-Coumaric Acid	Ferulic Acid	Apigenin	Rosmarinic Acid	Cinnamic Acid
Lavender	*0.14	3.37	10.70	7.41	0.67	15.20	5.03	0.18	7.80	10.13	0.98

*All the values in the same line are given as µg/g.

Table 4. LOD values, wavelengths, retention time (RT), and linear regression coefficients (R^2) for phenolic compounds.

	Gallic Acid (1)	3,4-dihydroxy benzoic Acid (2)	4-hydroxybenzoic Acid (3)	Chlorogenic Acid (4)	Vanillic Acid (5)	Caffeic Acid (6)	p-Coumaric Acid (7)	Ferulic Acid (8)	Apigenin (9)	Rosmarinic Acid (10)	Cinnamic Acid (11)
LOD (mg/L)	0.19	0.027	0.036	0.017	0.019	0.019	0.022	0.021	0.010	0.016	0.016
Detection wavelength (nm)	280	280	280	320	320	280	320	320	320	320	280
RT	7.8	12.2	16.9	19.4	21.7	24	29.3	34.7	64.1	66.7	70.7
R^2	0.999	0.999	0.999	0.999	0.999	0.999	0.999	0.999	0.999	0.999	0.999

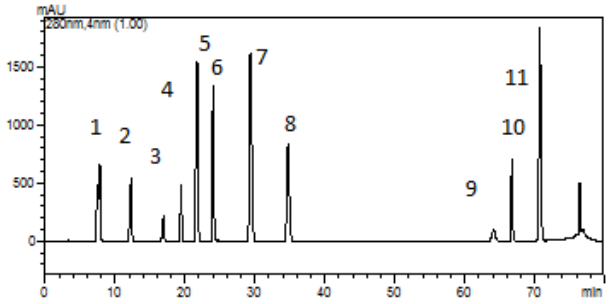

Figure 1. HPLC chromatogram of standard mixtures. 1. Gallic acid, 2. 3,4-dihydroxybenzoic acid, 3. 4-hydroxybenzoic acid, 4. chlorogenic acid, 5. vanillic acid, 6. caffeic acid, 7. p-coumaric acid, 8. ferulic acid, 9. apigenin, 10. rosmarinic acid, 11. cinnamic acid. (Agilent Eclipse C18 column (250*4.6 mm i.d., 5µm), flow rate: 0.8 mL min^{-1}, wavelength: 280 nm)

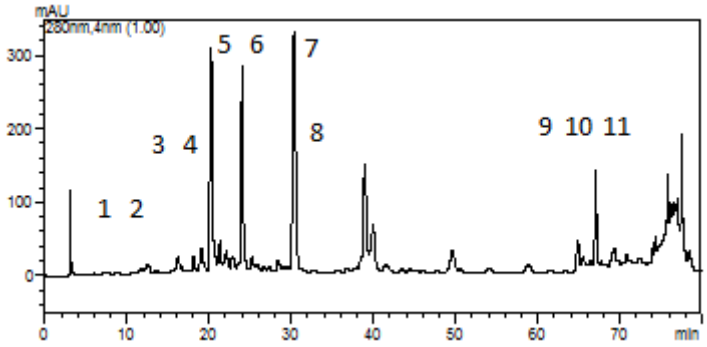

Figure 2. HPLC chromatogram of the sample. 1. Gallic acid, 2. 3,4-dihydroxybenzoic acid, 3. 4-hydroxybenzoic acid, 4. chlorogenic acid, 5. vanillic acid, 6. caffeic acid, 7. p-coumaric acid, 8. ferulic acid, 9. apigenin, 10. rosmarinic acid, 11. cinnamic acid. (Agilent Eclipse C18 column (250*4.6 mm i.d., 5 µm), flow rate: 0.8 mL min^{-1}, wavelength: 280 nm).

GC-MS Results

The Lavender essential oil is reported to be rich in linalyl acetate and linalool in the studies [34, 35]. The results of the analysis that we made also support these findings. Our results are given in Table 5.

Linalool, linalyl acetate, and α-terpineol have the highest ratio with 42.215%, 23.116% and 4.912%, respectively. The results can also be seen in Figure 3 as the chromatogram of the samples.

Lavender oil inhibited the growth of *C. Albicans*. Many researchers have also reported that especially essential oils rich in phenolics, aldehydes, and alcohols are effective in inhibiting pathogenic microorganisms and in preventing degradation [37]. Therefore, phenolic compounds are natural alternative to the synthetic antimicrobials used in the cosmetics, food and pharmaceutical industries [38] and they can be active even at low concentrations [37]. It is reported that linalool and α-terpineol have strong antimicrobial

activity against periodontopathic and cariogenic bacteria [36]. Furthermore, the antibacterial activity of lavender oil and its main components; *i.e.* 1,8-cineol, linalool, linalyl acetate, limonene, α-pinene, and β-pinene have been assayed against the human pathogenic bacteria and they have been successful [46]. These results are consistent with our findings.

Table 5. Essential oil composition of Lavender.

No	Component	RT*	Ratio(%)
1.	α-pinene	4.2	0.028
2.	Camphene	4.9	0.046
3.	β-pinene	5.5	0.019
4.	β-myrcene	6.2	0.341
5.	α-terpinene	6.5	0.007
6.	Limonene	6.7	0.234
7.	1,8 cineol	6.9	0.677
8.	Cymene	7.1	0.955
9.	3-octanone	7.4	0.163
10.	Acetic acid hexyl ester	7.5	0.257
11.	α –terpinolene	7.7	0.156
12.	3-octayl acetate	8.2	0.089
13.	n-hexyl isobutyrate	8.28	0.228
14.	1-hexene	8.3	0.033
15.	1-octen 3 yl acetate	8.5	0.193
16.	3-octanol	8.6	0.071
17.	Butanoic acid hexyl ester	8.9	1.323
18.	Hexyl -2-methyl butanoate	9	0.231
19.	Linalool oxide	9.1	0.592
20.	Linalool	9.8	42.215
21.	Linalyl acetate	10	23.116
22.	Cyclohexanone	10.1	2.053
23.	Neryl acetate	10.3	0.211
24.	Trans caryphyllene	10.4	0.935
25.	Farnesene	10.7	0.28
26.	α-terpineol	11	4.912
27.	Borneol	11.1	3.394
28.	Geranyl acetate	11.2	0.935
29.	Nerol	11.4	4.229
30.	Geraniol	12.2	2.975
31.	Caryophyllene oxide	14.5	4.5
	TOTAL		**95.398**
	Unknown		**4.602**

* RT: Retention time

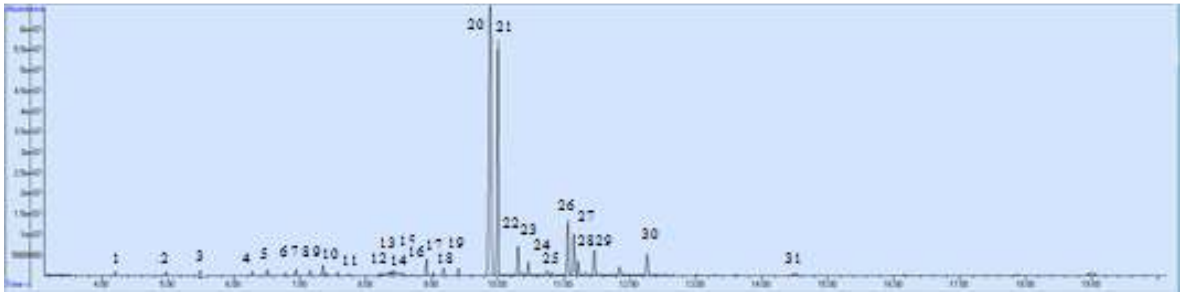

Figure 3. GC-MS Chromatogram of the sample.

Microbiological Results

According to the ISO 11930 standard challenge test was applied on lavender essential oil for 28 days and their logarithmic decreases were evaluated can be seen in Table 6-8.

Table 6. Microbial activity test performed according to the ISO standard.

Parameter	Unit	Results of the Analysis	Standard No	Limit Value
Total aerobic mesophilic microorganism	cfu/g	<1000 cfu/g	ISO 21149	<1000 cfu/g
Candida albicans	cfu/g	Negative	ISO 18416	Negative
Staphylococcus aureus	cfu/g	Negative	ISO 22718	Negative
Pseudomonas aeruginosa	cfu/g	Negative	ISO 22717	Negative
Mold-Yeast	cfu/g	<1000 cfu/g	ISO 16212	<1000 cfu/g

The antimicrobial activity of the essential oil studied on the microorganism strains was found to be pretty high. The results of the total aerobic mesophilic microorganism and Total Mold-Yeast counting, which determine the microbial quality of the oil were found to be coherent with the limit values. Moreover, *Candida albicans*, *Staphylococcus aureus*, *Pseudomonas aeruginosa,* and pathogenic microrganisms were not encountered in the analysis. The microbiologic quality of the product is sufficient for its usage in production of cosmetics can be seen in Table 6-8. In the analysis the ISO standards were applied in the microbiology of cosmetics were used and the analysis were made in an accredited laboratory.

Table 7. Logarithmic Evaluation Table.

Microorganism	1st Hour		7 th Day			14 th Day	28 th Day
	CFU/g	log CFU/g	CFU/g	log CFU/g	log reduction	CFU/g	CFU/g
Staphylococcus aureus ATCC 6538/ Lot 3221505	1.0E+06	6.00	9.8E+01	2.0	4.01	<10	<10
Pseudomonas aeruginosa ATCC 9027/ Lot 3270513	1.2E+06	6.09	1.5E+02	2.2	3.93	<10	<10
Candida albicans ATCC 10231/ Lot 8067507	2.3E+05	5.36	6.5E+01	1.8	3.55	<10	<10
Aspergillus brasiliensis ATCC 16404/ Lot 3175110	1.5E+04	4.18	1.5E+01	1.2	3.00	<10	<10

Many antimicrobial studies were made regarding *L. angustifolia* on various microorganisms [34, 35, 39-48] and our findings supported these results.

Table 8. Result Control Table.

Log decrease values (*Rx*= lg*N*0 - lg*Nx*) required [a]								
Microorganisms	**Bacteria**			***C. albicans***			***A.brasiliensis***	
Sampling Time	**T7**	**T14**	**T28**	**T7**	**T14**	**T28**	**T14**	**T28**
Criteria A	≥3	≥ 3 and NI[b]	≥ 3 and NI	≥ 1	≥ 1 and NI	≥ 1 and NI	≥ 0[c]	≥ 1
Criteria B	Not applied	≥ 3	≥ 3 and NI	Not applied	≥ 1	≥ 1 and NI	≥ 0	≥ 0 and NI

a: In this test, 0,5 log deviation are evaluated as acceptable.
b:NI: No increase in the time since the previous count
c :*Rx*= 0 lg*N*0 = When lgnx (no increase after the first count)

Lavender (*Lavandula angustifolia*) essential oil has been pretty effective on the mentioned microorganisms (Table7-8) and as of the 14th day, they could eliminate contamination completely.

CONCLUSION

The content of the essential oils extracted from *Lavandula angustifolia,* which were grown in Burdur Örtülü locality, was determined via HPLC and GC-MS analysis. Furthermore, the anti-microbial effect of the essential oil *L. angustifolia* was also investigated. To obtain lavandula oil, Clevenger and solvent extraction methods were used. Various phenolic compounds in the extracts were quantitatively determined by HPLC.

Eleven different phenolic compounds, which are gallic acid, 3,4-dihydroxybenzoic acid, 4-hydroxybenzoic acid, chlorogenic acid, vanillic acid, caffeic acid, p-coumaric acid, ferulic acid, apigenin, rosmarinic acid, and cinnamic acid were determined via HPLC analysis. In a quantitative sense, caffeic acid, rosmarinic acid, and 4-hydroxybenzoic acids were the most abundant phenolic acids in the content in decreasing order. It is known that the phenolic compounds in lavender extract show antimicrobial effect. Thirty-one different volatile compounds were determined by GC-MS analysis. It was found that linalool and linalyl acetate have the highest concentration. Anti-microbial effects of the essential oil of *L. angustifolia* were determined against the most frequently encountered microorganisms in the cosmetics such as *Candida albicans, Staphylococcus aureus, Pseudomonas aeruginosa, Aspergillus brasiliensis.* According to our results it is revealed that the essential oil, *L. angustifolia*, can be used either directly or incorporated into the cosmetics without the necessity for any other extra preservative against the

microrganisms mentioned above. Also, it was found that the essential oil of *L. angustifolia* completely removed the contamination caused by some microorganisms.

REFERENCES

1. Kan Y, Uçan US, Kartal M, Altun ML, Aslan S, Sayar E, Ceyhan T. GC-MS Analysis and Antibacterial Activity of Cultivated *Satureja cuneifolia*Ten. Essential Oil, Turkish Journal of Chemistry. 2006; 30: 253-259. URL: http://journals.tubitak.gov.tr/chem/issues/kim-06-30-2/kim-30-2-14-0506-6.pdf

2. Guenther, E., Haagen-Smit, A., Langenau, E., & Urdang, G. E. Guenther, D. Althausen, and F. Sterrett (vol. 2); E. Guenther (vols. 3-6). 1948-1952. The Essential Oils, 6. ISBN: 0882750739 9780882750736 0882751638 9780882751634 0882750747 9780882750743 0882750925 9780882750927.

3. Kara, N., Baydar, H., 2013. Determination of lavender and lavandin cultivars (*Lavandula sp.*) containing high quality essential oil in Isparta, Turkey. Turk J Field Crops, 18, 58-65. URL: http://www.field-crops.org/assets/pdf/product51d3c571594ef.pdf

4. Seçmen Ö, Gemici Y, Görk G, Bekat L, Leblebici E. Tohumlu Bitkiler Sistematiği. Ege Üniversitesi Fen Fakültesi Kitaplar Serisi No: 116. İzmir. 2000. ISBN: 9789754830286.

5. Baydar H. Tıbbi, Aromatik ve Keyf Bitkileri Bilimi ve Teknolojisi (2. Baskı). Süleyman Demirel Üniversitesi Yayın No: 51. Isparta. 2007. 288 s. ISBN: 9757929794, 9789757929796.

6. Boelens MH. Chemical and sensory evaluation of *Lavandula* oils. Perfum. Flavor. 1995; 20: 23-51. URL: http://kbd.kew.org/kbd/detailedresult.do?id=126386

7. Kara N. Uçucu Yağ Üretimine Uygun Lavanta (*Lavandula* sp.) Çeşitlerinin Belirlenmesi Ve Mikroçoğaltım Olanaklarının Araştırılması. Süleyman Demirel Üniversitesi, Fen Bilimleri Enstitüsü, Tarla Bitkileri Anabilim Dalı, Doktora Tezi. 2011; 178p. URL: http://ulusaltezmerkezi.com/ucucu-yag-uretimine-uygun-lavanta-lavandula-sp-cesitlerinin-belirlenmesi-ve-mikrocogaltim-olanaklarinin-arastirilmasi/2/

8. Beetham J, Entwistle T. The Cultivated Lavenders. Royal Botanic Gardens, Melbourne. 1982. URL: https://scholar.google.com.tr/scholar?q=The+Cultivated+Lavenders&btnG=&hl=tr&as_sdt=0%2C5

9. Hui L, He L, Huan L, Lan LX, Guo ZA. Chemical composition of *lavender* essential oil and its antioxidant activity and inhibition against rhinitisrelated bacteria. African Journal of Microbiology Research. 2010; 4(4) : 309-313. Article Number - AFB8DA511807. URL: http://www.academicjournals.org/journal/AJMR/article-abstract/AFB8DA511807

10. Venskutonis PR, Dapkevicius A, Baranauskiene M. Composition of the essential oil of lavender (*Lavandula angustifolia* Mill.) from Lithuania. Journal of Essential Oil Research. 1997; 9(1):107-110. DOI:10.1080/10412905.1997.9700727.

11. Tanker N, Koyuncu M, Coşkun M. Farmasötik Botanik. Ank.Ünv. Eczacılık Fak. Yayınları Ders Kitapları No:78. 1998. ISBN No. 975-482-411-8.

12. Smigielelski K, Raj A, Krosowiak K, Gruska R. Chemical composition of the essential oil of *Lavandula angustifolia* cultivated in Poland. Journal of Essential Oil Bearing Plants. 2008; 12(3):128-136. DOI: 10.1080/0972060X.2009.10643729.

13. Davis PH. Flora of Turkey and the Aegean Islands, Vol. 7. Edinburgh University Press, Edinburgh. 1982. 76 p. URL: http://link.springer.com/article/10.1007%2FBF02853097

14. Baytop T. Therapy with Medicinal Plants in Turkey (Past and Present). vol. 385. Therapy with Medicinal Plants in Turkey 385. İstanbul: University Press İstanbul. 1984. 316 p. URL:

https://scholar.google.com.tr/scholar?as_vis=0&q=baytop,+Therapy+with+Medicinal+Plants+in+Turkey+(Past+and+Present)&hl=tr&as_sdt=0,5

15. Gilani AH, Aziz N, Khan MA, Shaheen F, Jabeen Q, Siddiqui BS, Herzig JW. Ethnopharmacological evaluation of the anticonvulsant, sedative and antispasmodic activities of *Lavandula stoechas* L. Journal of Ethnopharmacology. 2000; 71: 161/167. DOI:10.1016/S0378-8741(99)00198-1.

16. Rabiei Z, Rafieian-Kopaei M, Mokhtari S, Alibabaei Z, Shahrani M. The effect of pretreatment with different doses of *Lavandula officinalis* ethanolic extract on memory, learning and nociception. Biomedicine & Aging Pathology. 2014; 4(1):71-76. DOI:10.1016/j.biomag.2013.10.006.

17. Dawson NL, Reinhardt DJ. Microbial flora of inuse, display eye shadow testers and bacterial challenges of unused eye shadows. Appl. and Environ. Microbiol. 1981;42:297-302. URL: http://aem.asm.org/content/42/2/297.short

18. USP. United States Pharmacopeia XXII, US: pharmacopeial convention, Rockville. 1990. URL: http://www.usp.org/.

19. Anelich LE, Korsten L. Survey of microorganisms associated with spoilage of cosmetic creams manufactured in South Africa. Int. J. Cosmet. Sci. 1996;18: 25–40. DOI: 10.1111/j.1467-2494.1996.tb00133.x.

20. Behravan J, Bazzaz F, Malaekeh P. Survey of bacteriological contamination of cosmetic creams in Iran (2000). Int J Dermatol. 2005; 44: 482–485. DOI: 10.1111/j.1365-4632.2005.01963.x.

21. Darmstadt GL. Oral antibiotictherapy for uncomplicated skin infections in children. Pediatr Infect Dis J. 1997; 16:227-240. URL: http://journals.lww.com/pidj/Citation/1997/02000/Oral_antibiotic_therapy_for_uncomplicated.12.aspx

22. Reid FR, Wood TO. Pseudomonas corneal ulser the causative role of contaminated eye cosmetics. Arch. Ophtalmol. 1979; 97:1640-1641. DOI: 10.1001/archopht.1979.01020020208002.

23. Flores M, Morillo M, Crespo ML.Deterioration of raw materials and cosmetic products by preservative resistant microorganisms.Ðnt. Biodeterioration and Biodegradation. 1997;40: 157-160. DOI:10.1016/S0964-8305(97)00037-1.

24. Kıvanç M. Kozmetik Ürünlerde Mikrobiyel Kontaminasyon. 2. Kozmetik Kongresi, 17-19 Subat 2012, Antalya. URL: http://kimyakongreleri.org/K2012/K2012-011.pdf

25. Lundov MD, Zachariae C. Recalls of microbiologycally contaminated cosmetics in EU from 2005 to May 2008. Int.J. of Cosmetic Sci. 2008; 30: 471-474. DOI: 10.1111/j.1468-2494.2008.00475.x

26. Kiselev KV, Dubrovina AS, Veselova MV, Bulgakov VP, Fedoreyev SA, Zhuravlev YN. The *rol*-B gene-induced over production of resveratrol in *Vitis amurensi*s transformed cells. Journal of Biotechnology. 2007; 128: 681-692. DOI:10.1016/j.jbiotec.2006.11.008.

27. Gomes T, Caponio F, Alloggio V. Phenolic compounds of virgin olive oil: influence of paste preparation techniques. Food Chemistry, 1999; 64: 203-209. DOI:10.1016/S0308-8146(98)00146-0.

28. Baydar H, Kuleasan H, Kara N, Secilmis-Canbay H, Kineci S. The effects of pasteurization, ultraviolet radiation and chemiclal preservatives on microbial spoilage and scent composition of rose water. Journal of Essential Oil Bearing Plants. 2013; 16(2): 151-160. DOI: 10.1080/0972060X.2013.794043.

29. Cowan MM. Plant Products as Antimicrobial Agent. Clin. Microbiol. Rev. 1999; 12(4):564. URL: http://cmr.asm.org/content/12/4/564.short

30. Karou D, Nadembega WMC, Ouattara L, Ilboudo DP, Canini A, Nikiema JB, Simpore J, Colizzi V, Traore AS. African Ethnopharmacology and New Drug Discovery. Medicinal and Aromatic Plant Science and Biotech. 2007. URL: http://citeseerx.ist.psu.edu/viewdoc/download?doi=10.1.1.525.7636&rep=rep1&type=pdf

31. Taguri T, Tanaka T, Kouno I. Antimicrobial Activity Of 10 Different Plant Polyphenols Against Bacteria Causing Food-Borne Disease. Biol.Pharm .Bull. 2004; 27(12):1965-1969. DOI: 10.1248/bpb.27.1965

32. Whitehead DC, Dıbb H, Hartley RD. Phenolic Compounds in Soil as Influenced by the Growth of Different Plant Species. Journal of Applied Ecology. 1982; 19:579-588. DOI: 10.2307/2403490.

33. Kang MS, Oh JS, Kang IC, Hong SJ, Choi CH. Inhibitory effect of methyl gallate and gallic acid on oral bacteria. The Journal of Microbiology. 2008; 46(6), 744-750. URL: http://link.springer.com/article/10.1007/s12275-008-0235-7

34. Hammer KA, Carson CF, Riley TV. Antimicrobial activity of essential oils and other plant extracts. J. Appl. Microbiol. 1999;86:985–990. DOI: 10.1046/j.1365-2672.1999.00780.x

35. de Rapper S, Kamatou G, Viljoen A, van Vuuren S. The in vitro antimicrobial activity of *Lavandula angustifolia* essential oil in combination with other aroma-therapeutic oils. J. Evid. Based Complement. Altern. Med., 2013; 2013:1–24. DOI: 10.1155/2013/852049.

36. Park SN, Lim YK, Freire MO, Cho E, Jin D, Kook JK. Antimicrobial effect of linalool and α-terpineol against periodontopathic and cariogenic bacteria. Anaerobe. 2012;18(3), 369-372. DOI:10.1016/j.anaerobe.2012.04.001.

37. Hammer KA, Carson CF. Antibacterial and antifungal activities of essential oils. H. Thormar (Ed.), Lipids and essential oils as Antimicrobial agents, Wiley, UK. 2010; 256–306. DOI: 10.1002/9780470976623.ch11.

38. Lang G, Buchbauer G. A review on recent research results (2008–2010) on essential oils as antimicrobials and antifungals. A review. Flavour and Fragrance Journal. 2012; 27(1), 13-39. DOI: 10.1002/ffj.2082.

39. Nelson RRS. In-vitro activities of five plant essential oils against methicillin-resistant *Staphylococcus aureus* and vancomycin-resistant *Enterococcus faecium*. Journal of Antimicrobial Chemotherapy. 1997; 40(2): 305–306. DOI: 10.1093/jac/40.2.305.

40. Adam K, Sivropoulou A, Kokkini S, Lanaras T, Arsenakis M. Antifungal activities of *Origanum vulgare* subsp. hirtum, *Mentha spicata*, *Lavandula angustifolia*, and *Salvia fruticosa* essential oils against human pathogenic fungi. Journal of Agricultural and Food Chemistry. 1998; 46(5): 1739–1745. DOI: 10.1021/jf9708296.

41. Hammer KA, Carson CF, Riley TV. *In-vitro* activity of essential oils, in particular *Melaleuca alternifolia* (tea tree) oil and tea tree oil products, against *Candida* spp. Journal of Antimicrobial Chemotherapy. 1998; 42(5): 591–595. DOI: 10.1093/jac/42.5.591.

42. Shin S, Lim S. Antifungal effects of herbal essential oils alone and in combination with ketoconazole against *Trichophyton* spp. Journal of Applied Microbiology. 2004; 97(6): 1289–1296. DOI: 10.1111/j.1365-2672.2004.02417.x.

43. Mayaud L, Carricajo A, Zhiri A, Aubert G. Comparison of bacteriostatic and bactericidal activity of 13 essential oils against strains with varying sensitivity to antibiotics. Letters in Applied Microbiology. 2008; 47(3):167–173. DOI: 10.1111/j.1472-765X.2008.02406.x.

44. Lodhia MH, Bhatt KR, Thaker VS. Antibacterial activity of essential oils frompalmarosa, evening primrose, lavender and tuberose. Indian Journal of Pharmaceutical Sciences. 2009;71(2):134–136. DOI: 10.4103/0250-474X.54278.

45. Agarwal V, Lal P, Pruthi V. Effect of plant oils on *Candida albicans*. Journal of Microbiology, Immunology and Infection. 2010;43(5):447–451. DOI:10.1016/S1684-1182(10)60069-2.

46. Sokovi´c M, Glamo˘clija J, Marin P. D. Antibacterial effects of the essential oils of commonly consumed medicinal herbs using an *in vitro* model. Molecules. 2010;15: 7532–7546. DOI: 10.3390/molecules15117532.

47. Tsai TH, Tsai TH, Wu WH, Tseng JTP, Tsai PJ. *In vitro* antimicrobial and anti-inflammatory effects of herbs against *Propionibacterium acnes*. Food Chemistry. 2010; 119(3): 964–968. DOI:10.1016/j.foodchem.2009.07.062.

48. Alexopoulos A, Kimbaris AC, Plessas S. Antibacterial activities of essential oils from eight Greek aromatic plants against clinical strains of *Staphylococcus aureus*. Anaerobe. 2011; 17;399–402. DOI:10.1016/j.anaerobe.2011.03.024.

Türkçe Öz ve Anahtar Kelimeler

Fitokozmetik Tür olarak *Lavandula angustifolia* Mill.'in Kimyasal Karakterizasyonu ve Kozmetik Ürünlerde Antimikrobiyal Etkisinin İncelenmesi

Aslıhan Cesur Turgut, Fatih Mehmet Emen, Hale Seçilmiş Canbay, Ruken Esra Demirdöğen, Neslihan Çam, Derya Kılıç, Tuncay Yeşilkaynak

Öz: Burdur-Örtülü'de yetişen *Lavandula angustifolia* türünden elde edilen ekstraktların bileşimi HPLC ve GC-MS analizleriyle belirlenmiştir ve *L. angustifolia*'nın esansiyel yağındaki antimikrobiyal etki araştırılmıştır. *L. angustifolia*'nın kurutulmuş çiçekleri ekstrakte edilmiş ve esansiyel yağı geri kalan kısmından damıtılmıştır. Ekstrakttaki çeşitli fenolik bileşikler HPLC ile kantitatif olarak belirlenmiştir. Kantitatif olarak kafeik asit, rosmarinik asit ve 4-hidroksibenzoik asitler, bu sırada azalacak şekilde, en bol bulunan fenolik asitler olarak bulunmuştur. GC-MS analizinde 31 farklı bileşik belirlenmiştir: Linalool ve linalil asetat en yüksek derişimlere sahiptir. *L. angustifolia*'nin esansiyel yağının antimikrobiyal aktivitesi, kozmetik ürünlerde en çok rastlanan mikroorganizmalara karşı tespit edilmiştir (*Candida albicans, Staphylococcs aureus, Pseudomonas aeruginosa* ve *Aspergillus brasiliensis*). *L. angustifolia*'nın esansiyel yağının 14.günden itibaren mikroorganizmalar tarafından oluşturulan kirliliği tamamen giderdiği görülmüştür. Sonuçlara göre, *L. angustifolia*'nın esansiyel yağının yukarıda bahsedilen mikroorganizmalara karşı başka bir koruyucu madde gereksinimi olmaksızın, kozmetik ürünlerde doğrudan veya dolaylı olarak kullanılabileceği anlaşılmaktadır.

Anahtar kelimeler: *Lavandula angustifolia* Mill.*;* kozmetik ürünler; fenolik bileşikler; esansiyle yağ; antimikrobiyal aktivite**.**

Sunulma: 04 Temmuz 2016**. Düzeltme:** 24 Kasım 2016**. Kabul:** 25 Kasım 2016**.**

JOTCS A
Journal of the Turkish Chemical Society
Section: A
Chemistry
TURKISH CHEMICAL SOCIETY

Syntheses and Structural Characterizations of First Paraben-Substituted Ferrocenyl Phosphazene Compounds

Yasemin Tümer[1]*, Efsun Şehirli[1], Çiğdem Yüksektepe Ataol[2]

[1]Karabük University, 78050, Karabük, Turkey
[2]Çankırı Karatekin University, 18100, Çankırı, Turkey

Abstract: The Cl replacement reactions of NO (**1**) or NN (**2–5**) spirocyclic monoferrocenyl cyclotriphosphazenes with the potassium salt of ethyl-4-hydroxybenzoate resulted in the full substituted phosphazenes (**6-10**). Their structures have been determined using elemental analysis, FTIR (Fourier transform), ^{1}H (one-dimensional-1D), ^{31}P NMR techniques and X-ray crystallography (for **9** and **10**).

Keywords: Ferrocenylphosphazenes; paraben, ethyl-4-hydroxybenzoate; spectroscopy.

Submitted: .July 11, 2016. **Revised:** November 21, 2016. **Accepted:** November 26, 2016.

Cite this: Tümer Y, Şehirli E, Yüksektepe Ataol Ç. Syntheses and Structural Characterizations of First Paraben-Substituted Ferrocenyl Phosphazene Compounds. JOTCSA. 2017;4(1):299–312.

DOI: To be assigned.

*Corresponding author. E-mail: yasemintumer@karabuk.edu.tr.

INTRODUCTION

The hexachlorocyclotriphosphazene (cyclic trimer, $N_3P_3Cl_6$) is an important compound in the improvement of cyclotriphosphazene derivatives [1], polyorganophosphazenes [2, 3], and phosphazene dendrimers [4, 5]. The phosphorus-nitrogen backbone with six Cl atoms provide an ideal structure for synthesis new cyclotriphosphazene derivatives.

Due to their bactericidal and fungicidal properties, parabens are a class of widely used as preservatives, especially in personal care products, pharmaceuticals, and food [6]. Recently, parabens have been mentioned as a significant substitute group to increase adjuvant [3, 7], water-solubility [3, 8], anti-cancer properties [9] of both the cyclophosphazenes and polyphosphazenes. In addition to that, paraben-substituted polyphosphazene compounds have been considered as hydrogels, membranes [3, 10], and polyelectrolyte materials [11].

In previous studies carried by our group, DNA interactions as well as cytotoxic and antimicrobial activities of ferrocenylphosphazene derivatives were investigated [12, 13, 14]. This study suggests that ferrocenylphosphazenes bearing a paraben derivative (ethyl-4-hydroxybenzoate) could show antimicrobial and cytotoxic activities, and DNA damaging properties. For this purpose, the tetrachloro spirocyclotriphosphazenes with ferrocenyl substituents on the spirocyclic unit (**1-5**) were synthesized as precursor materials which have four active P-Cl bonds [14, 15]. The substitution reactions of **1-5** with ethyl-4-hydroxybenzoate were carried out as emphasized. The structures of the new phosphazene derivatives (**6-10**) (Scheme 1) have been determined using FTIR (Fourier transform), ^{1}H (one-dimensional-1D), ^{31}P NMR techniques and elemental analyses. The molecular and solid-state structures of **9** and **10** were established using single crystal X-ray diffraction methods.

MATERIALS AND METHODS

Reagents

Hexachlorocyclotriphosphazene (Aldrich), ferrocenecarboxaldehyde (Aldrich), ethyl-4-hydroxybenzoate (Aldrich) and aliphatic amines (Fluka) were purchased. These compounds were used without further purification. All solvents we used were dried.

Instruments

The melting points of the new compounds **(6-10)** were determined with a Thermo Scientific apparatus. The ^{1}H NMR spectra were recorded on a Bruker DPX FT-NMR (300

MHz) spectrometer and ^{31}P NMR spectra were recorded on a Bruker Avance III HDNMR (600 MHz) spectrometer. The FTIR spectra were recorded on a Perkin Elmer FTIR (Fourier transform) spectrometer (650-4000 cm^{-1}).

Synthesis of Ferrocenylphosphazene Derivatives

The tetrachloroferrocenylphosphazenes (**1-5**) were synthesized from the reactions of $N_3P_3Cl_6$ with ferrocenylamines according to the methods reported in the literature [14, 15].

1. 4,4',4'',4'''-[(4-Ferrocenyl-1-oxa-4,6,8,10-tetraaza-5λ^5,7λ^5,9λ^5-triphosphaspiro[4.5] deca-5,7,9-triene-7,7,9,9-tetrayl)tetrakis(oxy)]tetrakis(ethyl benzoate) (**6**)

A solution of ethyl-4-hydroxybenzoate (1.24 g, 7.48 mmol) in dry THF (50 mL) was added to a solution of **1** (1.0 g, 1.87 mmol) and potassium carbonate (2.0 g) in dry THF (100 mL) with stirring and refluxing for 72 h. The reaction was followed on TLC silica gel plates using toluene-THF (10:1). After the solvent was evaporated, and the product **(6)** was purified by column chromatography with toluene-THF (10:1) as eluent. (1.54 g, 78 %) Anal. Calcd. for $C_{49}H_{51}FeN_4O_9P_3$: C, 55.90; H, 4.88; N, 5.32. Found: C, 55.89; H, 4.72; N, 5.24. FTIR: 1714 (C=O); 2982, 2930 (C-Haliph.); 1601, 1500, 1475 (C-Carom.); 1094 (C-O); 1265, 1158 (P=N).

2. 4,4',4'',4'''-[(7,11-Diferrocenyl-1,3,5,7,10-pentaaza-2λ^5,4λ^5,6λ^5-triphosphaspiro [4.5] deca-1,3,5-triene-2,4,4,4-tetrayl)tetrakis(oxy)]tetrakis(ethyl benzoate) (**7**)

The same procedure used for 6 was followed for the synthesis of **7**; using **2** (1.0 g, 1.37 mmol), ethyl-4-hydroxybenzoate (0.91 g, 5.47 mmol) and potassium carbonate (2.0 g). (1.44 g, 84%; mp: 154-157 ºC). Anal. Calcd. for $C_{60}H_{62}Fe_2N_5O_8P_3$: C, 57.66; H, 4.99; N, 5.60. Found: C, 57.34; H, 4.53; N, 6.13. FTIR: 1713 (C=O); 2979, 2918 (C-$H_{aliph.}$); 1600, 1502, 1464 (C-$C_{arom.}$); 1095 (C-O); 1272, 1149 (P=N).

3. 4,4',4'',4'''-[(1-Ferrocenyl-4-methyl-1,4,6,8,10-pentaaza-5λ^5,7λ^5,9λ^5-triphosphaspiro [4.5]deca-5,7,9-triene-7,7,9,9-tetrayl)tetrakis(oxy)]tetrakis(ethyl benzoate) (**8**)

The synthetic route used for **6** was followed for the synthesis of **8**; using **3** (1.0 g, 1.83 mmol), ethyl-4-hydroxybenzoate (1.22 g, 7.31 mmol) and potassium carbonate (2.0 g). (1.37 g, 70%; mp: 182-186 ºC). Anal. Calcd. for $C_{50}H_{54}FeN_5O_8P_3$: C, 56.30; H, 5.11; N, 6.57. Found: C, 55.75; H, 5.08; N, 6.21. FTIR: 1715 (C=O); 2981 (C-$H_{aliph.}$); 1600, 1503, 1464 (C-$C_{arom.}$); 1095 (C-O); 1265, 1154 (P=N).

4. 4,4',4'',4'''-[(1-Ferrocenyl-4-ethyl-1,4,6,8,10-pentaaza-5λ^5,7λ^5,9λ^5-triphosphaspiro [4.5]deca-5,7,9-triene-7,7,9,9-tetrayl)tetrakis(oxy)]tetrakis(ethyl benzoate) (**9**)

The experimental route used for **6** was followed, using **4** (1.0 g, 1.78 mmol), ethyl-4-hydroxybenzoate (1.19 g, 7.13 mmol) and potassium carbonate (2.0 g). (1.60 g, 83%; mp: 149-152 ^{o}C). The product **9** was dissolved in n-hexane/ THF mixture and crystallized at room temperature. Anal. Calcd. for $C_{51}H_{56}FeN_5O_8P_3$: C, 56.72; H, 5.23; N, 6.48. Found: C, 56.34; H, 5.26; N, 6.34. FTIR: 1715 (C=O); 2980 (C-$H_{aliph.}$); 1599, 1503, 1464 (C-$C_{arom.}$); 1094 (C-O);1258, 1150 (P=N).

5. 4,4',4'',4'''-[(7-Ferrocenyl-11-methyl-1,3,5,7,11-pentaaza-2λ^5,4λ^5,6λ^5-triphosphaspiro [5.5]undeca-1,3,5-triene-2,2,4,4-tetrayl)tetrakis(oxy)]tetrakis(ethyl benzoate) (**10**)
For the synthesis, the same procedure used for **6** was followed; using **5** (1.00 g, 1.78 mmol), ethyl-4-hydroxybenzoate (1.19 g, 7.13 mmol) and potassium carbonate (2.0 g). The product **10** was dissolved in n-hexane/ acetonitrile mixture and crystallized at room temperature. (1.56 g, 81%; mp: 170-172 ^{o}C). Anal. Calcd. for $C_{51}H_{56}FeN_5O_8P_3$: C, 56.72; H, 5.23; N, 6.48. Found: C, 57.22; H, 5.36; N, 6.34. FTIR: 1715 (C=O); 2981 (C-$H_{aliph.}$); 1600, 1503, 1464 (C-$C_{arom.}$); 1094 (C-O);1260, 1158 (P=N).

X-Ray Crystallography

Crystallographic data for **9** and **10** were recorded on a Bruker Kappa APEXII CCD area-detector diffractometer using Mo Kα radiation (λ= 0.71073 Å) at T = 296 K. Absorption corrections by multi-scan [21] were applied. Structures were solved by direct methods and refined by full-matrix least squares against F^2 using all data [22]. All non-H atoms were refined anisotropically. Atoms H3A and H3B (for CH_2 group) were placed in a difference synthesis and refined isotropically for **9**. Methyl, aromatic, methine, and methylene H atoms were positioned geometrically at distances of 0.93 (aromatic CH), 0.97 (CH_2), 0.98 (CH) and 0.96 (CH_3) from the parent C atoms; a riding model was used during the refinement process and the Uiso(H) values were constrained to be 1.2 Ueq (for aromatic, methine and methylene carrier atoms) and 1.5 Ueq (for methyl carrier atoms) for **9** and **10**. The principal mean square atomic displacements U of the some of atoms such as C1, C2, C15, C24, C51 and C33 are higher than the other atoms in the compound **10**. According to cif results, this means U values are admitted. The R1 and wR2 indices are obtained higher than expected due to high U displacements of some atoms.

RESULTS AND DISCUSSION

Synthesis and Characterization

The starting compounds (**1-5**) were synthesized in accordance with the published procedure [14, 15]. These precursor compounds have four reactive P-Cl bonds which

may be replaced by the nucleophiles. Utilizing these features tetra-substituted ferrocenylphosphazenes **(6–10)** were obtained from the reactions of **1-5** and potassium salt of ethyl-4-hydroxybenzoate in refluxing THF (Scheme 1). The new compounds in all the reactions were isolated by column chromatography.

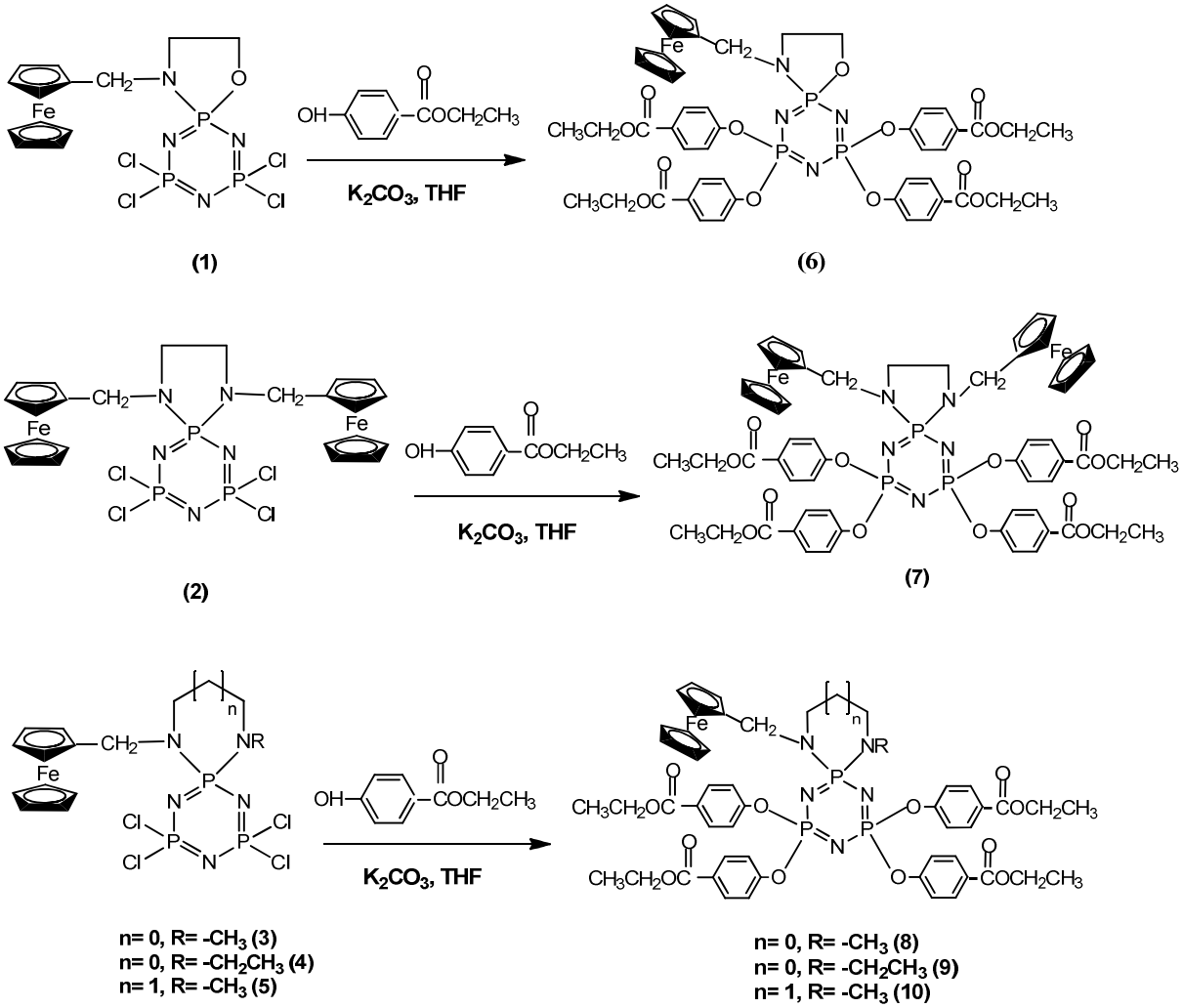

Scheme 1. The synthetic route for new phosphazene derivatives **(6-10)**.

The ^{1}H-decoupled ^{31}P NMR spectral data of **6-10** are listed in Table 1. The spin systems of the new compounds are interpreted as AX_2. Compounds **6-10** demonstrate a typical five-line resonance pattern, including a doublet for two substituted P atoms and a triplet for other P(spiro) atom.

The assignments of the ^{1}H NMR signals of the new ferrocenylphosphazene derivatives were made based on the chemical shifts, multiplicities, and coupling constants (Tables S1 and S2). The $FcCH_2N$ protons of paraben-substituted ferrocenylphosphazenes yield the doublets due to the vicinal coupling with the P-31 nucleus, indicating that both geminal

protons are equivalent. The $^{3}J_{PH}$ values of $FcCH_2N$ protons are in the range of 2.63-3.40 Hz. As expected, the nine protons belonging to the ferrocenyl groups are observed as a singlet (3.84-3.98 ppm).

Table 1. The ^{31}P NMR spectral data of **6-10**. [*J* values in Hz and chemical shifts (δ) are reported in ppm]. ^{31}P NMR measurements in $CDCl_3$ solutions at 293 K.

	δ(ppm)			O
Compound	**$P(NO)_{(spiro)}$**	**$P(NNR)_{(spiro)}$**	**$P(OAr)_2$**	**$^{2}J_{PP}$ (Hz)**
6	29.74 (t)	-	10.50 (d)	62.65
7	-	24.97 (t)	10.84 (d)	54.57
8	-	26.33 (t)	10.96 (d)	54.57
9	-	24.46 (t)	10.92 (d)	54.57
10	-	23.07 (t)	9.33 (d)	50.53

The spin system of all compounds is AX_2.

X-ray Structural Studies

The molecular structures of **9** and **10** are shown in Figures 1 and 2. The molecules are comprised of a cyclotriphosphazene core, a spirocyclic diamine with a ferrocenyl substituent, and four terminal ethylbenzoate groups.

The crystals are monoclinic, space groups $P2_1/c$, with *a* = 14.0306(12)Å and 14.3409(13)Å, *b* = 10.9976(8)Å and 10.9552(11)Å, *c* = 33.420(3)Å and 33.0730(32)Å, α, γ = 90° and 90°, β =94.212(3)° and 92.074(3)°, V = 5142.8(7) Å3 and 5192.6(9) Å3, and Z = 4 for **9** and **10**, respectively (Table S3). The phosphazene rings are not planar for **9** and **10**, with a total puckering parameter (Q_T) of 0.126(3)Å and 0.086(4)Å. The conformation of the phosphazene rings of **9** and **10** are twisted-boat [q_2= 0.045(3)Å and 0.033(4)Å, q_3=0.118(3)Å and -0.080(4)Å, Φ_2= 273(4)° and 85(6)° and θ_2= 21.0(14)° and 158(3)°, respectively]. The selected geometric parameters are listed in Table 2. The average endocyclic P−N bond lengths in phosphazene rings [1.636(4) Å for **9** and 1.651(5) Å for **10**] are shorter than the average exocyclic P−N bonds [1.633(4) Å for 9 and 1.643(5) Å for **10**]. There are regular variations with the distances from P1: P3−N2 ≈ P3−N3> P2−N1≈ P1−N1> P1−N2 ≈ P2−N3, P2−N1 ≈ P2−N2> P1−N3≈ P3−N3> P3−N2 ≈ P1−N1 for **9** and **10**, respectively. In the phosphazene rings, the endocyclic (α*)* and exocyclic (α^1) angles of **9** and **10** deviate slightly from those found in the standard compound $N_3P_3Cl_6$ [α 118.3(2)° and $\alpha^1$101.2(1)°] [17-19].

Table 2. Selected bond lenghts (Å) and angles (º) for **9** (α) and **10** (α^1)

Compound 9		**Compound 10**	
P(1)–N(1)	1.575(3)	P(1)–N(1)	1.556(5)
P(1)–N(2)	1.563(3)	P(1)–N(3)	1.588(4)
P(2)–N(1)	1.576(3)	P(2)–N(1)	1.611(5)
P(2)–N(3)	1.557(4)	P(2)–N(2)	1.600(5)
P(3)–N(2)	1.603(4)	P(3)–N(2)	1.566(5)
P(3)–N(3)	1.592(4)	P(3)–N(3)	1.577(5)
P(1)–O(6)	1.587(3)	P(1)–O(1)	1.604(4)
P(1)–O(7)	1.585(3)	P(1)–O(2)	1.605(4)
P(2)–O(1)	1.596(3)	P(3)–O(3)	1.594(4)
P(2)–O(4)	1.599(3)	P(3)–O(4)	1.594(4)
P(3)–N(4)	1.636(4)	P(2)–N(4)	1.651(5)
P(3)–N(5)	1.633(4)	P(2)–N(5)	1.643(5)
N(1)–P(1)–N(2)	118.23(2)	N(1)–P(1)–N(3)	118.8(3)
P(1)–N(1)–P(2)	119.80(2)	P(1)–N(3)–P(3)	119.9(3)
N(1)–P(2)–N(3)	118.47(2)	N(3)–P(3)–N(2)	118.8(3)
P(2)–N(3)–P(3)	124.90(2)	P(3)–N(2)–P(2)	123.7(3)
N(3)–P(3)–N(2)	111.99(2)	N(2)–P(2)–N(1)	113.9(3)
P(3)–N(2)–P(1)	124.30(2)	P(2)–N(1)–P(1)	123.9(3)
O(6)–P(1)–O(7)	98.07(2)	O(1)–P(1)–O(2)	97.0(2)
O(1)–P(2)–O(4)	97.71(1)	O(3)–P(3)–O(4)	97.9(2)
N(4)–P(3)–N(5)	94.25(2)	N(4)–P(2)–N(5)	102.7(3)

Full cif depositions, excluding structure factor amplitudes, are lodged with the Cambridge Crystallographic Data Centre, CCDC 1446475 for **9** and CCDC 1451311 for 10. These data can be obtained free of charge via http://www.ccdc.cam.ac.uk/conts/retrieving.html (or from the CCDC, 12 Union Road, Cambridge CB2 1EZ, UK; Fax: +44 1223 336033; E-mail: deposit@ccdc.cam.ac.uk).

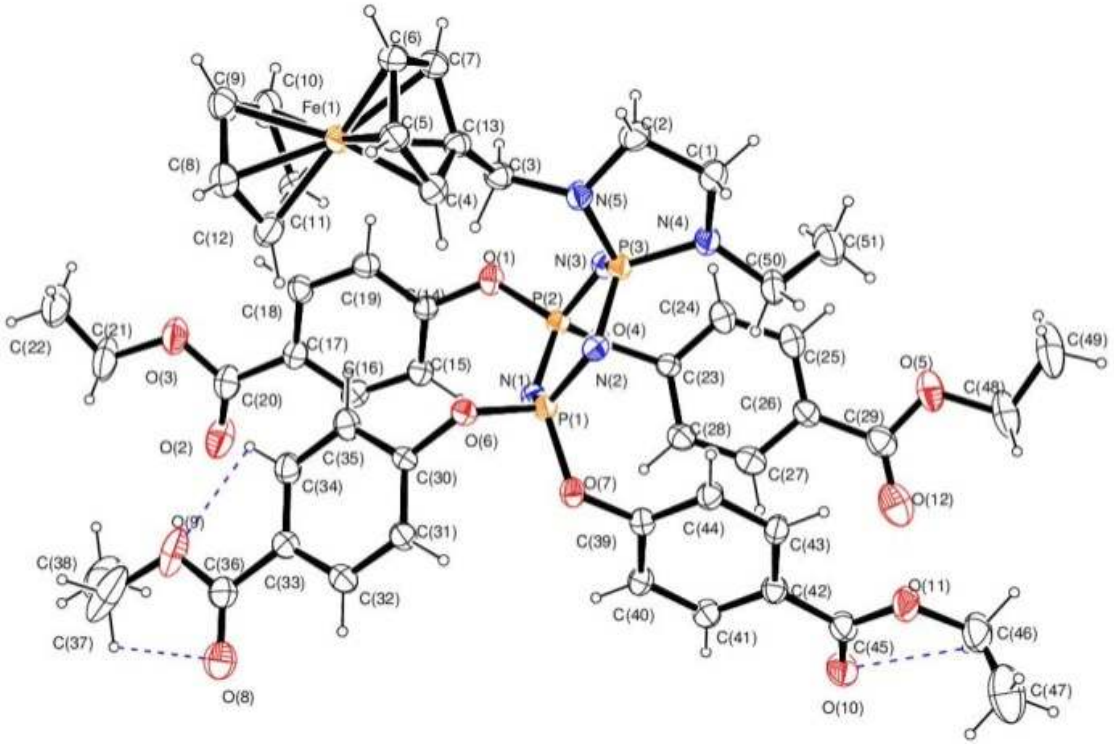

Figure 1. ORTEP-3 [16] drawing of **9** with the atom-numbering scheme. Displacement ellipsoids are drawn at the 30 % probability level.

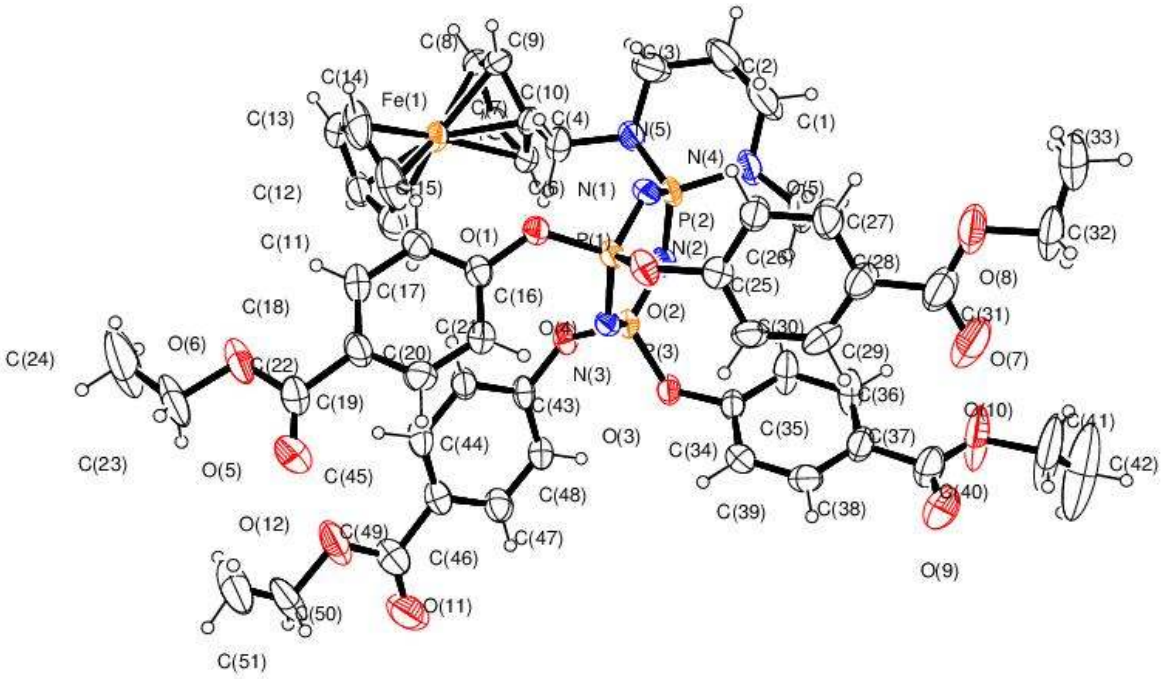

Figure 2. ORTEP-3 [16] drawing of **10** with the atom-numbering scheme. Displacement ellipsoids are drawn at the 30 % probability level.

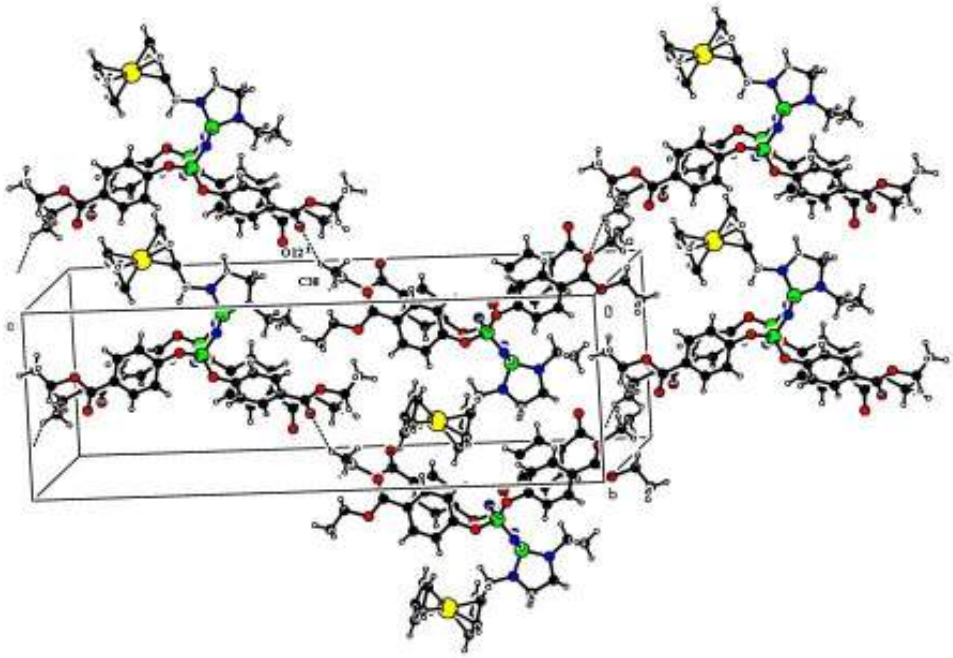

Figure 3. PLUTON [20] drawing of **9** with intermolecular C(38)−H(38A)…O(12)^{I} hydrogen bonding extending along *c* axis. Code of symmetry: (i) x,-1/2-y,1/2+z.

Compound **9** has intermolecular and intramolecular C−H…O hydrogen bonds; however, the hydrogen bonds are found in the compound **10**, which has intramolecular hydrogen bonds. The details of the intramolecular bonds are indicated in Table 3. Also, intramolecular C−H…O interactions can be seen in Figure 1. As seen in Figure 3, these intermolecular hydrogen bonds firstly link the molecules into centrosymmetric dimers, and then these dimers are linked to zig-zag form infinite chains running nearly along the c-axis. On the other hand, the *π* … *π* contact between the ferrocene rings, Cg(2)–Cg(3) [where Cg(2) and Cg(3) are the centroids of the rings (C4–C7/C13) and (C8–C12)] with the centroid–centroid distance of 3.286(3) Å and the C–H…*π* interaction may be effective in the stabilization of the crystal packing (Table 3 and Figure S1).

Table 3. Hydrogen-bond geometry (Å, °) of **9** and **10**. Symmetry codes: (i) x,-1/2-y,1/2+z; (ii) x, 1+y, z.

Compounds	Hydrogen bond(Å,°)	D–H	H…A	D…A	D–H…A
9	C(34)−H(34)...O(9)	0.93	2.38	2.703(7)	100
	C(37)−H(37A)...O(8)	0.97	2.23	2.657(12)	106
	C(46)−H(46A)...O(10)	0.97	2.29	2.663(8)	102
	C(38)−H(38A)...O(12)^{i}	0.96	2.60	3.402(12)	142
	C(6)−H(6)...Cg(7)^{ii}	0.93	2.93	3.698(5)	140
10	C(27)−H(27)...O(8)	0.93	2.40	2.715(10)	100
	C(41)−H(41B)...O(9)	0.97	2.14	2.590(20)	107
	C(45)−H(45)...O(12)	0.93	2.38	2.705(10)	100

CONCLUSIONS

In the current study, paraben-substituted ferrocenylphosphazene derivatives were synthesized. The structures of **9** and **10** were determined using X-ray crystallography. The compounds synthesized are the precursor molecules for further investigations by our research group.

ACKNOWLEDGMENT

The authors acknowledge the "Karabuk University, Scientific Research Unit" (GrantNo. YL20/2014-2) for the financial support and Scientific and Technological Research Application and Research Center, Sinop University, Turkey, for the use of the Bruker D8 QUEST diffractometer.

REFERENCES

1. Gleria M, Jaeger RD, editors. Applicative aspects of cyclophosphazenes. New York: Nova Science Publishers; 2004. 371 s. ISBN: 1-59454-026-8.

2. Allcock HR. Chemistry and applications of polyphosphazenes. Hoboken, N.J: Wiley-Interscience; 2003. 725 s. ISBN: 978-0-471-44371-1.

3. Andrianov AK, editor. Polyphosphazenes for biomedical applications. Hoboken, N.J: Wiley; 2009. 462 s. ISBN: 978-0-470-19343-3.

4. Tümer Y, Yüksektepe Ç, Batı H, Çalışkan N, Büyükgüngör O. Preparation and characterization of Hexakis[2-methoxy-4-(2,3-dimethylphenylimino)phenylato]cyclotriphosphazene. Phosphorus, Sulfur, and Silicon and the Related Elements. November 23 2010;185(12):2449–54. DOI: 10.1080/10426501003692078.

5. Çoşut B, Yeşilot S, Durmuş M, Kılıç A. Synthesıs and fluorescence propertıes of hexamerıc and octamerıc subphthalocyanınes based cyclic phosphazenes. Dyes And Pıgments. September 2013;98(3):442–9. DOI: 10.1016/j.dyepig.2013.03.028.

6. Bledzka D, Gromadzinska J, Wasowicz W. Parabens. From environmental studies to human health. Environ. Int., February 2014; 67: 27–42. DOI: 10.1016/j.envint.2014.02.007.

7. Andrianov AK, DeCollibus DP, Gills HA, Kha HH, Marin A, Prausnitz MR, Babiuk LA, Townsend H, Mutwiri G. Poly[di(carboxylatophenoxy)phosphazene] is a potent adjuvant for intradermal immunization. P Natl Acad Scı Usa. November 2009; 106 (45): 18936–18941. DOI: 10.1073/pnas.0908842106.

8. Stone ML, Wilson AD, Harrup MK, Stewart FF. An initial study of hexavalent phosphazene salts as draw solutes in forward osmosis. Desalination. March 2013; 312: 130–136. DOI: 10.1016/j.desal.2012.09.030.

9. Çiftçi GY, Şenkuytu E, İncir SE, Yuksel F, Ölçer Z, Yıldırım T, Kılıç A, Uludağ Y. First paraben substituted cyclotetraphosphazene compounds and DNA interaction analysis with a new automated biosensor. Biosensors and Bioelectronics. June 2016; 80: 331-338. DOI: 10.1016/j.bios.2016.01.061.

10. Allcock HR, Kwon S. An ionıcally cross-lınkable polyphosphazene: poly(bıs(carboxylatophenoxy)phosphazene) and its hydrogels and membranes. Macromolecules. February 1989; 22 (1): 75–79. DOI: 10.1021/ma00191a015.

11. Akgol Y, Hofmann C, Karatas Y, Cramer C, Wiemhofer HD, Schönhoff M. Conductivity spectra of polyphosphazene-based polyelectrolyte multilayers. J. Phys. Chem. B. May 2007; 111: 8532-8539. DOI: 10.1021/jp068872w.

12. Asmafiliz N, Kılıç Z, Hökelek T, Açık L, Koç LY, Süzen Y, Öner Y. Phosphorus–nitrogen compounds: Part 26. Syntheses, spectroscopic and structural investigations, biological and cytotoxic activities, and DNA interactions of mono and bisferrocenylspirocyclotriphosphazenes. Inorg. Chim. Acta. May 2013; 400: 250-261. DOI: 10.1016/j.ica.2013.03.001.

13. Tumer Y, Asmafiliz N, Kılıc Z, Hokelek T, Koc LY, Acık L, Yola ML, Solak AO, Oner Y, Dundar D, Yavuz M. Phosphorus–nitrogen compounds: Part 28. Syntheses, structural characterizations, antimicrobial and cytotoxic activities, and DNA interactions of new phosphazenes bearing vanillinato and pendant ferrocenyl groups. Journal of Molecular Structure. October 2013; 1049: 112–124. DOI: 10.1016/j.molstruc.2013.06.036.

14. Tumer Y, Koc LY, Asmafiliz N, Kılıc Z, Hokelek T, Soltanzade H, Acık L, Yola ML, Solak AO. Phosphorus–nitrogen compounds: part 30. Syntheses and structural investigations, antimicrobial and cytotoxic activities and DNA interactions of vanillinato-substituted NN or NO spirocyclic monoferrocenyl cyclotriphosphazenes. J Biol Inorg Chem. January 2015; 20: 165–178. DOI:10.1007/s00775-014-1223-5.

15. Ilter EE, Asmafiliz N, Kılıc Z, Acık L, Yavuz M, Bali EB, Solak AO, Buyukkaya F, Dal H, Hokelek T. Phosphorus–nitrogen compounds: Part 19. Syntheses, Structural and Electrochemical Investigations, Biological Activities and DNA Interactions of New Spirocyclic monoferrocenylcyclotriphosphazenes. Polyhedron. July 2010; 29: 2933-2944. DOI: 10.1016/j.poly.2010.07.017.

16. Farrugia LJ, ORTEP-3 for Windows- a version of ORTEP-III with a Graphical User Interface (GUI). J Appl. Cryst. 1997; 30; 565. DOI: 10.1107/S0021889897003117.

17. Tumer Y, Batı H, Çalışkan N, Yüksektepe Ç, Büyükgüngör O. Synthesis, Crystal Structure and Characterization of Hexakis[2-methoxy-4-formylphenoxy]cyclotriphosphazene. Z. Anorg. Allg. Chem. March 2008; 634(3): 597–599. DOI: 10.1002/zaac.200700389.

18. Kiliç A, Begeç S, Çetinkaya B, Kiliç Z, Hökelek T, Gündüz N, Yildiz M. Unusual products in the reactions of hexachlorocyclotriphosphazatriene with sodium aryloxides. Heteroatom Chem.December 1996; 7: 249-256. DOI: 10.1002/(SICI)1098-1071(199608)7:4<249::AID-HC6>3.0.CO;2-0.

19. Bullen GJ. An improved determination of the crystal structure of hexachlorocyclotriphosphazene (phosphonitrilic chloride). J. Chem. Soc. A. 1971; 1450-1453. DOI: 10.1039/J19710001450.

20. Spek AL, Acta Cryst., 1990; A 46, C34. PLATON, An Integrated Tool for the Analysis of the Results of a Single Crystal Structure Determination URL: http://journals.iucr.org/a/issues/1990/s1/00/a29681/a29681.pdf

21. Bruker, SADABS, Bruker AXS Inc., Madison, Wisconsin, USA, 2005.

22. Sheldrick GM. A short history of SHELX. Acta Crystallogr. Sect. A. January 2008; 64: 112–122. DOI: 10.1107/S0108767307043930.

İlk Paraben Sübstitüe Ferrosenil Fosfazen Bileşiğinin Sentezi ve Yapısal Karakterizasyonu

Yasemin Tümer, Efsun Şehirli, Çiğdem Yüksektepe Ataol

Öz: Etil 4-hidroksibenzoatın potasyum tuzu ile Cl yerdeğiştirme tepkimesi NO (**1**) veya NN (**2-5**) spirosiklik monoferrosenil siklotrifosfazenlerin (**6-10**) oluşumu ile sonuçlanmıştır. Elde edilen maddelerin yapıları elemental analiz, FTIR (Fourier dönüşüm kızılötesi spektroskopisi), ^{1}H (tek boyutlu 1D), ^{31}P NMR teknikleri ve X-ışını kristalografisi (**9** ve **10**) ile aydınlatılmıştır.

Anahtar kelimeler: Ferrosenilfosfazenler; paraben, etil 4-hidroksibenzoat; spektroskopi.

Sunulma: .11 Temmuz 2016. **Düzeltme:** 21 Kasım 2016. **Kabul:** 26 Kasım 2016.

Novel Metal Complexes of Mixed Piperaquine-Acetaminophen and Piperaquine-Acetylsalicylic acid: Synthesis, Characterization and Antimicrobial Activities

Ayipo Yusuf Oloruntoyin.[1*], Obaleye Joshua Ayoola.[2], Badeggi Umar Muhammad.[3]

[1*] Department of Chemical, Geological and Physical Sciences, Kwara State University, Malete, Ilorin, Nigeria.

[2] Department of Chemistry, University of Ilorin, Ilorin, Kwara State, Nigeria.

[3] Department of Chemistry, Ibrahim Badamasi Babangida University, Lapai, Niger State, Nigeria.

Abstract: Synthesis of coordination compounds of zinc(II), copper(II), nickel(II), cobalt(II), and iron(II) with mixed piperaquine-acetaminophen and piperaquine-acetylsalicylic acid has been studied. The complexes were characterized via the following: solubility test, melting point determination, conductivity measurement, atomic absorption spectroscopy, UV-Visible spectrophotometry, FTIR spectroscopy and magnetic susceptibility. The complexes were proposed to have a stoichiometry ratio of 1:1:1 between each metal salt and the ligands with tetrahedral and octahedral geometry following the reaction pattern of $MX.yH_2O + L_1L_{2/3}$ to give $ML_1L_{2/3}X.yH_2O$. Biological activities of the synthesized complexes have been evaluated against *Escherichia coli* and *Staphylococcus aureus*.

Keywords: Antimalarial activity; analgesic compounds; mixed ligands; spectroscopy; biological activities.

Submitted: October 05 2016. **Revised:** November 17, 2016. **Accepted:** November 21, 2016.

Cite this: Ayipo Y, Obaleye J, Badeggi U. Novel Metal Complexes of Mixed Piperaquine-Acetaminophen and Piperaquine-Acetylsalicylic acid: Synthesis, Characterization and Antimicrobial Activities. JOTCSA. 2017;4(1):313–26.

DOI: To be assigned.

***Corresponding author. E-mail: ayipochem@yahoo.com.**

INTRODUCTION

Malaria is one of the major devastating diseases affecting humans since the dawn of history. Over half a billion people are infected with malaria parasite while more than a million die annually from its effect [1]. Children and mostly people with low-income economy are more vulnerable; averagely 3000 children die daily from malaria in Africa [2]. Malaria is caused by an infection of the body by single-cell plasmodia protozoa; though being a very simple organism, it has a complex life cycle with many forms [3]. Since the discovery of the naturally-occurring alkaloids, quinine is an effective therapeutic drug against malaria, numerous antimalarial drugs such as quinacrine, chloroquine, sulfadoxine, *etc* have been in circulation, until the parasites developed resistance against most of them. Currently, pyrimethamine, sulfonamide, artemisinin, and its derivatives, halofantrine, clindamycin, piperaquine, *etc* are mostly in use [4]. The parasites are developing resistance against most of the monotherapy antimalarial drugs, making them less effective; thus, the emergence of combination therapy in forms of Artemisinin Combination Therapies (ACTs) *e. g.* Coartem$^{(R)}$, Artekin$^{(R)}$ *etc*. Fansidar$^{(R)}$ is another combination therapy containing sulfadoxine and pyrimethamine; which possess a better efficacy against the monotherapy-resistant malarial parasites than their respective single forms [5]. Piperaquine is a derivative of quinine, belonging to the 4-aminoquinoline groups. It was replaced for chloroquine in 1978 in China as a first line monotherapy for malaria and metric tons were dispensed for mass prophylaxis until resistant become too high [6]. Recently, piperaquine had become an object of renewed interest as a partner drug in ACTs. Dihydroartemisinin-piperaquine (Artekin) is one of the most common artemisinin combination for effective, short-course, and affordable malaria therapy with limited side effects and lower risks of recurrence of *falciparum* parasite [7]. Synriam$^{(R)}$, containing 150 mg arterolane maleate and 750 mg piperaquine phosphate is an oral fixed-dose combination antimalarial for *Plasmodium falciparum* and *Plasmodium vivax* in children and adults [8]. These and many more justify the aim of this research effort; to develop an antimalarial-analgesic fixed combination therapy against the strains of monotherapy-resistant *plasmodium* parasites especially those associated with fever and severe pain symptoms. Thus, the synthesis of piperaquine-acetaminophen and piperaquine-acetylsalicylic acid becomes a worth-taking approach of antimalarial research.

Materials

All chemicals used are of analytical and reagent grades, used as commercially obtained without further purification. Piperaquine phosphate (antimalarial ligand) was obtained from Zhuhai Runde Pharmaceutical Ltd., Guangzhou province, China, while acetaminophen and acetylsalicylic acid (analgesic ligands) were obtained from Rajrab Pharmeceutical Ltd., Ilorin. Transition metal salts and other solvents were obtained from Aldrich, BDH England.

EXPERIMENTAL

Synthesis of mixed piperaquine-acetaminophen metal complexes

The complexes were synthesized following some reported procedure with slight analytical modifications [5], [9], [10]. An aqueous-ethanolic solution of each metal salt (0.01 mol of each) was prepared in a round-bottomed flask. 5.355 g (0.01 mol) of piperaquine phosphate was mixed with 1.512 g (0.01 mol) of acetaminophen in a beaker. The mole ratio of the mixture of piperaquine phosphate, metal salt and acetaminophen was 1:1:1. The mixed ligands were dissolved in 20 mL of 5% lactic acid due to poor solubility of piperaquine in water even when fully ionized [19] and added to each solution of the corresponding metal salt dissolved previously in 10 mL of ethanol in a round-bottomed flask fitted with a condenser. The pH of the mixture was maintained by the addition of 10% methanolic ammonical solution. The mixture was refluxed at 70°C for 4 hours and kept thereafter in a refrigerator for 30 minutes for the metal chelate to crystallize. The crystals were then filtered and washed with dilute lactic acid and then distilled water to remove unreacted ligands and metals. The complexes were then dried in a desiccator for 3 days. The same procedure was applied for all metal salts.

Synthesis of mixed piperaquine-acetylsalicylic acid metal complexes

The procedure as reported above [5], [9], [10] was followed with some slight modifications such as change in analgesic ligands and the reflux time.

Determination of some properties of the complexes

Physical observations of the colors of the synthesized complexes were made and compared with those of the free ligands and the metal salts. The percentage yields were calculated and approximated to the nearest whole number. The melting points and conductivities were measured using Gallenkamp melting point apparatus and WTW conductimeter bridge, respectively and the values were recorded to a single whole number without range. Purity of the complexes was confirmed as a single spot on a thin layer chromatography (TLC) plate. Magnetic susceptibilities were deduced from the magnetic moment obtained on Sherwood Scientific Magnetic Susceptibility Balance. Infrared spectra of the synthesized complexes and the free ligands were recorded in KBr pellets using a Shimadzu FTIR-8400s (IR solution model) in the range of 4000 – 500 cm^{-1}. As a UV-Visible spectrometer, Beckman Coulter DU-730 was used to run the electronic transition of the complexes and the free ligands. Atomic Absorption Spectroscopy (AAS) analysis was used to determine the metal content of the complexes (which confirms evidence of coordination) was carried out using the Alpha 4 AAS PM 8251 single pen recorder.

Antimicrobial Screening

Antimicrobial activities of the free ligands and the complexes were deduced from their inhibitory potentials against *Escherichia coli* and *Staphylococcus aureus* on the basis of zones formed around their wells [5], [9].

Results

Table 1: Reaction pattern between ligands and metal salts to form complexes

$MX.yH_2O + L_1L_2 \rightarrow [ML_1L_2]X.yH_2O$
$MX.yH_2O + L_1L_3 \rightarrow [ML_1L_3]X.yH_2O$
Where M = Cu(II); Co(II); Zn(II) and Fe(II)
X = Cl_2, SO_4 and OAc_2
L_1, L_2 and L_3 = Piperaquine, Acetylsalicylic acid, Acetaminophen

Ligands + Metal salt	**Proposed chemical formula**
PQ + PC + $CuCl_2$	$Cu(PQ)(PC)Cl_2$
PQ + PC + $Co(OAc)_2$	$Co(PQ)(PC)(OAc)_2$
PQ + PC + $ZnSO_4$	$Zn(PQ)(PC)SO_4$
PQ + PC + $FeCl_2$	$Fe(PQ)(PC)Cl_2$
PQ + AS + $Cu(OAc)_2$	$Cu(PQ)(AS)(OAc)_2$
PQ + AS + $ZnSO_4$	$Zn(PQ)(AS)SO_4$

(See Fig. 1-3 below)

Proposed Complex Structures

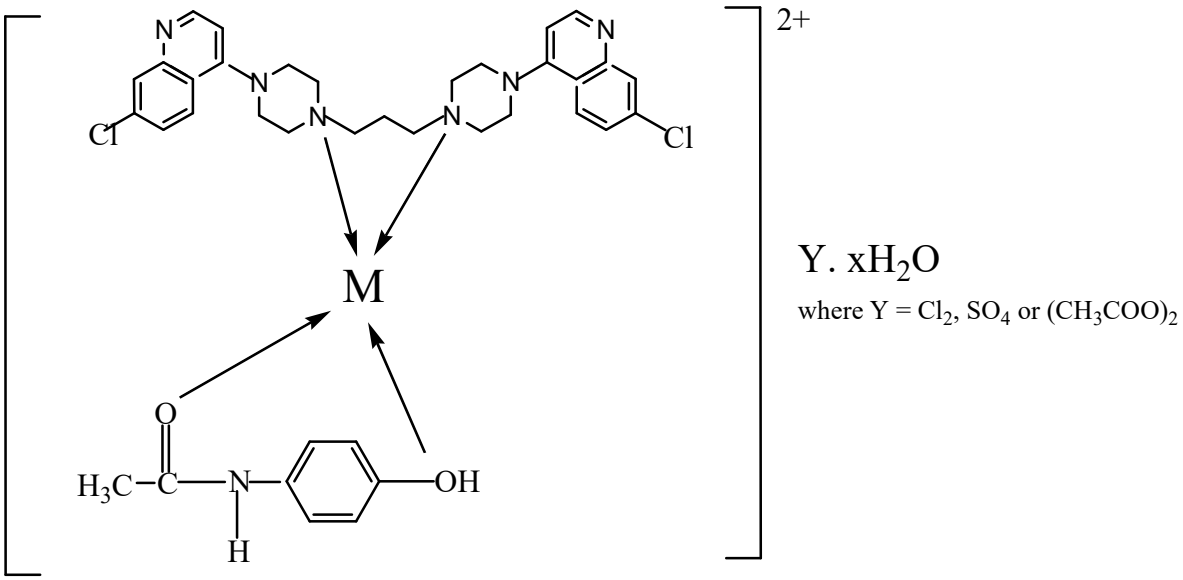

Figure 1: M-(PQ)(PC): Where M = Cu(II), Zn(II), Co(II), and Fe(II) ions.

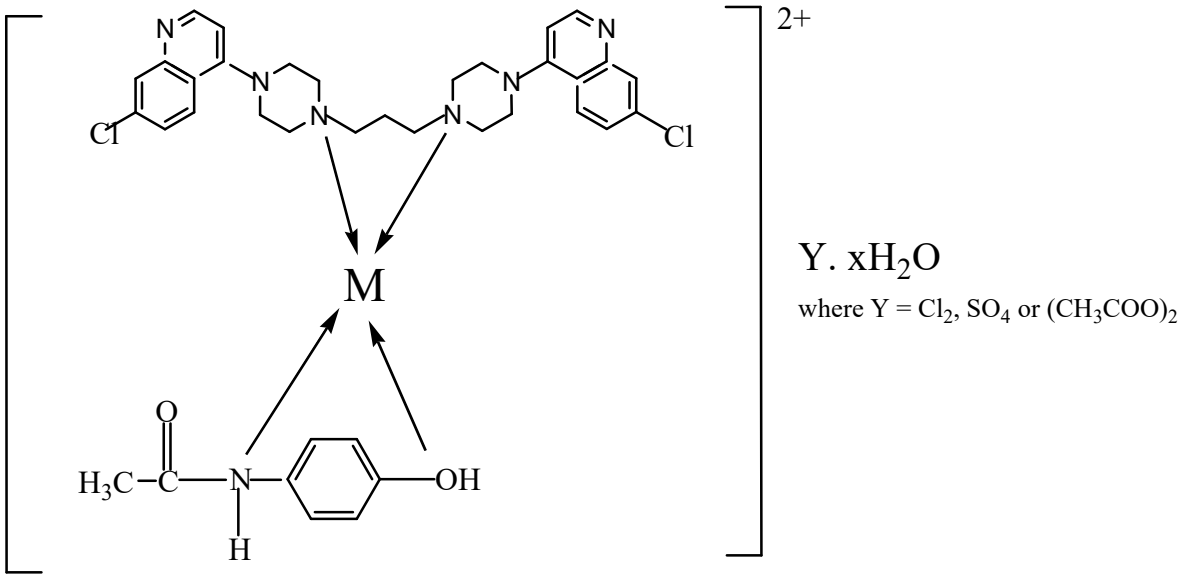

Figure 2: M-(PQ)(PC): Where M = Cu(II), Zn(II), Co(II), and Fe(II) ions.

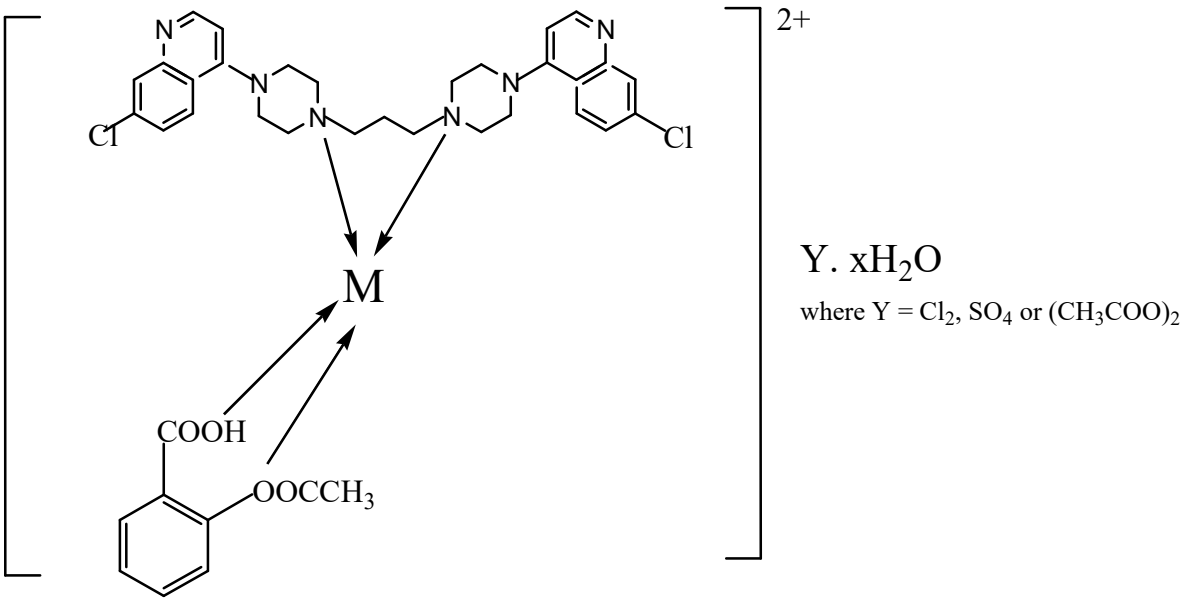

Figure 3: M-(PQ)(AS): Where M = Cu(II), Zn(II), Co(II), and Fe(II) ions.

Table 2: Some physical properties of the ligands and the complexes.

Sample	**Color**	**Yield (%)**	**M. P. (˚C)**	**Metal Content (%) Experimental (Calculated)**	**Conductivity ($\Omega^{-1}cm^{-1}$)**
PQ	White-yellow	-	249	-	6.2×10^{-6}
AS	White	-	138	-	3.3×10^{-4}
PC	White	-	169	-	4.1×10^{-4}
$Cu(PQ)(PC)Cl_2$	Blue	36	155	8.20 (7.93)	8.3×10^{-5}
$Co(PQ)(PC)(OAc)_2$	Faded pink	68	195	7.10 (6.85)	8.2×10^{-5}
$Zn(PQ)(PC)SO_4$	White	76	219	12.30 (14.26)	6.1×10^{-5}
$Fe(PQ)(PC)Cl_2$	Grey	25	205	6.60 (6.58)	6.5×10^{-5}
$Cu(PQ)(AS)(OAc)_2$	Blue	28	206	8.10 (7.57)	3.5×10^{-5}
$Zn(PQ)(AS)SO_4$	White	20	170	7.60 (7.52)	3.2×10^{-6}

Table 3: Solubility of the ligands and the complexes in some selected solvents.

Sample	**H_2O (r.t.p)**	**H_2O (100 °C)**	**Ethanol**	**Dil. Lactic Acid**	**Acetone**	**DMSO**	**Methanol**
PQ	SS	S	IS	S	IS	IS	IS
AS	SS	S	SS	SS	IS	S	S
PC	IS	IS	S	SS	SS	S	S
$Cu(PQ)(PC)Cl_2$	IS	S	IS	S	SS	SS	SS
$Co(PQ)(PC)(OAc)_2$	IS	SS	SS	S	IS	S	SS
$Zn(PQ)(PC)SO_4$	IS	SS	IS	S	IS	S	IS
$Fe(PQ)(PC)Cl_2$	SS	SS	IS	IS	IS	S	SS
$Cu(PQ)(AS)(OAc)_2$	SS	S	IS	S	IS	S	SS
$Zn(PQ)(AS)SO_4$	SS	S	IS	S	IS	S	IS

S = Soluble; SS = Sparingly soluble; IS = Insoluble.

Table 4: Magnetic moments, electronic transition and Some FTIR spectra assignment

Sample	**μ_{eff} (BM)**	**Water λ_{max} (nm)**	**V(N-H) cm^{-1}**	**V(O-H)cm^{-1}**	**V(C=O) cm^{-1}**
PQ	-	379	3433.41 m,b	-	-
AS	-	282	-	2999.41 m,b	1691.63 s,S
PC	-	306	3327.32 s,b	3161.43 m,	1654.98 s
$Cu(PQ)(PC)Cl_2$	2.23	392	3327.32 s,b	3163.36 b	1654.98 s,S
$Co(PQ)(PC)(OAc)_2$	4.78	389	3649.14 w	3055.35 m	1606.76 m
$Zn(PQ)(PC)SO_4$	1.89	392	3541.42 s,b	-	1633.76 m,b
$Fe(PQ)(PC)Cl_2$	5.10	250	3381.33 s,b	-	1624.12 m
$Cu(PQ)(AS)(OAc)_2$	2.30	390	3441.12 m,b	3234.73 w	1622.19 m
$Zn(PQ)(AS)SO_4$	1.76	393	3358.18 s,b	3066.92 m,b	-

m = medium; b = broad; s = strong; w = weak; S = sharp

Table 5: Biological activities of the ligands and the complexes

Sample	Concentration (%)	Zone of Inhibition in *Staphylococcus aureus* (mm)	Zone of Inhibition in *Escherichia coli* (mm)
PQ	1.0	3.55	5.60
AS	1.0	2.50	4.00
PC	1.0	2.00	3.50
$Cu(PQ)(PC)Cl_2$	1.0	5.00	5.00
$Co(PQ)(PC)(OAc)_2$	1.0	4.20	5.80
$Zn(PQ)(PC)SO_4$	1.0	4.80	5.00
$Fe(PQ)(PC)Cl_2$	1.0	5.20	5.80
$Cu(PQ)(AS)(OAc)_2$	1.0	3.25	5.00
$Zn(PQ)(AS)SO_4$	1.0	4.60	5.40

DISCUSSIONS

The complexes (Table 2) show different colors due to the presence of transition metal charge transfer to the ligands transition compared to the free ligands [11], [12]. The percentage yield of the complexes varied due to different factors such as the variation in electronic configuration of the metal ion in d-orbital, size of the ion, nature of the electron donation agent (donating atom on the ligand), functional groups of the ligands as Lewis bases and the reaction conditions [12]. The highest percentage yield was observed in $Zn(PQ)(PC)SO_4$ while the lowest was found in $Zn(PQ)(AS)SO_4$. The synthesized complexes were photo- and thermo-stable crystals with varied melting points due to the octahedral and tetrahedral geometry (Figures 1-3) of the transition metal complexes. The melting points of free piperaquine (PQ) ligand are higher than those of the complexes [9]. The percentage metal content as found experimentally is in good agreement with the calculated values as the data in Table 2 reveal. Molar conductivities of the metal complexes in water show non-electrolytic behavior of the free ligands and the complexes in the solvent.

The results of solubility tests (Table 3) show the solubility nature of the free ligands and the complexes in distilled water (at room temperature and at 100 ^{0}C), ethanol, dilute lactic acid, acetone, dimethylsulfoxide (DMSO), and methanol. Most of the complexes dissolved completely

in hot water and dilute lactic acid, some dissolved sparingly in DMSO and methanol, while others are practically insoluble in ethanol and acetone. None of the complexes is soluble in water, $Fe(PQ)(PC)Cl_2$, $Cu(PQ)(AS)(OAc)_2$ and $Zn(PQ)(AS)SO_4$ are sparingly soluble while $Cu(PQ)(PC)$, $Co(PQ)(PC)(OAc)_2$ and $Zn(PQ)(PC)SO_4$ are insoluble. In ethanol, none of them is soluble, $Co(PQ)(PC)(OAc)_2$ is sparingly soluble while others are insoluble. In dilute lactic acid, all the complexes are dissolved well except $Fe(PQ)(PC)Cl_2$ which is sparingly soluble. None is fully dissolved in acetone; only $Cu(PQ)(PC)Cl_2$ is sparingly soluble, others are practically insoluble. In DMSO, only $Cu(PQ)(PC)Cl_2$ is sparingly soluble, others dissolve well and none is insoluble. None of the complexes fully dissolves in methanol, $Zn(PQ)(PC)SO_4$ and $Zn(PQ)(AS)SO_4$ are insoluble while others are sparingly soluble.

The results of the magnetic moment (Table 4) show that Co(II) and Zn(II) complexes conform in a stoichiometric manner with tetrahedral geometry while Cu(II) and Fe(II) are proposed within the range of octahedral configuration. It also reveals that some of the $Zn(PQ)(PC)SO_4$ and $Zn(PQ)(AS)SO_4$ complexes are diamagnetic due to unavailable of unpaired electrons on d-orbital of the Zn^{2+} ion, $Fe(PQ)(PC)Cl_2$ are ferromagnetic, while $Cu(PQ)(PC)$, $Co(PQ)(PC)(OAc)_2$ and $Cu(PQ)(AS)(OAc)_2$ are paramagnetic due to the presence of unpaired electron on d-orbital of the Cu^{2+} and Co^{2+} ions. The analytical data obtained provides a supportive evidence for the stoichiometric ratio of 1:1:1 between the metal ion and the ligands [14], [15]. The free piperaquine, acetylsalicylic acid and acetaminophen show a λ_{max} of 379 nm, 282 nm and 306 nm respectively on UV-Visible spectroscopy. The shifting of these bands to a higher wavelength in $Cu(PQ)(PC)Cl_2$, $Co(PQ)(PC)(OAc)$, $Zn(PQ)(PC)SO_4$, $Cu(PQ)(AS)(OAc)_2$ and $Zn(PQ)(PC)SO_4$ confirmed the effective coordination and the formation of complexes between the metal ions and the ligands [9]. Although the λ_{max} values for $Cu(PQ)(PC)Cl_2$, $Cu(PQ)(AS)(OAc)_2$ and $Zn(PQ)(PC)SO_4$ did not really cross the border from UV to Visible region but could be approximated to the visible region and having slight evidences for d-d electron transition – hence the coloration [11]. The selective infrared spectral assignment of free ligands and the complexes have been carried out based on similar compounds [14, 16, 17]. The medium broad absorption band of 3433.41 cm^{-1} found in the spectrum of free piperaquine and the strong broad band of 3327.32 cm^{-1} in free acetaminophen due to N-H stretch have undergone a hyperchromic shifts to 3649.44 cm^{-1} and 3541.42 cm^{-1} in $Co(PQ)(PC)(OAc)_2$ and $Zn(PQ)(PC)SO_4$ respectively. The bands for N-H stretch in free piperaquine and acetaminophen have also undergone a hypsochromic shifts to 3381.33 cm^{-1}, 3441.12 cm^{-1} and 3358.18 cm^{-1} in $Fe(PQ)(PC)Cl_2$, $Cu(PQ)(AS)(OAc)_2$ and $Zn(PQ)(AS)SO_4$ respectively. Infrared spectra which can also probe coordination: The shifting of these N-H bands provides evidence of complex formation which is supported by the disappearance of broad 2999.41 cm^{-1} and 3161.43 cm^{-1} in free acetylsalicylic acid and acetaminophen spectra assigned to O-H in $Zn(PQ)(PC)SO_4$ and $Fe(PQ)(PC)Cl_2$. The strong absorption bands of 1691.63 cm^{-1} and 1654.98 cm^{-1} found in acetylsalicylic acid and acetaminophen respectively have disappeared in $Zn(PQ)(AS)SO_4$ and undergo various shifts in other complexes. The variation in the frequencies of the bands of the free ligands compared to

those of the complexes denotes the change in vibrational pattern of the ligands upon coordination to metal ions (see Figures 1, 2, and 3).

The presence of some anions such as Cl^-, SO_4^{2-} and CH_3COO^- are confirmed by the reaction of the solutions of the metal complexes with aqueous $AgNO_3$, aqueous $BaCl_2$ and neutral $FeCl_3$ [18]. The complexes containing Cl^- and SO_4^{2-} ions produce insoluble white precipitates on testing with aqueous $AgNO_3$ and aqueous $BaCl_2$. Those containing CH_3COO^- produce red color with $FeCl_3$ solution [18]. The formation of single spots on each TLC chromatography plate confirmed the purity of the complexes.

The proposed reaction pathways and chemical formulas as given in Table 4 above are derived from the cumulative characterization results.

Table 5 presents the results of the biological activities as antimicrobial tests of the free ligands and the complexes against a gram-positive *Staphylococcus aureus* and *Escherichia coli*. The inhibition growth effects of the complexes against these bacteria strains show significant differences in metal complex sensitivities as compared to the free ligands [9]. From the results, only $Cu(PQ)(AS)(OAc)_2$ have a lower inhibitory effect against *Staphylococcus aureus*, other complexes have higher effects compared to the free parent drugs. Against *Escherichia coli*, piperaquine was experimentally found to possess a higher inhibitory effect than the complexes while the effects of the free acetylsalicylic acid and acetaminophen are lower compared to the complexes. These provide supportive evidences that the metal complexes of mixed piperaquine-acetylsalicylic acid and piperaquine-acetaminophen have greater medicinal therapeutic potential against microorganism activities than their parent drugs.

CONCLUSION

The complexes were synthesized with the ligands (piperaquine, acetylsalicylic acid and acetaminophen) coordinating through N-H, O-H and C=O to the metal ions in the stoichiometric ratio of 1:1:1 to form both tetrahedral and octahedral complexes. Although some reactions yield low complexes while some are impressive, but solubility behaviors to the tested solvents, the melting point and the magnetic susceptibility of the complexes show distinct results from their parent ligands. The metal-ligand coordination is probed with UV-Vis and FTIR spectroscopy. The synthesized complexes were found to possess better physical and antimicrobial properties when compared to their free ligands. Thus, the complexes show a better therapeutic potential against some target bacteria compared to the free antimalarial piperaquine and free analgesic acetylsalicylic acid and acetaminophen and could also be suggested against malaria strains. This conclusion is also supported by the previous relevant research [5, 9, 10, 14, 16]. However, further characterization and *in vitro* and *in vivo* assessment of the complexes to confirm their therapeutic actions against *plasmodium* strains are needed.

ACKNOWLEDGEMENT

The authors wish to appreciate the Director, the Concord School, Ibadan and the Head of Chemistry Department, University of Ilorin, Ilorin, for their support in providing full access to laboratory work.

ABBREVIATIONS

PQ – Piperaquine

PC – Acetaminophen

AS – Acetylsalicylic acid

OAc – CH_3COO^-

TLC – Thin Layer Chromatography

FTIR – Fourier Transformation Infrared

UV – Ultraviolet

AAS – Atomic Absorption Spectroscopy

IUPAC – International Pure and Applied Chemistry

ACTs – Artemisinin Combination Therapies

IC50s – Concentrations for 50% parasite growth inhibition

^{1}H NMR – Proton Nuclear Magnetic Resonance

^{13}C NMR – Carbon-13 Nuclear Magnetic Resonance

XRD – X-ray Diffraction

M(II) – Cu^{2+}, Zn^{2+}, Co^{2+} and Fe^{2+}

REFERENCES

1. Wiesner J., Ortmann R., Jomaa H., and Schlitzer M., New Antimalarial Drugs, *Angew. Chem. Internat. Ed. Engl.,* 2003, 42 (43) , 5274-5293. https://dx.doi.org/10.1002/anie.200200569

2. Maribel N., Techniques used to Study MetalloDrugs-DNA interactions, *Ivic Instituto Venezolano De Investigaciones Cientifica*, 23-30 Julio, 2010. http://www.riidfcm-cyted.fq.edu.uy/archivos/Curso_Tecnicas_aplicadas_al_desarrollo_de_metalofarmacos/presentaciones_clases/hematina.pdf

3. World Health Organisation, Model Formulary for Children (2nd ed.), 2010,ISBN 978-92-4-159932-0. http://www.who.int/entity/selection_medicines/list/WMFc_2010.pdf. Retrieved 2011-03-30

4. World Health Organisation, Model List of Essential Medicines for Children (2nded.), 2010, http://www.who.int/entity/medicines/publications/essentialmedicines/Updated_second_children_list_en.pdf. Retrieved 2011-03-30.

5. Obaleye J. A., Amolegbe S. A. and Gbotoso G. O., Some metal-antimalarial drug complexes: synthesis, characterization and their effect against malaria parasites, http://www.journal.unaab.edu.ng/index.php/COLNAS/article/viewFile/193/190, 2006.

6. Olliaro P. L. and Taylor W. R., Antimalarial compounds: from bench to bedside. *J Exp Biol*, 2003, 206:3753-3759. DOI: 10.1242/jeb.00653

7. Marcus J. R., Rose M., Machteld E. B., Marion B., Stephane P., Mupawjay P., Pratap S. and Francois N., Dihydroartemisinin-Piperaquine Rescue Treatment of Multidrug-resistant Plasmodium Falciparum Malaria in Pregnancy. *American Journal of Tropical Medicine and* Hygiene, 2008, 78 (4) 543 – 545. https://ora.ox.ac.uk/objects/uuid:e21fb333-b72a-47f1-929d-5cea211bcc0f

8. Sanjukta B. Ranbaxy Laboratory Ltd., India. www.synriam.com/2synriamRanbaxy.pdf, 2013.

9. Ogunniran K. O., Ajani O. O., Ehi-Eromosele C. O., Obaleye J. A., Adekoya J. A. and Ajanaku C. O., Cu(II) and Fe(III) complexes of sulphadoxine mixed with pyramethamine: synthesis, characterization, antimicrobial and toxicology study. *International Journal of Physical Science*, 2012, Vol. 7(13), pp 1998 – 2005. DOI: 10.5897/IJPS11.1143

10. Shruti S. S., Jadhav W. N., Khade B. C. and Arbad B. R., Synthesis, characterization and antimicrobial study of some 3d metal complexes of sulfadoxine. *International Journal of ChemTech Research*, 2014, Vol. 6, No 4, pp 2291 – 2294. http://sphinxsai.com/2014/vol6pt4/1/(2291-2294)Jul-Aug14.pdf

11. Cotton F. A., Geoffrey W. and Carlos A. M., Advanced Inorganic Chemistry, *Wiley, New York, NY*, 1988, 6th Ed. ISBN: 978-0-471-19957-1

12. Miessler G. L.; Donald A. T., Inorganic Chemistry, *Pearson Education Inc., U. S. A.*, 1999, pp. 642. ISBN: 978-0321811059

13. Encyclopedia Britannica, https://en.wikipedia.org/wiki/**Encyclopædia_Britannica,** 2010.

14. Adediji J. F., Olayinka E. T., Adebayo M. A. and Babatunde O., Antimalarial mixed ligand metal complexes: Synthesis, physicochemical and biological activities. *International Journal of Physical Sciences,* 2009, 4 (9) 529 – 534. http://www.academicjournals.org/article/article1380628184_Adediji%20et%20al.pdf

15. Lee, J. D., Coincise Inorganic Chemistry; *Wiley: India*, 1999, pp 223 – 232. ISBN: 978-0-632-05293-6

16. Karunajeewa H., Lim C., Hung T. Y., Ilett K. F., Denis M. B., Socheat D. and Davis T. M., Safety evaluation of fixed combination piperaquine plus dihydroartemisinin (Artekin) in Cambodian children and adults with malaria. *Br J Clin Pharmacol,* 2004, 57:93-99. DOI: 10.1128/AAC.00555-07

17. Lawal A. and Obaleye J. A., Synthesis, characterization and antibacterial activity of aspirin and paracetamol-metal complexes. *BIOKEMISTRY,* 2006, *19* (1): 9-15. http://www.bioline.org.br/bk

18. Jeffery G. H., Basset J., Mendham J., Denney R. C.; Vogel's Textbook of Chemical Analysis, 5th Edition, *Wiley & Sons, Inc., N. Y.*, pp 339-340. ISBN: 0-582-44693-7

19. Hung T. Y., Davis T. M., Ilett K. F., Karunajeewa H., Hewitt S., Denis M. B., Lim C. and Socheat D.; Population pharmacokinetics of piperaquine in adults and children with uncomplicated falciparum or vivax malaria. *Br J Clin Pharmacol,* 2004, 57:253-262. https://www.ncbi.nlm.nih.gov/pubmed/14998421.

Piperakin-Asetaminofen ve Piperakin-Asetilsalisilik Asit İçeren Yeni Metal Kompleksleri: Sentez, Karakterizasyon ve Antimikrobiyal Aktiviteler

Ayipo Yusuf Oloruntoyin, Obaleye Joshua Ayoola, Badeggi Umar Muhammad

Öz: Çinko(II), nikel(II), kobalt(II) ve demir(II) komplekseleri, piperakin-asetaminofen ve piperakin-asetilsalisilik asit içeren komplekslerin sentezinde kullanılmıştır. Kompleksler şu yöntemlerle karakterize edilmiştir: Çözünürlük testi, erime noktası tayini, iletkenlik tayini, atomic soğurma spektroskopisi, UV-Görünür spektrofotometri, FTIR spektroskopisi ve manyetik duyarlılık ölçümleri. Komplekslerin her bir metal tuzu ve ligandlar arasında 1:1:1 şeklinde bir stokiyometrik orana sahip olduğu ve tetrahedral ve oktahedral geometrinin tercih edildiği bulunmuştur, kompleksleşme tepkimeleri $MX.yH_2O + L_1L_{2/3}$ tepkimesinden $ML_1L_{2/3}X.yH_2O$ komplekslerinin oluşması şeklindedir. Sentezlenen komplekslerin biyolojik aktiviteleri *Escherichia coli* ve *Staphylococcus aureus*'a karşı değerlendirildi.

Anahtar kelimeler: Antimalaryal aktivite; analjezik bileşikler; karışık ligandlar; spektroskopi; biyolojik aktiviteler.

Sunulma: 05 Ekim 2016. **Düzeltme:** 17 Kasım 2016. **Kabul:** 21 Kasım 2016.

Adsorption of Acid Red 114 onto Fe_3O_4@Caffeic acid Recyclable Magnetic Nanocomposite

Aylin YILDIZ*[1]

[1]Department of Textile Engineering, Faculty of Çorlu Engineering, Namık Kemal University 59860 Çorlu-Tekirdağ/TURKEY

Abstract: In this study, the adsorption capacity of caffeic acid (CFA) functionalized Fe_3O_4 magnetic recyclable nanocomposite (Fe_3O_4@CFA MNC) for removal of industrial dye Acid Red 114 (AR 114) was investigated. The maximum adsorption (q_m) of the Fe_3O_4@CFA MNC for AR114 was 333 mg/g without pH correction of the solution. Compared with other studies these adsorbent possess high adsorption capacity for AR114 dye. The adsorption isotherm data and the process of adsorption kinetics were fitted using the Langmuir equation and a pseudo-second-order kinetic model that showed chemisorption may be the rate controlling step in the adsorption processes. It was proved that the magnetic NMs technology was contributed by this study which can be a new and covetable alternative for organic contaminant adsorption. Furthermore, the reusability of the Fe_3O_4@CFA MNC was investigated and significant removal of AR114 obtained even after five cycles.

Keywords: Waste water treatment; Magnetic nanocomposite; Adsorption; Acid Red 114.

Submitted: September 28, 2016**. Revised:** November 20, 2016**. Accepted:** November 25, 2016**.**

Cite this: Yıldız A. Adsorption of Acid Red 114 onto Fe3O4@Caffeic acid Recyclable Magnetic Nanocomposite. JOTCSA. 2017;4(1):327–40.

DOI: To be assigned.

*Corresponding author. E-mail: ayildiz@nku.edu.tr.

INTRODUCTION

The textile industry is the main source of today's industrial wastewater due to its high water consumption. These types of wastewater are produced at the end of dyeing and finishing processes which release large amount of dyes to the environment. There are over 100,000 kinds of dyes commercially available (1). A serious number of these dyes are synthetic which contain carcinogenic and mutagenic aromatic rings (2). The presence of large amount of these stable organic compounds in industrial wastewater make their degradation/removal difficult for many methods which are coagulation, adsorption, precipitation, flocculation and ozonization (3,4). However, the adsorption is inexpensive and readily available. Due to its low maintenance, adsorption is an effective method for the dye removal (5-8).

Due to the potential for human exposure during production of bisazobiphenyl dyes which contains benzidine, a carcinogen chemical, Acid Red 114 was nominated for this study (9).

Since the presented Fe_3O_4@CFA MNC contains either carboxylate groups or magnetic component, it can be an excellent candidate for the application of adsorption of various different dyes (10). Zhang *et al*. studied the adsorption of methylene blue onto HA-coated Fe_3O_4 MNC. They reported typical superparamagnetic characteristics and great reactive activity for MB adsorption of Fe_3O_4@CFA MNC (11). Cao *et al.* studied the high adsorption capacity of magnetic Fe_3O_4/chitosan nanoparticles and removal of brilliant red (X-3B) (12). In another study, Chang *et al.* synthesized the Fe_3O_4/activated montmorillonite (Fe_3O_4/Mt) nanocomposite with co-precipitation method and found out over 83.73% color removal of MB (13). Mesoporous graphene/Fe_3O_4/chitosan nanocomposite was also used for the adsorption capacity for a textile dye (methylene blue) and found out that the adsorption capacity reached 98% within a contact time of 5 min at pH 9 and an initial dye concentration of 25 mg/L (14). Tan *et al*. used the activated maize cob impregnated with magnetic nanoparticles (Fe_3O_4 nanoparticles) for methylene blue (MB) adsorption found out 99.63% (15). Lee and Thinakaran *et al.* also reported on the removal of AR 114 by different techniques (16, 17). However, none of the studies reported on the remediation of AR 114 by adsorption method.

In this study, an inexpensive magnetic adsorbent, Fe_3O_4@CFA MNC, was easily synthesized (18, 19). The adsorption of the Acid Red 114 (Fig 1a) dye onto Fe_3O_4@CFA MNC (Fig 1b) has been studied, and the adsorption reactions were argued. Reutilizing the adsorbents saturated with dyes were evaluated and an efficient method was introduced.

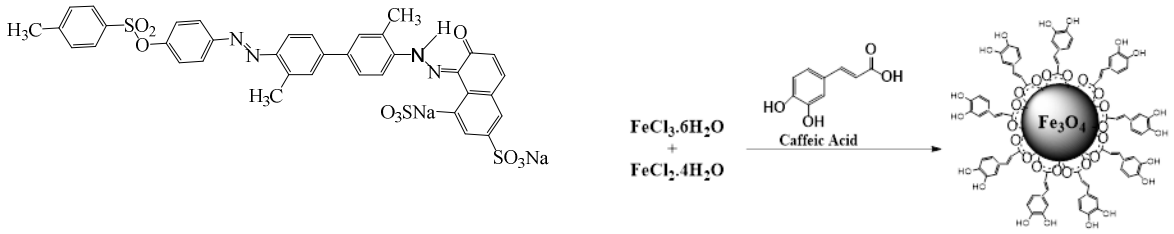

(a) **(b)**

Figure 1. The chemical structure of **a)** Acid Red 114 and **b)** Fe_3O_4@CFA MNC

MATERIALS AND METHODS

Materials

$FeCl_3.6H_2O$, $FeCl_2.4H_2O$, Magnetite (Fe_3O_4) Caffeic acid (CFA), NH_3, Acetic Acid, NaOH, Methanol, and HCl were purchased from Merck and used without further purification. The adsorbate AR 114 was purchased from Sigma–Aldrich.

Instrumentations

Thermo Spectronic Aquamate Visible Light Spectrophotometer 315 to 1100 nm wavelength range; 50/60 Hz. Light source was a Tungsten lamp.

Biosan PSU-10i Orbital Shaker was used to stir Fe_3O_4@CFA MNC with Acid Red 114.

EXPERIMENTAL PROCEDURE

Preparation of Adsorbate

For the synthesis of Fe_3O_4@CFA MNC, 10 mL of 0.4 M iron chloride solution ($FeCl_3$ $6H_2O$) and 10 mL of 0.2 M of iron chloride solution ($FeCl_2$ $4H_2O$) were mixed in distilled water. A specified amount of caffeic acid was added to the solution as a surfactant and coating material. A 1.5 M solution of sodium hydroxide (NaOH) was prepared and slowly added to the salt solution dropwise. The pH of the solution was constantly monitored as the NaOH solution was added. The reactants were constantly stirred using a magnetic stirrer until a pH level of 7–8 was reached. The liquid precipitate was then brought to a reaction temperature of 80 °C and stirred for 5 h. The product was then cooled to room temperature. To get particles free from sodium and chlorine compounds, the precipitate was washed twice with distilled water and then with ethanol to remove the excess surfactant from the solution. The obtained products were dried at 80 °C for 3 hrs. (18) AR114 stock solution (Stock solution) (200 mg/L) was prepared by dissolving 200 mg of

AR114 dye into 1 L of distilled water. Solutions of the required concentrations (20-200 mg/L) were prepared by consecutive dilution of this stock solution. Physical and chemical features of Acid Red 114 are given in Table 1 (2).

Table 1. Physical and chemical features of AR 144

Commercial name	Acid Red 114
Molecular formula	$C_{37}\,H_{28}\,N_4\,O_{10}\,S_3\,Na_2$
Purity	80%
Chromophore	Diazo
Molecular weight (g/mole)	830
λmax (nm)	522
View	Dark red powder

Batch adsorption study

Adsorption studies were applied at various initial concentrations (10, 20, 40, 60, 80, 100 and 200 mg/L) and different pH conditions (pH: 3, 5, without pH correction (7.3) and 11) which were applied at locked adsorbent dosage (0.03 g/50 mL) in the aqueous solution at room temperature. pH adjustment was done with 0.1 N HCl and 0.1 N NaOH. The effect of contact time (1, 5, 10, 15, 30, 45, 60, 90, 120 and 150 min) on color removal were also applied at a series of kinetic experiments. After adsorption process Fe_3O_4@CFA MNC were removed from the solution with a magnet and the concentration of the dye was evaluated at a wavelength which is maximum absorbance of AR114 by using a spectrophotometer.

The amount of adsorbed AR114 was calculated (Equation 1):

$$q_e = V(C_0 - C_e)/W \qquad \textbf{(Eq 1)}$$

q_e is the amount adsorbed (mg/g); C_0 and C_e are the initial and equilibrium AR114 concentrations in the solution (mg/L); V is the solution volume (L); and W is the mass of adsorbent (g).

Regeneration and reuse experiments

The practical applications of adsorbents are significantly dependent to the recycling and regeneration ability (11). Such adsorbents not only have an excellent adsorption capacity but also large desorption feature which will reduce secondary pollution and the overall cost. The optimum regeneration ability was found to be the mixture of methanol and acetic acid. 0.03 g of AR114-loaded adsorbents were added to 50 mL of a mixture of methanol and acetic acid (volume ratio of 9:1). After that Fe_3O_4@CFA MNC was prepared with a magnetic stirrer for 10 min. When the regeneration was complete Fe_3O_4@CFA MNC was separated with an external magnet. 5 g of Fe_3O_4@CFA MNC was added into the 1 L mixture of

methanol - acetic acid, and the final solution was shaken for 1 h to reach desorption equilibrium. To estimate the desorbed amount of AR114 in the concentration, a Thermospectronic spectrometer was used for the measurement at a wavelength of 522 nm. The experiment was repeated for three times (wavelength of 522 nm) until the AR114 concentration in the liquid decreased below 0.002 mmol/L (11). After the experiment was completed, the NPs were washed with ultrapure water. Next the NPs dried with air in oven. The adsorption and desorption of the AR114 on/from the Fe_3O_4@CFA MNC were evaluated for five times.

RESULTS AND DISCUSSION

The impact of initial pH, initial dye concentration and contact time on adsorption

To determine the impact of pH the adsorption experiments were applied for different pHs which were pH: 3, 5, without pH correction (7.3) and 11, at fixed adsorbent dosage (0.03 g/50 mL) in the aqueous solution and at room temperature (Fig. 2). It is seen from Fig. 2 that a high q_e values was achieved for AR114 at natural pH (without pH correction-pH:7.3). This can be explained by low solubility of Fe_3O_4@CFA MNC at neutral pH. The lower adsorption capacity may be because of the solubility of adsorbent in strong acid or base. (20). It can be seen from Figure 2 that lower AR114 removal was obtained at alkaline pH values than at acidic pH values. This is caused by the fact that surplus OH^- anions compete with the dye anions for the available adsorption sites at alkaline pH values. Since color removal was maximum without pH correction, the original solution pH (7.3) was selected for all adsorption experiments. It is known that colored dye anions are released from the acid dyes, into the solutions during the dissolutions. (2).

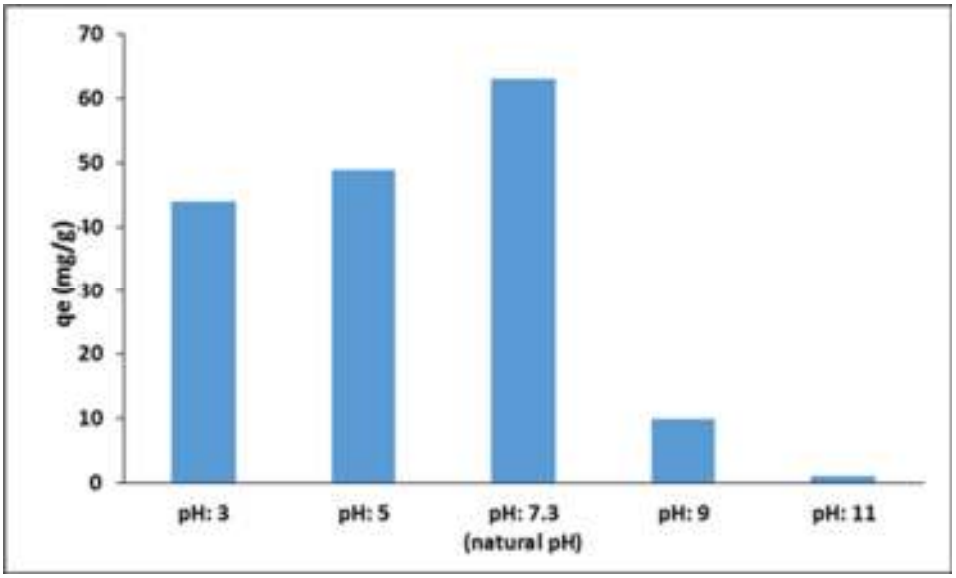

Figure 2. The variation of q_e values depending on pH values

The impact of initial dye concentration for the adsorption of AR 114 onto Fe_3O_4@CFA MNC is shown in Figure 3. The increase in the dye concentration from 10 mg/L to 200 mg/L resulted the increase of (mg/g) values from 12.65 mg/g to 214.92 mg/g. As it is shown in Figure 3 that the adsorption capacity increases with an increase in the initial concentration of AR114 which shows the favorable adsorption at high concentration (21). As it is known eliminate the mass change of dye between the liquid and solid phases are eliminated by a driving force which is provided by the initial dye concentration So the interaction between the adsorbent and dye increases along with initial dye concentration (22).

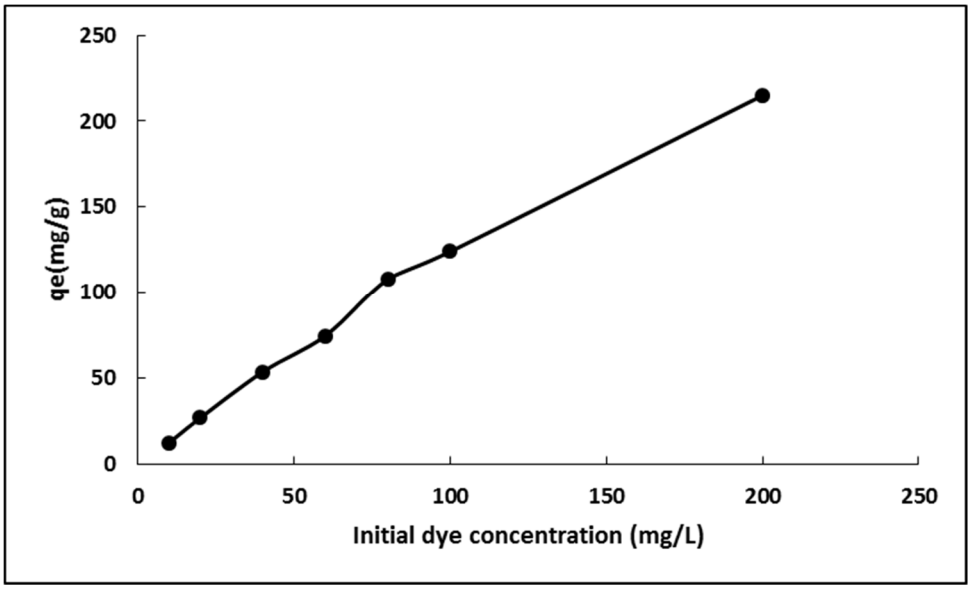

Figure 3. The impact of initial dye concentration on q_e values

Fig.4 presents the effects of contact time according to initial dye concentration for the adsorption of AR 114. The adsorption equilibriums of anionic dye on Fe_3O_4@CFA MNC are reached within 150 min as it is shown in Fig.4.

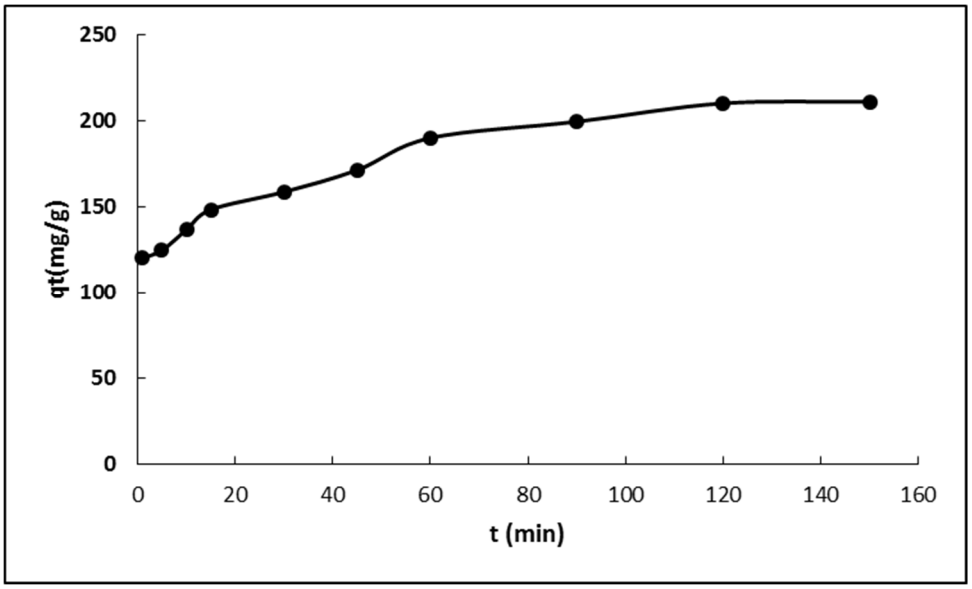

Figure 4. The impact of contact time for the adsorption of AR 114 onto Fe_3O_4@CFA MNC

Adsorption isotherms

For the determination of the adsorption capacity of the adsorbents, adsorption equilibrium studies were utilized by using Langmuir and Freundlich isotherm models. Adsorption isotherm experiments were employed by agitating dye solutions of various concentrations (10, 20, 40, 60, 80, 100 and 200 mg/L) with 0.03 g/50 mL Fe_3O_4@CFA MNC at room temperature.

The expression for the Langmuir isotherm is given below (23) (Equation 2):

$$\frac{C_e}{q_m} = \frac{1}{q_m K_L} + \frac{C_e}{q_m} \quad \textbf{(Eq. 2)}$$

The expression for the Freundlich isotherm is given below (24) (Eq. 3):

$$logq_e = \frac{1}{n} logc_e + logK_f \quad \textbf{(Eq. 3)}$$

Where, q_e (mg/g) expresses the AR 114 amount that each unit adsorbent adsorbs in the equilibrium condition, C_e (mg/L) stands for the AR 114 concentration that remains in the solution after the adsorption when the equilibrium condition is reached, K_L (L/mg) is the Langmuir constant, and q_m is the maximum adsorption capacity of the adsorbents (mg/g), K_f is the adsorption capacity that is calculated in the experiments, n is the adsorption density. q_m and K_L values were calculated by plotting of $1/q_e$ against $1/C_e$ by using Langmuir isotherm and n and K_f can be calculated from the slope and intercept by using Freundlich isotherm.

Langmuir and Freundlich isotherm plots and experimental values are shown in Fig 5. The adsorption constants derived from the Langmuir and Freundlich adsorption models are given in Table 2. As indicated from R^2 values given on Table 2, Langmuir model yielded a better fit than the Freundlich model for the adsorption of AR114 on Fe_3O_4@CFA MNC. According to this model adsorption appears at particular homogeneous sites within the adsorbent. Once an adsorbate molecule occupies a site, no further adsorption can be observed at the same site (23).

Table 2. The kinetic parameters of Freundlich and Langmuir isothermal equation (Natural pH:7.3, C_0=10, 20, 40, 60, 80, 100, 200 mg/L, m=0.03 g/50 mL)

Adsorbent	**Langmuir model**			**Freundlich model**		
	q_{max} (mg/g)	K_L (L/g)	R^2	K_f (mg/g)	1/n	R^2
Fe_3O_4@CFA MNC	333.3	0.025	0.9958	17.02	0.60	0.9818

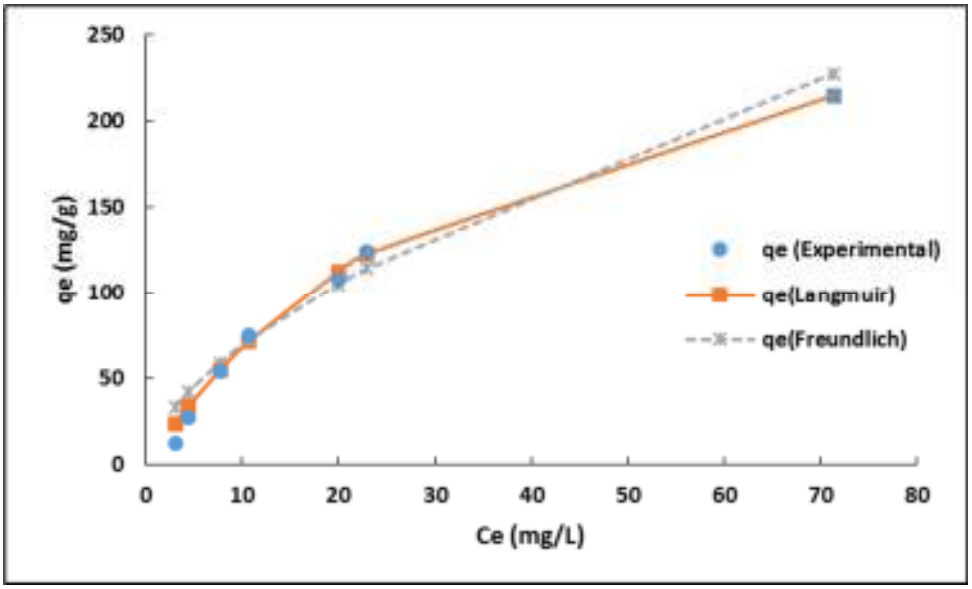

Figure 5. The fit of experimental adsorption data to Langmuir, Freundlich for the removal of AR 114 by Fe_3O_4@CFA MNC (t = 150 min, m = 0.03 g/50 mL).

The Langmuir isotherm could be indicated by a separation factor, R_L which is defined by McKay *et al.* (1989) as given below (25) (Equation 4):

$$R_L = 1/(1+K_L C_0) \qquad \textbf{(Eq. 4)}$$

Favorable adsorption is demonstrated by $0 < R_L < 1$. The R_L values were found to be between 0.16 and 0.8 for initial dye concentrations of 10-200 mg/L. R_L values between 0-1 show favorable adsorption of AR114 on Fe_3O_4@CFA MNC.

Table 3 shows the q_{max} value for AR114 adsorption obtained in this study in comparison with the q_{max} values obtained in the other studies carried out with various adsorbents. As it can be seen from Table 3, the maximum adsorption capacity (q_{max}) of Fe_3O_4@CFA MNC has the value of 333 mg/g for adsorption of AR114. It can be understood that these adsorbent possess high good adsorption capacity for AR114 dye.

Table 3. Adsorption capacities obtained from present study and other studies for the removal of AR114.

Adsorbent	Q_{max} (mg/g)	Reference
Activated pongam seed shells	204.08	(2)
Activated cotton seed shells	153.85	(2)
Activated sesame seed shells	102.04	(2)
Activated carbon-charcoal	101	(26)
Magnetic nanoparticle impregnated rice husk ash	111	(27)
Fe_3O_4@CFA MNC	333.3	This study

Adsorption kinetics

Pseudo-first order and pseudo-second order models were utilized to analyze the adsorption kinetics of AR 114 on Fe_3O_4@CFA MNC. The equations are integrated into form (Equation **5** and 6), using the boundary conditions $t = 0$, $q_t = 0$ and $t = t$, $q_t = q_t$. The linearized form of pseudo-first-order (Equation 5) and pseudo-second-order kinetic models (Equation 6) were expressed as follows (28):

$$\log(q_e - q_t) = log q_e - \frac{k_1}{2.303} t \qquad \textbf{(Eq.5)}$$

$$\frac{t}{q_t} = \frac{1}{k_2 q_e^2} + \frac{1}{q_e} t \qquad \textbf{(Eq. 6)}$$

Where, k_1 is pseudo-first order adsorption rate constant (min^{-1}), k_2 is pseudo-first order adsorption rate constant (g/mg.min), q_e, the amount that is adsorbed in equilibrium condition (mg/g), q_t is the adsorbed amount at time t (mg/g). The values of $q_{e1,calc}$ and k_1 (for pseudo-first order equation) were determined from linear plots of $\log(q_e - q_t)$ versus t. The values of $q_{e2,calc}$ and k_2 (for pseudo-second order equation) were determined from linear plots of t/q_t versus t.

Table 4 presents the kinetic parameters for the removal of AR114 by Fe_3O_4@CFA MNC. As given in Table 4 and Fig 6, R^2 of the pseudo-second order equation were 0.9955 and bigger than pseudo-first order kinetic model. As it could be seen from the Table 4 the calculated data ($q_{e2,cal}$) agreed well with the experimental data (qe_{exp}) for second order kinetics showing chemisorption that may be the rate controlling step in the adsorption processes (29). These results showed that adsorption was related to the amount of solute adsorbed on the adsorbent surface as well as the amount adsorbed at equilibrium (30).

Table 4. Kinetic parameters for the adsorption of AR 114 on Fe_3O_4@CFA MNC (C_0= 200 mg/L, natural pH)

	Pseudo-first-order kinetic model			**Pseudo-second-order kinetic model**		
$q_{e,exp}$(mg/g)	k_1 (min^{-1})	$q_{e1,calc}$(mg/g)	R^2	k_2(g/mg.min)	$q_{e2,calc}$(mg/g)	R^2
211.17	0.035	124.53	0.8993	0.0007	217.39	0.9955

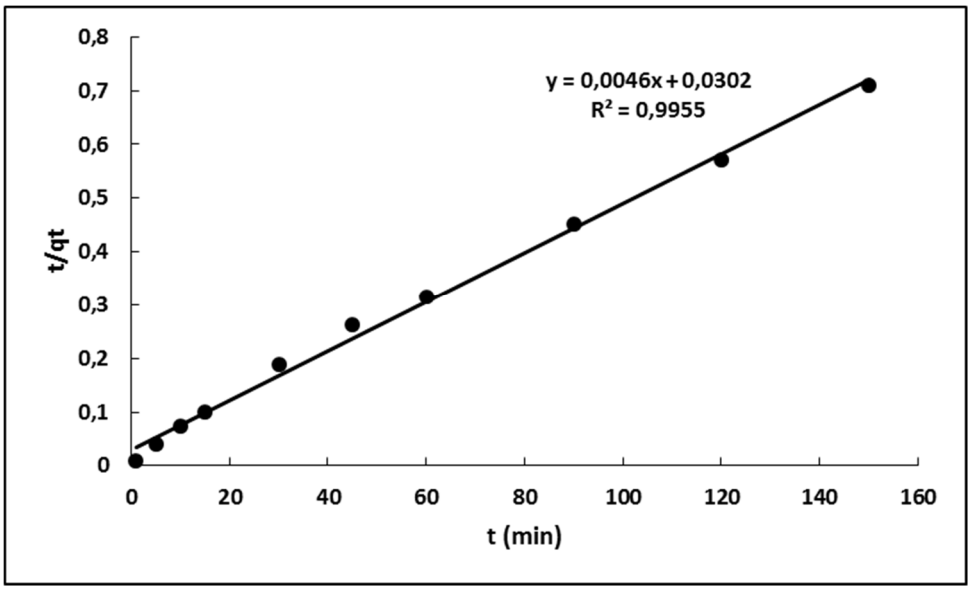

Figure 6. Plot of pseudo-second-order model for AR114 adsorption by Fe_3O_4@CFA MNC (Natural pH, C_0=200 mg/L, m= 0.03 g/50 ml)

Regeneration and reuse

Owing to economic and resource reasons, reuse of the adsorbents is significant. Eluting with organic solutions (The mixture of methanol:acetic acid as the volume ratio of 9:1) were examined in this study. The optimum regeneration ability was found to be the mixture of methanol and acetic acid. The recycling adsorption efficiency is shown in Figure 7 from which the adsorbed amount of AR114 onto the Fe_3O_4@CFA MNC was 74.7 mg/g, and the adsorbed amount of AR114 on the regenerated Fe_3O_4@CFA MNC, decreased each cycle from 74.7 mg/g to 45.5 mg/g.

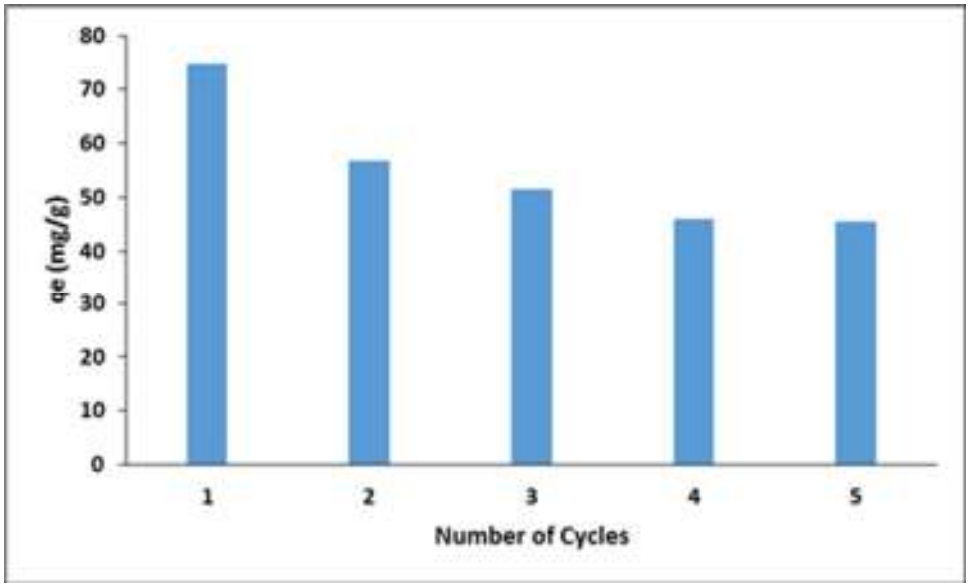

Figure 7. The recyclable adsorption of AR114 Fe_3O_4@CFA MNCs (C_0:60 mg/L, natural pH)

CONCLUSION

In the study the removal of AR114 by adsorption process, using the magnetic nanoparticle Fe_3O_4@CFA MNC were studied. Caffeic acid coated Fe_3O_4 MNC (Fe_3O_4@CFA MNC) were synthesized successfully by the simple chemical refluxing method. The MNC were proved and confirmed that it was covalently bonded to the Fe_3O_4 nanoparticle surface via carboxyl groups. The maximum q_e values for each adsorbent were obtained without correcting pH (pH=7.3). The Langmuir model well described equilibrium data. The maximum adsorption capacity of the Fe_3O_4@CFA MNC for AR114 was 333 mg/g at natural pH. Kinetic data were sufficiently adapted by the pseudo-second order kinetic model. The adsorbed amount of AR114 onto the regenerated Fe_3O_4@CFA MNC, for initial concentration of 60 mg/L, decreased from 74.7 mg/g to 45.5 mg/g after five cycles. This study showed that magnetic nanomaterials supported adsorbent are very attractive and can be a good alternative solution for waste water treatment due to its very efficient adsorbent capability and stability for reusable adsorbing materials used in the removal of hazardous dye. This work also showed that Fe_3O_4@CFA MNC has suitable adsorption ability towards the removal of AR 114 from the wastewater. Finally, Fe_3O_4@CFA MNC can be considered as an alternatives and efficient adsorbents for dye removal in wastewater treatment.

ACKNOWLEDGEMENTS

This work was supported in part by Scientific Research Unit of Namık Kemal University (NKUBAP.06.GA.16.047).

REFERENCES

1. Nasuha N, Hameed BH. Adsorption of methylene blue from aqueous solution onto NaOH-modified rejected tea. Chemical Engineering Journal. 2011; 166. 783-786. DOI: 10.1016/j.cej.2010.11.012.

2. Thinakaran N, Panneerselvam P, Baskaralingam P, Elango D, Sivanesan S. Equilibrium and kinetic studies on the removal of Acid Red 114 from aqueous solutions using activated carbons prepared from seed shells. Journal of Hazardous Materials. 2008; 158. 142–150. DOI: 10.1016/j.jhazmat.2008.01.043.

3. Dobrowski A. Adsorption--from theory to practice. Advence Colloids Interface Science. 2001; 93. 135–224. DOI: 10.1016/S0001-8686(00)00082-8.

4. Demirbas A. Agricultural based activated carbons for the removal of dyes from aqueous solutions: A review. Journal of Hazardous Materials. 2009; 167. 1-9. DOI: 10.1016/j.jhazmat.2008.12.114.

5. Abbas M, Trari M, Kinetic, equilibrium and thermodynamic study on the removal of Congo Red from aqueous solutions by adsorption onto apricot stone. Process Safety and Environmental Protection. 2015; 98. 424–436. DOI: 10.1016/j.psep.2015.09.015 .

6. Saiz J, Bringas E, Ortiz I, Functionalized magnetic nanoparticles as new adsorption materials for arsenic removal from polluted waters. J. Chem. Technol. Biotechnol. 2014.89. 909–918. DOI: 10.1002/jctb.4331.

7. Afkhami A, Moosavi R, Adsorptive removal of Congo red, a carcinogenic textile dye, from aqueous solutions by maghemite nanoparticles. Journal of Hazardous Materials. 2010; 174. 398–403. DOI: 10.1016/j.jhazmat.2009.09.066.

8. Pastora JG, Bringas E, Ortiz I. Recent progress and future challenges on the use high performance magnetic nano-adsorbents in environmental. applications. Chemical Engineering Journal. 2014; 256. 187–204. DOI.10.1016/j.cej.2014.06.119.

10. Chi Y, Geng W, Zhao L, Yan X, Yuan Q, Li N, Li X, Comprehensive study of mesoporous carbon functionalized with carboxylate groups and magnetic nanoparticles as a promising adsorbent. Journal of Colloid and Interface Science. 2012; 369. 366–372. DOI: 10.1016/j.jcis.2011.12.051.

11. Zhang X, Zhang P, Wu Z, Zhang L, Zeng G, Zhou C, Adsorption of methylene blue onto humic-acid coated Fe_3O_4 NPs. Colloids Surf. A Physicochem. Eng. Aspects. 2013;435. 85–90. DOI: 10.1016/j.colsurfa.2012.12.056.

12. Cao C, Xiao L, Chen C, Shi X, Cao Q, Gao L, In situ preparation of magnetic Fe_3O_4/chitosan nanoparticles via a novel reduction–precipitation method and their application in adsorption of reactive azo dye. Powder Techno. 2014;260. 90–97. DOI: 10.1016/j.powtec.2014.03.025.

13. Chang J, Ma J, Ma Q, Zhang D, Qiao N, Hu M, Ma H, Adsorption of methylene blue onto Fe_3O_4/activated montmorillonite nanocomposite. Appl. Clay Sci. 2016, 119. 132–140. DOI: 10.1016/j.clay.2015.06.038.

14 Hoa NV, Khong TT, Quyen TTH, Trung TS, One-step facile synthesis of mesoporous graphene/ Fe_3O_4/chitosan nanocomposite and its adsorption capacity for a textile dye. J. Water. Process. Eng, 2016, 9. 170–178. DOI: 10.1016/j.jwpe.2015.12.005.

15. Tan KA, Morad N, Teng TT, Norli I, Synthesis of magnetic nanocomposites (AMMC- Fe_3O_4) for cationic dye removal: Optimization, kinetic, isotherm, and thermodynamics analysis, J. Taiwan Inst. Chem. Eng, 2015, 54. 96–108. DOI: 10.1016/j.jtice.2015.03.014.

16. Thinakaran N, Panneerselvam P, Baskaralingam P, Elango D, Sivanesan S, Equilibrium and kinetic studies on the removal of Acid Red 114 from aqueous solutions using activated carbons

prepared from seed shells, J. Hazard. Mater,2008, 158. 142–150 DOI: 10.1016/j.jhazmat.2008.01.043.

17. Lin CC, Lin YS, Ho JM, Adsorption of Reactive Red 2 from aqueous solutions using Fe_3O_4 NPs prepared by co-precipitation in a rotating packed bed, J. Alloys Compd, 2016, 666. 153-158. DOI: 10.1016/j.jallcom.2016.01.015.

18. Baykal A, Amir MD, Güner S, Sözeri H. Preparation and characterization of SPION functionalized via caffeic acid. Journal of Magnetism and Magnetic Materials.2015; 395. 199–204. DOI: 10.1016/j.jmmm.2015.07.095.

19. Baykal A, Erdemi H, Amir MD. Temperature and Frequency Dependence on Electrical Properties of Fe_3O_4@ Caffeic Acid Nanocomposite. Journal of Inorganic and Organometallic Polymers and Materials. 2016;26. 190–196. DOI: 10.1007/s10904-015-0296-0.

20. Petrova TM, Fachikov L, Hristov J. The Magnetite as Adsorbent for Some Hazardous Species from Aqueous Solutions: a Review. International Review of Chemical Engineering. 2011; 3. 134-152. Bibliographic Code: 2011arXiv1104.5647P.

21. Jiang Z, Li Y. Facile synthesis of magnetic hybrid Fe3O4/MIL-101 via heterogeneous coprecipitation assembly for efficient adsorption of anionic dyes. Journal of the Taiwan Institute of Chemical Engineers. 2015;8. 1-7. DOI: 10.1016/j.jtice.2015.09.002.

22. Srivastava VC, Mall ID, Mishra IM. Competitive adsorption of cadmium(II) and nickel(II) metal ions from aqueous solution onto rice husk ash. Chemical Engineering and Processing. 2009;48. 370–379. DOI: 10.1016/j.cep.2008.05.001.

23. Langmuir I. The adsorption of gases on plane surfaces of glass, mica and platinum. Journal American Chemical Society. 1918; 40. 1362. DOI: 10.1021/ja02242a004.

24. Freundlich H, Over the adsorption in solution, Journal Physical Chemistry. 1906; 57. 385.

25. McKay G, Blair H, Gardiner JR. The adsorption of dyes onto chitin in fixed bed column and batch adsorbers. Journal Applied Polymer Science. 1989; 28. 1499-1544.

26. Choy KKH, McKay G, Porter JF. Sorption of acid dyes from effluents using activated carbon, Resources. Conservation and Recycling Resources. 1999;27. 57–71. DOI: 10.1016/S0921-3449(98)00085-8.

27. Kaykioglu G and Gunes E. Comparison of Acid Red 114 dye adsorption by Fe_3O4 and Fe_3O4 impregnated rice husk ash. Journal of Nanomaterials. 2016, 1-10. DOI: 10.1155/2016/6304096.

28. Lagergren S. Zur theorie der sogenannten adsorption geloester stoffe [About theory of so-called adsorption of soluble substances]. Kungliga Svenska Vetenskapsakad. Handl.1898; 24, 1–39.

29. Pirbazari AE, Saberikhah E, Gorabi NGA. Fe_3O_4 nanoparticles loaded onto wheat straw: an efficient adsorbent for Basic Blue 9 adsorption from aqueous solution. Desalination and Water Treatment. 2016; 57. 4110–4121. DOI: 10.1080/19443994.2014.989918.

30. Ouyang K, Zhu C, Zhao Y, Wang L, Xie S, Wang Q. Adsorption mechanism of magnetically separable Fe_3O_4/grapheneoxide hybrids. Applied Surface Science. 2015; 355, 562-569. DOI: 10.1016/j.apsusc.2015.07.109.

Türkçe Öz ve Anahtar Kelimeler

Asit Kırmızı 114'ün Fe_3O_4@Kafeik asit Geri Dönüştürülebilir Manyetik Nanokompoziti Üzerine Adsorpsiyonu

Aylin YILDIZ

Öz: Bu çalışmada, kafeik asit (CFA) ile fonksiyonlandırılmış Fe_3O_4 manyetik geri dönüştürülebilir nanokompozitinin (Fe_3O_4@CFA MNC) endüstriyel bir boyar madde olan Asit Kırmızısı 114 (AR 114) için adsorpsiyon kapasitesi incelenmiştir. Fe_3O_4@CFA MNC'nin AR114 için maksimum adsorpsiyonu (q_m), çözeltide pH düzeltmesi yapilmadan 333 mg/g olarak bulunmuştur. Diğer çalışmalarla karşılaştırıldığında, bu adsorbanın AR114 boyar maddesini yüksek bir adsorpsiyon kapasitesi ile tuttuğu görülmüştür. Adsorpsiyon izoterm verileri ve adsorpsiyon kinetik süreci Langmuir eşitliğine uydurulmuştur ve yalancı ikinci mertebe kinetik modele göre de adsorpsiyon sürecinde kemisorpsiyonun hız belirleyen basamak olduğu görülmüştür. Manyetik NM teknolojisinin bu çalışmada kullanılmasıyla organic kirleticilerin adsorpsiyonuna yeni bir boyut katacağına inanılmaktadır. Bunun ötesinde, Fe_3O_4@CFA MNC'nin beş çevrimde bile belirgin giderme sağladığı bulunmuştur.

Anahtar kelimeler: Atıksu islahı; manyetik nanokompozit; adsorpsiyon; Asit Kırmızısı 114.

Sunulma: 28 Eylül 2016**. Düzeltme:** 20 Kasım 2016**. Kabul:** 25 Kasım 2016**.**

Miscibility and Thermal Degradation Kinetics of Poly-β-Alanine/Poly(3-hydroxypropionate) Blends

Efkan ÇATIKER[1]*, Satılmış BASAN[2]

[1]Ordu University, Faculty of Art&Science, Department of Chemistry, 52200 Ordu, Turkey

[2]Hitit University, Faculty of Engineering, Chemical Engineering, 19930 Çorum, Turkey

Abstract: Poly-β-alanine (PBA) and poly(3-hydroxypropionate) (PHP) were synthesized via base-catalyzed hydrogen transfer polymerization (HTP) of acrylamide and acrylic acid, respectively. Blends of PBA/PHP with different composition (PHP content, 5% to 75%) were studied using FTIR, DSC, TGA, XRD and polarized optical microscope to reveal both miscibility and thermal degradation kinetics of PBA/PHP blends. Optical images of blends were transparent and entirely uniform. Characteristic FTIR bands of both components shifted in higher frequencies with increasing fraction of another component. Melting temperature (T_m), thermal decomposition temperatures (T_d), and enthalpy of fusion (ΔH_f) of PHP decreased with increasing PBA fraction in blends. Thermal degradation kinetics of both components were studied by Freeman-Carroll method. Activation energies of thermal degradations of blend components were determined with good regression coefficients (at least 0.994). Activation energies of decomposition decreased from 224.14 to 86.125 kJmol^{-1} with increasing PHP content. XRD spectra of blends exhibited lower peak intensities than those of neat polymers. The spectroscopic, thermal, and optical methods revealed that PBA and PHP were miscible with a good compatibility in amorphous phase.

Keywords: Thermal degradation; miscibility, poly-β-alanine, poly(3-hydroxypropionate).

Submitted: July 14, ,2016. **Revised:** November 19, 2016. **Accepted:** November 28, 2016.

Cite this: Çatıker E, Basan S. Miscibility and Thermal Degradation Kinetics of Poly-β-Alanine/Poly(3-hydroxypropionate). JOTCSA. 2017;4(1):341-54.

DOI: To be assigned.

*Corresponding author. E-mail: efkan@odu.edu.tr.

INTRODUCTION

Poly(3-hydroxypropionate) (PHP) or poly(β-propiolactone) is a well-known biodegradable [1] thermoplastic polyester with high tensile strength, elongation at breaking, and high moisture permeability. There are some reports on its potential utilization as scaffold material in tissue engineering [2] and polymeric matrix for drug delivery [3]. Although PHP has attracted much attention as an environmentally degradable polymer to be used for medical applications, it has limitations due to its brittleness (high crystallinity), narrow processability, and high hydrophobicity. Some studies were reported on blends [4-7] of PHP to eliminate these limitations. Similarly, various [8-11] copolymers of PHP have been prepared in order to combine its favorable properties with those of other components.

Comparing to aliphatic polyesters, aliphatic polyamides possess higher thermal stability, higher moduli, and higher tensile strength. Poly-β-alanine (PBA), sometimes described as nylon-3 or polyamide-3, is a crystalline poly(amino acid) with a high thermal (melts above 350 °C with decomposition [12]) and mechanical resistance [13].

Polymer blends are becoming more important in specific sectors of polymer industry, as they can frequently meet performance requirements that cannot be satisfied by the currently available commodity polymers. It is possible to obtain polymer blends of more desirable properties by mixing miscible polymers, and thus it is very important to examine the factors affecting the miscibility of polymer mixtures. Therefore, it is reasonable to combine the favorable properties of these two classes of polymers to produce a new polymeric material possessing good material properties and processability.

Thermal degradation of polymers and polymer blends is generally investigated by using thermogravimetry (TGA), differantial thermal analysis (DTA) and differantial scanning calorimetry (DSC). Mass losses and heat transfers due to the physical and chemical phenomena are examined by TGA and DSC or DTA, respectively.

The consideration of favorable properties of PHP and PBA motivated us to investigate their blends in the aspect of miscibility and thermal degradation behavior. Moreover, thermal stabilities of PHP, PBA and some of their blends were compared in the study.

MATERIALS AND METHODS

Acrylic acid (99%, Aldrich), acrylamide (99%, Aldrich), sodium tertiary butoxide (97%, Aldrich), phenyl-β-naphthylamine (97%, Aldrich), potassium chloride (99%, Sigma-

Aldrich), formic acid (99%, Sigma), o-dichlorobenzene (99%, Aldrich) were obtained commercially and used without purification.

Hydrogen transfer polymerization (HTP)

Acrylic acid ([M] = 0.07 mol) was placed into a three-necked flask. tBuONa ([I]=[M]/70) as initiator and catalyst, phenyl-β-naphthylamine (5 mg) as radicalic polymerization inhibitor and well-dried KCl ([KCl]=[M]/3) were added into the reaction flask. Reaction mixture was stirred under nitrogen flux at 90 °C in the dark for 48 h. The reaction mixture was poured into excess amount of diethyl ether to precipitate the PHP crystals out. The product was filtered and dried at room temperature and stored at 40 °C in a vacuum oven. PBA was prepared as described in Masamoto's report [14].

Blending and characterizations

Gel permeation chromatography (GPC) was performed using a Tosoh EcoSEC system equipped with a refractive index detector. Chloroform and hexafluoroisopropanol (HFIP) were used as solvents for PHP and PBA, respectively. The flow rate was 0.35 mL/min, and the column temperature was 35 °C. Monodispersed poly(methyl methacrylate) standards were used to calibrate the column. Number average molecular weights of PHP and PHP were determined as 3200 and 40000 $gmol^{-1}$, respectively. Polymer blends (10% w/v) were prepared using formic acid. PHP contents of the blends were in ratios of 5%, 10%, 25%, 50% and 75% by weight. The blend solutions were stirred vigorously overnight at room temperature. The solutions were cast into Petri dishes, dried at room temperature, and stored in vacuum oven overnight before analysis. DSC curves of neat polymers and blends were recorded using TA instrument 2920 Modulated DSC with 10 °C min^{-1} heating rate under nitrogen flux. Thermogram of neat polymers and blends were obtained using TA instrument Hi-Res TGA 2950 with 10 °C min^{-1} heating rate under nitrogen flux. XRD spectra of the film samples were recorded using a Bruker AXS Dimension D8 X-Ray System in a range of 7 to 35° (2-theta) using 20 kV with 5 mA current. FTIR spectra of neat polymers and blend films were recorded at room temperature using a Nicolet 380 FTIR spectrometer. The spectra were collected over the range 3400 to 1200 cm^{-1} with a resolution of 4 cm^{-1} using 32 scans.

RESULTS AND DISCUSSION

Optical Microscopy

Optical microscopic images of the blend films were recorded to obtain the first information about the compatibility of polymers. Although both PHP and PBA are white powders before

blending due to the high crystallinity of the polymers, solution-cast films of 10% and 25% PHP blends were completely transparent and uniform. This is a simple indication of miscibility of PHP and PBA. Optical microscopic images of blends were shown in Figure 1.

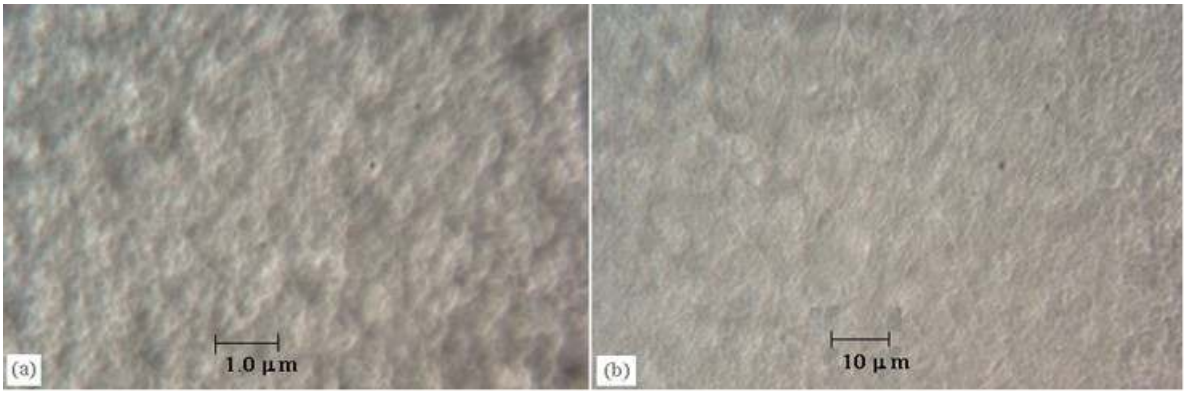

Figure 1. Polarized optical microscopic images of (a) 10% PHP and (b) 25% PHP blends.

FTIR Spectroscopy

FTIR spectroscopy provides crucial evidences on both crystallization and miscibility of polymer blends. Both PBA and PHP are highly crystalline due to the strong segmental interactions (dipole-dipole interactions in PHP and hydrogen bondings in PBA). The strong segmental interactions lead to decrements in the bond orders of corresponding functional groups ($C=O_{amide}$, NH_{amide} and $C=O_{ester}$) in the neat polymers. Consequently, FTIR spectra of the neat polymers give corresponding FTIR bands at lower frequencies than those in case of the strong interactions eliminated. Blending the polymers may destroy the strong interactions between the neat polymer chains resulting in increment in distance between the chains, decrement in crystallinity and hence increment in chain mobility. FTIR spectra of blends were expected to show corresponding bands at higher frequencies [15-18] than those in neat forms since chain mobility enhanced. Consequently, FTIR spectra of PBA/PHP blends were obtained to assess any structural changes that may have occurred upon blending as they affect the crystallinity and miscibility of the blend films. FTIR spectra of PBA/PHP blends with various compositions are shown in Figure 2.

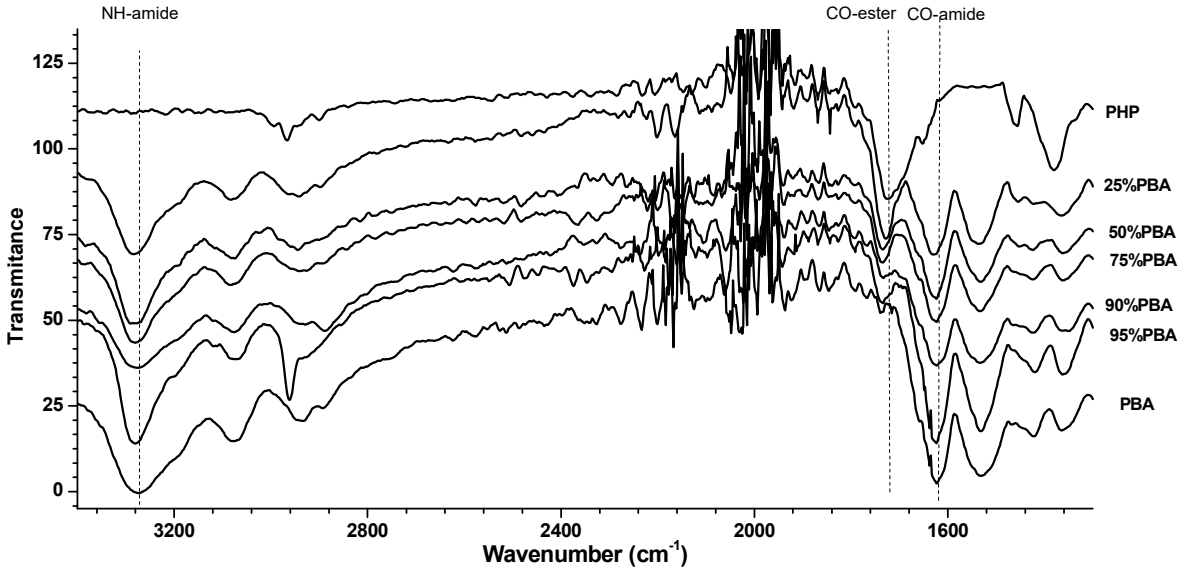

Figure 2. FTIR spectra of neat polymers and blends a) NH stretching b) CO_{ester} and CO_{amide} stretching.

Wavenumber shifts originating from blending for characteristic amide (N-H stretching and CO carbonyl stretching) and ester (CO carbonyl stretching) bands are summarized in Table 1. Examination of data listed in Table 1 reveals that, upon blending, wavenumber, $\nu_{C=O\ (ester)}$ value of 1725.0 cm^{-1} in neat PHP shifted up to 1737.2 cm^{-1} with increasing PBA content. These shifts to higher wavenumbers mean improvement of bond order for the corresponding group (ester CO) due to extinction of the previous segmental interactions (here, dipole-dipole interactions).

Similarly, $\nu_{NH(amide)}$ values in neat PBA (3272.5 cm^{-1}) also shifted to higher wavenumbers (3289.1 cm^{-1} for 75% PHP) with increasing PHP content, revealing increment in bond order for NH, and hence, the extinction of hydrogen bonding between amide CO and amide NH.

We also have observed shifts in ν_{CO} amide band (1622.8 cm^{-1}) to higher wavenumbers (1629.8 cm^{-1} for 75% PHP) by increasing the ratio of PHP in the blends. This result indicates enhancement in bond order for the corresponding amide CO group due to the extinction of self-associated hydrogen bonding, and it provides a clear evidence for penetration of PHP chains through the nylon crystal lattice.

Table 1. FTIR data of neat components and their blends.

	PBA	**5% PHP**	**10% PHP**	**25% PHP**	**50% PHP**	**75% PHP**	**PHP**
CO_{amide}	1622.8	1623.1	1623.7	1623.7	1624.3	1629.8	-
CO_{ester}	-	1737.2	1733.6	1735.4	1735.4	1729.3	1725.0
NH_{amide}	3272.5	3280.4	3280.6	3280.6	3284.9	3289.1	-

Differential Scanning Calorimetry

DSC curves for pure PHP and PBA/PHP blends are shown in Figure 3. Thermal behavior of PBA was not examined since PBA melted at around 350 °C and decomposition accompanied immediately after melting process began. The data derived from the first heating scans of DSC for PHP powder and PBA/PHP blends are listed in Table 2. The DSC curves show endothermic melting peak centered at 69.0 °C for pure PHP. The melting temperature of PHP in the blends decrease consistently with increasing PBA content. Even blends with minor PHP content (5% and 10% PHP) did not exhibit any melting peak. These decrements indicate that PHP chains acquire enhanced mobility after blending leading to lower T_m values. In general, a decrease in the melting point in a polymeric blend can be due to both morphological effects (decrease in lamellar thickness) and to thermodynamic factors [15] (polymer-polymer interactions).

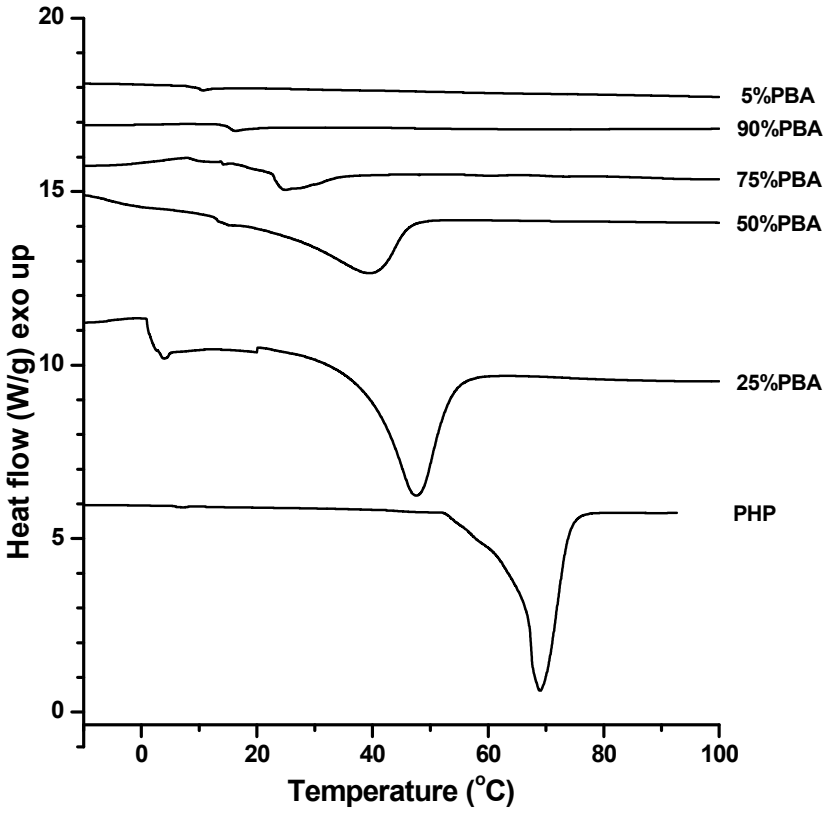

Figure 3. DSC curve of PHP and its blends with PBA.

Apparent enthalpy of fusion for PHP decreased in the blend samples. Percent crystallinities of PHP in the blend films were estimated by dividing the apparent fusion enthalpies of PHP in blends to fusion enthalpy of neat PHP [19], 140.9 J/g. Based on the data listed in Table 2, relative crystallinities of PHP in all blend samples were lower than that in neat PHP. Although both PHP and blend films were prepared using the same route (solvent, drying time, drying temperature), suppression of percent crystallinity of PHP in the blends may

be attributed to penetration of PBA to the crystal lattice of PHP. Another factor that lowers the degree of crystallinity for PHP is the difference in the molecular mobility between PHP and PBA. The difference in the glass-transition temperature between PBA and PHP (110-120 °C) influences the degree of crystallinity of their blends. Such a result is probably due to the trapped fraction of PBA in the interlamellar amorphous regions of PHP spherulitic behavior which is not allowed to crystallize. Therefore, the influence of PBA on the crystallinity of PHP can be considered to be the proof of miscibility (compatibility) of the two polymers. The DSC results in this work revealed that blending PBA with PHP suppressed the crystallinity of PHP in the blend films. In all, the DSC results supported our earlier finding in FTIR analysis that the crystallinities of PBA/PHP blends were suppressed compared with pure components.

Table 2. DSC data of neat PHP and blends.

	PHP	**25 % PHP**	**50% PHP**	**75% PHP**	**10% PHP**	**5% PHP**
T_m (°C)	69.0	28.4	39.5	48.4	-	-
ΔH_f (J g^{-1})	104.3	9.1	27.9	34,3	-	-
X_c	74.0	6.5	19.8	24.3	-	-

X-ray Diffraction Spectroscopy

XRD spectra patterns of crystalline polymers may be used to extract qualitative information on the degree of crystallinity of polymers and blends [17, 20]. In this study, XRD spectra of neat PHP /PBA and their blend films shown in Figure 4 were obtained to understand the effect of blending on the degree of crystallinity of each component. The XRD spectra reveal that diffraction intensities of blend films are lower than those of the individual components. The sharp peaks observed in the neat PHP film spectrum diminish in intensity with increasing PBA content in the spectra. Since the areas under these peaks can be used as measure of the degree of crystallinity, reduction in these areas may be attributed to suppression in the degree of crystallinity for both components (PHP and PBA) upon blending. Each blend component seems to trap the segments of the other in the amorphous phase hindering the mobility required for crystallization. This results in a lower degree of crystallinity.

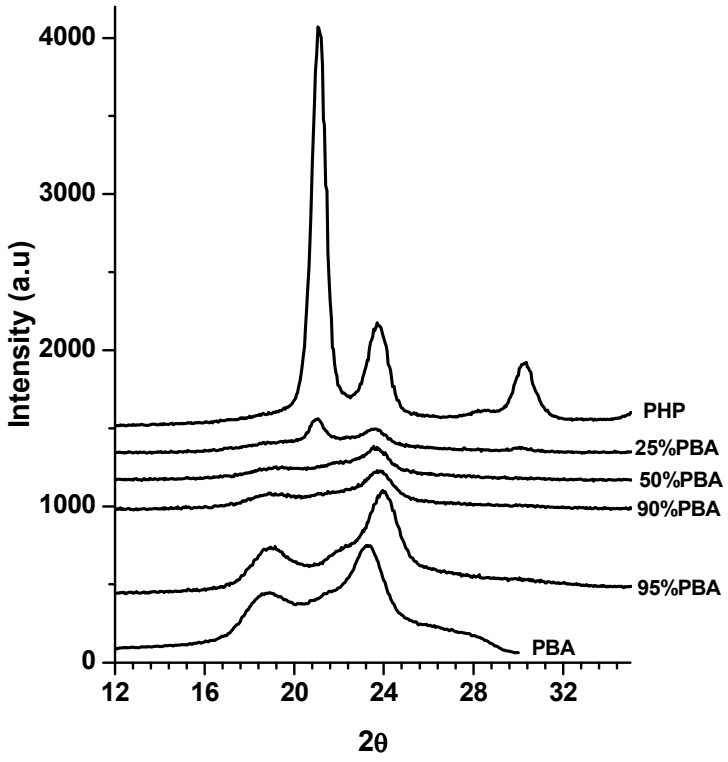

Figure 4. XRD spectra of the neat polymers and their blends.

Thermogravimetric Analysis

Thermogravimetric analyses of neat components and blend films were performed to see the effect of each component on the decomposition behavior over the others. The TGA and DTG decomposition curves of neat polymers and blends are shown in Figures 5 and 6. The TGA and DTG curves were used not only to compare thermal stabilities of neat polymers and their blends but also to investigate the kinetics of thermal degradation reactions [21]. It is obvious that both neat polymer decomposes through a fast reaction at single-step in different temperature domains.

Onset temperature of degradation (T_i), half-life temperature (T_h), maximum rate temperature (T_{max}), final temperature at degradation (T_f) and maximum mass loss rate (R_{max}) were listed in Table 3 to compare thermal stabilities of neat polymers and their blends. As easily shown in Figure 5 and 6, thermal stability of PBA is much higher than PHP. Moreover, PHP decomposes completely before PBA begins to decompose. It may be estimated that blending with PHP and PBA will result in elevation of thermal stability of PHP. Thus, the changes in T_i (488 to 492K), T_f (523 to 531K) and T_{max} (514 to 519) for 25% blend confirm this estimation. However, the values of T_i, T_f and T_{max} for the 50%, 75% and 90% blends (PBA dominant blends) are lower than those of neat PHP, that is an

indication of negative impact of PBA on the thermal stability of PHP. The values of T_i, T_f and T_{max} given in brackets, corresponding to the thermal degradation of PBA in the blends, increase with increasing PBA content in the blends. Similarly, the half-life temperatures (T_h), represent both degradation reactions, increase with increasing PBA content. Besides, addition of PBA causes depression in the rate of first degradation reaction, R_{max} and elevation in the rate of second degradation, R_{max} (in brackets).

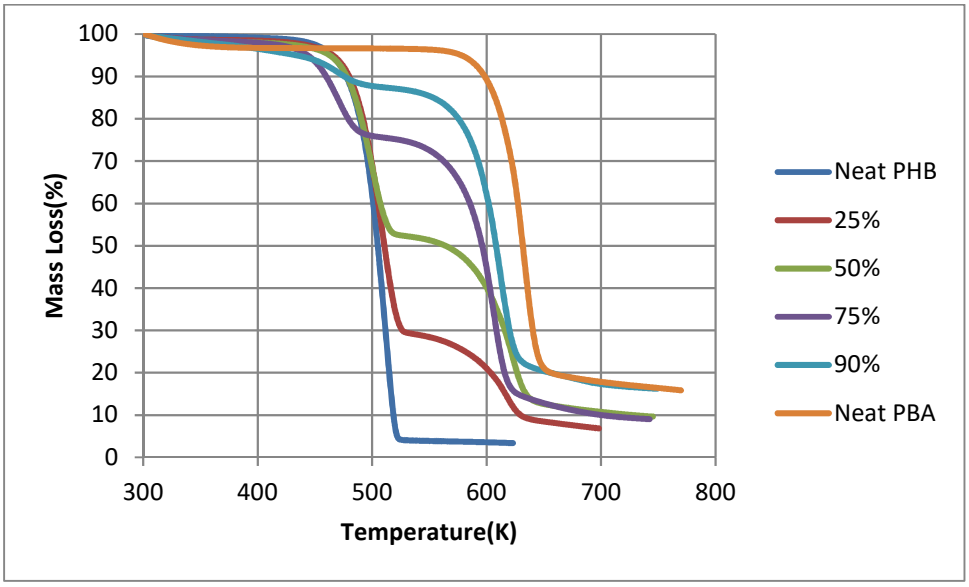

Figure 5. TGA curves of the neat polymers and their blends.

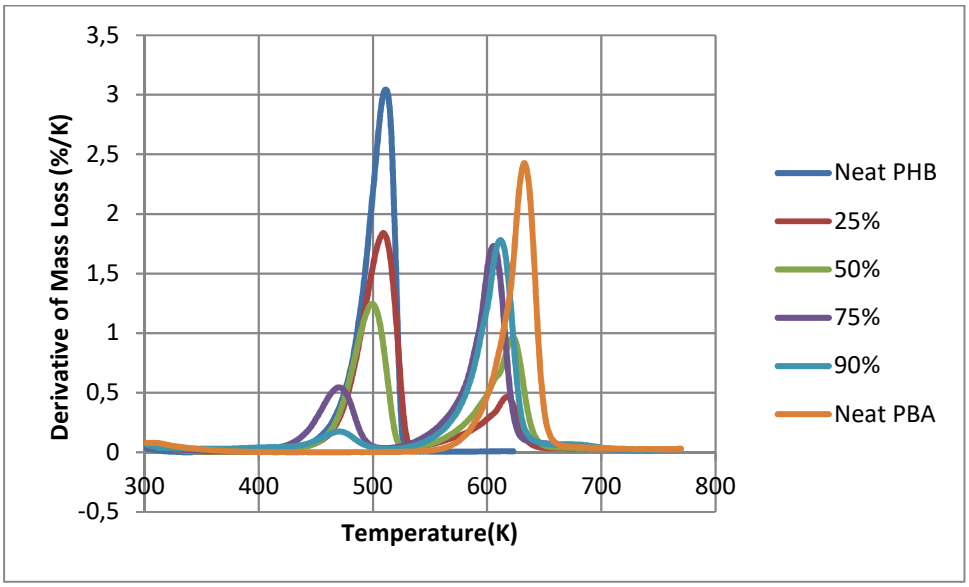

Figure 6. DTG curves of the neat polymers and their blends.

Table 3. Differential TGA curve data of the neat polymer and their blends. *The values given in brackets belong to the second thermal degradation.

PBA%	T_i(K)	T_f(K)	T_h(K)	T_{max}(K)	R_{max}(%/K)
0	488	523	507	514	3,04
25	492(592)	531(639)	520	519(627)	1.839(0.465)
50	484(602)	518(641)	571	505(630)	1.246(0.962)
75	475(612)	512(644)	623	497(633)	0.5446(1.73)
90	470(611)	507(646)	629	492(632)	0.175(1.780)
100	(610)	(644)	631	(633)	(2.427)

Freeman-Carroll method [22,23] is widely used in the kinetic analysis of thermal degradation of polymers and blends since it gives not only total reaction order but also activation energy of degradation. Since the activation energy of thermal degradation reaction obtained from the method belongs to overall of the thermal degradation, it is more useful than the parameters (T_i, T_{max}, T_h and T_f), which represents specific points of the reaction, for comparison of thermal stability of polymers.

Freeman-Carroll equation (Eq.1) has been used to determine the total reaction orders and activation energies of thermal degradation reactions. Graphs of $\Delta\ln(dC/dT)/\Delta\ln(1-C)$ versus $\Delta(1/T)/\Delta\ln(1-C)$ for each neat polymer and their blends have been plotted.

$$\frac{\Delta \ln(dC/dT)}{\Delta \ln(1-C)} = n - \frac{E_A}{R}\frac{\Delta(1/T)}{\Delta \ln(1-C)} \qquad \text{(Eq. 1)}$$

Figure 7 shows the Freeman-Carroll graph of 90% PBA blend. Intercept and slope of the straight line give total reaction order and activation energy of the thermal degradation, respectively. Activation energies of thermal degradations of blends were determined with good regression coefficient (at least 0.994). Activation energies of decomposition increased from 86.125 to 224.14 kJmol^{-1} with increasing PBA content. The results obtained for the all sample were listed in Table 4.

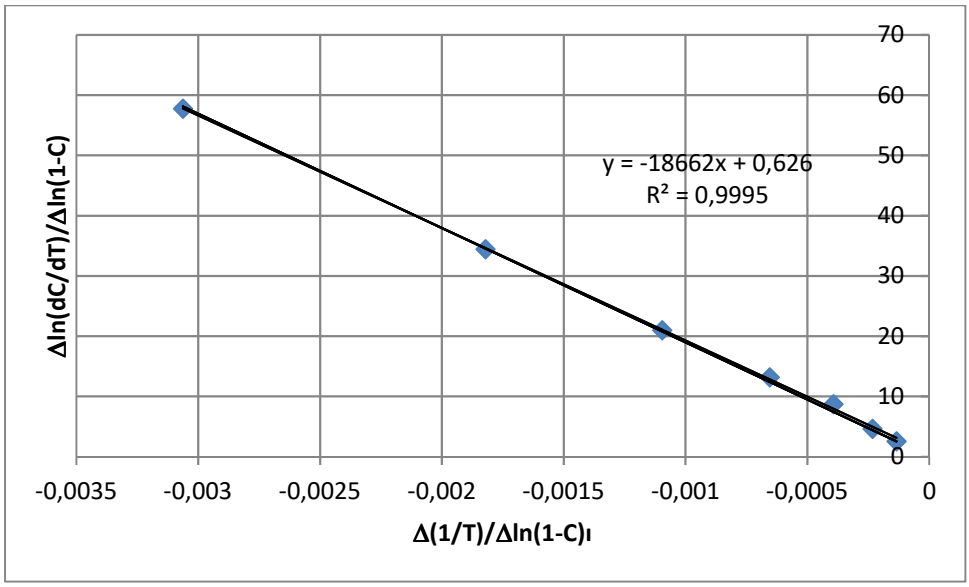

Figure 7. Freeman-Carroll graph of 90% PBA blend.

Table.4 Data obtained from Freeman-Carroll method for thermal degradations of neat PBA and PHP, and their blends.

PBA (%)	n	Slope	E_A(kJ/mol)	R^2
0	0.311	-10359	86	0.994
25	0.475	-10109	84	0.9961
50	-0.370	-13476	112	0.9985
75	0.198	-13702	113	0.9954
90	0.626	-18662	155	0.9995
100	-0.329	-26963	224	0.9996

CONCLUSION

In a thermodynamic sense, the formation of miscible PHP /PBA blends were favorable as attributed to the formation of strong hydrogen bonds between the components (enthalpic decrement), and suppression of high crystallinity in both the PHP and PBA components (entropic enhancement). Based on this point of view, the purpose of this work was to study the miscibility of PBA and PHP blends by using Differential Scanning Calorimetry (DSC), Fourier Transform Infrared Spectroscopy (FTIR), Thermogravimetric Analysis (TGA), X-Ray Diffraction Spectrometry (XRD), and Polarized Optical Microscopy (PEM).

These thermal, spectroscopic, and optical techniques revealed that the blends of PBA/ PHP are miscible in amorphous phase. The miscibility has been shown to be based mainly on suppression of crystallinity of both components in the blends. Such a decrease in the total crystallinity should be considered a very important factor for decreasing its brittleness and improving its other relevant material properties by tuning the amount of PBA to be blended.

PBA and PHP decompose thermally via fast and single step degradation. Thermal stability of PBA is higher than that of PHP. Moreover, PHP decomposes completely before PBA begins to decompose. Hence, blends of the polymers give TGA curves with two steps. Basically, PHP in the blends decomposes at the first step and then PBA decomposes at the second step. Increase in the PBA content (excluding 25%) in the blends depresses T_i, T_f and T_{max} values of first step and elevates T_i, T_f and T_{max} values of second step. Conversely, values of T_h and E_A, represent overall reaction, show that addition of PBA elevates the thermal stability of PHP. This behavior may be explained through wrapping of PHP chains by PBA chains, which is a result of miscibility. Blend with 25% PBA supports this approach. However, when PBA is dominant in blends (50%, 75% and 90%) it may behave as a barrier, hinder to remove of primary degradation product of PHP (acrylic acid), and then cause an autocatalytic effect on the thermal degradation of main polymer [24].

REFERENCES

1. Furuhashi Y, Iwata T, Kimura Y, Doi Y. Structural characterization and enzymatic degradation of α-, β-, and γ-crystalline forms for poly(β-propiolactone). Macromol. Biosci. 2003; 3:462–470. DOI: 10.1002/mabi.200350020.

2. Cortizo M S, Molinuevo M S, Cortizo A M. Biocompatibility and biodegradation of polyester and polyfumarate based-scaffolds for bone tissue engineering. J. Tissue. Eng. Regen. Med. 2008; 2:33–42. DOI: 10.1002/term.62.

3. Cortizo M S, Alessandrini J L, Etcheverr S B, Cortizo A M. A vanadium/aspirin complex controlled release using a poly(beta-propiolactone) film. Effects on osteosarcoma cells. J. Biomater. Sci. Polym. Ed. 2001;12: 945-959. DOI: 10.1163/156856201753252499.

4. Cao A, Asakawa N, Yoshie N, Inoue Y. Phase structure and biodegradation of the Bacterial poly(3-hydroxybutyric acid)/chemosynthetic poly(3-hydroxypropionic acid) blend. Polym. J. 1998; 30:743-752. DOI: 10.1295/polymj.30.743.

5. He Y, Asakawa N, Inoue Y. Biodegradable blends of high molecular weight poly(ethylene oxide) with poly(3-hydroxypropionic acid) and poly(3-hydroxybutyric acid) a miscibility study by DSC, DMTA and NMR spectroscopy. Polym. Int. 2000; 49:609–617. DOI: 10.1002/1097-0126(200006)49:6<609:AID-PI426>3.0.CO;2-6.

6. Kumagai Y, Doi Y. Enzymatic degradation of binary blends of microbial poly(3-hydroxybutyrate) with enzymatically active polymers. Polym. Degrad. Stabil. 1992;37: 253-256. DOI: 10.1016/0141-3910(92)90167-4.

7. Autran J P M. US Patent 7,265,188 B2 Sept 4 2007 assigned to The Procter&Gamble Company. URL: https://www.google.com/patents/US7265188.

8. Ichikawa M, Nakamura K, Yoshie N, Asakawa N, Inoue Y. Morphological study of bacterial poly(3-hydroxybutyrate-co-3-hydroxypropionate). Macromol. Chem. Phys. 1996; 197: 2467–2480. DOI: 10.1002/macp.1996.021970811.

9. Cerrai P, Tricoli M, Andruzzi F. Synthesis and characterization of polymers from β-propiolactone and poly(ethylene glycol)s. Polymer 1987; 28:831-836. DOI: 10.1016/0032-3861(87)90236-9.

10. Zhou Q, Shi Z Y, Meng D C, Wu Q, Chen J C, Chen G Q. Production of 3-hydroxypropionate homopolymer and poly(3-hydroxypropionate-co-4-hydroxybutyrate) copolymer by recombinant Escherichia coli. Metab. Eng. 2011; 13:777–785. DOI: 10.1016/j.ymben.2011.10.002.

11. Andreeßen B, Steinbüchel A. Biosynthesis and Biodegradationof 3-Hydroxypropionate-Containing Polyesters. Appl. Environ. Microbiol. 2010; 76:4919-4925. DOI: 10.1128/AEM.01015-10.

12. Camino G, Guaita M. A DTA Study of Crystallization on Heating of Branched Poly(imino(1-oxotrimethylene)), Nylon3. Euro. Polym. J. 1977; 13:903-905. DOI: 10.1016/0014-3057(77)90063-5.

13. Masamoto J. Nylon-3. Rep. Prog. Polym. Phys. Jpn. 2000; 43:867-876.

14. Yamamoto F, Misumi T. US Pat. 5,015,707, (1991) assigned to Asahi Chemical. URL: http://www.google.com/patents/US5015707

15. He Y, Zhu B, Inoue Y. Hydrogen-Bonds in Polymer Blends. Prog. Polym. Sci. 2004; 29:1021-1051. DOI: 10.1016/j.progpolymsci.2004.07.002.

16. Zakaria Z, Izzah Z, Jawaid M, Hassan A. Effect of degree of deacetylation of Chitosan on thermal stability and compatibility of Chitosan-polyamide blends. Bioresources.2012;7:5568-5580. URL: https://www.ncsu.edu/bioresources/BioRes_07/BioRes_07_4_5568_Zainoha_THJ_Deacetylation_Chitosan_Thermal_Stab_Amide_3078.pdf

17. Liu Y, Shao Z, Zhou P, Chen X. Thermal and crystalline behavior of silk fibroin/nylon 66 blend films. Polymer. 2004; 45:7705- 7710. DOI: 10.1016/j.polymer.2004.09.005.

18. Mousavioun P, Doherty W O S, George G. Thermal stability and miscibility of poly(hydroxybutyrate) and soda lignin blends. Ind. Crop. Prod. 2010; 32:656-661. DOI: 10.1016/j.indcrop.2010.08.001.

19. Watanabe M, Togo M, Sanui K, Ogata N, Kobayashi T, Ohtaki Z. Ionic conductivity of polymer complexes formed by poly(β-propiolactone) and lithium perchlorate. Macromolecules. 1984; 17:2908-2912. DOI: 10.1021/ma00142a079.

20. Guirguis O W, Moselhey M T H. Thermal and structural studies of poly(vinyl alcohol) and hydroxypropyl cellulose blends. Nat. Sci. 2012; 4:57-67. DOI: 10.4236/ns.2012.41009.

21. Shamshad Ahmed A A, Basfar M M. Comparison of thermal stability of sulfur, peroxide and radiation cured NBR and SBR vulcanizates, Polym. Degrad.Stab.2000;67:319-323. URL: http://www.iaea.org/inis/collection/NCLCollectionStore/_Public/31/016/31016367.pdf

22. Freeman E S, Carroll B. The Application of Thermoanalytical Techniques to Reaction Kinetics: The Thermogravimetric Evaluation of the Kinetics of the Decomposition of Calcium Oxalate Monohydrate J. Phys. Chem. 1958; 62:394-397. DOI: 10.1021/j150562a003.

23. Jerez A A. Modification to the Freeman and Carroll Method for the analysis of the kinetics of non-isothermel processes, J. Therm. Analysis. 1983; 26:315-318. DOI: 10.1007/BF01913218 S.

24. Aouachria K, Quintard G, Nageotte V M, Bensemra N B. The Effect of Di-(-2-ethyl hexyl) phthalate (DEHP) as Plasticizer on the Thermal and Mechanical Properties of PVC/PMMA Blends, Polímeros, 2014; 24:428-433, 2014. DOI: 10.1590/0104-1428.1588.

Türkçe Öz ve Anahtar Kelimeler

Poli-β-Alanin / Poli(3-hidroksipropiyonat) Karışımlarının Birbiri İçinde Çözünürlüğü ve Isıl Bozunma Kinetikleri

Efkan ÇATIKER, Satılmış BASAN

Öz: Poli-β-alanin (PBA) ve poli(3-hidroksipropiyonat) (PHP) sırasıyla akrilamid ve akrilik asidin baz katalizli hidrojen iletim polimerizasyonu (HTP) ile sentez edilmiştir. Farklı bileşimdeki (PHP içeriği %5 ile 75 arası) PBA/PHP karışımları FTIR, DSC, TGA, XRD ve polarize optik mikroskop çalışmalarıyla PBA/PHP karışımlarının birbiri içinde çözünebilirlik ve ısıl bozunma kinetiğini ortaya çıkarmıştır. Karışımların optik görüntüleri şeffaf ve tamamen tek biçimlidir. Her iki bileşenin karakteristik FTIR bantları, diğer bileşenin artan kısmı ile daha yüksek frekanslara kaymıştır. PHP'nin erime sıcaklığı (T_m), ısıl bozunma sıcaklığı (T_d) ve kaynaşma entalpisi (ΔH_f), karışımlardaki PBA kısmının artması ile azalma göstermiştir. Her bir bileşenin ısıl bozunma kinetiği Freeman-Carroll yöntemiyle çalışılmıştır. Karışımı oluşturan bileşenlerin ısıl bozunmalarının aktivasyon enerjileri iyi regresyon katsayıları ile (en az 0,994) belirlenmiştir. Bozunma aktifleşme enerjileri artan PHP içeriği ile 224,14'den 86,125 $kJmol^{-1}$'e azalmıştır. Karışımların XRD spektrumları, saf polimerlere oranla daha düşük pik şiddeti vermiştir. Spektroskopik, termal ve optik yöntemlere göre PBA ve PHP, amorf fazda iyi bir uyuma sahip olacak şekilde birbiri içinde çözünmektedir.

Anahtar kelimeler: Isıl bozunma; birbiri içinde çözünme; poli-β-alanin, poli(3-hidroksipropionat).

Sunulma: 14 Temmuz 2016. **Düzeltme:** 19 Kasım 2016. **Kabul:** 28 Kasım 2016.

Toxicity Modelling of Some Active Compounds Against K562 Cancer Cell Line Using Genetic Algorithm-Multiple Linear Regressions

David Ebuka Arthur[a]*, Adamu Uzairu[a], Paul Mamza[a], Abechi Eyeji Stephen[a], Gideon Shallangwa[a]

[a]Department of Chemistry, Ahmadu Bello University Zaria, Kaduna State, Nigeria

Abstract: This research entails the modelling of the toxicity of anticancer compounds on K562 cell line, where 112 compounds that make up the data set were divided into training and test sets to be used for developing and validating the model, respectively. The internal and external validation parameter R^2 for the training and test set given respectively as 0.845 and 0.5316, justifying the robustness and the ability of the model to predict toxicity of the compounds. WPSA-3 and minHBint7 molecular descriptor is responsible for about 50% of the overall effect on the model.

Keywords: QSAR; Modeling; External Validation; Molecular descriptors; Genetic algorithm.

Submitted: October 05, 2016. **Revised:** November 17, 2016. **Accepted:** November 21, 2016.

Cite this: Arthur D, Uzairu A, Mamza P, Stephen A, Shallangwa G. Toxicity Modelling of Some Active Compounds Against K562 Cancer Cell Line Using Genetic Algorithm-Multiple Linear Regressions. JOTCSA. 2017;4(1):355–74.

DOI: To be assigned.

*Corresponding author. E-mail: hanslibs@myway.com, phone: +2348138325431.

INTRODUCTION

Drugs are often modeled as various polygonal shapes, paths, graphs, *etc.* [1]. Each vertex in the polygonal path represents an atom of the molecule, and covalent bonds between atoms are represented by edges between the corresponding vertices. As the geometry of proteins play an important role in determining the function of the protein [2], molecular descriptors of chemical compounds can be correlated to their biological activity. Presently a large number of molecular descriptors have been reported as important for the study of molecular drug design, lead optimization, and for deriving regression models [3]. At present, cancer is one of the leading disease-related cause of death of the human population in the world, and it is predicted to continue to become the leading cause of death within the coming years [4]. The use of chemical compounds to inhibit cancer cell growth, is a mainstay in the treatment of malignancies. A major advantage of chemotherapy is its ability to treat metastatic cancers, whereas surgery and radiation therapies are limited to treating cancers that are confined to specific areas. Chemotherapy has aroused many researchers' interests and a great deal of current efforts has been focusing on the design and development of different anticancer drugs. The large and extensive library of discovered compounds with high activities have been compiled by drug databanks and institutes such as National Cancer Institute, but the most compelling problem other than the complications involved in developing a new drug has been the factor time and capital cost.

Quantitative Structure-Activity Relationship (QSAR) analysis is one of the most effective approaches for optimizing leading compounds and designing new drugs. QSAR can be employed in predicting the bioactivity such as toxicity, mutagenicity, and carcinogenicity based on structural parameters of compounds and appropriate mathematical models. With the rapid development of computer science and theoretical quantum chemical study, it can speedily and precisely obtain the quantum chemical parameters of compounds by computation. Moreover, these parameters, which have definite physical meaning, along with the introduction of the QSAR model can increase the chances of predicting the activities of the object compound and so quantum chemical theory is extensively applied in establishing QSAR models. The aim of this research is to find a new model which predicts the toxicity of chemicals with potent activities able to destroy K562 leukemic cell line using Genetic Algorithm-Multiple Linear Regression (GA-MLR) technique [5-8].

MATERIALS AND METHODS

Data sources

In this study, a data set of one hundred and twelve (112) anticancer compounds collected from the National Cancer Institute (NCI) database. These chemical structures were aligned with their respective bioactive component values on a 2D table after they were optimized at the density functional theory (DFT) level using Becke's three-parameter Lee-Yang-Parr hybrid functional (B3LYP) in combination with the 6-31G* basis set [9, 10]. The optimized structures were employed in the generation of quantum chemical and molecular descriptors. These were then divided into training and test sets by Kennard Stone algorithm [11]. The QSAR models were generated using the Genetic Function Approximation (GFA). The GFA technique is a conglomeration of Genetic Algorithm, Friedman's multivariate adaptive regression splines (MARS) algorithm and Holland's genetic algorithm to evolve population of equations that best fit the training set data [12, 13]. A distinctive feature of GFA is that it produces a population of models, instead of generating a single model, so do most other statistical methods. The established models were then subjected to internal and external validation and Y-randomization tests in order to institute their predictability and reliability [14].

Geometric optimization

Chemical structures of the compounds were drawn using the ChemDraw software (CambridgeSoft, 2010), while the molecular geometries were optimized using Spartan 14 software (Spartan 14v114) [15] at the density functional theory (DFT) level using Becke's three-parameter Lee-Yang-Parr hybrid functional (B3LYP) in combination with the 6-31G* basis set. The Spartan 14 software also resulted in the generation of a set of quantum chemical descriptors.

Descriptors calculation

The low energy conformers were then submitted for further generation of an additional set of molecular descriptors using the software "PaDel-Descriptor version 2.20" [16]. Different physicochemical descriptors were calculated for each molecule presented in Table 1. These descriptors included electronic, spatial, structural, and topological chemical descriptors. These were combined to the set of quantum chemical descriptors obtained from the low energy conformer of the structures generated by Spartan 14 Wavefunction software.

Data Pre-Treatment / Feature Selection

It is observed that constant value and highly correlated descriptors may cause difficulties in forming QSAR models, hence the predictability and generalization of the model fails under these conditions. In order to overcome this problem, the pre-processing for the generated molecular descriptors was done by removing descriptors having constant value and pairs of variables with correlation coefficient greater than 0.7 using " ***Data Pre-Treatment GUI 1.2"*** tool that uses V-WSP algorithm [17], [18].

Dataset Division

The dataset of eighty-five (85) molecular structures was split into training and test set by **Kennard Stone algorithm** technique using the software "Dataset Division GUI 1.2" [19]. This is an application tool used to perform rational selection of training and test set from the data set.

QSAR Model Development and Validation

The QSAR model were developed from the training set compounds where the independent variables (quantum chemical and molecular descriptors) and the dependent (response) variable (pGI_{50} and pLC_{50}) were subjected to multivariate analysis by Genetic Function Approximation (GFA) technique using the material studio software. GFA measures the fitness of a model during the evolution process by calculating the Friedman lack-of-fit (LOF). In Materials Studio, LOF is calculated using the expression:

$$LOF = \frac{SSE}{\left(1 - \frac{C + dp}{m}\right)^2}$$

Where ***SSE*** is the sum of squares of errors, ***C*** is the number of terms in the model, other than the constant term, and is a user-defined smoothing parameter, ***dp*** is the total number of descriptors contained in all model terms (again ignoring the constant term) and ***m*** is the number of samples in the training set [20].

Internal Model Validation

The developed models were validated internally by leave- one- out (LOO) cross- validation technique. In this technique, one compound is eliminated from the data set at random in each cycle and the model is built using the rest of the compounds. The model formed is

used for predicting the activity of the eliminated compound. The process is repeated until all the compounds are eliminated once. The cross-validated squared correlation coefficient, R^2_{cv} (Q^2) was calculated using the expression:

$$Q^2 = 1 - \frac{\sum(Y_{Obs} - Y_{Pred})^2}{\sum(Y_{Obs} - \bar{Y})^2}$$

Where Y_{OBS} represents the observed activity of the training set compounds, Y_{pred} is the predicted activity of the training set compounds and $\bar{Y}$ corresponds to the mean observed activity of the training set compounds.

External Model Validation

External validation was employed in order to determine the predictive capacity of the developed model as judged by its application for the prediction of test set activity values and calculation of predictive R^2(R^2pred) value as given by the expression:

$$R^2_{pred} = 1 - \frac{\sum\left(Y_{pred(Test)} - Y_{(Test)}\right)^2}{\sum\left(Y_{(Test)} - \bar{Y}_{(Training)}\right)^2}$$

Where $Y_{pred(Test)}$ and $Y_{(Test)}$ indicate predicted and observed activity values respectively, of the test compounds. $\bar{Y}_{(Training)}$ indicates the mean activity value of the training set. R^2_{pred} is the predicted correlation coefficient calculated from the predicted activity of all the test set compounds. It has been found that R^2_{pred} may not be sufficient to be indicated the external predictability of a model since its value is controlled by $\sum\left(Y_{(Test)} - \bar{Y}_{(Training)}\right)^2$.

RESULT AND DISCUSSION

Geometry Optimization and Descriptors Calculation

The observed activities for the various data sets were transformed to obtain a more uniformly distributed data as shown in Table 2. After minimization of the various compounds in the data set 32 descriptors were generated using the Spartan 14 software. These were combined to the 1875 descriptors generated using the paDEL software to give a total of 1907 descriptors.

Table 1: Experimental and Predicted toxicities (pLC_{50}) on different leukemia cell lines obtained with linear models based on GA-MLR technique.

Serial Number (ID)	NSC	K562 (Experimental pLC_{50})	K562 (Predicted pLC_{50})
1	606172	4.0	4.199
2	606173	4.0	4.013
3	643833	4.9	4.361
4	27640	2.6	2.815
5	95678	3.0	3.140
6	264880	2.6	2.592
7	127716	3.4 [b]	1.639
8	102816	2.7	3.065
9	107392	2.8	3.046
10	249910	4.0	4.203
11	629971	4.0	3.508
12	163501	3.0 [b]	3.125
13	406042	4.0 [b]	3.538
14	71851	2.3	2.951
15	132483	4.0	3.844
16	184692	4.0	4.427
17	134033	4.0 [b]	4.062
18	308847	3.6	3.457
19	623017	4.0	4.053
20	355644	4.1	3.946
21	303812	4.0	4.160
22	63878	3.3	2.635
23	167780	3.9 [b]	3.270
24	182986	3.7	3.906
25	139105	3.0	3.047
26	409962	3.4	3.105

27	71261	2.9	2.795
28	337766	4.3 [b]	4.167
29	368390	3.3 [b]	2.706
30	750	3.6 [b]	2.740
31	94600	4.0	4.209
32	295500	4.0	4.172
33	606985	4.0	3.846
34	295501	4.0	3.708
35	606499	4.0 [b]	4.168
36	606497	4.0 [b]	4.118
37	610459	4.0 [b]	4.043
38	610456	4.0 [b]	3.781
39	610457	4.0 [b]	4.957
40	610458	5.0 [b]	4.357
41	176323	4.0	4.082
42	95382	4.0	3.630
43	107124	4.1	4.025
44	100880	3.6	3.579
45	374028	4.0	4.179
46	618939	5.0	4.991
47	79037	3.3	3.279
48	3088	3.1	3.511
49	178248	2.9	3.009
50	338947	2.3 [b]	2.751
51	757	3.2	3.430
52	33410	4.9 [b]	3.677
53	357704	4.6	4.499
54	145668	3.0 [b]	2.707
55	348948	2.6 [b]	3.337
56	82151	4.2	4.247

57	267469	3.9	4.396
58	132313	3.8	3.221
59	126771	3.6	3.437
60	376128	*8.0	8.000
61	123127	4.7	4.417
62	73754	2.6	2.663
63	148958	3.0	3.259
64	364830	4.0	4.226
65	1895	2.0 [b]	2.187
66	329680	2.6	2.585
67	142982	4.2	4.107
68	32065	2.6	2.458
69	118994	2.6	2.423
70	153353	3.3 [b]	2.246
71	330500	4 [b]	4.145
72	249992	3.8	3.790
73	153858	4.0	3.668
74	8806	3.6	3.173
75	269148	4.1	4.322
76	740	3.6	3.412
77	174121	7.0	6.731
78	95441	3.6	3.432
79	26980	4.6	3.807
80	301739	4.9	4.877
81	353451	2.9	3.464
82	354646	5.0	4.962
83	224131	2.0	1.988
84	268242	*4.3	4.712
85	762	3.4	3.321
86	349174	3.6	4.015

87	95466	2.9	2.629
88	344007	3.0	3.180
89	135758	3.0	3.014
90	25154	3.3	3.742
91	56410	3.1	3.747
92	143095	2.3	2.567
93	366140	4.4	4.008
94	51143	2.0	2.180
95	332598	4.0	3.489
96	164011	4.1	3.988
97	172112	3.6	3.637
98	125973	4.6	3.895
99	296934	2.6 [b]	3.727
100	363812	*3.6	3.546
101	361792	4.0	3.649
102	752	3.6	3.868
103	6396	3.0	2.951
104	9706	4.0	3.845
105	352122	3.7	3.739
106	83265	3.9	3.499
107	34462	3.3	3.577
108	49842	5.6	5.458
109	67574	3.2	3.932
110	122819	4.6	4.313
111	141540	3.0	3.585
112	102627	2.0	2.132

Where superscript **letters (b)** represent test sets for the leukemia cell line, and ***** identifies compounds found outside the applicability domain (outliers) of the model, while **NSC** - represents the NCI's internal identification number of the database entry, and is derived from (part of) the acronym of the Cancer Chemotherapy National Service Center (CCNSC).

Feature Selection and Data Division

The created descriptor outcomes were exposed to data pre-treatment where descriptors with constant value and pairs of variables with correlation coefficient greater than 0.7 were removed using the software ***"Data Pre-Treatment GUI 1.2"*****.** This was done to be devoid of the model of intercorrelated descriptors. Data pre-treatment resulted in 681 descriptors from 1907 descriptors, thus removing 1226 invariable and highly correlated descriptors. Data division using "Dataset Division GUI 1.2" tool resulted in 90 molecular compounds (covering about 80% of the entire compounds) in the training set and 22 compounds (covering about 20% of the entire compounds) in the test set.

Model Development and Validation

About two hundred and fifty models were generated from the training set by Genetic Function Approximation using the Material Studio Software and the best model based on internal validatory statistical parameters was selected for their toxicity (LC_{50}). The developed model and the description of the molecular descriptors were shown in the equation pLC_{50} below with the model statistics. The predicted values for the training set by the QSAR model was generated by the Material Studio Software, while the predicted test set values was calculated using MSExcel 2013 [21] as reported in Table 2. The results for the model validation of the developed models are given as follows.

$$\begin{aligned} p\mathrm{LC}_{50} = \; & 6.602\,(\mathbf{Secondary\ butyl}) - 1.513\,(\mathbf{E-LUMO}) - 0.892\,(\mathbf{ALogp2}) \\ & + 1.560\,(\mathbf{GATS5p}) - 2.566\,(\mathbf{minHBint7}) + 0.795\,(\mathbf{maxHBint7}) \\ & - 0.539\,(\mathbf{maxHBint8}) + 1.503\left(\mathbf{ETA_{EtaP_L}}\right) + 1.159\,(\mathbf{nF10Ring}) \\ & + 4.269\,(\mathbf{WPSA-3}) - 3.795\,(\mathbf{RDF140u}) + 1.274\,(\mathbf{RDF145m}) + 3.079 \end{aligned}$$

$$N_{train} = 90, \quad R^2_{train} = 0.888,\ adjR^2_{train} = 0.871,\ F_{train} = 50.976, \quad Q^2_{CV} = 0.845,$$

$$N_{test} = 22,\ \text{Outliers} = 03$$

The high calculated Q^2_{LOO} value (0.845) for pLC_{50} proposes a good internal validation. A second validation method was also developed on the basis of an external validation method, here the test set constituting 20% of the data set were subjected to the developed model and the

result were found promising, since its value 0.532 which was higher than the standard value 0.50 for the toxicity model.

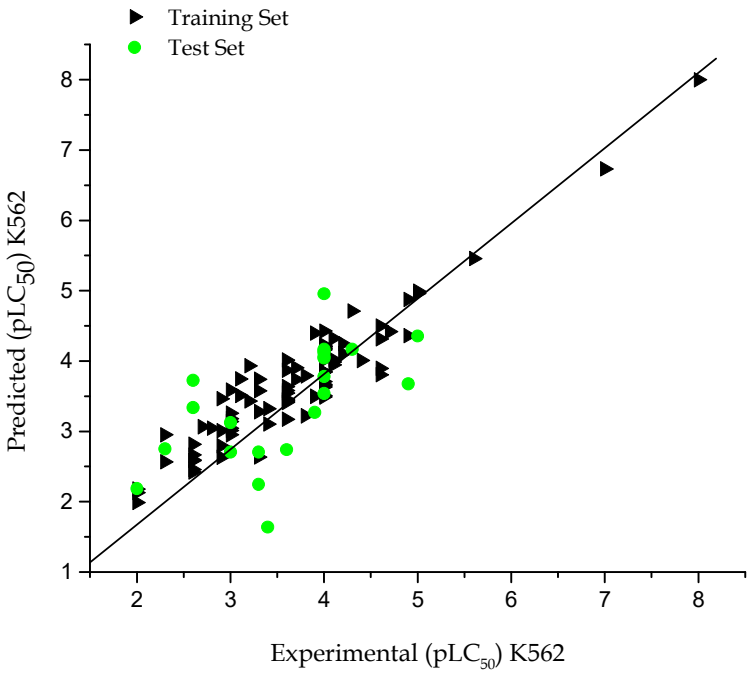

Figure 1: The predicted toxicity values (pLC_{50}) against the experimental values for the training and test sets of the compounds on K562 leukemia cell line.

These values indicate the robustness and stability of the constructed models, as can be seen that the model did not show any proportional and systematic errors, because the propagation of the residuals on both sides of zero is random. The built model was used to predict the test set data, and the prediction results are given in Table 1. The predicted values for pLC_{50} for the compounds in the training and test sets using pLC_{50} equation were plotted against the experimental pLC_{50} values in Figure 1, the calculated values for the pLC_{50} is in good agreement with those of the experimental values. Also, the plot of the standardized residual and leverages values for pLC_{50} is shown in Figure 2.

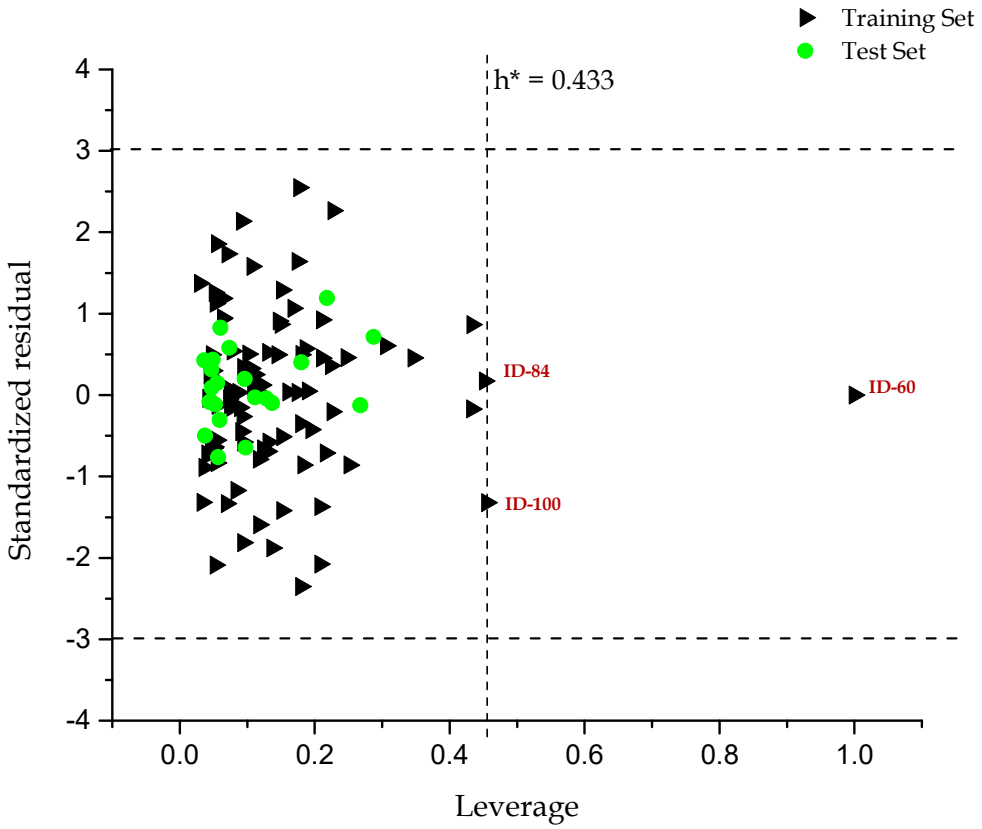

Figure 2: The Williams plot, the plot of the standardized residuals versus the Toxicity (pLC_{50}) leverage value for K-562 dataset.

The Williams plot in Figure 2 shows that the only three compounds were found outside the applicability domain of the molecule, these compounds with ID numbers 60, 84 and 100 were part of the training set. The plot indicates that these compounds structurally different, that is these compounds found outside the threshold value h*, have very few of the chemical descriptors which could be related to those in the model when compared to other compounds within the complete data set.

Table 2: External Validation Result for K-562 cell line.

Model biasness test	Systematic Error Result	Absent
Classical Metrics (for 100% data)	**R^2Test(100% data)**	0.5316
	R0^2Test(100% data)	0.4473
	Q2F1(100% data)	0.4268
	Q2F2(100% data)	0.4255
	Scaled Avg.Rm^2(100% data)	0.4003
	Scaled DeltaRm^2(100% data)	0.0755
	CCC(100% data)	0.7137
Error-based metrics (for 100% data)	**RMSEP(100% data)**	0.5769
	SD(100% data)	0.3636
	SE(100% data)	0.0813
	MAE(100% data)	0.4552

The external validation of the model in Table 2, showing that the mean absolute error (MAE) value is 0.455. Since the value is less than unity, deductions could be made that the predictions are close to the experimental outcomes and thereby supporting the value of the regression coefficient of the predicted test set (0.532), other classical statistical metrics such as Q^2_{F1} and Q^2_{F2} presented in Table 2, supports the result already stated in the discussion.

Interpretation of descriptors

Secondary butyl is a 2D molecular descriptor used in the model, it's defined as the number of secondary butyl group found in potent anticancer compounds. The mean effect reported in Table 3 indicates that the increase presence of this property diminishes the toxicity property of these molecules. Chemical descriptors like E LUMO and ALogp2 defined as energy of lowest occupied molecular orbital and square of AlogP respectively were also used in modelling the pLC50 property of these compounds gave a negative contribution to the model (-1.123 and -0.340).

GATs5p is 2D autocorrelation defined as Geary autocorrelation - lag 5 / weighted by polarizabilities, the descriptor was first stated by Todeschini and Consonni [22], in the book titled Molecular descriptors for chemoinformatics. It is an autocorrelation type descriptor depending on the polarizing ability of the active sites of a chemical drug compound. The descriptor was found to contribute positively to the model which is owned to the value of its

mean effect. The mean effect of GATs5p indicates that its presence decreases toxicity in anticancer drugs.

minHBint7, maxHBint7 and maxHBint8 are 2D Atom type electrotopological state molecular descriptors defined as Minimum E-State descriptors of strength for potential Hydrogen Bonds of path length 7, Maximum E-State descriptors of strength for potential Hydrogen Bonds of path length 7 and Maximum E-State descriptors of strength for potential Hydrogen Bonds of path length 8, respectively. Their mean effect was calculated and reported respectively as -1.637, 0.351 and -0.226. The mean effects of minHbint7 and maxHbint8 were negative indicating their direct involvement with the toxicity of the modeled compounds. The value of minHBint7 was most significant of all the three E-state type descriptors related to specific hydrogen bonds in a certain path length.

ETA_EtaP_L is a 2D Extended topochemical atom type descriptor defined as Local index Eta_local relative to molecular size, hence this topochemical descriptor is depend on the molecular size of the molecules. The mean effect given as 1.054 indicates that an increase in the molecular size of this type descriptor will decrease the toxicity of anticancer compounds.

nF10Ring, WPSA-3 and RDF140u which are the final descriptors in the model give the contributions 0.454, 1.657 and -0.705 respectively. They defined as the number of 10-membered fused rings, PPSA-3 multiplied by the total molecular surface area/1000 and the radial distribution function -140/unweighted respectively. WPSA-3 was found to give the highest contribution in the model, its value correlates with that of ETA_EtaP_L significantly, this similarity can be seen from their meanings which is a subject of the molecular size of this active compounds, thereby completing agreeing with the fact that large size molecules have less tendency of being toxic when used as anticancer drugs.

Table 3: Specification of entered descriptors in genetic algorithm multiple regression model of K-562.

Descriptors	**Definition**	**ME**
Secondary butyl	Number of secondary butyl group	0.119
E LUMO	Energy of lowest occupied molecular orbital	-1.123
ALogp2	Square of ALogP	-0.340
GATS5p	Geary autocorrelation - lag 5 / weighted by polarizabilities	1.227
minHBint7	Minimum E-State descriptors of strength for potential Hydrogen Bonds of path length 7	-1.637
maxHBint7	Maximum E-State descriptors of strength for potential Hydrogen Bonds of path length 7	0.351
maxHBint8	Maximum E-State descriptors of strength for potential Hydrogen Bonds of path length 8	-0.226
ETA_EtaP_L	Local index Eta_local relative to molecular size	1.054
nF10Ring	Number of 10-membered fused rings	0.454
WPSA-3	PPSA-3 * total molecular surface area / 1000	1.657
RDF145m	Radial distribution function - 145 / weighted by relative mass	0.554
RDF140u	Radial distribution function - 140 / unweighted	-0.705

CONCLUSION

The pLC_{50} for the leukemia cell line K562 was positively modelled for a sequence of anticancer drugs collected from NCI library, using highly interconnected descriptors computed using paDEL software, the statistical parameters of the model satisfy the criteria proposed by Tropsha, Roy and Grammatica for validating QSAR models. A few descriptors such as WPSA-3, minHBint7, GATS5p, E LUMO and ETA_EtaP_L with mean effects of 1.657, -1.637, 1.227, -1.123 and 1.054 respectively, were found to be significantly responsible for the toxicity of the compounds used in the data set.

COMPETING INTERESTS

The authors have declared no conflict of interest.

REFERENCES

1. Speck-Planche A, Kleandrova VV, Luan F, Cordeiro MNDS. Rational drug design for anti-cancer chemotherapy: Multi-target QSAR models for the in silico discovery of anti-colorectal cancer agents. Bioorganic & Medicinal Chemistry. 2012 Aug;20(15):4848–55. DOI: 10.1016/j.bmc.2012.05.071.

2. Dunnington BD, Schmidt JR. Molecular bonding-based descriptors for surface adsorption and reactivity. Journal of Catalysis. 2015 Apr;324:50–8. DOI: 10.1016/j.jcat.2015.01.017.

3. Andrada MF, Vega-Hissi EG, Estrada MR, Garro Martinez JC. Application of k-means clustering, linear discriminant analysis and multivariate linear regression for the development of a predictive QSAR model on 5-lipoxygenase inhibitors. Chemometrics and Intelligent Laboratory Systems. 2015 Apr;143:122–9. DOI: 10.1016/j.chemolab.2015.03.001.

4. Alanazi AM, Abdel-Aziz AA-M, Al-Suwaidan IA, Abdel-Hamide SG, Shawer TZ, El-Azab AS. Design, synthesis and biological evaluation of some novel substituted quinazolines as antitumor agents. European Journal of Medicinal Chemistry. 2014 May;79:446–54. DOI: 10.1016/j.ejmech.2014.04.029.

5. Gagic Z, Nikolic K, Ivkovic B, Filipic S, Agbaba D. QSAR studies and design of new analogs of vitamin E with enhanced antiproliferative activity on MCF-7 breast cancer cells. Journal of the Taiwan Institute of Chemical Engineers. 2016 Feb;59:33–44. DOI: 10.1016/j.jtice.2015.07.019.

6. Chen B, Zhang T, Bond T, Gan Y. Development of quantitative structure activity relationship (QSAR) model for disinfection byproduct (DBP) research: A review of methods and resources. Journal of Hazardous Materials. 2015 Dec;299:260–79. DOI: 10.1016/j.jhazmat.2015.06.054.

7. Speck-Planche A, Kleandrova VV, Luan F, Cordeiro MNDS. Chemoinformatics in anti-cancer chemotherapy: Multi-target QSAR model for the in silico discovery of anti-breast cancer agents. European Journal of Pharmaceutical Sciences. 2012 Aug;47(1):273–9. DOI: 10.1016/j.ejps.2012.04.012.

8. Zhao L, Xiang Y, Song J, Zhang Z. A novel two-step QSAR modeling work flow to predict selectivity and activity of HDAC inhibitors. Bioorganic & Medicinal Chemistry Letters. 2013 Feb;23(4):929–33. DOI: 10.1016/j.bmcl.2012.12.067.

9. Benarous N, Cherouana A, Aubert E, Durand P, Dahaoui S. Synthesis, characterization, crystal structure and DFT study of two new polymorphs of a Schiff base (E)-2-((2,6-dichlorobenzylidene)amino)benzonitrile. Journal of Molecular Structure. 2016 Feb;1105:186–93. DOI: 10.1016/j.molstruc.2015.10.037.

10. Bauernschmitt R, Ahlrichs R. Treatment of electronic excitations within the adiabatic approximation of time dependent density functional theory. Chemical Physics Letters. 1996 Jul;256(4–5):454–64. DOI: 10.1016/0009-2614(96)00440-X.

11. Kennard RW, Stone LA. Computer Aided Design of Experiments. Technometrics. 1969 Feb;11(1):137–48. DOI: 10.1080/00401706.1969.10490666.

12. Deb K, Pratap A, Agarwal S, Meyarivan T. A fast and elitist multiobjective genetic algorithm: NSGA-II. IEEE Transactions on Evolutionary Computation. 2002 Apr;6(2):182–97. DOI: 10.1109/4235.996017.

13. Leardi R, Boggia R, Terrile M. Genetic algorithms as a strategy for feature selection. Journal of Chemometrics. 1992 Sep;6(5):267–81. DOI: 10.1002/cem.1180060506.

14. Tropsha A. Best Practices for QSAR Model Development, Validation, and Exploitation. Molecular Informatics. 2010 Jul 6;29(6–7):476–88. DOI: 10.1002/minf.201000061.

15. Hehre WJ, Huang WW. Chemistry with computation: an introduction to SPARTAN. Irvine: Wavefunction, Inc.; 1995. ISBN: 9780964349520.

16. Yap CW. PaDEL-descriptor: An open source software to calculate molecular descriptors and fingerprints. Journal of Computational Chemistry. 2011 May;32(7):1466–74. DOI: 10.1002/jcc.21707.

17. Panagos P, Meusburger K, Ballabio C, Borrelli P, Alewell C. Soil erodibility in Europe: A high-resolution dataset based on LUCAS. Science of The Total Environment. 2014 May;479–480:189–200. DOI: 10.1016/j.scitotenv.2014.02.010.

18. Roy K, Kar S, Ambure P. On a simple approach for determining applicability domain of QSAR models. Chemometrics and Intelligent Laboratory Systems. 2015 Jul;145:22–9. DOI: 10.1016/j.chemolab.2015.04.013.

19. Barretina J, Caponigro G, Stransky N, Venkatesan K, Margolin AA, Kim S, et al. The Cancer Cell Line Encyclopedia enables predictive modelling of anticancer drug sensitivity. Nature. 2012 Mar 28;483(7391):603–307. DOI: 10.1038/nature11003.

20. Abdel-Atty MM, Farag NA, Kassab SE, Serya RAT, Abouzid KAM. Design, synthesis, 3D pharmacophore, QSAR, and docking studies of carboxylic acid derivatives as Histone Deacetylase inhibitors and cytotoxic agents. Bioorganic Chemistry. 2014 Dec;57:65–82. DOI: 10.1016/j.bioorg.2014.08.006.

21. Carlberg C. Statistical analysis: microsoft excel 2013. 1st edition. Indianapolis, IN: Que Pub; 2014. ISBN: 9780789753113.

22. Todeschini R, Consonni V. Molecular descriptors for chemoinformatics. Weinheim: Wiley-VCH; 2009. (Methods and principles in medicinal chemistry). ISBN: 9783527318520.

Türkçe Öz ve Anahtar Kelimeler

Genetik Algoritma-Çoklu Lineer Regresyon Kullanarak K562 Kanser Hücre Dizisine Karşı Bazı Aktif Bileşiklerin Zehirlilik Modellemesi

David Ebuka Arthur, Adamu Uzairu, Paul Mamza, Abechi Eyeji Stephen, Gideon Shallangwa

Öz: Bu araştırmada antikanser bileşiklerinin K562 hücre dizisi üzerindeki zehirliliğinin modellemesi araştırılacaktır, veri serisini oluşturan 112 bileşik, modelin sırasıyla geliştirilmesi ve doğrulanması için eğitim ve test setleri olarak ayrılmıştır. İç ve dış doğrulama parametresi olan R^2, eğitim ve test serisi için 0,845 ve 0,5316 olarak tespit edilmiştir, bu da modelin sağlamlığını ve bileşiklerin zehirliliğini tahmin etme yeteneğini belirlemek için kullanılmıştır. Modelin ortalama etkisinin %50 kadarından WPSA-3 ve minHBint7 moleküler tarifçi sorumludur.

Anahtar kelimeler: QSAR; modelleme; dış doğrulama; moleküler tarifiçiler; genetik algoritma.

Sunulma: 05 Ekim 2016. **Düzeltme:** 17 Kasım 2016. **Kabul:** 21 Kasım 2016.

JOTCS Journal of the Turkish Chemical Society Section: A Chemistry

TURKISH CHEMICAL SOCIETY

Sorption Study of Methylene Blue on Activated Carbon Prepared from *Jatropha curcas* and *Terminalia catappa* Seed Coats

Ismaila Olalekan Saheed[1*], Folahan Amoo Adekola[2] and Gabriel Ademola Olatunji[3]

[1]Department of Chemical, Geological and Physical Sciences, College of Pure and Applied Sciences, Kwara State University, Malete, P.M.B 1530, Ilorin, Nigeria
[2,3]Department of Industrial Chemistry, Faculty of Physical Sciences, University of Ilorin, P.M.B. 1515, Ilorin, Nigeria

[*]Corresponding author. Ismaila, Saheed. e-mail address: [1*]ismailolalekan2@gmail.com

Abstract: This research work targets the effectiveness of the prepared activated carbon from *Jatropha curcas* and *Terminalia catappa* seed coats for adsorption of methylene blue (MB) from aqueous solution. The prepared *Jatropha* activated carbon (JAC) and *Terminalia* activated carbon (TAC) were characterised using Fourier Transform Infrared Spectroscopy (FTIR), Scanning electron microscopy (SEM), and Brunauer- Emmett-Teller (BET) surface area analysis. Effects of initial concentration, pH, contact time, adsorbent dose and temperature on the adsorption experiments were studied and the concentration of methylene blue was monitored using spectrophotometry. The adsorption capacities of these adsorbents were found to be 37.84 mg/g and 17.44 mg/g for methylene blue uptake by JAC and TAC, respectively. The experimental data were analysed using Langmuir, Freundlich, and Dubinin-Radushkevich isotherms. The data fitted best into Langmuir isotherm for Methylene blue-JAC and Methylene blue-TAC systems. The kinetic studies fitted into pseudo second order kinetics model. The process chemistry was exothermic.

Keywords: Adsorption; activated carbon; methylene blue; kinetics; thermodynamics.

Submitted: November 14, 2016. **Revised:** November 23, 2016. **Accepted:** December 07, 2016.

Cite this: Saheed I, Adekola F, Olatunji G. Sorption Study of Methylene Blue on Activated Carbon Prepared from Jatropha curcas and Terminalia catappa Seed Coats. JOTCSA. 2017;4(1):375–94.

DOI: To be assigned.

*Corresponding author. E-mail: ismailolalekan2@gmail.com

INTRODUCTION

Organic dyes are used for textile dyeing and other purposes. Wastewaters emanating from these activities are discharged into aquatic environment as industrial wastes. These industrial effluents form part of the major environmental pollutants which in turn affect the survival of living organisms in the ecosystem [1]. Therefore, wastewaters from dyeing activities have to be treated for the protection of life and remediation of environmental pollution. Activated carbon is a known adsorbent of widely applied in the purification of polluted environment, treatment of gaseous effluents discharged from industry, and has additionally been effective for the removal of coloured substances in wastewater [2]. To improve the effluent quality before discharging into the environment, physical and/or chemical treatments comprising adsorption, photocatalytic degradation, electrochemical methods or reverse osmosis are necessary. Adsorption using activated charcoal is simple, cost effective, and efficient in removing organic and inorganic contaminants [3].

Activated carbon can be prepared from various wellsprings of biomaterials. The nature of the raw material utilised, activation process adopted, and processing conditions decide the properties and effectiveness of the activated carbon. The activation processes also have an influence on the surface properties of the activated charcoal [4]. Chemical activation uses chemical agents usually acids, bases or salts as activating agents while physical activation involves the use of carbon dioxide and steam as activating agents [4].

This research focuses on determining the potential of prepared activated carbon from seed coat of *Terminalia catappa* and *Jatropha curcas* for the removal of methylene blue (MB) in aqueous medium.

MATERIALS AND METHODS

Preparation of adsorbents

Termilania catappa and *Jatropha curcas* fruits were collected from University of Ilorin campus and a private estate at Oke Oyi, Kwara state respectively. The seed coats were appropriately washed, air-dried, and broken to pieces. The seed coats were then charred at 500 °C for 1h 30 minutes. The carbonised materials were ground and sieved with mesh that permits the entry of particles size < 90 μm [5]. The char was soaked in 0.5 M NaOH for 24 hours and then separated, washed to neutral pH, and air-dried. The subsequent material was later heated for 1 hour at a temperature of 200 °C to complete the process. The prepared activated carbons JAC and TAC were cooled and stored [6].

Characterization of the adsorbents

Proximate analysis

Moisture content: 0.20 g of the sample was heated at 105 °C for 2 hrs. The mass of the sample was determined after heating. *Ash content*: 0.20 g sample was heated at 750 °C for 1.5 h. The mass of the ash was determined after heating. *Bulk density*: 5.00 g of sample was weighed into a measuring cylinder and tapped until a steady volume is obtained. The mass was obtained by weighing [7].

Instrumental analysis

Morphological characterisation of the prepared JAC and TAC was done using SEM magnifying instrument (ASPEX 3020). 8400S Fourier transform infrared spectrometer was utilised to ascertain the functional groups on JAC and TAC. An ASAP 2020 BET instrument was employed to decide the BET surface area, pore volume and diameter of JAC & TAC [8].

Preparation of adsorbate solutions

Stock solution of 500 mg/L of methylene blue (see Figure 1 for the structure) was prepared and the required concentrations were obtained from the stock via serial dilution using deionised water. The concentration of MB was monitored using UV-Visible spectrophotometry (Beckman Coulter DU 730) at 664 nm. A calibration curve with the concentration extending from 5 to 100 mg/L was obtained [9].

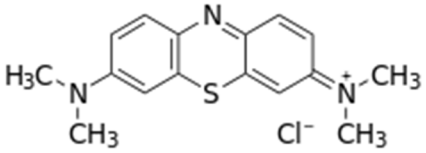

Figure 1: The structure of methylene blue.

Batch adsorption experiment

The influence of initial concentration, pH, contact time, adsorbent dose, and temperature on the adsorption of MB onto JAC and TAC were examined. A series of 20 mL MB solutions of different concentrations was prepared at controlled temperature of 28±2 °C. A 0.02 g of activated carbon was contacted with each solution and agitated in a mechanical shaker for 2 hours at 200 rpm. After centrifuging for 2 min, the final MB concentration in solution was monitored by UV- Vis spectrophotometer at the maximal absorbance wavelength of 664 nm. The amount of MB adsorbed was determined using Equation 1.

$$q_e = \frac{C_0 - C_e}{M} X\ V \qquad \text{(Eq. 1)}$$

where q_e denotes the quantity of MB adsorbed (mg/g), C_0 represents initial concentration of the MB (mg L^{-1}), C_e is the equilibrium concentration of the MB (mg L^{-1}) at time t, V is the

volume of the solution used (in litres, L) and m is the mass of the adsorbent utilised (g) [10, 11].

Adsorption isotherms

Freundlich isotherm

The linearised form of the equation is given by:

$$\log q_e = logK_f + \frac{1}{n}\, logC_e \qquad \text{(Eq. 2)}$$

q_e is the quantity adsorbed at equilibrium (mg/g), C_e is the equilibrium concentration of adsorbate (mg/L), 1/n is a heterogeneity factor, K_f is Freundlich's constant (mg/g) [12].

Langmuir isotherm

The linearised form of the Langmuir equation and the separation factor, R_L are given by Equations 3 and 4, respectively.

$$\frac{c_e}{q_e} = \frac{1}{k_L q_{max}} + \frac{1}{q_{max}} c_e \quad \text{....} \qquad \text{(Eq. 3)}$$

$$R_L = \frac{1}{1+K_L C_0} \qquad \text{.....} \qquad \text{(Eq. 4)}$$

Where C_e is the equilibrium concentration of the adsorbate (mg/L), q_e the amount adsorbed per adsorbent mass (mg/g), K_L is the Langmuir's constant and q_{max} is the maximal adsorption efficiency (mg/g). $0 < R_L < 1$ the adsorption is feasible [13].

Dubinin-Radushkevich isotherm

The D-R isotherm equation describes adsorption through multi-layer condensation [14, 15]. The linearised form is given by Equation 5:

$$In\ q_e = In\ q_d - \beta\ \varepsilon^2 \quad \text{.....} \qquad \text{(Eq. 5)}$$

where q_d is the D-R constant which relates to maximum adsorption efficiency (mg/g), β is a constant corresponding to free energy (mol^2/J^2) and ε is the Polanyi's potential which is defined in Equation 6 as:

$$\varepsilon = RT\ In\left[1 + \frac{1}{C_e}\right] \quad . \qquad \text{....(Eq. 6)}$$

where R is the gas constant and T is the absolute temperature. The mean free energy E is given by Equation 7 [14, 15].

$$E = \frac{1}{\sqrt{2\beta}} \quad \text{...} \qquad \text{..(Eq. 7)}$$

Adsorption kinetics

Kinetics study of the sorption experiment determines the adsorption efficiency and its potential applications. Pseudo first-order [16] and pseudo second-order [17] kinetics were used to assess the data obtained. The integrated forms of the equations are given by Equations 8 and 9, respectively:

$$log(q_e - q_t) = logq_e - \frac{k_1 t}{2.303} \quad \text{(Eq. 8)}$$

$$\frac{t}{q_t} = \frac{1}{k_2 q_e^2} + \frac{1}{q_e} t \quad \ldots \quad \text{.(Eq. 9)}$$

k_1 (min^{-1}) and k_2 (g/mg.min) are rate constants of pseudo first-order and pseudo second order respectively. q_e and q_t are the amount of dye adsorbed (mg/g) at equilibrium and at time t, respectively.

Adsorption thermodynamics

The thermodynamics parameters [18,19] were evaluated using Equations 10 and 11.

$$\Delta G^0 = -RT\ In\ K \quad \text{(Eq. 10)}$$

$$In\ K = \frac{\Delta S^0}{R} - \frac{\Delta H^0}{RT} \quad \text{(Eq. 11)}$$

K is given as q_e/c_e, T is the temperature and R is the gas constant.

RESULT AND DISCUSSION

Characterization of the adsorbent

The results of the proximate analysis of JAC and TAC (see Table 1) uncover that the adsorbents could be utilised for adsorption purpose due to their low ash content (n=3, 0 ≤ %E ≤ 0.88). The SEM micrographs of prepared JAC and TAC (Figure 2a & 2b) reveal that the surface of the prepared activated carbons possesses cavities, pores, and rough surface structure. The surface is also hollowed and fragmented [20,21]. The results of BET surface area, pore volume and pore size of JAC are 50.29 m^2/g, 0.0265 cm^3/g and 21.1 Å, respectively, while that of TAC were found to be 75.70 m^2/g, 0.0476 cm^3/g and 25.1 Å, respectively. This indicates that the surface of JAC and TAC are overwhelmed with mesopores [22].

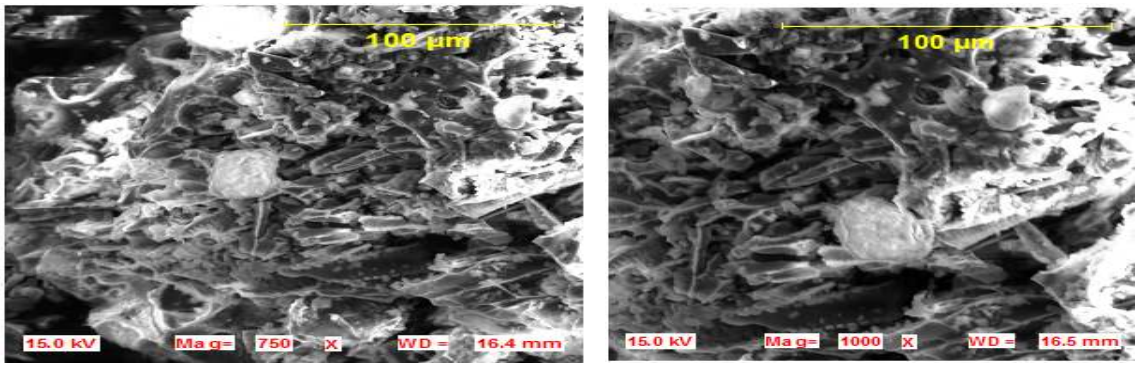

Figure 2(a): SEM image of JAC (left: mag=750; right: mag=1000).

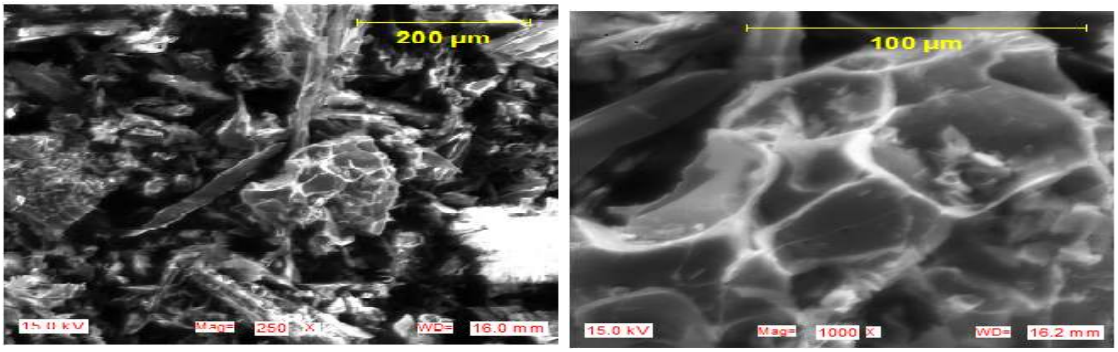

Figure 2(b): SEM image of TAC (left mag= 250; right: mag=1000).

Table 1: Proximate analysis of adsorbents and isothermal parameters for adsorption of MB onto JAC and TAC.

	Parameters	Values (JAC)	Values (TAC)
Proximate			
% Moisture Content		34	31.05
% Ash content		9.9	8.01
Bulk density (gcm^{-3})		1.33	2.00
Isotherms			
Langmuir	Q_{max} (mg/g)	44.05	23.26
	R_L	0.0182	0.172
	R^2	0.9916	0.9899
Freundlich	K_f (mg/g)	21.95	4.18
	n	2.62	2.24
	R^2	0.6935	0.9879
Dubinin-Radushkevich	β (mol^2/J^2)	$1x10^{-7}$	$2x10^{-6}$
	E ($Jmol^{-1}$)	$2.2x10^3$	500
	R^2	0.9627	0.8937

The FTIR spectra of JAC and TAC (Figure 3a & 3b) show a prominent signal at ~1570 cm^{-1} and 1370 cm^{-1} credited to graphitic structures that are expected to dominate activated carbons. The broad signal above 3400 cm^{-1} is attributed to OH stretching frequency in adsorbed water but also to surface OH groups not surprisingly for phenols, lactones, and carboxylic acid groups known to exist at the surface of activated carbon. The OH bending mode is usually observed around 1600 cm^{-1} and evidently adds to the broadening of the graphitic band. The signal at ~1200 cm^{-1} is allocated to the C-O stretching mode [23].

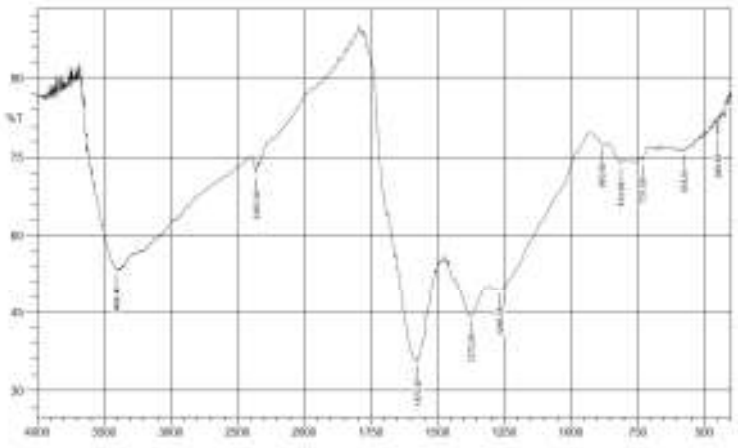

Figure 3(a): FTIR spectrum of JAC.

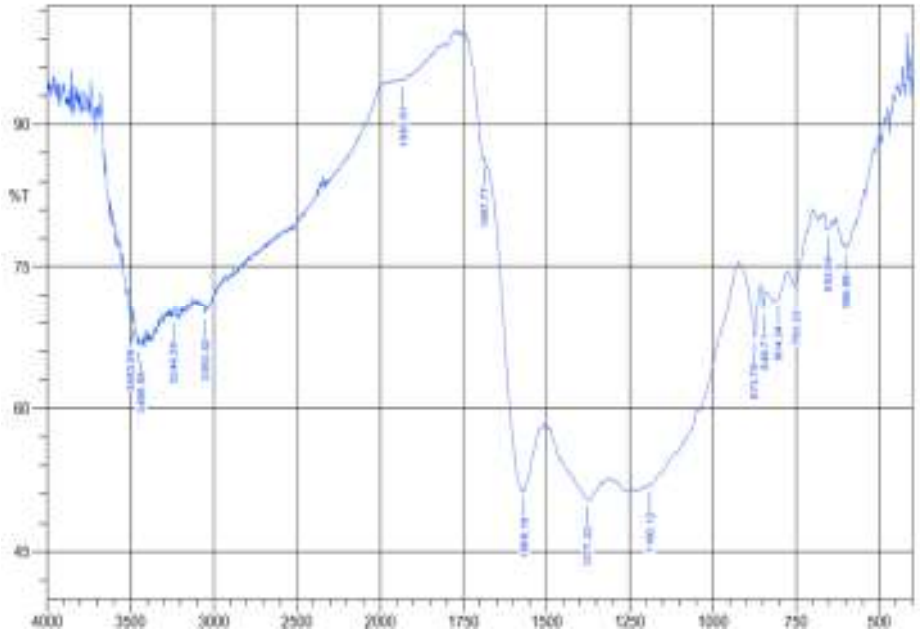

Figure 3(b): FTIR spectrum of TAC.

Effect of Initial Concentration

The quantity of MB adsorbed on JAC and TAC rises with increase in initial concentration of dye until saturation is reached (see Figure 4a). The adsorption limit of JAC is observed to be higher than that of TAC [24].

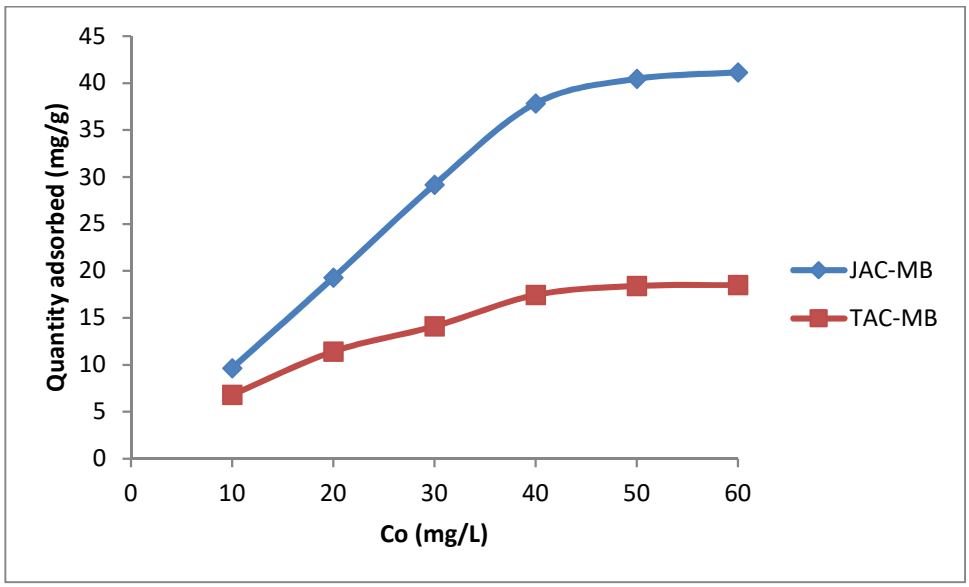

Figure 4(a): Effect of initial concentration (Conditions: pH=6.8, adsorbent dose=0.02 g, T=28±2°C, agitation time=120 min, agitation speed=200 rpm, n=3, 0 ≤ %E ≤ 0.90).

Effect of pH

The influence of pH on sorption of MB onto JAC and TAC was analysed (Figure 4b). The adsorption of MB under these conditions increases significantly as the pH increases from 2 to 4. However, at higher pH, the adsorption of dye molecules increases inconsequentially in JAC-MB system but diminishes due to the repulsive force between the adsorbent and adsorbate in TAC-MB system [25].

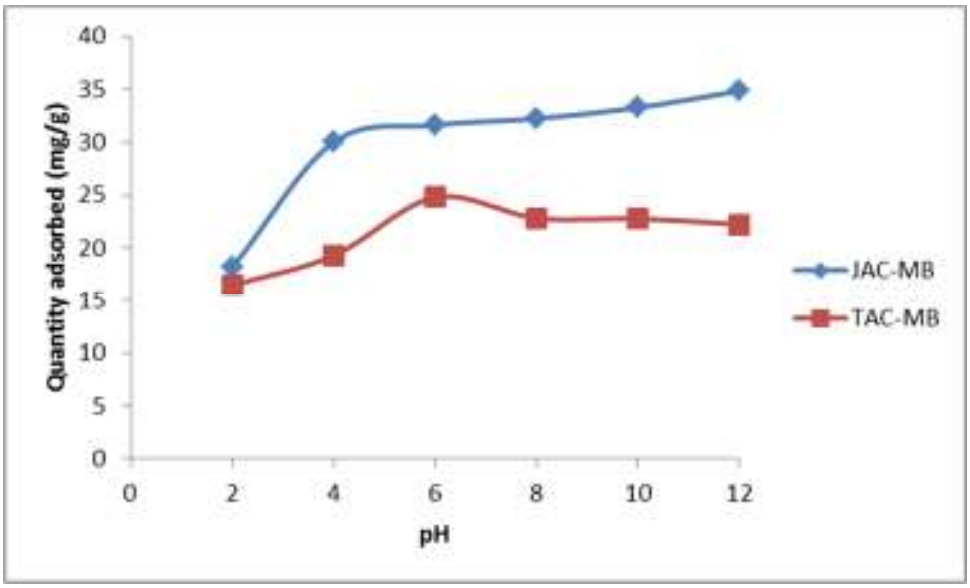

Figure 4(b): Effect of pH (Conditions: concentration= 40 mg/L, adsorbent dose=0.02 g, T=28±2°C, agitation time=120 min, agitation speed=200 rpm, n=3, 0 ≤ %E ≤ 0.92).

Effect of contact time

The progress of MB adsorption demonstrates a fast take-up at lower contact time (see Figure 4c). The quantity adsorbed increases thereafter until equilibrium was reached and no change in the quantity adsorbed could be seen beyond this point [26].

Effect of adsorbent dose

The influence of adsorbent dose on sorption experiment is presented in Figure 4d. The quantity of MB adsorbed diminishes with increase in dosage which shows that increasing the dose of adsorbent makes adsorbate molecules circulated over a larger amount of adsorbent [27].

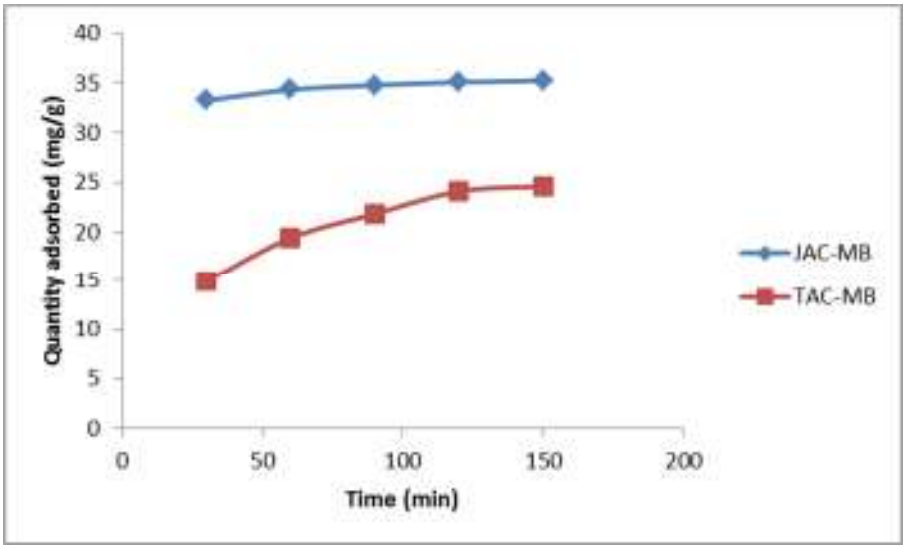

Figure 4(c): Effect of contact time (Conditions: concentration=40 mg/L, T=28±2°C, adsorbent dose=0.02 g, agitation time=120 min, agitation speed=200 rpm, n=3, 0 ≤ %E ≤ 0.90).

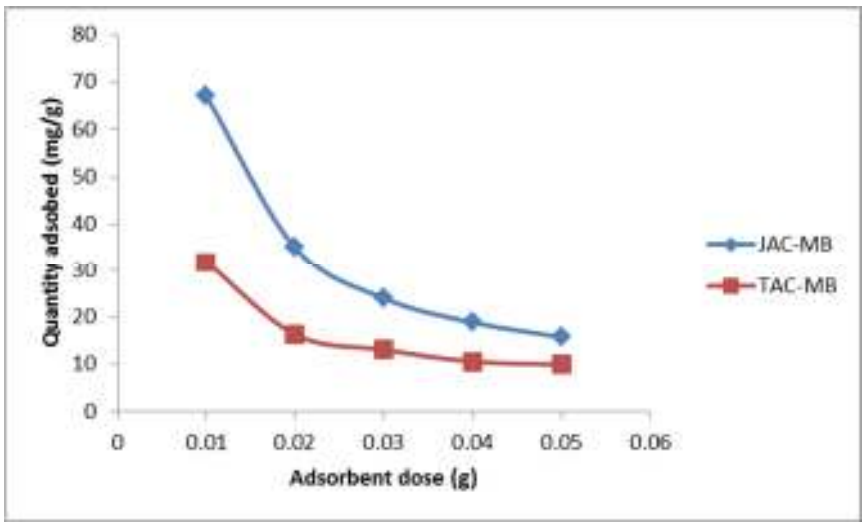

Figure 4d: Effect of adsorbent dose (Conditions: concentration=40 mg/L, pH=6, T=28±2°C, agitation time=120 min, agitation speed=200 rpm, n=3, 0 ≤ %E ≤ 0.24).

Effect of temperature

Figure 4e presents the impact of temperature on the sorption experiment. The quantity of MB adsorbed on JAC and TAC diminishes with a rise in temperature. This observation suggests that the force which binds the MB molecule to the activated carbon surface becomes weaker as the temperature of the medium is raised [28,29].

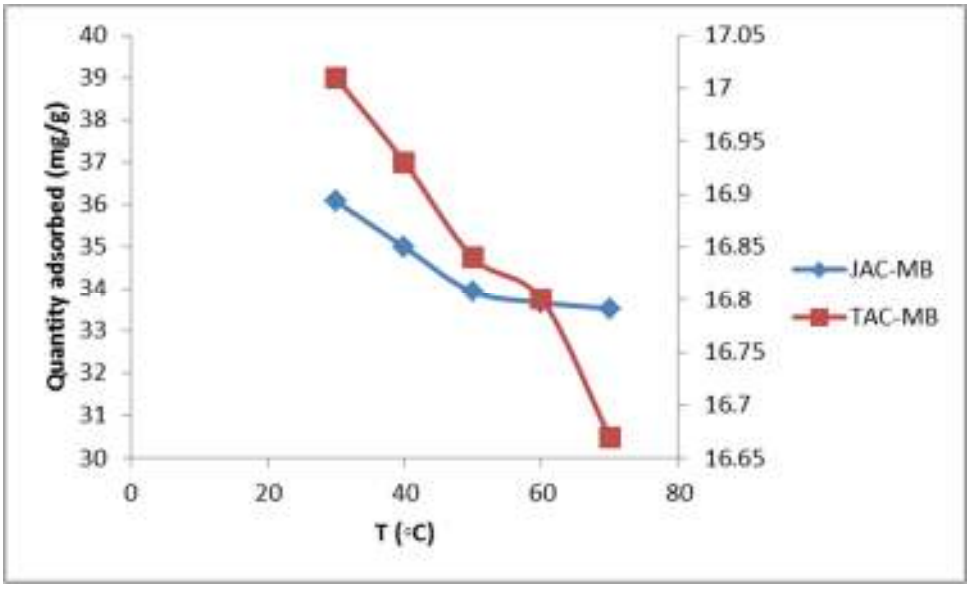

Figure 4e: Effect of Temperature (Conditions: concentration=40 mg/L, pH=6, adsorbent dose=0.02 g, agitation time=120 min, agitation speed=200 rpm, n=3, 0 ≤ %E ≤ 0.36).

Adsorption isotherms

The plots of Freundlich, Langmuir, and D-R isotherms model are shown in Figure 5. The R^2 values (see Table 1) of various isotherms reveal that Langmuir model fits the data well in both JAC-MB and TAC-MB systems [25]. Although D-R isotherm fits into JAC-MB system while Freundlich isotherm also describes adsorption data in TAC-MB system.

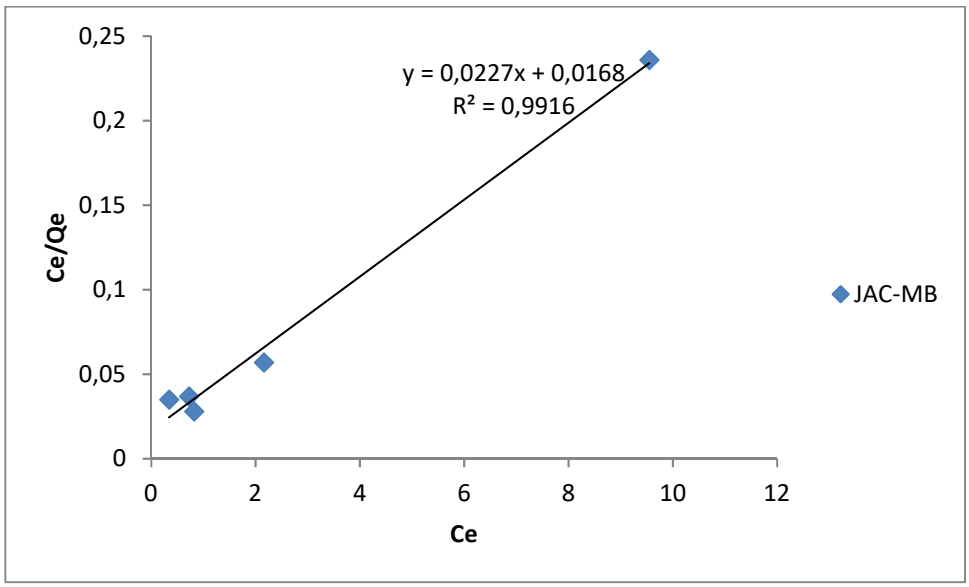

Figure 5(a): Langmuir plot of MB on JAC.

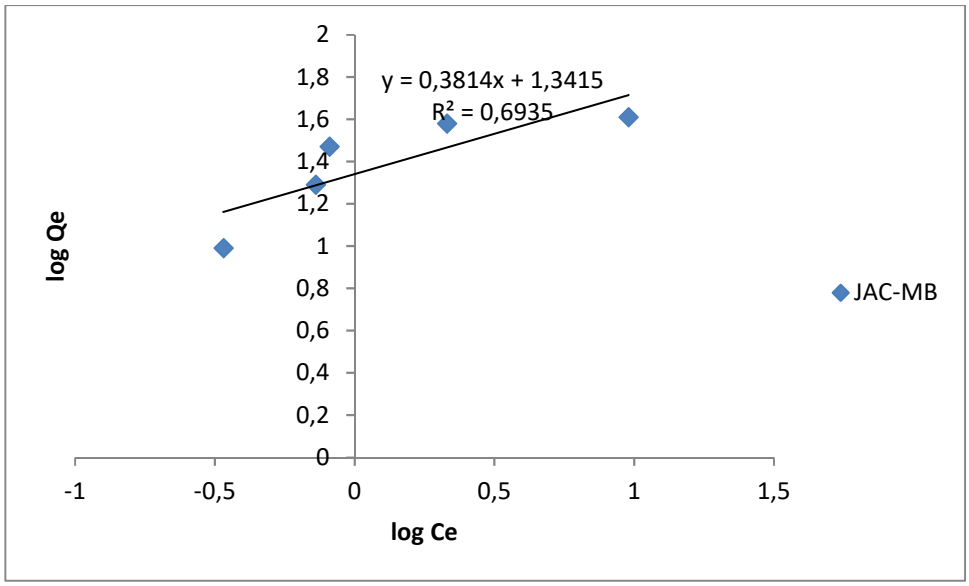

Figure 5(b): Freundlich plot of MB on JAC.

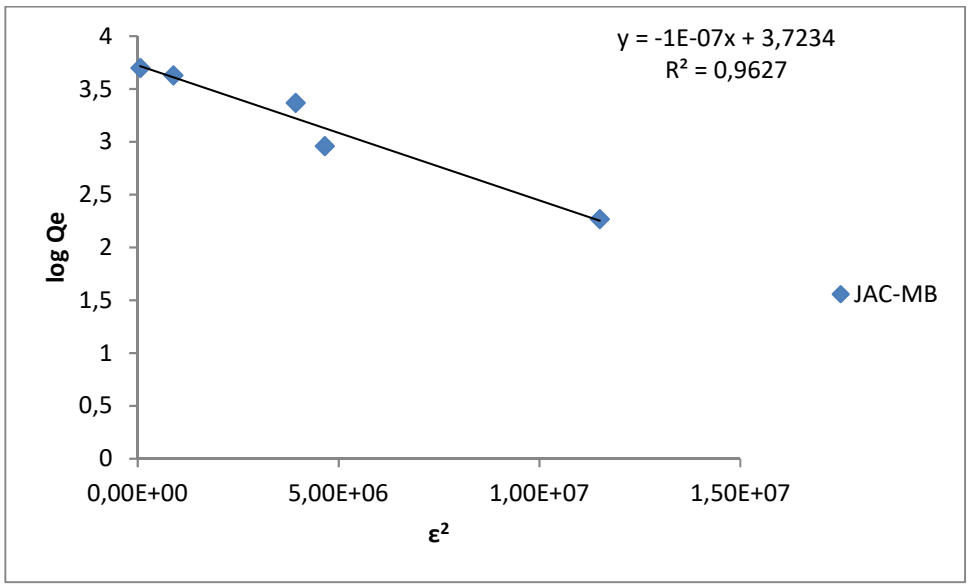

Figure 5(c): D-R isotherm plot of MB on JAC.

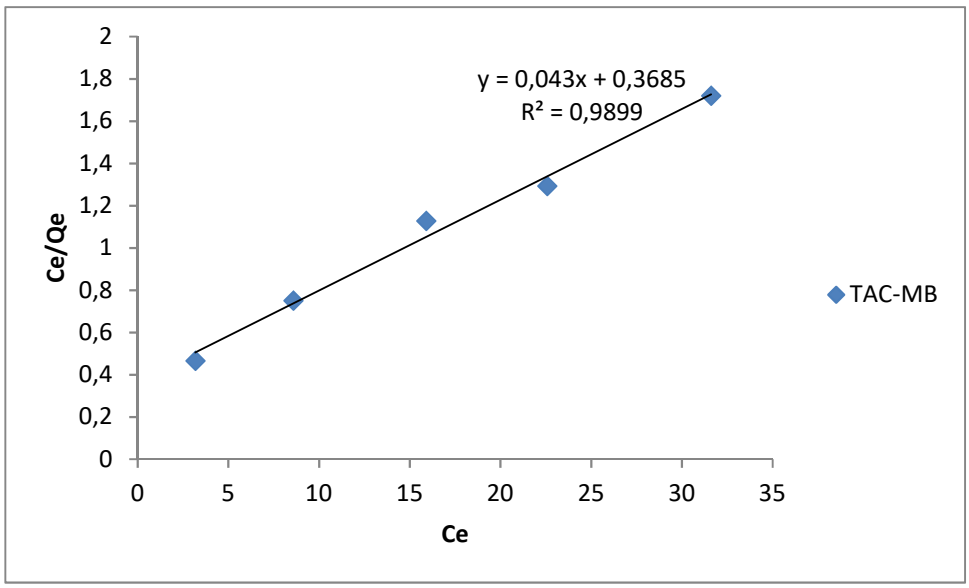

Figure 5(d): Langmuir plot of MB on TAC.

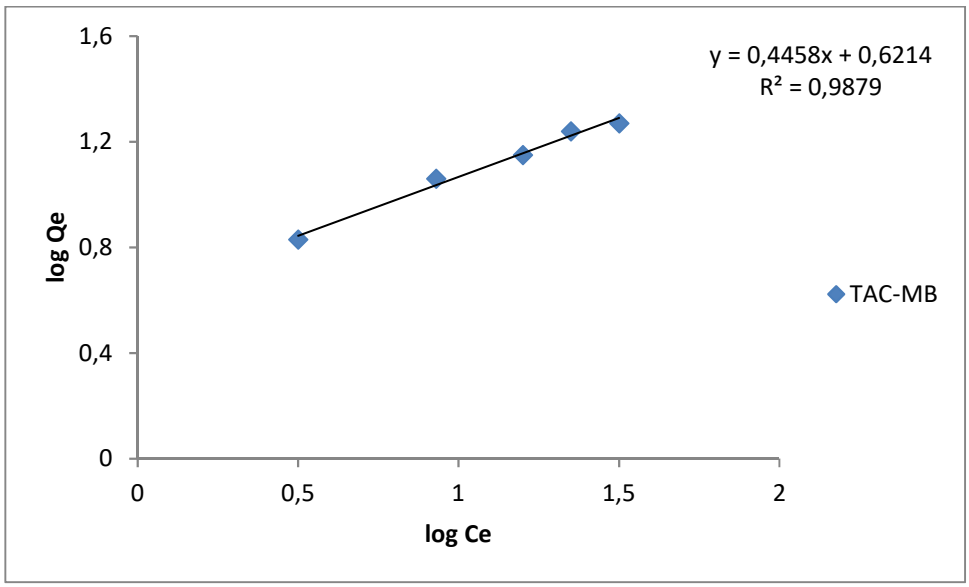

Figure 5(e): Freundlich plot of MB on TAC.

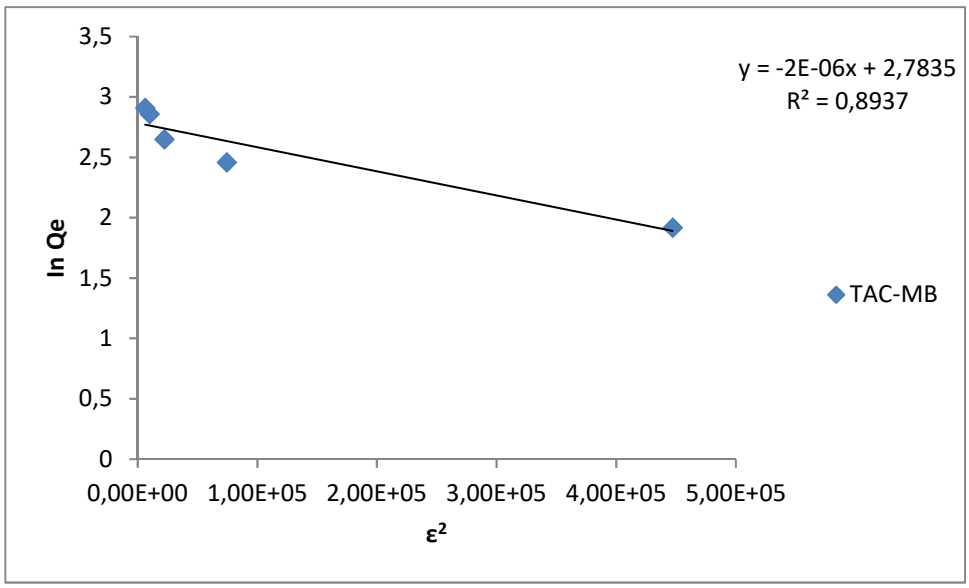

Figure 5(f): D-R isotherm plot of MB on TAC.

Adsorption kinetics

The pseudo first order and pseudo second order plots for MB-JAC and MB-TAC are presented in Figure 6. The correlation coefficients, R^2 observed is summarised in the Table 2 which suggests that pseudo second order fitted best for the sorption experimental data [30].

Table 2: Kinetics and Thermodynamic parameters for adsorption of MB onto JAC and TAC.

	Parameters	Values (JAC)	Values (TAC)
Kinetics Model			
Pseudo-first order	K_1 (min^{-1})	0.011	$8.75x10^{-3}$
	R^2	0.9485	0.9897
Pseudo-second order	K_2($gmg^{-1}min^{-1}$)	0.0112	$9.2x10^{-4}$
	R^2	1.000	0.9976
Thermodynamics			
	ΔH ($KJmol^{-1}$)	-12.68	-0.71
	ΔS ($Jmol^{-1}K^{-1}$)	-24.06	-4.85
	T (K)	ΔG (J/mol)	ΔG (J/mol)
	303	-5592	758
	313	-5048	804
	323	-4619	856
	333	-4623	894
	343	-4562	955

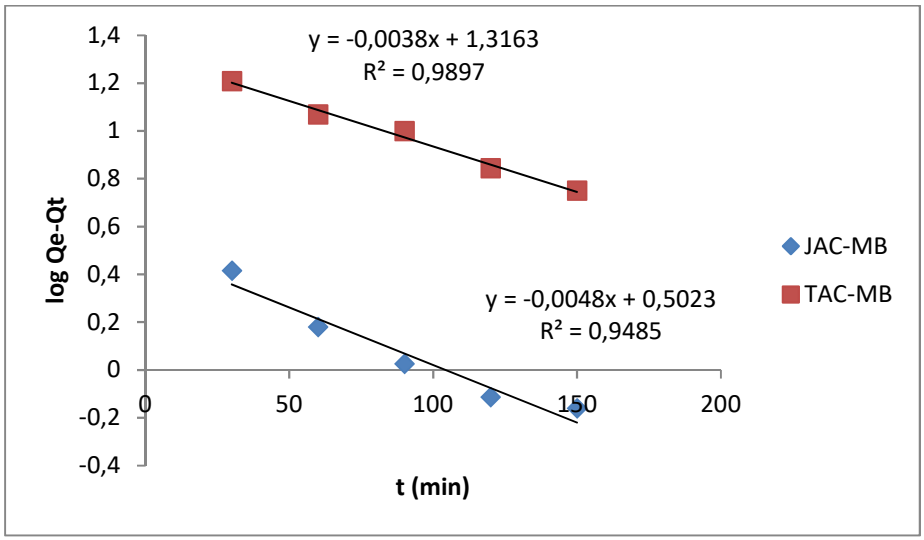

Figure 6a: Pseudo first order plots for the adsorption MB onto JAC and TAC.

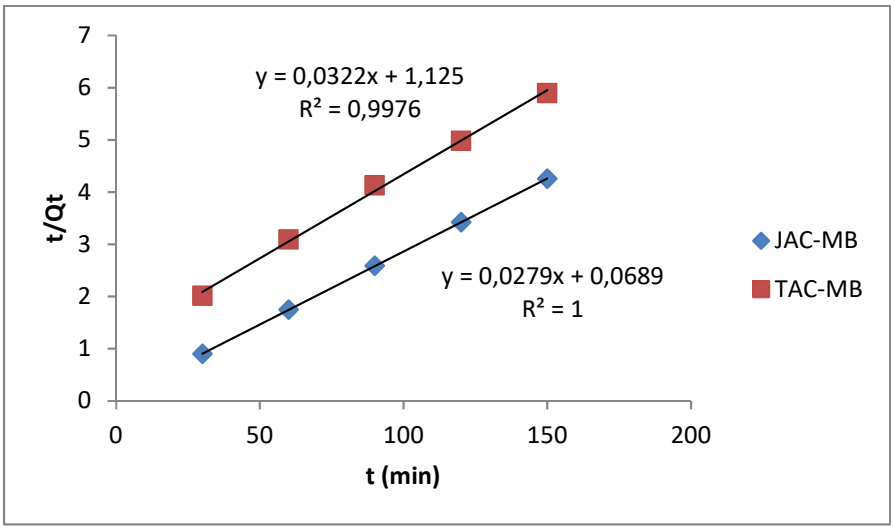

Figure 6b: Pseudo second order plots for the adsorption MB onto JAC and TAC.

Thermodynamics of adsorption

The thermodynamic parameters, free energy (ΔG^o), enthalpy (ΔH^o), and entropy (ΔS^o) assessed from the experimental data are presented using Van't Hoff's plot (see Figure 7). The values of ΔG^o, ΔH^o and ΔS^o acquired from the plots are introduced in Table 2. The values of ΔG^o obtained show that the adsorption process is more spontaneous at lower temperature. The negative value of ΔH^o was an indicative of the exothermic nature of the process. The negative value of ΔS^o proposes a diminished disorderliness at the solid-solute interface systems. This also proposes that the gain of entropy resulted from water molecules dislodged was not as much as that lost by the MB molecules [8].

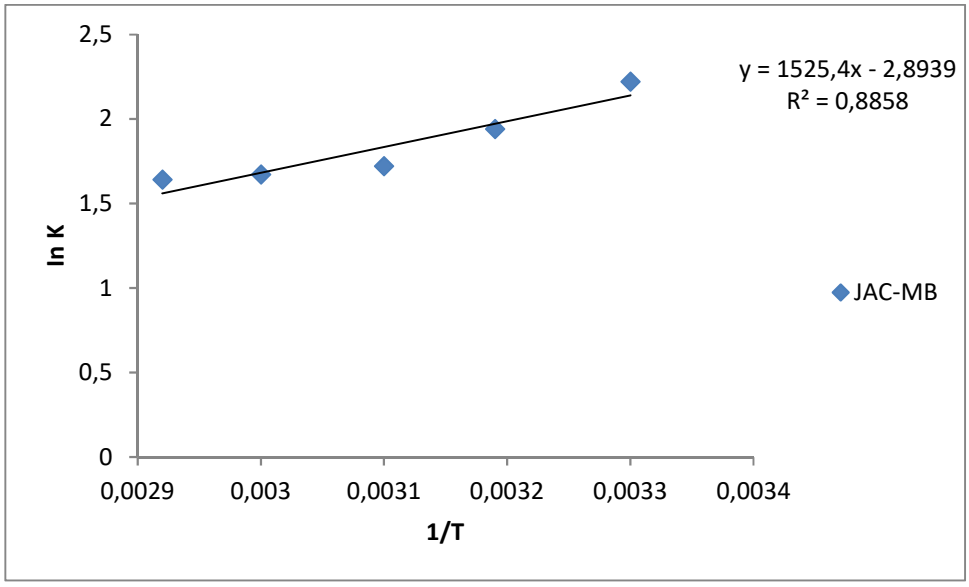

Figure 7a: Van't Hoff's plots for the adsorption of MB onto JAC.

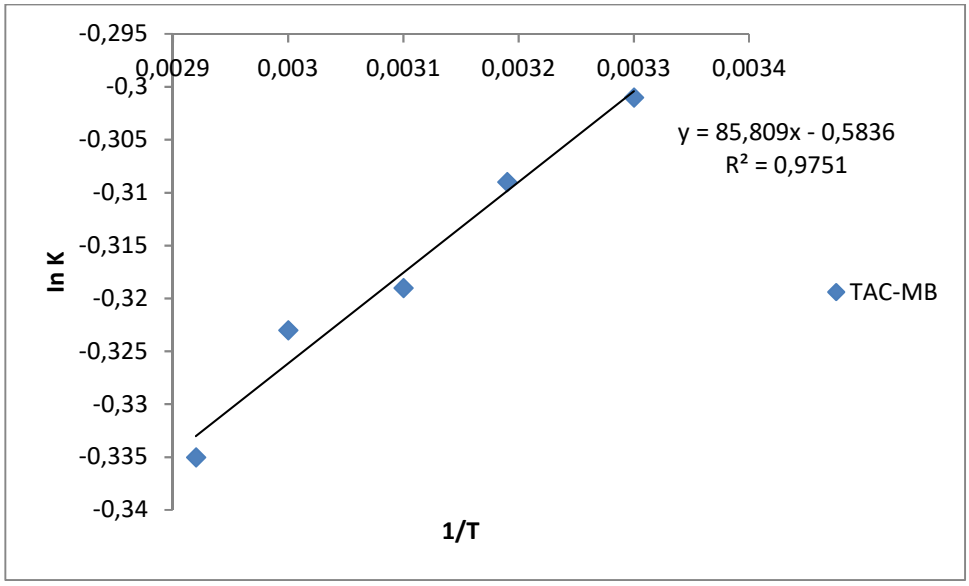

Figure 7b: Van't Hoff's plots for the adsorption of MB onto TAC.

CONCLUSIONS

The activated carbons (JAC and TAC) prepared were effective in the removal MB from aqueous medium. The sorption capacity of the prepared activated carbons was found to depend on the nature of the biomaterial used, experimental condition (initial concentration, pH, contact time, adsorbent dosage & temperature) adopted and the kinds of interaction that exist between the adsorbate and the adsorbent. The adsorption of MB on prepared JAC fitted into Langmuir and D-R isotherms; but Langmuir and Freundlich model fitted successfully for MB-TAC system. The kinetics studies best fitted into pseudo second order model. The process chemistry was found to be exothermic. The preferred disposal method of the spent adsorbent is by drying and burning or through landfill.

REFERENCES

1. Bansal RC, Goyal M. Activated Carbon Adsorption. Boca Raton: CRC Press/Taylor & Francis; 2005. 560 p. ISBN: 9780824753443.

2. Basso MC, Cukierman AL, Cerella EG. Activated Carbons Developed from a Rapidly Renewable Biosource for Removal of Cadmium(II) and Nickel(II) Ions from Dilute Aqueous Solutions. Ind. and Engineer. Chem. Research. 2002 DEC; 41: 180-189. DOI: 10.1021/ie010664x.

3. Bandosz TJ. Activated Carbon Surfaces in Environmental Remediation. Academic Press/Elsevier. 2006 Feb. 588 p. ISBN: 9780123705365.

4. Rouquerol F, Rouquerol I, Sing K. Adsorption by Powder and Porous Solids: Principles, Methodology and Applications. Academic press; 1999, pp. 237- 271. ISBN: 9780080977447.

5. Tan AI, Ahmad AH, Hameed BH. Preparation of activated carbon from coconut husk: optimization study on removal of 2, 4, 6-trichlorophenol using response surface methodology. Hazard. Mater. 2008 May; 153: 709–717. DOI: 10.1016/j.jhazmat.2007.09.014.

6. Ashly LP, Thirumalisamy S. Adsorption of hazardous cationic dyes from aqueous solution onto Acacia nilotica leaves as an eco-friendly. Sustain. Environ. Res. 2012; 22(2): 113-122. URL: http://ser.cienve.org.tw/index.php/list-of-issues/volume-22/207-22-2-2012/932-222-07.

7. Juejun K, Supunnee J, Chaiyot T. Comparison of Kinetic Models for CO_2 Gasification of Coconut-Shell Chars: Carbonization Temperature Effects on Char Reactivity and Porous Properties of Produced Activated Carbons Engineering Journal. 2012 August; 17: 269-278. DOI:10.4186/ej.2013.17.1.13.

8. Hassan MA, Ashfaq A. Inter. Conference on Chem., Biological and Environmental Engineering. 2011; 20. URL: http://www.icbee.org/ICBEE2011_program.pdf.

9. Garg VK, Gupta R, Yadav A. Kumar K. Dye removal from aqueous solution by adsorption on treated sawdust. Bioresource Technol. 2003 SEPT; 89:121 –124. DOI: 10.1016/S0960-8524(03)00058-0

10. Ünal G, Gülce O, Gizem ÇG. Removal of Methylene Blue from Aqueous Solution by Activated Carbon Prepared from Pea Shells (Pisum sativum). J. Chem. 2013 August; 2013. DOI: 10.1155/2013/614083.

11. Kannan N, Meenakshisundaram M. Adsorption of Congo Red on Various Activated Carbons. A Comparative Study. Water, Air and Soil Pollution. 2002 July; 138:289 –305. DOI: 10.1023/A:1015551413378

12. Ramalakshmi S, Muthuchelian K, Swaminathan K. Comparative Studies on Removal of Fast Green Dye from Aqueous Solutions by Activated Carbon Prepared from *Gloriosa superba* Waste and *Alternaria raphani* Fungal Biomass J. Environ. Sci. and Technol. 2012 Mar; 5: 222-231. DOI: 10.3923/jest.2012.222.231

13. Tang D, Zheng Z, Lin K, Luan J, Zhang J, Adsorption of p-nitrophenol from aqueous solutions onto activated carbon fiber. J. Harzard. Mater. 2007 May; 143: 49–56. DOI: 10.1016/j.jhazmat.2006.08.066

14. Federico I T. Salvation A., Marion B. Removal of phenol by adsorptive micellar flocculation: Multi-stage separation and integration of wastes for pollution minimisation. J. Colloid and Surface. 2005 October; 276 (1-3): 8-14 DOI: 10.1016/j.colsurfa.2005.10.003.

15. Jonas LA, Rehrmann JA. The rate of gas adsorption by activated carbon. Carbon. 1974 April; 12: 95-101. DOI:10.1016/0008-6223(74)90017-7

16. Odebunmi EO, Okeola OF. Preparation and characterization of activated carbon from waste material. J. Chem. Soc. Nigeria, 2001; 26(2): 149 – 155. URL: http://www.unilorin.edu.ng/publications/odebunmi/16.%20Preparation%20and%20characterization%20of%20activated%20carbon%20fro.pdf.

17. Mozammel HM, Masahiro O, Bhattacharya SC. Activated charcoal from coconut shell using $ZnCl_2$ activation. Biomass Bioenerg. 2002 May; 22(5):397–400. DOI: 10.1016/S0961-9534(02)00015-6

18. Saha B, Tai MH, Streat M. Study of Activated carbon after oxidation and subsequent treatment: Characterization. Process safety and environmental protection. 2001 July; 79:211-217. DOI:10.1205/095758201750362253.

19. Jun jie G, Ye-bo Q, Tao Z, Dong-dong C, Ping X, Danielle H, Yue-feim W. Adsorption of methylene blue onto activated carbon produced from tea (Camellia sinensis L.) seed shells: kinetics, equilibrium, and thermodynamics studies. J. Zhejiang Univ Sci. 2013 April**;** 14(7): 650–658. DOI:10.1631/jzus.B12a0225

20. Pala A, Tokat E. Color removal from cotton textile industry wastewater in an activated sludge system with various additives. Water Research. 2002 June; 36: 2920–2925. DOI: 10.1016/S0043-1354(01)00529-2

21. Ansari R, Masoudi M. Inter. J. Chemistry. 14(3) (2004) 139-142.

22. Tahir S, Rauf N. Removal of a cationic dye from aqueous solutions by adsorption onto bentonite clay. Chemosphere. 2006 Oct; 63: 1842-1848. DOI: 10.1016/j.chemosphere.2005.10.033.

23. Graham N, Chen XG, Jayaseelan S. The potential application of activated carbon from sewage sludge to organic dyes removal. Water Sci Technol. 2001; 43: 245-252. ISSN: 0273-1223. URL: http://wst.iwaponline.com/content/43/2/245

24. Vijayakumar G, Tamilarasan R, Dharmendirakumar M. Adsorption, Kinetic, Equilibrium and Thermodynamic studies on the removal of basic dye Rhodamine-B from aqueous solution by the use of natural adsorbent perlite. J Mater Environ Sci. 2012 SEPT; 3:157-170. ISSN : 2028-2508. URL: http://www.jmaterenvironsci.com/Document/vol3/16-JMES-139-2011-Tamilarasan.pdf.

25. Wood GO. Activated Carbon Adsorption Capacities for Vapors. Carbon. 1992; 30: 593-539. URL: http://gerryowood.com/uploads/3/4/3/1/3431344/carbon92.pdf

26. Dubinin MM. Progress in surface and membrane science. 1975, 9: 1-70. ISBN: 978-0-12-571809-7

27. Lagergren S. Zur Theorie der Sogenannten Adsorption Gelöster Stoffe, Kungliga Svenska Vetenskapsakademiens. Handlingar, 1898, Vol. 4 pp. 1-39.

28. Blanchard G, Maunaye M, Martin G. Removal of heavy metals from waters by means of natural zeolites. Water Research. 1984; 18:1501-1507. DOI:10.1016/0043-1354(84)90124-6.

29. Sumanjit, Prasad N. Adsorption of dyes on rice husk ash. Indian Journal of Chemistry. 2001 April; 40A: 388-391. URL: http://nopr.niscair.res.in/bitstream/123456789/18490/1/IJCA%2040A(4)%20388-391.pdf

30. Stephen I, Sulochana N. Basic dye adsorption on a low cost carbonaceous sorbent – kinetic and equilibrium studies. Indian Journal of Chemical Technology. 2002 Feb; 9: 201. ISSN: 0971-457X.

Türkçe Öz ve Anahtar Kelimeler

Jatropha curcas ve *Terminalia catappa* Tohum Kabuklarından Hazırlanan Aktif Karbon üzerinde Metilen Mavisinin Tutulma Çalışması

Ismaila Olalekan Saheed, Folahan Amoo Adekola ve Gabriel Ademola Olatunji

Öz: .Bu araştırma *Jatropha curcas* ve *Terminalia catappa* tohum kabuklarından üretilen aktif karbonun sudan metilen mavisi (MB) giderimi için etkinliğini bulmayı hedeflemiştir. *Jatropha* aktif karbonu (JAC) ve *Terminalia* aktif karbonu (TAC) Fourier Dönüşüm Kızılötesi Spektroskopisi (FTIR), taramalı electron mikroskopisi (SEM) ve Brunauer-Emmett-Teller (BET) yüzey alan analizi ile karakterize edilmiştir. Başlangıç derişimi, pH, temas süresi, adsorban dozu ve sıcaklığın adsorpsiyon deneyleri üzerindeki etkisi çalışılmıştır ve metilen mavisinin derişimi spektrofotometri ile takip edilmiştir. Bu adsorbanların adsorpsiyon kapasiteleri JAC ve TAC için sırasıyla 37,84 mg/g ve 17,44 mg/g olarak bulunmuştur. Deneysel veriler Langmuir, Freundlich ve Dubinin-Radushkevich izotermleri kullanılarak analiz edilmiştir. Veriler en iyi şekilde metilen mavisi-JAC sistemi ile metilen mavisi-TAC sistemine Langmuir izotermi üzerinden uyum göstermiştir. Kinetik çalışmaları yalancı ikinci derece kinetic modeline uyum sağlamıştır. Üreç kimyası eksotermiktir.

Anahtar kelimeler: Adsorpsiyon; aktif karbon; metilen mavisi; kinetik; termodinamik.

Sunulma: 14 Kasım 2016 . **Düzeltme:** 23 Kasım 2016. **Kabul:** 07 Aralık 2016.

JOTCS A
Journal of the Turkish Chemical Society
Section: A
Chemistry
TURKISH CHEMICAL SOCIETY

Pyrolysis of Isochrysis Microalgae with Metal Oxide Catalysts for Bio-Oil Production

Tevfik Aysu[1]*
[1]Yüzüncü Yıl University, 65080, Van, Turkey

Abstract: Pyrolysis of Isochrysis microalga was carried out in a fixed-bed reactor without and with metal oxide catalysts (CeO_2, TiO_2, Al_2O_3) for the first time at the temperatures of 450, 500 and 550 °C with a constant heating rate of 40 °C/min. The pyrolytic conditions including catalyst and temperature were studied in terms of their effects on the yields of pyrolytic products and quality. The amounts of bio-char, bio-oil, and gaseous products were calculated. The composition of the produced bio-oils was determined by Elemental analysis (EA), Fourier transform infrared spectroscopy (FT-IR), proton nuclear magnetic resonance (^{1}H NMR) and Gas chromatography/mass spectrometry (GC–MS) techniques. As a result of the pyrolysis experiments, it is shown that there have been significant effects of both catalyst and temperature on the conversion of Isochrysis microalgae into solid, liquid (bio-oil) and gas products. The highest bio-oil yield (24.30 %) including aqueous phase was obtained in the presence of TiO_2 (50%) as catalyst at 500 °C. 98 different compounds were identified by GC-MS in bio-oils obtained at 500 °C. According to ^{1}H NMR analysis, bio-oils contained ~60-64% aliphatic and ~17-19% aromatic structural units. EA showed that the bio-oils contained ~66-69% C and having 31-34 MJ/kg higher heating values.

Keywords: Energy; microalgae; isochrysis; pyrolysis; catalyst.

Submitted: July 12, 2016. **Revised:** November 20, 2016. **Accepted:** December 14, 2016.

Cite this: Aysu T. Pyrolysis of Isochrysis Microalgae with Metal Oxide Catalysts for Bio-Oil Production. JOTCSA. 2017;4(1):395–414.

DOI: To be assigned.

*Corresponding author. E-mail: tevfikaysu@yyu.edu.tr; Tel: +90 432 2251702

INTRODUCTION

In recent years, petroleum and crude oil prices have been highly flexible due to the increasing energy demand. Researchers have sought to produce renewable, alternative and sustainable fuels to meet this increasing energy demand and to stabilize prices. Biomass is a promising candidate in this regard as it is renewable, carbon-neutral, and highly productive [1]. However, biomass feedstocks should have some advantages such as being cheap, easily available, abundant, fast growing, not in competition with food industry, and with minimum by products and waste [2]. Algae, the microorganisms grow fastly in water, are considered as potential feedstocks for production of bio-fuels. Recently, algae have already attacted much attention [3,4]. There are different processes of bio-fuel production from algal biomass which include supercritical water gasification, bio-diesel production by solvent extraction, bio-gas production by anaerobic digestion and bio-oil production by pyrolysis. Algae are considered as promising feedstocks for the following reasons: (i) high yield per area, (ii) high growth rate (up to 20 g dry algae per m^2 per day) (iii) high efficiency in CO_2 capture and solar energy conversion, (iv) no competition with agricultural food. Algae can grow in open water such as sea water and ponds or in photobioreactors on non-arable areas. However, only a few microalgal species are currently cultivated in an industrial manner [5].

Algae contain mainly three components: carbohydrates, proteins, and lipids. Microalgae are suitable feedstocks for biodiesel production as some species may contain up to 80% of lipid content [6]. A great number of studies have been performed for commercialization of microalgae-based biodiesel production [7,8]. However, at present, commercialization of biodiesel from microalgae is still highly expensive [9,10]. Currently, biodiesel from algae is produced by lipid extaction using organic solvents, such as hexane, or by pressing of dry algae and this is followed by transesterification in methanol or ethanol in the presence of basic catalysts [11-13]. In biodiesel production, only one part (lipid) of organic content of algae is utilized for biofuel production. From an economic point of view, biofuel production from microalgae requires utilization of the complete biomass as efficiently as possible. Solid residues derived from algae processing contain minerals up to 10% and these can be fed back to the growth cycle as a soil amendment product [14]. However, the rest 60% of microalgae is considered as waste, and this process is neither attractive nor economical [2]. Therefore, all components need to be used completely based on the microalgae biorefinery concept to develop economically feasible processes for microalgae biofuels. Thermochemical processes can be used to utilize all organic contents of algal biomass completely for biofuel production [15].

There are various biomass conversion processes that can yield high quality liquid bio-fuels and value-added products. Pyrolysis is a processing technique that is applied to achieve

degradation of biomass thermally in inert atmosphere which produces solid, liquid and gases. The produced liquids, called bio-oil are used in direct combustion for energy generation, or can be upgraded into transportation fuels and/or biochemicals [16]. Algal biomass can be converted into bio-fuels through different methods such as thermochemical liquefaction, transesterification, and pyrolysis. Pyrolysis is more economical than organic solvent extraction or thermal-acid conversion methods and transesterification methods for conversion of algal biomass into bio-fuels since pyrolytic process is more efficient than other methods. Among the three products obtained from pyrolysis, bio-oil is the most important one while bio-char and gases have various uses as well. Bio-oil can be used as fuel for heat and power or as feedstock for chemical industry and is considered to be a very promising bio-fuel [17].

The conversion of biomass species to renewable bio-fuels and development of catalysts have received great attention because of negative environmental impacts fossil fuels exploitation. As biomass is considered as CO_2-neutral, its usage as a renewable energy source helps reducing the dependence on fossil fuels and the greenhouse effect [18]. Microalgal species such as *Chlorella, Nannochloropsis* and *Tetraselmis* have received growing interest recently due to their high oil content, high mass productivity, and the ability to grow in a wide range of conditions (climates and lands). High quality bio-oils can be produced from non-catalytic and catalytic pyrolysis of algae that have been widely studied as an alternative. In a previous study, Gopakumar *et al*. (2012) performed the catalytic pyrolysis of green algae (*Chlorella vulgaris*) using H^+ZSM-5 catalyst for hydrocarbon production. The results showed that a bio-oil yield of 52.7 wt% was obtained which contained aromatic and alkane compounds [19]. In another study performed by Chaiwong *et al*., bio-char and bio-oil have been produced at temperatures between 450 and 600 °C in slow pyrolysis of Spirulina sp. without catalyst. The components found in bio-oil were identified by GC-MS which showed saturated functional carbons in the range of heavy naphtha, kerosene, and diesel oil [20]. Campanella and Harold (2012) carried out the non-catalytic and catalytic (ZSM-5 catalysts) pyrolysis of microalgae to produce organic liquid fuel precursor. They observed that using catalyst has resulted in the formation of highest yields of desired fraction (hydrocarbons) whereas the highest bio-oil yield was obtained without catalyst. It was found that HZSM-5 catalyst has increased the hydrocarbon fraction yield significantly (from 21% to 43%) in the organic phase [21].

The chemical composition of lignocellulosic biomasses (feedstocks) such as wood are very different from microalgae. Lignocellulosic biomasses including wood are made up of hemicelluloses, cellulose, and lignin whereas microalgae are composed of mainly proteins and carbohydrates in addition to lipids and do not contain lignin. Therefore, microalgae pyrolysis bio-oils have different compounds than lignocellulosic biomass pyrolysis bio-oils. Microalgae pyrolysis bio-oils are mainly composed of linear hydrocarbons, nitrogen containing compounds which come from the decomposition of lipids, and proteins respectively along with some

amount of oxygenated compounds from carbohydrates' pyrolysis. In principle, improved properties of microalgal bio-oils such as low tar formation and high heating value are resulted from these differences between lignocellulosic and algal feedstocks. In addition, bio-char obtained from microalgae pyrolysis can be used in agriculture due to its high nitrogen content. However, there have been a small number of studies on the pyrolytic characteristics of algae so far [22]. As the selection of process conditions, catalysts, product yields, and quality are affected by the heterogeneous compositions of the different feedstocks, effective catalysts for lignocellulosic biomass conversion may not be suitable for conversion of marine (algal) feedstocks. There is lack of works available in the literature on the behavior of Isochrysis algal pyrolysis with metal oxide catalysts. Accordingly, the purpose of this study was to investigate the effects of ceria, titania, and alumina catalysts on microalgae conversion yields and products selectivity and to investigate the possibility of producing biofuels. In this work, catalytic pyrolysis of Isochrysis was performed in a fixed-bed tubular reactor at temperatures of 450 °C, 500 °C and 550 °C with a constant heating rate of 40 °C/min under N_2 atmosphere. Firstly, the amounts of all pyrolytic products (solid, liquid, gas) were determined which revealed the catalysts and temperature effects on the yields of products. Secondly, various techniques (EA, FT-IR, ^{1}H NMR) were used to analyze the pyrolytic products.

MATERIALS AND METHODS

Feedstock

Microalgal sample, isochrysis, was provided from Reed Mariculture. Chemical composition (protein, lipid, and carbohydrate) of microalgae was also provided from Reed Mariculture. The cells of microalgal sample were dried in an oven at 45 °C, and pulverized to a particle size of 80 mesh and then stored in a desiccator for further use.

Proximate and ultimate analysis

The proximate analyses were conducted according to ASTM standards (D2016, D1102-84, E872-82,). C, N and H were determined using LECO CHNS-932 analyzer, while O content was obtained by the difference. Higher heating values (HHV) of samples were obtained using the Dulong's Formula as given below.

HHV (MJ/kg) = 33.86 x C + 144.4 x (H-O/8) + 9.428 x S where C, H, O, and S are the mass fractions obtained from ultimate analysis.

Fourier transform infrared spectroscopy (FT-IR)

FT-IR analysis of bio-oils was performed using Perkin Elmer Spectrometer system to detect the characteristic peaks and their functional groups.

Proton nuclear magnetic resonance (^{1}H NMR)

Agilent 400-MR NMR Spectrometer operating at 400 MHz was used for the ^{1}H NMR analysis of *Isochrysis* bio-oils. The bio-oils were dissolved in $CDCl_3$ using 1:1 ratio by volume in 5 mm NMR tubes and TMS (tetramethylsilane) was used as the internal standard.

Gas chromatography–Mass spectrometry (GC–MS) analysis

An Agilent GC-MS 7890A/5975C series (column: HP 235–INNOWAX; transfer line at 270 °C, ion source at 250 °C and electron energy of 70 eV) was used for the GC-MS analysis of the bio-oils [28]. The bio-oil components were identified using mass spectral libraries (PMW_Tox3.l, Wiley7n.1 and NIST05a.L).

Pyrolytic experiments

The pyrolytic experiments of *Isochrysis* were performed using a fixed-bed reactor. The set-up was previously descibed [23]. The catalytic and non-catalytic algal pyrolysis experiments were performed at temperatures of 450 °C, 500 °C and 550 °C under N_2 atmosphere. The heating rate was 40 °C/min and the nitrogen flow rate was 100 mL/min. The reactor was kept constant at the final temperature for 60 min. The bio-oils were recovered in three Dreshel bottles. The remaining solid was recorded as bio-char yield (subtracting the catalyst weight). The gaseous products were not collected and calculated by difference (subtraction of total solid and liquid yields from the amount of initial feedstock).

The distribution of the parent algal material energy in the pyrolytic products was based on the pyrolytic material balance and HHV of bio-oils and bio-chars.

RESULTS AND DISCUSSION

Feedstock characterization

Table 1 shows the results of ultimate and proximate analysis and chemical composition of Isochrysis. The alga contains relatively high amount of proteins (44%) and carbohydrates (25%), and low lipids (19%). The high protein content of Isochrysis is in good agreement with other microalgal species reported in literature such as *Chlorella vulgaris* and *Scenedesmus almeriensis* [24]. Accordingly, the nitrogen content was high (6.63%) because of the protein component. Ultimate analysis shows that Isochrysis has relatively high amount of carbon (41.23%). This is good in terms of suitability for biofuel production. The proximate analysis shows that Isochrysis has 53.52% volatile matter, 18.14% ash and 22.78% fixed carbon, relatively high when compared to given values in literature [25].

Table 1 Main characteristics of Isochrysis.

Components	
Moisture (%)	5.56
Proximate analysis[a] (%)	
Ash	18.14
Volatile matter	53.52
Fixed carbon	22.78
Ultimate analysis[b](%)	
Carbon	41.23
Hydrogen	5.74
Nitrogen	6.63
Oxygen[c]	46.40
H/C molar ratio	1.67
O/C molar ratio	0.84
Empirical formula	$CH_{1.67}N_{0.14}O_{0.84}$
Higher Heating Value (MJkg^{-1})	
Dulong's formula	13.86
Chemical composition (%)	
Protein	44
Lipid	19
Carbohydrate	25

[a]Weight percentage (dry basis). [b] Weight percentage (daf). [c]By difference.

Effect of temperature on product distibution

Table 2 presents the conversion (total volatiles) and product distribution of pyrolysis of Isochrysis with (50%) and without catalyst. Heating rate of 40 °C/min and N_2 flow rate of 100 mL/min was used in the pyrolysis of Isochrysis. According to Table 1, temperature increase in 50 °C increments resulted in sharp increases in both conversion (total volatiles) and the gas yields, while the bio-char (solid) yields were decreased in all runs. For example, when temperature was increased from 450 to 500 °C, the conversion (total volatile) was increased from 62.14% to 66.04% in the non-catalytic runs and from 65.17% to 68.92% in the catalytic runs with CeO_2.

The gas yields were constantly increased with temperature (slightly at 500 °C, sharply at 550 °C). This was because the highest bio-oil yields were attained at 500 °C. The highest liquid (bio-oil) yield of 24.30% was achieved with TiO_2 at 500 °C. The bio-oil yields did not increase in a monotonic trend with temperature. A slight increase was observed in bio-oil yields at 500 °C, but a decrease again at 550 °C. This was due to the secondary cracking reactions of pyrolysis vapors which occured at high temperature [26]. Bio-char (solid) yields were decreased constantly with temperature because of the primary decomposition of Isochrysis components as well as the secondary decomposition of char residues. As the temperature of pyrolysis was increased from 450 to 550 °C, bio-char yields were decreased from 37.86% to 30.76% without catalyst and from 36.47% to 31.80% with alumina. Similar results were obtained for pyrolysis of not only algal biomass but also lignocellulosic biomass. Paddy husk

pyrolysis was studied recently using a drop-type pyrolyzer. The pyrolytic experiments were carried out at temperatures between 350 and 600 °C. The results showed that bio-oil yields were first increased and then decreased at 600 °C. The gas yields were increased, while bio-char yields were decreased with the incremental of pyrolysis temperature [27].

Table 2 The conversion[a] and product distribution of Isochrysis pyrolysis.

Temperature (°C)	Conversion (%)	Solid (%)	Liquid (%)	Gas (%)
No catalyst				
450 °C	62.14	37.86	16.82	45.32
500 °C	66.04	33.96	20.13	45.91
550 °C	69.24	30.76	18.07	51.17
CeO_2				
450 °C	65.17	34.83	20.82	44.35
500 °C	68.92	31.08	22.97	45.95
550 °C	71.52	28.48	19.91	51.61
TiO_2				
450 °C	66.82	33.18	22.41	44.41
500 °C	70.47	29.53	24.30	46.17
550 °C	73.61	26.39	21.10	52.51
Al_2O_3				
450 °C	63.53	36.47	19.36	44.17
500 °C	65.66	34.34	22.10	43.56
550 °C	68.20	31.80	20.03	48.17

[a]Mass fraction percentage of feedstock (daf)

Effect of catalysts on product distribution

Biomass can be converted into solid, liquid, and gaseous fuels by liquefaction and pyrolysis processes. However, bio-oils produced from thermal degradation of both lignocellulosic and algal biomass have generally a low quality as they are highly acidic with oxygenated compounds and have low higher heating values. For this reason, catalysts were applied in liquefaction and pyrolytic processes in biomass conversion to valuable chemical and bio-fuels. The studies reported in literature showed that most of the catalysts were effective in these processes [28]. The main aim of catalytic biomass pyrolysis is to decrease the amount of oxygen containing compounds in bio-oils generated from biomass pyrolysis. Generally, algal biomass contains 35–45% of oxygen.

Oxygen in biomass can be removed by two major deoxygenation reactions. These are decarboxylation and dehydration reactions in which oxygen is removed in the forms of carbon dioxide and water, respectively. The long chain carboxylic acids in biomass are cracked thermally during decarboxylation reaction which reduces the chain size and releases carbon dioxide. If an effective catalyst is used, it can enhance deoxygenation and improve the bio-oils' quality. The function of using a catalyst in biomass pyrolysis is to speed up deoxygenation including decaboxylation, dehydration, and decarbonylation which result in the production of

desired compounds such as hydrocarbons. Some amount of the hydrogen and carbon in feedstock are converted to water, hydrogen gas, and carbon monoxide during pyrolysis as well [29]. In recent years, many types of catalysts including Ni and Mg-based have been utilized in pyrolysis and gasification studies.

As for the present study, we see that catalysts had different effects on the yields of products and quality. Almost all used catalysts had positive effects and increased the total amounts of volatiles (conversions) with temperature increase when compared to runs without catalyst except alumina at 500 and 550 °C. Titania was the most effective catalyst in terms of conversion. The highest conversion of 73.61% was obtained with titania in the catalytic runs at 550 °C. The least effective one was alumina with the lowest conversion of 63.53% obtained at 450 °C in the catalytic runs. On the other hand, effects of catalysts on liquid yields were different from the effects of conversion. All catalysts increased the liquid yields compared to non-catalytic runs, with titania being the most effective. The solid (bio-char) yields obtained with and without catalyst were found to be decreasing with increasing the pyrolysis temperature and the lowest yield of 26.39% was obtained in the presence of titania at 550 °C. As for the gas yields, the effect of catalysts differed from each other. The highest gas yields 51.61% and 52.51% were obtained with ceria and titania at 550 °C respectively while the lowest yield (43.56 %) was obtained in the presence of alumina at 500 °C.

In terms of energy recovery, Figure 1a shows that most of the starting microalgal energy was recovered in the bio-oils. Titania and ceria were the most effective catalysts, which maintained 59.96% and 54.69 % of the starting energy in the bio-oils, repectively, while alumina was the least effective one and maintained only 50.12% of the starting energy. Figure 1b shows the nitrogen distribution in the products of catalytic and non-catalytic pyrolysis of Isochrysis at 500 °C. Bio-oil obtained without catalyst contained about 23.16 wt % of the nitrogen, while 18.28 wt % remained in the solid bio-char and 58.54 wt % went into the gas products. From a fuel quality point of view, nitrogen in bio-oil is detrimental. The use of catalyst did not have a significant effect on the nitrogen content in the bio-oils. Titania was the most effective catalyst in removing nitrogen from feedstock and released the most of nitrogen (59.22%) as uncondensable gases, while keeping only 15.81% in bio-char.

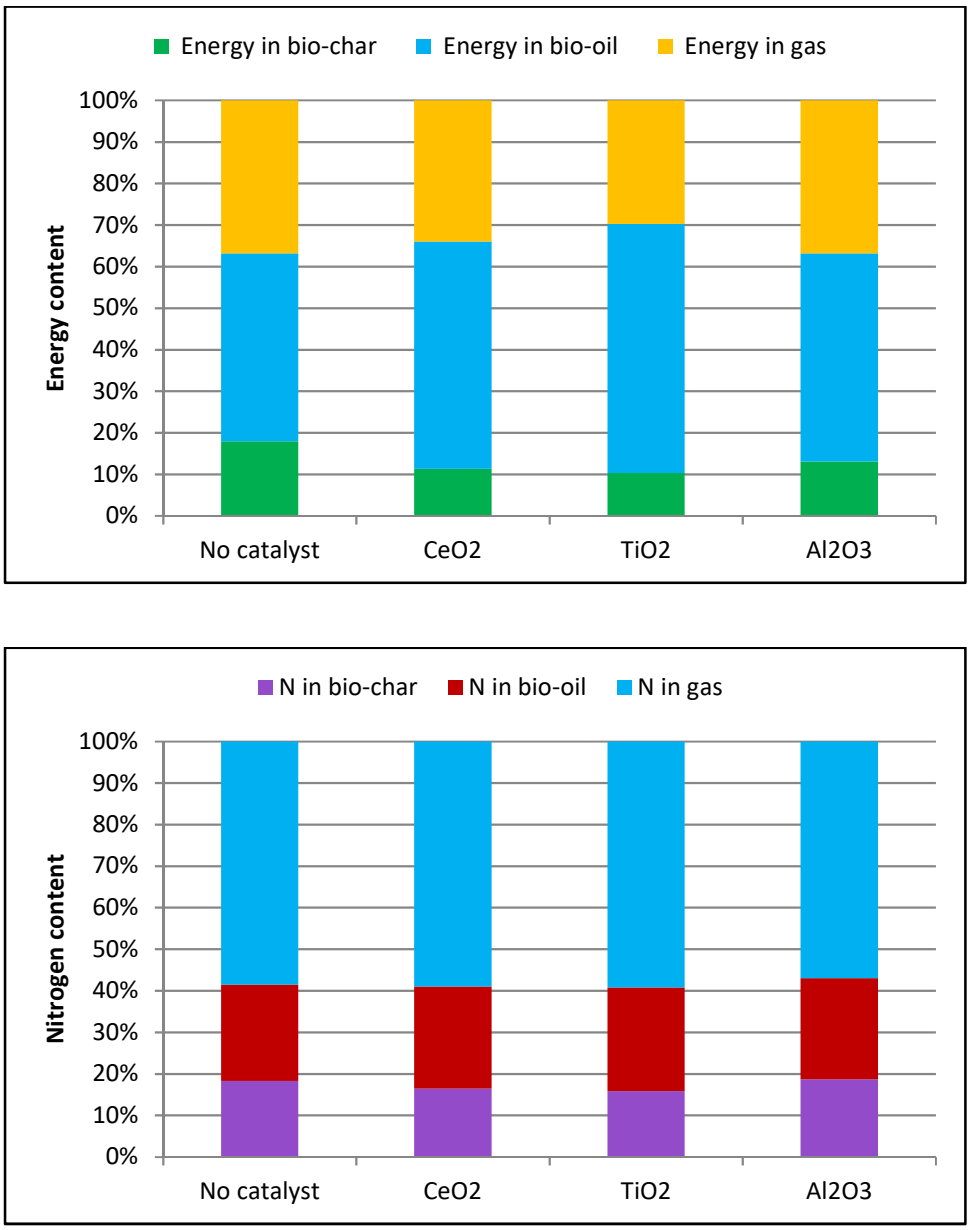

Figure 1. Energy and nitrogen contents of bio-oils obtained at 500 °C top: energy bottom: nitrogen.

EA, FT-IR, ^{1}H NMR and GC–MS analysis

The results of elemental (ultimate) analysis of bio-chars and bio-oils are given in Table 3. The elemental analysis of bio-chars obtained from Isochrysis pyrolysis showed their lower calorific values (4-7 MJ/kg) compared to that of feedstock (13.86 MJ/kg). This is because most of the starting microalgal energy was maintained in the bio-oils. Due to their low energy content, bio-chars may be utilized as soil amendment as they contain high ash and nitrogen (~3%) contents.

Table 3 The results of elemental analysis of Isochrysis bio-chars.

Elemental analysis [a] (Bio-chars)	No catalyst	CeO_2	TiO_2	Al_2O_3
Carbon	37.25	38.91	38.63	39.41
Hydrogen	1.31	1.40	1.36	1.37
Nitrogen	3.57	3.50	3.55	3.61
Oxygen[b]	57.87	56.19	56.46	55.61
H/C molar ratio	0.42	0.43	0.42	0.42
O/C molar ratio	1.16	1.08	1.09	1.06
HHV (MJ kg^{-1})	7.31	5.04	4.84	5.27
Elemental analysis (Bio-oils)				
Carbon	66.70	68.34	69.74	67.33
Hydrogen	8.14	8.82	9.14	8.15
Nitrogen	7.63	7.10	6.81	7.30
Oxygen[b]	17.53	15.74	14.31	17.22
H/C molar ratio	1.46	1.55	1.57	1.45
O/C molar ratio	0.19	0.17	0.15	0.19
HHV (MJ kg^{-1})	31.14	33.00	34.20	31.43

[a] Weight percentage (daf). [b]By difference.

When we look at the HHVs and elemental analysis of bio-oils from Isochrysis, we see that all catalysts increased C and H content in bio-oils and consequently enhanced their energy content. The most effective catalysts in improving bio-oil energy content were ceria and titania which increased the HHVs of bio-oils up to 33.00 and 34.20 MJ/kg, respectively, compared to non-catalytic run (31.14 MJ/kg). The decreasing amount of oxygen in bio-oils was due to the deoxygenation reactions which removed the oxygen in the form of carbon monoxide and/or carbon dioxide. The high nitrogen contents of bio-oils were obviously originated from proteins and chlorophyll present in Isochrysis. The pyrolysis bio-oil from Isochrysis had higher carbon and hydrogen content but lower oxygen content than the bio-oils from pyrolysis of lignocellulosic biomass, which makes it more suitable for fuel use.

GC-MS analysis of bio-oils produced at 500 °C was carried out in order to determine the main chemical compounds. The total ion chromatograms of bio-oils obtained at 500 °C are given in the Supplementary data (Figure S1,a-d). The list of the compounds identified by GC-MS in (Figure S1, a-d) is given in Table 4.

The presence of the metal oxide catalysts affected the distribution and number of the identified chemicals. The complete identification and quantification of all chemical compounds is not possible by GC-MS as the pyrolysis bio-oils have complex nature and may contain compounds with very high boiling points which can not pass through the GC column. Yet, elemental and FT-IR analysis of bio-oils were consistent and confirm the presence of compounds given in Table 4. As seen in Table 4, bio-oils from Isochrysis were composed of a mixture of different functionalities such as aliphatics, monoaromatics, oxygenates, nitrogenates and polycyclic compounds. As seen in Table 4, catalysts have formed aliphatics such as alkanes and alkenes.

Aliphatics (alkanes and alkenes) were mainly generated during the depolymerization of algal saturated and unsaturated fatty acids. Some examples are "Hexadecane", "Undecane", "Heptane, 2,4-dimethyl", "1,4-Pentadiene" and "2-Undecene". Aliphatics are valuable compounds which increase the high heating values of bio-oils. The nitrogen containing compounds in bio-oils, such as nitriles, amines, amides, pyrroles, and pyridines were assumed to be derived from protein degradation in algal cells. Oxygenated compounds, identified in pyrolysis bio-oils are represented with a wide range of compounds which include carboxylic acids, alcohols, esters, aldehydes, ethers and ketones. The main monoaromatics were phenol, phenol substitutes and benzene, which were produced from algal components thermal cracking, metal oxide promoted cracking, dehydration, decarbonylation, and decarboxylation reactions. A small number of phenolics were formed due to composition of microalga which has no lignin in its structure. The produced bio-oils had the carbon and hydrogen contents which are close to the conventional fossil fuels, however the oxygen and nitrogen contents are still high than desired amounts. The undesired NOx compounds are formed during combustion if nitrogen is found in bio-fuels. Therefore, the oxygen and nitrogen should be removed from bio-oils or lowered to a certain degree first if intented to be used as a transportation fuel. Hydrodenitrogenation and hydrodeoxygenation are the two main upgrading processes to lower the nitrogen and oxygen content in the bio-oils.

Table 4 Main chemical compounds present in bio-oils.

No	**Compound**	**Relative abundance (% area)**			
		No catalyst	**CeO_2**	**TiO_2**	**Al_2O_3**
1	2-Pentanone, 4-hydroxy-4-methyl-	75.80	–	–	–
2	3-Octanol	–	48.15	57.73	61.76
3	Aziridine, 1-(1-propenyl)-, (Z)-	–	–	–	1.09
4	Undecane	–	–	–	11.79
5	Heptane, 2,4-dimethyl-	–	–	4.14	–
6	Hexadecane	–	–	15.65	–
7	Methanamine, N,N-dimethyl-	–	0.27	–	–
8	Azetidine	–	0.88	0.56	–
9	Bicyclo[2.2.1]heptane-2-carbonitrile, 2-methyl-, exo-	–	0.30	–	–
10	(1S,3R,4R)-3-(Hydroxymethyl)-2-methyl-2-	–	–	1.09	–
11	1-Methyl-3-butenyl 3-methyl-3-hydroxybutyl ether	–	–	1.20	–
12	Ethenamine, N-methylene-	–	–	–	0.42
13	Dodecane	–	5.74	–	–
14	2(3H)-Furanone-3,3,4-d3, dihydro-4-D-	–	1.06	–	–
15	1-Octanol, 2-butyl-	–	20.08	–	2.67
16	2-Propynamide	–	0.36	–	–
17	Oxalic acid, isobutyl nonyl ester	–	5.04	–	–
18	Propiolonitrile	–	0.87	–	–
19	Decane	–	6.84	–	–
20	1,3-Butadiene, 2,3-dimethyl-	–	0.26	–	–
21	1,5-Hexadien-3-yne, 2-methyl-	–	0.25	–	–
22	Azetidine-D1	–	0.44	–	–
23	Methane, isocyanato-	–	0.26	–	–
24	Furan, 2,5-dihydro-	–	0.69	–	–

25	Ethene, methoxy-	0.39	–	–	0.38
26	Cyclopropane, 1,2-dimethyl-, trans-	–	–	–	0.81
27	Dodecane, 1,1-difluoro-	–	–	–	4.08
28	Oxalic acid, cyclobutyldecyl ester	8.90	–	–	–
29	2-Propenamide	1.04	–	–	0.47
30	2-Octanol formate	–	–	–	0.69
31	Dodecanal	–	1.78	–	–
32	1,3-Pentadiene, (e)-	–	1.21	–	–
33	3-Pentenenitrile, 2-oxo-	–	0.29	0.30	–
34	Bicyclo[4.3.1]dec-1(9)-ene oxide	–	–	3.33	–
35	1-Propanethiol, 2,2-dimethyl-	–	–	0.66	–
36	2-Oxaadamantan-6-ol	–	–	0.32	–
37	2-Propynenitrile	–	–	0.30	–
38	Pyridine, 2,3,4,5-tetrahydro-	–	–	0.87	–
39	2,4-Decadien-1-ol, (e,e)-	–	–	0.38	–
40	Trans-2-ethyl-3,3,5-trimethylcyclopentanone	–	0.25	–	–
41	Cyclopentanone, 2-methyl-3-(1-oxopropyl)-, trans-	–	–	0.33	–
42	Acetamide, 2-fluoro-	–	–	0.54	–
43	2-Butenedinitrile, (E)-	–	–	0.31	–
44	4-Isopropyl-5-methylhexa-2,4-dien-1-ol	–	–	0.50	–
45	1,5-Hexadiyne	–	–	0.36	–
46	3,7-Diazabicyclo[3.3.1]nonane, 9,9-dimethyl-	–	–	0.42	0.48
47	3-Furazancarboxamide, 4-(1-aziridinyl)-	–	–	–	0.53
48	2(1H)-Naphthalenone, octahydro-, trans-	–	–	0.50	–
49	9,9-Dimethyl-3,7-diazabicyclo[3.3.1]nonane	–	–	0.37	–
50	Pyridine, 2-methoxy-5-nitro-	–	–	0.58	0.51
51	Furazan-3-carbohydrazide, 4-methyl–N2-	–	–	0.41	–
52	2-Propenoic Acid, 3-(1-cyclopenten-1-yl)-, methyl	–	–	–	0.45
53	1H-Indene-2,5(3H,4H)-dione, tetrahydro-, cis-	–	–	–	0.38
54	1-Phenyl-3-hydroxy-2-fluoropropene-1	–	–	–	0.58
55	Phenol, 4-(aminomethyl)-2-methoxy-	–	–	0.39	–
56	Phenol, 3-methyl-2-nitro-	–	–	–	0.52
57	(2H) Benzene	–	0.24	–	–
58	1H-1,2,4-Triazole	–	0.35	–	–
59	Butane, 2-chloro-2-methyl-	–	0.66	–	–
60	1-Propanethiol	–	0.30	–	–
61	1-Dodecanol, 2-Methyl-, (S)-	3.16	–	–	–
62	1,3-Propylenimine	0.45	–	–	–
63	1H-Pyrrole	0.43	–	–	–
64	2,3-Dihydrofuran	1.27	–	–	–
65	8-Nonynoic acid	0.39	–	–	–
66	Acetonitrile, amino-	0.46	0.25	–	–
67	3-Pentanethiol	–	0.29	–	–
68	2-Propenenitrile, 2-methyl-	–	0.34	–	–
69	2-Azetidinecarboxylic acid, 1-nitroso-	–	0.27	–	–
70	2-Pentadecanone	–	2.23	–	–
71	N-Nitroso-methyl-D3-ethylamine	0.38	–	–	–
72	1,5-Pentanediol, 3-methyl-	1.10	–	–	1.78
73	1,4-Pentadiene	–	–	–	1.60
74	Acetonitrile, hydroxy-	–	–	–	0.50
75	Trimethylamine	–	–	–	2.28
76	1-Propanol, 2-methyl-	–	–	–	0.36
77	Carbon disulfide	–	–	–	0.42
78	2-Propenal	–	–	–	0.32

79	3,8,11-Trioxatetracyclo[4.4.1.0(2,4).0(7,9)]undecane, (1.alpha.,2.beta.,4.beta.,6.alpha.,7.beta.,9.beta.)-	0.48	–	–	–
80	Methyl vinyl ketone	0.57	–	–	–
81	3-Cyclohexen-1-one, 4-(1,5-dimethyl-4-hexenyl)-,	0.47	–	–	–
82	Propanenitrile	0.42	–	0.31	0.32
83	Dichloroacetic acid, 4-methylpentyl ester	–	–	3.46	–
84	Dodecane, 1,2-epoxy-	–	–	4.97	–
85	2-Undecene, (E)-	0.63	–	–	–
86	3-Butenenitrile	0.39	–	–	0.59
87	1-Heptadecanol	–	–	–	1.21
88	Cyclohexanone, 2,6-diethyl-	–	–	–	0.46
89	1-Heptyn-3-ol	–	–	–	0.71
90	Aziridine, 1-(1-propenyl)-, (E)-	–	–	–	0.31
91	[1R-(1Alpha.,5.alpha.,6.beta.)-6-N-propyl-3-azabicyclo[3.1.0]hexan-2-one	–	–	–	0.33
92	2-Cyclohexene-1-thione, 3,6,6-trimethyl-	–	–	–	0.59
93	(Z)-Cis-9,10-Epoxyheptadec-6-ene	–	–	–	0.61
94	2-Ethyl-3,3,5-methylcyclopentane	0.40	–	–	–
95	Pyridine-2,6-D2, 3-methyl-	0.54	–	–	–
96	2,3-Difluoro-2-(trifluoromethyl)-2H-azirine	0.81	–	–	–
97	2-Heptenal, 2-propyl-	0.66	–	–	–
98	3-Cyclopropylidene-1-propyne	0.85	–	–	–

FT-IR spectra of bio-oils obtained from pyrolysis of Isochrysis at 500 °C are given in Figure 2,a-d. FT-IR spectra, which represent the functional groups of bio-oils are consistent and confirm the presence of various types of compounds given in Table 4. The vibrations between 3000 and 3100 cm^{-1} are the characteristics of O–H groups, which indicate the presence of phenolics and alcohols. The sharp C–H and =C-H stretching vibrations between 2900 and 3000 cm^{-1} indicate the presence of aliphatics such as alkanes. The typical carbonyl group (C=O) streching vibrations at about 1700 cm^{-1} indicate the presence of aldehydes, ketones or carboxylic acids in bio-oils. Presence of alcohols and esters can be confirmed by C–H bending vibrations between 900 and 1350 cm^{-1} and C–O stretching vibrations between 1000 and 1350 cm^{-1} in bio-oils. Aromatic compounds are confirmed by the aromatic C=C stretching vibrations between 1350 and 1500 cm^{-1}.

Proton NMR spectra of the bio-oils obtained without and with metal oxide catalysts are given in Figure 3, a-d, while the integrations of selected regions of the spectra versus specific chemical shift ranges are presented in Table 5. NMR analysis is a powerful tool and of great importance, as it provides a complete overview of the chemical functionalities present in the bio-oils [30]. NMRs, which give an overview of the chemical functionalities present in the bio-oils, show that metal oxide catalysts altered the functionalities distribution. The aliphatic proton region of the metal oxide catalysts oils (0.0 to 1.5 ppm) was the most abundant. Among metal oxide catalysts, TiO_2 had the highest percentage of aliphatic protons (45.21% of all), while Al_2O_3 had the lowest (38.07% of all). The next integrated region from 1.5 to 3.0 ppm (aliphatic protons bonded to C=C double bond (aromatic or olefinic) or H two bonds away from a heteroatom)

did show slight differences between bio-oils obtained without and with catalyst, with CeO_2 having the lowest amount (19.43%) of protons in in this region. The region of the spectra (3.0-4.4 ppm) that characterises the aliphatic alcohol/ether protons, or methylene groups joining two aromatic rings were less in presence of metal oxide catalysts than without catalyst (9.54%). This sharp decrease in alcohols is mainly ascribed to the cracking of phytol, with TiO_2 being the most effective catalyst. The protons in the carbohydrates/aromatic ether (4.4-6.0 ppm) region were found to be in small amounts (~6-8 %) in all bio-oils, with lower levels in the presence of almost all metal oxide catalysts except Al_2O_3. These results are in accordance with the elemental (Table 3) and GC-MS (Table 4) analyses of bio-oils, which show lower oxygen contents when the catalysts were used. The aromatic region of the spectra (6.0-9.5 ppm) contain ~17-19 % of the protons in the bio-oils and the highest value of 19.44% was obtained without catalyst. Al_2O_3 produced the highest amount (18.57%) of aromatics while CeO_2 had the lowest (16.98%). This region represents hydrogen atoms both in benzenoid aromatic compounds and in heteroaromatics which contain oxygen and nitrogen such as furan and pyridine (Table 4). Negligible amount (~2 %) of aldehydes and carboxylic acids (9.0-10.1 ppm) were detected in bio-oils. The proton NMR results show that high percentages of the aliphatic structural units exist in the bio-oils obtained from pyrolysis of *Isochrysis*.

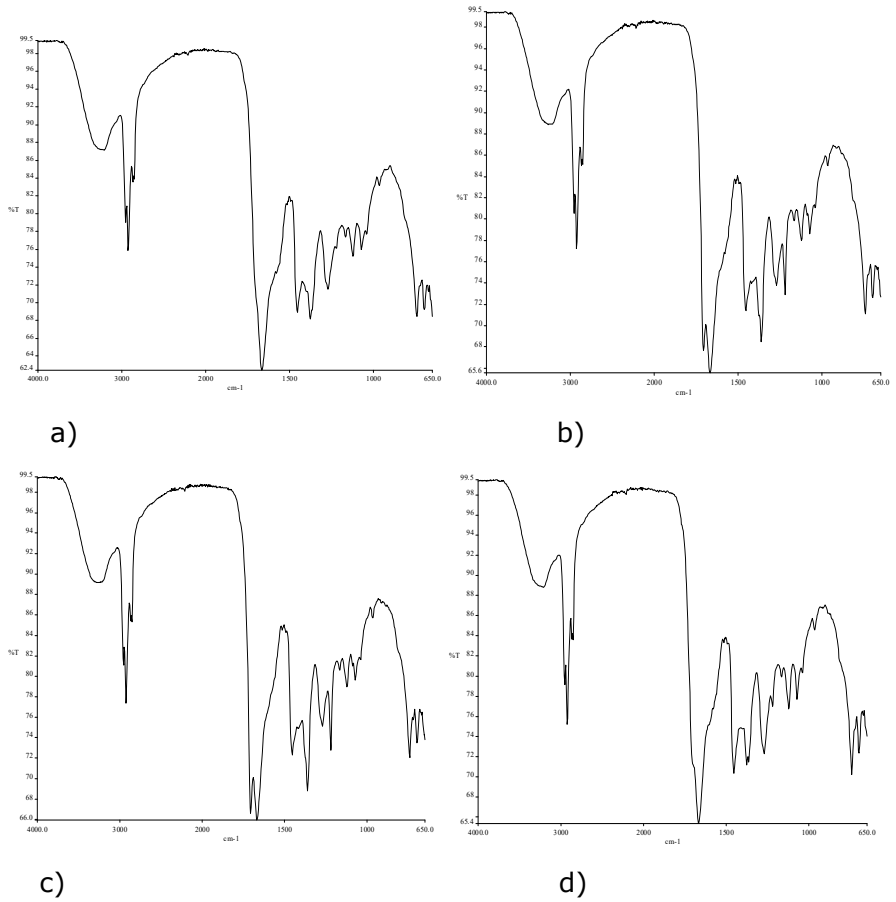

Figure 2 FT-IR spectra of bio-oils obtained at 500 °C a) without catalyst b) with ceria c) with titania d) with alumina.

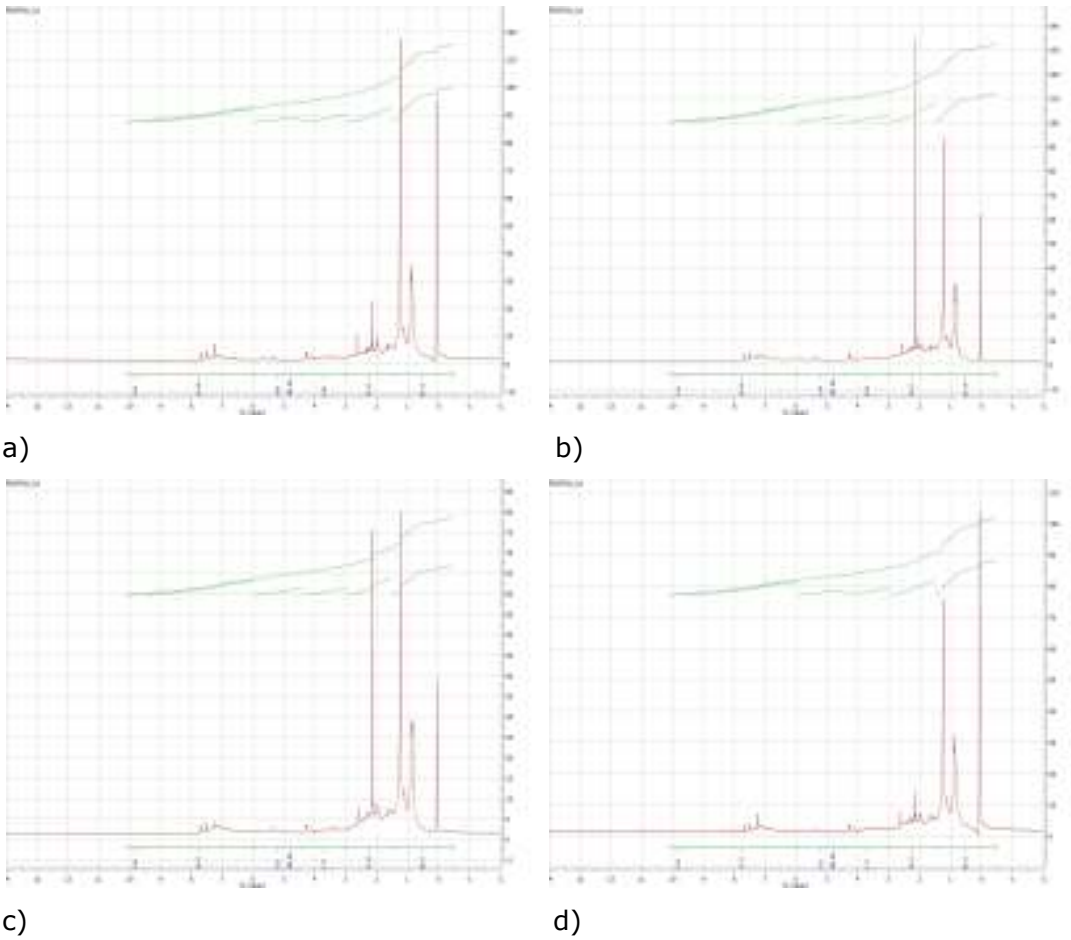

Figure 3 H^1-NMR spectra of bio-oils obtained at 500 °C a) without catalyst b) with ceria c) with titania d) with alumina.

Table 5 ^1H NMR Integrations of *Isochrysis* bio-oils obtained at 500 °C versus specific chemical shift ranges.

Chemical shift region (ppm)	**Proton assignment**	**Hydrogen content (% of all hydrogen)**			
		No catalyst	**TiO_2**	**CeO_2**	**Al_2O_3**
0.0 – 1.5	Alkanes	36.19	45.21	45.13	38.07
1.5 – 3.0	Aliphatics α-to heteroatom or unsaturation	24.07	19.51	19.43	23.42
3.0 – 4.4	Alcohols, methylene-dibenzene	9.54	9.11	9.30	9.12
4.4 – 6.0	Methoxy, carbohydrates	8.44	6.61	6.88	8.52
6.0 – 9.5	(Hetero-) aromatics	19.44	17.27	16.98	18.57
9.5 – 10.1	Aldehydes	2.31	2.29	2.28	2.30

CONCLUSION

In this study, an algal biomass (Isochrysis microalgae) was evaluated as feedstock for the catalytic (ceria, titania and alumina) production of bio-oils. The highest conversion of 73.61% and liquid (bio-oil) yield of 24.30% were obtained with titania at 550 and 500 °C respectively. The produced bio-oils were analyzed and characterized by EA, FT-IR, ^1H NMR and GC-MS which

indicated that temperature and catalyst have effected the product distribution. HHVs of bio-oils obtained in the presence of catalysts were higher than those obtained without. All bio-oils obtained with catalysts have suffered strong deoxygenation, with O level decreased from 46.40% in the starting feedstock to 14-17%. Elemental analysis showed that the bio-oils contained ~66-69% C and having 31-34 MJ/kg higher heating values. ^{1}H NMR analysis showed that all catalysts favoured the formation of aliphatics and lowered oxygen content of bio-oils. GC-MS analysis indicate that the bio-oils were enriched in alcohols, ketones and aliphatics.

REFERENCES

1. Le TA, Ly HV, Kim J, Kim S-S, Choi JH, Woo H-C, et al. Hydrodeoxygenation of 2-furyl methyl ketone as a model compound in bio-oil from pyrolysis of Saccharina Japonica Alga in fixed-bed reactor. Chemical Engineering Journal. 2014 Aug 15;250:157–63. DOI: 10.1016/j.cej.2014.04.003.

2. Babich IV, van der Hulst M, Lefferts L, Moulijn JA, O'Connor P, Seshan K. Catalytic pyrolysis of microalgae to high-quality liquid bio-fuels. Biomass and Bioenergy. 2011 Jul;35(7):3199–207. DOI: 10.1016/j.biombioe.2011.04.043.

3. Helwani Z, Othman MR, Aziz N, Fernando WJN, Kim J. Technologies for production of biodiesel focusing on green catalytic techniques: A review. Fuel Processing Technology. 2009 Dec;90(12):1502–14. DOI: 10.1016/j.fuproc.2009.07.016.

4. Neveux N, Yuen AKL, Jazrawi C, Magnusson M, Haynes BS, Masters AF, et al. Biocrude yield and productivity from the hydrothermal liquefaction of marine and freshwater green macroalgae. Bioresource Technology. 2014 Mar;155:334–41. DOI: 10.1016/j.fuproc.2014.08.014.

5. Duman G, Uddin MA, Yanik J. Hydrogen production from algal biomass via steam gasification. Bioresource Technology. 2014 Aug;166:24–30. DOI: 10.1016/j.biortech.2014.04.096.

6. Chisti Y. Biodiesel from microalgae beats bioethanol. Trends Biotechnol. 2008 Mar;26(3):126–31. DOI: 10.1016/j.tibtech.2007.12.002.

7. Nautiyal P, Subramanian KA, Dastidar MG. Production and characterization of biodiesel from algae. Fuel Processing Technology. 2014 Apr;120:79–88. DOI: 10.1016/j.fuproc.2013.12.003.

8. Wahlen BD, Barney BM, Seefeldt LC. Synthesis of Biodiesel from Mixed Feedstocks and Longer Chain Alcohols Using an Acid-Catalyzed Method. Energy Fuels. 2008 Nov 19;22(6):4223–8. DOI: 10.1021/ef800279t.

9. Yusuf NNAN, Kamarudin SK, Yaakub Z. Overview on the current trends in biodiesel production. Energy Conversion and Management. 2011 Jul;52(7):2741–51. DOI: 10.1016/j.enconman.2010.12.004.

10. Kim S-S, Ly HV, Kim J, Lee EY, Woo HC. Pyrolysis of microalgae residual biomass derived from Dunaliella tertiolecta after lipid extraction and carbohydrate saccharification. Chemical Engineering Journal. 2015 Mar 1;263:194–9. DOI:10.1016/j.cej.2014.11.045.

11. Umdu ES, Tuncer M, Seker E. Transesterification of Nannochloropsis oculata microalga's lipid to biodiesel on Al2O3 supported CaO and MgO catalysts. Bioresource Technology. 2009 Jun;100(11):2828–31. DOI: 10.1016/j.biortech.2008.12.027.

12. Xu H, Miao X, Wu Q. High quality biodiesel production from a microalga Chlorella protothecoides by heterotrophic growth in fermenters. Journal of Biotechnology. 2006 Dec 1;126(4):499–507. DOI: 10.1016/j.energy.2013.01.059.

13. Galadima A, Muraza O. Biodiesel production from algae by using heterogeneous catalysts: A critical review. Energy. 2014 Dec 15;78:72–83. DOI: 10.1016/j.energy.2014.06.018.

14. Grierson S, Strezov V, Shah P. Properties of oil and char derived from slow pyrolysis of Tetraselmis chui. Bioresource Technology. 2011 Sep;102(17):8232–40. DOI: 10.1016/j.biortech.2011.06.010.

15. Fatih Demirbas M. Biorefineries for biofuel upgrading: A critical review. Applied Energy. 2009 Nov;86, Supplement 1:S151–S161. DOI: 10.1016/j.apenergy.2009.04.043.

16. Miao X, Wu Q. High yield bio-oil production from fast pyrolysis by metabolic controlling of Chlorella protothecoides. Journal of Biotechnology. 2004 May 13;110(1):85–93. DOI: 10.1016/j.jbiotec.2004.01.013.

17. Hu Z, Zheng Y, Yan F, Xiao B, Liu S. Bio-oil production through pyrolysis of blue-green algae blooms (BGAB): Product distribution and bio-oil characterization. Energy. 2013 Apr 1;52:119–25. DOI: 10.1016/j.energy.2013.01.059.

18. Srirangan K, Akawi L, Moo-Young M, Chou CP. Towards sustainable production of clean energy carriers from biomass resources. Applied Energy. 2012 Dec;100:172–86. DOI: 10.1016/j.apenergy.2012.05.012.

19. Thangalazhy-Gopakumar S, Adhikari S, Chattanathan SA, Gupta RB. Catalytic pyrolysis of green algae for hydrocarbon production using H+ZSM-5 catalyst. Bioresource Technology. 2012 Aug;118:150–7. DOI: 10.1016/j.biortech.2012.05.080.

20. Chaiwong K, Kiatsiriroat T, Vorayos N, Thararax C. Study of bio-oil and bio-char production from algae by slow pyrolysis. Biomass and Bioenergy. 2013 Sep;56:600–6. DOI: 10.1016/j.biombioe.2013.05.035.

21. Campanella A, Harold MP. Fast pyrolysis of microalgae in a falling solids reactor: Effects of process variables and zeolite catalysts. Biomass and Bioenergy. 2012 Nov;46:218–32. DOI: 10.1016/j.biombioe.2012.08.023.

22. Harman-Ware AE, Morgan T, Wilson M, Crocker M, Zhang J, Liu K, et al. Microalgae as a renewable fuel source: Fast pyrolysis of Scenedesmus sp. Renewable Energy. 2013 Dec;60:625–32. DOI: 10.1016/j.renene.2013.06.016.

23. Aysu T. Catalytic pyrolysis of Eremurus spectabilis for bio-oil production in a fixed-bed reactor: Effects of pyrolysis parameters on product yields and character. Fuel Processing Technology. 2015 Jan;129:24–38. DOI: 10.1016/j.fuproc.2014.08.014.

24. Biller P, Ross AB. Potential yields and properties of oil from the hydrothermal liquefaction of microalgae with different biochemical content. Bioresource Technology. 2011 Jan;102(1):215–25. DOI: 10.1016/j.biortech.2010.06.028.

25. Marcilla A, Gómez-Siurana A, Gomis C, Chápuli E, Catalá MC, Valdés FJ. Characterization of microalgal species through TGA/FTIR analysis: Application to nannochloropsis sp. Thermochimica Acta. 2009 Feb 20;484(1–2):41–7. DOI: 10.1016/j.tca.2008.12.005.

26. Rover MR, Johnston PA, Whitmer LE, Smith RG, Brown RC. The effect of pyrolysis temperature on recovery of bio-oil as distinctive stage fractions. Journal of Analytical and Applied Pyrolysis. 2014 Jan;105:262–8. DOI: 10.1016/j.jaap.2013.11.012.

27. Naqvi SR, Uemura Y, Yusup SB. Catalytic pyrolysis of paddy husk in a drop type pyrolyzer for bio-oil production: The role of temperature and catalyst. Journal of Analytical and Applied Pyrolysis. 2014 Mar;106:57–62. DOI: 10.1016/j.jaap.2013.12.009.

28. Du S, Sun Y, Gamliel DP, Valla JA, Bollas GM. Catalytic pyrolysis of miscanthus × giganteus in a spouted bed reactor. Bioresource Technology. 2014 Oct;169:188–97. DOI: 10.1016/j.biortech.2014.06.104.

29. Akhtar J, Amin NAS. A review on process conditions for optimum bio-oil yield in hydrothermal liquefaction of biomass. Renewable and Sustainable Energy Reviews. 2011 Apr;15(3):1615–24. DOI: 10.1016/j.rser.2010.11.054.

30. Mullen CA, Strahan GD, Boateng AA. Characterization of Various Fast-Pyrolysis Bio-Oils by NMR Spectroscopy. Energy Fuels. 2009 May 21;23(5):2707–18. DOI: 10.1021/ef801048b.

Türkçe Öz ve Anahtar Kelimeler

Biyoyağ Üretimi için Isochrysis Mikroalginin Metal Oksit Katalizörleri ile Pirolizi

Tevfik Aysu[1]*

Öz: Isochryris mikroalginin pirolizi sabit yataklı bir reaktörde katalizörsüz ve metal oksit katalizörleri (CeO_2, TiO_2, Al_2O_3) ile ilk defa 450, 500 ve 550 °C sıcaklıklarda 40 °C/dak ısıtma hızı kullanılarak gerçekleştirilmiştir. Sıcaklık ve katalizör gibi piroliz parametrelerinin ürün verimleri üzerine etkileri incelenmiştir. Elde edilen katı, sıvı (biyoyağ) ve gaz ürünlerin miktarları hesaplanmıştır. Piroliz sonucu üretilen biyoyağların içerikleri elementel analiz (EA), Fourier Dönüşümlü Kızılötesi Spektroskopisi (FT-IR), proton nükleer manyetik rezonans (^{1}H NMR) ve Gaz Kromatografisi-Kütle Spektrometresi (GC-MS) teknikleri ile belirlenmiştir. Sonuçlardan, sıcaklık ve katalizörün Isochrysis mikroalginin katı, sıvı ve gaz ürünlere dönüşümü üzerine önemli etkilerinin olduğu görülmüştür. Sıvı faz dâhil en yüksek biyoyağ verimi %24.30 olarak TiO_2 (50%) katalizörü varlığında 500 °C sıcaklıkta elde edilmiştir. GC-MS analizi sonucu 500 °C'de elde edilen biyoyağlarda 98 farklı bileşiğin bulunduğu belirlenmiştir. ^{1}H NMR analizi biyoyağların ~60-64 % alifatik ve ~17-19 % aromatik yapısal birimlerden oluştuğunu göstermiştir. Elementel analiz sonuçlarına göre biyoyağların ~66-69 % karbon içerdiği ve 31-34 MJ kg^{-1} arasında ısıl değere sahip oldukları tespit edilmiştir.

Anahtar Kelimeler: Enerji; mikroalg; piroliz; *isochrysis*; katalizör.

Sunulma: 12 Temmuz 2016. **Düzeltme:** 20 Kasım 2016. **Kabul:** 14 Aralık 2016.

JOTCS A Journal of the Turkish Chemical Society Section: A Chemistry
TURKISH CHEMICAL SOCIETY

Simultaneous Determination of Different Anions in Milk Samples Using Ion Chromatography with Conductivity Detection

Orhan Destanoğlu and Gülçin Gümüş Yılmaz*
Istanbul Technical University, Faculty of Science and Letters, Department of Chemistry, 34469 Maslak, Istanbul, Turkey

Abstract: In this study, a simple method for simultaneous determination of chloride, nitrate, sulfate, iodide, phosphate, thiocyanate, perchlorate, and orotic acid in milk samples was investigated. The method involves the use of dialysis cassettes for matrix elimination, followed by ion chromatographic analysis of the anions on a high capacity anion exchange column with suppressed conductivity detection. The novelty of the proposed method was the use of dialysis process which did not need any chemical and organic solvent for elimination of macromolecules such as fat, carbohydrates and proteins from milk samples. External standard calibration curves for these analytes were linear with good correlation coefficients. The relative standard deviations of analyte concentrations were acceptable both inter-day and intra-day evaluations. Under optimized conditions, the limit of detection (Signal-to-Noise ratio = 3) for chloride, phosphate, thiocyanate, perchlorate, iodide, nitrate, sulfate, and orotate was found to be 0.012, 0.112, 0.140, 0.280, 0.312, 0.516, 0.520, and 0.840 mg L^{-1}, respectively. Significant results were obtained for various spiked milk samples with % recovery in the range of 93.88 - 109.75 %. The proposed method was successfully applied to milk samples collected from Istanbul markets. The advantages of the method described herein are reagent-free, simple, and reliable.

Keywords: Anions; dialysis; milk; ion chromatography; orotic acid.

Submitted: November 03, 2016. **Revised:** December 03, 2016. **Accepted:** December 24, 2016.

Cite this: Destanoğlu O, Gümüş Yılmaz G. Simultaneous Determination of Different Anions in Milk Samples Using Ion Chromatography with Conductivity Detection. JOTCSA. 2017;4(1):415–32.
DOI: To be assigned.
*Corresponding author. E-mail: ggumus@itu.edu.tr.

Table 1. List of notations/symbols and units.

Notations/Abbriviations		Units	
IC	Ion chromatography	mM	Millimolar
NIS	Sodium iodide symporter	L	Liter
N or n	Number of samples	mL	Milliliter
K_a	Dissociation constant of an acid	g	Gram
pK_a	Negative logarithm of K_a	mg	Milligram
LOD	Limit of detection	min	Minutes
LOQ	Limit of quantification	°C	Degrees celcius
SD	Standard deviation	h	Hours
RSD	Relative standard deviation	kDa	Kilodalton
t_R	Retention time	MWCO	Molecular weight cut-off

INTRODUCTION

Thyroid hormones are necessary for brain and neural development in fetuses and infants [1, 2]. In the cellular membrane of the cells from thyroid follicles, the protein responsible for iodide capture from the bloodstream was identified as sodium iodide symporter (NIS), which is present in the thyroid gland and also in the mammary glands. Iodide is an important trace element used by the thyroid gland to make thyroid functioning a human beings [3]. Deficiency or excess intake of iodine gives rise to disorders commonly referred to as iodine disorders. In the pregnant and lactating women, iodine deficiency leads to increased early and late loss of gestation, intellectual disability, cretinism, and growth retardation [4, 5]. A number of inorganic anions can block iodide (I^-) uptake at the thyroidal sodium iodide symporter (NIS) in a competitive manner. Among these, nitrate (NO_3^-), thiocyanate (SCN^-), and perchlorate (ClO_4^-) are of particular dietary and/or environmental importance [6]. Sufficient inhibition of iodide uptake can lead to decreased thyroid hormone production and, ultimately, results in adverse health effects secondary to hypothyroxinemia. In particular, infants under six months of age are very susceptible to nitrate poisoning. The solubility of $NaClO_4$ in water is 2 kg L^{-1}, and the compound is almost inert in surface waters. For this reason, perchlorate pollution can persist for long periods. Perchlorate is found as a common contaminant of food, water, milk, human milk [7-11]. Chloride (Cl^-) is one of the typical anions which its determination in milk has a great interest. The chloride determination in milk is a useful parameter to understand the degree of subclinical mastitis that may occur in cattle [12]. It is also important to determine phosphate (PO_4^{3-}) and sulfate (SO_4^{2-}) concentrations in milk because they are naturally present in the crude matter and may also be introduced during the industrial manipulations [13]. Orotic acid (1,3,5-trihydro-2,6-dioxo-pyrimidine-4-carboxylic acid) is an intermediate product in pyrimidine biosynthesis. The molecular structure of orotic acid is given in Figure 1. Recent experimental studies have demonstrated that it is involved in carcinogenesis, hepatic lipid storage and renal toxicity [14].

Several studies have shown that repeated dosing of orotic acid promotes the formation of tumors initiated by various known carcinogenic substances [15].

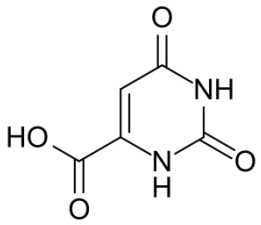

Figure 1. Molecular structure of orotic acid.

Sample preparation is an important part of the analysis of anions in a complex matrix especially in milk to manage a good analytical procedure. Because milk has high molecular mass compounds such as fats, proteins, and carbohydrates that can interfere with the analysis, some initial cleanup procedures are required before the analysis of anions. There are a number of matrix elimination methods, for example, dry ashing, wet digestion in closed system with microwave assistance are currently used [16, 17]. They involve generally laborious sample pre-treatments, too many steps, and time consuming nature, and the sample can lose its volatile species during the process. A micro-dialysis sampling technique is gentle and non-degrading procedure because of the fact that it can be used in multi-component analysis. Dialysis process depends on molecular diffusion occurring as a result of the concentration gradient of analyte of interest between donor and acceptor solutions. Dialysis procedure is mostly used in biological fields. In a representive study, cytochrome c, insulin, lysozyme, and ribonuclease A were separated from human serum albumin by using dialysis procedure [18]. In another study, the determination of inorganic anions in olive oil mill wastewater can be achieved by using dialysis procedure [19]. However, no previous research had focused on the analysis of anions and orotic acid in milk samples by using dialysis technique for sample preparation. This is the first paper on simultaneous determination of chloride, nitrate, sulfate, iodide, phosphate, thiocyanate, perchlorate, and orotic acid in milk by using dialysis as a sample preparation technique.

A wide range of techniques have been employed for the determination of anions and organic acids in milk, including voltammetry, flow injection methods, X- ray fluorescence spectroscopy, and neutron activation analysis [20, 21]. In a representative report, anions, including iodide, nitrate and nitrite in biological samples were analyzed by micellar electrokinetic capillary chromatography [22]. In another study, determination of iodine species in milk was done with using epithermal neutron activation analysis. In this method, pre-concentration of iodide anion was achieved by using polymer inclusion sorbent [4]. Another study showed that benzoic acid and sorbic acid in food products were analyzed by using electrokinetic flow injection analysis [23].

Ion chromatography has been used for determination of anions and organic acids with pK_a value below *ca*. 6, drawing analyst's attention to its capabilities of high sensitivity, rapidness, and the ease of operation, coupled with the advantage of simultaneous determinations [24]. However, up to now chloride, nitrate, sulfate, iodide, phosphate, thiocyanate, perchlorate, and orotic acid in milk are not analyzed using one method. In the present study, we demonstrated an ion chromatographic method for quantification of one organic acid and seven anions at the same time under a suppressed conductivity detector. The aim of this work is to present a simple and accurate procedure for milk pre-treatment. The sample's matrix elimination is carried out by using dialysis method with dialysis cassette. The proposed method of analysis has the following advantages: (a) addition of chemicals are not required; (b) proteins and lipids can be removed easily.

EXPERIMENTAL

1) Materials and Chemicals

Four milk samples from different brands were purchased from local markets in İstanbul. In addition, a raw milk sample was purchased from dairy farm. Additionally, a bottled daily milk sample was taken from a market. All solutions and reagents were prepared from highly pure analytical grade chemicals using ultra pure water. All chemicals used is in extra pure state (purity is up to > 99%). Sodium perchlorate monohydrate ($NaClO_4.H_2O$), potassium nitrate (KNO_3), potassium iodide (KI) and sodium chloride (NaCl) were obtained from Merck, Darmstadt, Germany. Sodium hydrogen phosphate dihydrate (dibasic) ($Na_2HPO_4.2H_2O$) and ammonium thiocyanate (NH_4SCN) were purchased from Riedel de Haën, Seelze, Germany. Anhydrous orotic acid ($C_5H_4O_4N_2$) and anhydrous sodium sulfate (Na_2SO_4) were provided by Sigma-Aldrich, Steinheim, Germany.

2) Instrumentation

Dionex ICS-3000 (Sunnyvale, CA, USA) ion chromatograph equipped with a suppressed conductivity detector (ASRS ULTRA II-2mm suppressor and conductivity cell) was used for analyses of anions in milk samples. Chromatographic separations were performed at 25 ºC with a Dionex IonPac® AS20 analytical column (2 x 250 mm) equipped with a Dionex IonPac® AG20 guard column (2 x 50 mm). Analytical column resin composition is super macroporous polyvinyl benzyl ammonium polymer cross-linked with divinylbenzene. Guard column's resin composition is microporous polyvinylbenzyl. Eluents' gradients were generated on-line from ultra pure water using the Dionex Eluent Generator, EGC II NaOH cartridge and then polished from the contaminants using Continuously Regenerating Trap Columns CR-ATCs. The eluent concentrations was controlled by Dionex Chromeleon® Client (6.80) software. The instrument was also equipped with a Pump and attached to an AS autosampler. 10 µL sample loop was used in all analyses unless otherwise stated.

Ultrapure water of 18.2 MΩ cm resistivity or better was obtained from a New Human Power I Scholar UV system (Human Corporation, Seoul, Korea). All solutions were prepared from highly pure analytical reagent grade compounds by using ultra pure water.

3.0 – 12 mL capacity of Slide-A-Lyzer® Dialysis cassette allowing passage of molecules (≤ 2 kDa) was supplied by Thermo Scientific (Rockford, IL 61101, U.S.A.). This cassette (molecular weight cut-off: 2K) facilitate simple and effective removal of ions from macromolecules that are larger than 2000 daltons. Membrane structure the cassette is cellulose.

3) Preparation of Stock and Standard Solutions

Stock solutions of the anions (Cl^-, NO_3^-, SO_4^{2-}, PO_4^{3-}, I^-, ClO_4^-, SCN^-) (1000 mg L^{-1}) were prepared by dissolving 0.165 g of NaCl, 0.141 of $NaClO_4.H_2O$, 0.163 g of KNO_3, 0.131 g of KI, 0.187 g of $Na_2HPO_4.2H_2O$, 0.131 g of NH_4SCN and 0.148 g of Na_2SO_4 in different 100 mL volumetric flasks and diluting to the mark with water. A stock solution of 100 mg L^{-1} of orotic acid was prepared by dissolving an appropriate amount of orotic acid in a 500 mL volumetric flask and diluting to the mark with water. The aqueous standard stock solutions of anions was prepared to obtain the calibration curves and to spike the milk samples.

4) Optimization of Dialysis Time

In order to optimize the dialysis time for chloride, nitrate, sulfate, iodide, phosphate, thiocyanate, perchlorate, and orotate, a 5.0 mL mixed standard aqueous solution containing 1.0 mg L^{-1} of each anion was loaded into the dialysis cassette. Subsequently, the cassette was submerged and fitted vertically into a plastic beaker containing 400 mL of ultrapure water. A magnetic stirrer was also utilized to accelerate the dialysis. 0.5 mL portions have been taken from the solution diffused to water in the beaker at different times and were immediately injected into the IC system under optimum ion chromatographic conditions.

5) Dialysis of Milk Samples

In proposed method, the newest sample preparation method including dialysis technique was investigated for matrix elimination of milk samples. The dialysis cassette was utilized for removing macromolecules such as milk fat, carbohydrates, and proteins from milk sample, because the macromolecules can affect ion chromatographic analysis of anions.

Good recoveries of the anions were obtained by using flat cassette chamber with two membranes provides high surface-area to volume ratio. The cassette does not require knots or clips that may result in leaking and sample loss. Rectangular cassette design (see Figure 2) maximizes recovery of entire sample volume with any one of the four corner injection ports.

Dialysis procedure was as follows: a) A syringe was filled with milk sample, b) the syringe needle was inserted through the gasket via one of the corner ports, c) 5 mL of spiked and unspiked milk sample were injected into the cassette, d) the excess air was withdrawn and the syringe was removed, e) a float buoy was attached onto the cassette, f) the sample was dialyzed to 400 mL ultra pure water in a plastic beaker in the presence of a magnetic stirrer, f) after a steady state time ~ 45 hours, which is described in the bottom paragraph, dialysis filtrate was analyzed by ion chromatography with conductivity detector using a computerized gradient elution program.

To clean the used cassette, an empty syringe was inserted to second corner port. Air was injected for expanding cassette chamber. Finally, the dialyzed sample was withdrawn.

Figure 2. Dialysis cassette; 2000 MWCO and 3 – 12 mL capacity.

6) Chromatographic conditions and Measurements

Many experiments targeting the optimal ion chromatographic separation for all anions in samples have been performed. The conditions of the suitable program is given in Table 2. Column temperature was 25 °C, cell temperature was 30 °C; current of the suppressor was 31 mA and injection volume was 10 µL.

External calibration curves drawn by peak areas versus concentrations were used for the quantification of analytes. Calculations were done by utilizing correlation equations ($y = mX + n$). A chromatogram obtained for a standard solution containing chloride, nitrate, sulfate, iodide, phosphate, thiocyanate, perchlorate and orotic acid of a 3 mg L^{-1} for each is shown in Figure 3.

Table 2. Optimum eluent (NaOH) program for separation of the anions on the anion exchange column.

Time (min.)	Concentration (mM)
0-1	3 isocratic
1.1-13	3-20 gradient
13.1-20	20 isocratic
20.1-21	20-50 gradient
21.1-24	50 isocratic
24.1-25	50-3 gradient
25.1-30	3 isocratic

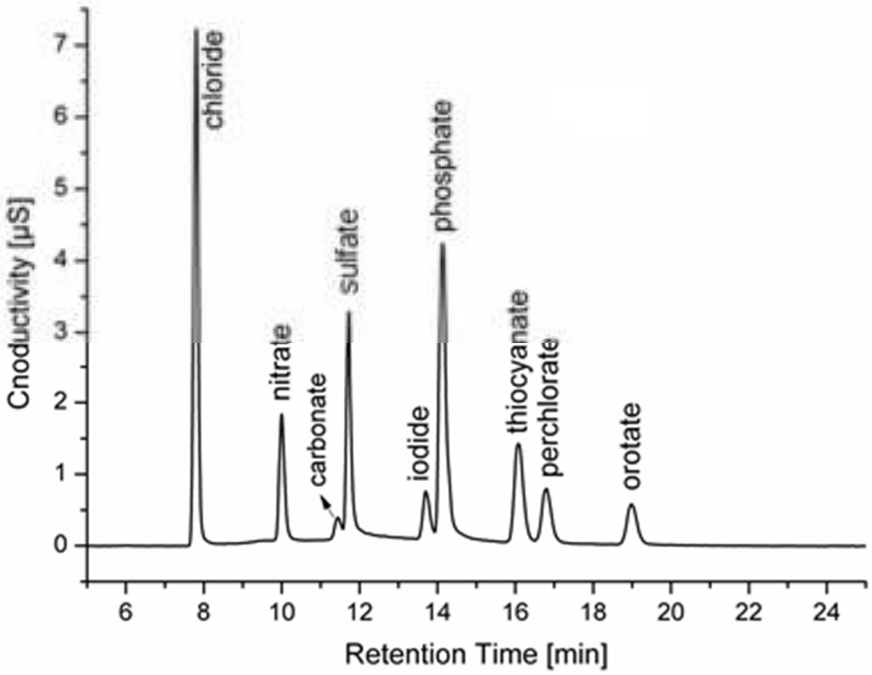

Figure 3. Chromatogram of a standard aqueous solution containing different anions.

7) Theoretical and statistical aspects

6.1) *LOD:* $\frac{signal}{noise} = 3$

LOQ: $\frac{signal}{noise} = 10$ [25]

6.2) *Standard Deviation:* $SD = \sqrt{\frac{(x-\bar{x})^2}{(n-1)}}$

(x: each measured value; $\bar{x}$: the mean value of population; n: number of measurement; $n-1$: degree of freedom)

Relative Standard Deviation: $RSD = \frac{SD}{\bar{x}}$

$RSD\ \% = \frac{SD}{\bar{x}} \times 100$

6.3) $Recovery\ \% = \frac{(\text{Found concentration} - \text{initial concentration})}{\text{added concentration}} \times 100$ [25]

6.4) *t value calculation:* $\text{tcal} = \frac{((\text{Recovery}\,\% - 100)\times\sqrt{\text{n}})}{SD}$ [26]

RESULTS AND DISCUSSION

Optimum dialysis time

After the filtrated 0.5 mL aqueous solutions had been collected at different times from plastic beakers during dialysis, these 0.5 mL portions were injected to the IC system and the recoveries were calculated. Figure 3 exhibits that all anions were completely transferred into 400 mL of water after 45 h during dialysis process. It was observed that recovery % values ranged from 96.5 % to 106.7 which are acceptable recovery values [26-28]. Thus, all of the other studies were carried out according to 45 h dialysis time.

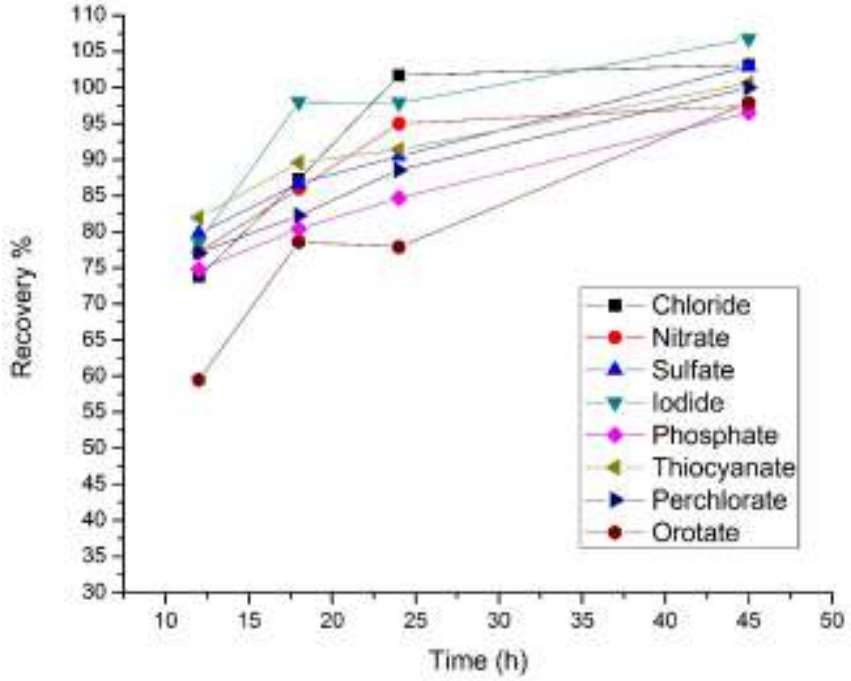

Figure 3. The plot of recovery % values for determination of optimum dialysis time for chloride, nitrate, sulfate, iodide, phosphate, thiocyanate, perchlorate, and orotate.

Validation of the method

To validate the proposed method, numerous analytical parameters such as linearity, limits of detection (LOD) and quantitation (LOQ), with-in run precision, intermediate precision, and accuracy have been evaluated. All of these parameters should be evaluated for validation of the method [25]. Microsoft Excel office software was used for all calculations.

Linearity, limit of detection and quantitation

External calibration method was used for determine the concentration of analytes in the samples. Linear concentration range, linear regression equations, correlation coefficients (r^2), LOD values, LOQ values and retention times are given in Table 3. Under the optimum ion chromatographic *(vice versa)* conditions, aqueous calibration standards have been injected five times into the IC

system. The linear relationships could be established with the linear regression equations, $y = ax + b$, wherein y is the peak area (μS min^{-1}) and x is concentration (mg L^{-1}). The experimental coefficients of the linear regression indicated a first-order correlation in all cases. LOD and LOQ values have been calculated from the peak height as the average concentration corresponding to the signal-to-noise ratio equal to 3 and 10, respectively. LOD and LOQ values for samples were again corrected for real samples by multiplying with dilution factor.

Table 3. Linear concentration range, regression equation, retention time, r^2, LOD and LOQ values.

Analyte	Linear Range (mg L^{-1})	Regression Equation	t_R (min)	r^2	LOD* (mg L^{-1})	LOQ* (mg L^{-1})
Chloride	0.01 - 9.0	y = 0.2131x – 0.017	7.76	0.9989	0.012	0.040
Nitrate	0.05 – 9.0	y = 0.0791x – 0.0067	10.01	0.9985	0.516	1.720
Sulfate	0.05 – 9.0	y = 0.0989x – 0.009	11.71	0.9999	0.520	1.733
Iodide	0.03 – 9.0	y = 0.0437x + 0.003	13.76	0.9989	0.312	1.040
Phosphate	0.01 – 9.0	y = 0.154x – 0.0219	14.29	0.9968	0.112	0.373
Thiocyanate	0.01 – 9.0	y = 0.123x – 0.0058	16.13	0.9968	0.140	0.467
Perchlorate	0.03 – 9.0	y = 0.0716x – 0.0114	16.87	0.9975	0.280	0.933
Orotate	0.07 – 9.0	y = 0.0661x – 0.0026	19.08	0.9953	0.840	2.800

***LOD and LOQ values were of the proposed method.

Precision

Repeatability is a criterion for precision. In addition, SD and RSD values are used for evaluation of repeatability. Therefore, a standard aqueous solution in which the concentration was 3.0 mg L^{-1} for each anion was injected five times to IC system and analyzed. High RSD values are acceptable for very low μg L^{-1} whereas accepted RSD values decrease as the concentrations increase. To illustrated, the acceptable RSD % is 5.3 for the analyte concentration of 100 mg L^{-1} while the acceptable RSD % is 30 for 1 μg L^{-1} concentration [28]. It is obvious from Table 4 that the repeatability of the IC system is excellent owing to very low RSD values of both peak areas and retention times. Moreover, milk sample 2 treated with dialysis has been injected five times into the IC system at three different days under optimized conditions and intermediate precision was evaluated. RSD values pointed that intermediate precision of the method was very well (see Table 5).

Table 4. Repeatabilities of the analytical signal and retention time for the 3 mg L^{-1} chloride, nitrate, sulfate, iodide, phosphate, thiocyanate, perchlorate, and orotate (n = 5).

Analyte	Area of the signal ($\mu S\ cm^{-1}\ min$)	RSD (%)	t_R (min)	RSD (%)
Chloride	0.97	0.48	7.76	0.15
Nitrate	0.28	0.58	10.01	0.07
Sulfate	0.43	3.55	11.71	0.01
Iodide	0.14	1.19	13.76	0.10
Phosphate	0.91	0.98	14.29	0.12
Thiocyanate	0.37	0.75	16.13	0.06
Perchlorate	0.21	1.49	16.87	0.05
Orotate	0.17	0.69	19.08	0.09

Table 5. RSD (%) values of within run and intermediate precisions of milk sample 2 for chloride, nitrate, sulfate, iodide, phosphate, and orotate.

	Chloride	Nitrate	Sulfate	Iodide	Phosphate	Orotate
$RSD_{with\text{-}in\ run}$(%) (n=5)	0.80	3.96	4.29	2.53	0.67	4.28
$RSD_{intermediate}$(%) (n=3)	2.96	12.74	3.31	6.46	2.40	3.41

Accuracy

The recovery values were taken into consideration to evaluate the accuracy of the method. Three different concentration levels (see Table 6) were added to milk sample #1, as described below. The significance test (t-test) at 95% confidence level was applied to recovery values. If the calculated t value is less than the tabulated value for 2 (n - 1) degree of freedom at 95 % significance level, the null hypothesis is accepted and the method is accurate [26]. We feel confident to note that the calculated t values were absolutely adequate for good accuracy as they were smaller than theoritical critical t value equal to 4.30 (see Table 5). At this point, we should emphasize that acceptable recovery percentage range is 70 – 120% with a precision about 20% in analytical studies [27,28].

Recovery studies were conducted by spiking a milk sample. Milk sample #1 was spiked with standard analyte solutions at three different concentrations. The added amounts for spike works are given in Table 6. Two mixed standard solutions were primarily prepared because the chloride and phosphate concentrations were very high comparing to the other anions. The first mixed solution contained chloride and phosphate whereas the other mixed solution included nitrate, sulfate, iodide, thiocyanate, perchlorate, and orotate anions. When dialysis time were finished, a 10-mL sample from 400 mL solution was filtered with PES (polyethersulfone) syringe filter and loaded into autosampler vials for IC-CD analysis. Another 10 mL from chloride and phosphate

recovery assay was additionally diluted 10 times prior to injection since the concentrations of chloride and phosphate were extremely high (especially in spiked solutions). Increasing concentrations of chloride caused interference with nitrate. On the other hand, additional ten-fold dilution of chloride and phosphate were convenient in terms of performing the analysis within the linear ranges. The concentration values in Table 6 are given after corrected by multiplying dilution factors.

Analysis of milk samples

Figure 4 presents the chromatogram for the milk sample 3. The ion chromatographic results of the anions in milk samples are given in Table 7. The milk samples between number 1 – 4 in Table 7 were different brands purchased from local markets in İstanbul. Sample #5 was a raw milk sample. The raw milk sample was also boiled and it was analyzed in same conditions as sample #6. It has been observed that the concentrations of anions in raw milk were dramatically changed after boiling. Concentrations of chloride, nitrate, sulfate, and orotic acid was increased whereas phosphate was decreased and thiocyanate peak disappeared in boiled milk. Moreover, a bottled daily milk sample (#7) was analyzed. Chloride, sulfate, phosphate, and orotate were observed in all samples. Chloride and phosphate concentrations were at the highest concentrations. Iodide was detected in two samples while thiocyanate were detected only in one sample. Perchlorate was not observed in the samples according to the present method. Nitrate was not detected in only one sample. Figure 5 also more apparently exhibits the concentration distribution of anions by samples. In brief, the found concentrations of anions in milk samples were also ordered as follows:

Sample #1: $[PO_4^{3-}] > [Cl^-] >> [SO_4^{2-}] > [Orotate] > [NO_3^-] > (I^-,\ ClO_4^-, SCN^-\ Not\ detected)$

Sample #2: $[Cl^-] > [PO_4^{3-}] >> [SO_4^{2-}] > [Orotate] > [NO_3^-] > (I^-, ClO_4^-, SCN^-\ Not\ detected)$

Sample #3: $[Cl^-] > [PO_4^{3-}] >> [SO_4^{2-}] > [Orotate] > [NO_3^-] > [I^-] > (ClO_4^-, SCN^-\ Not\ detected)$

Sample #4: $[Cl^-] > [PO_4^{3-}] >> [SO_4^{2-}] > [Orotate] > [NO_3^-] > [I^-] > (ClO_4^-, SCN^-\ Not\ detected)$

Sample #5: $[PO_4^{3-}] > [Cl^-] >> [Orotate] > [SO_4^{2-}] > [NO_3^-] > [SCN^-] > (I^-, ClO_4^-\ Not\ detected)$

Sample #6: $[Cl^-] > [PO_4^{3-}] >> [SO_4^{2-}] > [Orotate] > [NO_3^-] > (I^-, ClO_4^-, SCN^-\ Not\ detected)$

Sample #7: $[PO_4^{3-}] > [Cl^-] >> [SO_4^{2-}] > [Orotate] > (NO_3^-,\ I^-, ClO_4^-, SCN^-\ Not\ detected)$

Table 6. Recovery (%) and calculated t values for chloride, phosphate, nitrate, sulfate, iodide, thiocyanate, perchlorate, and orotate in milk sample 1.

Anion	**Concentration (mg L^{-1})**			**Recovery (%)**	**SD**	**RSD (%)**	t_{cal}
	Initial± SD	**Added**	**Found**	**(n=3)**			
Chloride	913±10	296	1208	99.83	4.13	4.14	0.07
		631	1598	108.56	4.45	4.10	3.33
		1215	2246	109.75	3.98	3.63	4.24
Phosphate	1678±19	496	2182	101.55	3.93	3.87	0.68
		664	2301	93.88	2.88	3.07	3.68
		1420	3133	102.44	2.38	2.32	1.78
Nitrate	4.72±0.16	2.0	6.79	103.31	11.3	10.94	0.51
		4.0	9.00	106.88	4.19	3.92	2.84
		13.2	18.67	105.67	4.20	3.97	2.34
		26.8	31.26	99.04	2.58	2.60	0.64
		53.2	59.23	102.46	1.50	1.46	2.84
Sulfate	97.60± 0.40	30.4	127.92	99.75	6.85	6.87	0.06
		200.0	329.72	116.06	7.83	6.75	3.55
		400.0	530.00	108.10	3.32	3.07	4.23
Iodide	N.D.[a]	44.36	44.48	100.27	0.81	0.81	0.58
		55.16	55.68	100.94	1.31	1.30	1.24
		115.16	116.43	101.11	0.97	0.96	1.98
Thiocyanate	N.D.	37.40	37.96	101.50	0.85	0.84	3.06
		50.0	49.56	99.12	1.24	1.25	1.23
		122.0	120.72	98.95	0.66	0.67	2.76
Perchlorate	N.D.	38.24	39.20	102.51	1.26	1.23	3.45
		41.44	42.38	102.27	0.94	0.92	4.18
		122.0	116.32	95.34	2.14	2.24	3.77
OA	74.60 ± 0.60	19.40	96.55	113.14	7.14	6.31	3.19
		37.48	112.07	99.97	5.73	5.73	0.01
		81.60	161.89	106.63	3.74	3.51	3.07

[a] N.D. : Not Detected

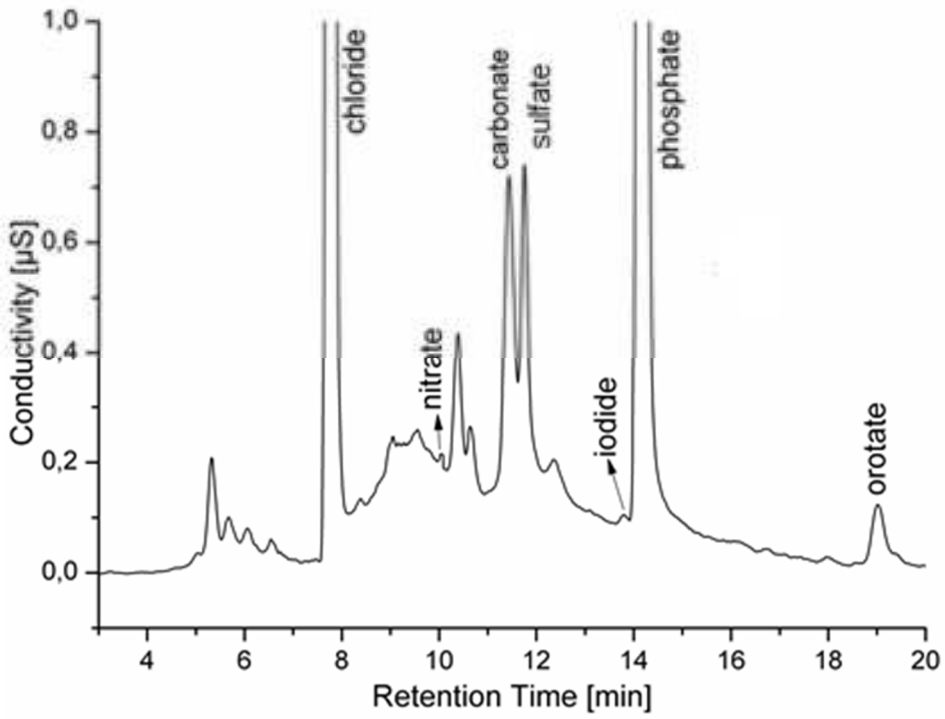

Figure 4. Chromatogram of milk sample 3.

Table 7. Concentration results of chloride, nitrate, sulfate, iodide, phosphate, thiocyanate, perchlorate, and orotate in real milk samples (n = 5).

Analyte anions		Sample 1	Sample 2	Sample 3	Sample 4	Sample 5	Sample 6 (Boiled)	Sample 7
Cl^-	C (mg L^{-1})	913	999	896	939	1177	1474	1099
	RSD %	1.1	0.8	0.1	0.7	0.5	0.1	0.7
NO_3^-	C (mg L^{-1})	4.72	6.37	8.06	9.30	3.86	4.98	N.D.
	RSD %	3.4	12.4	1.9	2.2	2.9	2.4	-
SO_4^{2-}	C (mg L^{-1})	97.6	156.5	79.9	80.1	43.4	85.7	56.0
	RSD %	0.4	4.3	0.8	1.5	2.2	1.8	3.0
I^-	C (mg L^{-1})	N.D.	N.D.	7.87	7.45	N.D.	N.D.	N.D.
	RSD %	-	-	2.29	3.76	-	-	-
PO_4^{3-}	C (mg L^{-1})	1680	730	799	673	1278	839	1107
	RSD %	1.2	0.7	0.6	0.1	0.4	0.4	0.4
SCN^-	C (mg L^{-1})	N.D.	N.D.	N.D.	N.D.	2.8	N.D.	N.D.
	RSD %	-	-	-	-	0.7	-	-
ClO_4^-	C (mg L^{-1})	N.D.	N.D.	N.D.	N.D.	N.D.	N.D.	N.D.
	RSD %	-	-	-	-	-	-	-
orotate	C (mg L^{-1})	74.6	52.6	62.7	58.1	52.1	67.4	49.1
	RSD %	0.8	4.3	3.4	1.0	1.5	1.8	3.6

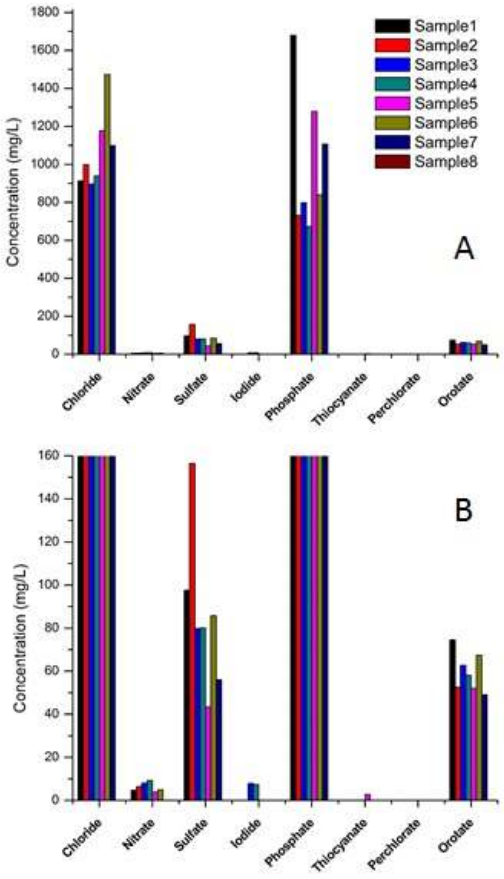

Figure 5. Distribition of results of anion concentrations in milk samples. A: Full scale distribition, B: zoomed image of A.

CONCLUSION

The most important advantage of this study is that this is the first study in the literature for the simultaneous determination of chloride, nitrate, sulfate, iodide, phosphate, thiocyanate, perchlorate, and orotate in milk by using dialysis technique for matrix elimination. This study may be a good alternative for studies related to needed difficult matrix elimination before analysis. The proposed method possesses many advantages which included easy preparation, the absence of chemicals, simple sample pretreatment procedure even if the dialysis time is long. The method was validated in terms of linearity, limits of detection and quantitation, intra-/inter-day accuracy, precision, and recovery. After hundreds of injections, no significant changes were observed on retention times. Very stable retention time values indicated that not only our method had good precision, but the life time of analytical column has also been prolonged as well. LOQ values were adequately small even though the analytes were diluted to 400 mL of water.

REFERENCES

[1] Martinelango PK, Gümüş G, Dasgupta PK. Matrix interference free determination of perchlorate in urine by ion association–ion chromatography–mass spectrometry. Analytica Chimica Acta. 2006 May;567(1):79–86. DOI:10.1016/j.aca.2006.02.022

[2] Niemann RA, Anderson DL. Determination of iodide and thiocyanate in powdered milk and infant formula by on-line enrichment ion chromatography with photodiode array detection. Journal of Chromatography A. 2008 Jul;1200(2):193–7. DOI: 10.1016/j.chroma.2008.05.064.

[3] Leung AM, Pearce EN, Braverman LE. Best Practice & Research Clinical Endocrinology & Metabolism Perchlorate , iodine and the thyroid. Best Pract Res Clin Endocrinol Metab. Elsevier Ltd; 2010;24(1):133–41. DOI: 10.1016/j.beem.2009.08.009.

[4] Bhagat PR, Pandey AK, Acharya R, Nair AGC, Rajurkar NS, Reddy AVR. Selective preconcentration and determination of iodine species in milk samples using polymer inclusion sorbent. Talanta 2007;71:1226–32. DOI: 10.1016/j.talanta.2006.06.018.

[5] Dorea JG. Iodine nutrition and breast feeding. Journal of Trace Elements in Medicine and Biology. 2002 Jan;16(4):207–20. DOI: 10.1016/S0946-672X(02)80047-5.

[6] Tonacchera M, Pinchera A, Dimida A, Ferrarini E, Agretti P, Vitti P, et al. Relative Potencies and Additivity of Perchlorate, Thiocyanate, Nitrate, and Iodide on the Inhibition of Radioactive Iodide Uptake by the Human Sodium Iodide Symporter. Thyroid. 2004 Dec;14(12):1012–9. DOI:10.1089/thy.2004.14.1012.

[7] Iannece P, Motta O, Tedesco R, Carotenuto M, Proto A. Determination of Perchlorate in Bottled Water from Italy. Water. 2013 Jun 13;5(2):767–79. DOI: 10.3390/w5020767.

[8] Sungur Ş, Atan MM. Determination of nitrate, nitrite and perchlorate anions in meat, milk and their products consumed in Hatay region in Turkey. Food Additives and Contaminants: Part B. 2013 Mar;6(1):6–10. DOI:10.1080/19393210.2012.717108

[9] Lin S-L, Lo C-Y, Fuh M-R. Quantitative determination of perchlorate in bottled water and tea with online solid phase extraction high-performance liquid chromatography coupled to tandem mass spectrometry. Journal of Chromatography A. 2012 Jul;1246:40–7. DOI:10.1016/j.chroma.2012.02.014.

[10] Kirk AB, Dyke JV, Martin CF, Dasgupta PK. Temporal Patterns in Perchlorate, Thiocyanate, and Iodide Excretion in Human Milk. Environmental Health Perspectives. 2006 Nov 20;115(2):182–6. DOI:10.1289/ehp.9558.

[11] Chen L, Chen H, Shen M, Zhou Z, Ma A. Analysis of Perchlorate in Milk Powder and Milk by Hydrophilic Interaction Chromatography Combined with Tandem Mass Spectrometry. Journal of Agricultural and Food Chemistry. 2010 Mar 24;58(6):3736–40. DOI: 10.1021/jf903801m.

[12] Jiang S, Li Y-S, Sun B. Determination of trace level of perchlorate in Antarctic snow and ice by ion chromatography coupled with tandem mass spectrometry using an automated sample on-line preconcentration method. Chinese Chemical Letters. 2013 Apr;24(4):311–4. DOI:10.1016/j.cclet.2013.02.011.

[13] Licata P, Naccari F, Di Bella G, Lo Turco V, Martorana V, mo Dugo G. Inorganic anions in goat and ovine milk from Calabria (Italy) by suppressed ion chromatography. Food Additives & Contaminants: Part A. 2013 Mar;30(3):458–65. DOI: 10.1080/19440049.2012.747222.

[14] Cataldi TRI, Nardiello D, Ciriello R, Guerrieri A. Pulsed electrochemical detection of orotic acid by an activated potential waveform at a gold working electrode following anion-exchange chromatography. Journal of Chromatography A. 2006 Feb;1107(1–2):130–8. DOI: 10.1016/j.chroma.2005.12.049.

[15] Manjeshwar S, Rao P, Rajalakshmi S, Sarma D. The regulation of ribonucleoside diphosphate reductase by the tumor promoter orotic acid in normal rat liver in vivo. Molecular Carcinogenesis. 1999;24(3):188–96. URL: http://onlinelibrary.wiley.com/doi/10.1002/(SICI)1098-2744(199903)24:3%3C188::AID-MC5%3E3.0.CO;2-%23/full.

[16] Noël L, Carl M, Vastel C, Guérin T. Determination of sodium, potassium, calcium and magnesium content in milk products by flame atomic absorption spectrometry (FAAS): A joint ISO/IDF collaborative study. International Dairy Journal. 2008 Sep;18(9):899–904. DOI:10.1016/j.idairyj.2008.01.003.

[17] Arnaud J, Bouillet MC, Alary J, Favier A. Zinc determination in human milk by flameless atomic absorption spectrometry after dry ashing. Food Chemistry. 1992 Jan;44(3):213–9. DOI: 10.1016/0308-8146(92)90190-D.

[18] Kjellström S, Appels N, Ohlrogge M, Laurell T, Marko-Varga G. Microdialysis—a membrane based sampling technique for quantitative determination of proteins. Chromatographia. 1999 Nov;50(9–10):539–46.. DOI: 10.1007/BF02493658.

[19] Buldini PL, Mevoli A, Quirini A. On-line microdialysis–ion chromatographic determination of inorganic anions in olive-oil mill wastewater. Journal of Chromatography A. 2000 Jun;882(1–2):321–8. DOI: 10.1016/S0021-9673(00)00434-9.

[20] Sam AK, Osman MM, El-Khangi FA. Determination of protein and trace elements in human milk using NAA and XFR techniques. Journal of Radioanalytical and Nuclear Chemistry. 1998 May;231(1–2):21–3. DOI: 10.1007/BF02387999.

[21] Cunha IIL, de Oliveira RM. Phosphorus determination in milk and bone samples by neutron activation analysis. Journal of Radioanalytical and Nuclear Chemistry. 1996 Jun;213(3):185–92. DOI: 10.1007/BF02165689.

[22] Bjergegaard C, Møller P, Sørensen H. Determination of thiocyanate, iodide, nitrate and nitrite in biological samples by micellar electrokinetic capillary chromatography. Journal of Chromatography A. 1995 Nov;717(1–2):409–14. DOI: 10.1016/0021-9673(95)00554-1.

[23] Han F, He Y-Z, Li L, Fu G-N, Xie H-Y, Gan W-E. Determination of benzoic acid and sorbic acid in food products using electrokinetic flow analysis–ion pair solid phase extraction–capillary zone electrophoresis. Analytica Chimica Acta. 2008 Jun;618(1):79–85. DOI: 10.1016/j.aca.2008.04.041.

[24] Buldini PL, Cavalli S, Sharma JL. Matrix removal for the ion chromatographic determination of some trace elements in milk. Microchemical Journal. 2002 Sep;72(3):277–84. DOI:10.1016/S0026-265X(02)00039-5.

[25] Magnusson B. The fitness for purpose of analytical methods: A laboratory guide to method validation and related topics. Eurachem; 2014. 57 p. (Eurachem Guide). URL: http://www.diva-portal.org/smash/record.jsf?pid=diva2%3A948751&dswid=-8752 .

[26] González AG, Herrador MA, Asuero AG. Intra-laboratory testing of method accuracy from recovery assays. Talanta. 1999 Mar;48(3):729–36. DOI: 10.1016/S0039-9140(98)00271-9.

[27] Silveira ELC, de Caland LB, Tubino M. Simultaneous quantitative analysis of the acetate, formate, chloride, phosphate and sulfate anions in biodiesel by ion chromatography. Fuel. 2014 May;124:97–101. DOI: 10.1016/j.fuel.2014.01.095.

[28] AOAC International, Guidelines for standard methods performance requirements, appendix F, AOAC official methods of analysis 2012.

Türkçe Öz ve Anahtar Kelimeler

Simultaneous Determination of Different Anions in Milk Samples Using Ion Chromatography with Conductivity Detection

Orhan Destanoğlu and Gülçin Gümüş Yılmaz*

Öz: Bu çalışmada, süt örneklerinde aynı anda klorür, nitrat, sülfat, iyodür, fosfat, tiyosiyanat, perklorat ve orotik asidin tayini incelenmiştir. Bu yöntem diyaliz kaset kullanarak matris ayrılması işlemini takiben söz konusu anyonların yüksek kapasiteli anyon değiştirme kolonu üzerinde ayıran baskılanmış iletkenlik dedektörlü iyon kromatografik analizini kapsamaktadır. Diyaliz prosesinin yeniliği yağ, karbohidrat ve protein gibi makromoleküllerin süt örneklerinden giderilmesi için hiç bir kimyasal veya organik çözücü ihtiyacı olmamasıdır. Bu analitlerin dış standart kalibrasyon eğrileri iyi korelasyon katsayıları ile doğrusal olarak elde edilmiştir. Analit derişimlerinin relatif standart sapmaları gün arası ve gün içi değerlendirmelerde kabul edilir seviyelerde bulunmuştur. En uygun koşullar altında, tespit sınırı (sinyal-gürültü oranı 3) klorür, fosfat, tiyosiyanat, perklorat, iyodür, nitrat, sülfat ve orotat için sırası ile 0,012, 0,112, 0,140, 0,280, 0,312, 0,516, 0,520 ve 0,840 mg L^{-1} olarak belirlenmiştir. Standart ilave edilmiş süt örneklerinde % geri kazanım değerleri %93,88 - %109,75 olarak göze çarpmaktadır. Önerilen yöntem İstanbul'dan satın alınan süt örneklerine başarı ile uygulanmıştır. Yöntemin avantajları reaktifsiz, kolay ve güvenilir olmasıdır.

Anahtar kelimeler: Anyonlar; diyaliz; süt; iyon kromatografisi; orotik asit.

Sunulma: 03 Kasım 2016. **Düzeltme:** 03 Aralık 2016. **Kabul:** 24 Aralık 2016.

JOTCS A
Journal of the Turkish Chemical Society
Section: A
Chemistry
TURKISH CHEMICAL SOCIETY

Preparation and Application of Biocompatible Carrier Implant to be Used in the Controlled Acquisition of Digoxin

Hesna URAL KAYALIK[1], Sema ÇETİN[2]

[1] University of Ufuk, Vocational School of Health Services, 06520, Ankara, Turkey

[2] University of Kırıkkale, Faculty of Sciences and Literature, Department of Biology, Kırıkkale, Turkey

Abstract: In this study, a persistent system is aimed to be established which contributes to slow basal digoxin release in the treatment of cardiac failure. Poly(2-hydroxyethyl-metacrylate-methylmetacrylate) (p(HEMA-MMA) copolymer that can swell by taking on water is prepared in cylindirical form by UV photopolymerization method for the controlled-release of digoxin and effective hydrogel implant formulation. A batch of p(HEMA-MMA) composition is prepared in different monomer ratios. Biocompatibility is improved by adding PEO, PEG and serum albumin to the structures of p(HEMA-MMA), respectively. Scanning electron microscope (SEM) studies are carried out for the surface structure of the prepared carrier implant material and differential scanning calorimetry (DSC) studies for the thermal stability analysis. Swelling behaviors are investigated by transferring solvent molecules to the hydrogels. Digoxin release kinetics are evaluated by applying three different accumulative digoxin doses (100, 250 and 500 U/mL) in the persistent flow release system containing physiological phosphate. Power law, level-zero, and Higuchi model equations are utilized so as to evaluate the release mechanism of digoxin. The most suitable results are acquired from the composition whose HEMA:MMA monomer ratio is 1:0.5 (v/v) in drug accumulation and release studies. It is observed from the SEM image that the carrier implant in the structure of the acquired hydrogel has a smooth surface. According to DSC results, it is seen that thermal stability decreases in the event that MMA comonomer is added to the structure of the pHEMA hydrogel. Balance water amount within the physiological phosphate buffer of the p(HEMA-MMA) copolymer is observed to be less than the pHEMA. Digoxin release loaded to carrier implants by different ratios takes a long-term period as expected. It is decided that the formulation established in the study can be successfully applied for the basal digoxin level over four weeks in the treatment of chronic cardiac failure.

Keywords: pHEMA; p[HEMA-MMA]; carrier implant; digoxin; controlled-release.**Submitted:** September 21, 2016. **Revised:** September 30, 2016. **Accepted:** December 20, 2016.

Cite this: Ural Kayalık H, Çetin S. Preparation and Application of Biocompatible Carrier Implant to be Used in the Controlled Acquisition of Digoxin. JOTCSA. 2017;4(1):415–30.

DOI: To be assigned.

*Corresponding author. E-mail: drhesnaural@gmail.com.

INTRODUCTION

Cardiac failure is a complex clinical syndrome with labored breathing, fatigue, and exercise intolerance because of impaired blood pumping or ventricular filling due to functional and anatomical disfunction. Cardiac failure is an important clinical issue that results in cardiovascular mortality and morbidity throughout the world. There have been at least 15 million patients with cardiac failure and a similar number of patients with asymptomatic ventricular disfunction in countries, which are the members of the European Society of Cardiology [ESC]. The cardiac failure prevalence is between 2-3% and the rate is significantly higher in elderly patients above 75 year-old [1].

A single extended prospective study has been carried out by applying digoxin to the patients of cardiac failure [2]. In this Digitalis Investigation Group's study, 6800 patients with (New York Heart Association) NYHA II-IV functional capacity are treated with randomized placebo; however, no positive effect was observed in terms of mortality.

Controlled release method is designed to release the active substance into the system at desired intervals by a specified rate in the required quantity. In the field of biomedical [medicine] studies, the main target is to minimize the drug dosage along with extending the dosing interval and increasing the quality of life while not causing any side effects on the patient. Controlled release systems are best options to meet these expectations. When the polymer [natural or synthetic] utilized in the controlled drug release is used along with the drug, the active substance is released as determined in advance. As reported by many researchers, the fact that toxic effects have been minimized thanks to the controlled release system and no continuous daily-usage is required providing convenience for the patients.

The materials with high biocompatibility are used in the formation of the devices that can be placed within the body. However, the studies are being carried out due to the fact that no material with the perfect biocompatibility has been created yet [3]. Hydrogels, which are insoluble in water, can absorb water at least 20% more than the dry mass, cross-linked, three-dimensional, hydrophilic and polymeric structures with high mechanical stability.

A hydrogel used in medical applications widely is cross-linked pHEMA. It is similar to the natural tissues because of the water content. It is inert in normal biological reactions. It is resistant to degradation, is not absorbed by the body, can be sterilized with heat, and can be prepared in many different shapes and forms [4-6]. The other hydrogel has the

medical importance is polyacrylamide. In addition to HEMA and acrylamide monomers, N-vinyl-2-pyrrolidone [NVP], metacrylic acid [MAA], methyl methacrylate [MMA], and maleic anhydride [MAH] are often found in medical hydrogel formulations. In addition, hydrogels may be combined with various ingredients in order to gain the desired properties. Acrylate origin polymers are long-lasting synthetic polymers. Poly[methyl methacrylate] [pMMA] placed in this group is used in numerous applications in biomedical and biotechnological fields as it is a biocompatible synthetic polymer.

The aim of this study is to develop a biologically compatible [pHEMA] materials of hydrogel-origin that can be used as biomaterial in the controlled drug release system. The amount of the released insulin is measured by applying digoxin with different dosages to the carrier implant material with hydrogel structure.

MATERIALS AND METHODS

2-Hydroxyethyl methacrylate [HEMA], methyl methacrylate [MMA], N,N-methylene bisacrylamide, polyethylene glycol [PEG], polyethylene oxide [PEO], and N,N-azobisisobutyronitrile [AIBN] were obtained from Sigma-Aldrich Chemie GmbH [Germany]. Human serum albumin, fibrinogen, γ-globulin, and bovine serum albumin were obtained from Sigma-Aldrich. All other chemicals in analytical grade were obtained from Merck AG [Wuppertal, Germany]. Distilled water used in each phase of the study were obtained from Mp Minipure Super Auto [Mes Medical, Turkey] brand ultra-pure water system.

Synthesis of Biomaterials

The polymerization mixture prepared with HEMA and MMA monomers were used as monomers in a ratio of 1:0-0:1 [v/v], N, N-methylene bisacrylamide as cross-linker, [BSA] [10 mg], and ammonium persulfate [AMP] as launcher [5 mg] and 5 mg of human serum albumin [HSA]. 10 mg of polyethylene glycol [PEG] or polyethylene oxide [PEO] was added to the structure to improve the biocompatibility property of carrier implant will be synthesized and nitrogen gas was passed through polymer solution for 2 minutes.

10% Tetramethylethylenediamine [TEMED] as accelerator was added to the polymerization mixture, passed nitrogen gas for the duration of 1 minute, poured into cylinder molds with diameter of 0.5 cm and 5 cm in length and it was synthesized at room temperature by UV light photopolymerization method. Different amounts of digoxin loading of polymeric carrier biomaterial to be used in controlled drug oscillation system were introduced by UV light-induced photo-polymerization method under the same

conditions as given above. Cylindrical polymeric carriers formed because of polymerization, they were washed with distilled water and were stored at 4 °C until use. The composite membranes that pHEMA-based hydrogel were synthesized by UV photo-polymerization method [5]. Human serum albumine (HSA) and polyethylene glycol (PEG) was added to the structure to achieve biocompatibility of pHEMA and p[HEMA-MMA] hydrogel synthesized in the controlled oscillation system and targeted efficient dosage in the drug oscillation system.

Characterization of Biomaterial

Designed systems for the controlled release of biologically active proteins, hormones, or drugs should have suitable surface morphology. The surface area is one of the important factors that determines the rate of drug oscillation [7]. It is known that the drug oscillation rate is quite low in the system that developed with non-porous biomaterials.

The scanning electron micrographs of the carrier systems were determined with JOEL brand apparatus and the thickness in the wet state of p[HEMA-MMA] membrane with a digital caliper to examine the surface morphology of the oscillation of the system that we developed in our study.

The density of hydrogel cylinder in shape determined with pycnometer by using [n-decane] non-solvent liquid for membranes. The mechanical strength of carrier implant, pHEMA and p[HEMA-MMA], were determined by DSC [Model DSC-60-DTG-60H, Shimadzu, Japan] analysis. The swelling property of biomaterial in hydrogel structure was determined by gravimetric method in salt solution [0.85%, NaCl] at room temperature in a buffer system [pH 4.5-8.5]. Firstly, examples were placed in an inflatable media, then the balance environment was changed. The swelling ratio of the biomaterial was calculated using the following equation.

$$\% \text{ Equilibrium water content [w/w]} = [(Wd - Wk)/Wk] \times 100 \qquad (\textbf{Eq. 1})$$

Here Wk, dry hydrogel weight; Wd, weight of hydrogel reached balance of water content.

Contact Angle and Surface Free Energy

The measurements of the contact angle in our study were carried out for the determination of carrier implant surface polarity since important results about the interaction with micro-environment of biomaterials can be determined by investigating the wettability properties. Left and right contact angles and drop size parameters on the surface of the polymer by creating a drop with the help of a micro-syringe were

calculated automatically from the digital image. Wettability with a liquid of solid surface and contact angle concept [θ], have been formulated for the first time by Young [8]. There is not a single agreed approach for the determination of the surface energy [sometimes is defined as solid surface tension] from contact angle data [9]. These results are analyzed according to four methods [10, 11]. These are; Zisman's critical surface tension, Fowkes' geometric expression, Wu's harmonic expression and van Oss' acid- base approach. The contact angle was calculated by using the formula created by the Young and solid surface tension is calculated with the four methods given above separately.

Adsorption of Serum Protein

pHEMA and P[HEMA-MMA], to determine the blood compatibility of biomaterials, was transferred into the human blood serum diluted phosphate buffer [7.5 ml, 50 mm, pH 7.4] at a rate of 1/5 and stirred for 120 minutes at 37 °C. The adsorption of serum proteins was studied in a batch system. It was performed for each protein with a specific initial concentration. It was determined the amount of protein adsorbed to the carrier implant by using fluorescence spectrophotometer [Jasco FP-750, Tokyo, Japan] [6].

Blood Compatibility Analysis

The carrier implants, pHEMA, p[HEMA-MMA], cut 0.5 cm long and was brought to equilibrium in 0.85% NaCl solution. A sample of venous blood from a healthy person was mixed with sodium citrate in a 1/9 ratio and 10 minutes, centrifuged at 3000 rpm, and the plasma was obtained. 300 µL of plasma with sodium citrate was contacted with the polymer tubes and were incubated for 1 hour. Plasma did not make contact with the polymer used as a control.

***In vitro* Oscillation Studies**

Digoxin is loaded to investigate the controlled release of digoxin to carrier support material by prepared arrest method in the matrix. Biomaterials loaded with digoxin are placed into a continuous system reactor and supplied to enter the physiologic buffer solution at a constant flow rate by a peristaltic pump [Ismatec, model IPG, Germany]. The amount of the released drug was determined by spectrophotometry [Shimadzu, Model 1601, Japan] at a wavelength of 450 nm at certain intervals.

Oscillation Mechanism of Digoxin from the Biocompatible Carrier Implant

The oscillation with diffusion from swelling hydrogels of the active substance is defined in the best way by act of Stefan-Maxwell or Fick [12].

$$J = - D \, dC_m/dx \qquad (\textbf{Eq. 2})$$

In this equation, J shows the release from the membrane of the active substance in the direction of decreasing concentration; $g.cm^{-2}$ / sec [quantity/surface. time]; D is the diffusion coefficient of the active substance which diffuses through the membrane; cm^2 / sec [space/time] and dC_m / dx are the change of the drug concentration in the membrane in the x distance.

Another empiric equation that is used to explain the release mechanism in the controlled release system is equation developed by Peppas and colleagues assuming that function depends on time [13].

$$M_t / M_\infty = k \, t^n \qquad (\textbf{Eq. 3})$$

In this equation, M_t shows the amount of molecules released at t time; M_∞ is the amount of the remaining oscillating molecules in the environment; k is the structural/geometric constant for the particular system and n is the release mechanism.

Initially, the ingredient is dispersed and dissolved in the carrier implant. The effective oscillation in the polymeric materials that is used as the carrier implant in the controlled drug oscillation system characterized by Fick, non -Fick [abnormal], Case II, or super case II depending on the temperature and thermodynamic behavior of the system.

The mathematical modeling widely used for the investigation of drug oscillation kinetics in controlled drug oscillation system is the first degree equality [$D_t = k_o \, t$] in [13]. In this equation D_t shows the mass of the drug released instantly t; k_o is the emission rate constant at the first degree.

Another kinetic equation is the Law of Strength that is used in the elucidation of oscillation mechanism in controlled drug oscillation systems [$M_t = M_\alpha \, k_p \, t^n$] [14, 15]. In this equation, M_t shows the mass of released drug; M_α is the mass of the released drug to reach at the balance time; k_p is the kinetic constant of the law and n is the component of oscillation.

Higuchi's equation is used for diffusion-controlled release of drugs from insoluble and biologically without degradation matrix. It is used the different formulations of Higuchi's equation depending on conditions such as homogeneous or heterogeneous matrix and the geometry of the matrix [16].

$$Q = [DC\,[2A-C]t]^{1/2} \quad \Rightarrow \quad Q = k_H\, t^{1/2} \qquad (\textbf{Eq. 4})$$

In the equation, Q shows the drug dose emitted per unit surface area at instantly t [mg cm^{-2}]; D is the diffusion coefficient of the substance in the matrix [cm^2 $time^{-1}$]; C is the solubility of the substance in the matrix [mg cm^{-3}]; A is the amount for per unit volume that is loaded initially [mg]; t, time [day]; k_H is the Hugichi's oscillation speed constant [mg cm^{-2} $t^{1/2}$].

RESULTS AND DISCUSSION

Results

Findings of the present study showed that the mechanical power of the membrane of p(HEMA-MMA), a synthetic polymer, varies depending on the ratio of the comonomer (Table 1). Since the hydrogel composition of p(HEMA-MMA) at a monomer ratio of 1:1 had sufficient mechanical strength; this ratio was used for further steps of the study.

Table 1: Effect of the composition of membrane preparation to the mechanical strength of composite hydrogel synthesized in different MMA rates.

HEMA:MMA ratio [v/v]	Polymerization	Mechanical strength
A] 1.00:0.00	+	Medium
B] 1.00:0.25	+	Medium
C] 1.00:0.50	+	Enough
D] 1.00:1.00	+	Enough
E] 0.00:1.00	-	Inadequate
F] 0.25:1.0	-	Inadequate
G] 0.5:1.0	-	Inadequate

Using a digital calliper, the thickness of the wet hydrogel was recorded as 2.70 mm. Hydrogel's density was found to be 1.10 g/cm^3 by using a non-solvent fluid for the material (n-decane) with the aid of Gay-Lussac pycnometry.

The composite hydrogel, dried in a vacuum incubator at a temperature of 30 °C, was covered with gold while being kept under reduced pressure and scanning electron microscopy of the membranes was performed to confirm the hydrogel had a smooth surface (Figure-1).

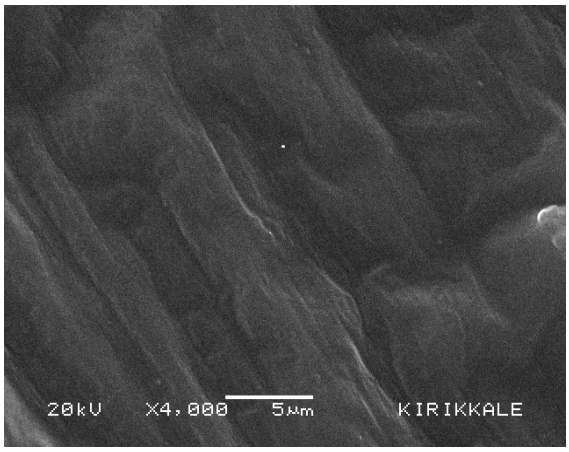

Figure 1: SEM image of the carrier implant used in the controlled oscillation system.

Figures 2 and 3 show the balanced inflation percentage under different medium buffer systems at 25 °C of pHEMA and p(HEMA-MMA) hydrogels prepared to be used for digoxin release.

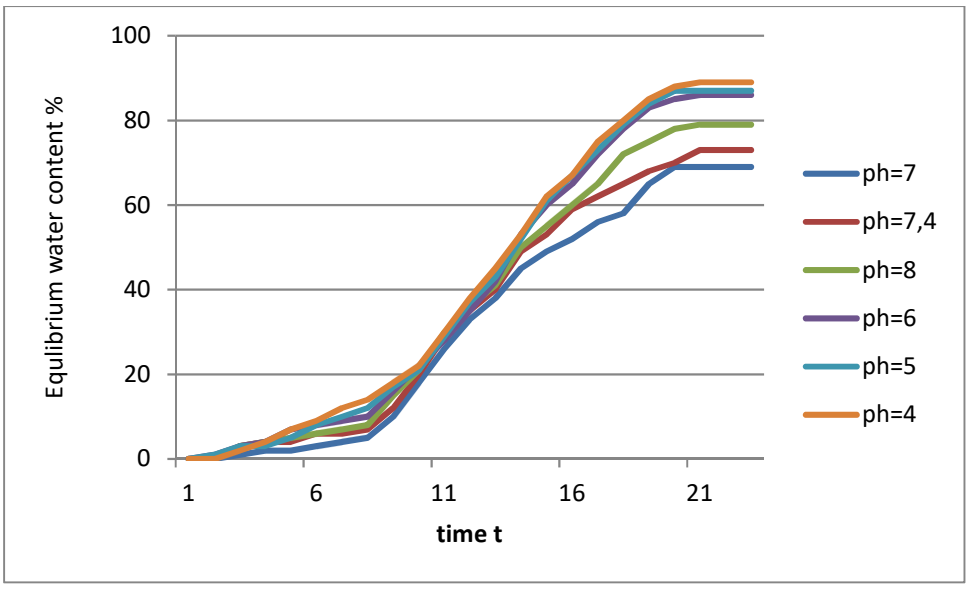

Figure 2: The swelling behavior of pHEMA hydrogel in different buffer systems (t = hours).

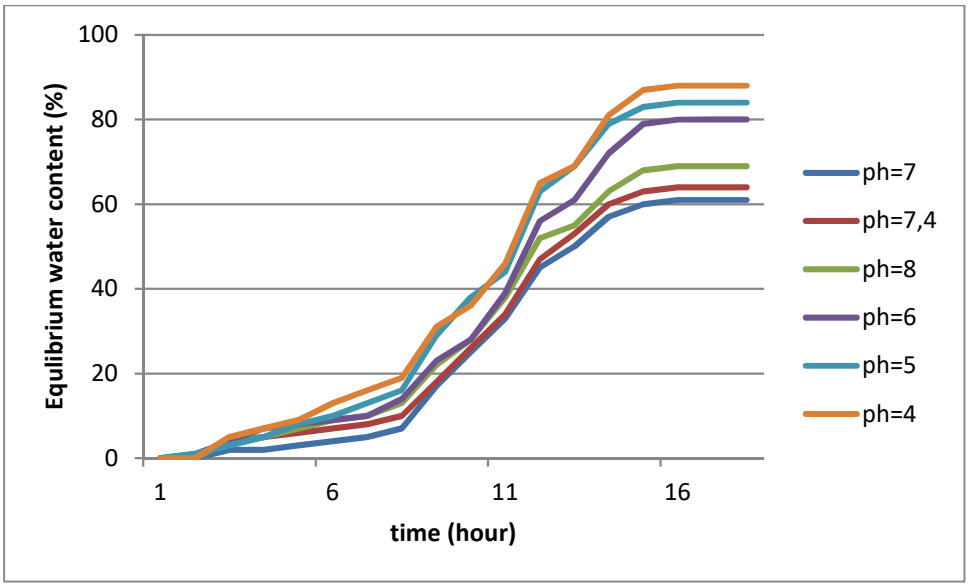

Figure 3: The swelling behavior of pHEMA-MMA hydrogel in different buffer systems.

Controlled release of the drugs varies depending on the structure of the polymer and glass transition temperature (T_g) value, which is a parameter indicating polymeric flexibility. Figure 4 shows the data obtained from DSC analyses performed under nitrogen gas at 10 °C/min heating ratio.

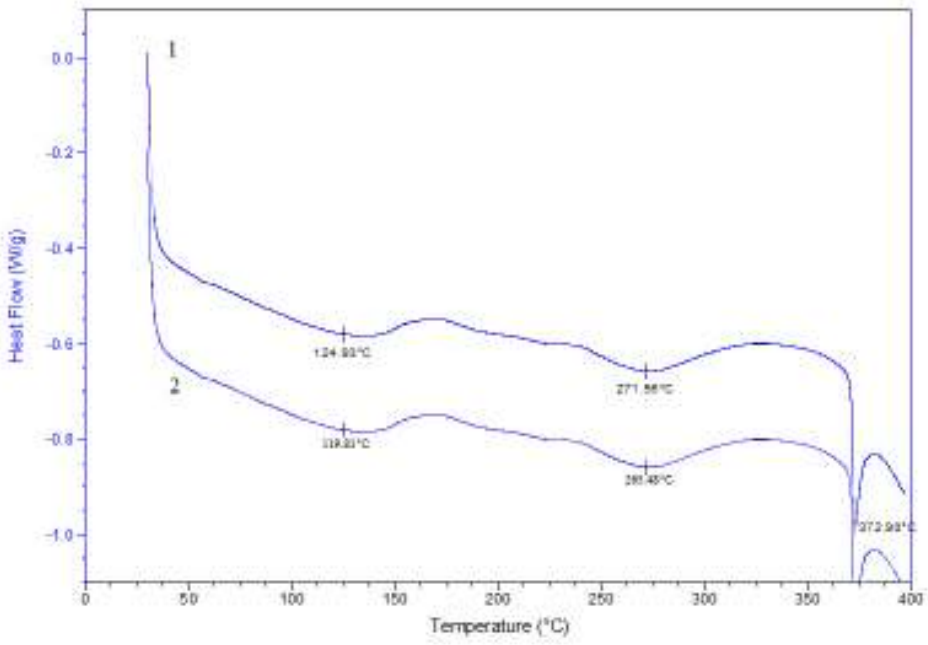

Figure 4: DSC chart of p[HEMA-MMA] [1] and pHEMA [2] hydrogels.

Contact angle values measured after dropping different test fluids (water, glycerol, diiodomethane) on pHEMA and p(HEMA-MMA) polymeric structures were determined by static drop method. (Table 2). Based on Young's equation, contact angles measured using the test fluids, which have lower surface tensions, should be smaller. Free surface

energy parameters of the polymeric structures were calculated using the contact angle values of the analyzed fluids. Total free surface energies (γ^{Total}) were calculated by van Oss' method. Table 3 shows the free surface energy parameters of the membranes based on van Oss' method.

Table 2: Surface contact angles [γerg: the surface tension of test liquid] measured with test fluids for the carrier implant.

Implant	Water [n=71.3] [Θ^0]	Glycerol [n=64.0][Θ^0]	Diiodomethane [n=50.8] [Θ^0]
PHEMA	59.2	55.5	34.3
p[HEMA-MMA]	52.4	60.0	31.1

[n: The test liquid and the surface tensions].

Table 3: Parameters of the surface free energy of the membranes [mJ/m^2] according to van Oss.

	γ^{LW}	γ^{+}	γ^{-}	γ^{AB}	γTotal	Polarity [%]
PHEMA	38.7	0.7	3.1	2.8	31.5	6.8
p[HEMA-MMA]	33.0	0.5	3.4	4.8	39.4	10.1

γ^{LW}[mN/m^2] Showing long-range interactions [dispersive interactions include dipole-dipole interaction and dipole-induced dipole interaction]

γ^{+}[mN/m^2] : It shows the acid component of the membrane.

γ^{-}[mN/m^2] : It shows some components of the membrane.

γ^{AB}[mN/m^2] : symptoms of acid-base interactions

γ^{Total}[mN/m^2] : The total surface free energy

Polarity F [%]: % polarity

Albumin adsorption to pHEMA and/or p(HEMA-MMA) carrier implant systems synthesized to be used for controlled digoxin release is important to increase biocompatibility of the prepared biomaterial. Moreover, fibrinogen adsorption to biomaterial surface reduces the biocompatibility of the prepared biomaterial. While albumin prevents thrombocytes binding to biomaterial surface, fibrinogen acts to initiate binding of thrombocytes to biomaterial surface. Therefore, albumin and PEG were placed into the prepared biomaterial by intra-matrix entrapment method, with an aim to increase blood-compatibility of the biomaterial. Serum protein levels adsorbed by pHEMA and p(HEMA-MMA) structures are shown in Table 4.

Table 4: The amounts of serum proteins adsorbed to the structure of pHEMA and P[HEMA-MMA].

	Plasma Proteins		
	HSA [ng/cm²]	**ɣ-globulins** [ng/cm²]	**Fibrinogen** [ng/cm²]
PHEMA	359	199	98
p[HEMA-MMA]	188	131	34

Release of digoxin loaded to p(HEMA-MMA) hydrogel was determined by analyses of the samples obtained from the controlled release system at regular time points over a period of 25 days. Cumulative release profile over time of p(HEMA-MMA) carrier implants was estimated. (Figure-5).

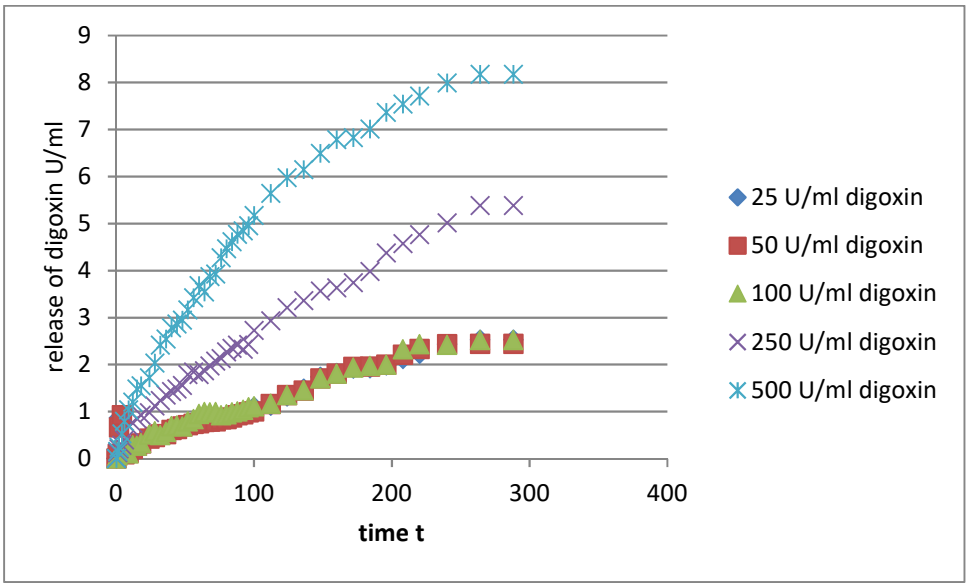

Figure 5: The oscillation profile of Digoxin from p[HEMA-MMA] hydrogel.

Figure-6 shows cumulative percent release profile over time of p(HEMA-MMA) hydrogels. The mechanism of the kinetics of controlled digoxin release from the biocompatible carrier implant was assessed using the semi-logarithmic method suggested by Korsmeyer-Peppas [9]. Experimental data obtained from controlled digoxin release system were adapted to that model in order to estimate n value. Table 5 shows the values obtained for pHEMA and p(HEMA-MMA) hydrogel with a cylindrical geometry. Values obtained for n and k release parameters in this study were consistent. Values estimated for n parameters of the biocompatible pHEMA ve p(HEMA-MMA) hydrogels prepared for controlled digoxin release were between 0.6-0.68 0.53-0.75 respectively, indicating that the kinetics of the release system represents a non-Fick transportation mechanism and the velocity of digoxin release depends on time. Another release

parameter, k, is a constant reflecting the structure and geometric characteristics of the carrier implant. Lower k values indicate slower digoxin release.

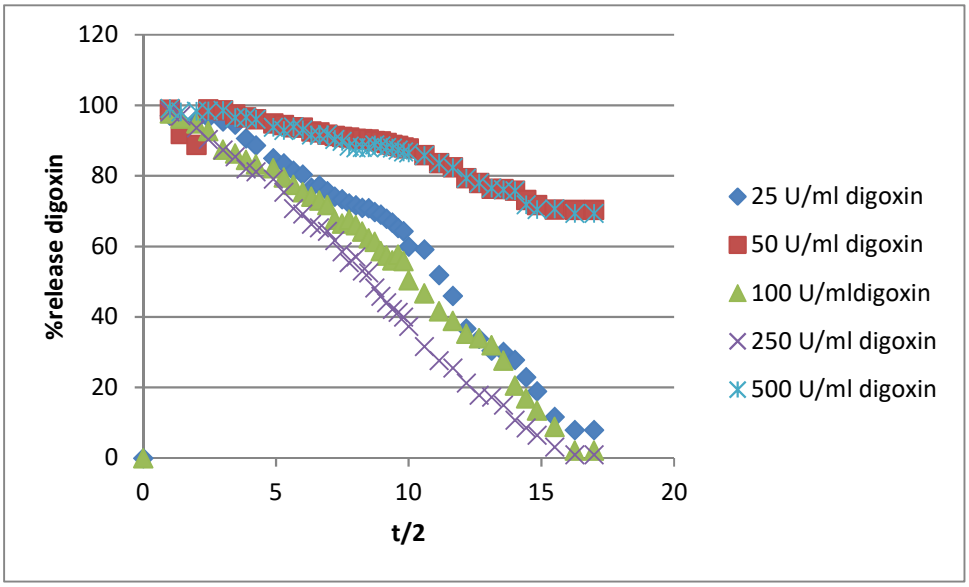

Figure 6: % cumulative oscillation chart of Digoxin from p[HEMA-MMA] hydrogel versus time (t = hours).

DISCUSSION

Controlled release parameters that should be taken into consideration while designing carrier implant systems include the characteristics of the active ingredient, the mode of administration of the drug, target region, duration of treatment, status of the disease, and the patient. Studies are performed with an idea to develop a controlled release system by loading digoxin into polymeric carrier implants, which can then be placed into cancerous tissues by surgical methods.

In the present study, pHEMA-based composite membranes in hydrogel structure, intended to bear the above listed characteristics, were synthesized using UV photopolymerization method. We believe that this newly synthesized composite membrane offers advantages to use for controlled drug release as;

i) it has sufficient mechanical power and is resistant to biological and chemical decay,

ii) it allows preparation of the required surface structure, at the required level of porosity,

iii) the drug can be loaded without causing any loss or decrease in drug activity while preparing the composite material and the carrier system allows adjusting the medication dose to any level,

iv) it has a hydrophilic structure.

Hydrogel images obtained using scanning electron microscopy indicate that the HEMA monomer, used as a component of the composite membrane, provides the material with

sufficient mechanical strength, while the pore size can also be adjusted by changing the concentration of pore-adjusting agents added to the polymerization mixture. This characteristic allows considerably fast and controlled drug release.

Inflation behavior of the hydrogels which can be inflated by solvent transfer was investigated and it was found to reduce polymer/co-polymer and co-polymer/drug interactions. pHEMA and p(HEMA-MMA) transited to aqueous structure and reached a balance in 21 and 12 hours, respectively. Water content at balanced state of p(HEMA-MMA) copolymer hydrogel in physiological phosphate buffer was found to be lower compared to pHEMA .

Presence of polar groups in the polymer increases Tg value as it reduces the motion around the main chain. Tg value of the polymer can be measured by DSC and DTA analyses. Thermal stability showed a reduction by the addition of MMA comonomer into the structure of pHEMA hydrogel.

Results of contact angle measurements showed that the surface energies of the membrane samples calculated based on Fowkes and Wu methods were comparable, but compared to the Fowkes' method, the Wu method indicated a lower polar component of the surface energy (γ^p). Both methods showed that the dispersive components made the major contribution to total free surface energy for all tested membranes. van Oss' method reflects the sum of Lifshitz-van der Waals (γ^{LW}) and acid-base components (γ^{AB}) applied at different values to all tested membranes. Base components (γ^-) of the membranes were found to be higher as compared to their acidic components (γ^+).

Presence of albumin and PEG in pHEMA and p(HEMA-MMA) structure lead to negligible levels of blood serum proteins adsorbed by the surface of the carrier implants.

Different release kinetic models were applied to experimental data to clarify the mechanism of digoxin release and the best model that defines kinetic model of release was investigated. The mechanism of the kinetics of controlled digoxin release from the biocompatible carrier implant was assessed using the semi-logarithmic model suggested by Korsmeyer-Peppas [13]. In release systems where the carrier implants used for controlled drug release have a cylindric geometry, the release mechanisms are determined by the values of the n parameter. Based on this model, an n parameter of 0.45 is defined by Fick's diffusion mechanism, while values between 0.45 - 0.89 reflect non-Fick mechanism, a value equal to 0.89 shows State II (relaxations) transportation and values higher than 0.89 indicate super State II tranportation mechanisms [13-15].

Another release parameter, k, is a constant reflecting the structure and geometric characteristics of the carrier implant. Lower k values indicate slower digoxin release. In the present study, estimated n and k release parameters were consistent. Values of the n parameters, calculated to be between 0.6-0.68 and 0.53-0.75, respectively, for the biocompatible pHEMA and p(HEMA-MMA) hydrogels prepared to be used for controlled digoxin release, indicated that the kinetics of the release system can be defined by a non-Fick transportation mechanism and the velocity of digoxin release depends on time. The compatibility of digoxin-release profile from the biocompatible p(HEMA-MMA) hydrogels with zero-degree kinetics and the Higuchi model was investigated, and analyses of the estimated model parameters showed that the results were consistent with both models.

Release-periods investigated after loading digoxin into p(HEMA-MMA) hydrogel demonstrated that the release process continued over a long period, as intended.

In conclusion, the present study showed that the developed formulation can be successfully used to provide basal digoxin levels for more than 3 weeks. These findings indicate that the hydrogel-based biocompatible implant materials prepared for this study provide several different advantages such as easy sterilization and drug loading, adjustment of the sample dose, biocompatibility of the system and elimination of the need to use organic solvents.

REFERENCES

1. Dickstein K, Cohen-Solal A, Filippatos G, McMurray JJ, Ponikowski P, Poole-Wilson PA, Strömberg A, van Veldhuisen DJ, Atar D, Hoes AW, Keren A, Mebazaa A, Nieminen M, Priori SG, Swedberg K; ESC Committee for Practice Guidelines (CPG). ESC guidelines for the diagnosis and treatment of acute and chronic heart failure 2008: the Task Force for the diagnosis and treatment of acute and chronic heart failure 2008 of the European Society of Cardiology. Developed in collaboration with the Heart Failure Association of the ESC [HFA] and endorsed by the European Society of Intensive Care Medicine [ESICM]. Eur J Heart Fail 2008;10:933-89. DOI: 10.1016/j.ejheart.2008.08.005.

2. Digitalis Investigation Group.The effect of digoxin on mortality and morbidity in patients with heart failure. The Digitalis Investigation Group. N Engl J Med 1997;336:525-33. DOI:10.1056/NEJM199702203360801.

3. Langer RS ve Peppas NA. Present and future applications of biomaterials in controlled drug delivery systems. Biomaterials 1981;2:201-14. DOI: 10.1016/0142-9612(81)90059-4.

4. Byrne ME, Park K, Peppas NA. Molecular imprinting within hydrogels. Adv Drug Deliv Rev. 2002 ;54(1):149-61. Review. DOI:10.1016/S0169-409X(01)00246-0.

5. Arıca MY, Bayramoğlu G, Bıçak N. Characterization of tyrosinase immobilised onto spacer-arm attached glycidyl methacrylate-based reactive microbeads. Process biochemistry. 2004;39: 2007-2017. DOI:10.1016/j.procbio.2003.09.030.

6. Arıca MY. Epoxy-Derived pHEMA Membrane for Use Bioactive Macromolecules Immobilization: Covalently Bound Urease in a Continuous Model System. Journal of Applied Polymer Science. 2000;77:2000-2008. DOI: 10.1002/1097-4628(20000829)77:9<2000::AID-APP16>3.0.CO;2-M.

7. Svec F, Fréchet JM. Modified poly(glycidyl methacrylate-co-ethylene dimethacrylate) continuous rod columns for preparative-scale ion-exchange chromatography of proteins. J Chromatogr A. 1995;70289-95. DOI: 10.1016/0021-9673(94)01021-6.

8. Blanco R, Arai A, Grinberg N, Yarmush DM, Karger BL.
Role of association on protein adsorption isotherms. Beta-lactoglobulin A adsorbed on a weakly hydrophobicsurface. J Chromatogr. 1989 Nov 17;482:1-12. DOI: 10.1016/S0021-9673(01)93202-9.

9. Mykhaylyk TA, Evans SD, Fernyhough CM, Hamley LW, Henderson JR. Ellipsometric study of adsorption on nanopatterned block copolymer substrates. J. Chem. Phys. 2005;122: 104902. DOI: 10.1063/1.1860371.

10. Zisman WA. Influence Of Constitution On Adhesion. Ind. Eng. Chem. 1963;55:18-38. DOI: 10.1021/ie50646a003.

11. Van Oss CJ, Good RJ, Chaudhury MK. Additive and nonadditive surface tension components and the interpretation of contact angles. Langmiur 1988;4:884-891. DOI: 10.1021/la00082a018.

12. Peppas NA, Huang Y, Torres-Lugo M, Ward JH, Zhang J.
Physicochemical foundations and structural design of hydrogels in medicine and biology. Annu Rev Biomed Eng. 2000;2:9-29. DOI: 10.1146/annurev.bioeng.2.1.9.

13. Siepmann J, Peppas NA. Modeling of drug
release from delivery systems based on hydroxypropyl methylcellulose (HPMC). Adv Drug Deliv Rev. 2001;48:39-57. Review. DOI: 10.1016/s0169-409x(01)00112-0.

14. Ritger PL, Peppas NA. A simple equation for description of solute release II. Fickian and anomalous release from swellable devices. J. Controlled Release. 1987;5:37-42. DOI:10.1016/0168-3659(87)90035-6.

15. Korsmeyer RW, Gurny R, Doelker E, Buri P, Peppas NA. Mechanisms of solute release from porous hydrophilic polymers. Int. J. Pharm 1983;15:25-35. doi:10.1016/0378-5173(83)90064-9.

16. Hıguchı T. Mechanism of Sustained Action Medication. Theorethical Analysis Of Rate of Solid Drugs Dispersed in Solid Matrices. J. Pharm. Sci. 1963;52:1145-1149.
DOI: 10.1002/jps.2600521210.

Türkçe Öz ve Anahtar Kelimeler

Kontrollü Digoksin Alımında Kullanılmak Üzere Biyo-uyumlu Taşıyıcı İmplantın Hazırlanması ve Uygulanması

Hesna URAL KAYALIK, Sema ÇETİN

Öz: Bu çalışmada, kalp yemezliğinin tedavisinde yavaş bazal digoksin salınımına katkıda bulunan sabit bir sistem ortaya konmuştur. Poli(2-hidroksietil metakrilat – metilmetakrilat) (p(HEMA-MMA)) kopolimeri UV fotopolimerizasyonu ile silindirik yapıda hazırlanır ve su tutarak şişer. Poli(HEMA-MMA) bileşimine sahip bir örnek farklı monomer oranlarında hazırlanmıştır. Biyo-uyumluluk PEO, PEG ve serum albuminat yapılarının p(HEMA-MMA)'ya ilave edilmesi ile geliştirilmiştir. Taramalı elektron mikroskobu (SEM) çalışmaları hazırlanan taşıyıcı implant malzemesinin yüzey yapısını çalışmak için kullanılmıştır. Diferansiyel taramalı kalorimetri (DSC) çalışmaları da ısıl kararlılık analizlerinde kullanılmıştır. Şişme davranışları, çözücü moleküllerini hidrojellere aktararak incelenmiştir. Digoksin salım kinetiği üç farklı akümülatif digoksin dozunun (100, 250 ve 500 U/mL) fizyolojik fosfat içeren sabit akış salım sistemine verilmesiyle değerlendirilmiştir. Güç yasası, sıfır seviyesi ve Higuchi model eşitlikleri uygulanarak digoksinin salım mekanizması değerlendirilmiştir En uygun sonuçlar, HEMA:MMA monomer oranının 1:0,5 (v/v) olduğu durum için ilaç birikmesi ve salım çalışmalarında elde edilmiştir. SEM görüntülerinden görüldüğü kadarı ile, alınan hidrojelin yapısı içinde taşıyıcı implant yumuşak bir yüzeye sahiptir. DSC sonuçlarına göre, ısıl kararlılığın MMA komonomerinin pHEMA hidrojeline eklendiği durumlarda azaldığı görülmüştür. Poli(HEMA-MMA) kopolimerinin fizyolojik fosfat tamponu içindeki denge suyu miktarı pHEMA'dan daha az olarak bulunmuştur. Taşıyıcı implantlara yüklenen digoksin salımı farklı oranlar kullanıldığında beklendiği gibi uzun dönem zaman almaktadır. Kronik kalp yetmezliğinin tedavisinde, çalışmada önerilen formülasyon temel digoksin seviyesinin dört haftadan daha uzun süre başarıyla uygulanabilmesini sağlamaktadır.

Anahtar kelimeler: pHEMA; p[HEMA-MMA]; taşıyıcı implant; digoksin; kontrollü salım.**Sunulma:** 21 Eylül 2016. **Düzeltme:** 30 Eylül 2016. **Kabul:** 20 Aralık 2016.

JOTCS Journal of the Turkish Chemical Society Section: A Chemistry

TURKISH CHEMICAL SOCIETY

Ion-Exchange properties of Diaion Cr 11, Amberlite Irc 748, and Dowex M 4195

Mahnur Jafarli[1*] and Aliaddin Abbasov[1]

[1]Institute of Natural Resources, Nakhchivan branch, National Academy of Sciences, Azerbaijan.

Abstract: Acid-base properties of ion-exchangers Diaion CR 11, Amberlite IRC 748, and Dowex M 4195 have been studied by potentiometry. Their conditional dissociation constants have been calculated from the Henderson-Hasselbach equation. Sorption regularities of Zn^{2+} and Pb^{2+} ions from aqueous solutions by ion exchangers of Diaion CR 11, Amberlite IRC 748 with iminodiacetic acid functional group, and Dowex M 4195 with bis-picolylamine functional group are investigated. Sorption isotherms are plotted. Isotherms are analyzed on the basis of known models. It is determined that with the exception of the Amberlite IRC 748-Pb^{2+} system, the isotherms in all remaining cases obey to the Langmuir and Freundlich equation. The corresponding equations are offered for each isotherm. The kinetic mechanisms of processes are determined, it is confirmed that the sorption at the concentration of 1.0 gMe·L^{-1} and above is controlled by pore diffusion, values of effective diffusion coefficients and pre-exponential factor are calculated. Thermodynamic parameters are calculated on the basis of kinetic data. Thermodynamic factor controlling processes is determined.

Keywords: Ion exchangers, Zn^{2+} and Pb^{2+} ions, sorption isotherms, Langmuir and Freundlich models, kinetic and thermodynamic parameters.

Submitted: July 29, 2016. **Revised:** September 06, 2016. **Accepted:** December 20, 2016.

Cite this: Jafarli M, Abbasov A. Ion-Exchange properties of Diaion Cr 11, Amberlite Irc 748, and Dowex M 4195. JOTCSA. 2017;4(1):449–62.

*__Correspondence to:__ Mahnur Jafarli. E-mail: nes.az.nil@mail.ru.

INTRODUCTION

The availability of data on the equilibrium of ion exchange is necessary for selection and optimization of the conditions of ion concentration, ejection of a concrete ion from a complex system and for its separation from the other ions, as well as for the calculation and designing of technological equipment. As a result, the investigation of equilibrium conditions of ion exchange brings to deriving of isotherm equations and to determination of the exchange constant and coefficient of selectivity. For this reason, the study of model solutions in the way of increase of sorption selectivity is regarded as an actual problem [1-7]. The aim of the present research work is to study the mutual influence of ion exchangers under consideration and ions of non-ferrous metals for the comparative evaluation of their sorption capacity. Studies are carried out at the follows chelate forming resins: Macroporous Dowex M 4195 (France) with bis-picolylamine functional group and macroreticular Amberlite IRC-748 (Germany) and highly porous Diaion CR 11 (Japan) with iminodiacetic acid functional groups [8].

EXPERIMENTAL

Sorption of the ions under investigation has been studied in static conditions, at the room temperature, at the ion exchanger-solution ratio of 1:100, at the concentration of metal ions 0,5-5,0 gMe•L^{-1}, in metal salt solutions corresponding to chemically pure grade. Concentration of Zn^{2+} ions has been determined complexometrically using Eriochrome black T: The solutions were first neutralized with sodium hydroxide. Then to 100 mL of each solution was added 2 mL of buffer solution (NH_4OH + NH_4Cl), and titrated to light red color transition in the blue. With the last drop of the titrant solution (EDTA), the reddish color shade disappears.

Concentration of Pb^{2+} ions – using xylenol orange: The sample solution containing not more than 50 mg in 100 mL Pb previously neutralized to pH 2-3 and then 3 mL of acetate buffer (CH_3COOH + CH_3COONa, pH = 4-6.5) solution was added. The solution should have a pH value of about 5. A few drops of indicator solution was added and titrated with EDTA solution until the color changes from red-purple to pure yellow [9]. In a series of experiments, the accuracy of the results was controlled by determining the concentration of Zn^{2+} and Pb^{2+} ions at atomic absorption spectrometer (Thermo Scientific iCE 3500 AA). The pH values of the solutions have been measured by Acvilon pH-meter pH-430. Quantity of Zn^{2+} and Pb^{2+} ions passing to the ionite phase at equilibrium condition has been calculated according to the formula (Eq. 1):

$$A = (C_0 - C_e)V / m \qquad \textbf{(Eq. 1)}$$

Here A is the Zn^{2+} and Pb^{2+}-ions adsorbed onto the ionites ($mg \cdot g^{-1}$) at equilibrium, C_o is the initial Zn^{2+} and Pb^{2+} ions concentration ($mg \cdot L^{-1}$), C_e is the final Zn^{2+} and Pb^{2+} ions concentration in the solution (mg/L^{-1}) is the volume (L) of the solution and m is the amount of ionites (g) used. Kinetics of processes have been studied by the limited volume method in ion solutions with the concentration 1.0 $gMe \cdot L^{-1}$. Values of effective diffusion coefficients were calculated according to the equation of G.Boyd and colleagues [10]:

$$F = Qt/Q\infty = 1 - \frac{6}{\pi^2}\sum\frac{1}{n^2}\exp\left(-\frac{D\pi^2 n^2 t}{r_0^2}\right) \quad \textbf{(Eq. 2)}$$

In Equation 2, Bt is defined as follows:

$$Bt = D_i\pi^2 \; t/r_0^2 \quad \textbf{(Eq. 3)}$$

Bt is called an intangible parameter or Fourier homochronous criterion. The value of effective diffusion coefficient has been calculated according to the formula:

$$D = B_t \cdot r_0^2 / t \cdot \pi^2 \; Bt\ r_o^2 / t\pi^2 \quad \textbf{. (Eq. 4)}$$

The value of activation entropy has been calculated according to the equation offered by R.M.Barrer and colleagues [11] (Eq. 5):

$$D_0 = D^2 \exp\left(kT/h\right)\cdot\exp\left(S/R\right) \quad \textbf{(Eq. 5)},$$

the value of entropy multiplier $\lambda^2 \exp(S/R)$ – according to the formula offered by S.Glasstone [12] (Eq. 6):

$$D = \lambda^2 \cdot \exp\left(S/R\right)\cdot \exp kT/h \exp\left(E_{akt}/RT\right) \quad \textbf{(Eq. 6)}.$$

Diaion CR 11 and Amberlite IRC 748 are characterized by the functional group $-CH_2-N(CH_2COONa)_2$, and Dowex M 4195 – by $C_5H_4N-CH_2-N-(matrix)-CH_2-C_5H_4N$. Sorption by the first two ionites is imagined as replacing of Na-ions by metal ions, and creation of coordination bond with nitrogen atoms, and sorption by Dowex M 4195 – as the formation of a complex bond between metal ions

and pyridine nitrogen [13,14]. As the salt forms of chelating ionites are more coordination active, the first two ionites were used in Na-form, and Dowex M 4195 – in SO_4^{2-}-form.

According to many researchers, the divalent metal ions form chelates with ionized iminodiacetic groups [13, 14]:

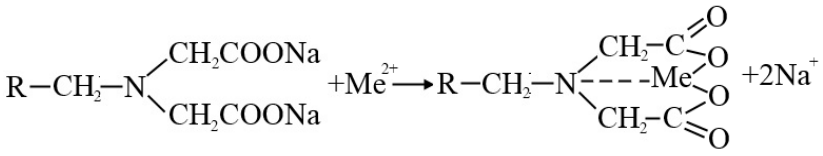

RESULTS AND DISCUSSION

Isoterms of sorption

Sorption isotherms have been plotted by variable concentrations method, they have a convex shape. These isotherms do not have noticeable refractions, it shows that complexing has a slight part in the sorption process, and absorption occurs and at the expense of replacement of metal ions with the opposing ions of functional groups (Diaion CR 11, Amberlite IRC 748). Optimum level of sorption acidity has been observed in the range of pH=5.5-6.5.

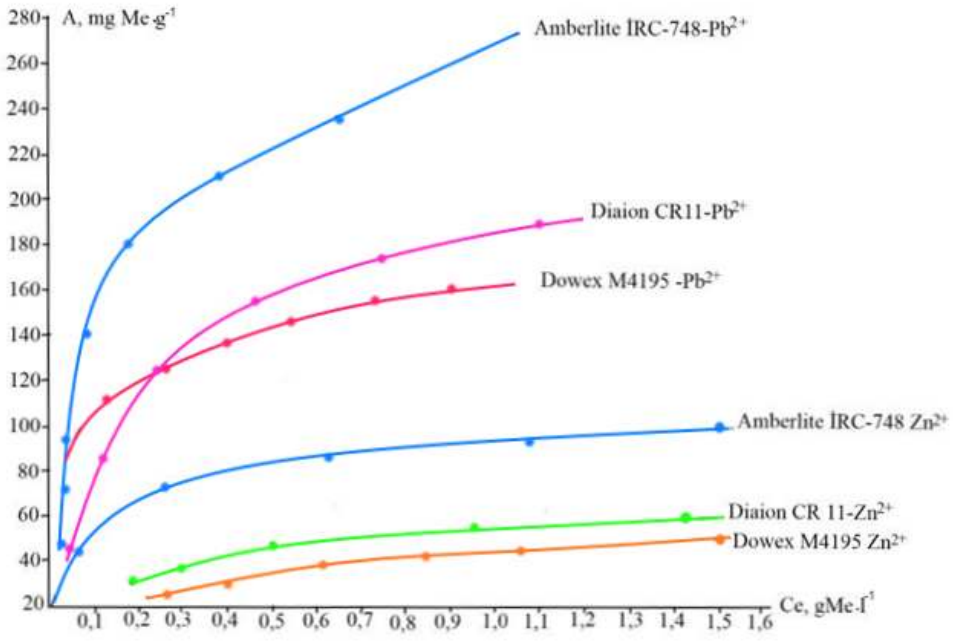

Figure 1. Isotherms of sorption of Zn^{2+} and Pb^{2+}-ions by ionites Diaion CR 11, Amberlite IRC 748, and Dowex M 4195.

Acid-base properties of Diaion CR 11, Amberlite IRC 748, and Dowex M 4195 are studied by potentiometry. Conditional dissociation constants of the ionites' functional groups are calculated using the Henderson-Hasselbach equation:

$$pK = pH - n \cdot \log(\alpha / 1 - \alpha) \quad \textbf{(Eq. 7)}$$

from the graphic dependence pH – lg(α/1-α) [15]. Experiments conducted on known methods, our results dissociation constants of functional groups with the appropriate structure of ionites, close values are characterized.

The following values have been obtained for Diaion CR 11 pK_1 = 4.7 ± 0.1; pK_2 = 8.8 ± 0.2, for Amberlite IRC 748 pK_1 = 5.5 ± 0.1; pK_2 = 9.2 ± 0.1, for Dowex M 4195 pK = 7.6 ± 0.3.

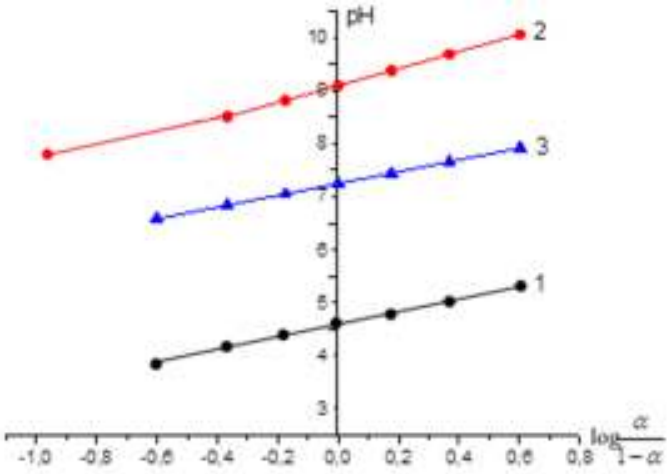

Figure 2. Dependence pH equilibrium solutions from log(α/1-α).

With the exception of the Amberlite IRC 748-Pb^{2+} system, sorption isotherms (Figure 1) in all remaining cases can be recorded by the Langmuir equation in the studied concentration region. Accuracy of determination of the Langmuir equation (Eq. 8):

$$A = A_{max} \cdot K \cdot C_e / 1 + K \cdot C_e \quad A = A_{max}.K \cdot C_e/1+K \cdot C_e \quad \textbf{(Eq. 8)}$$

The parameters have been checked by comparing values of A_{max} (maximum sorption in a monosurface) and K (pseudoequilibrium sorption constant). Sorption of both cations by the studied ionites is recorded by the linear dependence in C_e/A – C_e coordinates with the high correlation coefficient (R = 0.98-0.99) [8]. In addition, that allows us to determine A_{max} and K with satisfactory

reliability. Sorption of Pb^{2+} ions by Amberlite IRC 748 is expressed by a straight line in coordinates of absorbed amount A (distribution ratio). The parameters of the Freundlich equation:

$$x/m = K \cdot C_e^{\,n} \quad x/m = k \cdot C_e^{n} \qquad \textbf{(Eq. 9)}$$

Eq. 9 characterizes the isotherms under investigation have been found from the log A – log C_e graphic dependence [16] (Fig. 2).

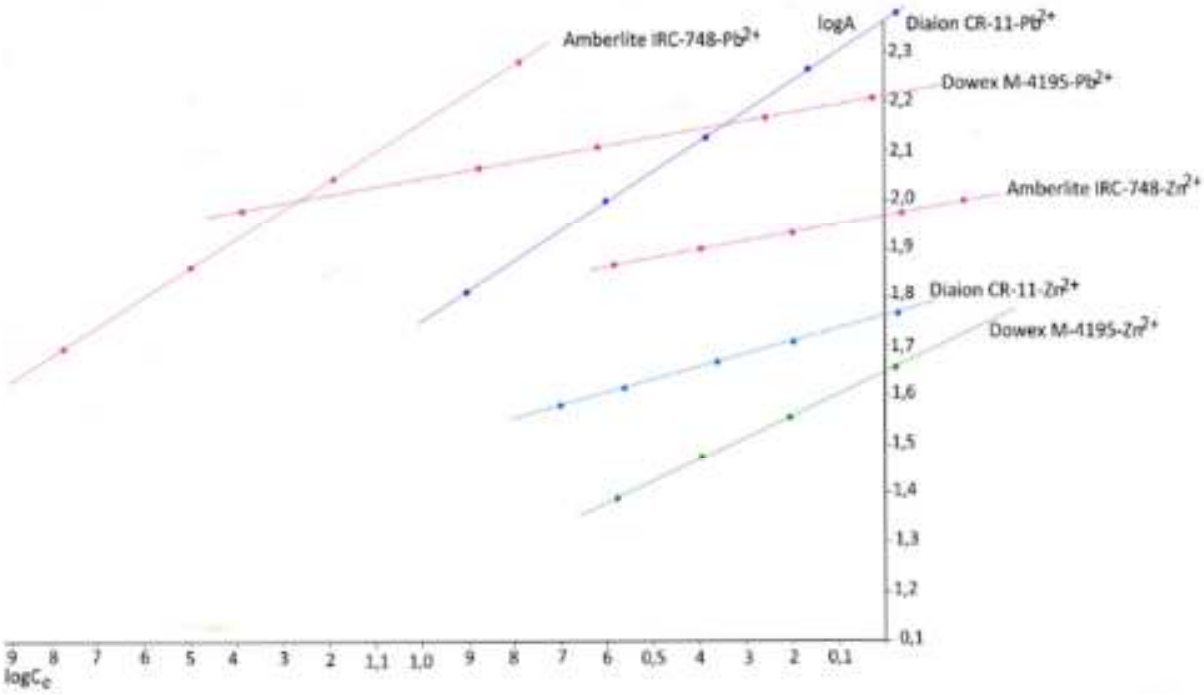

Figure 2. Establishment constants of Freundlich equation.

As illustrated here, the isothermal parts corresponding approximately to the range of 0.5-2.0 gMe•L^{-1} obey the Freundlich equation. The sorption isotherm for the Amberlite IRC 748-Zn^{2+} system obeys the Freundlich equation with high precision in the initial concentration range of 1.0-2.5 g Zn^{2+}. Also we intended to apply to these isotherms the Sips (Langmuir-Freundlich), Redlich-Petersson, and Toth equations [17], but that was unsuccessful. In our opinion, the cause of that should be explained by the fact that the mentioned models are based on a hybrid mechanism. The typical Langmuir and Freundlich equations characterizing the studied systems are given below:

Diaion CR 11-Zn^{2+}	$A = 68.7(4.19\pm0.04).C_e/1+(4.19\pm0.04).C_e$	$A = 57.74.C_e^{0.36}$
Diaion CR 11-Pb^{2+}	$A = 227.9(4.50\pm0.04).C_e/1+(4.50\pm0.04).C_e$	$A=234.40.C_e^{0.55}$
Dowex M 4195-Zn^{2+}	$A = 52.55(3.95\pm0.06).C_e/1+(3.95\pm0.06).C_e$	$A = 50.12.C_e^{0.59}$
Dowex M 4195-Pb^{2+}	$A=160.65(21.1\pm0.05).C_e/1+(21.1\pm0.05).C_e$	$A=245.5.C_e^{0.70}$

Amberlite IRC 748-Zn^{2+}	$A=99.70(10.56\pm0.06).C_e/1+(10.56\pm0.06)C_e$	$A= 56.25.C_e^{0.19}$
Amberlite IRC 748-Pb^{2+}		$A=276.80.C_e^{0.81}$

Amberlite IRC 748-Pb^{2+} system is not subject to an equation describing the isotherm Langmuir. Wide concentration range (0.5-5.0 $gPb\cdot L^{-1}$) sorption results of A – $P^{1/2}$ (distribution ratio) dependence is expressed.

The sorption capacity of these ionites against Cu^{2+} and Cd^{2+} ions has been investigated along with the studied ions, were assessed and selectivity rows registered by us are determined: for Diaion CR 11 and Amberlite IRC 748 – $Cu^{2+}>Pb^{2+}>Zn^{2+}>Cd^{2+}$, and for Dowex M 4195 – $Cu^{2+}>Zn^{2+} = Cd^{2+}>Pb^{2+}$. It is known that quantitative separation of ions in a two elements mixture from each other by selective sorption is only possible when at sorption of the given ions from a mixture the following condition is met for distribution coefficient: P_{Me1}>100-300 and P_{Me2}<3-10, then P_{Me1}/P_{Me2}>10-30 [18]. 0.5 g $Zn^{2+}\cdot L^{-1}$ + 0.5 g $Pb^{2+}\cdot L^{-1}$ concentration mixture of Dowex M 4195 and Amberlite IRC 748 with ionites optimum pH in a real during sorption of distribution coefficients for the specified ion accordance 2312.1; 82.57 and 2841.17; 67.64 $cm^3\cdot g^{-1}$ as the values obtained show that the allocation rate of 28 and 42. In both cases, these ionites showing high susceptibility to the Pb^{2+} ion, preferred to keep the Zn^{2+} ion in solution. The obtained results show that zinc and lead ions can be successfully divided by both ion exchangers in this concentration range.

Kinetics of sorption

With rise in temperature, the ion sorption rate at the ion exchangers increases, but up to various degrees. Thus, the rise in temperature from 25 to 55 °C causes an increase in the effective diffusion coefficients of the studied ions with ion-exchangers on the average in 1.5-2.75 times. The rise in temperature is more evident at sorption of lead ions with ion exchanger Dowex M 4195, *i.e.,* the higher is the activation energy, the more the sorption rate varies at temperature change (Figure 4). The values found for the effective activation energy are typical for ion exchange processes occurring in pore-diffusion area.

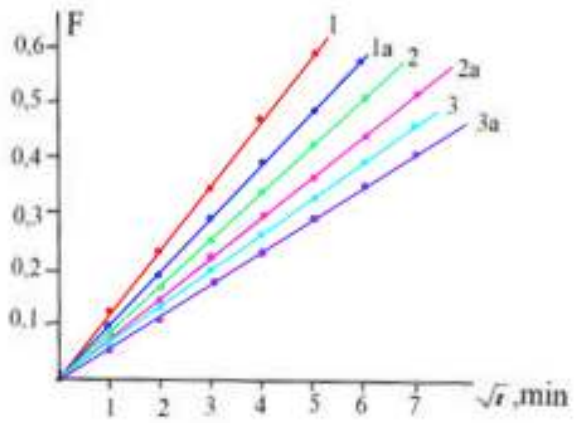

Figure 3. The dependence of equilibrium ions by ionites on the temperature improvement degree from $t^{1/2}$.

1-Diaion CR 11-Pb^{2+};1a-Diaion CR 11-Zn^{2+};

2-Amberlite IRC748-Zn^{2+};2a-Amberlite IRC748-Pb^{2+};

3-Dowex M4195-Zn^{2+};3a-Dowex M4195-Pb^{2+}.

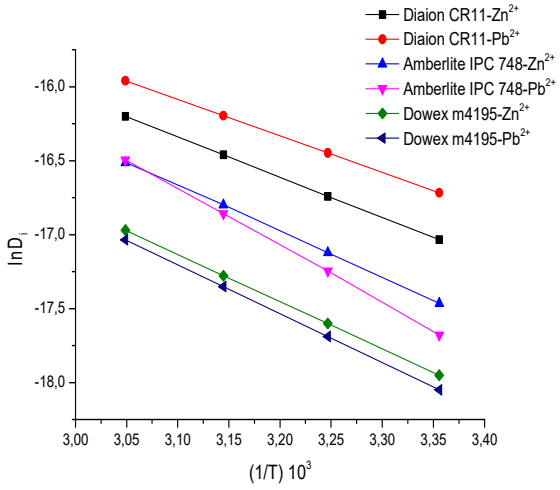

Figure 4. The dependence of the sorption of the studied ions.

It has been determined that the rate of processes in all cases is controlled by the internal diffusion in the selected concentration range (1.0 gMe·L^{-1}). The kinetic mechanism of these has been specified according to the Bio criterion. Diffusion coefficient and activation energy calculated values create a clear understanding for the speed of the process. As it can be seen from the table, the highest diffusion coefficient, but activation energy gets the lowest price in Diaion CR 11-Pb^{2+} system. This is shown occurred learned sorption equilibrium system more rapidly than other systems. Naturally, sorption equilibrium structures must also be considered in the creation of ionites' matrix. The prices

for Gibbs energy (ΔG <0) confirms that all processes were going spontaneously at room temperature. Enthalpic values show that there is an exothermic process. Dowex M 4195 - the highest values charged for Pb^{2+} system enthalpy (more heat allocation) constant change - not comparable with prices charged to other systems K is due to the high values -34.26.

Values obtained for the Bio criterion were in all cases more than 50 [19], also the dependence F-$t^{1/2}$ was expressed by straight lines (Figure 4) beginning in the origin of coordinates in all cases up to the values of F = 0.4-0.5 [20]. 0.0315 cm size radius of the Bio criterion ionite grain, according to the diffusion coefficients in accordance with the values calculated by formula Bi=β·ro/Di (9) and Diaion CR 11-Zn^{2+};Pb^{2+}, Amberlite IRC 748-Zn^{2+};Pb^{2+}, Dowex M4195-Zn^{2+};Pb^{2+} results were obtained for these systems: Bi=55, $\beta=0.7\cdot10^{-4}$; Bi=52, $\beta=0.91\cdot10^{-4}$; Bi=50, $\beta=0.42\cdot10^{-4}$; Bi=49, $\beta=0.33\cdot10^{-4}$; Bi=54, $\beta=0.275\cdot10^{-4}$; Bi=52, $\beta=0.24\cdot10^{-4}$.

Thermodynamics of processes

Thermodynamic of these processes is investigated at ideal ionite phase – the activity coefficients of absorbed ions in a solid phase have not been taken into account, and corresponding calculations are carried out [21]. It should be noted that, thermodynamic parameters calculated on the basis of information received from the experiences of kinetic values.

Enthalpy of the studied processes is determined as the ratio of quantity of heat given off and amount of absorbed ions [6]. The reactions under study are exothermic, and characterized by negative value of the entropic change. The processes of metal ions bonding are accompanied by negative values of the Gibbs energy that indicates thermodynamic permissibility of reactions studied in the forward direction. Though sorption processes are exothermic, observations show that exothermicity decreases parallel to the saturation of ionites with metal ions. Entropy of activation values were characterized by negative numbers in all cases. Expression of entropy of more selective processes by the minor values reveals itself also in the kinetics of these processes. It has been determined that during sorption from solution with the same density sorption rate is higher in the more selective systems. The minor values of the entropy factor are the indicator of more rapid termination of processes. The lowest value of the entropy factor obtained in the system of Zn^{2+}-Diaion CR 11 shows that equilibrium has been established sooner in this system, in comparison with the other studied systems.

Table 1. Kinetic and thermodynamic parameters of sorption of Zn^{2+} and Pb^{2+}-ions by studied resins.

Di, cm^2/sec	Do cm^2/sec	E_{akt} kC/mol	-ΔS, C/mol·K	$-\Delta H^0$, kC/mol	$-\Delta G^0$ kC/mol	K	$\lambda^2 exp(\Delta S/R)10^{-17}$ cm^2
			Diaion CR -11-Zn^{2+}				
$4.0\cdot10^{-8}$	$3.5.10^{-4}$	22.5	39.86	13.57	1.69	1.98	0.78
			Diaion CR- 11-Pb^{2+}				
$5.5\cdot10^{-8}$	$2.156\cdot10^{-4}$	20.50	43.88	16.43	3.36	3.38	12.76
			Amberlite İRC-748-Zn^{2+}				
$2.60\cdot10^{-8}$	$5.78\cdot10^{-4}$	24.8	35.69	15.76	5.12	7.91	3.42
			Amberlite İRC-748-Pb^{2+}				
$2.10\cdot10^{-8}$	$72.67\cdot10^{-4}$	31.60	14.64	9.84	5.47	9.12	$4.3.10^{-16}$
			Dowex M4195-Zn^{2+}				
$1.60\cdot10^{-8}$	$7.07\cdot10^{-4}$	26.50	34.00	11.25	1.12	1.57	41.80
			Dowex M4195-Pb^{2+}				
$1.45\cdot10^{-8}$	$9.59\cdot10^{-4}$	27.50	31.47	18.13	8.75	34.26	56.80

Later establishment of equilibrium with the ion exchanger Dowex M 4195 can be explained by the structure of the ion exchanger and as a result of the pyridine nitrogen screening by pyridine nucleus. From the viewpoint of thermodynamics absorption selectivity is controlled by enthalpy and entropy factors [22]. Therefore, during all processes studied by us, the selectivity at replacing of less selective ion (counter ion of a sorbent) by more selective ion (absorbed from the solution) is controlled by the enthalpic factor with calorification and entropy decrease.

CONCLUSIONS

Regularities of Zn^{2+} and Pb^{2+} ions sorption with salt forms of ion exchangers have been studied, it is determined that with the exception of the Amberlite IRC 748-Pb^{2+} system, the isotherms in all remaining cases obey to the Langmuir-Freundlich equation, and the corresponding equations are offered for each isotherm. Thermodynamic parameters characterizing the studied processes have been calculated on the basis of kinetic parameters and activation energies, it is specified that the selectivity is controlled by the enthalpy factor, calculated kinetic and thermodynamic values are presented in tabular form.

REFERENCES

1. Bilba D, Bejan D, Tofan L. Chelating Sorbents in Inorganic Chemical Analysis. Croatica Chimica Acta. 1998;71(1):155–78. URL: http://hrcak.srce.hr/file/195347.

2. Samczyński Z. Ion Exchange Behavior of Selected Elements on Chelex 100 Resin. Solvent Extraction and Ion Exchange. 2006 Oct;24(5):781–94. DOI: 10.1080/07366290600846174.

3. Malla M. Evaluation of sorption and desorption characteristics of cadmium, lead and zinc on Amberlite IRC-718 iminodiacetate chelating ion exchanger. Talanta. 2002 May 16;57(2):277–87. DOI: 10.1016/S0039-9140(02)00034-6.

4. Lin L-C, Juang R-S. Ion-exchange equilibria of Cu(II) and Zn(II) from aqueous solutions with Chelex 100 and Amberlite IRC 748 resins. Chemical Engineering Journal. 2005 Sep;112(1–3):211–8. DOI: 10.1016/j.cej.2005.07.009.

5. Wang F, Wang L, Li J, Sun X, Zhang L. Synthesis of modified D401 chelating resin and its adsorption properties for Pb2+. Journal of Central South University of Technology. 2009 Aug;16(4):575–80. DOI: 10.1007/s11771-009-0096-1.

6. Wołowicz A, Hubicki Z. Selective Adsorption of Palladium(II) Complexes onto the Chelating Ion Exchange Resin Dowex M 4195 – Kinetic Studies. Solvent Extraction and Ion Exchange. 2010 Feb;28(1):124–59. DOI: 10.1080/07366290903408953.

7. Dąbrowski A, Hubicki Z, Podkościelny P, Robens E. Selective removal of the heavy metal ions from waters and industrial wastewaters by ion-exchange method. Chemosphere. 2004 Jul;56(2):91–106. DOI: 10.1016/j.chemosphere.2004.03.006.

8. Chromatography.Products for analysis and purification. Sigma-Aldrich Chemie GmbH, 2003-2004, 453.

9. Shvartsenbakh G., Flashka G. Complexіmetric titration. 1970, 562 p. (in Russian).

10. Boyd GE, Adamson AW, Myers LS. The Exchange Adsorption of Ions from Aqueous Solutions by Organic Zeolites. II. Kinetics 1. Journal of the American Chemical Society. 1947 Nov;69(11):2836–48. DOI: 10.1021/ja01203a066.

11. Barrer RM, Bartholomew RF, Rees LVC. Ion exchange in porous crystals part I. Self- and exchange-diffusion of ions in chabazites. Journal of Physics and Chemistry of Solids. 1963 Jan;24(1):51–62. DOI: 10.1016/0022-3697(63)90041-6.

12. Glasstone S., Laidler K., Eyring H. The Theory of Rate Processes, 1941, 501 p.

13. Khering R. Chelatforming resins. 1971**,** 279 p.(in Russian).

14. Saldadze K.M., Kopylova-Valova V.D. Complexforming resins**.** 1980, 562 p (in Russian).

15. Soldatov VS. Potentiometric titration of ion exchangers. Reactive and Functional Polymers. 1998 Nov;38(2–3):73–112. DOI: 10.1016/S1381-5148(98)00018-2.

[16] Freundlich H.M.F. Die adsorption in lösungen. Z Phys Chem. 1906, 57, 385-470.

17. Redlich O, Peterson DL. A Useful Adsorption Isotherm. The Journal of Physical Chemistry. 1959 Jun;63(6):1024–1024. DOI: 10.1021/j150576a611.

18. Marhol M. Ion exchangers in analytical chemistry: their properties and use in inorganic chemistry. Amsterdam ; New York: Elsevier Scientific Pub. Co; 1982. 585 p. (Wilson and Wilson's Comprehensive analytical chemistry). ISBN: 978-0-444-99717-3.

19. Lykov A.V. Theory of heatconductance, 1967, 436 p. (in Russian)

20. Parfitt GD, Rochester CH, editors. Adsorption from solution at the solid/liquid interface. London ; New York: Academic Press; 1983. 416 p. ISBN: 978-0-12-544980-9.

21. Rengan K. Chelating resins: Sorption characteristics in chloride media. Journal of Radioanalytical and Nuclear Chemistry. 1997 May;219(2):211–5. DOI: 10.1007/BF02038502.

22. Lin L-C, Juang R-S. Ion-exchange kinetics of Cu(II) and Zn(II) from aqueous solutions with two chelating resins. Chemical Engineering Journal. 2007 Aug;132(1–3):205–13. DOI: 10.1016/j.cej.2006.12.019.

Türkçe Öz ve Anahtar Kelimeler

Diaion CR 11, Amberlite IRC 748 ve Dowex M 4195'in iyon değişim özellikleri

Öz : Diaion CR 11, Amberlite IRC 748 ve Dowex M 4195 iyon değiştiricilerinin asit baz özellikleri potansiyometri ile incelenmiştir. Şartlı ayrılma sabitleri Henderson-Hasselbalch denkleminden hesaplanmıştır. Zn^{2+} ve Pb^{2+} iyonlarının, Diaion CR 11, Amberlite IRC 748, iminodiasetik asit fonksiyonel grubu ve Dowex M 4195 ile bis-pikolilamin fonksiyonel grubu içeren iyon değiştiricilerinin süzgeç düzenlilikleri araştırılmıştır. Sorpsiyon izotermleri çizilmiştir. İzotermler, bilinen modeller temelinde analiz edilmiştir. Amberlite IRC 748- Pb^{2+} sistemi haricinde kalan tüm örneklerde izotermler Langmuir ve Freundlich denklemine uyulduğu tespit edilmiştir. Eşdeğer denklemler, her izoterm için verilmiştir. İşlemlerin kinetik mekanizmaları belirlenmiş ve 1.0 $gMe \cdot L^{-1}$ ve daha yukarı konsantrasyonda sorpsiyonun gözenek difüzyonu ile kontrol edildiği, etkin difüzyon katsayılarının değerleri ve ön-üslü faktörün hesaplandığı doğrulanmıştır. Termodinamik parametreler kinetik verilere dayanarak hesaplanmıştır. Termodinamik faktör kontrol süreçleri belirlenir.

Anahtar kelimeler: İyon değiştiriciler, Zn^{2+} ve Pb^{2+} iyonları, sorpsiyon izotermleri, Langmuir ve Freundlich modelleri, kinetik ve termodinamik parametreler.

Sunulma: 29 Temmuz 2016. **Düzeltme:** 06 Eylül 2016. **Kabul:** 20 Aralık 2016.

(This article was presented to the 28th National Chemistry Congress and submitted to JOTCSA as a full manuscript)

Chemical and Physical Investigations of Arabian Eye Kohl Brands as Cosmetic in Libya

Maher Mohamed Abed El-Aziz[a*], Mohamed Ammar Khalifa[b], Rabia Alhadi Ghariani[c], Hasan Daw Ashtawi Mohamed[b], and Mahmud Ashtewi S. Ashtewi[b]

[a]*Chemistry Department, Faculty of Education / Gaser Ben Ghashir, University of Tripoli, Tripoli, Libya*
[b] *Chemistry Department, Tarhuna Faculty of Arts and Sciences, Azzaytuna University, Tarhuna, Libya*
[c]*Janzour College of Education, Tripoli University, Tripoli, Libya*
**Correspondence Author*

Abstract: Three Arabian eye kohl brands were analyzed for the presence of lead and cadmium using atomic absorption spectroscopy (AAS) and X-ray diffraction techniques. In this work, the chemical analysis of the samples was studied according to the concentration of heavy metals, solubility in different medium, reaction with KI, moisture, and organic contents. XRD pattern proposed the presence of some crystalline material in an amorphous background for all investigated brands. Mineral data analysis shows that the main minerals found in the samples are Manganoshadlunite in Natural Arab Kohl (NAK), samarskite in Natural Black Al-Athmod Kohl (NBAK), and kitaibelite in Black Al-Hashemi kohl (BHK). Physical properties such as color, forms, touch, and transparency are nearly the same for all samples but different in density, average pore diameter, and specific surface area. Atomic absorption spectroscopy (AAS) showed that the average percentage of Pb was in the range 0.2411 to 6.173 %; and from zero to 0.0019 % for Cd. The maximum concentration of Pb and Cd was found in Natural Arab Kohl (NAK) sample and is equal to 30.865 mg/g and 9.50 µg/g respectively. The minimum concentration of heavy metal was found in Natural Black Al-Athmod Kohl (NBAK) sample. Moisture was present in a very low percent (~ 1%) while organics was being in a reasonable amount (maximum $\geq$ 69%). All eye kohl brands are soluble in acidic medium with different proportions and forms the yellow precipitate of PbI_2 when react with KI which is considered as a chemical evidence for the presence of lead. It is highly recommended to use Natural Black Al-Athmod Kohl (NBAK) only because it has low concentration of heavy metals (Pb and Cd), and has higher specific surface area. The risk factor for using these type of eye kohl is very low. The higher surface area helps in spreading the active ingredient leading to increase the treatability against eye disease.

Keywords: Eye Kohl; lead; cadmium; Atomic Absorption Spectrophotometry (AAS).
Cite this: Abed El-Aziz M, Ammar Khalifa M, Alhadi Ghariani R, Ashtawi Mohamed H, S. Ashtewi M. Chemical and Physical Investigations of Arabian Eye Kohl Brands as Cosmetic in Libya. JOTCSA. 2017;4(1):463-76.
DOI: To be assigned.
*Corresponding author. E-mail: hrshr152@gmail.com

INTRODUCTION

Eye kohl has been used by girls and mature women in the Middle East, Far East and North Africa cosmetically for eye makeup in many occasions, eye kohl has also been used for eye treatments against some diseases. Traditionally, in many countries, eye kohl is applied to newborn children; parents believe it works against pain and evil eyes [1, 2]. Most of the traditional eye kohl in Libyan markets comes from Africa, Asia and Middle East and all are made from stones contain elemental substances such lead, nickel, cadmium, and sulfur. Eye kohl is naturally occurring from the major amount of mineral sulfide, minor amount of mineral oxides and some of non-metals, especially carbon. The galena ore has a black-gray color with a shiny surface which is often used for making traditional eye kohl [1]. High considerations regarding the environment and human health in contact with heavy elements have been discussed, it has been reported that many medical products cause health risk and environmental contamination due to the presence of elements such as Pb, Hg, Cd, and Cr [3]. Heavy metals such as cadmium, chromium, lead, and nickel are highly toxic to humans and cause acute symptoms like nausea, vomiting, headache, and can damage kidneys and the liver [4-6]. Several studies reported that a strong correlation between the use of eye kohl and Pb levels in the human body and its relation to many diseases [7-10]. Lead compounds are toxic by ingestion, inhalation, and by skin exposure. Children are more prone to be affected by Pb than adults [11]. Lead toxicity has terrible effects on both children and adult's health, including intelligent quotient deficit, behavior disorder, impaired hearing, and slowed growth [12-15]. Severe Pb poisoning resulting brain damage when blood Pb concentration is about 70 μg/dL, the level usually proposed as the threshold for encephalopathy [16]. Pb replaces iron in blood, and more than 90% of Pb in the blood were found in the red cells and may cause severe illness, it has been reported that, in addition to other factors, a significant relation refers to the use eye kohl and the development of anemia [17, 18].

In recent studies, toxic heavy metals such as Hg, As, Cr, Se, and Pb have been detected quantitatively in eye cosmetic samples [19, 20]. These studies highlight the toxicity and risk of using such products. Many studies were done in North Africa and in the Middle East regarding the composition of traditional eye kohl. Among these studies were conducted on 18 traditional eye kohl samples purchased from markets in Cairo, 6 samples were found to be mainly PbS [1]. In Oman, 47 kohl samples were analyzed and reported that 14 of those sampled contain Pb in different concentrations [21]. Another study of 21 eye kohl samples was created in Saudi Arabia and Pb percentage was found between 2.9% and 34.1% in 4

samples and more than 84% in 10 samples, while 7 samples did not contain Pb [22]. Eye kohl products were studied in Tunisia, it was reported that Pb concentrations ranged between 51.1 μg/g and 4839.5 μg/g while Cd concentrations ranged between 1.0 μg/g and 158.6 μg/g [23].

A research carried on a different samples of eye kohl collected from state of Libya, Egypt and Kingdom of Saudi Arabia (KSA) and the results indicate that kohl samples are contaminated with a significant concentrations of semi and heavy metals such as As, Cd, Hg, and Pb [24]. In United Arab Emirates (UAE), a survey of minerals was carried out for 53 kohl samples. It was found that only 20 samples contain galena [25]. The above results were summarized in Table 1 which show that a significant difference in both chemical constituents and percent concentration of hazardous heavy metals between all samples investigated in many different countries, it is highly recommended to conduct further studies and researches in these fields. The present work aimed to investigate the physical and chemical characteristics of commercially available eye kohl samples commonly used by Libyan people as cosmetics. Physical investigations include the following: Density, particle radius, specific surface area, color, touch, forms, transparency and X-ray diffraction (XRD) analysis. Chemical investigations contain the analysis of lead and cadmium using atomic absorption spectroscopy (AAS), solubility in different medium, moisture contents, organic contents, and the effect of potassium iodide solution on the samples.

Table 1. Concentration of heavy metals in different kohl samples from different Arab countries.

Country	No. of kohl samples	Heavy metal concentrations	Tools of analysis	Reference No.
Cairo, Egypt	18	6 samples contain galena 10 samples contain amorphous carbon, calcite, cuprite, goethite and talc.	X-ray powder diffraction (XRPD) Scanning electron microscope (SEM)	[1]
Oman	47	14 samples contain Pb in different concentrations.	X-ray powder diffraction (XRPD) Scanning electron microscope (SEM)	[21]
Kingdom of Saudi Arabia (KSA)	21	Pb = 2.9-34.1 % (4 samples) Pb ≈ 84 % (10 samples) Nil (7 samples)	Energy dispersive X-ray (EDXR)	[22]
Tunisia	11	Pb concentrations ranged between 51.1 μg g^{-1} and 4839.5 μg g^{-1}. Cd concentrations ranged between 1.0 μg g^{-1} and 158.6 μg g^{-1}. Cu concentrations ranged between 2.5 μg g^{-1} and 162.5 μg g^{-1}. Zn concentrations ranged between 0.7 μg g^{-1} and 185.0 μg g−1.	Atomic absorption spectrophotometer (AAS)	[23]
Libya, Egypt and Kingdom of Saudi Arabia (KSA)	8	Kohl samples are contaminated with a significant concentrations of heavy metals As, Cd, Hg and Pb	Inductively coupled plasma & Optical emission spectrometer (ICP-OES)	[24]
United Arab Emirates (UAE)	53	20 samples contain galena 33 samples amorphous carbon, calcite/aragonite, hematite, goethite, sassolite, talc and zincite	X-ray powder diffraction (XRPD) and Scanning electron microscope (SEM)	[25]

Galena=PbS Calcite/aragonite=$CaCO_3$ Hematite=Fe_2O_3 Cuprite=Cu_2O
Goethite=FeO(OH) Sassolite=H_3BO_3 Zincite=ZnO Talc=$Mg_3Si_4O_{10}(OH)_2$

EXPERIMENTAL

Materials

All chemicals used were of analytical grade. Three types of eye kohl samples are available and were purchased from the local Libyan market as a shiny black solid powder. All obtained samples were investigated without any further pre-chemical treatment. Because of the morphological appearance of all samples are nearly the same, eye kohl brands were labeled according to their local/public commercial names as follows:

Common Arabic name	Symbol/Code	Brand
Natural Arab Kohl	NAK	Local public
Natural Black Al-Athmod Kohl	NBAK	Local public
Black Al-Hashemi kohl	BHK	Local public

The above names of the three investigated kohl samples are pure Arabic common names related to the Arabic culture. These names were used by public to differentiate between the source, the quality or the type of the kohl which they would used.

Instruments

Determination of Pb and Cd in the obtained eye kohl samples was carried out using the Atomic Absorption Spectrophotometer (AAS) (VARIAN system, 220FS Model, Made in USA). X-ray diffraction (XRD) patterns and crystallinity measurements were obtained using a PHILIPS X-ray diffractometer, model PW 1890, with a nickel filter and a Cu-K_α radiation.

Measurements

The radius of the particle of the sieved samples were determined according to El-Naggar method by measuring the diameter of 100 particles with an optical microscope. The particles were assumed to have a uniform spherical shape and a mean equivalent radius was calculated [26].

Procedure

The leaching process of lead and cadmium ions from solid eye kohl samples and preparation of Pb^{2+} and Cd^{2+} ion as concentrated solutions for analysis has been carried out according to the following steps:

1. Three times, 0.50 grams of each eye kohl sample were weighed and transferred into 100 mL beakers.
2. Concentrated solution of *aqua regia* containing a mixture of concentrated HCl and HNO_3 (3:2 vol. / vol. ratio) was prepared and 10 mL of the mixture was added to each beaker.
3. Samples were gently heated to almost dryness on a hot plate in a good ventilation hood.
4. Again 10 mL of the concentrated *aqua regia* solution was added to each beaker and heated again to almost dryness.
5. Samples were left to cool, then the desired amount of doubly distilled water was added and stirred with a glass rod to dissolve the residue.

6. Finally, dissolved samples were filtered into 50 mL volumetric flasks and completed to the mark with doubly distilled water.
7. The used glassware and filter papers were washed continuously with doubly distilled water to ensure that all Pb^{2+} and Cd^{2+} ions are completely leached from solid kohl samples.
8. The dissolved sample solutions were subjected directly to an air-acetylene flame atomic absorption spectrophotometer (UNICAM, 969) by the standard calibration technique for quantitative analysis.
9. Standardization and calibration curves take into consideration before measuring of Pb^{2+} and Cd^{2+} ions.

RESULTS AND DISCUSSION

Physicochemical characteristics of the three investigated eye kohl samples were presented in Tables 2 and 3. The physical properties include color, forms, bulk density, particle size, specific surface area, and crystallinity. While chemical analysis shows Pb and Cd contents, moisture content, organic content, reaction with KI, chemical stability in different medium, and pH of the sample solution. A complete identification of any sample should contain chemical, physical and mineralogical investigation. The obtained results will be discussed in the following parts.

Physical characteristics

The physical properties of the investigated Libyan eye kohl samples were shown in Table 2, from which we can notice that all samples have nearly the same color and the predominant color is black which absorbs all the wavelengths of the sunlight. Shiny black color may be due to the presence of naturally occurring mineral sulfide galena or coal. Powdered granular forms in all samples also support the homogeneous chemical constituent's hypothesis. Bulk density measurements prove that Natural Arab Kohl sample is the heavier sample with the value equal to ~ 3.53 g/mL. The bulk density sequence has the order: Natural Arab Kohl > Black Al-Hashemi Kohl > Natural Black Al-Athmod Kohl. These orders reflect the higher concentration of Pb (6.1730 %) and lower carbon (organic) contents ($\geq$60 %) in a Natural Arab Kohl sample as shown in Table 3. As a result, Natural Black Al-Athmod Kohl has low lead concentration (0.2411 %) and high carbon content ($\geq$69 %).

The particle size distribution shows that the average particle radius in mm are in the range from 0.12 ± 0.03 for NBAK sample to 0.18 ± 0.03 for NAK sample. The specific surface area

in m^2/g is in the range from 0.22 for NAK sample to 0.65 for NBAK sample. The data show that both the average particle radius and the specific surface area are in the opposite sequence:

The average particle radius: NBAK sample < BHK sample < NAK sample

The specific surface area: NBAK sample > BHK sample > NAK sample

Table 2. Physical characteristics of Libyan eye kohl samples.

Item	NAK	NBAK	BHK
Bulk density (g/c.c)	~ 3.53	~ 2.63	~ 2.78
Average particle radius (mm)	0.18 ± 0.03	0.12 ± 0.03	0.16 ± 0.03
Specific surface area (m^2/g)	0.22	0.65	0.38
Color	Black / Gray	Shiny black	Shiny black
Forms	Powdered granules	Powdered granules	Powdered granules
Touch	Greasy feel and stains fingers and skin	Greasy feel and stains fingers and skin	Greasy feel and stains fingers and skin
Transparency	Opaque	Opaque	Opaque
XRD pattern	Intensive continuum peaks at low 2θ value	Intensive continuum peaks at low 2θ value	Intensive continuum peaks at low 2θ value

The above results were attributed to the fact that the higher surface area of the solid samples is associated with the lower particle radius and *vice versa* [27]. The values of average particle radius and the specific surface area of the Black Al-Hashemi Kohl sample is in between values of Natural Arab Kohl sample and Natural Black Al-Athmod Kohl sample.

X-ray diffraction pattern of the three investigated kohl samples was obtained along a wide range of *2θ degree* and represented in Figure 1, which shows two separate peaks of crystallinity, one of them is the intensive continuum peaks at very low *2θ* value (*2θ = 12.6 degree, d = 7.02A*°) with relatively high intensity (*I = 60-80%*) for all investigated samples. Another peak at *2θ = 25.3 degree, d= 3.51A*° with relatively low intensity (*I = 10-30%*). This reveals that some crystallinity was found and all samples contain crystalline materials in an amorphous background [28]. Mineral analysis for NAK sample (Pb=6.173%) shows the presence of Manganoshadlunite which has the empirical formula $Mn^{2+}_{0.75}Pb_{0.25}Cu_6Fe^{2+}_2S_8$ at tolerance = 20 %. For NBAK sample (Pb=0.2411%), the major mineral found is samarskite with empirical formula $Yb_{0.09}$ $Er_{0.05}$ $Y_{0.05}$ $Dy_{0.05}$ $Lu_{0.01}$ $Nd_{0.01}$ $Tm_{0.01}$ $Ho_{0.01}$ $Gd_{0.01}$ $Sm_{0.008}$ $Tb_{0.005}$ $Ce_{0.004}$ $Pr_{0.001}La_{0.001}U_{0.12}Th_{0.12}Ca_{0.12}Fe^{2+}_{0.11}Mn^{2+}_{0.04}O_4$. All metals in samarskite was found as oxides and the mineral has shiny black color as shown in Figure 2. The mineral composition of NBAK sample was obtained at tolerance = 20. Finally, Figure 3 exhibits the shiny metallic lead gray color of kitaibelite which is the major mineralogical constituents of BHK sample (Pb=2.277%) at tolerance = 10%. The empirical formula of kitaibelite is $Ag_{10}PbBi_{30}S_{51}$ [29]. From the above-mentioned results, it was noticed that the obtained amount of Pb from both

chemical analysis by AAS and mineralogical analysis by XRD are closely related to each other and hence, the data analysis of XRD is in agreement with that of AAS for all investigated samples. In fact, mineralogical data analysis for Cd at trace concentration in eye kohl samples does not exhibit any specific major mineralogical constituents.

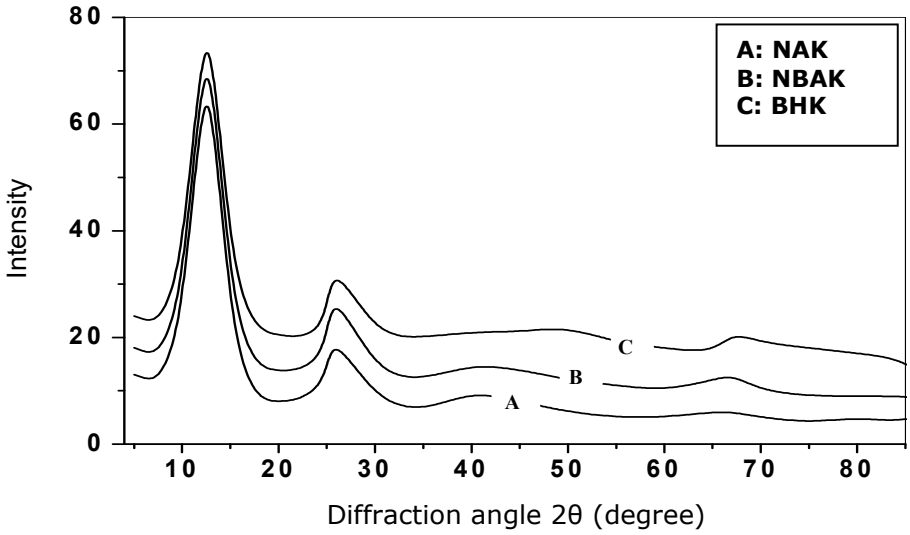

Fig. 1. XRD pattern for investigated Libyan eye kohl samples.

Fig. 2. Samarskite
shiny black color

Fig. 3. Kitaibelite
shiny metallic lead gray color

However, as shown in Table 2, all the investigated samples have the same general physical characteristics such as touch and transparency, they also have a greasy feeling in touching and stains fingers and skin while it is opaque. From the above-mentioned results, it can be concluded that Natural Arab Kohl has higher bulk density, higher particle size and lower specific surface area, but Natural Black Al-Athmod Kohl has a lower bulk density, lower particle size and higher specific surface area while Black Al-Hashemi Kohl is in between.

Chemical characteristics

The chemical properties of eye kohl samples commonly used in Libya were investigated according to lead concentration, cadmium concentration, moisture content, organic content, solubility in different media, and the reaction with potassium iodide which give a characteristic intensive yellow color with Pb^{2+} ion. Chemical properties of the investigated samples were shown in Table 3, from which we can conclude that the highest concentration of Pb and Cd was found in Natural Arab Kohl samples. This result is in agreement with the bulk density measurements mentioned above. The density of Pb and Cd is equal to 11.34 and 8.65 g/mL, respectively, and hence the presence of heavy metals in a sample will raise its bulk density. The concentration of Pb takes the following order: Natural Arab Kohl sample > Black Al-Hashemi Kohl sample > Natural Black Al-Athmod Kohl sample.

Table 3. Chemical characteristics of Libyan eye kohl samples.

Item	**NAK**	**NBAK**	**BHK**
Pb (% w/w)	6.1730 %	0.2411 %	2.2770 %
Cd (% w/w)	0.0019 %	Nil	0.0015 %
Pb concentration (mg/g)	30.8650	1.2055	11.385
Cd concentration (µg/g)	9.50	Nil	7.50
Reaction with KI	Yellow ppt. (+++)	Yellow ppt. (+)	Yellow ppt. (+)
Moisture content (%)	~ 1.0 %	~ 1.0 %	~ 1.0 %
Organic (carbon) content (%)	≥ 60 %	≥ 69 %	≥ 65 %
Solubility in H_2O (cold or hot)	-	-	-
Solubility in 3M HCl	++	+	+
Solubility in 3M HNO_3	++ Cloudy solution	+++	+++
Solubility in *aqua regia*	++++	++++	++++
pH of solution	7.9	7.3	7.4

(-) Insoluble (+) Sparingly soluble (++) Slightly soluble (+++) Soluble (++++) Highly soluble

It was calculated that for a Natural Arab Kohl sample, the concentration of Pb exceeded to the concentration of cadmium by about ≈ 3249 times. For Black Al-Hashemi Kohl sample, the concentration of Pb exceeded to the concentration of Cd by about ≈ 1518 times. A quantity of Pb in the samples is in tenths of milligrams per one-gram sample, while the quantity of Cd is in few micrograms per one-gram sample. The concentration of Cd is traced and in the range from 7.5 to 9.5 µg/g for Black Al-Hashemi Kohl sample and Natural Arab Kohl sample, respectively. These results refer to the lead is the main heavy metal affected on the chemical behavior of the eye kohl samples commonly used in Libya. The leached solution of three eye kohl samples was subjected to react with the potassium iodide solution and the preliminary tests show that the intense yellow color of lead iodide precipitate appeared with Natural Arab Kohl sample indicating to the presence of high lead

concentration. On the other hand, pale yellow color which appearing with Natural Black Al-Athmod Kohl sample and Black Al-Hashemi Kohl refers to the low concentration of Pb in these samples. The chemical reaction between lead ion as lead sulfide and potassium iodide can be expressed as follows:

$$PbS_{(aq)} + 2KI_{(aq)} \xrightarrow{yields} PbI_{2(s)} \downarrow + K_2S_{(aq)}$$

$$Pb(NO_3)_{2(aq)} + 2KI_{(aq)} \xrightarrow{yields} PbI_{2(s)} \downarrow + 2KNO_{3(aq)}$$

The moisture content does not exceed ~ 1.0 %, which can be attributed to the physically adsorbed water on the sample surfaces. The carbon / organic content was in the range from 60 to 69 %, and the relative high carbon content reflects availability and durability of carbon material in the environment. In addition to the economic and commercial factors affecting on the public, industry of the eye kohl.

Solubility results show that all samples are insoluble in cold and hot water, but soluble in acidic medium especially *aqua regia*. Natural Black Al-Athmod Kohl Sample and Black Al-Hashemi Kohl is sparingly soluble in hydrochloric acid solution. Because of oxidation of sulfur ion (S^{2-}) to sulfur in the presence of nitric acid, Natural Arab Kohl sample forms cloudy solution with nitric acid, indicating the presence of PbS [30] in Natural Arab Kohl sample. The values of pH were measured for the aqueous solution of the investigated samples and the results show that the solutions are between neutral and slightly alkaline.

From Tables 1 and 2 and according to the above mentioned results, we can indicate that:

1) Natural Arab Kohl was characterized by high bulk density, high particle size, high concentration of heavy metals, small specific surface area, and finally low carbon content.
2) Natural Black Al-Athmod Kohl was characterized by low bulk density, small particle size, low concentration of heavy metals, big specific surface area, and finally high carbon content.
3) Black Al-Hashemi Kohl was characterized by a relatively mild physical and chemical properties.

CONCLUSION

1) It is highly recommended that consumers use Natural Black Al-Athmod Kohl only because it has low concentration of heavy metals (Pb and Cd), and has a high specific surface area. The risk factor for using these type of eye kohl is very low. The higher surface area helps in spreading the active ingredient leading to increase the treatability against eye disease.
2) It is recommended that consumers avoid using Natural Arab Kohl and Black Al-Hashemi Kohl because these types of eye kohl have high concentrations of Pb and Cd, and this increase the risk factor for human and the environment.
3) To complete the profile of eye kohl commonly used in Libya, it was recommended to continue the chemical and physical research by further tools.

REFERENCES

1. Hardy AD, Walton RI, Vaishnav R. Composition of eye cosmetics (kohls) used in Cairo. International Journal of Environmental Health Research. 2004 Feb;14(1):83–91.
DOI: 10.1080/09603120310001633859.

2. Al-Ajel MM, Al-Ketbi MM, Al-Shehhi MA, Bastaki NA, Barss P, Grivna M, et al. Knowledge, Attitude & Practice of Mothers Regarding Lead Poisoning due to Use of Kohl Eye Cosmetic for Babies in Al Ain, UAE. In: UAE University Research Conference (Senior & Graduate Students). 2005. p. 18–24.

3. AI-Saleh I, Coate L. Lead exposure in Saudi Arabia from the use of traditional cosmetics and medical remedies. Environmental Geochemistry and Health [Internet]. 1995 Mar [cited 2016 Dec 14];17(1). Available from: http://link.springer.com/10.1007/BF00188629.

4. Vaglenov A, Creus A, Laitchev S, Petkova V, Pavlova S, Marcos R. Occupational exposure to lead and induction of genetic damage. Environ Health Perspect. 2001 Mar;109(3):295–8.
URL: https://www.ncbi.nlm.nih.gov/pmc/articles/PMC1240249/.

5. Lobner D, Asrari M. Neurotoxicity of dental amalgam is mediated by zinc. Journal of dental research. 2003;82(3):243–246.

6. Patnaik P. A comprehensive guide to the hazardous properties of chemical substances. 3rd ed. Hoboken, NJ: John Wiley; 2007. 1059 p. ISBN: 978-0-471-71458-3.

7. Alkhawajah AM. Alkohl use in Saudi Arabia. Extent of use and possible lead toxicity. Trop Geogr Med. 1992 Oct;44(4):373–7. URL: http://europepmc.org/abstract/med/1295151.

8. Al-Saleh I, Nester M, Devol E, Shinwari N, Al-Shahria S. Determinants of Blood Lead Levels in Saudi Arabian Schoolgirls. International Journal of Occupational and Environmental Health. 1999 Apr;5(2):107–14. DOI: 10.1179/oeh.1999.5.2.107.

9. Rahbar M, White F, Agboatwalla M, Hozhabri S, Luby S. Factors associated with elevated blood lead concentrations in children in Karachi, Pakistan. Bulletin of the World Health Organization. 2002;80(10):769–75. URL: http://www.scielosp.org/pdf/bwho/v80n10/8010a03.pdf.

10. Al-Ashban R., Aslam M, Shah A. Kohl (surma): a toxic traditional eye cosmetic study in Saudi Arabia. Public Health. 2004 Jun;118(4):292–8. DOI: 10.1016/j.puhe.2003.05.001.

11. Goyer R. Transplacental transport of lead. Environ Health Perspect. 1990;89:101–5.
URL: https://www.ncbi.nlm.nih.gov/pmc/articles/PMC1567784/.

12. Needleman HL, Schell A, Bellinger D, Leviton A, Allred EN. The Long-Term Effects of Exposure to Low Doses of Lead in Childhood: An 11-Year Follow-up Report. New England Journal of Medicine. 1990 Jan 11;322(2):83–8. DOI: 10.1056/NEJM199001113220203.

13. Schwartz J, Otto D. Lead and Minor Hearing Impairment. Archives of Environmental Health: An International Journal. 1991 Oct;46(5):300–5. DOI: 10.1080/00039896.1991.9934391.

14. Pocock SJ, Smith M, Baghurst P. Environmental lead and children's intelligence: a systematic review of the epidemiological evidence. BMJ. 1994 Nov 5;309(6963):1189–97.
DOI: 10.1136/bmj.309.6963.1189.

15. Chukwuma CS. Environmental Lead Exposure in Africa. Ambio. 1997;26(6):399–403.
URL: http://www.jstor.org/stable/4314625.

16. Khayat A, Menon NS, Alidina MR. Acute lead encephalopathy in early infancy--clinical presentation and outcome. Ann Trop Paediatr. 1997 Mar;17(1):39–44.
DOI: 10.1080/02724936.1997.11747861.

17. Hidayat A, Weatherhead R, Al-Rajhi A, Johnson F. Conjunctival and lacrimal sac pigmentation by kohl (eyeliner). Br J Ophthalmol. 1997;81(5):418.
URL: https://www.ncbi.nlm.nih.gov/pmc/articles/PMC1722203/.

18. Lee IW, Ahn SK, Choi EH, Whang KK, Lee SH. Complications of eyelash and eyebrow tattooing: reports of 2 cases of pigment fanning. Cutis. 2001 Jul;68(1):53–5.
URL: http://europepmc.org/abstract/med/11480149.

19. Soruraddin MH, Heydari R, Puladvand M, Zahedi MM. A New Spectrophotometric Method for Determination of Selenium in Cosmetic and Pharmaceutical Preparations after Preconcentration with Cloud Point Extraction. International Journal of Analytical Chemistry. 2011;2011:1–8.
DOI: 10.1155/2011/729651.

20. Hepp N, Mindak WR, Gasper JW, Thompson CB, Barrows JN. Survey of cosmetics for arsenic, cadmium, chromium, cobalt, lead, mercury, and nickel content. J Cosmet Sci [Internet]. 2014;65:125–45.URL:https://www.researchgate.net/profile/William_Mindak/publication/264091887_Survey_of_cosmetics_for_arsenic_cadmium_chromium_cobalt_lead_mercury_and_nickel_content/links/53fdf7170cf22f21c2f8be3b.pdf.

21. Hardy A., Vaishnav R, Al-Kharusi SS., Sutherland H., Worthing M. Composition of eye cosmetics (kohls) used in Oman. Journal of Ethnopharmacology. 1998 Apr;60(3):223–34.
DOI: 10.1016/S0378-8741(97)00156-6.

22. Al-Hazzaa SAF, Krahn PM. Kohl: a hazardous eyeliner. International Ophthalmology. 1995;19(2):83–8. DOI: 10.1007/BF00133177.

23. Nouioui MA, Mahjoubi S, Ghorbel A, Ben Haj Yahia M, Amira D, Ghorbel H, et al. Health Risk Assessment of Heavy Metals in Traditional Cosmetics Sold in Tunisian Local Markets. International Scholarly Research Notices. 2016;2016:1–12. DOI: 10.1155/2016/6296458.

24. Sherif M, Orabi M, Abdulrahem O. Study of Heavy Elements and Radioactivity Concentrations in Some Eye Cosmetics Commonly Used in Arabic Regions. International Journal of Chemical Engineering and Applications. 2015 Feb;6(1):66–70. DOI: 10.7763/IJCEA.2015.V6.453.

25. Hardy AD, Walton RI, Myers KA, Vaishnav R. Availability and chemical composition of traditional eye cosmetics ("kohls") used in the United Arab Emirates of Dubai, Sharjah, Ajman, Umm Al-Quwain, Ras Al-Khaimah, and Fujairah. J Cosmet Sci. 2006 Apr;57(2):107–25. URL: http://europepmc.org/abstract/med/16688375.

26. El-Naggar IM, Zakaria ES, Abou-Mesalam MM, Aly HF. Removal of some radioactive nuclides by in-situ precipitation with ion exchange materials. Czechoslovak Journal of Physics. 1999 Jan;49(S1):951–8.. DOI: 10.1007/s10582-999-1023-2.

27. Dąbrowski A, Tertykh VA, editors. Adsorption on new and modified inorganic sorbents. Amsterdam ; New York: Elsevier; 1996. 926 p. (Studies in surface science and catalysis). ISBN 0-444-82179-1.

28. El-Naggar I, Abdel-Galil E, Mahmoud M. Inorganic Ion Exchange Materials Based on Titanate: Synthesis, Characterization and Sorption Behaviour Of Zirconium Titanate for Some Hazardous Metal Ions from Aqueous Waste Solution. Isotope and Radiation Research. 2012;44(4):851–71. URL: https://inis.iaea.org/search/search.aspx?orig_q=RN:44113183.

29. http://www.webmineral.com.

30. Pough FH, Scovil JA, National Audubon Society, National Wildlife Federation, Roger Tory Peterson Institute. A field guide to rocks and minerals. Boston: Houghton Mifflin; 1996. ISBN: 978-0-395-72778-2.

Türkçe Öz ve Anahtar Kelimeler

Libya'da Kozmetik Ürünü Olarak Kullanılan Arap "Eye Kohl" Markalarının Kimyasal ve Fiziksel İncelemesi

Maher Mohamed Abed El-Aziz, Mohamed Ammar Khalifa, Rabia Alhadi Ghariani, Hasan Daw Ashtawi Mohamed, and Mahmud Ashtewi S. Ashtewi

Öz: Üç Arap "eye kohl" markası kurşun ve kadmiyum varlığı için atomik absorpsiyon spektroskopisi (AAS) ve X-ışını saçılması teknikleri ile incelenmiştir. Bu çalışmada, örneklerin kimyasal analizleri ağır metallerin derişimi, farklı ortamda çözünürlük, KI ile tepkime, nem ve organik içerik bakımından çalışılmıştır. XRD deseni bütün markalarda amorf artalan üzerinde bir kısım kristalize maddenin olduğunu göstermiştir. Mineral verilere göre örneklerde bulunan temel mineraller Manganoshadlunite (Natural Arab Koh., NAK), samarskit (Natural Black Al-Athmod Kohl, NBAK) ve kitaibelit (Black Al-Hashemi kohl, BHK) olarak bildirilmiştir. Renk, biçim, dokunuş ve şeffaflık bütün örneklerde neredeyse aynıdır, ancak yoğunluk, ortalama gözenek çapı ve özgül yüzey alanı bakımından farklılıklar göstermektedir. AAS'ye göre ortalama kurşun yüzdesi %0,2411 ile %6,173 arasındadır ve kadmiyum için yüzde değeri %0,0019 olarak bulunmuştur. Pb ve Cd'nin maksimum derişimi NAK örneğinde sırasıyla 30,865 mg/g ve 9,50 µg/g olarak tespit edilmiştir. Ağır metaller bakımından en düşük derişim NBAK örneğinde bulunmuştur. Nem çok düşük bir yüzdede (~%1) bulunmuştur, ancak organik maddeler en fazla %69'dan büyüktür. Bütün markalar asidik ortamda farklı oranlarda çözünmektedir ve KI ile tepkimeye sokulduğunda sarı renkli PbI_2 katısı oluşturmaktadır, bu da kurşunun varlığı için delil olarak kullanılmıştır. İncelenen markalar arasında NBAK'ın kullanılması son derece isabetli olur, çünkü ağır metaller (Pb ve Cd) açısından düşük yüzdeye sahiptir ve özgül yüzey alanı daha yüksektir. Bu tür kozmetik ürününün kullanılmasındaki risk faktörü çok düşüktür. Yüksek yüzey alanı, göz hastalıklarına karşı kullanılabilirlik olasılığını yükseltecek şekilde aktif içeriği yaymaktadır.

Anahtar kelimeler: "Eye kohl" kozmetik ürünleri; kurşun; kadmiyum; atomik absorpsiyon spektrometrisi (AAS).